Modelling the hydraulic behaviour of unsaturated soils and application to the numerical and experimental study of capillary barrier systems

Riccardo Scarfone

Submitted in fulfilment of the requirements for the
Degree of Doctor of Philosophy

James Watt School of Engineering
College of Science and Engineering
University of Glasgow

July 2020

List of publications

The work carried out in this PhD has led or is expected to lead to the following publications:

- **Scarfone, R.**, Lloret-Cabot, M., and Wheeler, S.J. (2018). Suction-enhanced geotechnical design through Capillary Barrier Systems. In *Proceedings of the 15th BGA Young Geotechnical Engineers' Symposium*, Guildford, UK, 2-3 July 2018.

  (Non-peer reviewed and published extended abstract, related to part of the content shown in Chapters 3, 6 and 7).

- **Scarfone, R.**, Lloret-Cabot, M., and Wheeler, S.J. (2018). Numerical modelling of water breakthrough in coarse soils initially at very low degree of saturation. In *Proceedings of the 7th International Conference on Unsaturated Soils*, Hong Kong, China, 3-5 August 2018.

  (Peer reviewed and published conference paper, related to part of the content shown in Chapter 6).

- **Scarfone, R.**, Wheeler, S.J., and Smith, C.C. (2019). Numerical study of the applicability of capillary barrier systems for prevention of rainfall-induced slope instabilities. MUSLOC 2019, Barcelona, 19-20 September 2019.

  (Non-peer reviewed and published abstract, related to part of the content shown in Chapter 8).

- **Scarfone, R.**, Wheeler, S.J., and Smith, C.C. (2020). Numerical study of the application of capillary barrier systems for prevention of rainfall-induced slope instabilities. In *Proceedings of the 4th European Conference on Unsaturated Soils*, Lisbon, Portugal, 19-21 October 2020.

  (Peer reviewed conference paper accepted for publication, related to the content shown in Chapter 8).

- **Scarfone, R.**, Wheeler, S.J., and Lloret-Cabot, M. (2020). A conceptual hydraulic conductivity model for unsaturated soils at low degree of saturation and application to the study of capillary barrier systems. *ASCE Journal of Geotechnical and Geoenvironmental Engineering*, 146(10): 04020106.

  (Peer reviewed journal paper, related to part of the content shown in Chapters 3 and 6).

- **Scarfone, R.**, Wheeler, S.J., and Lloret-Cabot, M. (2020). A hysteretic hydraulic constitutive model for unsaturated soils and application to capillary barrier systems.

  (Peer reviewed journal paper, accepted subject to minor corrections by *Geomechanics for Energy and the Environment*, related to part of the content shown in Chapters 3 and 6).

- **Scarfone, R.**, and Wheeler, S.J. (2020). Analytical and numerical modelling of air-entrapment during wetting of unsaturated soils.

  (Peer reviewed journal paper in preparation, related to the content shown in Chapter 5).

- **Scarfone, R.**, and Wheeler, S.J. (2021). Improved water storage capacity of multi-layered capillary barrier systems: an analytical, numerical and experimental study.

  (Peer reviewed journal paper in preparation for submission to *ASCE Journal of Geotechnical and Geoenvironmental Engineering*, related to the content shown in Chapter 7).

- **Scarfone, R.**, Wheeler, S.J., and Smith, C.C. (2021). Numerical parametric study of the application of capillary barrier systems for suction control purposes and prevention of rainfall-induced slope instabilities.

  (Peer reviewed journal paper in preparation for submission to *Géotechnique*, related to the content shown in Chapter 8).

Abstract

Nowadays, considerable research effort is addressed towards the mitigation of the effects of climate change. The development and application of low-carbon solutions in geotechnical engineering practice is essential for the mitigation of the effects of climate change. Under unsaturated conditions, suction has a beneficial effect on the shear strength of soils but it may easily vanish after intense rainfall. If suction can be maintained in the ground in the long term, its effect can be taken into account in geotechnical design as a natural soil reinforcement, and this can lead to low-carbon designs.

Capillary barrier systems can be used to prevent or limit the infiltration of water into the ground, thereby maintaining suction in the long term. Capillary barrier systems are soil covers made of a finer-grained layer overlying a coarser-grained layer. Under unsaturated conditions, the coarser layer is typically at very low degree of saturation and the corresponding unsaturated hydraulic conductivity is so low that it can be considered as impermeable. In these conditions, rainwater is stored in the finer layer and subsequently removed by evapotranspiration or lateral drainage.

Accurate modelling of the hydraulic behaviour of unsaturated soils is crucial for the interpretation of the behaviour of capillary barrier systems. The first part of this thesis is focused on the interpretation and modelling of the hydraulic behaviour of unsaturated soils. A critical review of the interpretation of the hydraulic behaviour of unsaturated soils leads to the identification of inaccuracies and inconsistencies in existing conventional hydraulic constitutive models for the soil water retention curve (SWRC) and the soil hydraulic conductivity curve (SHCC). These inaccuracies and inconsistencies relate particularly to the very high degree of saturation range and the very low degree of saturation range.

At very high values of degree of saturation, the apparent SWRC measured in a wetting test in the laboratory may differ from the true SWRC, because of the occurrence of air trapping. Analytical and numerical modelling of the phenomenon of gas trapping during wetting shows that, once air trapping occurs, the apparent SWRC depends upon many aspects of the wetting test conditions and is not a fundamental representation of the soil behaviour. The only correct way to represent the occurrence and influence of air trapping during wetting within numerical modelling of boundary value problems is to use the true SWRC in combination with a gas conductivity expression that goes to zero when the gas phase becomes discontinuous.

At low values of degree of saturation, conventional models for the SHCC are typically inaccurate. A new predictive hydraulic conductivity model, accurate for the full range of degree of saturation is developed. The hydraulic conductivity is divided into two components:

a bulk water component and a liquid film component; each of which varies with degree of saturation or suction. This model is coupled with SWRC models improved at low degree of saturation. Hydraulic hysteresis is subsequently introduced in the SWRC and SHCC by using an original bounding surface approach. The new hydraulic models were validated against experimental data. This set of hydraulic models forms a complete framework of hydraulic constitutive models for unsaturated soil, which was implemented in the numerical finite element software Code_Bright. Finally, these new models are applied to the numerical study of the hydraulic behaviour of capillary barrier systems (CBSs). The new hydraulic conductivity model is able to predict the behaviour of CBSs better than conventional models and the numerical modelling highlights the role of liquid film flow, which is often neglected. Water retention hysteresis is shown to have a significant impact on: i) movement and redistribution of water within the finer layer of a CBS; ii) the phenomenon of water breakthrough across the interface between the finer and coarser layers of a CBS and the subsequent restoration of the CBS after infiltration at the ground surface ceases; iii) the prediction of evaporation from a CBS into the atmosphere.

In the second part of this thesis, an original concept of multi-layered capillary barrier systems is presented and analysed. The use of multi-layered CBSs may lead to a substantial increase of the water storage capacity of CBSs, and hence their effectiveness. A simplified method of analysis of multi-layered CBSs is developed and validated against results from numerical finite element analyses and laboratory physical tests. Parametric analyses show the impact of number of layers, materials thickness of the CBS and infiltration rate on the water storage capacity of multi-layered CBS. Laboratory infiltration tests on different multi-layered CBSs are performed demonstrating the efficiency of multi-layered CBSs and clarifying their hydraulic behaviour.

In the third part of the thesis, advanced numerical thermo-hydraulic finite element analyses and limit analyses are performed to assess the application of CBSs for suction control and slope stability purposes in the long term. It is demonstrated that sloping CBSs are effective at maintaining suction in the ground and preventing rainfall-induced slope instability for different climatic conditions. In addition, the role of different parameters such as materials, thickness of the CBS and slope height are assessed. In particular, it is shown that CBSs with the finer layer made of a relatively fine material, such as silty sand, are more effective in dry and warm climates due to their ability of storing water, which can subsequently be removed by evaporation, whereas CBSs with a finer layer made of a slightly coarser material, such as fine sand, are more effective in wet and cool climates due to their ability of diverting water laterally down the slope. The effectiveness of solutions aimed to extend the application of CBS to slope of any height, such as the use of multi-layered CBSs and the use of multiple drains, is finally demonstrated.

Contents

List of Tables

List of Figures

Acknowledgements

First and foremost, I am sincerely grateful to my supervisor, Prof. Simon Wheeler, for giving me such amazing guidance during this path. In addition to benefiting from your brilliant technical knowledge and brightness, which are universally recognised, you have always shown great interest in my research work and in my technical, professional and academic growth. You have been a valuable mentor for me.

Thanks to Dr. Marti Lloret-Cabot and Dr. Colin Smith for their assistance to my supervision during my PhD. Marti, many thanks for the useful and interesting discussions that we had during the time you spent in Glasgow and afterwards. Colin, thank you for the help, support and technical advice that you gave me during the time I spent in Sheffield and for providing me with a modified version of the software LimitState:GEO, which has been important for my research.

Special thanks to various members of the technical staff at the University of Glasgow for the continuous support during my experimental work. Among these, I am particularly grateful to Mr. Bruce Robertson for the patience and interest that he has shown in managing the technical services that I needed, and to Mr. Timothy Montgomery for his continuous help and support in the soil mechanics lab and for the nice chats that we had about travels around the world.

I would like to thank Prof. Sebastia Olivella from UPC (Barcelona) for providing me with an open source version of the software Code_Bright. The use of this code has been fundamental for my work.

I wish to acknowledge the financial support of the European Commission via the Marie Skłodowska-Curie Innovative Training Networks (ITN-ETN) project TERRE 'Training Engineers and Researchers to Rethink geotechnical Engineering for a low carbon future' (H2020-MSCA-ITN-2015-675762). Within this network, I have had the pleasure to liaise with many important academic experts in the field of geotechnical engineering and to make new friends. Thanks for the lovely time spent together in the various project TERRE meetings.

The time I spent in Glasgow during my PhD was made cheerful and enjoyable by all the friends I made in this city. Working days would not have been so pleasant without our coffee breaks at the "Bar Feccia" and our nights out. Naming all of you would take too long, but you know who you are. Cheers guys! Similarly, also my best friends back in Italy deserve special thanks for the support during this period abroad and for making me feel that home was closer. Grazie ragazzi!

Last but not least, a warm thank you goes to my love Chloe, my brother Antonio, my

parents and all my family. This achievement and all achievements in my life have been and will be possible only thanks to your continuous, unconditional support and love.

Declaration

All work in this thesis was carried out by the author unless otherwise explicitly stated.

Chapter 1

Introduction

1.1 Motivation and aims

This research project is part of the network TERRE ("Training Engineers and Researchers to Rethink geotechnical Engineering for a low carbon future") which is a Marie Skłodowska-Curie Innovative Training Network funded from the EU H2020 Programme. TERRE aims to develop novel geo-technologies to address the competitiveness challenge of the European construction industry in a low carbon agenda, involving both universities and industrial partners across Europe. Industry and research bodies in the construction sector have been investing significantly in recent years to produce innovative low-carbon technologies. However, little innovation has been created in the geo-infrastructure industry, which is lagging behind other construction industry sectors. TERRE aims to close this gap through a network-wide training programme carried out by a close collaboration of Universities, Research Centres and Industrial Partners (Figure 1.1). More information about the project TERRE is available on http://www.terre-etn.com/.

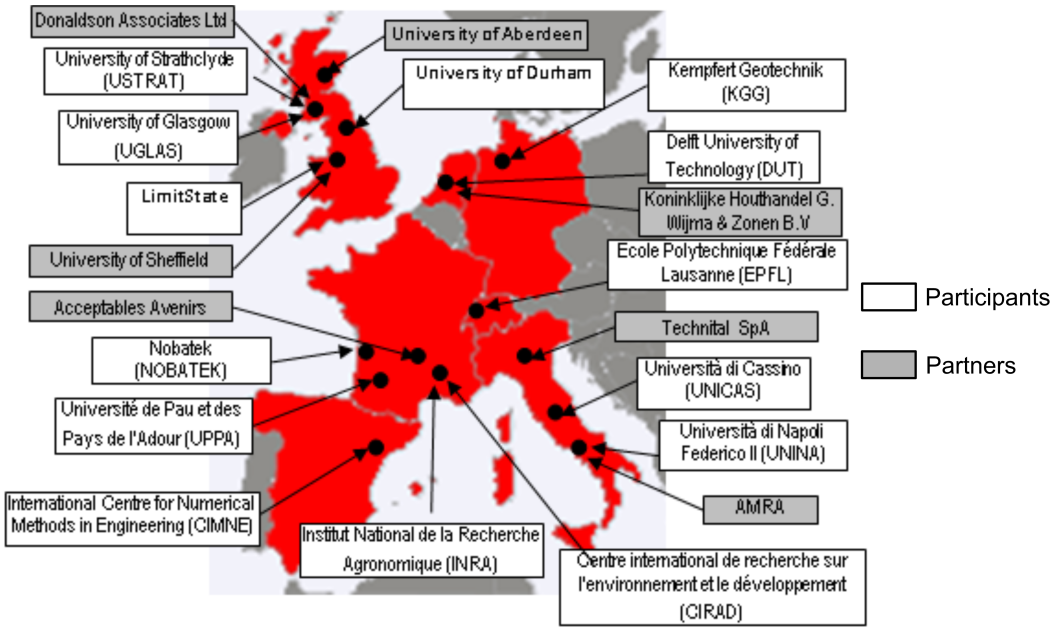

Figure 1.1: Project TERRE partners.

Nowadays, climate change is a very "hot" topic because it is considered the cause of potential catastrophic scenarios prospected by the scientific community [1–3]. Climate change and the rise of the mean earth temperature are partly related to the increase of the concentration of greenhouse gases in the atmosphere. In particular, several studies proved that the anthropogenic increase in greenhouse gas emissions, especially carbon dioxide (CO_2), is one direct cause of the climate change [1]. The concentration of CO_2 in the atmosphere increased from 280 ppm in 1750 to 440 ppm in 2015 and, consequently, global mean temperature has continuously risen [1, 4, 5]. For example, 2016 was recorded as the warmest year from 1880 [6].

Practices and activities in the construction field are considered the cause of a significant component of the overall carbon emission. For example, the production of cement, which increased by more than 700% from 1960 to 2016, generates almost 10% of the global carbon emission [7]. In the geotechnical engineering field, cement is widely employed in many applications (e.g. ground improvement by mixing and grouting). Thus, the development and application of low-carbon solutions also in geotechnical engineering practice is essential for the mitigation of the effects of climate change [8]. In general these solutions aim to reduce or avoid the use of non-sustainable materials like concrete and steel and to reduce or avoid the transportation of materials, which represents a significant source of carbon emissions. In this sense, many research efforts have been addressed to the development of low-carbon solutions for soil reinforcement [8]: chemical mixtures, geopolymers, geosynthetics, microbial organisms, biopolymers etc. In this context, the research work here presented has been addressed towards the use of a natural soil reinforcement: soil suction.

Although most textbooks on geotechnical engineering and most geotechnical design treat the behaviour of soils in fully dry or fully saturated conditions, unsaturated conditions are common in nature. Suction (i.e. negative pore-water pressure) occurs under unsaturated conditions and exists in many real situations. Figure 1.2 shows typical pore-water pressure profiles in the ground in (1) hydrostatic equilibrium, (2) during a downward flux at the surface (e.g. rainfall) and (3) during an upward flux at the surface (e.g. evapotranspiration), under the assumption of horizontal ground surface and horizontal water table. Below the water table the soil is typically in saturated conditions, the pore-water pressure is positive (relative to atmospheric pressure) and typically increases hydrostatically with depth. Above the water table, pore-water pressure is typically negative (relative to atmospheric pressure) and follows a hydrostatic profile in no-flux conditions (1), it is greater than hydrostatic in downward-flux conditions (2) and it is lower than hydrostatic in upward-flux conditions (3). Immediately above the water table there is a region where pore-water pressure is negative but the soil is still saturated and, above this is a region where the soil is unsaturated.

The presence of suction may impart significant strength gains to soil but this effect is generally neglected in geotechnical design because of its unreliability. Indeed, suction may easily vanish (or be reduced) after a heavy rainfall event. This is the cause, for example, of rainfall-induced slope instabilities. An existing slope which is stable thanks to the beneficial effect of soil suction may become unstable after a heavy rainfall which causes reduction or

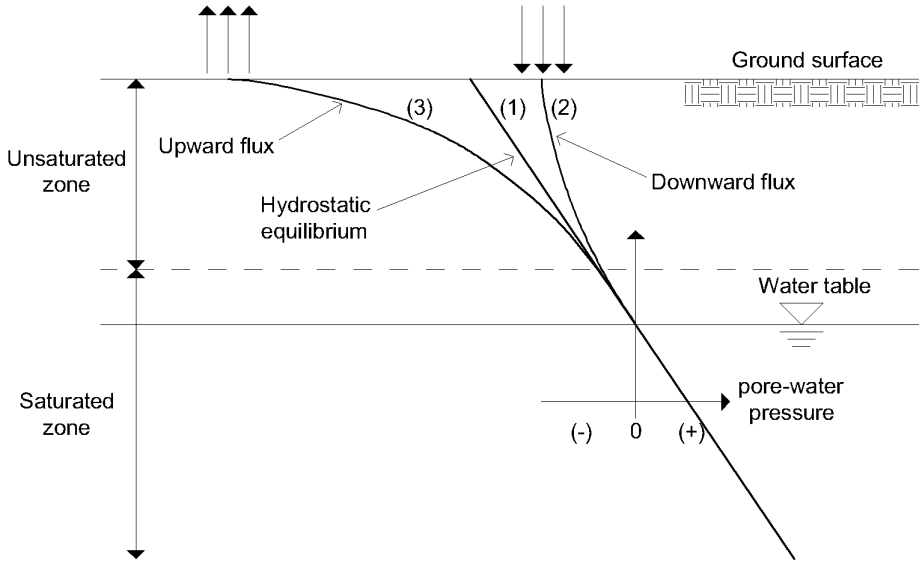

Figure 1.2: Typical pore-water pressure profiles in the ground.

loss of soil suction. If, however, one could find a way to maintain significant suction values in the ground even during rainfall and predict the minimum value of suction expected over the design life, geotechnical design could take into account the maintenance of suction and the effect of unsaturated conditions. In this way, soil suction could be used by geotechnical engineers as a natural soil reinforcement. This can be potentially obtained by using soil covers which avoid the infiltration of rainwater into the ground.

In the last few decades, the need of making efficient landfill cover systems has led to development of different types of surface covering barriers mainly aimed to prevent the infiltration of water into the underlying soil in order to avoid the contamination of the water itself. Figure 1.3 shows three of the main conventional landfill cover systems: a monolithic cover (Figure 1.3a), a compacted clay cover (Figure 1.3b) and a capillary barrier system (Figure 1.3c).

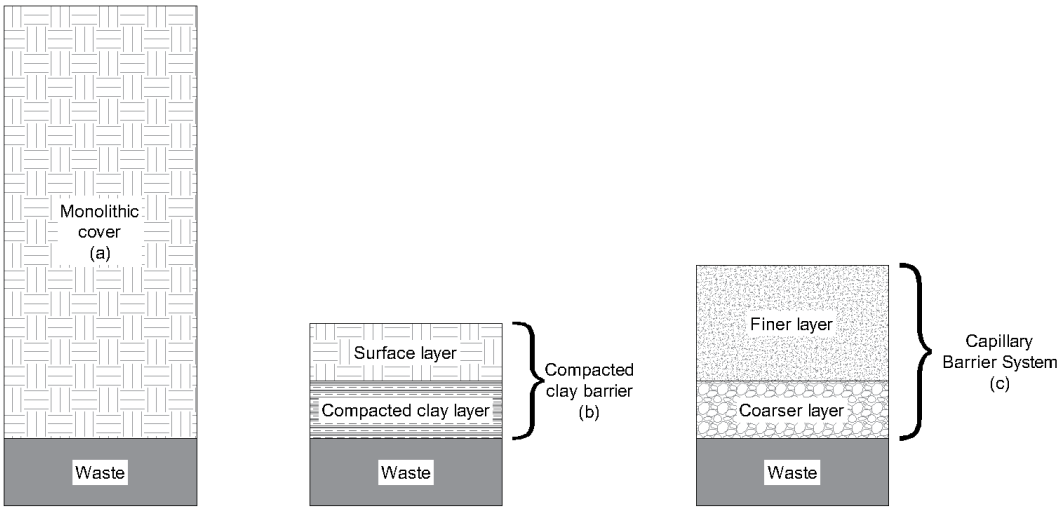

Figure 1.3: Conventional landfill covers: (a) monolithic cover, (b) compacted clay cover and (c) capillary barrier system.

A monolithic cover is an evapotranspirative cover which consists of a single layer placed directly over the waste [9]. In arid regions, the water content fluctuations are confined to the upper metres of soil [10]. Thus, the monolithic cover, which is mainly used in arid regions, is designed to store rainwater which is then removed by evapotranspiration. However, since the thickness of the cover must be high enough that water content fluctuations are restricted to the cover itself, very thick layers may be required for this type of cover.

A compacted clay cover [11] is made of a compacted clay layer, which acts as a low-permeability barrier due to its very low value of saturated hydraulic conductivity ($<10^{-9}$ m/s), underlying a surface cover layer which is intended to protect the clay layer from erosion and desiccation and to support plant growth. The rainwater is mainly removed by surface runoff. This type of cover may be expensive [12] and its long-term performance may be undermined by construction aspects [13] and cracking caused by desiccation and freeze-thaw cycling [14–19]. If cracking occurs, the saturated hydraulic conductivity of the compacted clay layer may increase by two or more orders of magnitude, compromising the effectiveness of the barrier. In order to reduce costs and avoid cracking, the compacted clay layer may be replaced by a Geosynthetic Clay Liner (GCL) although deterioration of the material may still be an issue [12, 19–21].

A capillary barrier system [22, 23] is made of an upper finer-grained layer, typically ranging from a fine sand to a low-plasticity silt, overlying a coarser-grained layer, typically ranging from a gravel to a medium sand. Note that, in a capillary barrier, even the finer-grained layer is considerably coarser than the main layer of a compacted clay cover. The coarser layer of a capillary barrier system is typically at very low degree of saturation and hence the corresponding unsaturated hydraulic conductivity, which decreases by many orders of magnitude with decreasing degree of saturation, is also very low. Thus, the coarser layer acts as an almost impermeable barrier and the rainwater is stored in the upper finer layer. The rainwater stored in the finer layer is then removed by evapotranspiration or lateral drainage. The coarser layer will continue to behave as an impermeable layer unless it reaches a critical condition (breakthrough), which typically corresponds to high saturation of the finer layer [23]. The coarser layer can be also substituted by a porous geosynthetic (e.g. a nonwoven geotextile) but the sustainability of these geosynthetics requires further study, given their possible ecotoxic effect on the environment from the leakage into the ground of additives and residual products from degradation of polymeric or metallic materials [24–26].

Capillary barrier systems are often preferred to compacted clay covers for their low-cost [12], possibility to use recycled low-cost materials [27] and high durability [14, 28–30]. The high durability is due to the use of materials with low susceptibility to weather conditions (i.e. negligible deformations upon wetting and drying) and to the low potential for surface runoff and thus surface erosion, due to the use of a surface material (the upper finer-grained layer) with relatively high saturated permeability. For these reasons, capillary barrier systems, in which both the coarser and finer layers are made of soils or recycled materials, were selected for this research.

Fully understanding the hydraulic behaviour of unsaturated soils is crucial for the inter-

pretation and modelling of the behaviour of capillary barrier systems. Existing constitutive models describing the hydraulic behaviour of relatively coarse-grained soils (gravel, sand and silt) in unsaturated conditions have weaknesses at very low degree of saturation. These weaknesses are particularly relevant in modelling the behaviour of capillary barrier systems because the coarser layer is typically at very low degree of saturation. Reliable numerical modelling of the ability of a capillary barrier system to act as a low-permeability barrier therefore strongly relies on accurate prediction of hydraulic behaviour at very low degree of saturation. Also water retention hysteresis, i.e. different soil water retention behaviour between wetting and drying, needs to be included for accurate modelling. Water retention hysteresis is important because a capillary barrier system may be subjected to multiple cycles of rain and evapotranspiration.

Therefore, the initial aim of this work is the development of constitutive models able to describe accurately the hydraulic behaviour of unsaturated soils, particularly addressing weaknesses of existing models at low degree of saturation and incorporating retention hysteresis. The consequences of the use of these more accurate hydraulic constitutive models on the predicted fundamental behaviour of capillary barrier systems will be studied numerically. In addition, a deeper knowledge of the hydraulic behaviour of unsaturated soils will also lead to a more accurate interpretation of the formation of trapped air, a phenomenon which often occurs in unsaturated soils during wetting.

The second aim of this work is the study of the possibility of improving the water storage capacity of capillary barrier systems using multiple layers, i.e. more than a single finer layer and a single coarser layer. This will be done through an analytical, numerical and experimental study.

The final aim of the project will be the investigation of the use of capillary barrier systems that inhibit or reduce the percolation of water into the ground, thereby helping to maintain high suction values in the ground in the long-term and reducing the risk of full saturation. This could lead to enhanced soil strength and hence use of reduced soil quantities or lower quality soils (e.g. recycled materials), leading to reduced embedded carbon. This concept will be applied to the analysis of the prevention of rainfall-induced slope instability.

1.2 Objectives

Specific objectives of this research work are listed below:

- To carry out a critical review of the hydraulic behaviour of unsaturated soils. Aspects like the role of bulk water, liquid film water and trapped air, which are often misunderstood or neglected in the literature, will be highlighted. This will lay the basis for the development of improved hydraulic constitutive models for unsaturated soils.

- To develop a framework of improved hydraulic constitutive models for unsaturated soils including the following key ingredients: distinct roles of bulk water and liquid film water on the hydraulic conductivity, water retention hysteresis and gas conductivity.

- To implement the new hydraulic constitutive models in the numerical Finite Element code Code_Bright.
- To provide a more accurate and physics-based interpretation of the phenomenon of air entrapment which occurs during wetting. This will be done through simple analytical modelling and more complex numerical simulations.
- To assess, by means of numerical simulations, the influence of the new improved hydraulic constitutive models on the prediction of the fundamental behaviour of capillary barrier systems. In particular, the role of bulk water and liquid film water will be highlighted as well as the role of the water retention hysteresis.
- To develop a new simplified method of analysis of multi-layered capillary barrier systems and validate the method through numerical FEM analyses and laboratory 1D infiltration column tests on different multi-layered capillary barrier systems.
- To assess potential improvements in the water storage performance of multi-layered capillary barrier systems. Particular attention will be given to the role played by the different parameters, by performing a parametric study.
- To develop an *ad hoc* code in Matlab able to link thermo-hydraulic finite element analyses performed with Code_Bright and limit analyses performed with the code LimitState:GEO.
- To perform an advanced numerical study on the application of capillary barrier systems for suction control and slope stability purposes when subjected to European weather conditions. In particular, the role of different parameters like geometry of the underlying soil, geometry of the capillary barrier system, materials and weather conditions will be highlighted.

1.3 Thesis structure

This thesis is organised in 9 chapters, including this. The content of the next 8 chapters is outlined below.

Chapter 2 provides the general research background for this thesis, including fundamental concepts of unsaturated soils and a literature review regarding the hydraulic constitutive modelling of unsaturated soils, the behaviour and application of capillary barrier systems and the modelling of soil-atmosphere interaction.

Chapter 3 presents a critical review of the hydraulic behaviour of unsaturated soils and describes the development and validation of new hydraulic constitutive models for unsaturated soils, including improved modelling of hydraulic conductivity at low degree of saturation and hydraulic hysteresis.

Chapter 4 describes the numerical codes used in this thesis (i.e. Code_Bright and LimitState:GEO), the implementation of new hydraulic constitutive models for unsaturated soils in Code_Bright and the development of a Matlab code linking Code_Bright and LimitState:GEO.

Chapter 5 presents an original interpretation of the phenomenon of air trapping in unsaturated soils developed through analytical and numerical modelling.

Chapter 6 presents the results of numerical analyses involving the fundamental behaviour of capillary barrier systems and investigates the impact of the use of the new hydraulic constitutive models introduced in Chapter 3 on the response of capillary barrier systems.

Chapter 7 describes the working mechanism of an original concept of multi-layered capillary barrier systems and presents a new simplified method for the analysis of their hydraulic behaviour. Subsequently, the behaviour of these multi-layered CBSs is studied analytically, numerically and experimentally.

Chapter 8 presents results from advanced numerical analyses regarding the application of capillary barrier systems in the long term for suction control and slope stability purposes.

Chapter 9 summarises the key conclusions of this thesis and offers recommendations for future work.

Chapter 2

Research background

In this chapter, the research background and the current state of the art are analysed and presented in order to identify gaps in the literature and to provide the reader with sufficient information required for understanding of the work presented in this thesis. In particular, fundamental concepts and definitions about unsaturated soils are initially described since they will recur throughout the thesis. A literature review of existing constitutive models describing the hydraulic behaviour of unsaturated soils is then presented. The existing state of knowledge about the fundamental behaviour and applications of capillary barrier systems is subsequently described. Finally, the theoretical background about the modelling of soil-atmosphere interaction is presented.

2.1 Fundamental concepts and definitions about unsaturated soils

2.1.1 Surface tension, pore pressures and matric suction

Unsaturated soils are mixtures of three or more phases. In this work, the three phases considered are: the solid phase (i.e. the soil grains), the liquid phase and the gas phase. The liquid phase and the gas phase fill the void spaces. The liquid phase is an aqueous solution mostly made of water with a small concentration of dissolved air (dissolved salts are not considered in this work) and the gas phase is a mixture mostly made of dry air with a small concentration of water vapour. Because of the coexistence of both liquid and gas phases within the pores, the interface between the two phases assumes a significant role. When considered at a continuum level, the interface behaves as an elastic membrane which is able to exert a tensile pull. This property is commonly known as "surface tension" [31], expressed as a force per unit length. The surface tension is the result of unbalanced intermolecular forces exerted on water molecules which are located at the liquid-gas interface. As shown in Figure 2.1, a water molecule within the liquid phase is subjected to intermolecular forces acting uniformly in all directions, thus resulting in balanced forces. By contrast, a resulting unbalanced intermolecular force directed towards the interior of the liquid phase acts on

a water molecule located at the liquid-gas interface. This resulting intermolecular force is equilibrated by the surface tension.

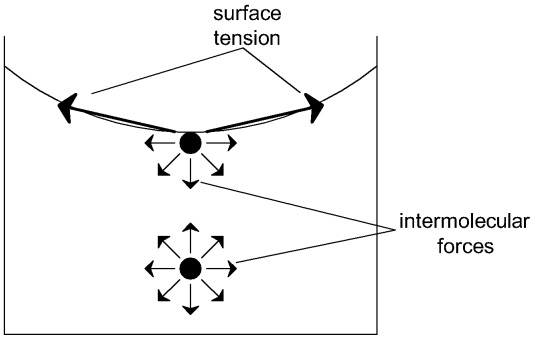

Figure 2.1: Intermolecular forces and surface tension

Because of the presence of surface tension at the liquid-gas interface, the pore-gas pressure p_g is not equal to the pore-liquid pressure p_l if the interface is curved. The matric suction s can be defined as:

$$s = p_g - p_l \tag{2.1}$$

In Equation 2.1, it makes no difference whether p_g and p_l are expressed as absolute pressures or relative to atmospheric pressure. However, in this thesis, there are situations where it is necessary to be explicit about whether the values of p_g and p_l are expressed as absolute pressures or relative to atmospheric pressure. Throughout this thesis, the symbols p_g and p_l are used for absolute values of pore-gas pressure and pore-liquid pressure respectively.

The definition of matric suction must not be confused with the definitions of osmotic suction and total suction [32]. Aitchison [33] proposed the following definitions:

- *Total suction - The negative gauge pressure, relative to the external gas pressure on the soil-water, to which a pool of pure water must be subjected in order to be in equilibrium through a semipermeable (permeable to water molecules only) membrane with the soil-water.*

- *Matric suction - The negative gauge pressure, relative to the external gas pressure on the soil-water, to which a solution identical in composition with the soil-water must be subjected in order to be in equilibrium through a porous permeable wall with the soil-water.*

- *Solute (osmotic) suction - The negative gauge pressure to which a pool of pure water must be subjected in order to be in equilibrium through a semipermeable membrane with a pool containing a solution identical in composition with the soil-water.*

Total suction is the sum of matric suction and osmotic suction. Flow of liquid water through the soil (see Section 2.1.5) is driven by gradients of total suction (after accounting for elevation differences). Total suction is also a relevant variable when considering a state of equilibrium across a gas-liquid interface (see Section 2.1.2). In contrast, matric suction is a key variable when considering both retention behaviour (see Section 2.1.4) and mechanical behaviour (see

Section 2.1.6). Changes in pore liquid chemistry may also affect mechanical and retention behaviour (particularly in clays), but these effects cannot be described simply by the use of the same osmotic suction that is a component of the total suction governing liquid flow [34]. In this work, the contribution of the osmotic suction to liquid flow was neglected, because the major focus was addressed to study of the hydraulic behaviour of coarse-grained soils wetted by non-saline liquids. Therefore, the matric suction will be considered equal to the total suction and both terms will be referred to simply with the term suction in this work, unless differently specified.

The shape of the gas-liquid interface and matric suction are linked via the Young-Laplace equation [35, 36], which can be derived by considering force equilibrium of an infinitesimal element of the curved interface (see Figure 2.2):

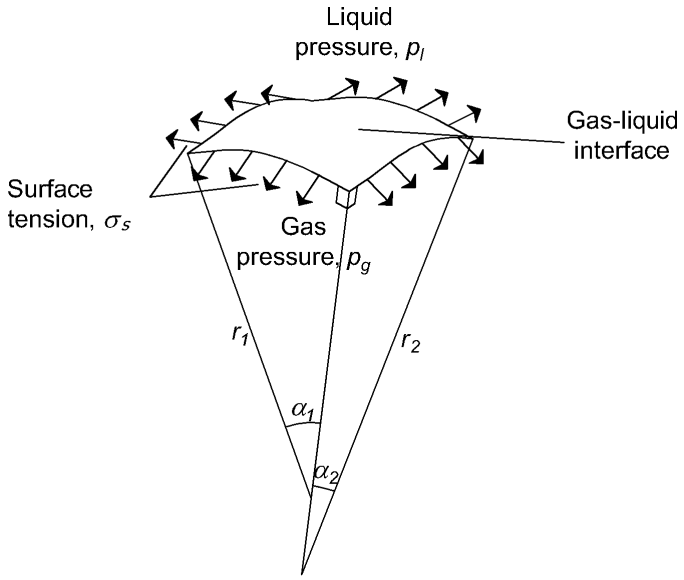

Figure 2.2: Infinitesimal portion of three-dimensional liquid-gas interface

$$p_g - p_l = \sigma_s \cdot \left(\frac{1}{r_1} + \frac{1}{r_2} \right) \tag{2.2}$$

where r_1 and r_2 are the principal radii of curvature of the interface, with the positive sign when they are measured on the gas side of the interface, and σ_s is the surface tension ($\sigma_s = 0.072\,57\,\mathrm{N/m}$ for an air-water interface at 20 °C [37]). When the gas-liquid interface is in contact with a solid, like a soil grain, there is a certain contact angle between the interface and the solid surface. The value of the contact angle (measured on the liquid side), which depends upon the properties of the liquid, the gas and the solid, is very low (approximately equal to 0°) for an air-water interface in contact with a wetted soil grain (see Figure 2.3). It follows that the gas-liquid interface is generally convex on the liquid side, and hence, from Equation 2.2:

$$p_g \geq p_l \tag{2.3}$$

For most geotechnical applications, the gas is connected to the atmosphere, the pore-gas pressure is considered equal to atmospheric and matric suction is identified as the negative

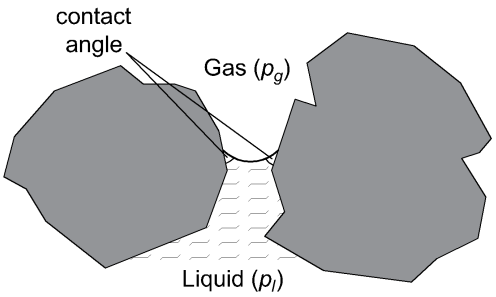

Figure 2.3: Air-water interface in contact with soil grains

pore-liquid pressure relative to atmospheric. In this case, the pore-liquid pressure is negative, relative to atmospheric pressure.

2.1.2 Air-water interaction

The liquid phase is typically a mixture of water (the major component) and a small concentration of dissolved air. Under equilibrium conditions across a gas-liquid interface, the mass concentration of air dissolved in the liquid phase depends upon the absolute air pressure within the gas phase. At equilibrium, the mass concentration of air in the liquid phase ω_l^a (a dimensionless quantity) is governed by Henry's law [38], which can be expressed as:

$$\omega_l^a = p_a \cdot \left(\frac{1}{H} \frac{M_a}{M_w} \right) \tag{2.4}$$

where p_a is the absolute pressure of the air in the gas phase, M_a is the molecular mass of air ($M_a = 28.964\,\mathrm{kg/kmol}$), M_w is the molecular mass of water ($M_w = 18.016\,\mathrm{kg/kmol}$) and H is Henry's constant [$\mathrm{ML^{-1}T^{-2}}$].

The air concentration within the liquid phase may be non-uniform. For example, as shown in Figure 2.4, the air pressure p_{a1} in a smaller gas bubble present in the liquid phase is higher than the air pressure p_{a2} in a bigger gas bubble, due to the difference in curvature of the gas-liquid interface surrounding the bubbles (see Equation 2.2). Thus, according to Equation 2.4, assuming uniform temperature and liquid pressure, the mass concentration of dissolved air in the liquid close to the smaller gas bubble is higher than that in the liquid close to the bigger gas bubble. A gradient in dissolved air concentration drives diffusion of air within the liquid phase from higher to lower dissolved air mass concentrations. The diffusive flux of air within the liquid phase $\boldsymbol{i}_l^a$ [$\mathrm{ML^{-2}T^{-1}}$] is governed by Fick's law, expressed in this case as:

$$\boldsymbol{i}_l^a = -D_l^a \nabla \left(\rho_l \omega_l^a \right) \tag{2.5}$$

where D_l^a [$\mathrm{L^2T^{-1}}$] is the diffusion coefficient for the diffusion of air in the liquid phase and ρ_l is the liquid density [$\mathrm{ML^{-3}}$]. The product $\rho_l \omega_l^a$ represents the concentration of dissolved air in the liquid phase, expressed as the mass of dissolved air per unit volume of liquid.

The gas phase is typically a mixture of dry air (the major component) and a small fraction of water vapour. According to Dalton's law, the behaviour of a particular gas in a mixture

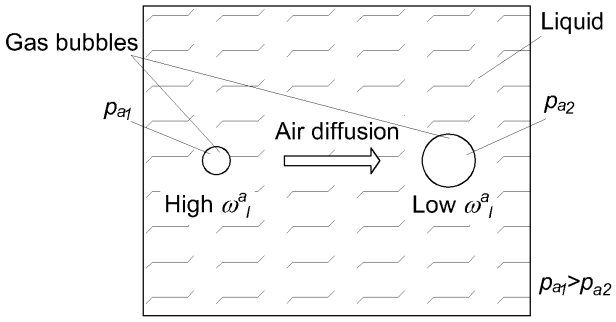

Figure 2.4: Air diffusion mechanism

of gases is independent of the other gases. Mathematically, Dalton's law in this case can be expressed as:

$$p_g = p_a + p_v \tag{2.6}$$

where p_g is the pressure of the gas mixture, p_a is the partial absolute pressure of dry air and p_v is the partial absolute pressure of water vapour. Each partial pressure is a fraction of the total pressure, as follows:

$$p_a = X_a \cdot p_g \tag{2.7a}$$

$$p_v = X_v \cdot p_g \tag{2.7b}$$

where X_a and X_v are respectively the molar fractions of the air component and of the vapour component.

The state of the water (i.e. solid, liquid or gas) depends on pressure and temperature, as shown in the state diagram for water in Figure 2.5. Focusing only on the liquid and gas states, the vaporization curve (AB) represents the set of pressure-temperature combinations in which liquid water and gas water can coexist in equilibrium for a flat liquid-gas interface. On the vaporization curve the water vapour is "saturated". Thus, the vaporization curve can be described by a unique relationship between the saturated vapour pressure p_{v0} and the temperature T. However, if the liquid-gas interface is curved, as happens with unsaturated soils, the pressure of vapour in equilibrium with the soil water p_v is lower than the pressure of vapour in equilibrium with a flat liquid-gas interface p_{v0} (see Figure 2.5) [31]. In this case the water vapour is "undersaturated". Relative humidity RH is defined as:

$$RH = \frac{p_v}{p_{v0}} \tag{2.8}$$

The relationship between relative humidity RH and suction s for a state of equlibrium across a liquid-gas interface is governed by Kelvin's equation [31]:

$$RH = \exp\left(-\frac{M_w}{RT\rho_w}s\right) \tag{2.9}$$

where R is the universal gas constant (8.314 J/(mol K)), T is the absolute temperature and ρ_w is the density of pure water (998 kg/m^3 at 293 K). The suction term s in Equation 2.9 is the

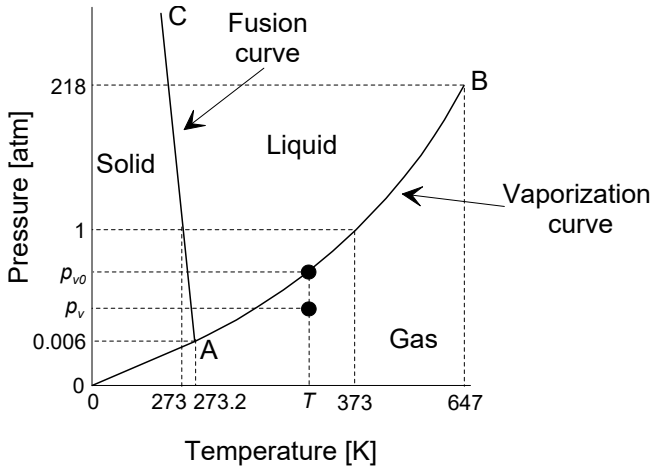

Figure 2.5: State diagram for water

total suction but, as discussed in Section 2.1.1 above, in this thesis it was taken as the matric suction, neglecting the role of osmotic suction.

Once the vapour pressure p_v is known, the ideal gas law can be used to calculate the vapour density ρ_v, as follows:

$$\rho_v = \frac{p_v M_w}{RT} \tag{2.10}$$

A similar expression can be used to calculate the dry air density ρ_a, replacing p_v and M_w with the dry air pressure p_a and the molecular mass of air M_a, respectively. The mass concentration of vapour in the gas phase ω_g^w is thus obtained as:

$$\omega_g^w = \frac{\rho_v}{\rho_v + \rho_a} = \frac{p_v M_w}{p_v M_w + p_a M_a} \tag{2.11}$$

Similarly to the case of air dissolved in the liquid phase, the water vapour concentration may not be uniform within the gas phase of an unsaturated soil. The gradient in vapour concentration drives the diffusion of water vapour within the gas phase, which can be expressed by Fick's law, as follows:

$$\boldsymbol{i}_g^w = -D_g^w \nabla \left(\rho_g \omega_g^w\right) \tag{2.12}$$

where $\boldsymbol{i}_g^w$ is the diffusive flux of water vapour in the gas phase, D_g^w is the diffusion coefficient for the diffusion of vapour in the gas phase and ρ_g is the gas density. The product $\rho_g \omega_g^w$ represents the concentration of water vapour in the gas phase, expressed as the mass of vapour per unit volume of gas.

2.1.3 Liquid water forms in unsaturated soils

In unsaturated soils, the liquid water exists in three forms: i) bulk water, ii) meniscus water and iii) liquid film water (see Figure 2.6). The bulk water and the meniscus water are also known as the capillary component of the water retained by the soil since their presence is governed by the action of capillary forces, namely the forces of adhesion and cohesive surface tension [39]. Adhesive forces are forces of attraction between the water molecules

and other substances (e.g. the soil grain surface) and (cohesive) surface tension is due to the unbalanced mutual attraction occurring between the water molecules located at the interface between water and a different fluid (e.g. air), as described in Section 2.1.1. The liquid film water represents the adsorptive component of the water retained by the soil grains because adsorptive forces govern this phenomenon. In essence, adsorption is a surface phenomenon in which substances from a gaseous or liquid solution (e.g. water molecules in the gas phase) move onto a solid surface (e.g. a soil grain surface), to which they become bonded by means of chemical or physical attraction forces [40].

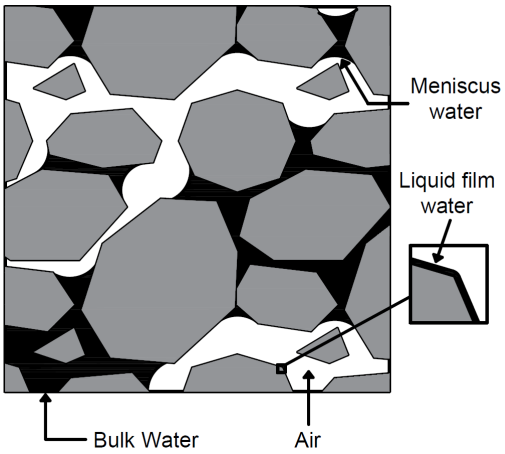

Figure 2.6: Liquid water forms in unsaturated soils: bulk water, meniscus water and liquid film water

The bulk water is the water present within liquid-filled voids, namely the same form of water as in saturated soils. Meniscus water bridges, also called liquid bridges, are formed at the inter-particle contacts surrounded by air-filled voids (see Figure 2.6). The properties and the behaviour of the liquid bridges were initially analysed by the pioneering work of Haines [41] and Fisher [42]. In particular, they found that dimensions and volume of a single meniscus water bridge decrease with increasing suction.

As suction in the soil varies, the configuration of the liquid phase and of the gas phase changes. Hence, the configurations of bulk water and meniscus water vary as well, as shown in Figure 2.7 where a drying path (a-c) and a wetting path (d-e) are qualitatively represented. Starting from an initial configuration where a pore is filled with bulk water (Figure 2.7a), as suction increases, the curvature of the gas-liquid interface increases (Figure 2.7b) according to the Young-Laplace equation (Equation 2.2). If suction increases beyond a certain value corresponding to the maximum curvature of the liquid-gas interface that can be sustained at the throat connecting two pores, the water may retreat from a pore which hence gets filled with gas (Figure 2.7c). From this condition (Figure 2.7d), if the process is reversed and suction decreases, the curvature of the gas-liquid interface decreases (Figure 2.7e). When the curvature decreases to a value corresponding to the coalescence of the menisci surrounding a pore filled with gas, the gas phase retreats and the pore gets filled with liquid (Figure 2.7f). Therefore, an increase in suction generally corresponds to a decrease in the degree of saturation (i.e. the volume fraction of voids filled with liquid) and, vice versa, a decrease in suction

generally corresponds to an increase in the degree of saturation. Moreover, at the same suction value, a pore can be either filled with liquid during drying (Figure 2.7b) or can be filled with gas during wetting (Figure 2.7e). Thus, at the same value of suction, the degree of saturation is generally higher during a drying process with respect to a wetting process. This effect, also called "ink bottle" effect, is the main cause of water retention hysteresis, which is discussed in Section 2.1.4.

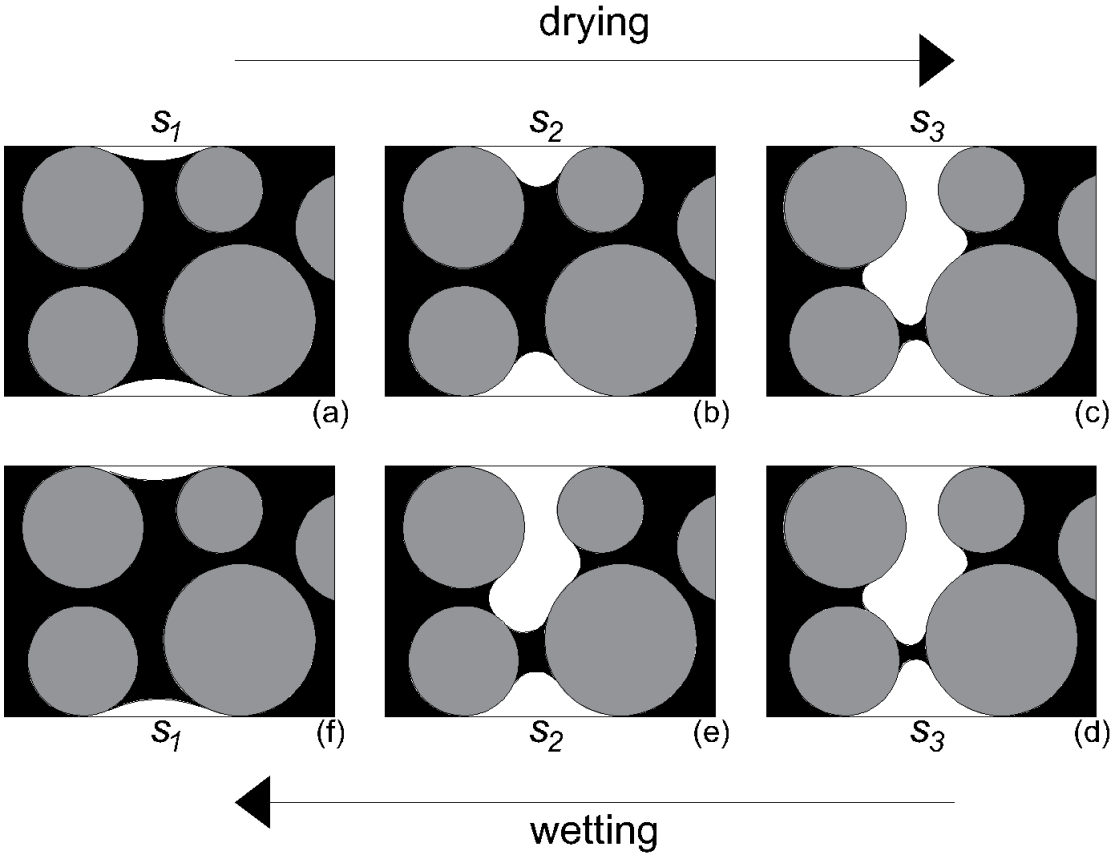

Figure 2.7: Liquid-gas distributions during drying (a-c) and wetting (d-f), corresponding to three different values of suction, $s_1 < s_2 < s_3$

Thin liquid films generally cover the surface of unsaturated soil grains when pores are filled with gas (see Figure 2.6), due to the adsorption forces. Unlike in geotechnical engineering, the role of these liquid films is better understood in fields like hydrology, hydrogeology and geochemistry. However, also in geotechnical engineering the liquid films can play an important role, e.g. the description of the behaviour of unsaturated soils at low degree of saturation.

In the very dry range, the process of adsorption was shown to be well represented by the Brunauer-Emmett-Teller theory [43], which extended the Langmuir adsorption model from the monolayer adsorption process to the multilayer adsorption process. This applies when relative humidity is lower than 35%, which, at a temperature of 293 K, corresponds to matric suction values greater than approximately 150 MPa, which is beyond the limit of interest of this work. For lower values of matric suction, the adsorption process causes the formation of multilayer films which can be seen as part of a thinned liquid phase. This can be described by

the disjoining pressure isotherm [44], defined as:

$$\Pi\left(t_{Film}\right) = p_g - p_l \tag{2.13}$$

where Π is the disjoining pressure, t_{Film} is thickness of the liquid film, p_g is the pressure in the gas phase and p_l is the pressure in the bulk liquid phase. Using this definition, it follows that the disjoining pressure in the case of planar liquid films (i.e. no capillary interactions) is equal to the matric suction s. The disjoining pressure Π is made of different components linked to different types of surface forces governing the physical phenomenon. The forces considered in the study of thin films covering soil particles are generally ionic-electrostatic and molecular. In this case, the disjoining pressure can be defined as the sum of two components [45], as follows:

$$\Pi\left(t_{Film}\right) = \Pi_e\left(t_{Film}\right) + \Pi_m\left(t_{Film}\right) \tag{2.14}$$

with Π_e and Π_m the ionic-electrostatic and the molecular components of the disjoining pressure, respectively.

The ionic-electrostatic component of the disjoining pressure was studied by the the Nobel Prize winner Langmuir [46]. He studied the problem of a planar film of an ionic solution bounded by an infinitely extended planar charged substrate. The charge of the substrate induces a high concentration of ions close to the surface due to Coulombic attractions. This high concentration forces ions to diffuse away from the surface. This layer of surface charges and counter-ions is called "diffuse double layer". Generally speaking, this problem is governed by the Poisson-Boltzmann equation, from which Langmuir [46] derived an expression for the thickness of the diffuse double layer, for a low-concentration symmetric ionic solution bounded by a high-potential substrate. The expression derived by Langmuir is the following:

$$\Pi_e\left(t_{Film}\right) = \frac{\varepsilon_r \varepsilon_0}{2}\left(\frac{\pi k_B T}{eZ}\right)^2 \frac{1}{{t_{Film}}^2} \tag{2.15}$$

where ε_r is the static relative permittivity of the liquid phase, ε_0 is the permittivity of free space, k_B is the Boltzmann constant, T is the absolute temperature, e is the charge of an electron and Z is the valence change.

The molecular component of the disjoining pressure is due to long-range van der Waals attraction interacting between solid, liquid and vapour. Israelachvili [47] considered the simple case of a thin planar liquid film adsorbed to a indefinetely extended flat solid substrate, and in contact with undersaturated vapour. The whole system is assumed to be in contact with a reservoir of liquid (the bulk water in the case of soils) at temperature T and liquid pressure p_l, such that $\Pi_m = p_g - p_l$, where p_g is the pressure in the gas phase. From considerations about thermodynamic equilibrium, the following expression for the molecular component of the disjoining pressure was obtained:

$$\Pi_m\left(t_{Film}\right) = -\frac{A_{svl}}{6\pi {t_{Film}}^3} \tag{2.16}$$

where A_{svl} is the Hamaker constant for solid-vapour interactions via an intervening liquid phase. The Hamaker constant A_{svl}, which represents interaction between macroobjects (e.g. soil particles surface and liquid) due to short-range van der Waals forces, generally ranges between -1×10^{-20} J and -1×10^{-19} J but, for natural soils, it is suggested to be assumed as -6×10^{-20} J [48].

Equations 2.13, 2.14, 2.15 and 2.16 can be combined to describe the relationship between the liquid film thickness and the matric suction in unsaturated soils, even though the effect of shape and rugosity of the soil grains and the interaction between liquid films surrounding different adjacent particles are neglected. The values of all the constants in Equations 2.15 and 2.16 are shown in Table 2.1. Figure 2.8 shows the relationship between the liquid film thickness and suction (disjoining pressure), and the contribution of the ionic-electrostatic and the molecular components, for a monovalent ionic solution (e.g. water) adsorbed to natural soil grains at the temperature $T = 20\,^{\circ}\mathrm{C}$. For film thicknesses greater than approximately 5 nm (suction lower than approximately 100 kPa) the ionic-electrostatic component is dominant, for film thicknesses lower than approximately 0.3 nm (suction greater than approximately 1×10^5 kPa) the molecular component is dominant. When the film thickness is approximately between 0.3 nm and 5 nm (suction approximately between 100 kPa and 1×10^5 kPa), both the ionic-electrostatic component and the molecular component are significant.

Table 2.1: Values of the constants related to the ionic-electrostatic and the molecular components of the expression of the disjoining pressure (Equations 2.15 and 2.16)

Permittivity of free space, $\varepsilon_0\,[\mathrm{C^2\,J^{-1}\,m^{-1}}]$	8.85×10^{-12}
Static relative permittivity of water, ε_r	78.41
Boltzmann constant, $k_B\,[\mathrm{J\,K^{-1}}]$	1.38×10^{-23}
Electron charge, $e\,[\mathrm{C}]$	1.60×10^{-19}
Hamaker constant, $\mathrm{A}_{svl}\,[\mathrm{J}]$	-6.00×10^{-20}

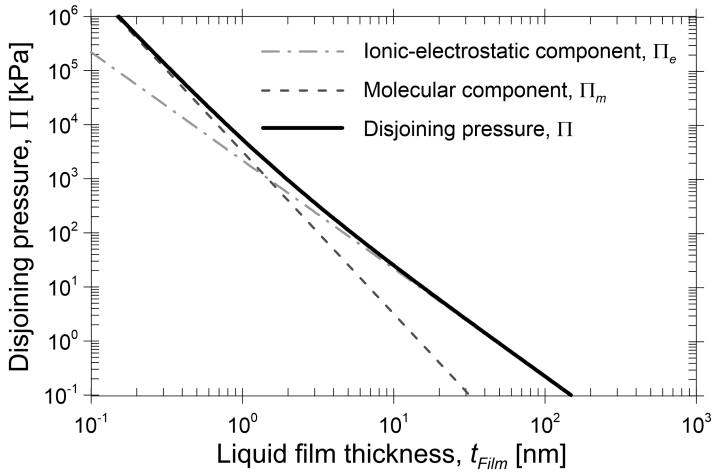

Figure 2.8: Liquid film thickness as a function of the disjoining pressure for a monovalent ionic solution (e.g. water) adsorbed to natural soil grains at the temperature $T = 20\,^{\circ}\mathrm{C}$ (after Lebeau and Konrad [49])

2.1.4 Water retention behaviour

The soil water retention curve (SWRC) describes the relationship between the water content (in terms of volumetric water content θ_l, gravimetric water content θ_{gl} or degree of liquid saturation S_l) and the matric suction s. The volumetric water content is defined as:

$$\theta_l = \frac{V_l}{V_{tot}} \tag{2.17}$$

where V_l is the volume of liquid and V_{tot} is the total volume of soil. The gravimetric water content θ_{gl} is defined as:

$$\theta_{gl} = \frac{m_l}{m_s} \tag{2.18}$$

where m_l is the mass of liquid and m_s is the mass of solid. The degree of liquid saturation is defined as:

$$S_l = \frac{V_l}{V_v} \tag{2.19}$$

where V_v is the volume of voids or pore spaces. The volumetric water content θ_l and the degree of saturation S_l are linked via the following equation:

$$S_l = \frac{\theta_l}{\Phi} \tag{2.20}$$

where the porosity Φ is defined as:

$$\Phi = \frac{V_v}{V_{tot}} \tag{2.21}$$

Unless differently specified, where the term "water content" is used within this thesis it can be taken to be the volumetric water content, defined by Equation 2.17.

Figure 2.9 shows qualitative SWRCs for different materials plotted as degree of saturation S_l against suction s. Suction is plotted on a logarithmic scale, which is common for the representation of SWRCs. In all cases, the degree of saturation S_l decreases with increasing suction s. Starting from full saturation $S_l = 1$, as a soil is dried, the liquid retreats into smaller and smaller voids, the gas-liquid interface becomes increasingly more curved and the corresponding suction s increases accordingly (see Figure 2.7). Comparing the different materials, because the void pores are much smaller in a finer material (e.g. a clay) than in a coarser material (e.g. a sand), much higher values of curvature, and hence suction, are required to reduce the degree of saturation to a particular value in a finer material than in a coarser material.

For a given soil, the water retention curve is not unique, with different retention behaviour during a drying path and during a wetting path [50]. This effect is known as water retention hysteresis. In addition, water retention behaviour is affected by changes in the void ratio of the soil. Figure 2.10 qualitatively shows, for a given soil, the water retention hysteresis and how the void ratio affects the water retention behaviour. Three limit or boundary curves can be identified: the "primary drying curve", the "main drying curve" and the "main wetting curve" [51]. The primary drying curve represents a drying process which starts from full saturation.

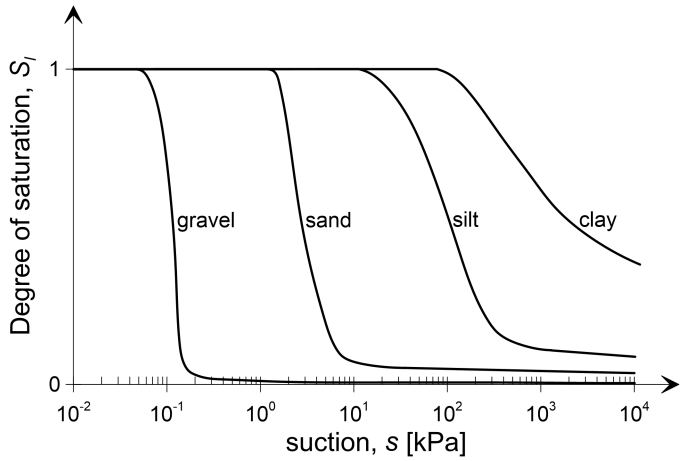

Figure 2.9: Qualitative soil water retention curves (SWRCs) for different materials

The main wetting curve represents a wetting process which start from dry conditions and ends in general at a degree of saturation lower than 1 because of the formation of trapped air. The main drying curve represents a drying process which starts from the end of a main wetting process, namely from $s = 0$ but from a degree of saturation value in general lower than 1. Moreover, "scanning curves" describe paths included between the limit curves, occurring when drying or wetting are reversed at intermediate degrees of saturation.

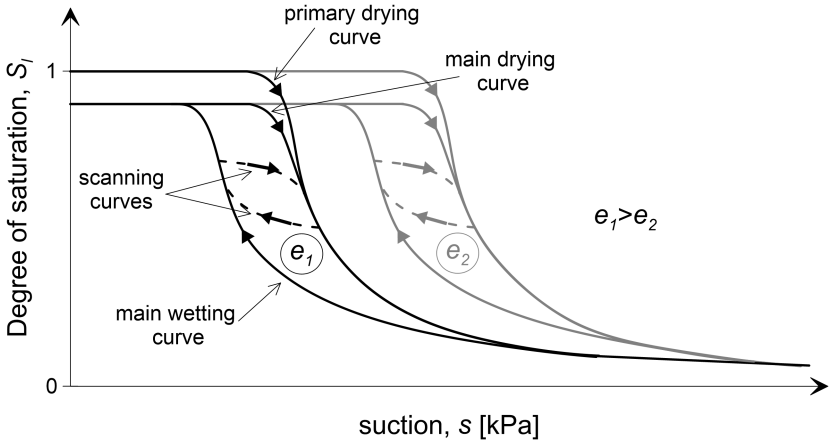

Figure 2.10: Water retention hysteresis and effect of void ratio on the SWRC

As was mentioned in Section 2.1.3, the mechanisms of drying and wetting of a pore are different (see Figure 2.7) and, for a given value of suction, the corresponding degree of saturation during drying is greater than during wetting. This effect, also known as "ink bottle effect" [50], is the main cause of water retention hysteresis in unsaturated soils. However, other phenomena also contribute to the hysteretic retention behaviour of unsaturated soils [52], like the hysteresis of the contact angle, the formation of trapped air during wetting and change of soil structure during wetting and drying.

The contact angle of the gas-liquid interface in contact with moist soil grains is approximately equal to 0 but, during a first wetting process, when the soil grains are dry, the contact angle values can be significantly higher [53].

During a wetting process, full saturation is often not achieved even though the applied

suction becomes zero or negative (see Figure 2.10), due to the formation of trapped air which, consequently has an effect on the wetting SWRCs [54–56]. During a wetting process, the liquid phase enters the smaller pores of the soil first and subsequently the larger pores, and the gas phase is consequently expelled. However, in order for the gas to flow out of the soil during wetting, the gas phase must create continuous gas flow channels. When high degree of saturation values are attained, exceeding 70-80% [56], larger pores filled with gas may be surrounded by smaller pores filled with liquid and the passageway for the gas flow may be blocked. From this point, further decreases in the applied suction result in an increase in the gas pressure in the trapped air. In this situation, the gas is expelled only through the slow process of diffusion of air in the liquid phase [57], driven by a gradient in the dissolved air concentration between the pore liquid around the trapped air (higher concentration) and the pore liquid adjacent to free air (lower concentration).

Finally, the hydraulic and mechanical behaviours of unsaturated soils are in general coupled. In particular, changes of void ratio e, caused by volumetric straining (i.e. mechanical behaviour), lead to different SWRCs, as shown in Figure 2.10 (i.e. mechanical behaviour influences hydraulic behaviour). In particular, if a soil with an initial void ratio e_1 is compressed, resulting in a smaller void ratio e_2, the mean size of the pores decreases. Consequently, according to Equation 2.2, higher values of suction are required to attain the same degree of saturation [58].

2.1.5 Flow processes

The advective flux (volume flow rate through unit cross-sectional area) of liquid $\boldsymbol{q}_l$ and gas $\boldsymbol{q}_g$ through porous media (e.g. soils) is governed by Darcy's law. For the liquid flux, this can be expressed as:

$$\boldsymbol{q}_l = -k_l \cdot \nabla h_l \tag{2.22}$$

where k_l is the hydraulic conductivity [LT^{-1}] and ∇h_l is the hydraulic gradient. In the absence of osmotic effects, the hydraulic head h_l is defined as:

$$h_l = z + \frac{p_l}{\gamma_l} \tag{2.23}$$

where z is the elevation relative to an arbitrary horizontal reference datum and γ_l is the unit weight of the liquid, defined as $\gamma_l = \rho_l g$ where ρ_l is the liquid density and g is the gravitational acceleration. Equations 2.22 and 2.23 can be applied also to the description of the advective gas flux $\boldsymbol{q}_g$, replacing k_l, h_l, p_l, γ_l and ρ_l with the gas conductivity k_g, the gas head h_g, the pore gas pressure p_g, the unit weight of gas γ_g and the gas density ρ_g, respectively.

The hydraulic conductivity k_l is a property of soils which represents the ease with which the liquid can flow through pores. For saturated conditions, the hydraulic conductivity is often assumed to be constant for a given soil, although it actually varies with the porosity Φ [59]. By contrast, under unsaturated conditions, the hydraulic conductivity strongly varies also with the degree of saturation S_l. The hydraulic conductivity depends on the number and the

size of the continuous paths formed by the liquid. In particular, the more and larger are these liquid paths, the higher is the hydraulic conductivity. It should be pointed out that, although water movement through soils may also occur under the form of water vapour flow, this is not related to the hydraulic conductivity k_l because vapour flow is not governed by Darcy's law. Similar concepts apply to the gas conductivity k_g.

Figure 2.11 shows the qualitative dependence of the hydraulic conductivity k_l and the gas conductivity k_g on the (liquid) degree of saturation S_l and on the gas degree of saturation S_g, which is defined as $S_g = 1 - S_l$. Under saturated conditions ($S_l = 1$) the hydraulic conductivity is equal to the saturated value k_{ls}. As S_l decreases from 1, the hydraulic conductivity falls dramatically, because:

- the cross-sectional area of voids available for the liquid flow (the voids filled with liquid) is reduced;
- the continuous liquid paths are restricted to smaller voids, because the larger voids are the first to empty of liquid;
- the length of continuous liquid paths is increased because, in order to avoid pores filled with gas, the tortuosity of these paths increases;
- the thickness of liquid films adsorbed to the soil grain surfaces reduces thereby reducing the transport of liquid water within these liquid films.

Similar concepts apply also to the relationship between gas conductivity k_g and gas degree of saturation S_g (see Figure 2.11), where the saturated gas conductivity k_{gs} is the gas conductivity value in fully dry conditions (i.e. $S_l = 0$ or $S_g = 1$).

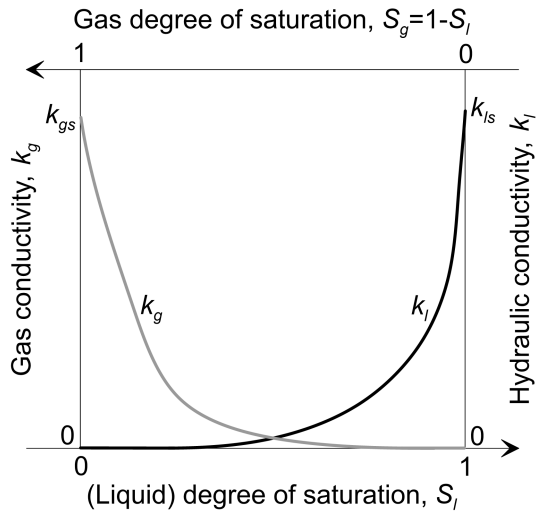

Figure 2.11: Typical hydraulic conductivity and gas conductivity curves as functions of the (liquid) degree of saturation and gas degree of saturation

The soil hydraulic conductivity curve (SHCC) is the relationship between hydraulic conductivity k_l and either degree of saturation S_l or suction s. The SHCC is generally

represented by the following expression:

$$k_l(S_l) = k_{ls} \cdot k_{lr}(S_l) \tag{2.24}$$

where $k_{lr}(S_l)$ is the relative hydraulic conductivity, which ranges between 1 ($k_l = k_{ls}$) and 0 ($k_l = 0$). Similarly, the relative gas conductivity k_{rg} is the ratio between $k_g(S_g)$ and k_{gs}.

The advective movement of liquid in unsaturated soils is often described by Richards equation [60], a non linear partial differential equation. Richards equation was obtained by applying Darcy's law to the liquid mass conservation under the assumptions of no phase transfer (i.e. water storage or transfer in vapour form is ignored), non-deformable soil and incompressible water. This equation can be written as:

$$\frac{\partial \theta_l}{\partial t} = -\frac{\partial}{\partial x}\left[k_{lx}(\theta_l)\frac{\partial h_l}{\partial x}\right] - \frac{\partial}{\partial y}\left[k_{ly}(\theta_l)\frac{\partial h_l}{\partial y}\right] - \frac{\partial}{\partial z}\left[k_{lz}(\theta_l)\frac{\partial h_l}{\partial z}\right] \tag{2.25}$$

where k_{lx}, k_{ly} and k_{lz} are the hydraulic conductivities in the x-, y- and z-directions respectively, in the general case of anisotropic hydraulic conductivity. A similar equation can be written to represent the gas flow, with corresponding assumptions of no phase transfer (i.e. air storage or transfer in dissolved form is ignored) and non-deformable soil, although the effect of gas compressibility does need to be included.

In addition to the advective flows of liquid water and gaseous air (each described by Darcy's law), also the following flow processes occur in unsaturated soils:

- flow of water vapour within the gas phase by advection of the gas phase;
- flow of water vapour within the gas phase by diffusion (see Equation 2.12);
- flow of dissolved air within the liquid phase by advection of the liquid phase;
- flow of dissolved air within the liquid phase by diffusion (see Equation 2.5).

2.1.6 Mechanical behaviour

In unsaturated soils, bulk water and meniscus water interact in a different way with the soil skeleton, hence affecting differently the mechanical behaviour. The liquid film water has generally a negligible effect on the mechanical behaviour of coarse-grained soils whereas it can be significant for fine-grained soils [61].

The pressure in bulk water acts in the same way as in saturated soils, influencing both normal and tangential forces at inter-particle contacts adjacent to liquid-filled voids. By contrast, the pressure in meniscus water produces an additional stabilizing inter-particle force, normal to the inter-particle contact, at each contact where a meniscus water bridge is present (i.e. where voids are gas-filled), with no addition to the tangential force [62, 63].

Fisher [42] studied the force equilibrium in a meniscus water bridge connecting two identical spherical soil particles of radius R_p in contact with each other (see Figure 2.12a).

Figure 2.12b shows the dependency of ΔN upon suction s, where ΔN is the additional inter-particle normal force due to the presence of the meniscus water bridge. As suction increases:

- more voids become gas-filled and the number of inter-particle contacts affected by meniscus water bridges increases;
- the additional inter-particle normal force ΔN increases, but reaches a limiting value as suction tends to infinity that is only 50% greater than the value of ΔN produced by a meniscus water bridge at $s = 0$.

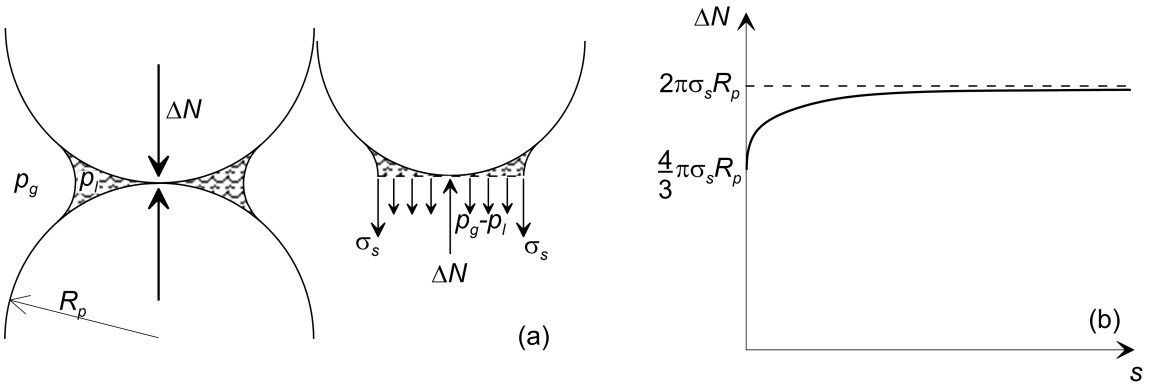

Figure 2.12: Equilibrium in the meniscus water bridge

To a first approximation, ΔN can be assumed to be constant when the meniscus water bridge is present but it disappears when the surrounding voids become liquid-filled [62].

To describe the mechanical behaviour of unsaturated soils, Bishop [64] proposed a definition for a single effective stress σ':

$$\sigma' = \sigma - p_g + (p_g - p_l) \cdot \chi \tag{2.26}$$

where σ is the total stress and χ is a function of the degree of saturation ($\chi = \chi(S_l)$), with the following properties: $\chi(S_l = 1) = 1$ and $\chi(S_l = 0) = 0$.

The validity of the use of Bishop's effective stress to represent the mechanical behaviour of unsaturated soils was, however, first challenged by Jennings and Burland [65]. A single effective stress is in fact unable to represent all the aspects of the mechanical behaviour of unsaturated soils. Figure 2.13 qualitatively shows the change in void ratio e of two samples of an unsaturated soil when wetted under two different values of constant total stresses σ. When the soil is wetted under a relatively low total stress, the soil "swells", i.e. the void ratio increases. When the soil is wetted under a relatively high total stress, the soil initially swells but then the void ratio decreases [66]. The reduction of void ratio during wetting is called "collapse" compression. The single Bishop's effective stress is unable to represent the collapse compression phenomenon.

A single effective stress would be able to represent only the effect of bulk water on the mechanical behaviour of unsaturated soils but it is unable to represent the role of meniscus water. As suction increases within a single meniscus water bridge (pore-liquid pressure decreases),

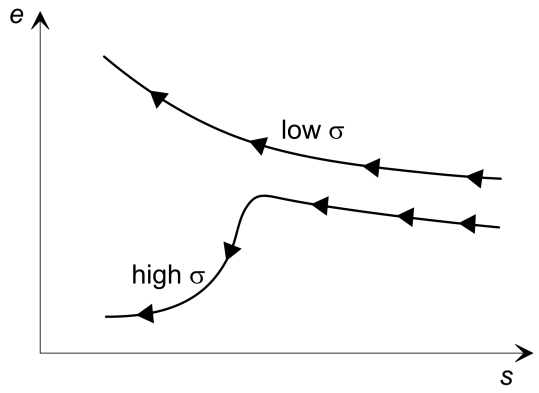

Figure 2.13: Volumetric behaviour upon wetting: swelling and collapse compression

the normal force at the inter-particle contact increases with no increase in the tangential force (see Figure 2.12). This has the following effects on the macroscopic mechanical behaviour:

- Elastic strains: it causes compression of the grains and elastic compression of the soils (like an increase in effective stress in saturated soils).
- Plastic strains: it has a stabilizing effect on the inter-particle frictional contact against particle slippage because the normal inter-particle force increases but the tangential force does not increase; this reduces the possibility of plastic strains (like a decrease in effective stress in saturated soils).
- Shear strength: shear strength increases because the normal inter-particle forces increase (like an increase in effective stress in saturated soils).

Collapse compression on wetting can be thus interpreted microscopically. When a soil is loaded by increasing total stress, normal and tangential forces at the inter-particle contacts increase and slippage (plastic strain) can occur. However, at some inter-particle contacts, the presence of meniscus water bridges may prevent this slippage. This stabilizing effect is lost during wetting because meniscus water bridges are replaced by bulk water. If wetting occurs at relatively high value of total stress, the loss of inter-particle stability as meniscus water bridges disappear is sufficient to bring the soil to a point of instability, slippage at inter-particle contacts commences and collapse compression occurs. However, if the applied total stress is relatively low, the tangential inter-particle forces are also low and slippage will not occur even if the stabilizing effect of meniscus water bridges is lost during wetting. This explains why collapse compression does not occur at relatively low values of applied total stress.

Therefore, in order to represent the mechanical behaviour of unsaturated soils, the definition of two stress variables is required. Commonly, net stress $\sigma - p_g$ and matric suction $p_g - p_l$ are used [66, 67], although many other possible combinations of stress state variables have also been proposed [68].

Many full mechanical constitutive models for unsaturated soils have been proposed since the original Barcelona Basic Model (BBM) of Alonso et al. [69]; some of these employ net stress and matric suction as stress variables [e.g. 69, 70] whereas others employ alternative

pairs of stress variables [e.g. 62, 71–73]. However, in this thesis, the only aspect of mechanical behaviour that is significant is the shear strength, and therefore the remaining review of mechanical behaviour of unsaturated soils is restricted to shear strength.

Shear strength in unsaturated conditions is greater than that in saturated conditions and it generally increases with increasing suction. Fredlund et al. [74] proposed the following relationship to model the shear strength τ_f of unsaturated soils:

$$\tau_f = c' + (\sigma - p_g)\tan\phi' + (p_g - p_l)\tan\phi_b \tag{2.27}$$

where $\sigma - p_g$ is the net stress normal to failure plane, c' and ϕ' are respectively the effective cohesion and the effective friction angle for saturated conditions and ϕ_b is the friction angle with respect to matric suction. In addition to the conventional Mohr-Coulomb for saturated soils, the presence of the term $(p_g - p_l)\tan\phi_b$ predicts a linear increase of shear strength with suction, given that ϕ_b was prescribed to be a constant. The validity of this last aspect was challenged by subsequent works [e.g. 75, 76], which showed that ϕ_b is not constant with suction.

Figure 2.14 shows data of shear strength τ_f against suction s at different values of applied net stress $\sigma - p_g$, obtained by Escario and Saez [75] for a clayey sand. It can be seen that the relationship between τ_f and s is clearly non linear and a constant value of ϕ_b is not appropriate to represent the shear strength of unsaturated soils. For $s = 0$ the soil is in saturated conditions and hence τ_f increases approximately linearly with increasing $\sigma - p_g$. As s increases, τ_f initially increases linearly with a slope approximately equal to ϕ', which is the effective friction angle. Indeed, at relatively low values of suction, the soil is still saturated and only bulk water is present. In these conditions, a variation in suction has the same effect as in saturated conditions. Increasing suction, the presence of bulk water decreases, meniscus water bridges are formed at the inter-particle contacts but the stabilizing inter-particle forces which they generate reach a limiting value as suction tends to infinity (see Figure 2.12). Therefore, as suction increases and the degree of saturation decreases, the slope of the $\tau_f : s$ curves decreases from the initial value ϕ'.

Several other relationships representing the shear strength of unsaturated soils have been proposed [e.g. 67, 74, 77–79]. Among these, Bishop and Blight [67] replaced the effective stress in the conventional Mohr-Coulomb model with the Bishop's effective stress defined by Equation 2.26, thereby obtaining:

$$\tau_f = c' + [(\sigma - p_g) + (p_g - p_l)\cdot\chi]\cdot\tan\phi' \tag{2.28}$$

A good approximation of the parameter is $\chi = S_l$ [77]. This relationship (with $\chi = S_l$) is able to capture the non-linearity of the relationship between τ_f and s and it is adequate to represent the shear strength of unsaturated soils [80]. For this reason and for its simplicity, it will be used in this thesis.

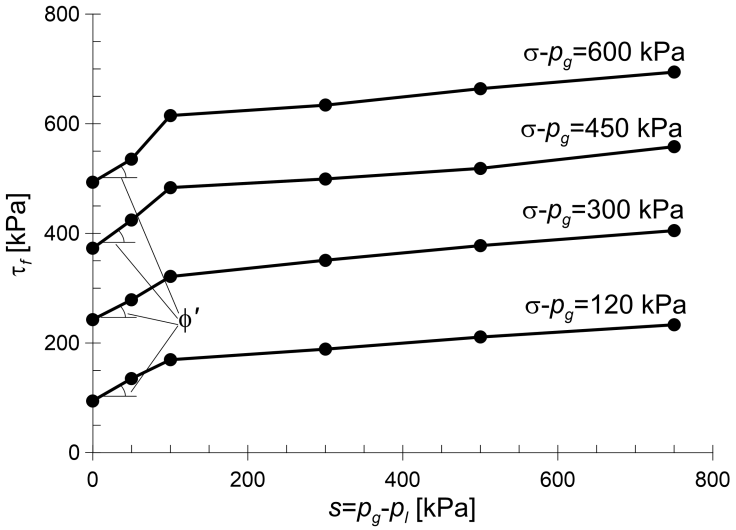

Figure 2.14: Dependency of shear strength on suction (data for a clayey sand from Escario and Saez [75])

2.2 Hydraulic constitutive models for unsaturated soils

The soil water retention curve (SWRC) and the soil hydraulic conductivity curve (SHCC) can be expressed mathematically by different constitutive models. This section provides a review of the main hydraulic constitutive models describing the SWRC and the SHCC, including the effects of water retention hysteresis and trapped air.

2.2.1 Soil water retention curve

Conventionally, water retention models are empirical and their parameter values, for a given soil, are typically calibrated with experimental data. The conventional water retention models proposed by Brooks and Corey [81], van Genuchten [82] and Kosugi [83] are amongst the most well-known. The three models all assume that as suction s varies, the degree of saturation S_l varies between a maximum value S_{ls} at $s = 0$ and a minimum value, the residual degree of saturation S_{lr}, as s tends to infinity, where S_{ls} and S_{lr} are both soil constants. Each of the three models then gives the degree of saturation S_l at any specific value of s by:

$$S_l = S_{lr} + S_{le} \cdot (S_{ls} - S_{lr}) \tag{2.29}$$

where S_{le} is termed the effective degree of saturation (with a value between 0 and 1). The three models differ in the predicted variation of the effective degree of saturation S_{le} with suction s.

The Brooks and Corey model can be expressed as:

$$S_{le} = \begin{cases} 1 & \text{if } s \leq s_{AE/AEX} \\ \left(\frac{s_{AE/AEX}}{s}\right)^n & \text{if } s > s_{AE/AEX} \end{cases} \tag{2.30}$$

where the air entry or air exclusion value of suction $s_{AE/AEX}$ and n are parameters of the

model (soil constants).

The van Genuchthen model can be expressed as:

$$S_{le} = \left[\frac{1}{1 + \left(\frac{s}{P_0} \right)^n} \right]^m \tag{2.31}$$

where P_0, n and m are parameters of the model (soil constants). Parameters m and n are often correlated as $m = 1 - 1/n$ [82].

The Kosugi model can be expressed as:

$$S_{le} = Q \left(\frac{\ln (s/s_m)}{\sigma_m} \right) \tag{2.32}$$

where Q is the complementary normal distribution function and s_m and σ_m are parameters of the model (soil constants).

For all three models, the maximum degree of saturation S_{ls} is the degree of saturation value at $s = 0$ and it is typically considered as $S_{ls} = 1$ because it represents the saturated condition. Sometimes, however, it is considered as $S_{ls} < 1$ in order to represent situations in which full saturation is not achieved at $s = 0$ during wetting, due to the formation of trapped air. According to Equation 2.29 used in conjunction with Equation 2.30, 2.31 or 2.32, the residual degree of saturation S_{lr} is the value of S_l as s tends to infinity. More typically, however, it is simply treated as a fitting parameter, to optimise the fit to the experimental variation of S_l at intermediate values of degree of saturation.

Figure 2.15 shows an example of comparison between SWRCs obtained with the three models described above, with model parameter values selected to provide approximate matching. All the models lead to a similar shape of the SWRC. However, with the Brooks and Corey [81] model the degree of saturation is constant ($S_l = S_{ls}$) at low values of suction and starts decreasing for $s > s_{AE/AEX}$, at which the gradient of the SWRC is discontinuous. By contrast, the van Genuchten [82] model and the Kosugi [83] model predict a SWRC which decreases monotonically (i.e. the gradient is continuous) but it starts decreasing more dramatically at suction values around the parameter $s_{AE/AEX}$ of the Brooks and Corey model.

All three of these empirical models for the SWRC can generally provide a good match to the SWRC at high and moderate values of degree of saturation, but they cannot accurately represent the SWRC at low values of S_l. In fact, these models predict that S_l tends asymptotically to a minimum value (i.e. the residual degree of saturation S_{lr}), as suction tends to infinity. However, experimental results [84], supported by thermodynamic considerations [85], showed that the value of S_l reduces to zero at a finite value of suction of approximately 1 GPa, regardless of the type of soil. In particular, at low degree of saturation when only meniscus water and liquid film water are present in the soil, the SWRC decreases approximately linearly with the logarithm of suction. Hence, some more recently proposed SWRC models are specifically intended to extend the range of application to lower degree of saturation. Some of these models involve new mathematical expressions [86] whereas others are modified forms

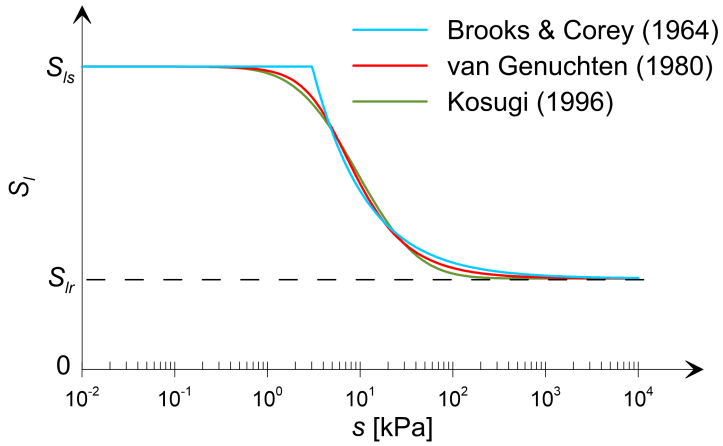

Figure 2.15: Conventional SWRC models

of previous conventional models [84, 87–93].

Campbell and Shiozawa [84] modified the van Genuchten model and Rossi and Nimmo [87] modified the Brooks and Corey model, both adding an extra-term in order to capture the log-linear behaviour of the SWRC in the low degree of saturation range.

Fredlund and Xing [86] proposed a new expression able to capture the water retention behaviour from saturation to complete dryness. According to this model, the SWRC can be expressed as:

$$S_l = C(s)\frac{S_{ls}}{\{\ln[e+(s/p_0)^n]\}^m} \tag{2.33}$$

where p_0, n and m are parameters of the model and $C(s)$ is a correction function defined as:

$$C(s) = \frac{\ln(1+s/s_r)}{\ln[1+(1\,\text{GPa}/s_r)]} \tag{2.34}$$

The correction function $C(s)$ forces the SWRC to drop slowly to $S_l = 0$ at $s = 1\,\text{GPa}$ and the parameter s_r represents the suction at which the SWRC starts to drop approximately linearly in a semi-logarithmic plot [86].

Fayer and Simmons [88] and Zhang [89] modified in similar ways both the van Genuchten and the Brooks and Corey models, replacing a constant residual degree of saturation S_{lr} with a function decreasing with suction $S_{lr}(s)$. In particular, according to Fayer and Simmons [88], this function can be expressed as:

$$S_{lr} = \xi \ln\left(\frac{s_{dry}}{s}\right) \tag{2.35}$$

where ξ is a fitting parameter and s_{dry} is the suction at oven dryness, i.e. $s_{dry} = 1\,\text{GPa}$. Therefore, joining Equations 2.29, 2.30, 2.31 and 2.35, the modified versions of the Brooks and Corey model and of the van Genuchten model [88] can be expressed respectively as:

$$S_l = \begin{cases} S_{ls} & \text{if } s \le s_{AE/AEX} \\ \xi \ln\left(\frac{s_{dry}}{s}\right) + \left(\frac{s_{AE/AEX}}{s}\right)^n \cdot \left[S_{ls} - \xi \ln\left(\frac{s_{dry}}{s}\right)\right] & \text{if } s > s_{AE/AEX} \end{cases} \tag{2.36}$$

$$S_l = \xi \ln\left(\frac{s_{dry}}{s}\right) + \left[\frac{1}{1+\left(\frac{s}{P_0}\right)^n}\right]^m \cdot \left[S_{ls} - \xi \ln\left(\frac{s_{dry}}{s}\right)\right] \tag{2.37}$$

In the same way, Khlosi et al. [90] modified the Kosugi model introducing the residual degree of saturation function of Equation 2.35 in Equations 2.29 and 2.32, leading to the following expression:

$$S_l = \xi \ln\left(\frac{s_{dry}}{s}\right) + Q\left(\frac{\ln(s/s_m)}{\sigma_m}\right) \cdot \left[S_{ls} - \xi \ln\left(\frac{s_{dry}}{s}\right)\right] \tag{2.38}$$

Figure 2.16 shows the qualitative comparison between the conventional van Genuchten model (Equations 2.29 and 2.31) and the modified version proposed by the Fayer and Simmons model (Equation 2.37), with $S_{ls} = 1$ in both cases. The two SWRCs, which were obtained using the same values for n, m and P_0, are almost coincident at high and medium values of degree of saturation. However, the Fayer and Simmons model is able to represent effectively also the state at low degree of saturation, where the degree of saturation decreases approximately linearly with the logarithm of suction down to a completely dry state [84].

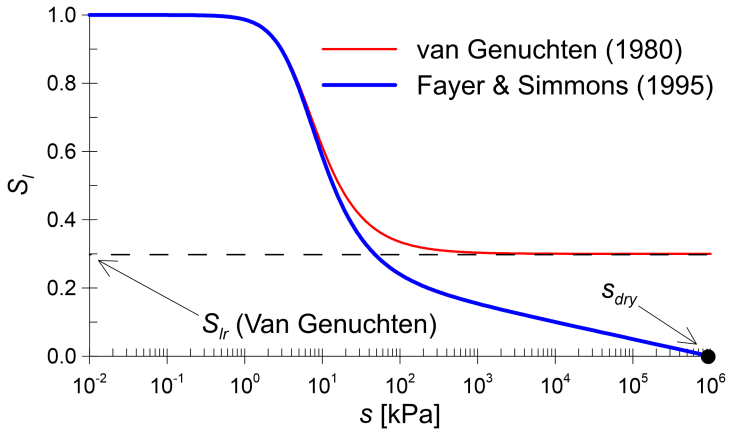

Figure 2.16: Comparison between the van Genuchten [82] model and the Fayer and Simmons [88] model

More recently, Peters [91] proposed an empirical model where the total degree of saturation is split into the capillary and adsorptive liquid components, where the former represents the component related to bulk and meniscus water and the latter represents the component related to liquid film water. This model also solved some difficulties arising in the Fayer and Simmons [88] model and in the Khlosi et al. [90] model for soils with wide grain-size distributions. Since the model was not continuously differentiable at the connection point between the capillary and the adsorptive regions, Iden and Durner [92] modified Peter's model introducing a different empirical expression for the adsorptive component.

2.2.2 Soil hydraulic conductivity curve

In contrast with the water retention models which are typically calibrated with experimental data, direct measurements of unsaturated hydraulic conductivity are time-consuming, tech-

nically complex and expensive and their use is therefore generally limited to the research field or important projects. For this reason, most research effort has been addressed towards the use of predictive models for the unsaturated hydraulic conductivity function (SHCC), based on the SWRC properties. A direct physical link exists between the SHCC and SWRC properties, namely they are both linked to the pore-size distribution. The size of a single pore and the sizes of connections to neighbouring pores are important to determine whether, for a given suction, a pore is filled with liquid or gas, thus controlling the SWRC, and the sizes and connectivity of pores filled with liquid controls the hydraulic conductivity, i.e. the SHCC. In most predictive models for unsaturated hydraulic conductivity, only one extra parameter (other than those defining the SWRC) is needed to describe the conductivity function, which is typically the saturated hydraulic conductivity k_{ls}.

Similar to the water retention models, many conventional models for the SHCC provide realistic modelling of the variation of hydraulic conductivity at medium and high values of degree of saturation but they do not perform well at low values of degree of saturation. Among these, Burdine [94] and Mualem [95] proposed statistical models making use of the fact that the unsaturated hydraulic conductivity depends on the pore-size distribution. They modelled the soil pores as a bundle of cylindrical tubes, with each individual tube either filled or empty of water with the liquid flow attributed to the former. In contrast with the Burdine [94] model, the Mualem [95] model considers in a statistical way also the role of cylindrical tubes of different diameter connected to each other along the flux direction. According to Burdine [94], the relative hydraulic conductivity (see Equation 2.24) can be expressed as:

$$k_{lr} = {S_{le}}^2 \frac{\int_{S_{lr}}^{S_l} \frac{dS_l}{s^2}}{\int_{S_{lr}}^{S_{ls}} \frac{dS_l}{s^2}} = {S_{le}}^2 \frac{\int_0^{S_{le}} \frac{dS_{le}}{s^2}}{\int_0^1 \frac{dS_{le}}{s^2}} \tag{2.39}$$

whereas the Mualem [95] model can be expressed as:

$$k_{lr} = {S_{le}}^{0.5} \left[\frac{\int_{S_{lr}}^{S_l} \frac{dS_l}{s}}{\int_{S_{lr}}^{S_{ls}} \frac{dS_l}{s}} \right]^2 = {S_{le}}^{0.5} \left[\frac{\int_0^{S_{le}} \frac{dS_{le}}{s}}{\int_0^1 \frac{dS_{le}}{s}} \right]^2 \tag{2.40}$$

The Burdine model and the Mualem model were subsequently used in conjunction with expressions for the SWRC. For instance, Brooks and Corey [81] substituted the SWRC expression for S_{le} (see Equation 2.30) in the Burdine SHCC expression of Equation 2.39, obtaining:

$$k_{lr} = {S_{le}}^{3+2/n} \tag{2.41}$$

Similarly, van Genuchten [82] and Kosugi [83] used the Mualem SHCC expression (Equation 2.40) in conjunction with their expressions for the SWRC (Equations 2.31 and 2.32

respectively). van Genuchten [82] obtained the following expression:

$$k_{lr} = {S_{le}}^{0.5} \left[1 - \left(1 - {S_{le}}^{1/m} \right)^{m} \right]^{2} \tag{2.42}$$

whereas Kosugi [83] model for the relative hydraulic conductivity can be expressed as:

$$k_{lr} = {S_{le}}^{0.5} \left\{ Q \left[Q^{-1} \left(S_{le} \right) + \sigma_m \right] \right\}^{2} \tag{2.43}$$

Fayer and Simmons [88] adapted the modified versions which they proposed of the Brooks and Corey and van Genuchten SWRC models (Equations 2.36 and 2.37 respectively) to the Mualem model for the SHCC.

Both the Burdine SHCC model and the Mualem SHCC model are inappropriate at low values of degree of saturation where few if any pores are entirely filled with water and these do not form continuous liquid paths. In these conditions, the liquid flow occurs only within thin liquid films covering the surfaces of the soil particles and in meniscus water bridges at the inter-particle contacts. While there were different studies trying to extend conventional water retention models to the low degree of saturation range, the studies aimed to model the hydraulic conductivity in the the low degree of saturation range where liquid flow occur in the adsorbed liquid films covering the soil grain surfaces were initially poor. Rossi and Nimmo [87] and Fayer and Simmons [88] simply replaced the effective degree of saturation with the actual degree of saturation in the Mualem SHCC model. The first important contribution in this sense was given by Tuller and Or [96]. They studied analytically the unsaturated hydraulic conductivity due to liquid flow occurring within the liquid films covering the soil grains and within the corners occupied by meniscus liquid water. The problem was studied at the microscopic level and an upscaling algorithm was proposed. However, the model which they proposed is mathematically very complex and it requires input data not easy to obtain, like the pore geometries and the specific surface area. Peters and Durner [97] proposed a hydraulic conductivity expression made of the linear superposition of a simple power-law expression for the liquid film conductivity and a conventional Mualem model for the bulk water conductivity. The model is not fully predictive and, in order to be used, it requires additional empirical parameters calibrated with unsaturated hydraulic conductivity data at low values of degree of saturation, which are difficult to obtain. Tokunaga [98] analytically studied the problem of liquid flow occurring within liquid films in an idealized soil consisting of identically-sized smooth spherical particles, coming up with an expression for the component of the hydraulic conductivity related to liquid film flow, for the situation where none of the voids are filled with bulk water and hence all of the particles are covered by liquid films. According to this model, the liquid film component of the hydraulic conductivity ${k_l}^{Film}$ can be estimated as:

$${k_l}^{Film} = \frac{4\pi^2 \rho_l g \left(1 - \Phi\right)}{\mu_l D} \left(\frac{\varepsilon_r \varepsilon_0}{2} \right)^{1.5} \left(\frac{k_B T}{Ze} \right)^{3} \left(\frac{2\sigma_s}{D} + s \right)^{-1.5} \tag{2.44}$$

where ρ_l and μ_l are the liquid density and viscosity respectively, Φ is the porosity, D is the

spherical particle diameter, σ_s is the liquid-gas interface tension, T is the absolute temperature, Z is the ion valence change and ε_r, ε_0, k_B and e are physical constants shown in Table 2.1. This equation, although is able to capture the functional relationship between ${k_l}^{Film}$ and s at relatively low values of suction, cannot predict accurately the absolute values of ${k_l}^{Film}$ because it contains many simplifying assumptions (e.g. perfectly spherical particles, smooth surface, lack of consideration of increased liquid tortuosity due to the 3d shape of the particles) and because of the uncertainty in the choice of some parameters (e.g. a representative value of D for a natural porous medium).

Lebeau and Konrad [49] coupled the Kosugi model for the bulk water conductivity (Equation 2.43) with a version of the liquid film conductivity model proposed by Tokunaga [98] (Equation 2.44), which was improved at high values of suction and extended to wider grain-size distributions. However, this model requires the measurement of SWRC data at very high values of suction (i.e. as close as possible to 10 MPa). Also Zhang [89] adopted the model proposed by Tokunaga [98] to model the liquid film component of the hydraulic conductivity, introducing a correction factor which needs to be obtained experimentally. Peters [91] proposed a model where the hydraulic conductivity is split into capillary and liquid film components. However, a prediction from the SWRC cannot be done since two additional empirical parameters are required to predict the film conductivity.

In conclusion, the literature analysed lacks a model able to predict accurately the hydraulic conductivity down to very low values of degree of saturation, which does not require experimental data difficult to obtain and which is easy to apply. A model with these features was developed in this work and it will be discussed in Chapter 3.

2.2.3 Water retention hysteresis

Several hydraulic models have been proposed with the aim of describing the soil water retention hysteresis. Pham et al. [99] presented a detailed review of hysteretic water retention models proposed until 2003. These models can be divided in two groups: the conceptual (or physically based) models and the empirical models.

The conceptual hysteretic SWRC models are based on the domain concept. Among the different domain models, the one proposed by Néel [100, 101] and firstly applied in a hysteretic SWRC model by Everett [102] is probably the most used. It was assumed that every pore in the soil is either filled or empty of liquid. In particular, when suction increases to a certain value $s_{p,d}$, the initially filled pore drains, whereas, when the suction decreases to a certain value $s_{p,w}$, the initially empty pore is filled with liquid. A domain is made of a certain group of pores, whose properties are characterized by two infinitesimal ranges of suction ($s_{p,d}$; $s_{p,d} + ds_{p,d}$) and ($s_{p,w}$; $s_{p,w} + ds_{p,w}$). When suction increases to a value included between $s_{p,d}$ and $s_{p,d} + ds_{p,d}$ the pores in the corresponding domain dries out of water whereas when suction decreases to a value included between $s_{p,w}$ and $s_{p,w} + ds_{p,w}$ the pores in the corresponding domain are filled with water. The soil is seen as made of different domains. If the state of a pore in a domain is assumed to be independent of the surrounding

pores, the model is called an "independent domain" model [e.g. 102–108]. On the contrary, if the effect of surrounding pore blockages against liquid and gas entry is taken into account, and thus the state of a pore is dependent on the surrounding pores, the model is called a "dependent domain" model [e.g. 109–111]. In a domain model, the degree of saturation of a soil can be represented using the three dimensional diagram shown in Figure 2.17b. When suction s reaches a maximum value s_{max} all the pores are empty of water and the degree of saturation reaches the minimum value $S_{l,min}$. When suction reaches a minimum value s_{min} all the pores are filled with liquid and the degree of saturation attains the maximum value $S_{l,max}$. These two points represent the meeting points for the main wetting and the main drying curves. According to this model, for $s > s_{max}$ or $s < s_{min}$ the SWRC is assumed to be non-hysteretic. The water distribution function calculated at the point $(s^0_{p,d}, s^0_{p,w})$, namely $f\left(s^0_{p,d}, s^0_{p,w}\right)$, represents the volume of pores which are filled at a suction of $s^0_{p,w}$ and dry at $s^0_{p,d}$. Since the suction at which a pore is filled with liquid is always lower than the suction at which it dries, i.e. $s_{p,d} > s_{p,w}$, the water distribution function is zero outside the triangle ABC in Figure 2.17b.

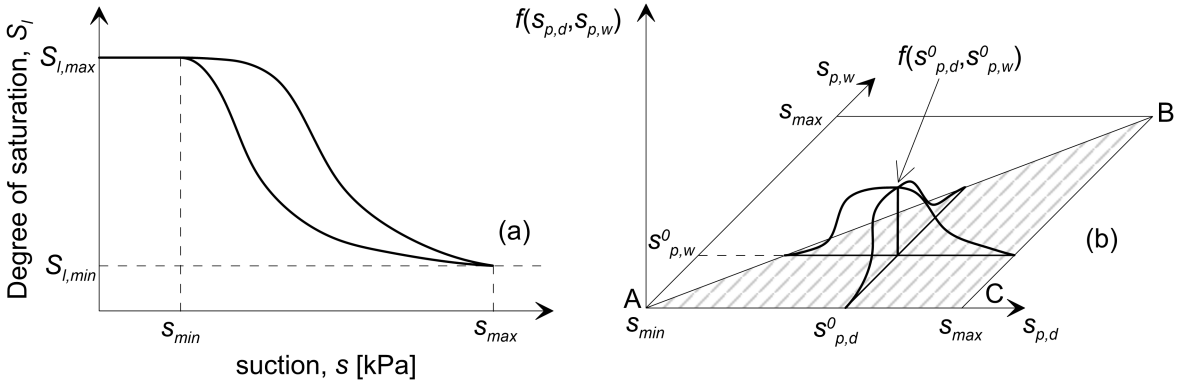

Figure 2.17: Schematic representation of (a) the main wetting and main drying curves and (b) the corresponding Néel diagram (after Pham et al. [99])

According to this model [100, 101], the maximum degree of saturation $S_{l,max}$ can be expressed as:

$$S_{l,max} = S_{l,min} + \int_{s_{min}}^{s_{max}} \int_{s_{min}}^{s_{max}} f\left(s_{p,d}, s_{p,w}\right) ds_{p,d} ds_{p,w} \tag{2.45}$$

Figure 2.18 shows a main drying process and a main wetting process presented on the Néel diagram. The main drying curve $S_{l,Md}(s)$ can be thus expressed as:

$$S_{l,Md}(s) = S_{l,min} + \int_{s_{min}}^{s_{max}} \int_{s}^{s_{max}} f\left(s_{p,d}, s_{p,w}\right) ds_{p,d} ds_{p,w} \tag{2.46}$$

whereas the main wetting curve can be expressed as:

$$S_{l,Mw}(s) = S_{l,min} + \int_{s}^{s_{max}} \int_{s}^{s_{max}} f\left(s_{p,d}, s_{p,w}\right) ds_{p,d} ds_{p,w} \tag{2.47}$$

A drying scanning curve $S_{l,d}(s_1, s)$ (not shown in the diagram) starting from suction s_1 on

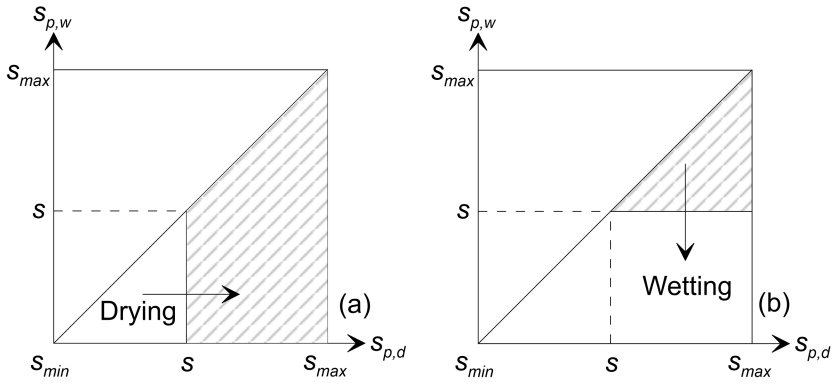

Figure 2.18: (a) Main drying and (b) main wetting processes on the Néel diagram (after Pham et al. [99])

the main wetting curve can be expressed as:

$$S_{l,d}(s_1,s) = S_{l,Mw}(s_1) - \int_{s_1}^{s}\int_{s_1}^{s} f\left(s_{p,d},s_{p,w}\right) ds_{p,d}ds_{p,w} \tag{2.48}$$

whereas a wetting scanning curve $S_{l,w}(s_2,s)$ (not shown in the diagram) starting from suction s_2 on the main drying curve can be expressed as:

$$S_{l,w}(s_2,s) = S_{l,Md}(s_2) + \int_{s}^{s_2}\int_{s}^{s_2} f\left(s_{p,d},s_{p,w}\right) ds_{p,d}ds_{p,w} \tag{2.49}$$

The function $f\left(s_{p,d},s_{p,w}\right)$ is calibrated over experimental data of the main wetting curve and the main drying curve and at least a family of scanning curves (either drying or wetting). An alternative domain diagram was also proposed by Mualem [106] in which the variables $s_{p,d}$ and $s_{p,w}$ were replaced by the neck pore diameter $\bar{r}$ and by the body pore diameter $\bar{\rho}$.

The first application of Néel's domain model by Everett [102] represented the basis for applications and new developments of physically based models. Poulovassilis [103] was the first to apply Everett's model on a porous material (i.e. glass beads). He divided the suction range into n intervals and, consequently, the Néel's diagram into $(n^2+n)/2$ sub-areas, each one representing an unknown. Since the two main curves provide only $2n$ equations, the remaining $(n^2+n)/2-2n$ equations must be obtained through the scanning curves. Philip [104] simplified the water distribution function $f\left(s_{p,d},s_{p,w}\right)$ introducing a "similarity hypothesis" stating: "the distribution of geometrical relationships between wetting and drying meniscus curvatures is independent of pore size". Using this hypothesis, the water distribution function can be expressed as:

$$f\left(s_{p,d},s_{p,w}\right) = \frac{l\left(s_{p,w}\right) h\left(s_{p,d}/s_{p,w}\right)}{s_{p,w}} \tag{2.50}$$

where $l\left(s_{p,w}\right)$ and $h\left(s_{p,d}/s_{p,w}\right)$ are two additional functions. Using the similarity hypothesis, the model requires fewer experimental data for calibration (i.e. only the main drying and main wetting curves). Also Mualem [105] proposed a similarity hypothesis where the water distribution function is the product of two independent functions $h\left(s_{p,d}\right)$ and $l\left(s_{p,w}\right)$, as

follows:

$$f\left(s_{p,d}, s_{p,w}\right) = h\left(s_{p,d}\right) l\left(s_{p,w}\right) \tag{2.51}$$

Based on this similarity hypothesis, Mualem proposed a series of other models [105, 106, 108, 111]. A more detailed review of each physically based model and their comparison can be found in Pham's works [99, 112].

The empirical hysteretic SWRC models are directly fitted to the observed shape of the hysteretic SWRC, once the mathematical formulation is given. In recent years, they found more applications than the physically based models, in particular when coupled with mechanical models for unsaturated soils. In 1969, Hanks et al. [113] were the first to propose the linear model. According to this model, once the boundary curves are defined, the scanning curves are approximated by straight lines with a slope lower than the slope of the main curves at the intersection point. This approach was used subsequently in other hysteretic water retention models. Wheeler et al. [62] proposed a model coupling hydraulic hysteresis and mechanical behaviour, in which the scanning curves were modelled as straight lines in the semi-logarithmic plot $S_l : \ln s$. A similar approach was used subsequently also, among others, by Khalili et al. [114] and by Nuth and Laloui [115].

In 1975, Dane and Wierenga [116] proposed an empirical "point" model representing water retention hysteresis. According to this, the shape of a scanning curve is governed by an empirical expression which is a function of the mutual distance between s_{min} and s_{max} and of the position of last reversal point (i.e. suction and degree of saturation) compared to the two boundary curves. This model found little application, because of its complexity.

Jaynes [117] proposed a "slope" model, which is a modification of the point model. According to this model, the slope of a scanning curve is proportional to the slope of the corresponding main curve at the same value of suction and the proportionality depends on the mutual vertical distance (difference in degree of saturation) between the scanning curve and the two main curves, in a plot where S_l is the vertical axis and s is the horizontal axis. The slope of a wetting scanning curve $\frac{dS_{l,w}}{ds}$ can be expressed as a fraction of the slope of the main wetting curve at the same suction value $\frac{dS_{l,Mw}}{ds}$ (see Figure 2.19a), as follows:

$$\frac{dS_{l,w}}{ds} = \frac{\left[S_{l,Md}\left(s\right) - S_{l,w}\left(s\right)\right]}{\left[S_{l,Md}\left(s\right) - S_{l,Mw}\left(s\right)\right]} \frac{dS_{l,Mw}}{ds} \tag{2.52}$$

The slope of a wetting scanning curve at a point on the main drying curve will be 0. However, the slope of a wetting scanning curve will tend to the slope of the main wetting curve as the wetting scanning curve gets closer to the corresponding main wetting curve. Similar concepts apply to a drying scanning curve although, in this case, a correction must be introduced in the corresponding equation for suction values lower than the air-entry value. This concept is the precursor of more recent bounding surface hysteretic water retention models [118–120], which however considered a proportionality factor depending on the horizontal distance (difference in suction) between the scanning curve and the main curves instead of the vertical distance (difference in degree of saturation).

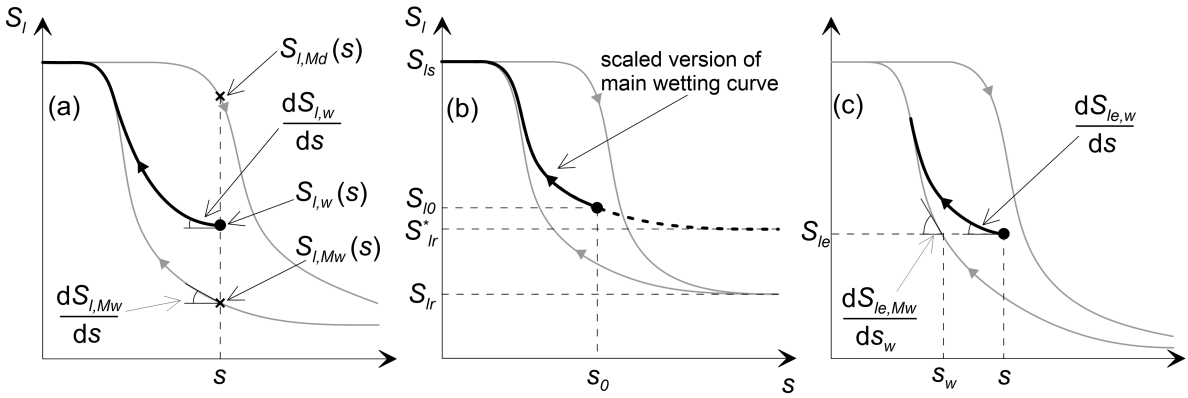

Figure 2.19: Empirical hysteretic water retention models: (a) Jaynes [117] model (b) Kool and Parker [121] model and (c) Zhou et al. [119] model

Nimmo [122] proposed a semi-empirical hysteretic water retention model which requires, as calibration data, the main drying curve and two points on the main wetting curve. The model assumes that: (i) the ratio of the slopes of wetting and drying curves in the $S_l : s$ plot is a constant at any value of suction; (ii) the body-to-neck size ratio in the biggest pore of the soil is equal to the ratio between air-entry and air-exclusion suction values, where the former is the suction value at which the degree of saturation starts decreasing from 1 during drying and the latter is the suction value at which the soil becomes saturated during wetting (excluding the effect of air trapping). The model was, however, relatively complex to apply in engineering practice.

In 1983, Scott et al. [123] proposed the scaling-down model. They modelled the main drying and main wetting curves using the Gardner [124] model. The scaling-down model was subsequently applied also by Kool and Parker [121] who instead used the van Genuchten [82] model (Equation 2.31) to represent the main curves. In this type of hysteretic model, the scanning curves are determined by scaling down the main curves. In particular, a drying scanning curve starting from the reversal point (suction s_0 and degree of saturation S_{l0}) is a scaled version of the main drying curve, which is forced to pass through the reversal point. To obtain this, in the description of the drying scanning curve the maximum degree of saturation S_{ls} is replaced by a fictitious value S^*_{ls}, expressed as:

$$S^*_{ls} = \frac{S_{l0} - S_{lr} \cdot \left[1 - S_{le,Md}(s_0)\right]}{S_{le,Md}(s_0)} \tag{2.53}$$

where S_{lr} is the residual degree of saturation and $S_{le,Md}(s_0)$ is the effective degree of saturation value on the main drying curve at the reversal suction value s_0. Similarly, a wetting scanning curve (see Figure 2.19b) starting from the reversal point (suction s_0 and degree of saturation S_{l0}) is a scaled version of the main wetting curve which is forced to pass through the reversal point. In this case, to obtain this, the residual degree of saturation S_{lr} is replaced by a fictitious value S^*_{lr}, expressed as:

$$S^*_{lr} = \frac{S_{l0} - S_{ls} \cdot S_{le,Mw}(s_0)}{1 - S_{le,Mw}(s_0)} \tag{2.54}$$

where $S_{le,Mw}(s_0)$ is the effective degree of saturation value on the main wetting curve at the reversal suction value s_0. The scaling-down model has found many applications in numerical codes, like HYDUS [125], SWAP [126] and UNSAT-H [127] for its relatively simple and realistic form.

Unfortunately, the scaling-down model of Scott et al. [123] or Kool and Parker [121] may predict unrealistic results when used to model cyclic variations of suction, leading to the artificial "pumping effect" [128] that can move the scanning curves outside the main curves. In order to solve this drawback, Parker and Lenhard [129] proposed a modification to the model. This consisted in enforcing that the scanning wetting-drying loops must be closed, e.g. after reverting a drying path going from a point A to point B, the subsequent wetting path starting from B has to pass through point A. Let us consider an arbitrary wetting scanning curve starting at point $\left(s_{0,d-w}, S_{le0,d-w}\right)$, which is the most recent reversal point from drying to wetting, and passing through point $\left(s_{0,w-d}, S_{le0,w-d}\right)$, which is the reversal point from wetting to drying of the previous drying path. Both $S_{le0,d-w}$ and $S_{le0,w-d}$ are expressed as effective degrees of saturation. The wetting scanning $S_{le,w}(s)$ curve can be expressed as a scaled version of the main wetting curve $S_{le,Mw}(s)$ (both expressed in terms of the effective degree of saturation) to interpolate the two reversal point:

$$S_{le,w}(s) = \frac{\left[S_{le,Mw}(s) - S_{le,Mw}\left(s_{0,w-d}\right)\right] \cdot \left[S_{le0,d-w} - S_{le0,w-d}\right]}{S_{le,Mw}\left(s_{0,d-w}\right) - S_{le,Mw}\left(s_{0,w-d}\right)} + S_{le0,w-d} \tag{2.55}$$

Similarly, an arbitrary drying scanning curve $S_{le,d}(s)$ starting at point $\left(s_{0,w-d}, S_{le0,w-d}\right)$, which is the most recent reversal point from wetting to drying, and passing through point $\left(s_{0,d-w}, S_{le0,d-w}\right)$, which is the reversal point from drying to wetting of the previous drying path, can be expressed as a scaled version of the main drying curve $S_{le,Md}(s)$:

$$S_{le,d}(s) = \frac{\left[S_{le,Md}(s) - S_{le,Md}\left(s_{0,d-w}\right)\right] \cdot \left[S_{le0,w-d} - S_{le0,d-w}\right]}{S_{le,Md}\left(s_{0,w-d}\right) - S_{le,Md}\left(s_{0,d-w}\right)} + S_{le0,d-w} \tag{2.56}$$

Although this model solved the artificial pumping effect of the Kool and Parker [121] model, it has two drawbacks: (i) the prediction of wetting-drying loops which are always closed may be unrealistic; (ii) when implemented in a numerical code, the model may require high memory capacity because all the reversal points at all the positions of the numerical model must be saved.

More recently, various "bounding surface"-based models were proposed to represent the water retention hysteresis [118–120, 130]. In all these models, the slope of a scanning curve (e.g. a drying scanning curve) in the $S_{le} : s$ plot is proportional to the slope of the corresponding main curve (e.g. the main drying curve) at the same effective degree of saturation. Unlike the Jaynes [117] model, the proportionality factor depends on the horizontal distance (i.e. suction difference) between the current point on the scanning curve and the corresponding point on the main curve at the same effective degree of saturation: the closer the current state is to the corresponding main curve, the more similar is the slope of the scanning curve to that of the main curve. Li [118] was the first to adopt this type of bounding surface approach to describe

the hysteretic SWRC behaviour. Zhou et al. [119] slightly simplified Li's hysteretic SWRC model by removing a varying "projection centre", which is needed to define the mapping rule for the scanning curves, and locating it either at $s = 0$ for drying scanning curves or at $s = +\infty$ for wetting scanning curves. Gallipoli et al. [120] subsequently applied the Zhou et al. hysteretic water retention model, in conjunction with the van Genuchten [82] model for the main SWRC curves, in a coupled hydro-mechanical constitutive model. According to Zhou et al. [119], the slope of a wetting scanning curve $\frac{dS_{le,w}}{ds}$ can be expressed as a proportion of the slope of the main wetting curve $\frac{dS_{le,Mw}}{ds}$ at the same degree of saturation (both expressed in terms of the effective degree of saturation) (see Figure 2.19c), as follows:

$$\frac{dS_{le,w}}{ds} = \left(\frac{s_w}{s}\right)^{\gamma_w} \frac{dS_{le,Mw}}{ds_w} \tag{2.57}$$

where s_w is the image value of suction on the main wetting curve, namely the suction corresponding to the main wetting curve at the same effective degree of saturation as the current point on the wetting scanning curve. The parameter γ_w is a positive fitting parameter which controls the gradient of the scanning curve: for $\gamma_w = 0$ the wetting scanning curve has the same shape as the main wetting curve (with a fixed horizontal translation), for $\gamma_w \to +\infty$ the predicted wetting scanning curve tends to a horizontal straight line until it reaches the main wetting curve. Similarly, the slope of a drying scanning curve $\frac{dS_{le,d}}{ds}$ and the slope of the main drying curve $\frac{dS_{le,Md}}{ds}$ at the same degree of saturation are linked via:

$$\frac{dS_{le,d}}{ds} = \left(\frac{s}{s_d}\right)^{\gamma_d} \frac{dS_{le,Md}}{ds_d} \tag{2.58}$$

where s_d is the image value of suction on the main drying curve and γ_d is a positive fitting parameter. Bounding surface hysteretic water retention models have the potential to be applied extensively because they can predict realistic results, they have a relatively simple form, which makes them also applicable in numerical codes and in coupled hydro-mechanical constitutive models, and they need a maximum of two parameters (γ_w and γ_d) to describe scanning wetting and scanning drying curves.

All the models presented for the water retention hysteresis have a common weakness: they are generally coupled with conventional SWRC models which, as discussed before, are not able to predict accurately the hydraulic behaviour of unsaturated soils at low values of degree of saturation. Moreover, although the hysteresis of the SWRC has been modelled extensively, little research effort has been put into coupling hysteretic SWRC models with unsaturated hydraulic conductivity models. When a SHCC model is used in conjunction with a hysteretic SWRC model, the SHCC is typically considered non-hysteretic when expressed as a function of the degree of saturation [31, 121, 131], i.e. as $k_l(S_l)$. By contrast, the SHCC presents a highly hysteretic behaviour when expressed as a function of suction, i.e. as $k_l(s)$, due to the indirect effect of the hysteresis in the SWRC.

Recently, Rudiyanto et al. [132] proposed a complete hydraulic model for unsaturated soils accounting for hydraulic hysteresis and for improved modelling of SWRC and SHCC

at low degree of saturation. In particular, they combined the model proposed by Peters [91] and Iden and Durner [92] for the main SWRCs and for the SHCC and the model proposed by Parker and Lenhard [129] to introduce water retention hysteresis in the SWRC and in the SHCC. This model represents an interesting contribution towards a complete hydraulic model for unsaturated soils, improved at low degree of saturation and including water retention hysteresis. However, it is affected by some weaknesses: (i) the bulk water component of the hydraulic conductivity is overpredicted at low degree of saturation (this aspect will be discussed in more detail in Chapter 3); (ii) the liquid film component of the hydraulic conductivity is not predictive, i.e. it needs SHCC data at very low degree of saturation to be calibrated; (iii) the hysteretic water retention model proposed by Parker and Lenhard [129] is affected by weaknesses discussed above. For this reason, a new hydraulic constitutive model for unsaturated soils was proposed and it is described in Chapter 3.

Finally, the effect of air trapping during wetting has been included in several hydraulic models [e.g. 121, 129, 133, 134]. All of them propose wetting curves which do not reach full saturation even when suction is equal to zero. Although this represents a pragmatic and useful approach, these wetting SWRCs are not realistic because they are based on the use of an apparent suction, which is the suction imposed or monitored at the boundaries. However, once the air is trapped, the pore-gas pressure in the trapped air bulbs increases with respect to that imposed at the boundaries and the actual suction within the soil is consequently higher than that applied and monitored at the boundaries. The apparent SWRC is therefore not only a property of the material but also a result of the specific test conditions, like the degree of saturation at the beginning of the wetting process [135], the rate of wetting and the physical size of the test specimen or the boundary value problem. On the other hand, the actual SWRC is only a property of the soil and reaches full saturation when suction is sufficiently decreased. In order to fill this gap between the physics of the phenomenon of air trapping and the way it is typically modelled, a new interpretation of the phenomenon will be discussed in Chapter 5 through the use of analytical modelling and numerical simulations.

2.3 Capillary barrier systems

2.3.1 Basic principles

In the last three decades, the need of making efficient landfill covers has led to development of different surface cover systems aimed to prevent or limit the infiltration of water into the underlying soil in order to avoid contamination. Among these, one of the most important is the capillary barrier system [21].

A conventional capillary barrier system (CBS) is a geotechnical system made of two layers, an upper finer-grained layer (FL), generally ranging from a sandy silt to a fine sand, overlying a coarser-grained layer (CL), generally ranging from a coarse sand to a gravel, placed over the landfill material or a generic original soil (see Figure 1.3c).

The working principle of a CBS [23] is based on the contrast between the hydraulic

properties (soil water retention curve (SWRC) and soil hydraulic conductivity curve (SHCC)) of the two materials (see Figure 2.20). In saturated conditions, the hydraulic conductivity of the coarser layer is typically many orders of magnitude higher than that of the finer layer. By contrast, in unsaturated conditions, at relatively high values of suction the situation may be significantly different. At a given value of suction, the coarser layer will typically be at much lower degree of saturation than the finer layer, because of differences in the water retention behaviour (see Figure 2.20a). As a consequence, the coarser layer will typically be much less hydraulically conductive than the finer layer (see Figure 2.20b). Hence, prior to significant water breakthrough into the coarser layer, it is this coarser layer that acts as the low permeability barrier, as long as it remains at high suction values (low degree of saturation). If these conditions are maintained, the infiltrating water is stored in the finer layer and then removed by evapotranspiration and, if the barrier is sloped, lateral drainage.

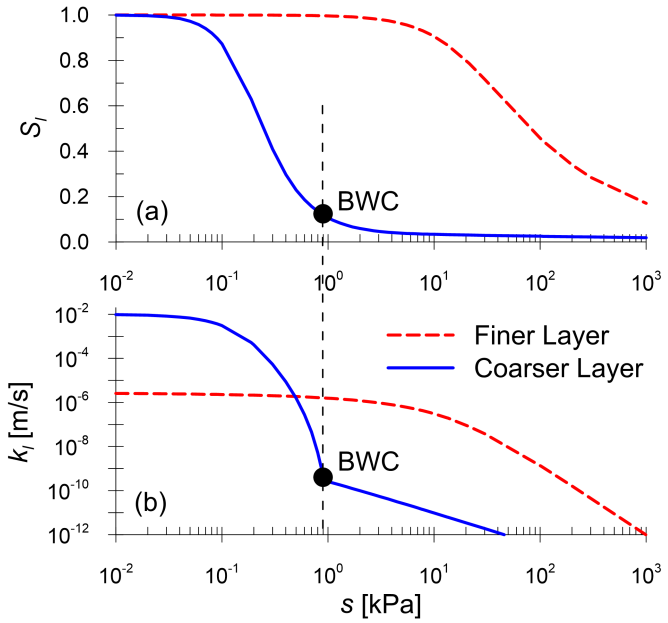

Figure 2.20: Typical (a) water retention curves and (b) hydraulic conductivity curves for the materials of a capillary barrier system

The conditions in which capillary barriers are effective (relatively high suction values at the interface between coarser layer and finer layer) may be lost if sustained heavy rainfall events occur. If a large amount of water is stored in the lower part of the finer layer, near the interface between the two layers, suction decreases in that position. Equilibrium of the liquid phase means that the matric suction s has to be continuous across the interface between the two layers. Thus, as suction decreases at the bottom of the finer layer, it also decreases at the top of the coarser layer. If this suction at the interface decreases sufficiently, the coarser layer becomes hydraulically conductive (its hydraulic conductivity increases significantly), breakthrough occurs and water starts flowing easily from the finer layer to the coarser layer and ultimately into the underlying soil, making the capillary barrier system fail. Breakthrough, which can be identified with a rapid increase of percolation into the coarser layer, can then be defined as the moment when bulk water first forms a continuous liquid network in the coarser layer and significant amounts of water start entering it [23].

2.3.2 Water balance

The hydraulic behaviour of capillary barrier systems [136] is governed by the following water balance equation (see Figure 2.21), applied to the finer layer:

$$P - ET = R_{off} + Br + LD + \frac{d(WS)}{dt} \tag{2.59}$$

where P is the precipitation rate, ET is the evapotranspiration rate, R_{off} is the surface runoff, Br is the percolation rate across the interface between the finer layer and the coarser layer following water breakthrough, LD is the lateral drainage flow rate and $\frac{d(WS)}{dt}$ is the variation of the water storage in the finer layer WS over time. All the terms here can be expressed as a volume (or as a mass) per unit time per unit plan area [LT^{-1}] (or [$ML^{-2}T^{-1}$]).

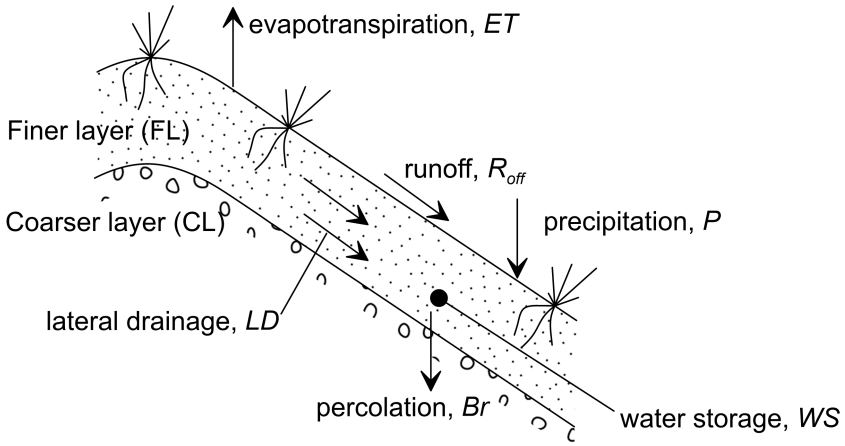

Figure 2.21: Water balance for capillary barrier systems

Runoff R_{off} occurs when suction at the soil surface becomes equal to zero, which is generally caused by maintaining a rainfall intensity higher than the saturated hydraulic conductivity of the finer layer [137–139]. Typically, runoff is very limited for CBSs because even the finer layer is made of a relatively coarse-grained material, which has a saturated hydraulic conductivity higher than usual precipitation rates. Percolation Br, which occurs at breakthrough, is the term that should be minimised, according to the aim of the barrier. Once breakthrough occurs, water percolated into the coarser layer quickly reaches the underlying soil. When a CBS is applied as a landfill cover, suggested limit values are 10 mm/year percolation in semi-arid climates and 30 mm/year percolation for humid climates [140]. Lateral drainage LD, which occurs only in sloping CBSs, and water storage WS are the most studied terms by researchers studying the fundamental behaviour of capillary barrier systems, because maximising these will reduce the risk of significant percolation Br. These terms (LD and WS) are analysed further in the following sections.

2.3.3 Horizontal capillary barrier systems

In a horizontal capillary barrier system (i.e. non-sloping) no lateral drainage occurs ($LD = 0$). In addition, if runoff is considered negligible ($R_{off} = 0$) and the CBS is to be perfectly

effective in preventing percolation ($Br = 0$), Equation 2.59 becomes:

$$P - ET = \frac{d(WS)}{dt} \tag{2.60}$$

In these conditions, the only way to handle the rainfall water in wet periods (i.e. when $P > ET$) is using the storage ability of the finer layer. A significant research effort has been addressed towards the evaluation of the "water storage capacity" (WSC) of CBSs, defined as the maximum amount of water that can be stored in the finer layer before water breakthrough occurs through the interface between finer layer and coarser layer. The water storage capacity can be evaluated through the following steps (after Stormont and Morris [141]):

1. evaluate the SWRCs of the materials expressed in terms of volumetric water content, $\theta_l(s)$;

2. evaluate the suction profile in the finer layer at breakthrough $s_{br}(z)$, where z is the elevation;

3. obtain the volumetric water content profile at breakthrough $\theta_{l,br}(z)$, by means of the SWRC and the suction profile at breakthrough (i.e. $\theta_{l,br}(z) = \theta_{l,br}(s_{br}(z))$);

4. calculate the WSC, by integrating the volumetric water content profile at breakthrough over the thickness of the finer layer t_f, as follows:

$$WSC = \int_0^{t_f} \theta_{l,br}(z)\, dz \tag{2.61}$$

   where z is here the elevation starting from the interface between coarser and finer layer ($z = 0$) and directed upward.

The understanding of the conditions at breakthrough (particularly the suction profile and the corresponding volumetric water content profile in the finer layer) is a crucial point for the assessment of the water storage capacity. For this reason, several experimental studies have been carried out in order to identify the properties of the breakthrough phenomenon [23, 138, 142, 143] and the key concepts are summarised below.

Before breakthrough, no significant movement of water across the interface between the finer layer (FL) and the coarser layer (CL) was observed experimentally [23]. Significant amounts of water start moving across the interface when the water filling the soil pores (i.e. the bulk water) starts forming a continuous liquid path across the interface between the FL and the CL [23]. In this thesis, as discussed later in Section 3.1, the point at which the bulk water starts forming a continuous liquid path during a wetting process in an unsaturated soil will be called the "bulk-water continuity" (BWC) point. From infiltration tests in different capillary barrier systems, Stormont and Anderson [23] showed that the bulk water continuity suction value of the coarser layer can be identified approximately as the bend in the main wetting SWRC of the coarser layer at low degree of saturation (see Figure 2.20). They also showed that the suction at the interface at the time of breakthrough does not vary with the

infiltration rate (i.e. the vertical flow rate into the soil at the ground surface) since it is a property of the material (the value of suction at the BWC point). At the bulk water continuity point, the hydraulic conductivity of an unsaturated soil increases dramatically since water starts flowing through the pores filled with bulk water. Thus, water breakthrough in a CBS occurs when the suction at the interface attains the bulk water continuity suction value s_{BWC} of the coarser layer.

Unlike the suction value at the interface between F.L. and C.L. at breakthrough, the suction profile in the finer layer at breakthrough depends on the infiltration rate [23, 138, 141]. Figure 2.22a shows, for a given pair of materials for the C.L. and the F.L., the suction profiles in the finer layer at breakthrough corresponding to the application of different constant infiltration rates i_1, i_2, i_3 and i_4 to a CBS initially at a relatively dry state. In these conditions, when a water infiltration is applied from the surface at a constant rate i, water velocity at all depths in the finer layer (at all times) must be less than or equal to i, because the entire finer layer experiences monotonic wetting (i.e. no element of soil can have greater water outflow at bottom than inflow at top). As breakthrough time is approached, water storage capacity has been achieved at all depths within the finer layer (i.e. there is no net inflow to soil elements at any depth in the finer layer) and hence the water velocity is now equal to the infiltration rate i throughout the entire finer layer. Hence, according to Darcy's law, at the time of breakthrough, the product of hydraulic conductivity of the material of the finer layer $k_{l,f}$ and hydraulic gradient $\partial h_l/\partial z$ must be equal to i at all depths in the finer layer. The suction value at the interface is the BWC suction value of the coarser layer, regardless of the applied infiltration rate (see Figure 2.22a). Thus, at the bottom of the F.L. the material of the F.L. will be at a high value of degree of saturation and a correspondingly high value of $k_{l,f}$, that is much larger than the value of i. As a consequence, the value of hydraulic gradient $\partial h_l/\partial z$ at this location must be much less than 1, i.e. almost zero, indicating a suction variation with elevation that is indistinguishable from a hydrostatic variation. Moving upwards through the F.L., the value of suction increases, according to the (almost) hydrostatic variation, and hence the degree of saturation falls and so does the hydraulic conductivity $k_{l,f}$. However, there will typically be a significant part of the finer layer where the value of $k_{l,f}$ is still much larger than the value of i, indicating that the value of $\partial h_l/\partial z$ is still much less than 1, and hence the suction variation is still approximately hydrostatic. If the infiltration rate is very low (see i_1 in Figure 2.22a), the situation described above will apply throughout the entire finer layer, and the suction variation will be approximately hydrostatic right up to the ground surface. If, however, the infiltration rate is higher (see i_2, i_3 and i_4 in Figure 2.22a), there will come a point on moving upward through the finer layer where it is no longer true to say that k_l is much greater than the water velocity i and hence the hydraulic gradient must start to become significantly greater than zero i.e. the suction variation begins to diverge from a hydrostatic profile. Moving upward, the suction profile may ultimately attain a suction value s^* at which the hydraulic conductivity of the F.L. reaches a critical value that is equal to the water velocity i, i.e. $k_{l,f}(s^*) = i$ (see Figure 2.22b). At this point, Darcy's law indicates that the hydraulic gradient $\partial h_l/\partial z$ must have a value of 1. A hydraulic gradient of 1 corresponds to a situation

where suction is not changing with elevation. Hence, from this point up to the ground surface the suction remains constant at this value. Any decrease or increase of suction with elevation from this point would lead to logical inconsistencies. Given that the nature of the SHCC means that large changes of k_l can occur for relatively small changes of suction in particular for coarse-grained materials, the transition from a situation where k_l is much greater than i (quasi-hydrostatic profile) to a situation where k_l is equal to i (constant profile) can occur over a relatively small change of elevation. Hence, a simplified bi-linear suction profile is a reasonable approximation of the true suction profile.

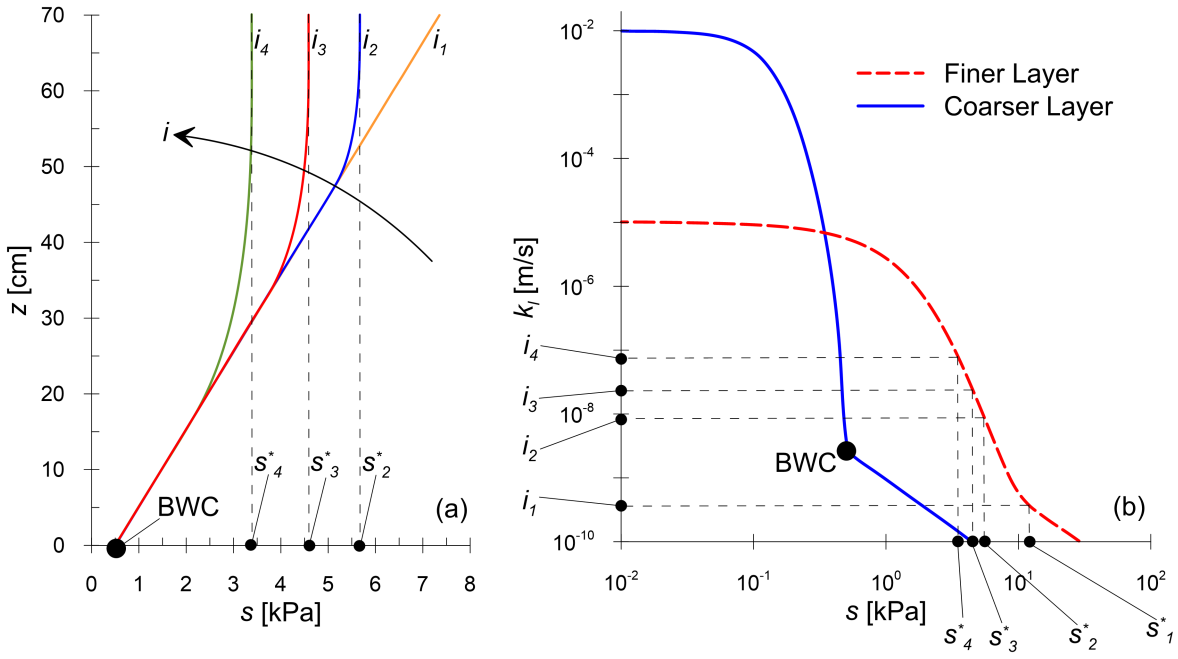

Figure 2.22: (a) Suction profiles in the finer layer at breakthrough for different applied infiltration rates and (b) corresponding SHCCs

Stormont and Morris [141] and Khire et al. [144] performed parametric numerical analyses on horizontal capillary systems to investigate the effects of different parameters on the water storage capacity of CBSs and, more generally, on the hydraulic response of CBSs when subjected to different weather conditions. Weather conditions were identified as a key variable: cooler and wetter climates represent more demanding conditions for effective functioning of CBSs and the winter period is typically critical because the total amount of rainfall is often higher than in summer and the evapotranspiration is lower. The choice of materials for the finer layer strongly affects the efficiency of the barrier: the use of coarse materials (e.g. sand) or overly fine materials (e.g. clay) led to higher amounts of percolation into the coarser layer whereas intermediate materials, such as silt, silty sand, sandy silts, loam, silt loam and clayey sands were found to be the optimum for horizontal CBSs [141, 144]. Moreover, the use of too fine-grained materials also generates other problems compromising the durability of CBSs, like desiccation cracking and surface erosion [14]. For the coarser layer, the use of materials with lower BWC values leads to an increased water storage capacity because the suction profile in the finer layer at breakthrough will attain lower values of suction and

hence higher values of degree of saturation. The thickness of the coarser layer was found not to be an important parameter: Khire et al. [144] suggest a value of 30 cm whereas Yang et al. [145] suggest a minimum value of $s_{c,BWC}/\gamma_l$, where $s_{c,BWC}$ is the bulk-water continuity suction value of the coarser layer and γ_l is the unit weight of liquid. On the other hand, the thickness of the finer layer is an important parameter: in general, as the thickness of the finer layer increases the water storage capacity of the CBS increases. However, the gain in water storage capacity obtained by increasing the thickness of the finer layer is negligible beyond a certain value. This thickness value depends on the material of the FL: the coarser the soil, the lower is this thickness [141].

From experimental infiltration column tests, Yang et al. [145] suggested that, in order to generate a sufficiently effective contrast in the hydraulic properties of the FL and CL, the saturated hydraulic conductivity of the CL should be between 2 and 3 orders of magnitude higher than that of the FL. With the same purpose, Rahardjo et al. [146] suggested that the ratio between the bulk water continuity suction value of the finer layer $s_{f,BWC}$ and the bulk water continuity suction value of the coarser layer $s_{c,BWC}$ should be higher than 10. They also suggested that $s_{c,BWC}$ should be lower than 1 kPa for effective operation of the CBS.

The behaviour of the CBS during and after breakthrough has also been studied. Experimental research works show that breakthrough is always a relatively sudden phenomenon, compared to the overall period of rainfall infiltration, even when the infiltration rate is low and the time to breakthrough is correspondingly long. Figure 2.23 provides the result of a one-dimensional infiltration laboratory test carried out on a capillary barrier by Stormont and Anderson [23]. It can be seen that breakthrough, which occurred after approximately 48 days from the beginning of the experiment, was a very fast phenomenon if compared to the duration of the experiment. During percolation into the coarser layer (from day 48 to day 57.7) the steady-state condition in the barrier was rapidly reached and the percolation rate equalled the applied infiltration rate. After the infiltration was stopped (day 57.7), "restoration of the barrier" was observed: the percolation into the coarser layer decreased until it ceased and suction at the interface increased up to the suction value at which the bulk water in the coarser layer became discontinuous and the corresponding hydraulic conductivity decreased dramatically. In this thesis, this point is referred to as the "bulk water discontinuity" (BWD) point, which is defined as the point at which the bulk water becomes discontinuous along a main drying path (see Section 3.1). Similar to the BWC point (which is taken from a main wetting SWRC), the BWD point can be identified as the bend in the main drying SWRC at low degree of saturation. Beyond this point in the infiltration test (see Figure 2.23), no changes in suction at the interface and water content of the coarser layer were observed and a "static non-equilibrium condition" [147] was reached. In this condition the maximum suction values that develop during drainage in the coarser layer are approximately the same as those developed at the bulk water discontinuity point BWD. Although not in hydrostatic equilibrium, this condition will persist for long time without other mechanisms of moisture transport (i.e. liquid film flow or vapour flow). The time required for the restoration of the barrier depends on the hydraulic properties of the materials: the coarser the soil, the faster is

the restoration of the barrier [23].

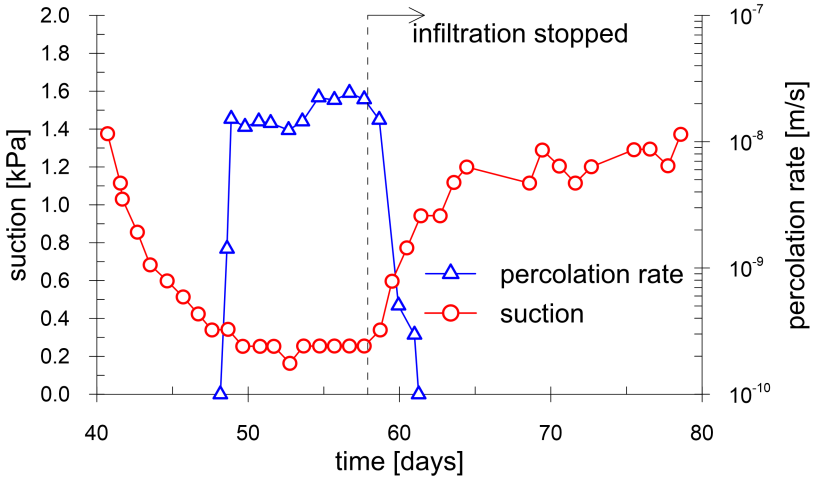

Figure 2.23: Time history of the percolation rate into the coarser layer and suction at the bottom tensiometer location (10 mm above interface) before, during and after breakthrough for initial infiltration $i = 3.2 \times 10^{-8}$ m/s into a silty sand over pea gravel column (after Stormont and Anderson [23])

The numerical simulation of the processes discussed above has often been performed using conventional hydraulic constitutive models which are not accurate at low degree of saturation (see Section 2.2). An improved hydraulic constitutive model at low degree of saturation developed in this thesis (Chapter 3) was applied to the numerical study of the fundamental behaviour of CBSs, as will be discussed in Chapter 6.

2.3.4 Sloping capillary barrier systems

Sloping capillary barriers have the capacity of diverting water laterally within the finer layer ($LD > 0$ in Equation 2.59). Figure 2.24 shows a simplified model demonstrating how lateral diversion works within the barrier when a uniform constant infiltration rate i is applied at the surface and a steady-state condition is reached. At the top of the slope, infiltrating water starts entering the finer layer, suction at the interface between finer and coarser layers is relatively high since the water content is low, the coarser layer behaves as an impermeable layer and water is diverted laterally down the finer layer due to the effect of gravity. Moving down the slope, the amount of water flowing laterally within the finer layer increases. Hence the water content at the base of the finer layer is greater than that up the slope, and the suction at the interface decreases. If the suction at the interface decreases down to a point where suction equals the BWC suction value of the coarser layer this becomes highly hydraulically conductive (breakthrough occurs). Beyond that point, no more water can be diverted laterally and infiltrating water becomes percolation into the coarser layer, i.e. in the lower part of the slope the percolation into the coarser layer is equal to the infiltration rate [148]. The "diversion capacity" $Q_{D,max}$ of the barrier is defined as the amount of water flowing laterally per unit thickness out of plane (i.e. units are L^2/T) beyond the point where breakthrough commences (see Figure 2.24). Therefore, $Q_{D,max}$ represents the maximum quantity of infiltrating water

that the barrier can divert. The "diversion length" L_D of the barrier is the length in the down-dip direction to a point where breakthrough commences and the barrier does not divert any additional water [149].

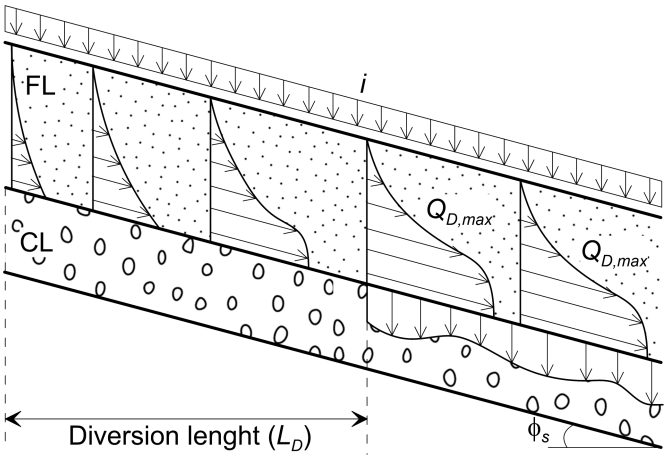

Figure 2.24: Lateral water diversion in a sloping capillary barrier system (after Parent and Cabral [150])

The first important study regarding the diversion capacity of CBSs was done by Ross [148] who obtained a simple analytical upper bound solution for the diversion capacity $Q_{D,max}$ and the corresponding diversion length L_D, expressed in the following relationships:

$$Q_{D,max} < \frac{k_{ls,f} \tan \phi_s}{\alpha_k} \tag{2.62}$$

$$L_D = \frac{Q_{D,max}}{i} < \frac{k_{ls,f} \tan \phi_s}{\alpha_k i} \tag{2.63}$$

where $k_{ls,f}$ is the saturated hydraulic conductivity of the finer layer, ϕ_s is the slope angle, i is the infiltration rate and α_k is the sorptivity number of the finer layer, where Ross [148] assumed that the SHCC could be described by an exponential relationship between hydraulic conductivity k_l and suction s ($k_l = k_{ls} e^{-\alpha_k s/\gamma_l}$ where k_{ls} is the saturated hydraulic conductivity and γ_l is the unit weight of liquid). Ross' solution was obtained under the following assumptions: deep water table, very thick layers, linear approximation between the logarithm of hydraulic conductivity and suction ($k_l = k_{ls} e^{-\alpha_k s/\gamma_l}$) for the SHCC, inclined interface much longer than the diversion length, constant vertical infiltration rate applied uniformly and steady-state condition.

Steenhuis et al. [151] revised Ross' solution using a different assumed form for the SHCC, suggesting that the log-linear approximation of Ross may not be reliable for water contents close to saturation (low suction values).

Stormont [152] expanded Ross' solution in order to take into account the effect of anisotropy in the hydraulic conductivity of the finer layer. Stormont's solution, in terms of both $Q_{D,max}$ and L_D, is a sum of two terms: the first is related to the diversion due to the capillary barrier effect (similar to Ross' solution) and the second refers to the anisotropy of the finer layer. The latter term varies approximately linearly with the ratio between the principal hydraulic conductivities of the finer layer.

Oldenburg and Pruess [153] studied the behaviour of sloping CBSs numerically using the finite difference method. They supported the theoretical solution of Ross, by comparing Ross' predictions and numerical results obtained using the log-linear approximation for the SHCC. The use of the log-linear approximation was validated by Webb [154] who obtained similar results using the theoretical Ross' formula and numerical analyses where the van Genuchten [82] model was used for the SWRC coupled with the Mualem [95] model for the SHCC.

The validity and the reliability of Ross' solution has also been proved experimentally, although it was found to be slightly conservative (i.e. it slightly underestimated the value of $Q_{D,max}$) [155–157].

As for the breakthrough condition for sloping barriers, different authors [150, 153, 158] showed that the phenomenon is more complicated than the assumptions of Ross who, in his steady-state analysis, assumed no percolation up to the diversion length and constant uniform percolation (equal to the infiltration rate i) beyond the diversion length. In fact, breakthrough in capillary barriers appears to be a more gradual phenomenon along the interface. Moreover, Oldenburg and Pruess [153] showed that at breakthrough, percolation greater than the infiltration rate tends to take place, thereby partially drying out the finer layer. In this way, the barrier becomes effective again in the down-dip direction. Webb [154], however, subsequently showed that this was due to the assumption of a shallow water table by Oldenburg and Pruess [153].

Kämpf and Montenegro [159] proved the ability of capillary barriers at diverting water by means of field tests, laboratory tests and numerical analysis. They found good agreement between the different results, although they recognized that temperature effects need to be considered moving from laboratory tests to field tests. They also pointed out that numerical modelling is able to describe with reasonable accuracy the lateral diversion behaviour.

Zhan et al. [156] analysed the effects of studying the diversion process by means of transient simulations instead of using solutions based on the assumption of steady-state conditions. They carried out numerical infiltration tests on a slope for the case where infiltration at a constant rate commences at the time $t = 0$. They recorded, from the beginning of the test, the position where a significant amount of percolation occurred, which can be seen as the diversion length in transient analysis but, in this case, this length is not constant. The corresponding diversion length in transient analysis has a maximum value at the beginning of the analysis which is limited by the length of the slope, and this diversion length then decreases over time, tending to an asymptotic value that is slightly higher than that obtained by Ross' steady-state solution, which is recognized to be moderately conservative. A similar result was obtained by Lacroix Vachon et al. [157] who also recognized a better agreement of their asymptotic result with the steady-state model proposed by Parent and Cabral [150].

The model proposed by Parent and Cabral [150] to calculate the diversion capacity and the diversion length of the sloping barrier uses a similar approach to that used by Ross but they considered a more realistic representation of the suction profile at breakthrough. In addition, unlike Ross' model, any SHCC model can be used in their relationship. They ultimately

obtained the following equations:

$$Q_{D,max} = k_{ls,f} \tan \phi_s \int_{s_{BWC,c}}^{s_f^*} \frac{k_{lr,f}(s)}{\gamma_l} ds \tag{2.64}$$

$$L_D = \frac{Q_{D,max}}{i} \tag{2.65}$$

where $k_{lr,f}(s)$ is the relative hydraulic conductivity of the finer layer, $s_{BWC,c}$ is the bulk water continuity value of the coarser layer and s_f^* is the maximum suction attained in the finer layer, which depends on the infiltration rate and the SHCC of the finer layer (see Section 2.3.3).

2.3.5 Multi-layered capillary barrier systems

The effectiveness of capillary barriers has been proved in arid and semi-arid climates but they have been found to be ineffective in preventing water percolation in humid climates [160]. In order to improve the effectiveness of CBSs, in both horizontal and sloping configurations, different non-conventional CBSs have been proposed (see Figure 2.25).

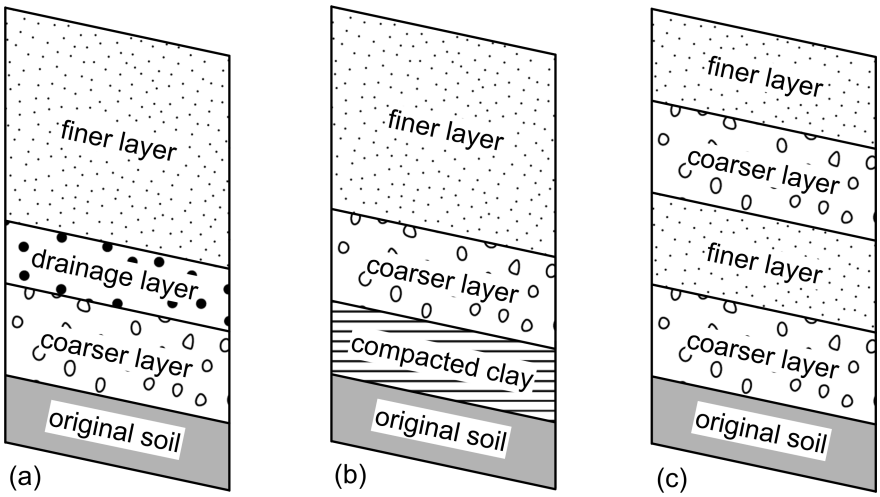

Figure 2.25: Non conventional capillary barrier systems: (a) capillary barrier with drainage layer [161], (b) three-layer capillary barrier [162] and (c) dual capillary barrier [27]

Different studies demonstrated that the inclusion of an unsaturated drainage layer between the finer layer and the coarser layer (see Figure 2.25a) causes a significant improvement of the diversion capacity of sloping CBSs [29, 136, 149, 150, 156, 160, 161]. The drainage layer must have high values of hydraulic conductivity for a range of suction from low to moderate such that the diversion capacity $Q_{D,max}$ expressed in Equation 2.64, now used for the intermediate sand layer, is maximized. The most suitable material was identified as a uniform, fine-to-medium grained sand that is generally coarser than the overlying finer layer and finer than the underlying coarser layer.

The three-layer barrier of Figure 2.25b [162] relies on the inclusion of a compacted clay layer under a classical capillary barrier. In wet periods, the upper capillary barrier may fail and the compacted clay layer becomes useful in preventing downward water movement because of its very low hydraulic conductivity even in saturated conditions; in dry periods, the upper

capillary barrier is effective, the unsaturated hydraulic conductivity of the two upper layers is so low as to prevent evaporation of water from the clay layer which, otherwise, might be affected by desiccation cracking. Ng et al. [163] and Ng et al. [164] demonstrated that the three-layer barrier is also very effective in diverting water laterally. Indeed, in wet conditions the clay layer behaves as an impermeable layer and the coarser layer behaves as a transport layer.

The concept of the dual capillary barrier (see Figure 2.25c) was firstly introduced by Harnas et al. [27]. This barrier relies on a double capillary barrier effect at the interfaces between a finer layer and an underlying coarser layer. The use of the dual CBS was shown to lead to a higher water storage capacity [27] and to an increase of the diversion capacity [165].

Although the dual capillary barrier was shown to be more effective than a single capillary barrier [27, 165], the role of the parameters affecting the gain in water storage capacity obtained by layering was not clear. In this thesis, the concept of dual capillary barrier was extended to multi-layered capillary barrier systems and it will be discussed in Chapter 7. The role of the different parameters was identified through a parametric study. Moreover, a simplified theoretical method for determining the optimum design of a multi-layered CBS was proposed and validated by means of numerical simulations and experimental laboratory tests.

2.3.6 Effect of water retention hysteresis

Water retention hysteresis is expected to be relevant in the modelling of the behaviour of capillary barrier systems since they are subjected to multiple cycles of rain (wetting) and evapotranspiration (drying). Nevertheless, surprisingly, water retention hysteresis is very often neglected in the numerical analysis of capillary barriers. One of the very few contributions to address this was by Zhang et al. [166], who demonstrated the importance of considering water retention hysteresis in numerical modelling of capillary barriers. They modelled the SWRC and the SHCC of finer and coarser layers during main wetting and main drying using the van Genuchten [82]-Mualem [95] model whereas the scanning curves were modelled using the Kool and Parker [121] scaling model. They concluded that the most important effects of retention hysteresis on the behaviour of capillary barriers are:

- higher water storage;
- higher evaporation rate at the ground surface once infiltration stops (hence quicker re-charge of storage capacity);
- lower percolation into the coarser layer.

Therefore, Zhang et al. [166] showed that water retention hysteresis has beneficial effects for capillary barriers. However, given the lack of studies on this aspect, further investigation is required. In this thesis, a new hysteretic hydraulic model (see Section 3.4) was applied to the numerical study of CBSs (see Section 6.2), providing further insights into the significance of water retention hysteresis for the performance of CBSs.

2.3.7 Application of capillary barrier systems

As previously stated, capillary barriers have been mostly studied as landfill cover systems [29] and, only recently, they have started to be seen as a means of controlling suction in the ground [167]. Moreover, it was shown that CBSs can be constructed using low quality and recycled materials, like recycled asphalt [165] and recycled concrete aggregates [168].

Recent studies have particularly addressed the application of CBSs for slope stabilization. The stability of slopes is often achieved by the effect of suction, which imparts higher strength to the soil, compared to fully dry and fully saturated conditions. However, suction may vanish or greatly decrease after prolonged and heavy rainfall. In these cases, significant reductions in shear strength may induce slope instability. Capillary barriers may represent an efficient means to stabilize slopes against rain because of their ability of avoiding or limiting the percolation of water into the underlying soil.

The effectiveness of CBSs for slope stability purposes was proven by Rahardjo et al. [168–170] by means of three different field tests. They constructed CBSs in three different areas in Singapore which had previously experienced rainfall-induced slope instabilities. They monitored the slopes covered by CBSs and the original bare slopes with tensiometers and piezometers. They showed that, compared to the original slopes, in all slopes covered by CBSs lower values of pore-liquid pressure were maintained even during rainfall events, with a consequent increase in the calculated factor of safety of the slopes.

Harnas et al. [165] carried out numerical analyses focusing on a particular case study and they compared the results obtained from three models: slope without capillary barrier, slope with a standard capillary barrier and slope with a dual capillary barrier (Figure 2.25c). They showed that the use of both the barriers reduced the risk of slope instability and that the dual capillary barrier was the most effective at maintaining suction in the original soil.

More recently, the concept of a Geobarrier system was introduced by Rahardjo et al. [171] as an alternative retaining wall design. A Geobarrier system combines the concepts of a geobag type of wall [172], which serves as a retaining wall, and a capillary barrier system, which serves as a means to prevent water infiltration. This combined system, which can be made of recycled low quality materials, has lower environmental impact, lower cost, better aesthetics and shorter construction time than conventional retaining wall design. The proposed system was constructed and monitored for a field study and analysed numerically [171]. It was shown that suction in the compacted backfill was maintained also during rainfall and that the local stability of the Geobarrier system was not affected by rainfall. Although promising, this system still requires further research.

Although recent studies showed the potential of CBSs for suction control and slope stabilization purposes, further research on this aspect is still required. In particular, the following literature gaps were identified and were studied in the research presented in this thesis:

- **Advanced numerical modelling of the application of CBSs.** The behaviour of capillary barriers has been often studied numerically by means of simplified analyses, e.g.

without considering water retention hysteresis, with a poor description of the hydraulic behaviour of unsaturated soils at low degree of saturation and with poor modelling of the complex phenomenon of soil-atmosphere interaction in the long term. Advanced numerical modelling procedures covering all these aspects were used in the current work.

- **Role of the parameters.** The roles of the different parameters affecting the application of CBSs for suction control and slope stability (e.g. geometry of the slope, geometry of the CBS, materials and weather conditions) have not previously been thoroughly investigated, and they were analysed numerically in the current study.

- **Application to wet and cool climates.** Different studies have been carried out in order to try to extend the applicability of CBSs to wet climates like those in Hong Kong [164], Singapore [173] and some regions of China [174]. Although these areas are characterized by high amounts of rainfall, the high temperatures mean that evaporation rates are also very high. In the current work, the application of capillary barriers in areas where the amount of precipitation is high and the amount of evapotranspiration is low, due to relatively low temperature (e.g. in the UK), namely where the term $P - ET$ of the water balance equation (Equation 2.59) is higher than zero over the entire year, was studied numerically.

2.4 Modelling soil-atmosphere interaction

The term soil-atmosphere interaction refers to all those phenomena of mass (liquid and gas) exchange and energy exchange occurring between soil and atmosphere and to the many phenomena affecting the state or the structure of the soil which are caused by environmental and atmospheric conditions, e.g. desiccation cracking and freeze-thaw cycles. The term interaction means a bi-directional activity: the soil is directly affected by atmospheric conditions but also the atmosphere is affected by the conditions of the soil. For instance, evaporation into the atmosphere from a soil surface at high water content will occur at higher rate than from a similar soil surface at lower water content and the incoming solar radiation will be less reflected from a darker surface (e.g. a bare soil) than from a lighter surface (e.g. a grassed surface).

Soil-atmosphere interaction plays a crucial role in many geotechnical problems although is has been often treated with grossly simplifying assumptions. However, more recently the geotechnical community understood the need for more accurate modelling of soil-atmosphere interaction. For example, Blight [175] gave the 37th Rankine Lecture on the interpretation of soil-atmosphere interaction and on the measurement of the different significant components, Fredlund et al. [176] dedicated a chapter of their book to this topic and Elia et al. [177] published an interesting review about modelling strategies of soil-atmosphere interaction with particular reference to slope stability.

This section provides the reader with an overview of key phenomena involved in soil-atmosphere interaction, modelling approaches and effects on evaporation from soils.

2.4.1 Water balance and energy balance

Several phenomena of mass and energy transfer occur between the soil surface and the atmosphere. Figure 2.26 shows the complex of key phenomena involved in the soil-atmosphere interaction.

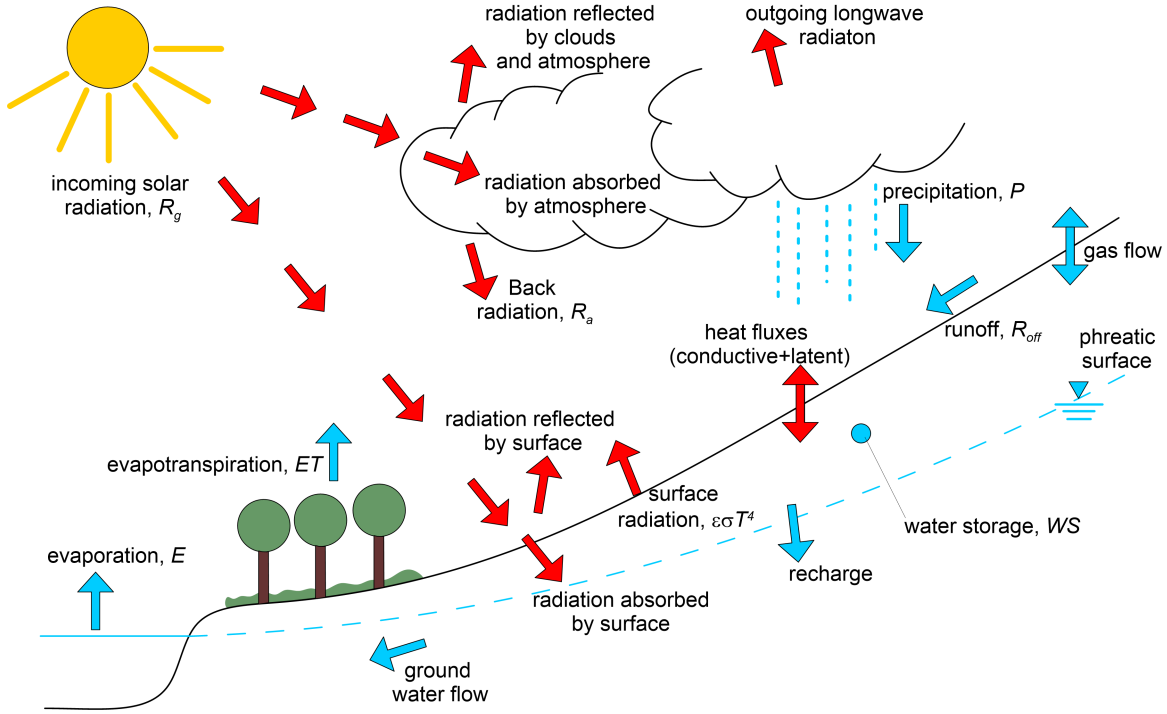

Figure 2.26: Soil-atmosphere interaction components

The water budget equation applied to a layer of soil between the surface and the water table, which expresses the conservation of water mass, can be written as follows [175]:

$$P - \left(I_{nt} + R_{off}\right) = ET + R_{ech} + \frac{d\left(WS\right)}{dt} \tag{2.66}$$

where P is the precipitation rate, I_{nt} is the rate of water intercepted by the plant cover and does not infiltrate the soil, R_{off} is the surface runoff rate, ET is the evapotranspiration rate, R_{ech} is the rate of water recharged to the water table and $d\left(WS\right)/dt$ is the rate of increase of water stored in the reference layer. The terms above are expressed in $\mathrm{kgm^{-2}s^{-1}}$. Equation 2.66 represents a more general version of Equation 2.59. A budget equation could also be written for the air mass but this, as well as advective gas flows occurring at the surface, will be neglected in this discussion.

The evaporation process occurring at the soil surface consumes energy. In order for the liquid water to evaporate, energy must be supplied and used in the form of latent heat of vaporization. The energy balance applied to a surface layer of soil, which expresses the

conservation of energy, can be written as follows [178]:

$$R_n - L_e E - H_s - G_s + H_c = \frac{dW}{dt} \tag{2.67}$$

where R_n is the net incoming radiation flux at the soil surface, L_e is the latent heat of evaporation, E is the evaporation rate, H_s is the sensible heat flux into the atmosphere, G_s is the specific energy flux leaving the layer at the lower boundary, H_c is the convective heat flux into the layer and dW/dt is the increase of energy storage per unit area in the layer over time. The units of the terms above (including the product $L_e E$) are W/m^2 (or Jm^{-2}s^{-1}). Most of the incoming solar radiation is transformed into an increase of internal energy. Subsequently, this increase of internal energy is partitioned into an increase of soil temperature, surface outward radiation, upward and downward heat convection and downward heat conduction. The vaporization process requires a large amount of energy given the high value of latent heat of vaporization of water. This large amount of energy is subsequently released through condensation of water vapour in the atmosphere into precipitation. Therefore, the amount of evaporation plays an important role in controlling the climate.

Evaporation E, sensible heat flux H_s and net incoming radiation R_n are discussed further in the following sections. The transpiration phenomenon, i.e. water extraction from the soil by plants, will not be discussed although it can often have a significant role.

2.4.2 Evaporation into the atmosphere

Evaporation and sensible heat flux into the atmosphere are the result of a complex interaction between atmosphere and soil surface. The key atmospheric variables governing the phenomenon of evaporation and sensible heat flux are the atmospheric temperature T_a, the atmospheric absolute humidity ρ_{va} and the wind speed v_a. ρ_{va} is the density of vapour in the gas phase, namely the mass of water vapour per unit volume of gas. The key variables regarding the soil surface are the surface temperature T_s and the surface value of absolute humidity in gas-filled soil pores ρ_{vs}, which in turn is a function of the surface temperature T_s and pore-liquid pressure p_l and pore-gas pressure p_g at the soil surface.

The problem of the evaporation into the atmosphere can be treated analytically if various simplifying assumptions are made [178]. The various simplifying assumptions required include: no phase changes; uniform density of moist air in the atmosphere; uniform diffusivity coefficient of water vapour in the atmosphere; negligible impact of atmospheric gas pressure variation on the compressibility of the moist air; and constant viscosity of the moist air. The key equations for this simplified problem are the conservation of water vapour, the conservation of moist air, the conservation of momentum and the conservation of energy. The problem is analytically complex to solve for two reasons: (i) fluxes in the atmosphere are turbulent and, in general, any set of equations of motion containing turbulent fluxes has more unknowns than the number of equations, due to the presence of some higher order moments; (ii) also the mean motion of the atmosphere involves phenomena of high complexity. Nevertheless, the analytical problem can be further simplified while still obtaining meaningful

results, with the following additional assumptions:

- in the atmospheric boundary layer, i.e. the lower part of the atmosphere between 500 m and 2000 m thick, variations of temperature, humidity and wind speed in the horizontal direction are negligible compared to those in the vertical direction;
- dimensional analysis can be applied to describe the turbulence in the lowest part of the atmospheric boundary layer.

Using this approach, it can be demonstrated [178] that the profiles of mean wind speed $v_a(z)$, mean absolute humidity $\rho_{va}(z)$ and mean temperature $T_a(z)$ are all semi-logarithmic at sufficiently low heights (i.e. up to approximately 10 m from the surface) whereas evaporation E and sensible heat flux H_s are constant over height. Moreover, the following relationships can be obtained for these profiles:

$$v_a(z) = \frac{v_*}{k^*} \ln\left(\frac{z}{z_{0m}}\right) \tag{2.68}$$

$$\rho_{va}(z) = \rho_{vs} - \frac{E}{k_v^* v_*} \ln\left(\frac{z}{z_{0v}}\right) \tag{2.69}$$

$$T_a(z) = T_s - \frac{H_s}{k_h^* v_* \rho_{ga} c_p} \ln\left(\frac{z}{z_{0h}}\right) \tag{2.70}$$

where z is the height starting from the soil surface, k^*, k_v^* and k_h^* are respectively the Von Karman's constants for wind speed, water vapour and sensible heat, z_{0m}, z_{0v} and z_{0h} are integration constants (unit is [L]), ρ_{ga} is the atmospheric gas density, c_p is the specific heat for constant pressure and v_* is the friction velocity, defined from boundary layer theory as:

$$v_* = \sqrt{\frac{\tau_{w0}}{\rho_{ga}}} \tag{2.71}$$

where τ_{w0} is the shear stress at the surface due to the wind flow. The Von Karman's constants can be approximated as $k^* = k_v^* = k_h^* = 0.4$ [178].

Figure 2.27 shows typical profiles of wind speed, absolute humidity and temperature in the lower atmosphere. The profiles, which generally are semi-logarithmic in the lower atmosphere, deviate from the semi-logarithmic trend very close to the soil surface. Thus, the integration constants z_{0m}, z_{0v} and z_{0h} can be interpreted as the intercepts of the semi-logarithmic profiles at the values of v_a, ρ_{va} and T_a attained at the surface (see Figure 2.27), which in the case of wind speed is always 0. The values of z_{0m}, z_{0v} and z_{0h} depend on the surface roughness (suggested values can be found in the literature for different types of surface). As stated above, the semi-logarithmic trend of the profiles is valid only in the lower atmosphere (up to 10 m). At higher elevations, these profiles deviate from the semi-logarithmic trend.

The evaporation rate E (in kg/m^{2}s) and the sensible heat flux H_s (in J/m^{2}s) can be estimated if the following quantities are known: wind speed v_{a1} at a height z_1, absolute humidity ρ_{va2} and temperature T_{a2} at a height z_2 and absolute humidity ρ_{vs} and temperature T_s at the soil surface. In fact, using Equations 2.68, 2.69 and 2.70, the following relationships can be

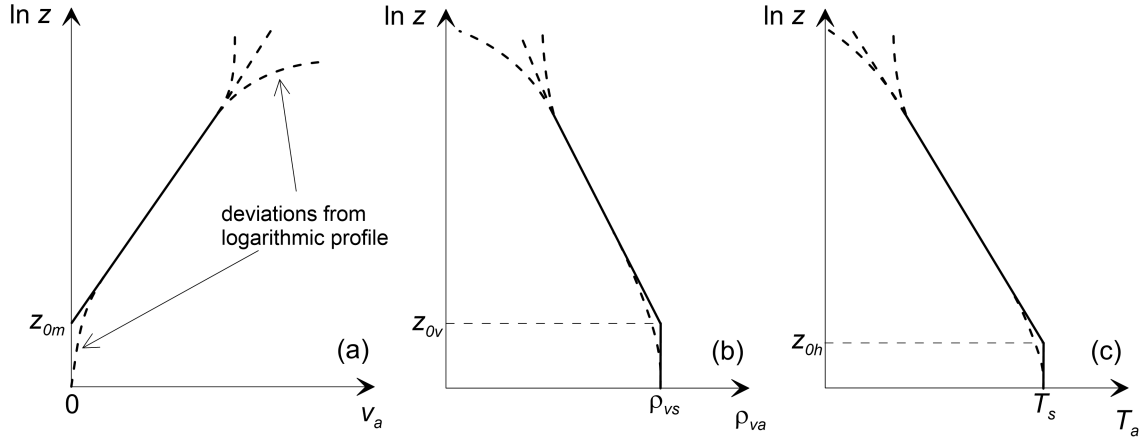

Figure 2.27: Profiles of (a) wind speed, (b) atmospheric absolute humidity and (c) atmospheric temperature

obtained [178]:

$$E = \frac{k_v^* k^* v_{a1}}{\ln\left(\frac{z_2}{z_{0v}}\right) \ln\left(\frac{z_1}{z_{0m}}\right)} (\rho_{vs} - \rho_{va2}) \tag{2.72}$$

$$H_s = \frac{k_h^* k^* v_{a1} \rho_{ga} c_p}{\ln\left(\frac{z_2}{z_{0h}}\right) \ln\left(\frac{z_1}{z_{0m}}\right)} (T_s - T_{a2}) \tag{2.73}$$

From inspection of Equations 2.72 and 2.73, the driving forces of evaporation E and sensible heat flux H_s can be identified. Both E and H_s increase linearly with wind speed v_a. During a mean horizontal motion, the wind also creates vertical turbulent air fluxes which cause air volumes at different vapour concentration and temperature to mix, thereby driving evaporation and sensible heat flux into the atmosphere.

Evaporation E is also linearly proportional to the difference in absolute humidity between the gas-filled soil pores at the soil surface ρ_{vs} and the atmosphere ρ_{va}. A difference in water vapour concentration drives the evaporation flux from a zone at higher vapour concentration (typically the soil surface) to a zone at lower vapour concentration (typically the atmosphere). However, this relationship strongly depends on the water availability at the soil surface, more precisely on the corresponding suction at the soil surface. Figure 2.28 shows the dependency of the absolute humidity at the soil surface ρ_{vs} and the evaporation rate E upon suction s at the soil surface, under the assumptions of constant absolute humidity in the atmosphere ρ_{va} and constant wind speed v_a. The absolute humidity at the soil surface ρ_{vs} is related to the suction at the soil surface s by means of Kelvin's equation and the law of ideal gases (see Equations 2.8, 2.9 and 2.10). Starting from $s = 0$, as suction in the soil at the surface increases the absolute humidity in the soil pores at the soil surface ρ_{vs} decreases and the evaporation rate, driven by the difference between ρ_{vs} and ρ_{va}, decreases accordingly. Thus, the evaporation rate is higher if the soil surface is at lower suction and at higher degree of saturation. The evaporation rate decreases as the soil surface progressively dries.

Similarly, the sensible heat flux H_s is linearly proportional to the difference between the

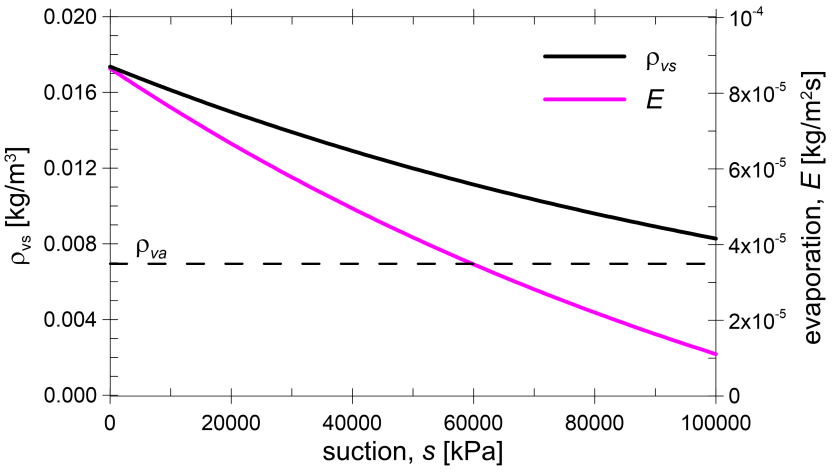

Figure 2.28: Dependency of absolute humidity at the soil surface ρ_{vs} and evaporation rate E upon suction s at the soil surface ($k_v^* = k^* = 0.4$, $v_{a1} = 3\,\mathrm{m/s}$, $\rho_{va2} = 0.00695\,\mathrm{kg/m^3}$, $z_1 = z_2 = 2\,\mathrm{m}$, $z_{0m} = z_{0v} = 0.001\,\mathrm{m}$ and $T_s = 293.15\,\mathrm{K}$)

temperature at the soil surface T_s and the temperature in the atmosphere T_a. Sensible heat flux occurs intuitively from a zone at higher temperature to a zone at lower temperature.

2.4.3 Radiation

The net incoming radiation absorbed by the soil surface has an important role in the phenomenon of evaporation. Most of the latent heat of evaporation required for the liquid water to evaporate is given by the radiation.

The net incoming radiation absorbed from the soil surface R_n is the result of the combination of different terms and it can be written as follows [178]:

$$R_n = R_s\,(1 - A_l) + \varepsilon_s R_{ld} - R_{lu} \tag{2.74}$$

where R_s is the global short-wave solar radiation, A_l is the surface albedo, ε_s is the emissivity of the surface, R_{ld} is the downward atmospheric long-wave radiation and R_{lu} is the upward long-wave radiation from the soil surface.

The global short-wave solar radiation R_s which reaches the soil surface is strongly affected by the latitude and the position of the Sun: higher at midday, null at night; on a yearly average basis, higher at lower latitudes. The value of R_s is also affected by the presence of clouds, which represent a cover for the surface from solar radiation, thereby reducing its effect. Part of the solar radiation reaching the soil surface is then reflected into the atmosphere by the surface: the reflected fraction is $R_s \cdot A_l$ whereas the absorbed fraction is $R_s \cdot (1 - A_l)$. The surface albedo depends on the colour of the surface (e.g. snow, which is lighter, reflects more than deep oceans, which are darker).

The downward atmospheric long-wave radiation R_{ld} is the radiative flux emitted by the atmosphere and absorbed by the soil surface. It is affected by humidity, cloudiness and in

particular atmospheric temperature. It can be expressed as [178]:

$$R_{ld} = C_{cloud}\varepsilon_a\sigma_R {T_a}^4 \tag{2.75}$$

where σ_R is the Stefan-Boltzmann constant ($5.67 \times 10^{-8}\,\mathrm{W/m^2/K^4}$), ε_a is the emissivity of the atmosphere in clear sky conditions, T_a is the atmospheric temperature and C_{cloud} is a correction parameter for cloudiness.

The emissivity of the surface ε_s depends on the surface properties but it is generally close to unity [178].

The upward long-wave radiation from the soil surface R_{lu} is the radiative flux emitted by the surface and it can be written as:

$$R_{lu} = \varepsilon_s\sigma_R {T_s}^4 \tag{2.76}$$

where T_s is the soil surface temperature [178].

2.4.4 Modelling approaches

Three fundamental approaches can be adopted in numerical modelling of problems in geotechnical engineering that might involve soil-atmosphere interaction [177]. From the simpler, to the more advanced:

- hydraulic modelling;
- thermo-hydraulic modelling;
- thermo-hydro-mechanical modelling.

Hydraulic modelling

The hydraulic modelling approach is the most simple but also the most used approach. Only water and air balance equations are solved whereas temperature is assumed to be constant and the soil is assumed to be non-deformable. Often, the problem is further simplified by considering a uniform and constant gas pressure, and only the water mass balance is solved. Further simplifications may involve neglecting water diffusion in the gas phase and dissolution of air into the liquid phase. If also the liquid density is considered as a constant, the water mass balance equation reduces to the Richards' equation [60]. Given this uncoupled approach, the evapotranspiration of water from the soil surface must be modelled as an input boundary outflow at the ground surface. In this case, evapotranspiration must be estimated using phenomenological interpretations and semi-empirical laws, which relate atmospheric and vegetation conditions to the evapotranspirative flux imposed at the surface. In these models, water budget and energy budget equations (see Equations 2.66 and 2.67) are not employed explicitly (they are implicitly combined in estimating the applied evapotranspiration rate).

One of the most popular models introduced to estimate the evapotranspiration was introduced by Penman [179]. More precisely, the model aimed to estimate the evaporation from

an open-water surface or a completely wet land. According to this model, evaporation E is expressed as:

$$E = \frac{\Delta_v \cdot R_n + \dfrac{\rho_g \cdot c_p \left(p_{v0,a} - p_{v,a}\right)}{r_a}}{L_e \cdot \left(\Delta_v + \gamma_{ps}\right)} \tag{2.77}$$

where $p_{v,a}$ and $p_{v0,a}$ are respectively the vapour pressure and the saturation vapour pressure of air at some reference level, Δ_v is the slope of the saturation vapour pressure curve $p_{v0}(T)$ at the atmospheric temperature T_a (i.e. $\left.\dfrac{dp_{v0}}{dT}\right|_{T_a}$), ρ_{ga} is the atmospheric gas density, γ_{ps} is the psychrometric constant and r_a is the aerodynamic resistance, which is an increasing function of the wind speed. The psychrometric constant γ_{ps} relates the partial pressure of water in the gas phase to the gas temperature and it is defined as:

$$\gamma_{ps} = \frac{c_p \cdot p_{ga}}{L_e \cdot \dfrac{M_w}{M_a}} \tag{2.78}$$

where p_{ga} is the atmospheric gas pressure, M_w is the molecular weight of water and M_a is the molecular weight of dry air. The aerodynamic resistance r_a determines the resistance to the transfer of heat and water vapour into the atmosphere as a function of wind speed v_a. For instance, in Equation 2.72, the aerodynamic resistance is the following term:

$$r_a = \frac{\ln\left(\dfrac{z_2}{z_{0v}}\right)\ln\left(\dfrac{z_1}{z_{0m}}\right)}{k_v^* k^* v_{a1}} \tag{2.79}$$

In Penman's model, the terms G_s, H_c and dW/dt of the the energy budget equation (Equation 2.67) are neglected.

Penman's model was subsequently modified and improved. Monteith [180] modified Penman' model in order to introduce also the term G_s from the energy balance equation and to consider the effect of transpiration. Therefore, the potential evapotranspiration ET, which is the evapotranspiration which is obtained in case the soil surface is fully saturated, can be estimated as:

$$ET = \frac{\Delta_v \cdot \left(R_n - G_s\right) + \dfrac{\rho_g \cdot c_p \left(p_{v0,a} - p_{v,a}\right)}{r_a}}{L_e \cdot \left[\Delta_v + \gamma_{ps} \cdot \left(1 + \dfrac{r_s}{r_a}\right)\right]} \tag{2.80}$$

In comparison to Equation 2.77, in Equation 2.80 the downward specific energy flux in the soil G_s and the stomatal resistance r_s are introduced. The parameter G_s is difficult to measure and r_s, which is the resistance to the transfer of heat and water vapour into the atmosphere due to the presence of vegetation and depends on plant properties, is often unknown.

Priestley and Taylor [181] proposed a model in which the dependency on the observations (excluding radiation) was removed. They observed that, after some time, an air mass moving over a saturated vegetated surface tends to become vapour-saturated. In this condition, the term $\left(p_{v0,a} - p_{v,a}\right)$ in Penman's equation becomes 0. Priestley and Taylor [181] proposed the

following expression for the evaporation E:

$$E = \alpha_e \cdot \frac{\Delta_v \cdot R_n}{L_e \cdot (\Delta_v + \gamma_{ps})} \tag{2.81}$$

where α_e is an empirical constant which was found to be approximately equal to 1.26, with similar values obtained for open water surfaces and lands covered by grass.

Other models were proposed [e.g. 182, 183] but, at the moment, the FAO Penmann-Monteith method [184] is one of the most commonly used to provide realistic estimation of evapotranspiration. According to this model, a reference evapotranspiration ET_0 is initially calculated from a reference surface, using the Penmann-Monteith equation (Equation 2.80). The reference surface is a hypothetical wet grass crop with an assumed crop height of 0.12 m, a fixed stomatal resistance of $r_s = 70\,\mathrm{s\,m^{-1}}$ and an albedo $A_l = 0.23$. Under these assumptions, the reference evapotranspiration ET_0 is calculated as:

$$ET_0 = \frac{0.408\Delta_v \cdot (R_n - G_s) + \gamma_{ps}\dfrac{900}{T+273} v_{a,2m}\,(p_{v0,a} - p_{v,a})}{\Delta_v + \gamma_{ps} \cdot (1 + 0.34 v_{a,2m})} \tag{2.82}$$

where, in this equation, ET_0 is in mm day^{-1}, R_n and G_s are in MJ m^{-2} day^{-1}, T is in °C, $v_{a,2m}$ is the wind speed at 2 m height and is in m s^{-1}, $p_{v0,a}$ and $p_{v,a}$ are in kPa and Δ_v and γ_{ps} are in kPa °C^{-1}. Once the reference evapotranspiration ET_0 is calculated, the crop evapotranspiration ET_c is obtained by multiplying the reference evapotranspiration ET_0 by a correction factor (termed crop coefficient K_c) which takes into account differences from the reference conditions in terms of leaf anatomy, stomatal characteristics, aerodynamic properties and albedo, presence of pests and diseases, soil salinity, low soil fertility, water shortage or waterlogging etc.

Thermo-hydraulic modelling

Thermo-hydraulic modelling involves the simultaneous resolution of the equations describing the mass balances of both water and air and the energy balance. In this type of analysis, the numerical problems is characterized by three unknowns in the soil: pore-liquid pressure p_l, pore-gas pressure p_g and temperature T. Even in this case, p_g is often assumed as a constant and equal to the atmospheric gas pressure. This modelling strategy can include different multi-physics transfer phenomena in the soil: advective liquid flow, advective gas flow (if p_g is not assumed as a constant), water vapour diffusion in the gas phase, air diffusion in the liquid phase, heat convection, heat advection, changes of phase (e.g. vaporization of liquid water into the gas phase) etc.

The simultaneous resolution of mass balance and energy balance equations, with the consequent prediction of pore-liquid pressure p_l, pore-gas pressure p_g and temperature T at the soil surface, allows the simultaneous application of the water budget equation (see Equation 2.66) and the energy budget equation (see Equation 2.67) at the soil surface to represent the soil-atmosphere interaction. Equations 2.72 and 2.73 can be directly employed

to model evaporation and sensible heat fluxes. It is worthy noting that, in this in case, evaporation from the surface is not an input boundary condition but it is an output result of the interaction between the soil surface and the atmosphere. Parameters representing atmospheric conditions and surface type are the input parameters for the soil-atmosphere interaction in this modelling approach.

This modelling approach is rarely used because of the complexity of the analysis and the large amount of input data required [177]. Nevertheless, this approach is more accurate than the basic hydraulic modelling approach, the dependency of the evaporation rate upon the hydraulic state of the soil surface is considered and overly simplifying assumptions regarding heat fluxes are not introduced. This approach will be used in the modelling of soil-atmosphere interaction in this thesis.

Thermo-hydro-mechanical modelling

Thermo-hydro-mechanical modelling involves the simultaneous resolution of the equations describing the mass balances of both water and air, the energy balance and the momentum balance (i.e. equilibrium). In addition to the features of the thermo-hydraulic modelling, this approach also includes the representation of the mechanical behaviour of soils and how this is affected by thermal and hydraulic aspects. Fully coupled mechanical constitutive models may include the influences of temperature, suction and degree of saturation on stress-strain behaviour [185]. In turn, if soil deformation (i.e. mechanical behaviour) involves changes of void ratio, this can cause changes in the hydraulic behaviour, affecting both water retention behaviour (see Section 2.1.4) and hydraulic conductivity (see Section 2.1.5).

The introduction of the mechanical behaviour may have a significant impact also on the soil-atmosphere interaction. For instance, periods of dryness and high temperatures can cause desiccation cracking in the soil at the surface. This phenomenon has an important effect on the increase of the hydraulic conductivity and changes in water retention behaviour of the soil at a surface affected by desiccation cracking. The variation of properties like permeability and water retention strongly affect the water transport around the soil surface, thus impacting also evapotranspiration, runoff, heat flux etc.

This modelling approach, which is more relevant for fine-grained soils because they are more affected by coupling phenomena like desiccation cracking, is even more complex than the thermo-hydraulic modelling approach and will not be used in this thesis.

2.4.5 Effect of evaporation on soils

Several experimental and numerical studies addressed the response of soils during evaporation [e.g 186–189]. Typical experimental tests are 1D column tests where evaporation is enhanced by an imposed flux of dry (sometimes hot) air and/or a lamp placed at the top simulating the solar radiation.

Han and Zhou [189] performed an evaporation test on a column of sand, starting from relatively wet conditions in the soil and simulating solar radiation with a lamp placed at the

top of the column. They also analysed the test numerically. Figures 2.29a and 2.29b show the result of the predicted time history of water outflows from the soil surface in terms of total evaporative flux, liquid flux component and vapour flux component arriving at the surface (positive sign means upward flux), whereas Figure 2.29c provides a schematic interpretation of the phenomenon of evaporation from soil. The liquid component and the vapour component represent the water which reaches the soil surface during evaporation by means of a liquid flux and a vapour flux respectively. The time history of evaporation can be divided into three stages [186, 189].

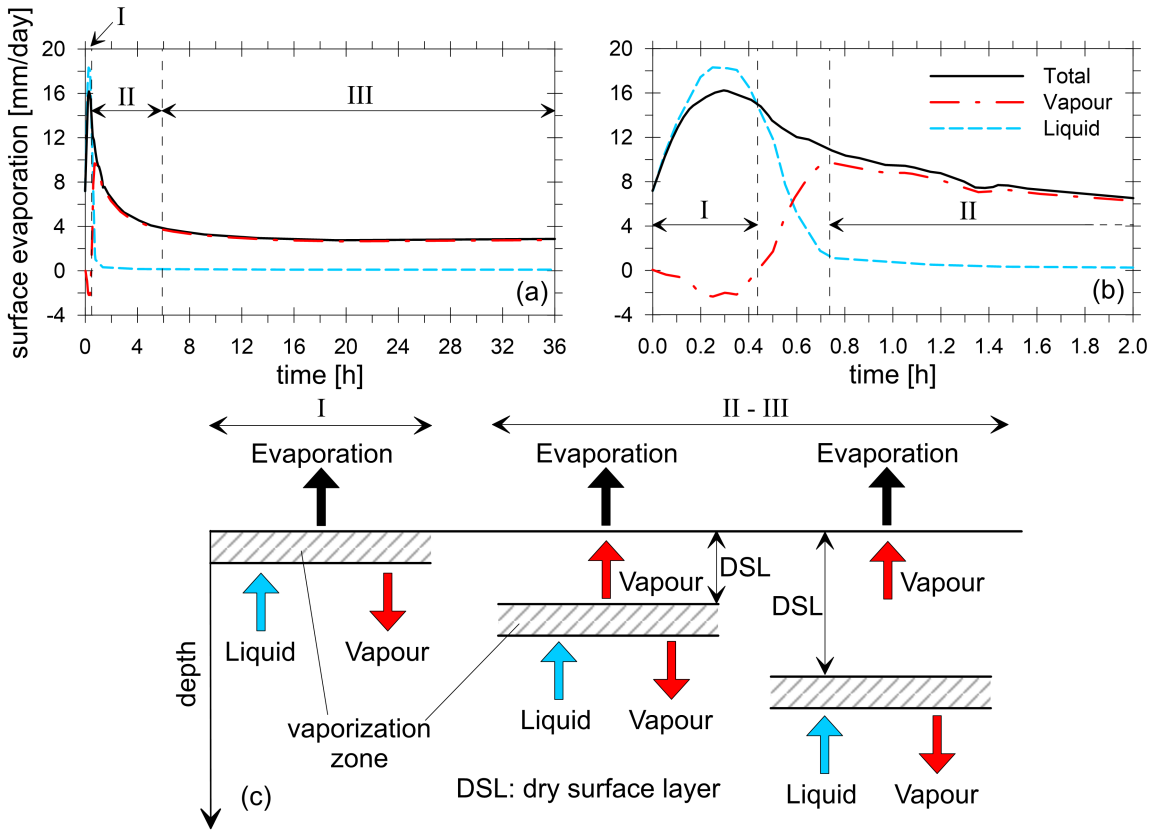

Figure 2.29: (a) Time history of surface evaporation from soil (with (b) zoom at initial times) (from Han and Zhou [189]) and (c) schematic interpretation

During stage I, the soil surface was relatively wet and the corresponding suction was low. In this condition the evaporation rate was high (see Figure 2.28 about the relationship between evaporation rate and suction at the soil surface in isothermal conditions). More precisely, the evaporation rate increased during the first part of stage I, from the beginning of the test until approximately 0.3 h, because the soil surface temperature increased due to the effect of radiation. An increase of temperature caused an increase in vapour concentration at the soil surface and hence an increase of the evaporation rate. On the other hand, the generation of a temperature gradient in the soil at this stage, with higher values of temperature at the soil surface and a decreasing trend with depth, caused a gradient in vapour concentration within the soil, i.e. higher vapour concentration at the soil surface and decreasing with depth. As a consequence, a downward vapour flux starting from the soil surface was generated (see negative values of vapour flux in Figure 2.29a,b and the schematic diagram in Figure 2.29c).

During stage I, the water outflow from the soil surface was supplied by an excess of upward liquid water flux over downward vapour flux which evaporated directly at the soil surface.

In the transition between stage I and stage II, the liquid component of flow arriving at the soil surface rapidly dropped almost to zero and the vapour component rapidly changed from downward to upward.

During stage II, almost all the evaporation from the soil surface was supplied by an upward vapour flow to the soil surface, whereas the liquid water flow to the soil surface was almost nil (see Figure 2.29). During this stage, the evaporation from the soil surface gradually decreased because the soil surface became drier and drier and suction at the soil surface increased. During this stage, most of the phase change from liquid to vapour occurred in the "vaporization zone" which was located under the soil surface (see Figure 2.29c). Above this zone, a dry surface layer was generated, in which water transfer was mainly due to an upward vapour flow since the hydraulic conductivity was zero or extremely low. Below the vaporization zone, the degree of saturation was high and water moved upwards by means of liquid flow. On the other hand, because of the high concentration of water vapour at the location of the vaporization zone, vapour flow was also directed downwards from the vaporization zone.

During stage III, the evaporation mechanism was similar to that described for stage II. However, the location of the vaporization zone progressively moved deeper and the dry surface layer progressively became thicker. Temperature and suction at the soil surface did not significantly vary further during this stage but the suction at the ground surface attained very high values. Therefore, at this stage, the rate of evaporation from the soil surface was almost constant (slightly decreasing) but very low.

The interpretation of the response of the soil during evaporation can be further clarified from the observation of the results obtained by Gran et al. [188]. They performed experimental tests similar to those performed by Han and Zhou [189]. They also simulated the tests numerically, comparing numerical and experimental results in terms of degree of saturation, temperature and salt concentration profiles at the end of the test (12 days). The good quality of the match between numerical and experimental results served as a validation of the numerical model. Figure 2.30 shows the profiles of water and heat fluxes predicted numerically at different times during the test.

Figure 2.30a shows the liquid water flux profiles at different times during the test. According to the pattern described above, at the beginning of the test water moved by means of a liquid flux to the soil surface, where it evaporated. As the test progressed, a vaporization zone progressively moved deeper in the soil. Above this zone, the liquid water flux was approximately zero whereas, below the vaporization zone, liquid water flowed upwards towards the vaporization zone. The location of the vaporization zone can be identified as the sharp variation (almost a discontinuity) of the liquid water flux in Figure 2.30a.

The pattern described above about the vapour flux during evaporation can be recognized in the vapour flux profiles at different times shown in Figure 2.30b. At the beginning of the test, a temperature gradient in the soil drove downward vapour fluxes from the vaporization zone

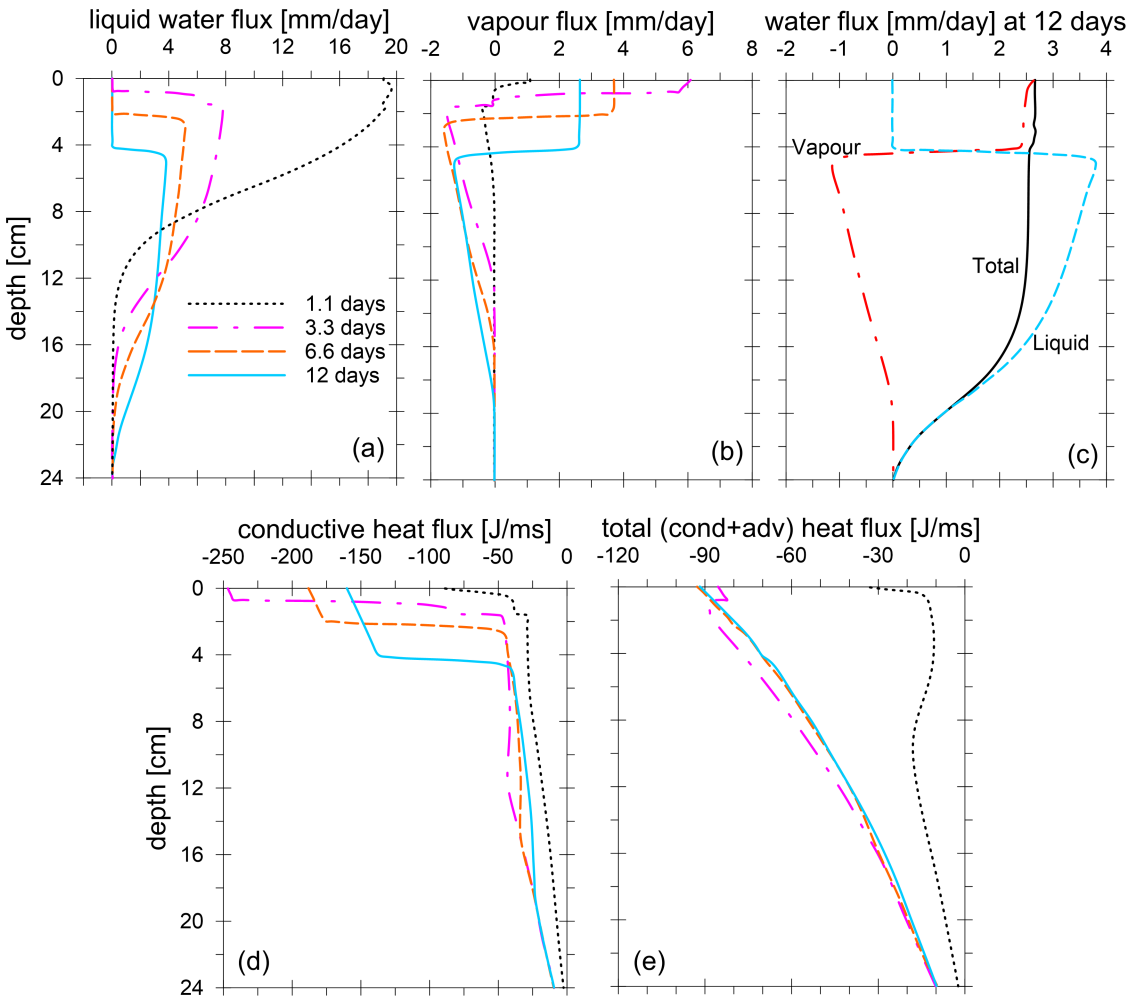

Figure 2.30: Profiles during evaporation from soil of (a) liquid water flux at different times, (b) vapour water flux at different times, (c) water fluxes at 12 days, (d) conductive heat flux at different times and (e) total heat flux at different times, with positive sign indicating upward fluxes (from Gran et al. [188])

located at the soil surface. Upward and downward vapour fluxes starting from the vaporization zone occurred as this moved deeper because peaks of vapour concentration were attained at the location of the vaporization zone.

Inspection of Figure 2.30c, which shows the liquid, vapour and total water flux profiles at 12 days from the beginning of the test, clarifies the roles of liquid and vapour transfer during evaporation from the ground surface. At a later stage during evaporation (12 days), the total water flux was approximately constant with depth (to a maximum depth greater than the location of the vaporization zone) and directed upwards. However, above the vaporization zone the water transport is dominated by vapour flow and under the evaporation zone the water transport is dominated by liquid flow.

Figure 2.30d and 2.30e show respectively the conductive heat flux and the total (conductive+advective) heat flux profiles at different times. Negative values means that the heat fluxes are directed downwards. At the early stage of the test (until approximately 3.3 days) the radiative flux provided at the top surface was transformed into an increase of temperature in the soil. After 3.3 days, temperature profiles remained approximately constant in time as well

as the total heat flux (see Figure 2.30e). However, above the vaporization zone, much greater downward values of conductive heat flux occurred which were partially offset by upward advective heat flux, i.e. heat related to the internal energy of vapour flowing upwards.

Chapter 3

Development of improved hydraulic constitutive models for unsaturated soils

A review of existing constitutive models describing the hydraulic behaviour of unsaturated soils (see Section 2.2) identified a lack of a SHCC model able to predict accurately the hydraulic conductivity at low degree of saturation, once the SWRC and the saturated hydraulic conductivity are known, and which includes water retention hysteresis.

This chapter initially provides a critical review of the hydraulic behaviour of unsaturated soils and some key transition points on the SWRC and SHCC are identified and defined. This serves as the physical basis for the selection of an appropriate SWRC model and the development of a new SHCC model, which is presented and validated against experimental data. This new SHCC model can be applied for relatively coarse-grained soils (i.e. gravel, sand and silt). Subsequently, water retention hysteresis is introduced in the new model (both SWRC and SHCC) using a bounding surface approach and also the water retention hysteretic component of the new model is finally validated against experimental data.

3.1 Critical review of the hydraulic behaviour of unsaturated soils

The definition and explanation of liquid-gas arrangement states at key transition points is often unclear and inconsistent in the literature. For instance, the “residual degree of saturation” is defined in different ways by different authors [190]: the horizontal asymptote of the SWRC [81], the degree of saturation at s=1500 kPa [82], the degree of saturation corresponding to the maximum amount of water in a soil not contributing to liquid flow [191] or simply a fitting parameter [82, 83, 191]. In this thesis, the term "residual degree of saturation" will be used only to refer to the fitting parameter for some SWRC models (e.g. the van Genuchten [82] model) representing the horizontal asymptote of the SWRC. Similar lack of clarity applies to the definition of the “water-entry” value [192, 193]. Therefore, it is important to give a consistent and clear explanations and definitions of the different liquid-gas arrangement states at key transition points on the SWRC and SHCC, as a basis for subsequent development of

hydraulic constitutive models.

The SWRC of a soil is directly related to the liquid-gas distribution states. Figure 3.1a shows typical main wetting curve, main drying curve and scanning curves in a semi-logarithmic plot. Figure 3.1a shows also the relationship between SWRCs and pore-water forms in unsaturated soils and some key transition points on the SWRCs are highlighted. As shown in Figure 3.1a, different gas-liquid distribution states can be identified, depending on the degree of saturation: they are defined as capillary state, funicular state and pendular state [194]. In the capillary state, at low suction, the soil is saturated $S_l = 1$, all the pores are filled with liquid water and only bulk water is present. For intermediate values of degree of saturation and suction, in the funicular state, gas and liquid phases coexist. In this case, water is present in the forms of bulk water, meniscus water bridges and liquid films. For low degree of saturation and high suction, the soil is in the pendular state, all the pores contain air, there is no bulk water left and water is present only in the forms of meniscus water bridges and liquid films.

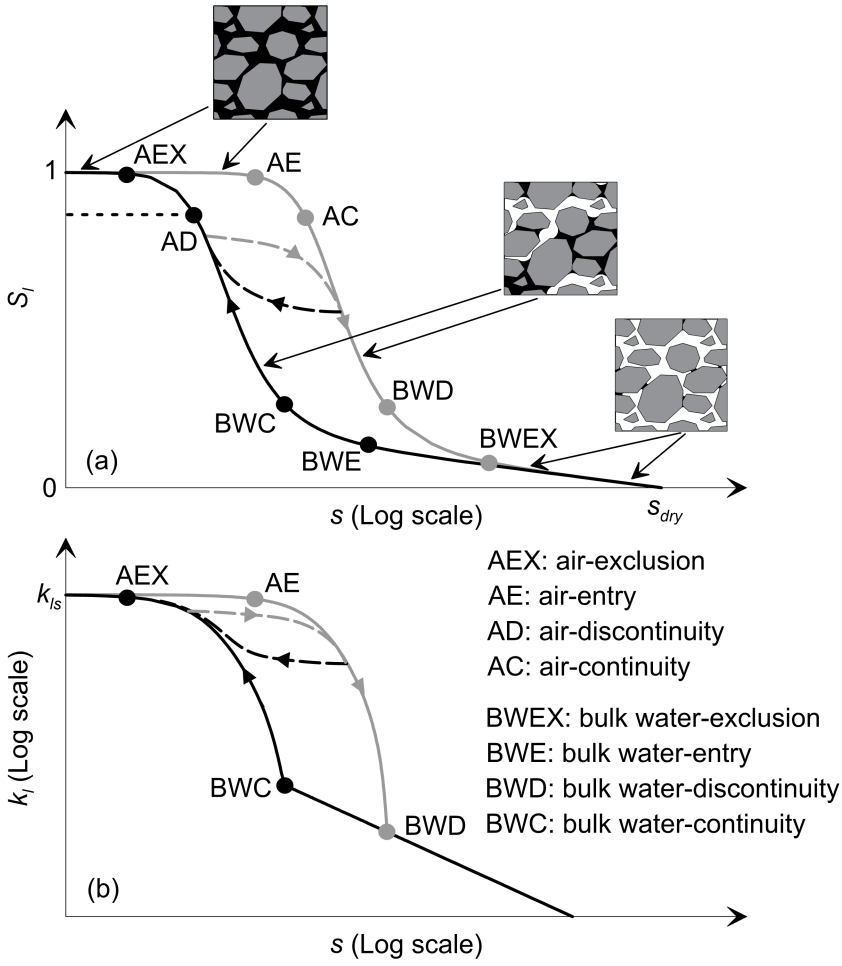

Figure 3.1: Typical (a) SWRC and (b) SHCC, with key transition points indicated

Following a drying path starting from a saturated state (see the main drying curve shown in Figure 3.1a), the soil is in the capillary state until suction is increased up to the air-entry value (AE). At this point, air starts entering the voids, firstly into the voids with the largest entry throats, and the soil enters the funicular state. As the suction increases from the air-entry value, air breaks through into more voids, with smaller and smaller entry throats. The degree of saturation gradually falls, mainly because the volume of bulk water decreases but also

because, although the number of meniscus water bridges and the area of particle surfaces covered by liquid films both increase as new pores fill with air, the volume of each individual meniscus water bridge decreases with increasing suction [42] and the thickness of the liquid films also decreases with increasing suction [98]. When the degree of saturation reduces to the air-continuity value (AC), the gas phase starts forming continuous gas paths within the soil. At the bulk-water discontinuity point (BWD), although bulk water is still present in the soil, it occupies so few voids that the bulk water no longer forms continuous liquid paths. Decreasing the degree of saturation further, the bulk water-exclusion point (BWEX) represents the filling of the last voids with air, so that there is no longer any bulk water, and this corresponds to the transition from the funicular state to the pendular state. From this point onwards, a large increase in suction corresponds to a small decrease in degree of saturation, due only to the reduction in size of meniscus water bridges and reduction in thickness of liquid films. Ultimately, the soil completely dries for a suction value s_{dry} of approximately 1 GPa [84, 85], although Lu and Khorshidi [195] have shown that this value ranges approximately between 0.5 GPa and 1 GPa for different soils, by means a water vapour sorption-based method used to determine the maximum suction in the soil.

Similar concepts apply to a wetting path starting from a dry state (see the main wetting curve shown in Figure 3.1a). At the bulk water-entry point (BWE), bulk water starts filling the smallest voids, representing a transition from the pendular state to the funicular state. At the bulk water-continuity point (BWC), sufficient voids are filled with bulk water to form a continuous liquid path, whereas at the air-discontinuity point (AD) the gas phase becomes discontinuous. Eventually, at the air-exclusion point (AEX), air is totally removed and the soil enters the capillary state. When a main wetting SWRC is obtained experimentally, air can remain trapped in the soil and complete saturation may not be reached even when zero suction is imposed on the external boundary of the soil sample. In this case, the wetting SWRC appears to be approximately horizontal from the point AD where the gas phase becomes discontinuous, as shown by the dashed line in Figure 3.1a. However, this dashed line does not represent true equilibrium states, because the trapped air is at elevated pressure (i.e. the internal value of suction within the soil sample is greater than the value applied at the boundary) and the trapped air is then expelled very slowly by the processes of air dissolution and diffusion in the liquid phase. This aspect will be treated in more detail in Chapter 5.

Water retention hysteresis is clearly evident in the funicular state, mainly due to the ink-bottle effect, hysteresis of the contact angle and air trapping (see Section 2.1.4). In the capillary state there cannot be hysteresis because the soil is fully saturated ($S_l = 1$). In the pendular state, where only meniscus water and liquid film water is present, water retention hysteresis has been observed for certain soils, i.e. clays mainly consisting of expandable minerals such as montmorillonite. For these soils, sorption and desorption of interlayer cations require different energy levels, and thus different suctions [195]. For fine-grained soils mainly consisting of non-expandable minerals (e.g. kaolinite) and for coarse-grained soils, water retention hysteresis in the pendular state is absent or negligible [196].

Points AE, AEX, BWEX and BWE are directly related to the shape of the SWRC. AE

and AEX can be identified as the points where the main drying curve and main wetting curve respectively diverge from a fully saturated condition $S_l = 1$. Since the degree of saturation has been shown to decrease approximately linearly with the logarithm of suction in the pendular state (i.e. no bulk water) [84], BWEX and BWE can be identified as the points where the two curves (in the semi-logarithmic plot) diverge from an approximately linear relationship at low degree of saturation (see Figure 3.1a). In contrast, the points AC, AD, BWD and BWC are not related to the shape of the SWRC. BWD and BWC are related to the shape of the SHCC (see Figure 3.1b), as they represent transitions between states where bulk water flow occurs (in which case this completely dominates the hydraulic conductivity) and states where liquid water flow occurs only through liquid films. AC and AD are important in the variation of gas conductivity, with the gas conductivity as zero for suction values lower than these points because the gas phase becomes discontinuous.

In the literature, there is often no distinction between the bulk water-exclusion point BWEX, bulk water-entry point BWE, bulk water-continuity point BWC and bulk water-discontinuity point BWD (see Figure 3.1). They are all often defined as the "residual" point, which is typically identified as the bend in the SWRC at low degree of saturation, when plotted in semi-logarithmic form [190, 197, 198].

Liquid water flow in unsaturated soils may occur within continuous liquid paths formed by the bulk water and/or by the thin liquid films, connected to each other at the inter-particle contacts by means of meniscus water bridges (see Figure 3.2). Thus, the hydraulic conductivity k_l of unsaturated soils can be split in two components: the bulk water component k_l^{Bulk} and the liquid film component k_l^{Film}. The film flow component is ignored in many SHCC models, which assume that liquid water flows only through pores filled with bulk water. This assumption is reasonable for very fine soils (e.g. clays) because, in these soils, the role of the adsorbed liquid films becomes dominant over the bulk water only at very high values of suction (typically >10 MPa for a clay). At these values of suction, the thickness of the adsorbed liquid films, which decreases with increasing suction (see Figure 2.8), is so small (typically <1 nm) that the attractive molecular forces between water molecules and the surfaces of the soil particles impede any mobility of the water within the liquid films. However, for coarser soils (e.g. sand), the role of adsorbed liquid films becomes dominant at much lower values of suction than in fine-grained soils (typically <10 kPa for sands and gravels), and at these values of suction the thickness of the films may be orders of magnitude higher (typically >20 nm) (see Figure 2.8). In this case, the molecular attractions, strong only in the first molecular layers next to the soil particle surfaces, do not impede the liquid film flow [49, 96, 199]. In contrast with the hydraulic conductivity, the role of adsorbed liquid films in water retention behaviour and mechanical behaviour is more important for finer-grained soils than for coarser-grained soils [61].

The value of hydraulic conductivity depends on the number and the size of the continuous liquid paths formed by the water. In particular, the more and larger are these liquid paths, the higher is the hydraulic conductivity. Figure 3.1b shows typical main drying and main wetting SHCCs in a log-log plot. The difference between these two curves is mainly due to

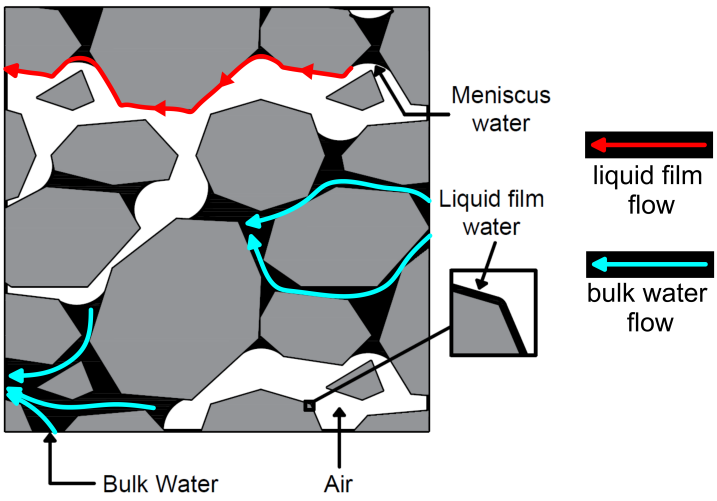

Figure 3.2: Bulk water flow and liquid film flow in unsaturated soils

the water retention hysteresis, because the hydraulic conductivity variation generally shows very little hysteresis when k_l is plotted against S_l [31, 121, 131, 200]. In the capillary state, the soil is saturated ($S_l = 1$) and thus, the hydraulic conductivity is equal to the saturated value k_{ls}. In this condition, $k_l^{Film} = 0$ and $k_l = k_l^{Bulk} = k_{ls}$. In the funicular state, as suction increases, k_l^{Bulk} reduces from the saturated value, because the continuous flow channels formed by bulk water are fewer and fewer and restricted to the smaller channels and voids. Moreover, the lengths of the continuous flow channels also increase because the tortuosity of these paths increases. Although k_l^{Film} is greater than zero in this condition, it is negligible if compared to k_l^{Bulk} in almost all the funicular range. In the pendular state, no bulk water is present within the soil. More precisely, it is at the bulk water-discontinuity point BWD during drying that k_l^{Bulk} falls to zero or at the bulk water-continuity point BWC during wetting that k_l^{Bulk} starts increasing from zero (see Figure 3.1b), because at these points the liquid paths formed by the bulk water become respectively discontinuous or continuous. For suctions above the bulk water-discontinuity point (during drying) or the bulk water-continuity point (during wetting), the hydraulic conductivity is very small (several orders of magnitude smaller than the saturated value) and related only to the liquid paths formed by the thin liquid films connected by meniscus water bridges at the inter-particle contacts, so that $k_l^{Bulk} = 0$ and $k_l = k_l^{Film}$. Moreover, as suction increases, the hydraulic conductivity $k_l = k_l^{Film}$ decreases (see Figure 3.1b), because the thickness of liquid films and the size of liquid bridges both decrease with increasing suction.

3.2 Water retention modelling

As explained in Section 2.2.1, conventional SWRC models like the Brooks and Corey [81] model (see Equation 2.30), the van Genuchten [82] model (see Equation 2.31) and the Kosugi [83] model (see Equation 2.32) are not appropriate at low degree of saturation.

In this thesis, in order to model accurately the water retention behaviour of unsaturated soils at low degree of saturation, the non-conventional modified version of the van Genuchten

model (modVG) (see Equation 2.37) proposed by Fayer and Simmons [88] will be used extensively as a reference SWRC model. In order to generalize the application of the new proposed hydraulic conductivity model (see Section 3.3) and the new hydraulic hysteretic model (see Section 3.4), also the modified version of the Brooks and Corey model (modBC) [88] (see Equation 2.36) and the modified version of the Kosugi model (modK) [90] (see Equation 2.38) will be considered.

A comparison between the performance of the van Genuchten (VG) model and the modified van Genuchten (modVG) model is shown in Figure 3.3a, where the two models are employed to fit experimental data in the full saturation range. The experimental data set is for Shonai sand [201] and will be discussed in more detail in Section 3.3.2 (soil 6). The SWRCs obtained with the VG model and the modVG model are almost coincident in the capillary and funicular states, where both models fit the experimental data well. However, the modVG model is able to represent effectively also the pendular state, where the degree of saturation decreases approximately linearly with the logarithm of suction down to a completely dry state [84].

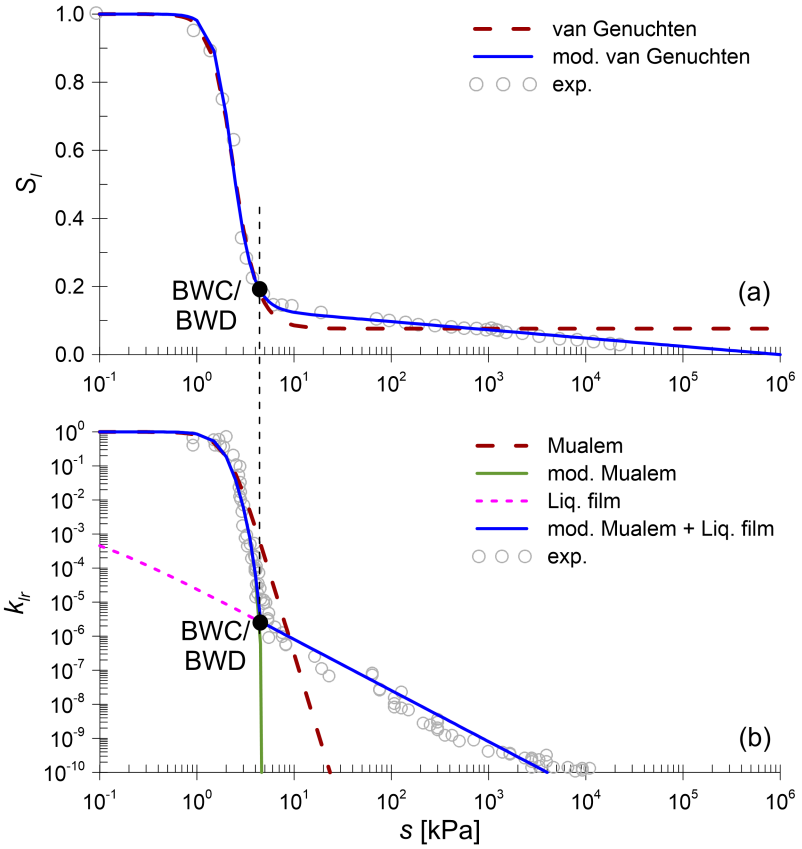

Figure 3.3: Comparison between the hydraulic constitutive models and experimental data for Shonai sand (experimental data from Mehta et al. [201]): (a) SWRC and (b) SHCC

3.3 Hydraulic conductivity modelling

3.3.1 SHCC model

The Mualem [95] (M) model (see Equation 2.40) is commonly used to describe the SHCC, in particular when it is coupled with the van Genuchten [82] model for the SWRC. In the Mualem model, the soil is assumed as a homogeneous porous medium with a certain statistical pore size distribution, which is indirectly related to the shape of the SWRC. The water is assumed to flow only in bulk water-filled pores which are modelled as bundles of cylindrical capillary tubes of different radii. If the Mualem model is coupled with the van Genuchten SWRC model, the hydraulic conductivity k_l is given by Equation 2.42. According to Equation 2.42, once the SWRC is defined by the VG model, only one extra parameter is needed (i.e. k_{ls}) for the description of the SHCC by the M model.

The accuracy of the Mualem model, when coupled with the van Genuchten model, deteriorates as the degree of saturation decreases, failing completely when the degree of saturation is so low that the bulk water is discontinuous. The model has two main weaknesses. Firstly, the model is not able to represent the liquid flow occurring in the liquid films and in the meniscus water bridges at very low values of degree of saturation. Secondly, applying Equation 2.31 (the VG SWRC model) in Equation 2.42 (the M SHCC model), the hydraulic conductivity goes to zero only when suction tends to infinity. This is physically unreasonable if this model is used only to represent the bulk water component of the hydraulic conductivity, as k_l^{Bulk} must, in reality, go to zero at the BWD point during drying and diverge from zero at the BWC point during wetting.

Due to these shortcomings of the conventional M model, a new hydraulic conductivity model, that is more accurate than the M model at low degree of saturation, is now proposed. In the new model, the hydraulic conductivity k_l is considered as the sum of two terms, as also proposed by Peters [91]:

$$k_l = k_l^{Bulk} + k_l^{Film} \tag{3.1}$$

where the bulk water component of the hydraulic conductivity k_l^{Bulk} is related to the liquid flow occurring within bulk water-filled pores whereas the liquid film component of the hydraulic conductivity k_l^{Film} is related to the liquid flow occurring within the liquid films adsorbed to the soil particle surfaces, which are inter-connected to each other by means of meniscus water bridges at the inter-particle contacts.

The bulk water component of the SHCC k_l^{Bulk} is modelled with an expression similar to the M model (Equation 2.42) but the variable S_{le} occurring twice in Equation 2.42 is replaced by two different variables. The term $\sqrt{S_{le}}$ occurring in the right hand-side of Equations 2.40 and 2.42 was introduced by Mualem [95] to model the increase of tortuosity and decrease of connectivity between bulk water-filled pores with decreasing degree of saturation. According to Equation 2.31 (VG or modVG SWRC models), S_{le} goes to zero only when suction goes to infinity, which produces unreasonable results in Equation 2.42. In reality, the connectivity of the bulk water is lost for suction values equal to or higher than the BWD point (drying) or the

BWC point (wetting). Thus, a new term $\sqrt{S_l^C}$ is used instead of $\sqrt{S_{le}}$, where S_l^C is defined by:

$$S_l^C = \frac{S_l - S_{l,BWD}}{1 - S_{l,BWD}} \quad \text{for drying} \tag{3.2a}$$

$$S_l^C = \frac{S_l - S_{l,BWC}}{1 - S_{l,BWC}} \quad \text{for wetting} \tag{3.2b}$$

where $S_{l,BWD}$ and $S_{l,BWC}$ are the values of degree of saturation at the BWD point and at the BWC point respectively.

The second appearance of S_{le} in the right hand-side of Equation 2.42 derives from solving the integrals in the right hand-side of Equation 2.40, in which S_l is substituted by the SWRC van Genuchten model (see Equations 2.29 and 2.31). The term in the right hand-side of Equation 2.40 was introduced by Mualem [95] to model the decrease of the number and size of pores filled with bulk water with decreasing degree of saturation. Again, using S_{le} from Equation 2.31 is unreasonable, because this implies that the quantity of bulk water goes to zero only when suction goes to infinity. In reality, the volume of the bulk water is zero for suction values equal to or higher than the BWEX point (drying) or the BWE point (wetting). Thus, a new variable S_l^B is used instead:

$$S_l^B = \frac{S_l - S_{l,BWEX}}{1 - S_{l,BWEX}} \quad \text{for drying} \tag{3.3a}$$

$$S_l^B = \frac{S_l - S_{l,BWE}}{1 - S_{l,BWE}} \quad \text{for wetting} \tag{3.3b}$$

where $S_{l,BWEX}$ and $S_{l,BWE}$ are the values of the degree of saturation at the BWEX and BWE points respectively.

Thus, the bulk water component of the relative hydraulic conductivity can be expressed with a new modified version of the Mualem model (modM model), as follows:

$$k_l^{Bulk} = k_{ls}\sqrt{S_l^C}\left[1 - \left(1 - S_l^{B\,1/m}\right)^m\right]^2 \tag{3.4}$$

The values of $S_{l,BWD}$, $S_{l,BWC}$, $S_{l,BWEX}$ and $S_{l,BWE}$ (for use in Equations 3.2 and 3.3) may be difficult to identify experimentally. Akin and Likos [202] identified the BWE point (which they defined as the adsorption-capillary transition point) as the change in slope of water sorption isotherms (i.e. curves of water content plotted against relative humidity obtained in isothermal conditions). Values of $S_{l,BWD}$ and $S_{l,BWC}$ are particularly difficult to identify experimentally, given that they should strictly be determined from high quality experimental SHCC data at low values of S_l and this type of data is rarely available. However, in the absence of more precise data, a simplified pragmatic procedure can be used, which assumes $S_{l,BWD} = S_{l,BWEX}$ and $S_{l,BWC} = S_{l,BWE}$. This simplified graphical procedure, which uses only the SWRC, is similar to that suggested by Vanapalli et al. [203] and is illustrated in Figure 3.4. With the fitted SWRC (based on the modVG model of Equation 2.37) presented in a semi-logarithmic plot, the intersection point of the tangent through the inflection point of the main

drying curve and the straight line formed by the final linear portion of the main drying curve defines a suction $s_{BWD/BWEX}$ (see Figure 3.4). The value of $S_{l,BWD} = S_{l,BWEX}$ is then taken as the value of S_l on the fitted main drying curve at the suction $s_{BWD/BWEX}$ (see Figure 3.4). A corresponding procedure using the main wetting curve gives the value of $S_{l,BWC} = S_{l,BWE}$ (see Figure 3.4). Assuming $S_{l,BWD} = S_{l,BWEX}$ means that $S_l^C = S_l^B$ during drying and, similarly, assuming $S_{l,BWC} = S_{l,BWE}$ means that $S_l^C = S_l^B$ during wetting (see Equations 3.2 and 3.3). This simplified procedure is likely to underestimate the values of $S_{l,BWD}$ and $S_{l,BWC}$ and overestimate the values of $S_{l,BWEX}$ and $S_{l,BWE}$ (see Figure 3.1), resulting in overestimation of S_l^C and underestimation of S_l^B. These errors will therefore partially compensate when Equation 3.4 is used to determine the value of k_l^{Bulk}.

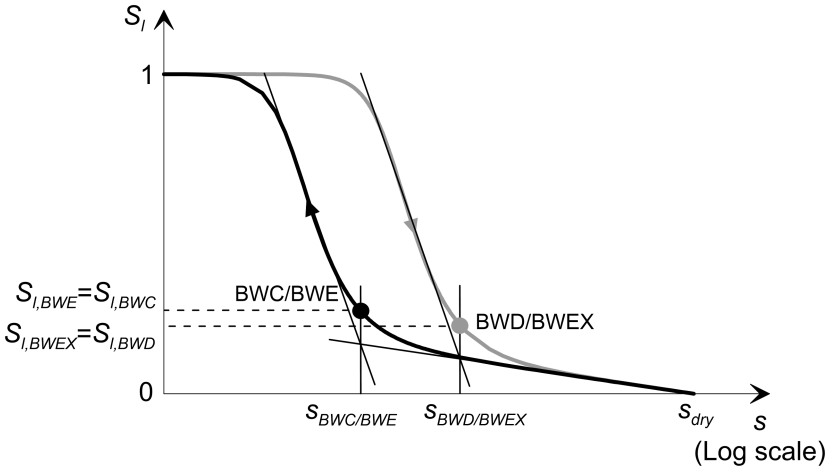

Figure 3.4: Graphical procedure for simplified estimation of $S_{l,BWD}$, $S_{l,BWC}$, $S_{l,BWEX}$ and $S_{l,BWE}$

In order to model the liquid film component of the hydraulic conductivity k_l^{Film}, a predictive semi-empirical model is proposed (LF model). In the pendular state, where the flow occurs only within the liquid films, the relationship between hydraulic conductivity and suction has been shown to be approximately linear in the log-log plot, with a slope of approximately -1.5 [91, 98]. As discussed in Section 2.2.2, the relationship for the liquid film conductivity k_l^{Film} proposed by Tokunaga [98] (see Equation 2.44) is able to capture the functional relationship between $k_l{}^{Film}$ and s at relatively low values of suction but cannot predict accurately the absolute values of $k_l{}^{Film}$ because it is the result of many simplifying assumptions. Therefore, maintaining the same functional form of Equation 2.44, the following relationship is proposed:

$$k_l^{Film} = C^{Film} \cdot \left(a^{Film} + s\right)^{-1.5} \tag{3.5}$$

where C^{Film} and a^{Film} are model parameters (soil constants). Equation 3.5 represents the liquid film component of the hydraulic conductivity as if the liquid film water was always present in the soil. However, liquid film is gradually replaced by bulk water as suction is reduced in the funicular state and hence k_l^{Film} should drop to zero at full saturation. A pragmatic approach is simply to choose the value of the parameter a^{Film} so that k_l^{Film} is negligible compared to k_l^{Bulk} at high values of S_l. a^{Film} is a dummy parameter, because it is

needed simply to ensure that the predicted value of k_l^{Film} does not tend to infinity as suction tends to zero, but its effect should be negligible in the range of suction where liquid films govern the liquid flow [98]. The value of a^{Film} must be small enough that it does not affect the linearity of the log-log plot at very low values of S_l (in the pendular range), but large enough that the predicted value of k_l^{Film} is negligible compared to k_l^{Bulk} at high values of S_l. Using a value of the parameter a^{Film} between $s_{BWD}/100$ and $s_{BWD}/10$ for drying and between $s_{BWC}/100$ and $s_{BWC}/10$ for wetting is typically acceptable.

If high quality experimental SHCC data at low values of S_l are available for the particular soil, these can be used to determine the value of the soil constant C^{Film} in Equation 3.5. However, such data are rarely available, because the hydraulic conductivity in this range is very low and thus not easy to measure. In the absence of such data, the value of C^{Film} can be estimated from knowledge of a representative particle size of the soil and of the porosity Φ. Tokunaga [98] showed analytically that, for a soil made of identical spherical particles of diameter D, the value of k_l^{Film} varies linearly with $(1-\Phi)/D$ (see Equation 2.44). Hence, the following relationship is proposed for the estimation of the parameter C^{Film}:

$$C^{Film} = X_D \frac{1-\Phi}{D} \tag{3.6}$$

where D is a representative particle size for the soil and X_D is a model parameter (a soil constant). The effective particle size D_{10} is suggested for the parameter D, because liquid film flow is likely to be predominantly controlled by the size of the smaller soil particles (because of their high specific surface area). This was confirmed by finding a better statistical correlation of experimental data from different soils when using D_{10}, rather than when using D_{50} or D_{90} (see Section 3.3.2). However, values of D_{10} are not always available (e.g. when the fines content is high and hence D_{10} is very small) and, in this case, the value of D_{50} can be used instead. The parameter X_D accounts for factors not appearing in Equation 3.6, such as differences in particle shapes, particle-size distribution and soil fabric between different soils. However, the value of X_D is expected to vary over a limited range for different coarse-grained soils, and hence, in the absence of data to determine a soil-specific value for X_D, a default value, applicable to all coarse-grained soils, can be assumed. The choice of this default value for X_D will depend upon whether D_{10} or D_{50} is used for D in Equation 3.6, as described below in Section 3.3.2.

A comparison between the hydraulic conductivity models presented above is shown in Figure 3.3b, which is plotted in terms of relative hydraulic conductivity k_{lr}, defined as $k_{lr} = k_l/k_{ls}$, with the models used to predict the bulk water component of the hydraulic conductivity of the Shonai sand [201] (see soil 6 in Section 3.3.2) and to fit the liquid film component. At high values of S_l, the conventional M model and the new modM+LF model lead to very similar SHCCs but, as S_l decreases, greater differences arise between the two models. In particular, around the BWC point the conventional M model tends to overestimate the hydraulic conductivity (sometimes by several orders of magnitude), whereas the new modM+LF model predicts much lower values of k_l, because k_l^{Bulk} goes to zero at the BWC

point. The overestimation of k_l in this region by the conventional M model is most evident for coarse-grained soils [204]. In contrast, at high values of suction the conventional M model underestimates the hydraulic conductivity, because it does not take into account the role of liquid film flow. Finally, it can be seen that in the new modM+LF model the hydraulic conductivity is governed almost entirely by k_l^{Bulk} at relatively low suction values and almost entirely by k_l^{Film} at relatively high suction values. The predicted transition between the two, occurring around the BWC point, is sharper and more distinct for coarser soils.

Figure 3.5 shows a qualitative comparison between the predicted SHCCs for two fictitious soils: a coarser-grained soil and a finer-grained soil. The coarser soil has a higher saturated hydraulic conductivity but it desaturates at a lower value of suction and, thus, the liquid film component of the hydraulic conductivity becomes dominant at a lower value of suction than for the finer soil. Comparing the two soils in the suction range where the hydraulic conductivity is governed by the liquid film component, it can be seen that, at the same value of suction (points A_f and A_c), the hydraulic conductivity is higher for the finer soil. At the same value of suction, the thickness of the adsorbed liquid films is the same for the two soils but the finer soil has a higher specific surface area and thus a higher number of liquid film flow channels. However, at the two different suction values where the liquid film component of the hydraulic conductivity becomes dominant over the bulk water component for the two soils (points B_f and B_c), the hydraulic conductivity of the coarser layer (point B_c) is higher than that of the finer layer (point B_f), because the thickness of the adsorbed liquid films at point B_c for the coarser layer is considerably higher than that at point B_f for the finer layer. This explains why considering the role of liquid films in hydraulic conductivity is more relevant for coarser-grained soils.

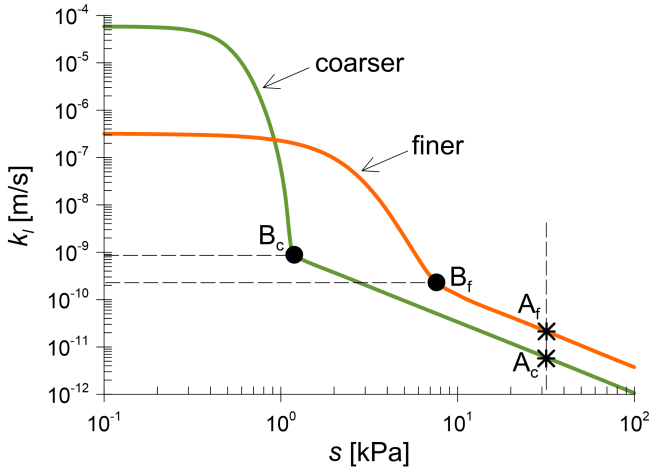

Figure 3.5: Qualitative comparison between predicted SHCCs for a finer-grained soil and a coarser-grained

At extremely high suction values, approaching s_{dry}, the liquid film flow becomes so small that water movement will be dominated by vapour flow (i.e. diffusion of water within the gas phase) [91]. However, unlike the advective liquid water flux, which is governed by Darcy's law, the diffusive flux of water vapour in the gas phase is a different physical process and it is governed by Fick's law. Thus, water vapour flow cannot be included in the hydraulic

conductivity k_l. Some numerical codes, e.g. Code_Bright [205], allow the resolution of coupled thermo-hydraulic problems in which water vapour diffusion is modelled by Fick's law whereas advective liquid flux is modelled by Darcy's law. In this way, the two different phenomena of advective liquid water flux and diffusive water vapour flux are both correctly modelled.

It should be noted that the proposed new hydraulic constitutive model has a small element of inconsistency, in that the modVG SWRC model predicts that the value of S_l reduces to zero (i.e. no liquid water present in the soil) at a finite (but extremely high) value of suction s_{dry}, whereas the proposed modM+LF SHCC model predicts that the hydraulic conductivity only goes to zero as suction tends to infinity. For most practical problems this inconsistency has negligible effects because, at very high suction values approaching s_{dry}, water movement is governed by vapour diffusion.

Throughout this thesis, the reference improved models will be the modVG model for the SWRC and the modM+LF model for the SHCC. However, similar hydraulic models improved at low degree of saturation can be obtained starting from the conventional Brooks and Corey [81] model and the Kosugi [83] model. For the SWRC, the modified Brooks and Corey model (modBC) proposed by Fayer and Simmons [88] (see Equation 2.36) and the modified Kosugi model (modK) proposed by Khlosi et al. [90] (see Equation 2.38) can be used. For the SHCC, the new proposed model expressed by Equation 3.1 can be applied. In a similar fashion to what was proposed for the modVG-modM model, k_l^{Bulk} can be calculated also for the modBC and the modK model by replacing the variable S_{le} present in Equation 2.39 (for the modBC model) and in Equation 2.40 (for the modK model), with the new variables S_l^C and S_l^B. Thus, the term k_l^{Bulk} for the modBC model can be expressed as:

$$k_l^{Bulk} = k_{ls}\left(S_l^C\right)^2\left(S_l^B\right)^{1+2/n} \tag{3.7}$$

whereas, for the modK model, it can be expressed as:

$$k_l^{Bulk} = k_{ls}\sqrt{S_l^C}\left\{Q\left[Q^{-1}\left(S_l^B\right)+\sigma_m\right]\right\}^2 \tag{3.8}$$

where S_l^C and S_l^B are expressed by Equation 3.2 and Equation 3.3 respectively. For the modBC and the modK models, the liquid film component of the hydraulic conductivity k_l^{Film} is the same as for the modVG-modM+LF model (see Equations 3.5 and 3.6).

3.3.2 Experimental validation

Data from the literature involving tests on 11 relatively coarse-grained soil samples were used for experimental validation of the new hydraulic model modVG-modM+LF. Properties of these soils (soil type, reference, saturated hydraulic conductivity k_{ls} and porosity Φ) are shown in Table 3.1. The experimental data come from three different sources: one journal paper [201], the unsaturated soil hydraulic database UNSODA [206] and an unsaturated soil hydraulic catalogue [207]. Experimental data defining the SWRC and the SHCC were

Table 3.1: General properties of soils 1-11

Soil n.	Soil type	Reference*	k_{ls} [m/s]	Φ	D_{10} [mm]	D_{50} [mm]
1	Sand	N (4660)	7.240×10^{-5}	0.460	0.0647	0.3013
2	Sand	N (4661)	1.320×10^{-4}	0.430	0.0722	0.3113
3	Sand	N (4650)	6.791×10^{-5}	0.380	0.0722	0.3195
4	Loamy sand	N (4011)	2.176×10^{-6}	0.419	0.0174	0.1121
5	Loamy sand	N (4062)	1.508×10^{-6}	0.320	0.0265	0.1041
6	Shonai sand	Me	1.093×10^{-4}	0.430	0.1317	0.3099
7	Sandy Loam	N (4172)	3.738×10^{-6}	0.420	-	0.0915
8	Silt Loam	N (4182)	7.014×10^{-6}	0.435	-	0.0296
9	Gilat Loam	Mu	2.000×10^{-6}	0.440	-	-
10	Rehovot sand	Mu	1.330×10^{-4}	0.400	-	-
11	Grenoble 3 sand	N (4442)	5.000×10^{-5}	0.385	0.1409	0.2859

* N (ID code): Nemes et al. [206]; Me: Mehta et al. [201]; Mu: Mualem [207].

available for all 11 soils. For soil 8, unlike the other soils, the SHCC data points were only available in the $k_l : S_l$ plot, but they were converted to the $k_l : s$ plot by using the modVG model for the SWRC. This operation was considered reasonable, because the modVG model was able to fit the experimental SWRC points extremely well over the full range of suction for this soil.

Experimental SHCC data in the suction range where hydraulic conductivity was governed by the liquid film component (low values of S_l) were available for soils 1-10. For these soils, the expression for k_l^{Film} given by Equation 3.5 (LF model) was fitted to the experimental SHCC data points in the suction range where these points are aligned on a straight line with slope -1.5 in the log-log scale, as shown in Figure 3.6 (which is plotted in terms of relative hydraulic conductivity k_{lr}). In this fitting operation, the slope of the straight line in the log-log plot was fixed a priori to -1.5 whereas the parameter C^{Film} was fitted. In all 10 soils, the LF model fits the experimental data very well. This confirms the validity of Equation 3.5, including the value of the exponent (-1.5). The resulting values of the parameter C^{Film} are shown in Table 3.2. The units employed for C^{Film} in Table 3.2 are appropriate if suction s and parameter a^{Film} are expressed in kPa and k_l^{Film} is required in units of m/s.

Among soils 1-10, values of D_{10} were available for soils 1-6 and values of D_{50} were available for soils 1-8 (see Table 3.1). For each of these soils, the fitted value of C^{Film} shown in Table 3.2 was combined with the soil porosity Φ and the appropriate value of D_{10} or D_{50} to back-calculate a corresponding soil-specific value of the parameter X_D (see Table 3.2), by using Equation 3.6. The units employed for X_D in Table 3.2 are appropriate if suction s and parameter a^{Film} are expressed in kPa, representative particle size D (i.e. D_{10} or D_{50}) is expressed in mm and k_l^{Film} is required in units of m/s. When using D_{10}, the geometric mean of the 6 soil-specific values of X_D listed in Table 3.2 was calculated as 2.35×10^{-9} mm.m s^{-1}.kPa$^{1.5}$ (see Table 3.2), and this is recommended as a general default value of X_D to use in Equation 3.6 (with a value of D_{10}) in cases where experimental values of

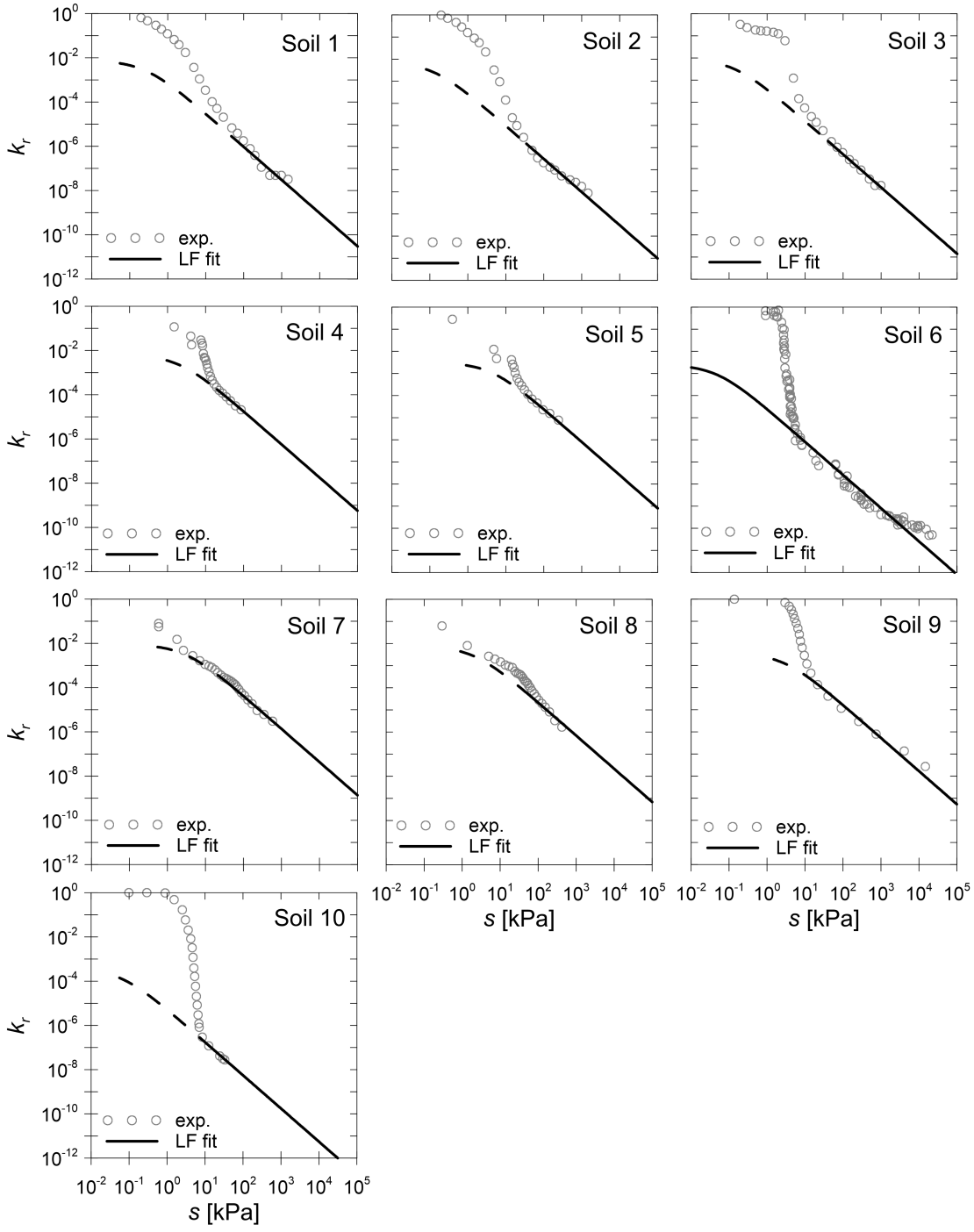

Figure 3.6: Liquid film component of the hydraulic conductivity (Equation 3.5) fitted to experimental data in the range where the hydraulic conductivity is governed by the liquid film component (soils 1-10)

Table 3.2: Fitted values of C^{Film} and X_D for soils 1-10

Soil n.	C^{Film} [ms^{-1}.kPa$^{1.5}$]	$X_D\,(D_{10})$ [mm.ms^{-1}.kPa$^{1.5}$]	$X_D\,(D_{50})$ [mm.ms^{-1}.kPa$^{1.5}$]
1	6.8420×10^{-8}	8.20×10^{-9}	3.82×10^{-8}
2	4.0919×10^{-8}	5.18×10^{-9}	2.23×10^{-8}
3	3.0120×10^{-8}	3.51×10^{-9}	1.55×10^{-8}
4	3.9372×10^{-8}	1.18×10^{-9}	7.60×10^{-9}
5	3.8297×10^{-8}	1.49×10^{-9}	5.86×10^{-9}
6	2.7805×10^{-9}	6.42×10^{-10}	1.51×10^{-9}
7	1.6153×10^{-7}	-	2.55×10^{-8}
8	1.5310×10^{-7}	-	8.02×10^{-9}
9	3.3616×10^{-8}	-	-
10	7.3879×10^{-10}	-	-
Default	-	2.35×10^{-9}	1.08×10^{-8}

k_l in the pendular range (low values of S_l) are not available. If a value for D_{10} is not available, but D_{50} is known, the corresponding default value of X_D is 1.08×10^{-8} mm.m s^{-1}.kPa$^{1.5}$ (see Table 3.2). However, it is preferable to use D_{10}, if possible, because statistical analysis showed that the variance in the D_{10} soil-specific values of X_D shown in Table 3.2 is less than the variance in the D_{50} soil-specific values of X_D. The statistical analysis of the D_{10} soil-specific values of X_D indicated a 95% confidence level that the value of X_D for a soil should fall between a lower bound of 0.2 times the default value and an upper bound of 5 times the default value.

Experimental and modelled SWRCs and SHCCs for all the 11 soils are shown in Figure 3.7, with the SHCCs plotted in terms of relative hydraulic conductivity k_{lr}. In the graphs representing the SWRCs, the experimental points are compared to the conventional VG model and the proposed modVG model, both fitted to the experimental SWRC points. In both cases, the constraint $m = 1 - 1/n$ was used and the parameter S_{ls} was set as $S_{ls} = 1$. Values of the remaining model parameters are shown in Table 3.3. In the graphs representing the SHCCs, the experimental points are compared to the conventional M model (coupled with the VG model) and the new modM+LF model (coupled with the modVG model for the prediction of k_l^{Bulk}). In the k_l^{Bulk} component (i.e. modM) of the new SHCC model, the value of the parameter $s_{BWD} = s_{BWEX}$ for each soil (see Table 3.3), and hence the value of $S_{l,BWD} = S_{l,BWEX}$, was obtained from the SWRC using the graphical construction described in Section 3.3.1 (see Figure 3.4). In the k_l^{Film} (i.e. LF) component of the new SHCC model, the value of C^{Film} was taken either as a fitted value, from Table 3.2, where SHCC data from the pendular range were available (soils 1-10), or as a predicted value, calculated from Equation 3.6, using the appropriate default value of X_D (see Table 3.2) and the value of D_{10}, where this was available (soils 1-6, 11), or the value of D_{50} (soils 7, 8).

For soils where SWRC data were available in the pendular range (i.e. soils 3, 6, 9 and 10), the modVG model fits the experimental data much better than the VG model (see Figure 3.7). However, in the capillary and funicular ranges, the two models are indistinguishable.

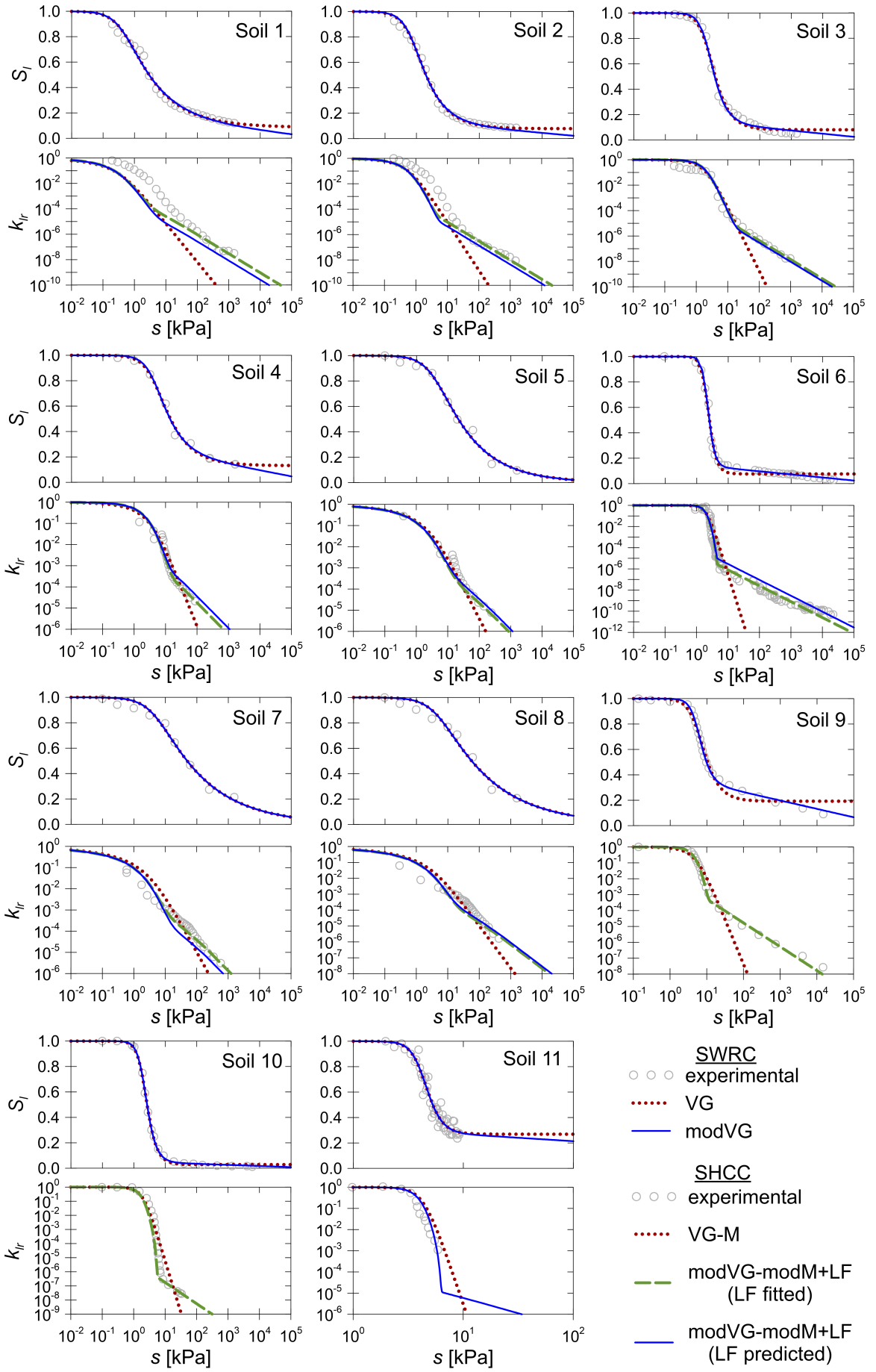

Figure 3.7: Comparison between experimental data and SWRC and SHCC models for soils 1-11

Table 3.3: Model parameter values for soils 1-11

Soil n.	n (VG)	P_0 (VG) [kPa]	S_{lr} (VG)	n (modVG)	P_0 (modVG) [kPa]	ξ (modVG)	s_{BWD} (modM) [kPa]
1	1.4153	0.4524	0.0864	1.4643	0.4302	0.0125	50
2	1.7129	0.7469	0.0780	1.7820	0.7378	0.0096	12
3	2.1980	2.2553	0.0810	2.4487	2.2738	0.0108	40
4	1.6767	4.2589	0.1314	1.8519	4.2176	0.0204	40
5	1.3739	3.5386	0.0000	1.3739	3.5386	0.0000	400
6	3.9820	2.1749	0.0762	4.6368	2.1547	0.0105	4.70
7	1.2844	4.4385	0.0000	1.2844	4.4385	0.0000	200
8	1.2664	4.3745	0.0000	1.2664	4.3725	0.0000	600
9	2.4417	5.8514	0.1919	3.3255	5.6370	0.0287	14
10	3.1295	2.1529	0.0289	3.2450	2.1441	0.0038	8
11	6.3045	4.4563	0.2691	6.4199	4.4267	0.0232	6.48

Figure 3.7 also shows that in general the modM model predicts k_l^{Bulk} better than the M model. Exceptions are soil 3 where the two models lead to very similar results and soils 1 and 2 where both models are not in a good agreement with the experimental data. This mis-match for soils 1 and 2 is probably related to an underlying weakness of the Mualem approach or to inaccurate experimental determination of the value of k_{ls} (note that the experimental values of k_l within the funicular range have not been used at all in determining the parameter values in the M and modM+LF models). The difference between the M model and the modM model may lead to significant differences of hydraulic conductivity for certain values of suction. For instance, at the BWD point of soil 10 ($s = 8$ kPa)), the conventional M model overestimates the hydraulic conductivity by approximately three orders of magnitude, whereas for soil 9 at a very high suction of 10 MPa the conventional M model underestimates the hydraulic conductivity by approximately 11 orders of magnitude.

Figure 3.7 shows that the liquid film branch of the SHCCs for the different soils is very well modelled by Equation 3.5 when this is fitted to experimental data (i.e. using a fitted value of C^{Film}). Moreover, it can be seen that, in absence of experimental data of hydraulic conductivity at very low degree of saturation, k_l^{Film} may be predicted adequately by Equations 3.5 and 3.6, if an appropriate default value of X_D, presented in Table 3.2, is used.

For soil 11, experimental SHCC points were not available at very low degree of saturation and the liquid film component of the SHCC model could only be predicted. This is an example of how the predictive SHCC model should be used in the absence of experimental data.

3.4 Hydraulic hysteresis modelling

The improved models presented for the SWRC (see Section 3.2) and for the SHCC (see Section 3.3) can be used only to represent a main drying or a main wetting process. In this section, the models are extended to include the effects of hydraulic hysteresis, by using a bounding surface approach. The extended hydraulic model requires the definition of the

following elements:

- main drying and main wetting SWRCs;
- scanning retention curves;
- effect of hydraulic hysteresis on the SHCCs.

In this thesis, main drying (Md) and main wetting (Mw) SWRCs are modelled using the modVG model as a reference model. However, the hysteretic water retention modelling approach can also be applied to other models for the main SWRCs, such as the modBC model and the modK model, as demonstrated within this section.

3.4.1 Initial modelling approach

The scanning curves are modelled using a bounding surface approach. In the initial modelling approach, which is similar to that followed by Gallipoli et al. [120], the gradient of a scanning drying curve $\left(\frac{dS_l}{d\log s}\right)_d$ and the gradient of a scanning wetting curve $\left(\frac{dS_l}{d\log s}\right)_w$ (in the semi-logarithmic $S_l : \log s$ plot) at the point (s, S_l) are related to the corresponding gradient of the main drying curve $\left(\frac{dS_l}{d\log s_d}\right)_{Md}$ or main wetting curve $\left(\frac{dS_l}{d\log s_w}\right)_{Mw}$ respectively:

$$\left(\frac{dS_l}{d\log s}\right)_d = \left(\frac{s}{s_d}\right)^{\gamma_d} \left(\frac{dS_l}{d\log s_d}\right)_{Md} \tag{3.9a}$$

$$\left(\frac{dS_l}{d\log s}\right)_w = \left(\frac{s_w}{s}\right)^{\gamma_w} \left(\frac{dS_l}{d\log s_w}\right)_{Mw} \tag{3.9b}$$

s_d and s_w are the image values of suction, namely the suction values corresponding to the horizontal projection (at the same degree of saturation S_l) of the point (s, S_l) onto the main drying curve or the main wetting curve (see Figure 3.8). $\left(\frac{dS_l}{d\log s_d}\right)_{Md}$ and $\left(\frac{dS_l}{d\log s_w}\right)_{Mw}$ are respectively the gradients of the main drying curve and of the main wetting curve at their image points (see Figure 3.8). The terms γ_d and γ_w are parameters of the model (soil constants) for the scanning drying curve and scanning wetting curve respectively and they always assume positive values. The closer is the current value of suction s to its image value, s_d or s_w, the closer is the gradient of the scanning curve to the gradient of its corresponding Md or Mw curve. The main curve thus represents an asymptotic limit for the corresponding scanning curve.

The parameters γ_d and γ_w control the shape of the scanning curves, as shown in Figure 3.9. As the value of γ_d or γ_w increases, the variation of the gradient of the scanning curve becomes sharper. At the upper limit, i.e. $\gamma_d \to \infty$ or $\gamma_w \to \infty$, the scanning curve is horizontal in the $S_l : \log s$ plot until reaching the corresponding main curve. At this point, the gradient of the scanning curve changes sharply and the scanning curve follows the corresponding main curve. At the lower limit, i.e. $\gamma_d = 0$ or $\gamma_w = 0$, the scanning curve is exactly parallel to the corresponding main curve (i.e. they have the same gradient) regardless of the distance of the current suction value from the corresponding image suction value.

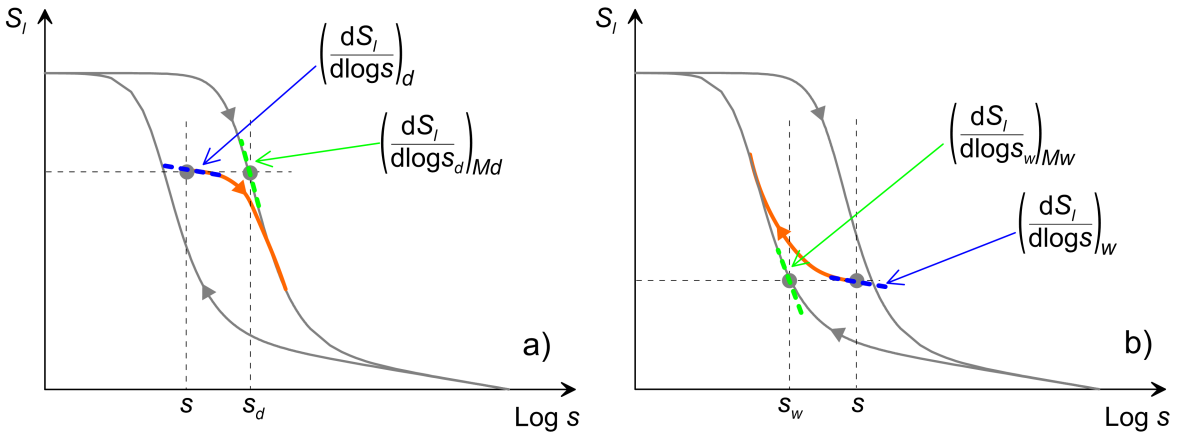

Figure 3.8: Qualitative water retention a) drying scanning curve and b) wetting scanning curve

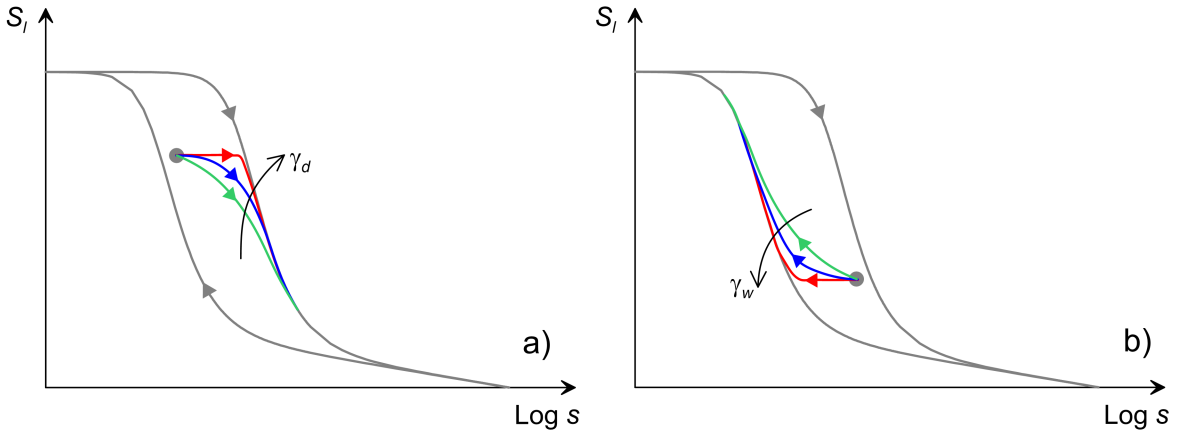

Figure 3.9: Role of parameters a) γ_d and b) γ_w

Given that the differential term $d\log s$ can be written as:

$$d\log s = \log_{10} e \cdot \frac{ds}{s} \tag{3.10}$$

Equation 3.9 can be expressed as:

$$\log_{10} e \cdot \frac{s \cdot dS_l}{ds} = \left(\frac{s}{s_d}\right)^{\gamma_d} \log_{10} e \cdot \frac{s_d \cdot dS_l}{ds_d} \tag{3.11a}$$

$$\log_{10} e \cdot \frac{s \cdot dS_l}{ds} = \left(\frac{s_w}{s}\right)^{\gamma_w} \log_{10} e \cdot \frac{s_w \cdot dS_l}{ds_w} \tag{3.11b}$$

Simplifying Equation 3.11, the following expressions are obtained:

$$\frac{s}{ds} = \left(\frac{s}{s_d}\right)^{\gamma_d} \frac{s_d}{ds_d} \tag{3.12a}$$

$$\frac{s}{ds} = \left(\frac{s_w}{s}\right)^{\gamma_w} \frac{s_w}{ds_w} \tag{3.12b}$$

Equation 3.12 can be thus written in the following integral form:

$$\int s^{(\gamma_d-1)}ds = \int s_d^{(\gamma_d-1)}ds_d \tag{3.13a}$$

$$\int s^{(-\gamma_w-1)}ds = \int s_w^{(-\gamma_w-1)}ds_w \tag{3.13b}$$

By integrating Equation 3.13, the following expressions are obtained:

$$\frac{s^{\gamma_d}}{\gamma_d} = \frac{s_d^{\gamma_d}}{\gamma_d} + A_{d0} \tag{3.14a}$$

$$-\frac{s^{-\gamma_w}}{\gamma_w} = -\frac{s_w^{-\gamma_w}}{\gamma_w} + A_{w0} \tag{3.14b}$$

where A_{d0} and A_{w0} are integration constants. Equation 3.14 can be simplified and written in the following way:

$$s^{\gamma_d} = s_d^{\gamma_d} + A_d \tag{3.15a}$$

$$s^{-\gamma_w} = s_w^{-\gamma_w} + A_w \tag{3.15b}$$

where s_d and s_w are respectively the inverse function of the main drying curve $s_d = s_d(S_l)$ and the main wetting curve $s_w = s_w(S_l)$, and A_d and A_w are integration constants which are obtained by imposing the condition that the scanning curve passes through the reversal point (s_0, S_{l0}). In particular, the integration constants are obtained as:

$$A_d = s_0^{\gamma_d} - s_d(S_{l0})^{\gamma_d} \tag{3.16a}$$

$$A_w = s_0^{-\gamma_w} - s_w(S_{l0})^{-\gamma_w} \tag{3.16b}$$

Equations 3.15a and 3.15b define the scanning drying and scanning wetting curves respectively, once the inverse function of the main drying curve $s_d(S_l)$, the inverse function of the main wetting curve $s_w(S_l)$ and the position of the last reversal point (s_0, S_{l0}) are known. Closed-form solutions to Equations 3.15a and 3.15b can always be obtained if the main SWRC can be inverted to a closed-form relationship (i.e. if $s_d(S_l)$ and $s_w(S_l)$ can be expressed by closed-form relationships).

3.4.2 Revised modelling approach and application to modVG SWRC model

Unfortunately, if the function representing the main SWRCs is not invertible to a closed-form (i.e. if a closed-form expression for $s_d(S_l)$ and $s_w(S_l)$ cannot be obtained), Equation 3.15 can be solved only using iterative procedures, which may increase the computational effort if the model is used in numerical codes. This is the case for the modified van Genuchten (modVG) model (see Equation 2.37). In this case, however, a revised form of bounding surface approach can be applied to obtain a closed-form expression for the scanning curve.

In this revised form of bounding surface approach, the relationship between the gradient of the scanning curve and the gradient of the corresponding main curve (see Equation 3.9) is replaced by an equivalent expression in terms of the effective degree of saturation S_{le} instead of the actual degree of saturation S_l:

$$\left(\frac{dS_{le}}{d\log s}\right)_d = \left(\frac{s}{s_d}\right)^{\gamma_d}\left(\frac{dS_{le}}{d\log s_d}\right)_{Md} \tag{3.17a}$$

$$\left(\frac{dS_{le}}{d\log s}\right)_w = \left(\frac{s_w}{s}\right)^{\gamma_w}\left(\frac{dS_{le}}{d\log s_w}\right)_{Mw} \tag{3.17b}$$

As a consequence, revised versions of Equations 3.11 and 3.15 can be written by substituting S_l with S_{le}. In particular, s_d and s_w in Equation 3.15 are respectively the inverse function of the main drying curve $s_d = s_d(S_{le})$ and the main wetting curve $s_w = s_w(S_{le})$, now each expressed as a function of the effective degree of saturation S_{le}. The function $S_{le}(s)$ expressed by Equation 2.31 can now be inverted to a closed-form, thereby obtaining:

$$s_d = P_{0d}\cdot\left({S_{le}}^{-1/m_d} - 1\right)^{1/n_d} \tag{3.18a}$$

$$s_w = P_{0w}\cdot\left({S_{le}}^{-1/m_w} - 1\right)^{1/n_w} \tag{3.18b}$$

where P_{0d}, n_d and m_d are the parameters of the modVG model for the main drying SWRC and P_{0w}, n_w and m_w are the parameters of the modVG model for the main wetting SWRC. Therefore, replacing the terms s_d and s_w in Equation 3.15 with those expressed by Equation 3.18 and after some algebraic manipulation, the following closed-form relationships describing the scanning curve in terms of the effective degree of saturation S_{le} can be obtained:

$$S_{le,d} = \left\{1 + \left[\frac{(s^{\gamma_d} - A_d)^{1/\gamma_d}}{P_{0d}}\right]^{n_d}\right\}^{-m_d} \tag{3.19a}$$

$$S_{le,w} = \left\{1 + \left[\frac{(s^{-\gamma_w} - A_w)^{-1/\gamma_w}}{P_{0w}}\right]^{n_w}\right\}^{-m_w} \tag{3.19b}$$

The integration constants A_d and A_w are calculated as:

$$A_d = s_0^{\gamma_d} - \left[P_{0d}\cdot\left(S_{le0}^{-1/m_d} - 1\right)^{1/n_d}\right]^{\gamma_d} \tag{3.20a}$$

$$A_w = s_0^{-\gamma_w} - \left[P_{0w}\cdot\left(S_{le0}^{-1/m_w} - 1\right)^{1/n_w}\right]^{-\gamma_w} \tag{3.20b}$$

where S_{le0} is the effective degree of saturation at the reversal point and it can be obtained

from the actual degree of saturation at the reversal point S_{l0} as:

$$S_{le0} = \frac{S_{l0} - \xi_d \ln\left(\frac{s_{dry}}{s}\right)}{S_{ls,d} - \xi_d \ln\left(\frac{s_{dry}}{s}\right)} \quad \text{for drying} \tag{3.21a}$$

$$S_{le0} = \frac{S_{l0} - \xi_w \ln\left(\frac{s_{dry}}{s}\right)}{S_{ls,w} - \xi_w \ln\left(\frac{s_{dry}}{s}\right)} \quad \text{for wetting} \tag{3.21b}$$

where $S_{ls,d}$ and ξ_d are the parameters of the modVG model for the main drying SWRC and $S_{ls,w}$ and ξ_w are the parameters of the modVG model for the main wetting SWRC.

Thus, using Equations 2.29 and 2.35 and the terms $S_{le,d}$ and $S_{le,w}$ obtained from Equations 3.19a and 3.19b (with A_d and A_w given by Equation 3.20), the following closed-form relationships describing the scanning curves in terms of the actual degree of saturation S_l can be obtained:

$$S_{l,d} = \xi_d \ln\left(\frac{s_{dry}}{s}\right) + S_{le,d}(s) \cdot \left(S_{ls,d} - \xi_d \ln\left(\frac{s_{dry}}{s}\right)\right) \tag{3.22a}$$

$$S_{l,w} = \xi_w \ln\left(\frac{s_{dry}}{s}\right) + S_{le,w}(s) \cdot \left(S_{ls,w} - \xi_w \ln\left(\frac{s_{dry}}{s}\right)\right) \tag{3.22b}$$

The combination of Equations 3.19, 3.20 and 3.22 forms a simple but effective method to include water retention hysteresis in the modVG SWRC model. This model is referred to as the hysteretic modVG SWRC model throughout the remainder of this thesis.

The logic behind the revised modelling approach described in this section is that water retention hysteresis is implicitly related solely to the effective degree of saturation S_{le}, which can be considered an expression of the bulk water present in the soil. As a consequence, in this revised modelling approach, water retention hysteresis is related solely to the bulk water, in agreement with the description of water retention hysteresis given in Section 3.1.

If this new proposed hysteretic hydraulic model is implemented in a numerical code, the following constraints are suggested:

$$\xi_d = \xi_w \tag{3.23}$$

$$S_{ls,d} = S_{ls,w} = 1 \tag{3.24}$$

Equation 3.23 ensures that water retention hysteresis is not present in the pendular range and that main drying curve and main wetting curve never cross each other. Equation 3.24 guarantees that full saturation (i.e. $S_l = 1$) can always be achieved in the soil. In the literature, the formation of trapped air occurring during wetting has been often modelled adopting a main wetting SWRC which does not reach full saturation even at $s = 0$ (i.e. $S_{ls,w} < 1$). However, as discussed in Chapter 5, this wetting SWRC is not a fundamental representation of the soil behaviour and depends on various aspects of the wetting test conditions. The real fundamental main wetting SWRC should satisfy Equation 3.24 and, in numerical analyses, the effect of trapped air should be captured according to a procedure discussed in Chapter 5.

3.4.3 Impact on modM+LF SHCC model

The bulk water component of the SHCC k_l^{Bulk} is typically recognized as non-hysteretic when plotted against the degree of saturation [31, 121, 131, 200], and thus hysteretic if plotted against suction, due to the hysteresis in the SWRC (see Figure 3.10). In order to satisfy the requirement that k_l^{Bulk} is non-hysteretic when plotted against the degree of saturation, the following restrictions must be applied to the parameters of the modVG SWRC model, when coupled with the SHCC model:

$$m_d\,(=1-1/n_d) = m_w\,(=1-1/n_w) \tag{3.25}$$

$$S_{l,BWC} = S_{l,BWD} \tag{3.26}$$

$$S_{l,BWE} = S_{l,BWEX} \tag{3.27}$$

which are typically realistic [51]. The relationship between k_l^{Bulk} and degree of saturation is still given by Equation 3.4, which is the same for main wetting curve, main drying curve and scanning curves under the assumptions of Equations 3.25, 3.26 and 3.27.

The liquid film component of the hydraulic conductivity k_l^{Film} is still given by Equation 3.5, with a^{Film} and C^{Film} as soil constants, and thus the relationship between k_l^{Film} and s is independent of wetting or drying. Consequently, k_l^{Film} is non-hysteretic when plotted against suction s.

Figure 3.10 qualitatively shows the performance of the new hysteretic hydraulic modVG-modM+LF model in the $S_l : s$ plot, the $k_l : s$ plot and the $k_l : S_l$ plot, by simulating a virtual sequence of wetting and drying paths (starting at point A and ending at point K). Results in Figure 3.10 were obtained assuming $S_{ls,d} = S_{ls,w} = 1$, $\xi_d = \xi_w$ and $s_{dry} = 1\,\text{GPa}$. The results shown in Figure 3.10 are valid for both the use of the initial modelling approach of Section 3.4.1 (i.e. Equation 3.9) and the use of the revised modelling approach of Section 3.4.2 (i.e. Equation 3.17). Under saturated conditions (capillary state) and at very low degree of saturation (i.e. in the pendular state) the water retention behaviour is non-hysteretic. Scanning curves (e.g. A-B) reasonably describe the hysteresis in the water retention behaviour in the funicular range.

The bulk water component of the hydraulic conductivity k_l^{Bulk} is non-hysteretic when plotted against the degree of saturation S_l (see Figure 3.10c) whereas k_l^{Bulk} is hysteretic when plotted against suction s (see Figure 3.10b) due to hysteresis in the SWRC. The liquid film component k_l^{Film} is non-hysteretic when plotted against suction s (see Figure 3.10b). From the physical point of view, the liquid film conductivity is related to the thickness of the liquid films, which is solely a function of suction for a given soil. At very low degree of saturation, i.e. in the pendular range, k_l^{Film} is non-hysteretic also when plotted against S_l because only liquid film water and meniscus water are present and, in this condition, also the SWRC is non-hysteretic. However, k_l^{Film} is slightly hysteretic in the $k_l : S_l$ plot at the transition between bulk water-dominated hydraulic conductivity and liquid film-dominated hydraulic conductivity (see Figure 3.10c), in particular for values of the degree of saturation between the BWC/BWD points and the BWE/BWEX points, i.e. $S_{l,BWE/BWEX} < S_l < S_{l,BWC/BWD}$.

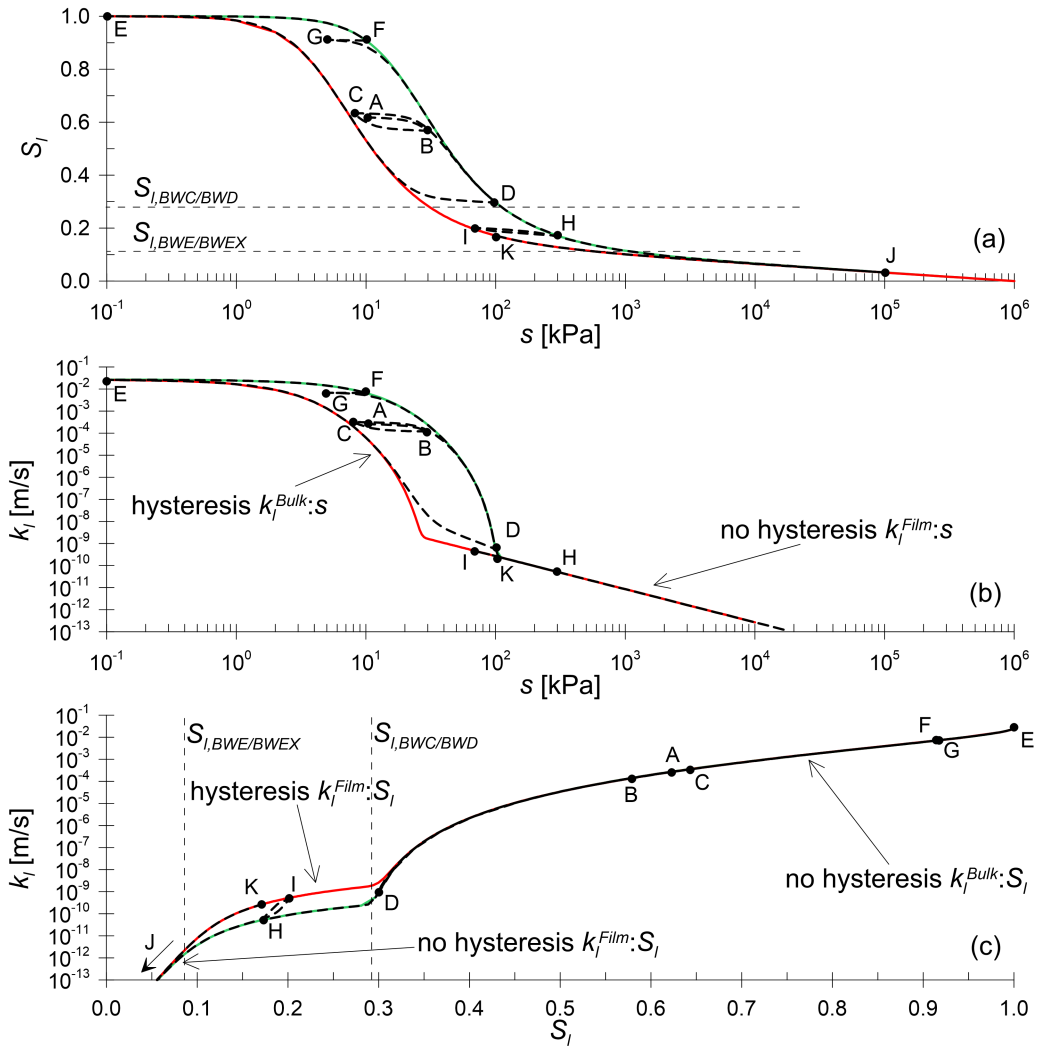

Figure 3.10: Performance of the hydraulic hysteretic model: a) SWRC, b) SHCC plotted against suction s and c) SHCC plotted against degree of saturation S_l

This prediction of the model has a physical explanation. Since $S_l < S_{l,BWC/BWD}$, bulk water is not continuous and the liquid flow is governed by the liquid film hydraulic conductivity but, since $S_l > S_{l,BWE/BWEX}$, a small amount of bulk water is present in the soil although it does not contribute to liquid flow. The bulk water influences the hysteresis in the SWRC whereas liquid film water and meniscus water do not have a hysteretic behaviour. Therefore, $k_l^{Film} : S_l$ is hysteretic because the bulk water still present in the soil contributes to the hysteresis in the SWRC, although not to the SHCC. In other words, if k_l^{Film} was plotted against the component of the degree of saturation only related to liquid film water and meniscus water, k_l^{Film} would always be non-hysteretic.

3.4.4 Application to modBC and modK SWRC models

As mentioned above, the hysteretic approach of hydraulic modelling described in Sections 3.4.1 and 3.4.2 leads to closed-form expressions for any models characterized by a SWRC equation for main drying and for main wetting curves which can be inverted to a closed-form expression. If the initial bounding surface approach of Equation 3.9 is applied,

it is the main drying/wetting curve expression for S_l that must be inverted to closed form, whereas if the revised bounding surface approach of Equation 3.17 is applied, it is the main drying/wetting curve expression for S_{le} that must be invertible to a closed form. The revised hysteretic hydraulic modelling approach of Equation 3.17, which above is applied to the modVG model (i.e. the reference model throughout this thesis), can be applied also to the modified Brooks and Corey (modBC) model (see Equation 2.36) and the modified Kosugi (modK) model (see Equation 2.38). For the hysteretic modBC model, the scanning curves in terms of the effective degree of saturation are expressed as:

$$S_{le,d} = \begin{cases} 1 & \text{if } s \leq s_{AE} \\ s_{AE}^{n_d} \left(s^{\gamma_d} - A_d\right)^{-n_d/\gamma_d} & \text{if } s > s_{AE} \end{cases} \tag{3.28a}$$

$$S_{le,w} = \begin{cases} 1 & \text{if } s \leq s_{AEX} \\ s_{AEX}^{n_w} \left(s^{-\gamma_w} - A_w\right)^{n_w/\gamma_w} & \text{if } s > s_{AEX} \end{cases} \tag{3.28b}$$

where s_{AE} and n_d are the parameters of the modBC model for the main drying SWRC, s_{AEX} and n_w are the parameters of the modBC model for the main wetting SWRC, and the integration constants A_d and A_w are obtained as:

$$A_d = s_0^{\gamma_d} - \left(\frac{s_{AE}}{S_{le0}^{1/n_d}}\right)^{\gamma_d} \tag{3.29a}$$

$$A_w = s_0^{-\gamma_w} - \left(\frac{s_{AEX}}{S_{le0}^{1/n_w}}\right)^{-\gamma_w} \tag{3.29b}$$

For the hysteretic modK model:

$$S_{le,d} = Q\left[\frac{\ln\left(\frac{s^{\gamma_d} - A_d}{s_{md}^{\gamma_d}}\right)}{\gamma_d \sigma_{md}}\right] \tag{3.30a}$$

$$S_{le,w} = Q\left[\frac{\ln\left(\frac{s^{-\gamma_w} - A_w}{s_{mw}^{-\gamma_w}}\right)}{-\gamma_w \sigma_{mw}}\right] \tag{3.30b}$$

where s_{md} and σ_{md} are the parameters of the modK model for the main drying SWRC, s_{mw} and σ_{mw} are the parameters of the modK model for the main wetting SWRC and the constants A_d and A_w are obtained as:

$$A_d = s_0^{\gamma_d} - s_{md}^{\gamma_d} \exp\left[\gamma_d \sigma_{md} Q^{-1}\left(S_{le0}\right)\right] \tag{3.31a}$$

$$A_w = s_0^{-\gamma_w} - s_{mw}^{-\gamma_w} \exp\left[-\gamma_w \sigma_{mw} Q^{-1}\left(S_{le0}\right)\right] \tag{3.31b}$$

Equations 3.28 for the modBC model and 3.30 for the modK model are then combined with Equation 3.22 to obtain the equations for the scanning curves expressed in terms of the actual

degree of saturation.

Finally, as discussed for the modVG model, also the modBC and the modK hysteretic water retention models can be coupled with the corresponding SHCC models (see Equations 3.1, 3.5, 3.7 and 3.8). In order to guarantee that k_l^{Bulk} is non-hysteretic in the $k_l^{Bulk} - S_l$ plot, in addition to the constraints given by Equations 3.26 and 3.27, the following restriction must be applied within the modBC SWRC model:

$$n_d = n_w \tag{3.32}$$

and in the modK SWRC model:

$$\sigma_{md} = \sigma_{mw} \tag{3.33}$$

3.4.5 Experimental validation

The hysteretic component of the new hydraulic model for unsaturated soils was validated against experimental data coming from different sources in the literature.

Figure 3.11 shows experimental SWRC data for Tottori sand, obtained by Sakai and Toride [208], covering the full range of degree of saturation and including scanning drying and scanning wetting curves. The experimental data were fitted using the hysteretic modVG model (the reference model in this thesis) (see Figures 3.11a,d), the hysteretic modBC model (see Figures 3.11b,e) and the hysteretic modK model (see Figures 3.11c,f). The SWRCs are shown in terms of the volumetric water content θ_l, which, assuming no deformation of the soil, can be expressed as $\theta_l = \theta_{ls} \cdot S_l$ where θ_{ls} is the water content when the soil is fully saturated. The primary drying curve and the main wetting curve were firstly best-fitted to the corresponding experimental data. Note that the main wetting curve does not reach a fully saturated condition as suction approaches zero, indicating the likely occurence of air trapping (see Chapter 5). Subsequently, the scanning curves were fitted by imposing the curves to pass through the previous reversal point and fitting Equations 3.19, 3.28 and 3.30 to the experimental data, where only γ_d for drying and γ_w for wetting were the fitting parameters. Table 3.4 shows the model parameters obtained with this procedure. In general, all three models fitted well the experimental data for the primary drying and main wetting SWRCs over the full range of degree of saturation, although the modBC model was slightly imprecise around the air-entry value (i.e. the point on the primary drying curve where the degree of saturation starts decreasing from 1) due to the prediction of a discontinuity in the gradient of the SWRC at this point (see Figure 3.11e). The scanning curves were well fitted by all three models, which are thus able to capture an entire scanning loop with a single pair of parameters (γ_d for drying and γ_w for wetting). This showed that the new hysteretic approach can be coupled with different SWRC models designed to work well at very low degree of saturation (e.g. modified van Genuchten, modified Brooks and Corey and modified Kosugi). In the remaining part of this section, only the reference hysteretic modVG model will be used.

Two slightly different versions of the hysteretic approach were described in Sections 3.4.1 and 3.4.2. The scanning curves predicted by the two different approaches are compared in

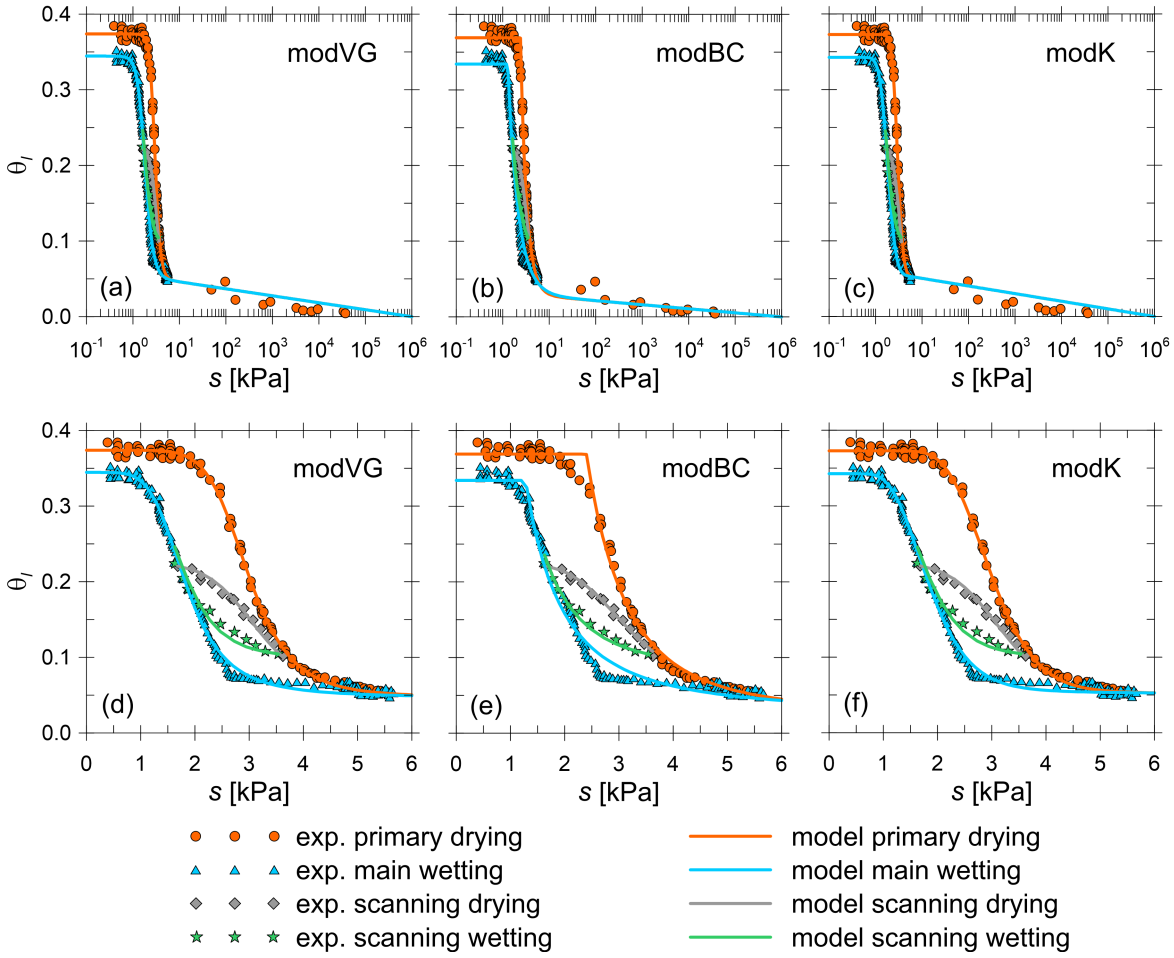

Figure 3.11: Comparison between experimental data for Tottori sand (data from Sakai and Toride [208]) and (a) modVG model ((d) zoom at low suction), (b) modBC model ((e) zoom at low suction) and (c) modK model ((f) zoom at low suction)

Figure 3.12. For the initial approach (based on Equation 3.9 and described in Section 3.4.1) an iterative procedure was required to calculate the scanning curves shown in Figure 3.12, whereas for the revised approach (based on Equation 3.17 and described in Section 3.4.2) the closed form expressions of Equations 3.19, 3.20 and 3.22 were used for the scanning curves. Using the approach based on Equation 3.9, the best-fit values of γ_d and γ_w were 6.09 and 5.35 respectively, i.e. slightly different to the best-fit values when using Equation 3.17, which are shown in Table 3.4a. Inspection of Figure 3.12 shows that the scanning curves predicted by the two slightly different hysteretic approaches are indistinguishable. Therefore, the revised approach (based on Equation 3.17), which is much simpler to apply to the modVG model than the initial approach (based on Equation 3.9) is used throughout the remainder of this thesis, as the hysteretic modVG model.

Figure 3.13 shows the comparison between the hysteretic modVG model and experimental SWRC data for Wray sand obtained by Gillham et al. [209]. For this soil, different scanning drying curves (see Figure 3.13b) and different scanning wetting curves (see Figure 3.13c) were available. The modVG model was initially best-fitted to the main drying and main wetting experimental curves (see Figure 3.13a). Subsequently, all the experimental scanning curves

Table 3.4: Hysteretic SWRC model parameter values for Tottori sand (see Figures 3.11 and 3.12)

(a) Hysteretic modVG model

	Drying curves					Wetting curves				
θ_{ls}	$S_{ls,d}$	ξ_d	$P_{0,d}$	n_d	γ_d	$S_{ls,w}$	ξ_w	$P_{0,w}$	n_w	γ_w
[-]	[-]	[-]	[kPa]	[-]	[-]	[-]	[-]	[kPa]	[-]	[-]
0.374	1.00	0.0107	2.90	7.77	6.25	0.92	0.0107	1.73	5.45	5.41

(b) Hysteretic modBC model

	Drying curves					Wetting curves				
θ_{ls}	$S_{ls,d}$	ξ_d	s_{AE}	n_d	γ_d	$S_{ls,w}$	ξ_w	s_{AEX}	n_w	γ_w
[-]	[-]	[-]	[kPa]	[-]	[-]	[-]	[-]	[kPa]	[-]	[-]
0.369	1.00	0.0063	2.40	3.27	6.07	0.91	0.0063	1.28	1.94	3.23

(c) Hysteretic modK model

	Drying curves					Wetting curves				
θ_{ls}	$S_{ls,d}$	ξ_d	$s_{m,d}$	$\sigma_{m,d}$	γ_d	$S_{ls,w}$	ξ_w	$s_{m,w}$	$\sigma_{m,w}$	γ_w
[-]	[-]	[-]	[kPa]	[-]	[-]	[-]	[-]	[kPa]	[-]	[-]
0.373	1.00	0.0117	2.96	0.221	6.10	0.92	0.0117	1.82	0.314	5.62

of a family, i.e. wetting or drying, were fitted by the hysteretic modVG model using a single value for γ_d (for all scanning drying curves) or γ_w (for all scanning wetting curves). Note that a single value of γ_d valid for all the family of the scanning drying curves was obtained by best-fitting the hysteretic modVG model to all the scanning drying curves simultaneously and a similar operation was done also for the wetting scanning curves to determine a single value of γ_w. The parameter values are shown in Table 3.5. From Figures 3.13b and 3.13c, it can be seen that the model provided a very good fit to all the scanning curves. Therefore, the use of a single pair of values for the parameters γ_d and γ_w was sufficient to model the different scanning curves starting from different reversal points, corresponding to different degree of saturation values.

Table 3.5: Hysteretic modVG SWRC model parameter values for Wray sand (see Figure 3.13

	Drying curves					Wetting curves				
θ_{ls}	$S_{ls,d}$	ξ_d	$P_{0,d}$	n_d	γ_d	$S_{ls,w}$	ξ_w	$P_{0,w}$	n_w	γ_w
[-]	[-]	[-]	[kPa]	[-]	[-]	[-]	[-]	[kPa]	[-]	[-]
0.301	1.00	0.0281	3.166	9.45	6.34	1.00	0.0277	1.834	5.46	5.30

Figure 3.14 shows experimental SWRC and SHCC data, obtained by Londra [210], in three different plots, i.e. $\theta_l : s$, $k_l : s$ and $k_l : \theta_l$, for three different mixtures of peat and perlite: 100% peat; 75% peat - 25 % perlite; 50% peat - 50 % perlite. The main drying and the main wetting SWRC data were initially fitted by the modVG model. Given the value of the saturated hydraulic conductivity k_{ls}, the SHCCs were predicted using the modM model (the LF model was not used since no data were available at very low degree of saturation) and then compared to the experimental data. The constraints given by Equations 3.23, 3.25, 3.26, and 3.27 were

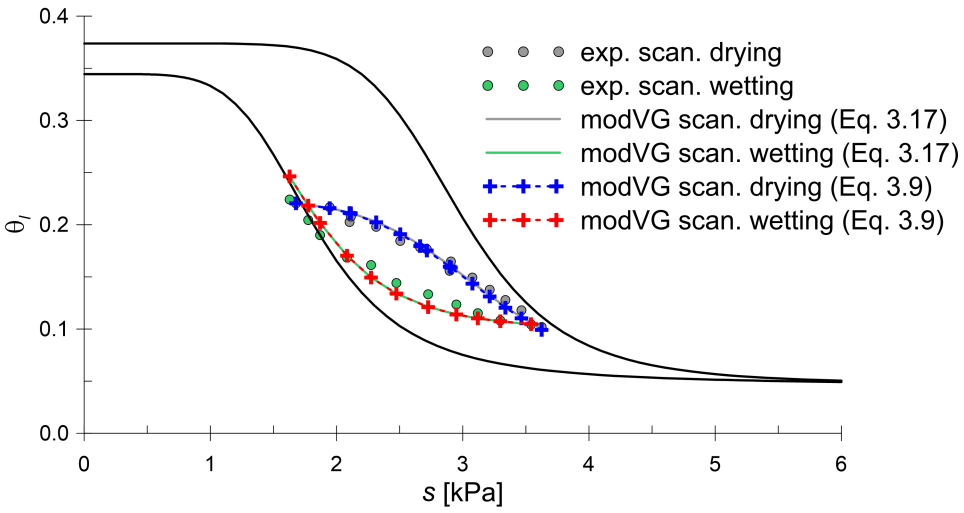

Figure 3.12: Comparison between the two different versions of the hysteretic modVG model (initial version based on Equation 3.9 and revised version based on Equation 3.17), fitted to experimental data for Tottori sand [208]

used in this case during the fitting operations in order to guarantee the absence of hysteresis in the bulk water component of the hydraulic conductivity when plotted in the $k_l : \theta_l$ plot. The relevant model parameters are shown in Table 3.6. For these soils, little water retention hysteresis was observed, as shown in Figures 3.14a,d,g. The main wetting and the main drying experimental curves were fitted well by the modVG model. The maximum volumetric water content θ_{ls} was known, and thus fixed in the model, although the corresponding point (at $s = 0$) cannot be shown in the semi-logarithmic plot. The predicted main drying and main wetting SHCCs showed hysteresis when plotted against suction s but not when plotted against the water content θ_l. These predicted SHCCs were in very good agreement with the experimental data in both plots (i.e. against s and θ_l) and for all the three soil mixtures.

Table 3.6: ModVG-modM SWRC and SHCC model parameter values for different mixtures of peat and perlite (see Figure 3.14) and for Edosaki sand (see Figure 3.15)

Soil	θ_{ls} [-]	Drying curves $S_{ls,d}$ [-]	Drying curves $P_{0,d}$ [kPa]	Wetting curves $S_{ls,w}$ [-]	Wetting curves $P_{0,w}$ [kPa]	ξ [-]	n [-]	k_{ls} [m/s]	$S_{l,BWC/BWD}$ [-]
100%Peat	0.820	1.00	0.640	1.00	0.411	0.0346	1.89	2.22E-4	0.363
75%Peat 25%Perlite	0.780	1.00	0.439	1.00	0.253	0.0376	1.90	5.84E-4	0.46
50%Peat 50%Perlite	0.750	1.00	0.253	1.00	0.167	0.0154	1.32	1.19E-3	0.26
Edosaki sand	0.440	1.00	2.700	0.79	1.707	0.0191	2.67	4.40E-5	0.12

The same operation described for the three peat-perlite mixtures was applied to Edosaki sand (see Figure 3.15), with experimental data from Gallage et al. [211] and modVG-modM parameter values given in Table 3.6. In this case, however, the maximum water content obtained during main wetting was lower than that recorded on the primary drying curve due

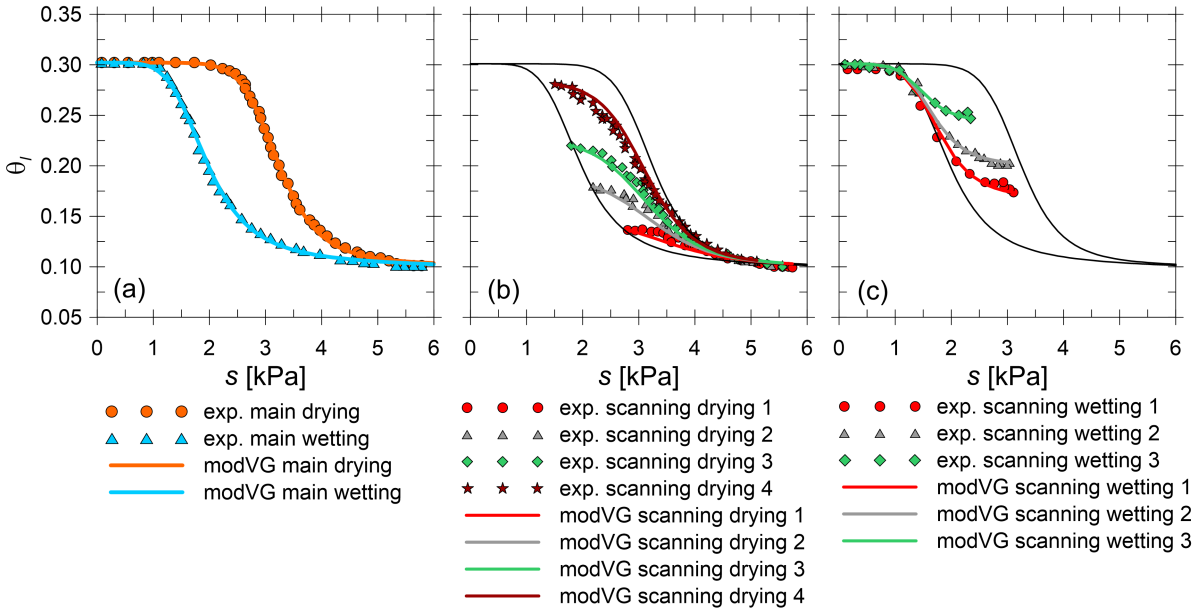

Figure 3.13: Comparison between experimental data for Wray sand [209] and hysteretic modVG model: (a) main drying and main wetting curves, (b) scanning drying curves, (c) scanning wetting curves

to the occurrence of trapped air. This led to a lower value of the hydraulic conductivity at zero value of suction in the case of the main wetting curve compared to the primary drying curve (see Figure 3.15b). This, however, did not have any effect of the SHCC when plotted against the water content θ_l. Experimental SHCC data showed negligible hysteresis when plotted against the volumetric water content θ_l. In general, the SWRCs were fitted well by the modVG model although the constraints given by Equations 3.23 and 3.25 were used. The modM model gave a good prediction of the SHCC data, although the values of hydraulic conductivity were slightly underestimated.

Topp and Miller [212] obtained experimental data for aggregated glass beads, covering primary drying, main drying and main wetting SWRC curves and SHCC curves ($k_l : \theta_l$), a family of 5 scanning drying SWRC curves and a family of 6 scanning wetting SWRC curves (see Figure 3.16). Primary drying, main drying and main wetting SWRC experimental data were simultaneously fitted by the modVG model using the constraints given by Equations 3.23, 3.25, 3.26 and 3.27. The scanning curves were fitted by the hysteretic modVG model using a single value of γ_d or γ_w for each family of scanning curves, as was described for the Wray sand. The primary drying, main drying and main wetting SHCCs predicted using the modM model were subsequently compared to the experimental data. The resulting model parameters are shown in Table 3.7. The SWRC data were fitted reasonably well by the modVG model applied to the primary drying curve, the main drying curve and the main wetting curve (see Figure 3.16a). The quality of the fitting is slightly lower at low degree of saturation, due to the constraints used on all the three SWRCs. The comparison between the predicted SHCCs and the experimental data, plotted in terms of the relative hydraulic conductivity k_{lr}, showed a good match in the full saturation range (see Figure 3.16b). However, a small amount of

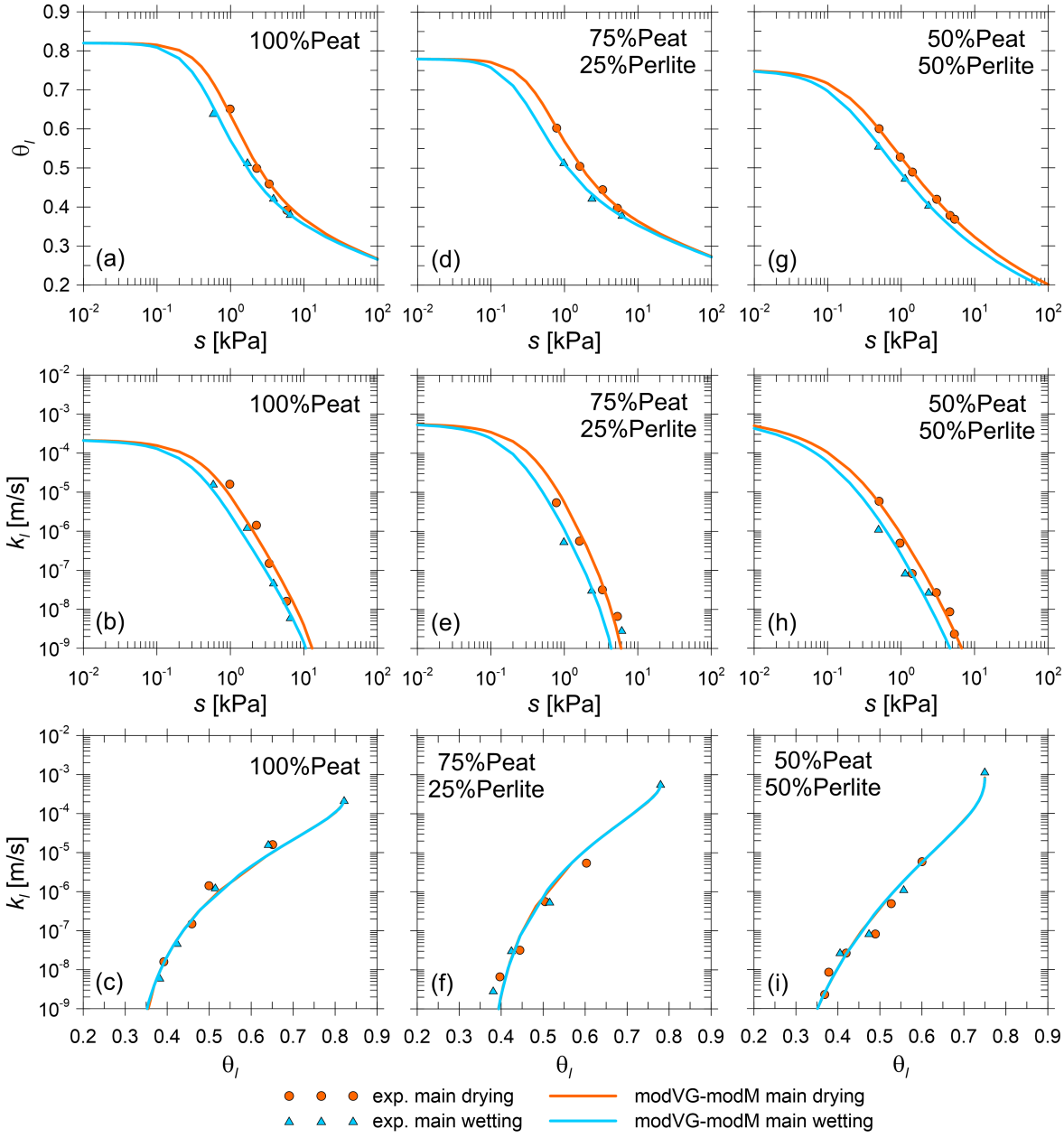

Figure 3.14: Comparison between experimental data for different peat-perlite mixtures (data from Londra [210]) and modVG-modM model: 100% peat ((a) $\theta_l : s$, (b) $k_l : s$ and (c) $k_l : \theta_l$), 75% peat - 25% perlite ((d) $\theta_l : s$, (e) $k_l : s$ and (f) $k_l : \theta_l$) and 50% peat - 50% perlite ((g) $\theta_l : s$, (h) $k_l : s$ and (i) $k_l : \theta_l$)

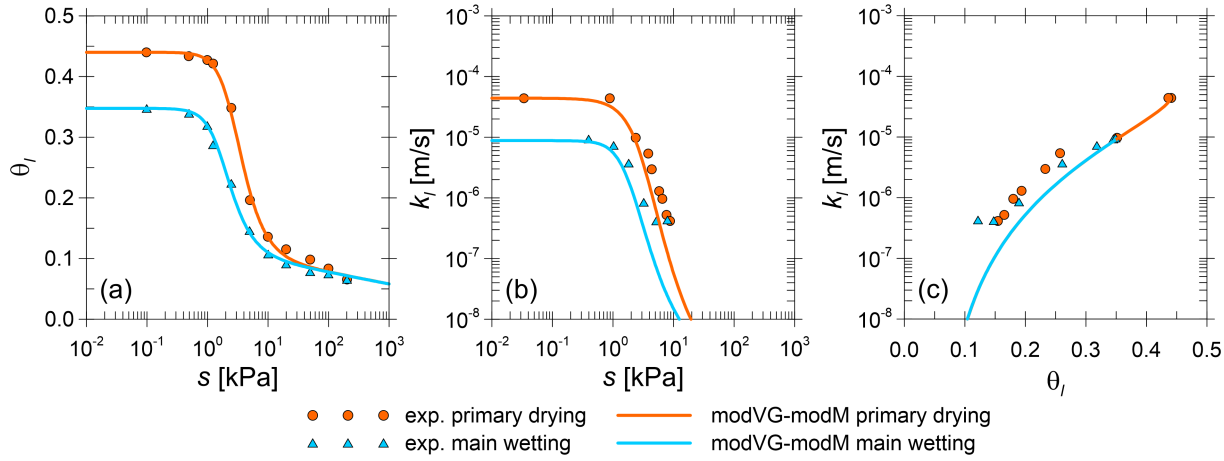

Figure 3.15: Comparison between experimental data for Edosaki sand [211] and hysteretic modVG-modM model: (a) $\theta_l : s$, (b) $k_l : s$ and (c) $k_l : \theta_l$

hysteresis in the SHCC experimental data was observed when plotted against θ_l. In particular, at a given value of θ_l in the range of high degree of saturation values, k_l obtained during primary drying was slightly higher than that obtained during main wetting, which in turn was slightly higher than that obtained during main drying (see Figure 3.16b). The predicted SHCC was intermediate between these points (Figure 3.16b) and the error was very little. Similar to what was observed for the Wray sand (see Figure 3.13), the use of a single value for γ_d and a single value for γ_w led to a very good fitting of the scanning drying curves (see Figure 3.16c) and the scanning wetting curves (see Figure 3.16d) for the aggregated glass beads. The only exception for the scanning wetting curve 1. This scanning curve predicted by the hysteretic modVG model followed the main wetting curve, leading to a slight underestimation of the volumetric water content values (see Figure 3.16d). This was due to the poor fitting of the main wetting curve at low degree of saturation (see Figure 3.16a).

Table 3.7: Hysteretic modVG-modM SWRC and SHCC model parameter values for aggregated glass beads (see Figure 3.16)

(a) SWRC

	Primary drying		Main drying		Main wetting					
θ_{ls}	$S_{ls,d}$	$P_{0,d}$	$S_{ls,d}$	$P_{0,d}$	$S_{ls,w}$	$P_{0,w}$	ξ	n	γ_d	γ_w
[-]	[-]	[kPa]	[-]	[kPa]	[-]	[kPa]	[-]	[-]	[-]	[-]
0.609	1.00	3.969	0.90	3.898	0.90	2.452	0.0162	12.24	9.65	7.91

(b) SHCC

k_{ls}	$S_{l,BWC/BWD}$
[m/s]	[-]
3.30E-4	0.25

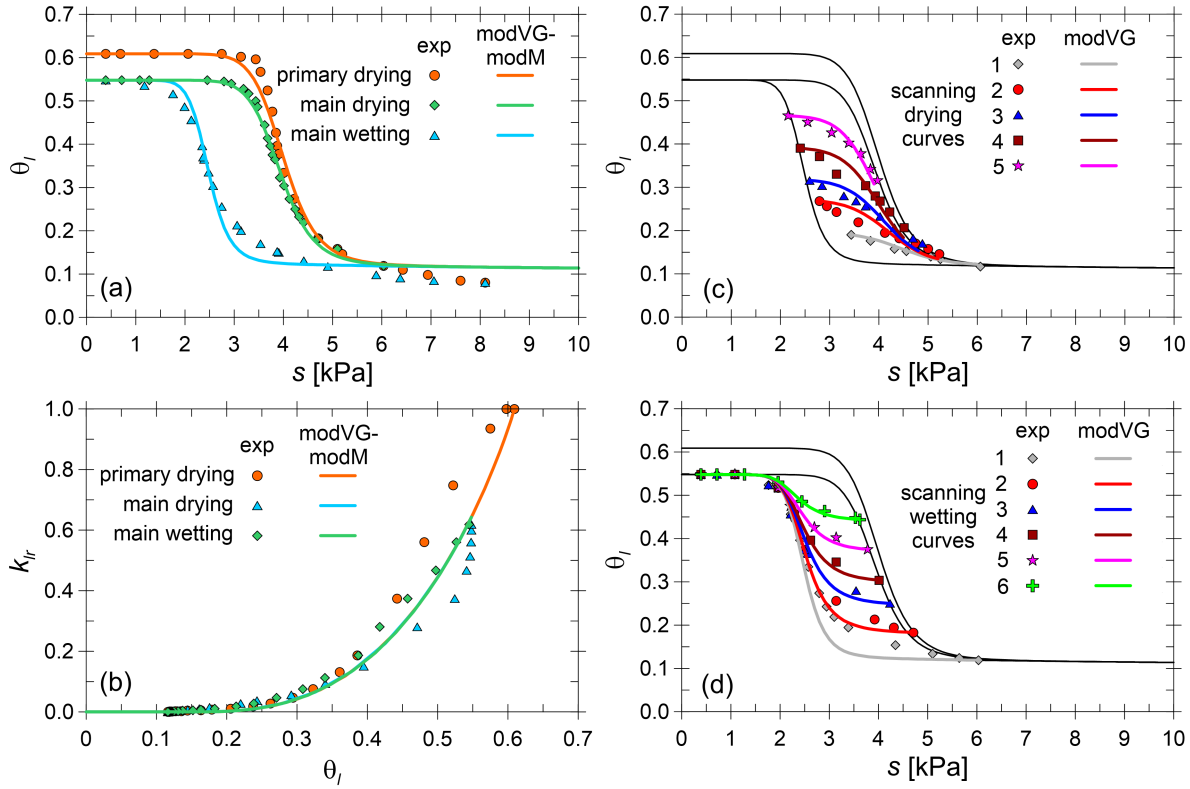

Figure 3.16: Comparison between experimental data for aggregated glass beads [212] and hysteretic modVG-modM model: primary drying curve, main drying curve and main wetting curve ((a) $\theta_l : s$ and (b) $k_{lr} : \theta_l$), (c) scanning drying curves ($\theta_l : s$) and (d) scanning wetting curves ($\theta_l : s$)

3.5 Concluding remarks

In the first part of this chapter, a critical review of the hydraulic behaviour of unsaturated soils was carried out, highlighting the roles of the different water forms (bulk water, meniscus water and liquid film water) in the SWRC and SHCC. In particular, key transition points for the water retention behaviour, hydraulic conductivity behaviour and gas conductivity behaviour were identified and defined: air-entry (AE) point, air-exclusion (AEX) point, air-continuity (AC) point, air-discontinuity point (AD), bulk water-discontinuity (BWD) point, bulk water-continuity (BWC) point, bulk water-exclusion (BWEX) point and bulk water-entry (BWE) point. This served as a physical basis for the development of new hydraulic constitutive models for relatively coarse-grained (gravels, sands and silts) unsaturated soils.

A new hydraulic conductivity model for unsaturated soils was subsequently proposed. This model is reliable, predictive, easy to apply and avoids inconsistencies present in conventional models. The hydraulic conductivity is split into two components: the bulk water component and the liquid film component. The bulk water component is modelled with a new modified version of the Mualem [95] model (modM model), which is able to capture the fact that bulk water flow ceases at a finite value of suction i.e. when the bulk water becomes discontinuous within the soil. The bulk water component can be predicted simply from knowledge of the saturated hydraulic conductivity k_{ls} and the SWRC, as in the conventional Mualem model.

The liquid film component is modelled by a semi-empirical relationship (LF model). This semi-empirical relationship involves the definition of a soil constant, which can be either fitted to experimental SHCC data at low degree of saturation where liquid film governs the flow process or, in the absence of these data, it can be estimated from knowledge of porosity Φ and effective particle size D_{10}. The formulation of this new hydraulic conductivity model was developed coupling it with three different SWRC models improved at low degree of saturation: the modified van Genuchten (modVG) model, the modified Brooks and Corey (modBC) model and the modified Kosugi (modK) model. The modVG SWRC model is used as a reference model for this thesis. The new model was validated against experimental data from different soils.

Hydraulic hysteresis was subsequently introduced. ModVG, modBC and modK were considered as models for the main SWRCs for the development of the formulation of this hysteretic model. However, it was shown that the use of any SWRC model which can be inverted in a closed-form expression will lead to scanning curves which can be expressed by closed-form expressions. Scanning curves were modelled using a bounding surface approach. Introducing certain parameter constraints in the hysteretic SWRC model means that the bulk water component of hydraulic conductivity k_l^{Bulk} is assumed non-hysteretic when plotted against degree of saturation S_l, whereas the liquid film component k_l^{Film} is non-hysteretic when plotted against suction s. The new hysteretic hydraulic constitutive model was validated against experimental SWRC and SHCC data from different soils. The model was able to represent well the hysteretic hydraulic behaviour of relatively coarse-grained unsaturated soils (gravels, sands and silts) over the full range of degree of saturation. The model is easy to apply (it involves simple closed-form expressions), flexible (the same approach can be applied with different expressions for the main drying and main wetting SWRCs) and it requires a relatively low number of parameters (once the main SWRCs and SHCCs are defined, only a single pair of additional parameters, γ_d and γ_w, are required for the definition of the scanning SWRC and SHCC curves).

The simplicity of the new hydraulic models developed make them suitable for implementation in numerical codes, as was done successfully in Code_Bright in this thesis work (see Chapter 4).

Chapter 4

Numerical codes

A major component of the research work done in this thesis was numerical. Hydraulic and coupled thermo-hydraulic analyses involving unsaturated soils were performed using the finite element code Code_Bright (see Chapters 5, 6, 7, and 8) whereas limit analyses applied to the assessment of the stability of slopes in unsaturated conditions were performed using the software LimitState:GEO (see Chapter 8).

This chapter provides an overview of the functioning of Code_Bright and the description of the implementation within Code_Bright of the new hydraulic constitutive models presented in Chapter 3. Similarly, the functioning of the software LimitState:GEO is subsequently presented. Finally, the implementation of a new code, called CB-LS, is explained. The code CB-LS was developed by the author to link the results from thermo-hydraulic analyses performed with Code_Bright and limit analyses for unsaturated soils performed with LimitState:GEO (see Chapter 8).

4.1 Code_Bright

4.1.1 Theoretical background

Code_Bright (CB) [205, 213] is a finite element code developed at the Universitat Politècnica de Catalunya (UPC) in Barcelona. It is able to model numerically thermo-hydro-mechanical processes in multi-phase geological media in a coupled way, including multi-physics processes (e.g. diffusion of water vapour in the gas phase, advection of liquid water in the liquid phase, dissolution and diffusion of air in the liquid phase etc.). Code_Bright works in combination with the GiD system [214] for pre- and post-processing, where pre-processing refers to the creation of the numerical model and post-processing refers to the visualization and the processing of the output results. The software GiD is developed by the International Center for Numerical Methods in Engineering (CIMNE) in Barcelona. The following versions of the codes were used in this thesis: GiD v.13.0.4 and Code_Bright v.8.2.

In the formulation of Code_Bright, the simultaneous mutual interaction of a large number of phenomena is considered. For instance, thermal expansion of water in the pores causes an increase of the degree of saturation in partially saturated soils or an increase of pore-water

pressure in saturated or almost saturated soils. Variation of temperature also affects vapour diffusion and liquid viscosity, thereby affecting water transport processes. In addition, changes of the hydraulic conditions affect the thermal response of soils, e.g. changes in the degree of saturation significantly affect the thermal conductivity. Many other interaction phenomena are considered in Code_Bright.

Three phases are considered in Code_Bright: solid (s), liquid (l) and gas (g). Three species are considered: solid (s) (coincident with the solid phase), water (w) (as liquid water or water vapour in the gas phase) and air (a) (dry air, as gas or dissolved in the liquid water).

The following assumptions are made in the formulation of Code_Bright:

- Dry air is considered as a single species (rather than separating into nitrogen, oxygen, carbon dioxide etc.) and it is the main component of the gas phase. Henry's law is used to establish the equilibrium concentration of dissolved air in the liquid phase.
- The three phases are always in thermal equilibrium, i.e. at the same temperature.
- Vapour concentration is always in equilibrium with the liquid phase. Kelvin's law relates vapour concentration to the suction and temperature.
- State variables, also called unknowns, are: solid displacements $\boldsymbol{u}$ (three-dimensional vector), liquid pressure p_l, gas pressure p_g and temperature T.
- Balance of momentum for the medium is reduced to the equation of equilibrium together with a mechanical constitutive law relating stresses and strains. Strains are expressed from displacements.
- Small strains and small strain rates are assumed for solid deformation.
- Balance of momentum for fluid phases and for dissolved species are reduced to constitutive equations, i.e. Darcy's law and Fick's law.
- Physical parameters in constitutive laws (e.g. surface tension, dynamic viscosity, liquid and gas density etc.) are expressed as functions of pressures and/or temperature.

Moreover, in Code_Bright it is also possible to consider the presence of dissolved salts in the liquid phase and the presence of water inclusions in the solid phase but these were not considered in this thesis and thus they will not be treated in the description of Code_Bright.

Four types of governing equations are implemented in Code_Bright: balance equations, constitutive equations, equilibrium relationships and definition constraints. A summary of these equations and the corresponding variables is given in Table 4.1.

Mass balance equations are written for the three species (solid, water, air). The equation of the momentum balance is reduced to that of stress equilibrium. The energy balance equation is written for the medium as a whole.

The mass balance of solid is expressed as:

$$\frac{\partial}{\partial t}\left(\theta_s\left(1-\Phi\right)\right)+\nabla\cdot\left(\boldsymbol{j}_s\right)=0 \tag{4.1}$$

Table 4.1: Equations and variables in Code_Bright (after Olivella et al. [213])

Equation name	Variable	Equation number
Balance equations		
Solid mass balance	Φ	4.1
Water mass balance	p_l	4.3
Air mass balance	p_g	4.6
Stress equilibrium	$\dot{\boldsymbol{u}}$	4.9
Internal energy	T	4.10
Definition constraints		
$\dot{\boldsymbol{\varepsilon}} = \frac{1}{2}(\nabla\dot{\boldsymbol{u}} + \nabla\dot{\boldsymbol{u}}^t)$	$\dot{\boldsymbol{\varepsilon}}$	4.11
$\omega_l^w + \omega_l^a = 1$	ω_l^w	4.12
$\omega_g^w + \omega_g^a = 1$	ω_g^a	4.13
$S_l + S_g = 1$	S_g	4.14
$\boldsymbol{i}_g^a + \boldsymbol{i}_g^w = 0$	$\boldsymbol{i}_g^a$	4.15
$\boldsymbol{i}_l^a + \boldsymbol{i}_l^w = 0$	$\boldsymbol{i}_l^w$	4.16
Equilibrium restrictions		
Henry's law	ω_l^a	4.17
Kelvin's law	ω_g^w	4.18
Constitutive equations		
Liquid density	ρ_l	4.21
Liquid viscosity	μ_l	4.22
Gas density (gases law)	ρ_g	
Gas viscosity	μ_g	4.23
SWRC	S_l	4.24, 4.25
Darcy's law (liquid and gas)	$\boldsymbol{q}_l$, $\boldsymbol{q}_g$	4.26, 4.27
Fick's law (water and air)	$\boldsymbol{i}_g^w$, $\boldsymbol{i}_l^a$	4.32, 4.34
Mechanical constitutive model	$\boldsymbol{\sigma}$	
Fourier's law	$\boldsymbol{i}_c$	4.36

where θ_s is the mass of solid per unit volume of solid [ML^{-3}], Φ is the porosity and $\boldsymbol{j}_s$ is the flux of solid [ML^{-2}T^{-1}], which is expressed as:

$$\boldsymbol{j}_s = \theta_s (1-\Phi) \frac{d\boldsymbol{u}}{dt} \tag{4.2}$$

The mass balance of water is expressed by the following relationship:

$$\frac{\partial}{\partial t}\left(\theta_l^w S_l \Phi + \theta_g^w S_g \Phi\right) + \nabla \cdot \left(\boldsymbol{j}_l^w + \boldsymbol{j}_g^w\right) = f^w \tag{4.3}$$

where θ_l^w is the mass of water per unit volume of liquid [ML^{-3}], θ_g^w is the mass of water per unit volume of gas [ML^{-3}], S_l is the (liquid) degree of saturation, S_g is the gas degree of saturation, $\boldsymbol{j}_l^w$ is the total mass flux of water in the liquid phase [ML^{-2}T^{-1}], $\boldsymbol{j}_g^w$ is the total mass flux of water in the gas phase [ML^{-2}T^{-1}] and f^w is an external supply of water [ML^{-3}T^{-1}]. The total mass fluxes of water in the liquid phase $\boldsymbol{j}_l^w$ and in the gas phase $\boldsymbol{j}_g^w$ are each the sum of three components: a non-advective (diffusive) component, an advective component due to the

fluid motion and an advective component due to the solid motion. Therefore, $\boldsymbol{j}_l^w$ and $\boldsymbol{j}_g^w$ are expressed as:

$$\boldsymbol{j}_l^w = \boldsymbol{i}_l^w + \theta_l^w \boldsymbol{q}_l + \theta_l^w S_l \Phi \frac{d\boldsymbol{u}}{dt} \tag{4.4}$$

$$\boldsymbol{j}_g^w = \boldsymbol{i}_g^w + \theta_g^w \boldsymbol{q}_g + \theta_g^w S_g \Phi \frac{d\boldsymbol{u}}{dt} \tag{4.5}$$

where $\boldsymbol{i}_l^w$ and $\boldsymbol{i}_g^w$ are the non-advective fluxes of water in the liquid and gas phase respectively [$ML^{-2}T^{-1}$] and $\boldsymbol{q}_l$ and $\boldsymbol{q}_g$ are the advective volumetric fluxes of liquid and gas respectively [LT^{-1}], relative to the solid skeleton.

The mass balance of air is expressed by the following relationship:

$$\frac{\partial}{\partial t}\left(\theta_l^a S_l \Phi + \theta_g^a S_g \Phi\right) + \nabla \cdot \left(\boldsymbol{j}_l^a + \boldsymbol{j}_g^a\right) = f^a \tag{4.6}$$

where θ_l^a is the mass of air per unit volume of liquid [ML^{-3}], θ_g^a is the mass of air per unit volume of gas [ML^{-3}], $\boldsymbol{j}_l^a$ is the total mass flux of air in the liquid phase [$ML^{-2}T^{-1}$], $\boldsymbol{j}_g^a$ is the total mass flux of air in the gas phase [$ML^{-2}T^{-1}$] and f^a is an external supply of air [$ML^{-3}T^{-1}$]. The total mass fluxes of air in the liquid phase $\boldsymbol{j}_l^a$ and in the gas phase $\boldsymbol{j}_g^a$ are expressed as:

$$\boldsymbol{j}_l^a = \boldsymbol{i}_l^a + \theta_l^a \boldsymbol{q}_l + \theta_l^a S_l \Phi \frac{d\boldsymbol{u}}{dt} \tag{4.7}$$

$$\boldsymbol{j}_g^a = \boldsymbol{i}_g^a + \theta_g^a \boldsymbol{q}_g + \theta_g^a S_g \Phi \frac{d\boldsymbol{u}}{dt} \tag{4.8}$$

where $\boldsymbol{i}_l^a$ [$ML^{-2}T^{-1}$] and $\boldsymbol{i}_g^a$ [$ML^{-2}T^{-1}$] are the non-advective fluxes of air in the liquid and gas phase respectively.

The momentum balance is reduced to the equilibrium of stresses if the inertial terms are neglected:

$$\nabla \cdot \boldsymbol{\sigma} + \boldsymbol{b} = 0 \tag{4.9}$$

where $\boldsymbol{\sigma}$ is the stress tensor [$ML^{-1}T^{-2}$] and $\boldsymbol{b}$ [$ML^{-2}T^{-2}$] is the vector of body forces.

The energy balance equation for the porous medium is written as follows:

$$\frac{\partial}{\partial t}\left(E_s \rho_s (1-\Phi) + E_l \rho_l S_l \Phi + E_g \rho_g S_g \Phi\right) + \nabla \cdot \left(\boldsymbol{i}_c + \boldsymbol{j}_{Es} + \boldsymbol{j}_{El} + \boldsymbol{j}_{Eg}\right) = f^Q \tag{4.10}$$

where E_s, E_l and E_g are the internal energies (per unit mass) of the solid phase, the liquid phase and the gas phase respectively [L^2T^{-2}], ρ_s, ρ_l and ρ_g are the densities of the solid phase, the liquid phase and the gas phase respectively [ML^{-3}], $\boldsymbol{i}_c$ is the energy flux due to heat conduction through the porous medium, $\boldsymbol{j}_{Es}$, $\boldsymbol{j}_{El}$ and $\boldsymbol{j}_{Eg}$ are the energy fluxes due to advection of solid, liquid and gas respectively [MT^{-3}] and f^Q is an internal/external energy supply [$ML^{-1}T^{-3}$].

Different definition constraints are used in Code_Bright. The compatibility of deforma-

tions is expressed by the following definition constraint:

$$\dot{\boldsymbol{\varepsilon}} = \frac{1}{2}\left(\nabla \dot{\boldsymbol{u}} + \nabla \dot{\boldsymbol{u}}^t\right) \tag{4.11}$$

where $\dot{\boldsymbol{\varepsilon}}$ is the strain rate tensor and $\dot{\boldsymbol{u}} = d\boldsymbol{u}/dt$ is the solid displacement rate (the solid velocity). The strain rate tensor $\dot{\boldsymbol{\varepsilon}}$ is used in the mechanical constitutive model where it is related to the stress rate tensor $\dot{\boldsymbol{\sigma}}$.

Since the liquid phase is made of water and dissolved air, the following definition constraint is used:

$$\omega_l^w + \omega_l^a = 1 \tag{4.12}$$

where ω_l^w is the fraction of water in the liquid phase (i.e. mass of water per mass of liquid) and ω_l^a is the fraction of dissolved air in the liquid phase (i.e. mass of dissolved air per mass of liquid). Note also that $\rho_l = \theta_l^w + \theta_l^a$, $\omega_l^w = \theta_l^w/\rho_l$ and $\omega_l^a = \theta_l^a/\rho_l$. Similarly, the following definition constraint for the gas phase is used:

$$\omega_g^w + \omega_g^a = 1 \tag{4.13}$$

where ω_g^w is the fraction of water in the gas phase (i.e. mass of water per mass of gas) and ω_g^a is the fraction of dissolved air in the gas phase (i.e. mass of dissolved air per mass of gas). Note also that $\rho_g = \theta_g^w + \theta_g^a$, $\omega_g^w = \theta_g^w/\rho_g$ and $\omega_g^a = \theta_g^a/\rho_g$.

Since the volume of voids is occupied either by the gas phase or by the liquid phase, the following definition constraint is used:

$$S_l + S_g = 1 \tag{4.14}$$

The concept of binary diffusion [215] applied to the diffusive fluxes in the gas phase is expressed by the following definition constraint:

$$\boldsymbol{i}_g^a + \boldsymbol{i}_g^w = 0 \tag{4.15}$$

which means that the diffusive flux of water vapour in the gas phase is balanced by an opposite and equal diffusive flux of air in the gas phase. A similar definition constraint is used for the liquid phase:

$$\boldsymbol{i}_l^a + \boldsymbol{i}_l^w = 0 \tag{4.16}$$

The concentration of species in phases is governed by equilibrium restrictions: Henry's law and Kelvin's law. Henry's law governs the concentration of dissolved air in the liquid phase and, in Code_Bright, it is expressed as:

$$\omega_l^a = p_a \cdot \left(\frac{1}{H}\frac{M_a}{M_w}\right) \tag{4.17}$$

where p_a is the partial pressure of air in the gas phase, M_a is the molecular mass of air, M_w is the molecular mass of water and H is Henry's constant [$ML^{-1}T^{-2}$]. Note that Equation 4.17

coincides with Equation 2.4. In Code_Bright, default values for these parameters are: $M_a = 0.02895\,\mathrm{kg/mol}$, $M_w = 0.01802\,\mathrm{kg/mol}$ and $H = 10000\,\mathrm{MPa}$.

Kelvin's law governs the concentration of water vapour in the gas phase and, in Code_Bright, it is expressed in terms of the vapour density in the gaseous phase θ_g^w as:

$$\theta_g^w = \left(\theta_g^w\right)^0 \exp\left(\frac{-(p_g - p_l)M_w}{R(T+273.15)\rho_l}\right) \tag{4.18}$$

where $\left(\theta_g^w\right)^0$ is the vapour density in the gaseous phase in contact with a planar gas-liquid interface (i.e. when $p_g - p_l = 0$), R is the universal gas constant (8.314 J/(mol K)) and T is the temperature in °C. Making use of the law of ideal gases, $\left(\theta_g^w\right)^0$ is calculated as:

$$\left(\theta_g^w\right)^0 = \frac{p_{v0}M_w}{R\,(273.15+T)} \tag{4.19}$$

where p_{v0} is the vapour pressure in the gaseous phase in contact with a planar gas-liquid interface. The value of p_{v0} is calculated by the following empirical relationship:

$$p_{v0} = 136075 \exp\left(-5239.7/\left(273.15+T\right)\right) \tag{4.20}$$

where p_{v0} is expressed in MPa and T is expressed in °C.

Constitutive equations describe the behaviour of the materials and relate dependent quantities (e.g. S_l, $\boldsymbol{q}_l$, $\boldsymbol{q}_g$, $\boldsymbol{i}_c$, $\boldsymbol{i}_g^w$ etc.) to the unknowns (i.e. $\boldsymbol{u}$, p_l, p_g and T). The relevant constitutive equations for this thesis are discussed in Section 4.1.2.

Code_Bright allows the user to solve full thermo-hydro-mechanical problems or more restricted problems, e.g. a hydraulic problem. In this thesis, the mechanical part of Code_Bright was not used (the soil was assumed to be rigid). It follows that Equations 4.1, 4.2, 4.9 and 4.11 were not considered, the porosity Φ was treated as a constant equal to the initially assigned value and all the terms $d\boldsymbol{u}/dt$ appearing in Equations 4.4, 4.5, 4.7 and 4.8 were considered equal to 0. Most simulations in this thesis, with the exception of those presented in Chapter 5, were performed excluding the solving of the air mass balance equation and, consequently, Equations 4.6, 4.7 and 4.8 were not considered. In this case, the pore-gas pressure p_g was considered as uniform and constant and it was assigned at the beginning of the analyses, and the presence of dissolved air in the liquid phase was excluded (i.e. $\omega_l^a = 0$ and $\omega_l^w = 1$). Some of the simulations in this thesis were performed excluding the solving of the energy balance equation and, consequently, Equation 4.10 was excluded. In this case, the temperature T was considered as uniform and constant and it was assigned at the beginning of the analyses, and the presence of the water vapour in the gas phase was automatically excluded (i.e. $\omega_g^w = \theta_g^w = 0$, $\omega_g^a = 1$ and $\boldsymbol{i}_g^w = 0$).

4.1.2 Constitutive equations

Code_Bright allows the user to choose among a large number of constitutive models. In this section, only the constitutive models relevant for this thesis are presented.

The phase properties relevant to the numerical simulations presented in this thesis are: the specific heat of solid phase C_s, liquid density ρ_l, liquid viscosity μ_l, gas density ρ_g and gas viscosity μ_g. Default laws and parameter values for the phase properties suggested in Code_Bright and by Olivella et al. [216] were used in this thesis and they are shown in Table 4.2. Since the phase properties were not changed in the different analyses, they will not be shown again in the rest of this thesis. Specific heats of water and air, which depend on the corresponding phase (i.e. solid, liquid or gas), are internally modelled in the code and cannot be set by the user. It should be noticed that the physical properties in Code_Bright are functions of the different unknowns (i.e. p_g, p_l and T).

Table 4.2: Models for phase properties

Solid phase specific heat		$C_s = 1000\,\mathrm{J kg^{-1} K^{-1}}$
Liquid density $\rho_l = \rho_{l0} \exp\left(\beta\left(p_l - p_{l0}\right) + \alpha T\,[^\circ\mathrm{C}]\right)$	(4.21)	$\rho_{l0} = 1002.6\,\mathrm{kg m^{-3}}$ $\beta = 4.5 \times 10^4\,\mathrm{MPa^{-1}}$ $p_{l0} = 0.1\,\mathrm{MPa}$ $\alpha = -3.4 \times 10^{-4}\,^\circ\mathrm{C^{-1}}$
Liquid viscosity $\mu_l = A \exp\left(\dfrac{B}{273.15 + T\,[^\circ\mathrm{C}]}\right)$	(4.22)	$A = 2.1 \times 10^{-12}\,\mathrm{MPa\,s}$ $B = 1808.5\,\mathrm{K}$
Gas density - law of ideal gases Dissolved air concentration - Henry's law for dry air		$M_a = 0.028\,95\,\mathrm{kg/mol}$ $M_w = 0.018\,02\,\mathrm{kg/mol}$ $H = 10\,000\,\mathrm{MPa}$
Gas viscosity $\mu_g = \dfrac{A\sqrt{273.15 + T\,[^\circ\mathrm{C}]}}{\left(1 + \dfrac{B}{273.15 + T\,[^\circ\mathrm{C}]}\right)\left(1 + \dfrac{C - Dk}{p_g}\right)}$ k: intrinsic permeability	(4.23)	$A = 1.48 \times 10^{-12}\,\mathrm{MPa\,s}$ $B = 119.4\,^\circ\mathrm{C}$ $C = 0.14$ $D = 1.2 \times 10^{15}$

Different models are available in Code_Bright for the definition of the soil water retention curve (SWRC). In this thesis, two models were used: the conventional van Genuchten [82] (VG) model and the modified van Genuchten (modVG) model proposed by Fayer and Simmons [88]. In Code_Bright, every constitutive law is identified by the the definition of two codes: ICL and ITYCL. The code ICL identifies the type of constitutive law (e.g. for the SWRC ICL=6). The code ITYCL identifies the specific model used for the constitutive law (e.g. for the VG model ITYCL=1, for the modVG model ITYCL=17). For every constitutive law, a maximum of 10 parameters can be defined, consecutively ordered from P1 to P10. For all the constitutive laws used in this thesis work and presented below, the list of parameters to be used in Code_Bright and the corresponding units are shown in Table 4.3.

The VG model (ICL=6, ITYCL=1) is expressed as:

$$S_{le} = \frac{S_l - S_{lr}}{S_{ls} - S_{lr}} = \left(1 + \left(\frac{p_g - p_l}{P_0}\right)^{1/(1-m)}\right)^{-m} \qquad P_0 = \bar{P}_0 \frac{\sigma_s}{\bar{\sigma}_s} \tag{4.24}$$

where S_{lr}, S_{ls}, P_0 and m are parameters of the VG model (see Section 2.2.1). In CB, the

Table 4.3: Parameters for constitutive models in Code_Bright

model	P1	P2	P3	P4	P5	P6	P7	P8	P9	P10
SWRC - VG	$\bar{P}_0$	$\bar{\sigma}_s$	m	S_{lr}	S_{ls}	-	-	-	-	-
Eq. 4.24	[MPa]	$\left[\frac{\mathrm{N}}{\mathrm{m}}\right]$	[-]	[-]	[-]					
SWRC - modVG	$\bar{P}_0$	$\bar{\sigma}_s$	m	S_{lr}	S_{ls}	s_{dry}	ξ_0	-	-	-
Eq. 4.25	[MPa]	$\left[\frac{\mathrm{N}}{\mathrm{m}}\right]$	[-]	[-]	[-]	[MPa]	[-]			
Intrinsic permeability, $\boldsymbol{k}$	$k_{11,0}$ $[\mathrm{m}^2]$	$k_{22,0}$ $[\mathrm{m}^2]$	$k_{33,0}$ $[\mathrm{m}^2]$	-	-	-	-	-	-	-
Rel. hydr. conduct.	-	-	m	S_{lr}	S_{ls}	-	-	-	-	-
k_{rl}, Eq. 4.29			[-]	[-]	[-]					
Rel. gas conduct.	-	A_g	λ_g	S_{gr}	S_{gs}	-	-	-	-	-
k_{rg}, Eq. 4.30		[-]	[-]	[-]	[-]					
Diffus. water in gas	D	n	τ_0	-	-	-	-	-	-	-
$\boldsymbol{i}_g^w$, Eqs. 4.32,4.33	$\left[\frac{\mathrm{m}^2\mathrm{Pa}}{\mathrm{sK^n}}\right]$	[-]	[-]							
Diffus. air in liquid	D	Q	τ_0	-	-	-	-	-	-	-
$\boldsymbol{i}_l^a$, Eqs. 4.34,4.35	$\left[\frac{\mathrm{m}^2}{\mathrm{s}}\right]$	$\left[\frac{\mathrm{J}}{\mathrm{mol}}\right]$	[-]							
Thermal conduct.	λ_{dry}	λ_{sat}	$(\lambda_{solid})_0$	λ_{gas}	λ_{liq}	a_1	a_2	a_3	-	-
$\boldsymbol{i}_c$, Eqs. 4.38,4.39	$\left[\frac{\mathrm{W}}{\mathrm{mK}}\right]$	$\left[\frac{\mathrm{W}}{\mathrm{mK}}\right]$	$\left[\frac{\mathrm{W}}{\mathrm{mK}}\right]$	$\left[\frac{\mathrm{W}}{\mathrm{mK}}\right]$	$\left[\frac{\mathrm{W}}{\mathrm{mK}}\right]$	[-]	[-]	[-]		

parameter P_0 is a function of surface tension σ_s, which in turn is a function of temperature T. The parameter $\bar{P}_0$ represents the value of P_0 measured at a certain temperature and $\bar{\sigma}_s$ represents the value of σ_s measured at the same temperature. If the user sets $\bar{\sigma}_s = 0$, P_0 is considered as $P_0 = \bar{P}_0$. In Code_Bright, the constraint suggested by van Genuchten [82], $m = 1 - 1/n$, is used. The parameters P6, P7 and P9 of this model are used to model the influence of the variation of porosity Φ on the SWRC but, since in this thesis the soil was considered as non-deformable and the porosity as a constant, these parameters were not considered.

The modVG model (ICL=6, ITYCL=17) is not presented in the User's Guide of Code_Bright but it is implemented in the code. The model is expressed as:

$$S_{le} = \frac{S_l - \xi_0 \cdot S_{lr} \ln\left(\frac{s}{s_{dry}}\right)}{S_{ls} - \xi_0 \cdot S_{lr} \ln\left(\frac{s}{s_{dry}}\right)} = \left(1 + \left(\frac{p_g - p_l}{P_0}\right)^{1/(1-m)}\right)^{-m} \qquad P_0 = \bar{P}_0 \frac{\sigma_s}{\bar{\sigma}_s} \tag{4.25}$$

where ξ_0 and s_{dry} are two extra parameters compared to the VG model. The parameter s_{dry} represent the suction value at which the degree of saturation S_l decreases to zero (see Section 2.2.1) and, in this thesis, it was always considered as $s_{dry} = 1000\,\mathrm{MPa}$. Comparing the version of the model implemented in Code_Bright (Equation 4.25) to the expression of the modVG model given by Equation 2.37, the product $\xi_0 \cdot S_{lr}$ coincides with the parameter ξ. In the rest of the thesis, only the value of the parameter ξ will be given.

Liquid and gas advective flows are modelled in CB using Darcy's law. The liquid flow $\boldsymbol{q}_l$

is modelled as:

$$\boldsymbol{q}_l = -\frac{\boldsymbol{k} k_{rl}}{\mu_l}\left(\nabla p_l - \rho_l \boldsymbol{g}\right) \tag{4.26}$$

and the gas flow $\boldsymbol{q}_g$ is modelled as:

$$\boldsymbol{q}_g = -\frac{\boldsymbol{k} k_{rg}}{\mu_g}\left(\nabla p_g - \rho_g \boldsymbol{g}\right) \tag{4.27}$$

where $\boldsymbol{k}$ [L^2] is the intrinsic permeability, k_{rl} is the relative hydraulic conductivity, k_{rg} is the relative gas conductivity and $\boldsymbol{g}$ is the gravitational acceleration.

The intrinsic permeability $\boldsymbol{k}$ (ICL=7), which is treated as a tensor in Code_Bright, can be modelled in different ways. In this thesis, the intrinsic permeability was modelled as constant and isotropic. The code ITYCL=1 was used and the intrinsic permeability values in the three principal directions $k_{11,0}$, $k_{22,0}$ and $k_{33,0}$ were considered as $k_{11,0} = k_{22,0} = k_{33,0} = k$. In Code_Bright, the parameters P4 and P5 of this model are used to model the influence of the variation of porosity Φ on the intrinsic permeability but, since in this thesis the soil was considered as non-deformable and the porosity as a constant, these parameters were not considered. The intrinsic permeability k is related to the saturated hydraulic conductivity k_{ls} via the following relationship:

$$k = \frac{\mu_l}{\rho_l g} k_{ls} \tag{4.28}$$

In this thesis, two models were used for the relative hydraulic conductivity (ICL=14): the conventional Mualem (M) model, used in conjunction with the VG model, and the new modified Mualem (modM) model + liquid film (LF) model, used in conjunction with the modVG model. The M model was already present in the original version of Code_Bright whereas the modM+LF model was implemented in this thesis work and its implementation is described in Section 4.1.5. The M model (ITYCL=1) is expressed as:

$$k_{rl} = \sqrt{S_{le}}\left(1 - \left(1 - S_{le}^{1/m}\right)^m\right)^2 \tag{4.29}$$

By default, the term S_{le} in Equation 4.29 coincides with that obtained from the SWRC (Equations 4.24 and 4.25). However, the user can re-define the term S_{le} to be used in Equation 4.29 by prescribing different values for S_{ls} and S_{lr} (see Table 4.3) from those used for the SWRC model. As will be shown in Section 4.1.5, this approach was used to distinguish the conventional M model and the new modM model for the modelling of the bulk water component of the hydraulic conductivity.

In simulations where the air mass balance equation was solved (see Chapter 5), the relative gas conductivity (ICL=19) was modelled using a power-law expression (ITYCL=6), which can be written as follows:

$$k_{rg} = A_g {S_{ge}}^{\lambda_g} \tag{4.30}$$

where A_g and λ_g are model parameters (soil constants) and S_{ge} is expressed as:

$$S_{ge} = \begin{cases} \frac{S_g - S_{gr}}{S_{gs} - S_{gr}} & \text{if } S_g \geq S_{gr} \\ 0 & \text{if } S_g < S_{gr} \end{cases} \tag{4.31}$$

where S_{gr} and S_{gs} are respectively the residual gas saturation and the maximum gas saturation. By default, these parameters are considered as $S_{gr} = 1 - S_{ls}$ and $S_{gs} = 1 - S_{lr}$, but the user can choose different appropriate values (see Table 4.3).

Diffusive (non-advective) fluxes of water vapour in the gas phase and of dissolved air in the liquid phase are modelled in CB using Fick's law. The diffusive flux of water vapour in the gas phase $\boldsymbol{i}_g^w$ (ICL=11) is modelled as:

$$\boldsymbol{i}_g^w = -\left(\tau_0 \Phi \rho_g S_g D_g^w \boldsymbol{I}\right) \nabla \omega_g^w \tag{4.32}$$

where τ_0 is the tortuosity factor, D_g^w is the diffusion coefficient for the diffusion of water in the gas phase and $\boldsymbol{I}$ is the identity matrix. In this thesis, the diffusion coefficient D_g^w was modelled using the following constitutive law (ITYCL=1):

$$D_g^w = D\left(\frac{(273.15 + T[^\circ\mathrm{C}])^n}{p_g}\right) \tag{4.33}$$

where D and n are model parameters. The tortuosity factor τ_0 was considered as a constant. In this thesis, the values suggested by Olivella et al. [216] for these parameters (i.e. the default values in Code_Bright) were used: $D = 5.9 \times 10^{-6}\,\mathrm{m^2 s^{-1} K^{-n} Pa}$, $n = 2.3$ and $\tau_0 = 1$.

The diffusive flux of air in the liquid phase $\boldsymbol{i}_l^a$ (ICL=12) is modelled as:

$$\boldsymbol{i}_l^a = -\left(\tau_0 \Phi \rho_l S_l D_l^a \boldsymbol{I}\right) \nabla \omega_l^a \tag{4.34}$$

where τ_0 is the tortuosity factor and D_l^a is the diffusion coefficient for the diffusion of air in the liquid phase. In this thesis, the diffusion coefficient D_l^a was modelled using the following constitutive law (ITYCL=1):

$$D_l^a = D \exp\left(\frac{-Q}{R\,(273.15 + T[^\circ\mathrm{C}])}\right) \tag{4.35}$$

where D and Q are model parameters. The tortuosity factor τ_0 was considered as a constant. In this thesis, the values suggested by Olivella et al. [216] for these parameters (i.e. the default values in Code_Bright) were used: $D = 1.1 \times 10^{-4}\,\mathrm{m^2 s^{-1}}$, $Q = 24\,530\,\mathrm{J mol^{-1}}$ and $\tau_0 = 1$.

The energy flux due to heat conduction $\boldsymbol{i}_c$ is modelled using Fourier's law. This is expressed as:

$$\boldsymbol{i}_c = -\lambda \nabla T \tag{4.36}$$

where λ is the thermal conductivity of the porous medium. The thermal conductivity λ depends on the porosity Φ and on the degree of saturation S_l. The dependency on the degree

of saturation (ICL=20) was modelled using the following law (ITYCL=1):

$$\lambda = \lambda_{sat}\sqrt{S_l} + \lambda_{dry}\left(1 - \sqrt{S_l}\right) \tag{4.37}$$

where λ_{sat} is the thermal conductivity in fully saturated conditions (i.e. $S_l = 1$) and λ_{dry} is the thermal conductivity in fully dry conditions (i.e. $S_l = 0$). The dependency of the thermal conductivity on porosity (ICL=9) was modelled using the following law (ITYCL=1):

$$\lambda_{dry} = \lambda_{solid}^{(1-\Phi)}\lambda_{gas}^{\Phi} \tag{4.38a}$$

$$\lambda_{sat} = \lambda_{solid}^{(1-\Phi)}\lambda_{liq}^{\Phi} \tag{4.38b}$$

where λ_{solid}, λ_{gas} and λ_{liq} are respectively the thermal conductivities of the solid phase, the gas phase and the liquid phase. The thermal conductivity of the solid phase λ_{solid} was modelled as follows:

$$\lambda_{solid} = (\lambda_{solid})_0 + a_1 T + a_2 T^2 + a_3 T^3 \tag{4.39}$$

The thermal conductivity of the solid phase depends on the mineralogy, e.g. quartz minerals have higher thermal conductivity ($7.7\,\mathrm{Wm^{-1}K^{-1}}$ [217]) than clay minerals (between $1.3\,\mathrm{Wm^{-1}K^{-1}}$ and $3\,\mathrm{Wm^{-1}K^{-1}}$ [218]). In this work, since mainly relatively coarse-grained soils (e.g. sand), more likely to be made of quartz minerals, were analysed, the thermal conductivity of the solid phase was assumed to be as $(\lambda_{solid})_0 = 7.7\,\mathrm{Wm^{-1}K^{-1}}$ [217] and not dependent on temperature, i.e. $a_1 = 0$, $a_2 = 0$, $a_3 = 0$. The thermal conductivity of the gas phase was considered as $\lambda_{gas} = 0.024\,\mathrm{Wm^{-1}K}-1$ and the thermal conductivity of the liquid phase was considered as $\lambda_{liq} = 0.6\,\mathrm{Wm^{-1}K}-1$ [217]. In Code_Bright, no values were assigned to the parameters λ_{dry} (P1) and λ_{sat} (P2) (see Table 4.3) because they were calculated using Equation 4.38. The parameters λ_{dry} (P1) and λ_{sat} (P2) must be considered only in case no values are assigned to the parameters $(\lambda_{solid})_0$, λ_{gas} and λ_{liq}.

4.1.3 Boundary conditions

One-dimensional and two-dimensional simulations were performed in this thesis work. Boundary conditions are incorporated in Code_Bright by assigning a mass flux or an energy flux at the boundary nodes of the mesh, directed perpendicular to the boundaries. This process is applied even when the required boundary condition is a prescribed value of an unknown (e.g. p_l, p_g or T), as described below. Two types of boundary conditions were used in Code_Bright: "standard" boundary conditions and "atmospheric" boundary conditions. The sign convention for all boundary conditions is: positive sign for fluxes entering the model, negative sign for fluxes leaving the model.

Standard boundary conditions

Standard boundary conditions for mass fluxes are made of the combination of three terms. The following equation represents the boundary condition for the mass flux of air in the liquid

phase j_l^a:

$$j_l^a = (\omega_l^a)^0 j_l^0 + (\omega_l^a)^0 \gamma_l \left(p_l^0 - p_l\right) + \beta_l \left((\rho_l \omega_l^a)^0 - (\rho_l \omega_l^a)\right) \tag{4.40}$$

where the superscript ^{0} stands for the parameter values assigned at the boundary nodes whereas the parameters without the superscript ^{0} are the actual values at the boundary nodes, ω_l^a is the mass fraction of air in the liquid phase, ρ_l is the liquid density, p_l is the liquid pressure, j_l^0 is the prescribed mass liquid flow and γ_l and β_l are two parameters termed leakage coefficients. The first term in the right hand-side of Equation 4.40 represents the mass flow which takes place when a mass flow rate (in this case liquid) is prescribed at the boundary. The second term represents the mass flow which takes place when a phase pressure (in this case liquid) is prescribed at the boundary. The third term represents the mass flow which takes place when a species mass fraction (in this case air in liquid) is prescribed at the boundary. For realistic numerical predictions, only one of the three terms shown in the right hand-side of Equation 4.40 should be activated at any given time: if a mass flow rate is prescribed at the boundary the following parameters should be used $\gamma_l = 0$ and $\beta_l = 0$, if the liquid pressure is prescribed at the boundary the following parameters should be used $j_l^0 = 0$, $\gamma_l \neq 0$ and $\beta_l = 0$, if a species mass fraction is prescribed at the boundary the following parameters should be used $j_l^0 = 0$, $\gamma_l = 0$ and $\beta_l \neq 0$. The leakage coefficient γ_l represents the "strength" with which the boundary liquid pressure is prescribed: an extremely high value of γ_l may lead to numerical difficulties (matrix ill conditioning) whereas a low value of γ_l may produce inaccurate prescriptions of the liquid pressure at the boundary. An appropriate value for γ_l can be obtained easily by means of a few trials. Similar concepts applies to the leakage coefficient β_l representing the "strength" with which the boundary species mass fraction is prescribed. If a negative value is assigned to the parameter γ_l, only outflow is allowed and it occurs when $p_l = p_l^0$ whereas, for $p_l < p_l^0$, an impermeable boundary condition is automatically assigned (i.e. $j_l^0 = 0$).

Similar concepts are applied to the other possible boundary conditions for mass fluxes. The mass flux of water in the liquid phase j_l^w at the boundary is calculated as:

$$j_l^w = (\omega_l^w)^0 j_l^0 + (\omega_l^w)^0 \gamma_l \left(p_l^0 - p_l\right) + \beta_l \left((\rho_l \omega_l^w)^0 - (\rho_l \omega_l^w)\right) \tag{4.41}$$

The mass flux of air in the gas phase j_g^a at the boundary is calculated as:

$$j_g^a = \left(\omega_g^a\right)^0 j_g^0 + \left(\omega_g^a\right)^0 \gamma_g \left(p_g^0 - p_g\right) + \beta_g \left(\left(\rho_g \omega_g^a\right)^0 - \left(\rho_g \omega_g^a\right)\right) \tag{4.42}$$

The mass flux of water in the gas phase j_g^w at the boundary is calculated as:

$$j_g^w = \left(\omega_g^w\right)^0 j_g^0 + \left(\omega_g^w\right)^0 \gamma_g \left(p_g^0 - p_g\right) + \beta_g \left(\left(\rho_g \omega_g^w\right)^0 - \left(\rho_g \omega_g^w\right)\right) \tag{4.43}$$

where γ_g and β_g are leakage coefficients for the boundary gas fluxes. Note that in the other chapters of this thesis the symbols γ_l and γ_g are defined as the unit weights of liquid and gas whereas only in this chapter they represent the leakage coefficients. This inconsistency

in the definition of γ_l and γ_g in this thesis was considered acceptable, in order to use the conventional symbol for unit weight throughout the majority of the thesis while also, in this chapter, maintaining consistency with the parameter definitions used in Code_Bright.

The boundary condition for the energy flux j_e is calculated as:

$$j_e = j_e^0 + \gamma_e \left(T^0 - T\right) + E_l^a \left(j_l^a\right) + E_l^w \left(j_l^w\right) + E_g^a \left(j_g^a\right) + E_g^w \left(j_g^w\right) \tag{4.44}$$

where, similar to the boundary conditions for mass fluxes, j_e^0 is the energy flux prescribed at the boundary, T^0 is the temperature prescribed at the boundary and γ_e is the corresponding leakage coefficient. In addition, the terms $E_l^a \left(j_l^a\right)$, $E_l^w \left(j_l^w\right)$, $E_g^a \left(j_g^a\right)$ and $E_g^w \left(j_g^w\right)$ are the advective energy fluxes related respectively to the fluxes j_l^a, j_l^w, j_g^a and j_g^w. For realistic numerical predictions, only one of the terms j_e^0 and γ_e shown in the right hand-side of Equation 4.44 should be activated at any given time.

Atmospheric boundary conditions

The "atmospheric" boundary conditions are used in Code_Bright to perform advanced simulations modelling soil-atmospheric interactions (see Section 2.4).

In CB, the parameters used to model the atmosphere are: atmospheric temperature T_a [°C], atmospheric gas pressure p_{ga} [MPa], atmospheric relative humidity RH_a [-], net incoming radiation R_n [$\mathrm{J\,m^{-2}\,s^{-1}}$], cloud index I_n [-], rainfall P [$\mathrm{kg\,m^{-2}\,s^{-1}}$] and wind velocity v_a [$\mathrm{m\,s^{-1}}$]. Two strategies can be used in Code_Bright to model the variation of these parameters with time: interpolation and simulation. According to the first strategy, i.e. interpolation, the user defines a list of data points in terms of times and corresponding parameter values, and the code automatically applies a linear interpolation of the parameter values between the different data points. According to the second strategy, i.e. simulation, the variation of the atmospheric parameter values with time can be modelled using the following sinusoidal law:

$$x(t) = x_m + x_a \sin\left(2\pi \frac{t - t_a}{d_a}\right) + x_d \sin\left(2\pi \frac{t - t_d}{d_d}\right) \tag{4.45}$$

where $x(t)$ is the value of the generic atmospheric parameter at time t, x_m is its mean value, x_a is its annual amplitude, x_d is its daily amplitude, t_a is the start of the annual variation, t_d is the start of the daily variation, d_a is the duration of a year and d_d is the duration of a day. Equation 4.45 is characterized by the superposition of two sinusoidal functions: one simulates the annual variation of the atmospheric parameter and the other one simulates its daily variation.

In addition to the simulation and interpolation strategies, the variation of the radiation R_n can be also calculated using a model implemented in Code_Bright. According to this model [219], the radiation is an output result and measured data of radiation are thus not needed. Radiation is calculated according to Equation 2.74, which is here reminded:

$$R_n = R_s (1 - A_l) + \varepsilon_s R_{ld} - R_{lu}$$

where R_s is the solar radiation, R_{ld} is the downward atmospheric long-wave radiation, R_{lu} is the upward long-wave radiation and both albedo A_l and emissivity ε_s are calculated as functions of the degree of saturation of the soil at the ground surface:

$$A_l = A_{ld} + (A_{ld} - A_{lw})\left(S_l^2 - 2S_l\right) \tag{4.46}$$

$$\varepsilon_s = 0.9 + 0.05 S_l \tag{4.47}$$

where A_{ld} and A_{lw} are the dry and wet albedos respectively.

The upward long-wave radiation from the soil surface R_{lu} is calculated as given by Equation 2.76, that is:

$$R_{lu} = \varepsilon_s \sigma_R {T_s}^4$$

where T_s is the soil surface temperature (i.e. temperature at the boundary nodes) and σ_T is the Stefan-Boltzmann constant ($5.67 \times 10^{-8}\,\mathrm{Wm^{-2}K^{-4}}$).

The downward atmospheric long-wave radiation R_{ld} is calculated as a function of atmospheric temperature T_a and atmospheric absolute humidity ρ_{va}, as follows:

$$R_{ld} = \sigma_R T_a^4 \left(0.605 + 0.048\sqrt{1370\rho_{va}}\right) \tag{4.48}$$

In Equation 4.48, ρ_{va} must be expressed in units of kg/m^3. Note that the temperatures T_s and T_a appearing in Equations 2.76 and 4.48 regarding radiative fluxes are expressed in units of K in order to be consistent with the format used by Code_Bright whereas in the rest of the thesis temperatures are expressed in units of °C unless stated otherwise.

The calculation of the solar radiation R_s takes into account the time of the day and of the year, according to the following relationship:

$$R_s = \begin{cases} \dfrac{\pi \bar{R}_S}{2 d_s} \sin\left(\dfrac{(t - t_m + 0.5 d_s)\,\pi}{d_s}\right) & \text{if } t_m - 0.5 d_s \le t \le t_m + 0.5 d_s \\ 0 & \text{otherwise} \end{cases} \tag{4.49}$$

where d_s is the time span between sunrise and sunset, t_m is the time at noon and $\bar{R_S}$ is the daily solar radiation, which is calculated by the following empirical expression:

$$\bar{R_S} = \int_{t_m - 0.5 d_s}^{t_m + 0.5 d_s} R_s dt = R_A\,(0.29 \cos\varphi_l + 0.52 I_n) \tag{4.50}$$

where φ_l is the latitude, I_n is the cloud index (=1 for a clear sky, =0 for a completely clouded sky) and R_A is the daily solar radiation in the absence of the atmosphere, calculated as:

$$R_A = S_0 r_s \left[\frac{d_d}{\pi} \cos\varphi_l \cos\delta_s \sin\left(\frac{\pi d_s}{d_d}\right) + d_s \sin\varphi_l \sin\delta_s\right] \tag{4.51}$$

where S_0 is the solar constant (=1367 $\mathrm{J\,m^{-2}\,s^{-1}}$), r_s is the ratio between the average distance between the sun and the earth and the distance at a given time t, d_d is the duration of a day (=86400 s) and δ_s is the declination of the sun. The parameters d_s, r_s and δ_s are calculated as

follows:

$$d_s = \frac{d_d}{\pi} \arccos\left(-\tan\varphi_l \tan\delta_s\right) \tag{4.52}$$

$$\begin{aligned} r_s = 1.00011 + 0.034221\cos\left(2\pi\frac{t-t_0}{d_a}\right) + 0.00128\sin\left(2\pi\frac{t-t_0}{d_a}\right) \\ +0.000719\cos\left(4\pi\frac{t-t_0}{d_a}\right) + 0.000077\sin\left(4\pi\frac{t-t_0}{d_a}\right) \end{aligned} \tag{4.53}$$

$$\delta_s = -\delta_{s,max}\sin\left(2\pi\frac{t-t_s}{d_a}\right) \tag{4.54}$$

where d_a is the duration of a year (=365.241 days=$3.155\,68\times10^7$ s), t_0 is the time at the 1st of January, t_s is the time when autumn starts (21st of September for the northern hemisphere) and $\delta_{s,max}$ is the maximum declination of the sun (=0.4119 rad=23.26°).

Once the atmospheric parameters are defined, the different mass and energy fluxes at the boundary can be calculated as a result of the soil-atmosphere interaction. In this type of analysis, the boundary fluxes are output results. The calculation of the different mass and energy fluxes at the boundary is presented below.

- Air flux

The mass gas flux at the boundary q_g is calculated as:

$$q_g = \gamma_g\left(p_g - p_{ga}\right) \tag{4.55}$$

where γ_g [m s] is the leakage coefficient for gas flow, p_g is the gas pressure at the boundary nodes and p_{ga} is the atmospheric gas pressure assigned by the user. As far as the parameter γ_g is concerned, the use of $\gamma_g = 0$ implies boundary impermeable to gas flow, whereas a large value of γ_g will ensure $p_g \approx p_{ga}$, i.e. a value of gas pressure at the ground surface equal to the prescribed value of atmospheric gas pressure. Note that, unlike the term $\boldsymbol{q}_g$ used previously (e.g. in Equation 4.27) which is a volumetric flux, the term q_g in Equation 4.55 is a mass flux, in consistency with the convention used in Code_Bright. The air flux is then calculated as:

$$j_a = \omega_g^a q_g = \left(1-\omega_g^w\right) q_g \tag{4.56}$$

- Water flux

Evaporation E (expressed in CB as positive when it is a flux from the atmosphere into the soil) is calculated using the following aerodynamic diffusion relationship:

$$E = \frac{k^{*2} v_a \psi}{\left(\ln\dfrac{z_a}{z_0}\right)^2}\left(\rho_{va} - \rho_v\right) \tag{4.57}$$

where ρ_{va} and ρ_v are respectively the absolute humidity (calculated by relative humidity RH and temperature T) of the atmosphere and at the boundary node, k^* is the Von Karman's constant (=0.4), v_a is the wind velocity, ψ is the stability factor (which, if different from 1,

takes into account deviations from the logarithmic profile of wind speed with height), z_0 is the roughness length and z_a is the screen height at which the different atmospheric parameter values (including v_a and ρ_{va}) are measured. Equation 4.57 is similar to Equation 2.72 presented in Section 2.4.2. However, in Equation 4.57, the stability factor ψ is added and the following assumptions are implicitly made: $k_v^* = k^* = 0.4$ and $z_{0v} = z_{0m} = z_0$. These assumptions are typically reasonable [178].

The advective mass flux of vapour in the gas phase is calculated as:

$$j_g^w = \begin{cases} \omega_g^w q_g & \text{if } p_g > p_{ga} \\ \dfrac{\rho_{va}}{\rho_{ga}} q_g & \text{if } p_g \leq p_{ga} \end{cases} \tag{4.58}$$

where ρ_{ga} is the atmospheric gas density and q_g is the mass flux of gas given by Equation 4.55.

Surface runoff j_{sr} is calculated as:

$$j_{sr} = \begin{cases} \gamma_l \left(p_l - p_{ga}\right) & \text{if } p_l > p_{ga} \\ 0 & \text{if } p_l \leq p_{ga} \end{cases} \tag{4.59}$$

where γ_l is a leakage coefficient (it must be negative and must have a high absolute value in this case). Note that the use of the leakage coefficient γ_l in Equation 4.59 valid for the atmospheric boundary condition is different from the use of the leakage coefficient γ_l in Equations 4.40 and 4.41 valid for the standard boundary condition. According to Equation 4.59, no runoff occurs if $p_l \leq p_{ga}$ ($s > 0$) whereas runoff occurs when $p_l \approx p_{ga}$ ($s \approx 0$) and, in this case, the infiltration in the soil is the result of an applied liquid pressure at the boundary instead of an applied flux.

The total flux of water at the boundary is thus calculated as:

$$j_w = P + E + j_g^w + j_{sr} \tag{4.60}$$

- Energy flux

The sensible heat flux H_s (positive when directed into the soil) is calculated as:

$$H_s = \frac{k^{*2} v_a \psi}{\left(\ln \dfrac{z_a}{z_0}\right)^2} \rho_{ga} C_a \left(T_a - T\right) \tag{4.61}$$

where C_a is the specific heat of the gas. Equation 4.61 is similar to Equation 2.73 presented in Section 2.4.2. However, in Equation 4.61, the stability factor ψ is added and the assumptions $k_v^* = k^* = 0.4$ and $z_{0v} = z_{0m} = z_0$ are implicitly made.

The convective heat flux H_c is calculated as the sum of the convective components related to liquid water, vapour and air:

$$H_c = h_v \left(E + j_g^w\right) + h_l \left(P + j_{sr}\right) + h_a j_a \tag{4.62}$$

where h_v, h_l and h_a are the free energy of vapour, liquid water and air, which depend on temperature.

The total energy flux at the boundary is thus calculated as:

$$j_e = R_n + H_s + H_c \tag{4.63}$$

A summary of the parameters needed for the modelling of the atmospheric boundary condition in Code_Bright is shown in Table 4.4.

Table 4.4: Parameters for atmospheric boundary condition in Code_Bright

Parameters	Unit	Parameters	Unit
Atmospheric parameters		**General parameters**	
Atm. temperature, T_a	°C	Latitude**, φ_l	rad
Atm. gas pressure, p_{ga}	MPa	Time when autumn**, t_s	s
Atm. relative humidity, RH_a	-	Time at noon**, t_m	s
Radiation*, R_n	$\mathrm{J\,m^{-2}\,s^{-1}}$	Roughness length, z_0	m
Cloud index**, I_n	-	Screen height, z_a	m
Rainfall, P	$\mathrm{kg\,m^{-2}\,s^{-1}}$	Stability factor, ψ	-
Wind velocity, v_a	$\mathrm{m\,s^{-1}}$	Atm. gas density, ρ_{ga}	$\mathrm{kg\,m^{-3}}$
		Dry albedo**, A_{ld}	-
		Wet albedo**, A_{lw}	-
		Leakage coeff. for gas, γ_g	$\mathrm{kg\,m^{-2}\,s^{-1}\,MPa^{-1}}$
		Leakage coeff. for liquid, γ_l	$\mathrm{kg\,m^{-2}\,s^{-1}\,MPa^{-1}}$

* Only needed if radiation data are provided by the user.
** Only needed if radiation is calculated according to the model present in Code_Bright.

4.1.4 Numerical approach

In Code_Bright, the system of partial differential equations shown in Section 4.1.1 is solved numerically [205]. The finite difference method is used for time discretization whereas the finite element method is used for spatial discretization. The time discretization is linear and an implicit integration scheme is used. Four times are considered in this time discretization: two consecutive time steps t^k and t^{k+1} and two intermediate times $t^{k+\theta}$ and $t^{k+\varepsilon}$, where $0 \leq \theta \leq 1$ and $0 \leq \varepsilon \leq 1$. Given that the numerical problem is non-linear, the Newton-Raphson iterative method is used to solve the system of governing equations.

The mass balance equation of solid (Equation 4.1), unlike the other balance equations, is solved using an explicit integration scheme and intermediate times are not needed because variations of porosity are expected to be slow. Thus, values at the time t^k are used for porosity.

For the other balance equations (Equations 4.3, 4.6, 4.9 and 4.10), the residuals for a single finite element are calculated as:

$$\boldsymbol{r}\left(\boldsymbol{X}^{k+1}\right) = \frac{\boldsymbol{d}^{k+1} - \boldsymbol{d}^{k}}{t^{k+1} - t^{k}} + \boldsymbol{A}\left(\boldsymbol{X}^{k+\varepsilon}\right)\boldsymbol{X}^{k+\theta} + \boldsymbol{b}\left(\boldsymbol{X}^{k+\theta}\right) = \boldsymbol{0} \tag{4.64}$$

where $\boldsymbol{r}$ is the vector of residuals, $\boldsymbol{X}$ is the vector of the unknowns calculated at a certain time

(i.e. $\boldsymbol{X} = (\boldsymbol{u}, p_l, p_g, T)$), $\boldsymbol{d}$ is the storage or accumulation term of the balance equations, $\boldsymbol{A}$ is the conductance term and $\boldsymbol{b}$ is the sink/source term. The residuals are calculated at the time t^{k+1}, the storage or accumulation terms at the times t^k and t^{k+1}, the conductance terms at the time $t^{k+\varepsilon}$ and the unknowns multiplying the conductance terms and used in the sink/source terms are calculated at the time $t^{k+\theta}$. The application of the iterative Newton-Raphson solution method is written as:

$$\frac{\partial \boldsymbol{r}\left(\boldsymbol{X}^{k+1}\right)}{\partial \boldsymbol{X}^{k+1}}\left(\boldsymbol{X}^{k+1,l+1} - \boldsymbol{X}^{k+1,l}\right) = -\boldsymbol{r}\left(\boldsymbol{X}^{k+1,l}\right) \tag{4.65}$$

where l indicates the iteration. The values of θ and ε are chosen by the user: the default values $\theta = 1$ and $\varepsilon = 1$ were used in this thesis, which correspond to a fully implicit integration scheme.

In terms of the space discretization, the concept of cell is used in Code_Bright (see Figure 4.1). Once the space is discretized with a mesh defined by the user, made of nodes and elements, the code assigns a cell to each node of the mesh. The cell is centred on the corresponding node (see node i in Figure 4.1) and it is made of fractions of the different elements which share this node. The standard Galerkin method is used for application of the finite element (FE) method. The balance equations are written for each cell associated to each node. In Code_Bright, the unknowns $\boldsymbol{u}$, p_l, p_g and T are nodal quantities whereas many dependent variables, such as degree of saturation S_l, intrinsic permeability k, relative hydraulic conductivity k_{rl}, relative gas conductivity k_{rg}, thermal conductivity λ etc., are elemental quantities. When a balance equation is solved for a cell, the contributions of the different elements to a single cell are summed. As a result, a sort of "average" of the elemental quantities are considered for each nodal cell. Further information about how the different terms appearing in the balance equations are treated from the numerical point view can be found in the work of Olivella et al. [205].

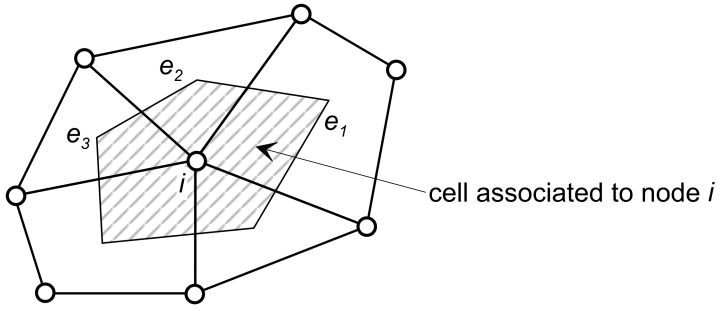

Figure 4.1: Schematic representation of the cell used in Code_Bright (after Olivella et al. [205])

Hydraulic conductivity k_l and gas conductivity k_g are elemental quantities. Different options are available in Code_Bright for the calculation of k_l and k_g, depending on the value assigned to the parameter IOPTPC.

- If IOPTPC=0, the elemental k_l is calculated from the elemental suction. This means that the elemental suction is firstly calculated as the average of the suction values at

the nodes of the element. The elemental degree of saturation is then calculated as a function of the elemental suction. The elemental hydraulic conductivity k_l is finally calculated as a function of this elemental degree of saturation. The derivative of the hydraulic conductivity $\partial k_l / \partial S_l$ is calculated as a function of the elemental degree of saturation.

- If IOPTPC=-1 (default option), the elemental k_l is calculated from the average nodal degrees of saturation. This means that nodal value of degree of saturation are calculated at each node of the element as a function of suction at the same node. The elemental degree of saturation is then calculated as the average of the nodal degrees of saturation. The elemental hydraulic conductivity k_l is finally calculated as a function of this elemental degree of saturation. The derivative of the hydraulic conductivity $\partial k_l / \partial S_l$ is calculated as a function of the elemental degree of saturation.

- If IOPTPC=-2, the elemental k_l is calculated from the average nodal relative permeabilities. This means that nodal degrees of saturation are calculated at each node of the element as a function of suction at the same node. Nodal hydraulic conductivities are then calculated at each node of the element as a function of the nodal degree of saturation. The elemental hydraulic conductivity k_l is finally calculated as the average of the nodal hydraulic conductivities. The derivative of the hydraulic conductivity $\partial k_l / \partial S_l$ is calculated as a function of the elemental degree of saturation, which is calculated as the average of the nodal degrees of saturation.

- If IOPTPC=-3, the elemental k_l is calculated from the average nodal relative permeabilities (applies also for derivatives). The elemental hydraulic conductivity k_l is calculated as for IOPTPC=-2. However, in this case, the derivative of the hydraulic conductivity $\partial k_l / \partial S_l$ is calculated differently. The nodal derivatives of the hydraulic conductivity are calculated at each node of the element as a function of the nodal degree of saturation. The elemental derivative of the hydraulic conductivity $\partial k_l / \partial S_l$ is calculated as the average of the nodal derivatives of the hydraulic conductivity.

- If IOPTPC=-4, the elemental k_l is calculated from the maximal nodal relative permeability. This means that nodal degrees of saturation are calculated at each node of the element as a function of suction at the same node. Nodal hydraulic conductivities are then calculated at each node of the element as a function of the nodal degree of saturation. The elemental hydraulic conductivity k_l is finally calculated as the maximum of the nodal hydraulic conductivities. The elemental derivative of the hydraulic conductivity $\partial k_l / \partial S_l$ is taken as the same as the nodal derivative of the hydraulic conductivity of the node with the maximum nodal hydraulic conductivity.

- If IOPTPC=-5, the elemental k_l is calculated from the minimal nodal relative permeability. This means that nodal degrees of saturation are calculated at each node of the element as a function of suction at the same node. Nodal hydraulic conductivities are

then calculated at each node of the element as a function of the nodal degree of saturation. The elemental hydraulic conductivity k_l is finally calculated as the minimum of the nodal hydraulic conductivities. The elemental derivative of the hydraulic conductivity $\partial k_l / \partial S_l$ is taken as the same as the nodal derivative of the hydraulic conductivity of the node with the minimum nodal hydraulic conductivity.

The same options described above for the hydraulic conductivity k_l apply also to the gas conductivity k_g.

In the analyses performed, the options IOPTPC=-1, IOPTPC=-2 and IOPTPC=-3 lead to negligible differences. The default option IOPTPC=-1 was used in most of the analyses because it leads to correct results in shorter computing times. However, in some particular "extreme" cases the option IOPTPC=-3 should be preferred. For instance, when simulating water breakthrough from the finer layer to the coarser layer of a CBS, subsequent to the application of a very high infiltration rate and with the coarser layer at very high values of suction, IOPTPC=-1 leads to numerical problems whereas it was found that IOPTPC=-3 leads to more reliable results. These results are not shown in this thesis. A comparison between the results obtained with options IOPTPC=-1 and IOPTPC=-3 is in general always suggested.

The FE mesh for space discretization can be generated automatically by Code_Bright, according to the user preferences. For 1D and 2D problems, either triangular or quadrilateral mesh elements can be used. Both structured meshes and unstructured meshes were used in this thesis work. A structured mesh is characterised by a regular topological pattern and it is defined as a mesh where all inner nodes have the same number of elements around them. An unstructured mesh is characterised by an irregular topology. Typically, quadrilateral elements are used in structured meshes and triangular elements are used in unstructured meshes.

The size of the elements of a structured mesh can be defined in different ways. One of these, used in this thesis, consists of assigning the number of elements that are required along a given orientation. Practically, the number of elements is assigned in each boundary line and this number must be the same for all lines that are opposite to each other on each surface. A mesh refinement gradient can be defined for each line in order to concentrate or enlarge the size of the elements towards the two ends of the lines. In Code_Bright, the mesh refinement along a direction is defined by assigning a pair of numbers along a boundary line (e.g. 0.2/-0.3) with a given orientation. The first number is the concentration weight related to the initial extremity of the line, the second number is the concentration weight related to the final extremity of the line. If the weight is positive the elements will be concentrated (smaller elements) towards the extremity of the line; if negative, the elements will be enlarged. As a reference for the values given in this thesis, the orientation of the mesh refinement will be left/right and down/up, meaning that, in the following chapters in which FE meshes are described, the first number will refer to left or down sides and the second number will refer to right or up sides. As the magnitude of the weight increases, the difference between element sizes will be greater.

The size of the elements of an unstructured mesh can be defined as the average side length. The maximum value of the size can be assigned by the user. In addition, it is possible to

assign different sizes to different boundary lines. This means that in the vicinity of these lines, the unstructured mesh elements will be approximately of that size. The transition between different sizes at different locations can be controlled by means of a given parameter. Increasing this parameter, the transition between the mesh sizes at different locations is faster.

4.1.5 Implementation of the new hydraulic conductivity model for unsaturated soils

In this thesis work, changes and new developments were introduced in Code_Bright, which is written in the programming language Fortran. Given the potential and all the possible features that CB provides, the code is big and complex. The changes and new developments of the code resulted in substantial work, involving many different components of the program. In this section and in Sections 4.1.6 and 4.1.7, changes and new developments in the code are described only qualitatively. For users accessing the modified source files of Code_Bright, all changes and new developments done in this thesis work were marked by the text "!RS" plus the corresponding date (e.g. "!RS 25/07/18") written next to the corresponding commands, in order to facilitate the tracking of these changes.

The new hydraulic conductivity model modM+LF presented in Section 3.3.1 (see Equation 3.1) was implemented in CB. The bulk water conductivity of the new model k_l^{Bulk} (modM) (see Equation 3.4) can be used in the original version of the code using appropriate parameters for the conventional Mualem model whereas the liquid film component of the new hydraulic conductivity model k_l^{Film} (see Equation 3.5) was implemented in this thesis work.

The modM model for the bulk water component of the hydraulic conductivity (see Equation 3.4) can be used in the original version of Code_Bright by choosing an appropriate value for the parameter S_{lr} (P4) of the Mualem model (ICL=14, ITYCL=1) (see Equation 4.29 and Table 4.3). Indeed, assuming that $S_{l,BWD} = S_{l,BWEX}$ for drying and $S_{l,BWC} = S_{l,BWE}$ for wetting, as suggested in Section 3.3.1, the modM model can be obtained by imposing $S_{lr} = S_{l,BWD/BWC}$ as the value of the parameter P4 in the conventional Mualem model (ICL=14, ITYCL=1). This will ensure that k_l^{Bulk} goes to zero when the degree of saturation falls to the value of $S_{lr} = S_{l,BWD/BWC}$ specified in the Mualem model. This will always occur at a finite value of suction if the modVG model is used for the SWRC, but it will also occur if the VG model is used, provided that the value of S_{lr} specified in the M model is greater than the value of S_{lr} specified in the VG model.

The LF model for the liquid film component of the hydraulic conductivity (see Equation 3.5) was implemented in Code_Bright. A specific subroutine (i.e. a sub-unit of the code), called "*liquid_permeability*", is dedicated to the calculation of the relative hydraulic conductivity k_{rl}. Therefore, the liquid film component of the relative hydraulic conductivity k_{lr}^{Film} was introduced in this subroutine, using the following equation:

$$k_{lr}^{Film} = C_r^{Film} \cdot \left(a^{Film} + p_g - p_l\right)^{d^{Film}} \tag{4.66}$$

where C_r^{Film}, a^{Film} and d^{Film} are three new material parameters introduced in CB for the LF model. The parameter a^{Film} coincides with that shown in Equation 3.5. The parameter d^{Film} is the exponent -1.5 in Equation 3.5. However, in the model implemented in Code_Bright, the user has the possibility to choose any value for the parameter d^{Film}. The coefficient C_r^{Film} is related to the coefficient C^{Film} of Equation 3.5 by the following relationship:

$$C_r^{Film} = \frac{C^{Film}}{k_{ls}} \tag{4.67}$$

where k_{ls} is the saturated hydraulic conductivity, which is related to the prescribed intrinsic permeability k via Equation 4.28.

In the same subroutine dedicated to the calculation of the relative hydraulic conductivity, also the partial derivatives of the relative hydraulic conductivity with respect to liquid pressure $\partial k_{lr}/\partial p_l$, gas pressure $\partial k_{lr}/\partial p_g$ and temperature $\partial k_{lr}/\partial T$ are calculated. These are used by the iterative solving algorithm implemented in the code. Using the additivity rule and the chain rule of derivatives and given the form of the new modM+LF model (see Equation 3.1), the following relationships are calculated:

$$\frac{\partial k_{lr}}{\partial p_l} = \frac{\partial k_{lr}^{Bulk}}{\partial S_l}\frac{\partial S_l}{\partial p_l} + \frac{\partial k_{lr}^{Film}}{\partial s}\frac{\partial s}{\partial p_l} \tag{4.68}$$

$$\frac{\partial k_{lr}}{\partial p_g} = \frac{\partial k_{lr}^{Bulk}}{\partial S_l}\frac{\partial S_l}{\partial p_g} + \frac{\partial k_{lr}^{Film}}{\partial s}\frac{\partial s}{\partial p_g} \tag{4.69}$$

$$\frac{\partial k_{lr}}{\partial T} = \frac{\partial k_{lr}^{Bulk}}{\partial S_l}\frac{\partial S_l}{\partial T} + \frac{\partial k_{lr}^{Film}}{\partial s}\frac{\partial s}{\partial T} \tag{4.70}$$

Since k_{lr}^{Bulk} is an explicit function of S_l whereas k_{lr}^{Film} is an explicit function of s, their partial derivatives are calculated respectively with respect to S_l and s, i.e. $\partial k_{lr}^{Bulk}/\partial S_l$ and $\partial k_{lr}^{Film}/\partial s$. The terms $\partial k_{lr}^{Bulk}/\partial S_l$, $\partial S_l/\partial p_l$, $\partial S_l/\partial p_g$ and $\partial S_l/\partial T$ were already present in the original version of Code_Bright. The term $\partial k_{lr}^{Film}/\partial s$ was written as:

$$\frac{\partial k_{lr}^{Film}}{\partial s} = C_r^{Film} \cdot d^{Film} \cdot \left(a^{Film} + p_g - p_l\right)^{d^{Film}-1} \tag{4.71}$$

and the remaining terms were written as:

$$\frac{\partial s}{\partial p_l} = -1 \tag{4.72}$$

$$\frac{\partial s}{\partial p_g} = 1 \tag{4.73}$$

$$\frac{\partial s}{\partial T} = 0 \tag{4.74}$$

Other changes in other parts of the code were made in order to guarantee consistency between the values of suction s adopted in the LF model and the values of the degree of saturation S_l adopted in the modM model. When elemental values of S_l were used in the

modM model, elemental values of suction of s at the same time (e.g. $t^{k+\varepsilon}$) were used in the LF model, calculated as the average of the nodal values for each element. Similarly, when nodal values of S_l were used in the modM model, nodal values of suction s at the same time were used in the LF model.

Finally, Table 4.5 shows the list of parameters, and the corresponding units, needed in order to use the modM+LF model implemented in Code_Bright.

Table 4.5: Parameters for the modM+LF model implemented in Code_Bright

ICL	ITYCL	P2	P3	P4	P5	P6	P7
14	1	C_r^{Film} [MPa$^{-d^{Film}}$]	m [-]	$S_{l,BWC/BWD}$ [-]	S_{ls} [-]	a^{Film} [MPa]	d^{Film} [-]

4.1.6 Implementation of the new hysteretic hydraulic model for unsaturated soils

Hydraulic hysteresis was introduced in Code_Bright using the bounding surface approach described in Section 3.4. Water retention hysteresis was implemented for use in conjunction with the van Genuchten model (ICL=6, ITYCL=1, see Equation 4.24) and the modified van Genuchten model (ICL=6, ITYCL=17, see Equation 4.25). A new subroutine called "*hyst_liquid_saturation*" was written in the code with this purpose. Some assumptions on the material parameters were made in the implementation of water retention hysteresis:

- For both the VG model and the modVG model, the maximum degree of saturation is the same for drying and wetting, i.e. $S_{ls,d} = S_{ls,w} = S_{ls}$;
- for both the VG model and the modVG model, the slopes of the main drying curve and the main wetting curve are the same, i.e. $m_d = m_w = m$;
- for the VG model, the residual degree of saturation is the same for drying and wetting, i.e. $S_{lr,d} = S_{lr,w} = S_{lr}$;
- for the modVG model, the main drying curve and the main wetting curve coincide in the pendular state, i.e. $\xi_d = \xi_w = \xi$;
- for the modVG model, the suction at oven-dryness is fixed and equal to $s_{dry} = 1000\,\text{MPa}$.

The input variables of this subroutine are the material parameters (i.e. $\bar{P}_{0d}$, $\bar{P}_{0w}$, $\bar{\sigma}_s$, m, S_{ls}, γ_d and γ_w for both models, S_{lr} for the VG model, ξ for the modVG model), history variables about the previous hydraulic state, i.e. at the previous time step, (s_0 and S_{l0}) and the current values of the unknowns (T, p_g and p_l). The output variables of this subroutine are the liquid degree of saturation S_l and its derivatives with respect to temperature $\partial S_l/\partial T$, pore-gas pressure $\partial S_l/\partial p_g$ and pore-liquid pressure $\partial S_l/\partial p_l$ at the current time step.

Figure 4.2 shows a schematic flow chart regarding the functioning of the subroutine *hyst_liquid_saturation*. This subroutine is called by the program only if water retention hysteresis is activated in the model. The activation of water retention hysteresis is identified by the value attained by a flag parameter iopthys (=1 for the hysteretic model, =0 for the non-hysteretic model). An appropriate value is assigned to iopthys in an external code, called "Transb", which reads the information of the model created in the program GiD and generates input files for Code_Bright accordingly. Changes were made to the code Transb in this thesis work, so that the model is considered hysteretic (i.e. 1 is assigned to iopthys) if ITYCL=1 (VG model) or 17 (modVG model), $\gamma_d > 0$ and $\gamma_w > 0$, otherwise the model is considered non-hysteretic (i.e. 0 is assigned to iopthys). Therefore, the new subroutine *hyst_liquid_saturation* is called only if iopthys=1, otherwise the non-hysteretic models already implemented in Code_Bright are used.

The subroutine *hyst_liquid_saturation* firstly checks the current suction value: if $s < 0$ the soil is in saturated conditions and the following quantities are calculated $S_l = S_{ls}$, $\partial S_l/\partial p_l = \partial S_l/\partial p_g = \partial S_l/\partial T = 0$. In this case, before exiting the subroutine, the history variables s_0 and S_{l0} are updated with the corresponding current values, i.e. $s_0 = s$ and $S_{l0} = S_l$, for use of the subroutine in the next time step.

If the suction value is $s > 0$ the soil is in an unsaturated condition. The parameter P_{0d} and the parameter P_{0w} are firstly initialized as follows:

$$P_{0w} = \bar{P}_{0w}\frac{\sigma_s}{\bar{\sigma}_s} \tag{4.75a}$$

$$P_{0d} = \bar{P}_{0d}\frac{\sigma_s}{\bar{\sigma}_s} \tag{4.75b}$$

and the derivatives $\partial\sigma_s/\partial T$ and $\partial\sigma_s/\partial p_l$ are calculated. The calculation of σ_s, $\partial\sigma_s/\partial T$ and $\partial\sigma_s/\partial p_l$ is done in a different subroutine which was already present in the original version of Code_Bright.

The value of the parameter S_{lr0}, which represents the corresponding residual degree of saturation at the previous time step, is then assessed: if the VG model is used, the material parameter assigned by the user S_{lr} is directly employed whereas, if the modVG model is used, S_{lr0} is calculated as a function of suction:

$$S_{lr0} = S_{lr} \qquad \text{for the VG model} \tag{4.76a}$$

$$S_{lr0} = \xi \ln\left(\frac{s_{dry}}{s_0}\right) \quad \text{for the modVG model} \tag{4.76b}$$

The parameter S_{lr0} is then used to calculate the effective degree of saturation at the previous time step S_{le0}, as follows:

$$S_{le0} = \frac{S_{l0} - S_{lr0}}{S_{ls} - S_{lr0}} \tag{4.77}$$

The parameter S_{le0} is used subsequently for the calculation of the integration constants A_w or A_d.

At this point the subroutine recognizes if the current hydraulic state is on a wetting curve

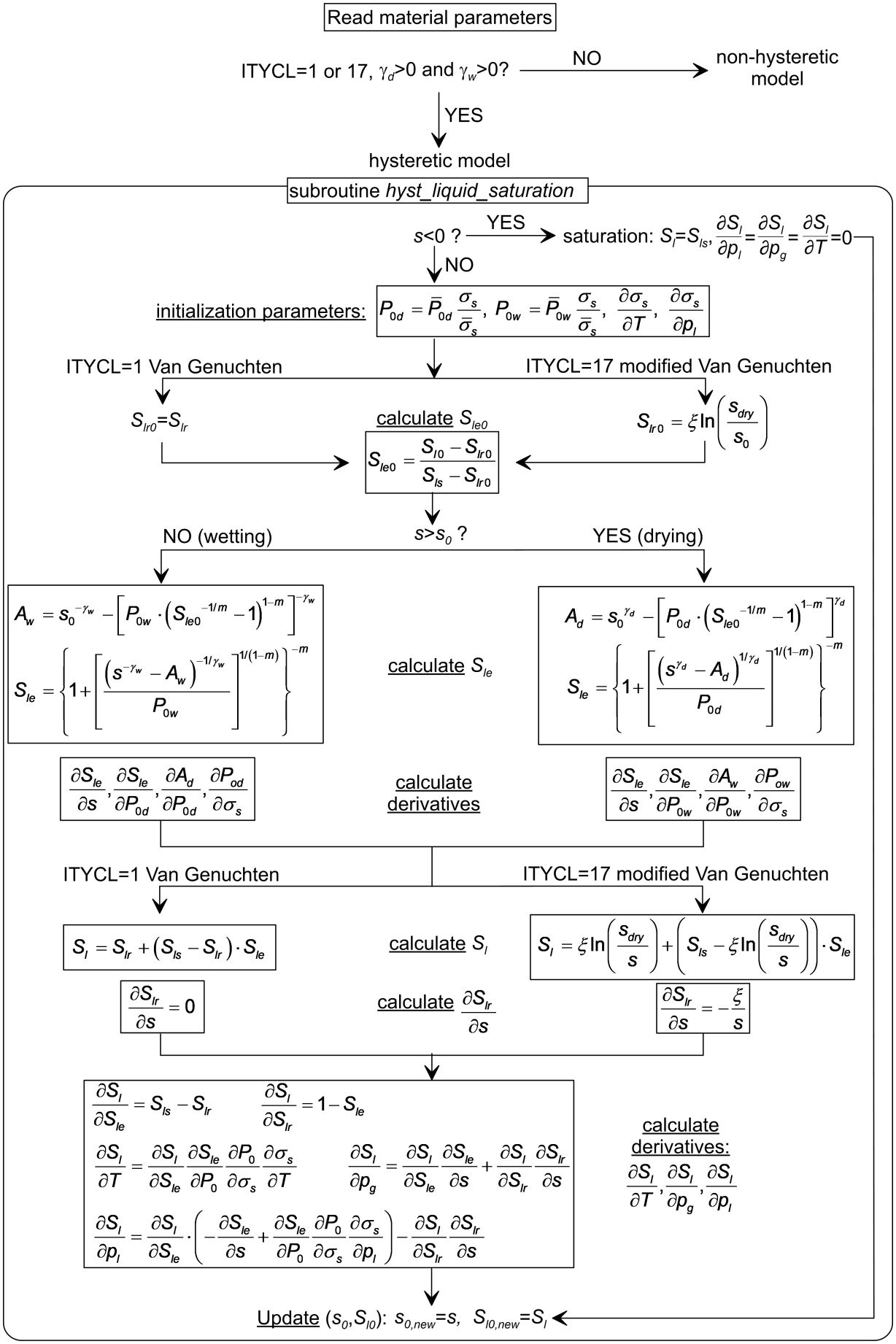

Figure 4.2: Implementation of the subroutine *hyst_liquid_saturation* for the hysteretic soil water retention models in Code_Bright

or a drying curve. If the current value of suction is greater than the previous value of suction, i.e. $s > s_0$, the current hydraulic state is on a drying curve, otherwise it is on a wetting curve. The integration constant, A_w or A_d, is calculated accordingly:

$$A_w = s_0^{-\gamma_w} - \left[P_{0w} \cdot \left(S_{le0}^{-1/m} - 1 \right)^{1-m} \right]^{-\gamma_w} \quad \text{for wetting} \tag{4.78a}$$

$$A_d = s_0^{\gamma_d} - \left[P_{0d} \cdot \left(S_{le0}^{-1/m} - 1 \right)^{1-m} \right]^{\gamma_d} \quad \text{for drying} \tag{4.78b}$$

The effective degree of saturation S_{le} is then calculated as:

$$S_{le} = \left\{ 1 + \left[\frac{\left(s^{-\gamma_w} - A_w \right)^{-1/\gamma_w}}{P_{0w}} \right]^{1/(1-m)} \right\}^{-m} \quad \text{for wetting} \tag{4.79a}$$

$$S_{le} = \left\{ 1 + \left[\frac{\left(s^{\gamma_d} - A_d \right)^{1/\gamma_d}}{P_{0d}} \right]^{1/(1-m)} \right\}^{-m} \quad \text{for drying} \tag{4.79b}$$

Also some partial derivatives are calculated at this point, i.e. $\partial S_{le}/\partial s$, $\partial S_{le}/\partial P_{0d}$ or $\partial S_{le}/\partial P_{0w}$, $\partial A_d/\partial P_{0d}$ or $\partial A_w/\partial P_{0w}$ and $\partial P_{0d}/\partial \sigma_s$ or $\partial P_{0w}/\partial \sigma_s$ (see Equations 4.88, 4.89, 4.90 and 4.86). These derivatives are used at the end of the subroutine for the calculation of $\partial S_l/\partial T$, $\partial S_l/\partial p_g$ and $\partial S_l/\partial p_l$.

Subsequently, the residual degree of saturation at the current hydraulic state is assessed, depending on the model used:

$$S_{lr} = \text{assigned parameter } S_{lr} \quad \text{for the VG model} \tag{4.80a}$$

$$S_{lr} = \xi \ln\left(\frac{s_{dry}}{s} \right) \quad \text{for the modVG model} \tag{4.80b}$$

The actual degree of saturation S_l is finally calculated as:

$$S_l = S_{lr} + (S_{ls} - S_{lr}) \cdot S_{le} \tag{4.81}$$

For the modVG model, Equation 4.80b used with Equation 4.81 coincides with:

$$S_l = \xi \ln\left(\frac{s_{dry}}{s} \right) + \left(S_{ls} - \xi \ln\left(\frac{s_{dry}}{s} \right) \right) \cdot S_{le} \tag{4.82}$$

Also the partial derivative of $\partial S_{lr}/\partial s$ is calculated at this point (see Equation 4.91), depending on the model used.

In the subroutine the derivatives $\partial S_l/\partial T$, $\partial S_l/\partial p_g$ and $\partial S_l/\partial p_l$ are calculated in the following way:

$$\frac{\partial S_l}{\partial T} = \frac{\partial S_l}{\partial S_{le}} \frac{\partial S_{le}}{\partial P_0} \frac{\partial P_0}{\partial \sigma_s} \frac{\partial \sigma_s}{\partial T} \tag{4.83}$$

$$\frac{\partial S_l}{\partial p_g} = \frac{\partial S_l}{\partial S_{le}} \frac{\partial S_{le}}{\partial s} \frac{\partial s}{\partial p_g} + \frac{\partial S_l}{\partial S_{lr}} \frac{\partial S_{lr}}{\partial s} \frac{\partial s}{\partial p_g} \tag{4.84}$$

$$\frac{\partial S_l}{\partial p_l} = \frac{\partial S_l}{\partial S_{le}} \cdot \left(\frac{\partial S_{le}}{\partial s}\frac{\partial s}{\partial p_l} + \frac{\partial S_{le}}{\partial P_0}\frac{\partial P_0}{\partial \sigma_s}\frac{\partial \sigma_s}{\partial p_l} \right) + \frac{\partial S_l}{\partial S_{lr}}\frac{\partial S_{lr}}{\partial s}\frac{\partial s}{\partial p_l} \tag{4.85}$$

where $P_0 = P_{0d}$ for drying and $P_0 = P_{0w}$ for wetting and S_{lr} is calculated using Equation 4.80a or 4.80b depending on the model used. The derivatives $\partial\sigma_s/\partial T$ and $\partial\sigma_s/\partial p_l$ are calculated in a different subroutine which was already present in the original version of Code_Bright. The derivatives $\partial s/\partial p_l$, $\partial s/\partial p_g$ and $\partial s/\partial T$ are calculated according to Equations 4.72, 4.73 and 4.74. Given Equations 4.75a and 4.75b, the derivative $\partial P_0/\partial\sigma_s$ is calculated as:

$$\frac{\partial P_0}{\partial \sigma_s} = \frac{\bar{P}_0}{\bar{\sigma}_s} \tag{4.86}$$

where $\bar{P}_0 = \bar{P}_{0w}$ for wetting and $\bar{P}_0 = \bar{P}_{0d}$ for drying. Given Equations 4.79a and 4.79b, the partial derivative $\partial S_{le}/\partial s$ is calculated as:

$$\begin{aligned} \frac{\partial S_{le}}{\partial s} = &- \left[\frac{s}{P_{0w} \cdot \left(S_{le}^{-1/m} - 1 \right)^{1-m}} \right]^{-\gamma_w - 1} \\ &\cdot \left[\frac{m \cdot S_{le}^{1+1/m} \cdot \left(S_{le}^{-1/m} - 1 \right)^{m}}{P_{0w} \cdot (1-m)} \right] \qquad \text{for wetting} \end{aligned} \tag{4.87}$$

$$\begin{aligned} \frac{\partial S_{le}}{\partial s} = &- \left[\frac{s}{P_{0d} \cdot \left(S_{le}^{-1/m} - 1 \right)^{1-m}} \right]^{\gamma_d - 1} \\ &\cdot \left[\frac{m \cdot S_{le}^{1+1/m} \cdot \left(S_{le}^{-1/m} - 1 \right)^{m}}{P_{0d} \cdot (1-m)} \right] \qquad \text{for drying} \end{aligned} \tag{4.88}$$

The derivative $\partial S_{le}/\partial P_{0w}$ for wetting and $\partial S_{le}/\partial P_{0d}$ for drying are calculated as:

$$\frac{\partial S_{le}}{\partial P_{0w}} = \frac{m \cdot S_{le}^{1+1/m} \cdot \left(S_{le}^{-1/m} - 1 \right)^{1+\gamma_w/n} \cdot \left[-\frac{\partial A_w}{\partial P_{0w}} + \frac{\gamma_w}{P_{0w}} \left(s^{-\gamma_w} - A_w \right) \right]}{(1-m) \cdot \gamma_w \cdot P_{0w}^{-\gamma_w}} \tag{4.89a}$$

$$\frac{\partial S_{le}}{\partial P_{0d}} = -\frac{m \cdot S_{le}^{1+1/m} \cdot \left(S_{le}^{-1/m} - 1 \right)^{1-\gamma_d/n} \cdot \left[-\frac{\partial A_d}{\partial P_{0d}} - \frac{\gamma_d}{P_{0d}} \left(s^{\gamma_d} - A_d \right) \right]}{(1-m) \cdot \gamma_d \cdot P_{0d}^{\gamma_d}} \tag{4.89b}$$

where the derivatives of the integration constants $\partial A_w/\partial P_{0w}$ for wetting and $\partial A_d/\partial P_{0d}$ for drying are calculated as:

$$\frac{\partial A_w}{\partial P_{0w}} = \gamma_w P_{0w}^{-\gamma_w - 1} \left(S_{le0}^{-1/m} - 1 \right)^{-\gamma_w \cdot (1-m)} \tag{4.90a}$$

$$\frac{\partial A_d}{\partial P_{0d}} = -\gamma_d P_{0d}^{\gamma_d - 1} \left(S_{le0}^{-1/m} - 1 \right)^{\gamma_d \cdot (1-m)} \tag{4.90b}$$

Given the definition of the parameter S_{lr} for the VG model (Equation 4.80a) and the modVG

model (Equation 4.80b), the following derivatives are calculated:

$$\frac{\partial S_{lr}}{\partial s} = 0 \qquad \text{for the VG model} \tag{4.91a}$$

$$\frac{\partial S_{lr}}{\partial s} = -\frac{\xi}{s} \quad \text{for the modVG model} \tag{4.91b}$$

Finally the derivative $\partial S_l / \partial S_{le}$ is calculated as:

$$\frac{\partial S_l}{\partial S_{le}} = S_{ls} - S_{lr} \tag{4.92}$$

and the derivative $\partial S_l / \partial S_{lr}$ is calculated as:

$$\frac{\partial S_l}{\partial S_{lr}} = 1 - S_{le} \tag{4.93}$$

Outside the subroutine *hyst_liquid_saturation*, Code_Bright was modified in order to get the history variables s_0 and S_{l0} tracked and saved throughout the code. Two arrays are used with this purpose: "hystvc" is used to save and update the history variables for elements and "hystvn" is used to save and update the history variables for nodes.

In CB, initial conditions are assigned in terms of the unknowns (p_l, p_g and T) whereas the initial dependent variables, such as the degree of saturation S_l, are calculated as functions of the unknowns. Unlike non-hysteretic models, for hysteretic water retention models the relationship between S_l and s is not unique. Thus, assigning initial conditions for p_l, p_g and T in the numerical FE model is not sufficient to calculate the initial degree of saturation S_l. The history variables s_0 and S_{l0} are updated and saved at each step during the simulations. However, the initial values need to be assigned by the user for the first step of the analysis. Therefore, by means of a modification to the code, the degree of saturation at the beginning of the analysis is initialized using the subroutine *hyst_liquid_saturation* with values of s_0 and S_{l0} assigned by the user as material parameters. In the particular cases in which the user wants to prescribe the initial hydraulic state to be located on the main wetting curve or on the main drying curve, the use of the following initial values for s_0 and S_{l0} is suggested:

- for the VG model, on the main wetting curve, $s_0 = 1000\,\text{MPa}$ and $S_{l0} = S_{lr}$;
- for the VG model, on the main drying curve, $s_0 = 0\,\text{MPa}$ and $S_{l0} = S_{ls}$;
- for the modVG model, on the main wetting curve, $s_0 = 1000\,\text{MPa}$ and $S_{l0} = 0$;
- for the VG model, on the main drying curve, $s_0 = 0\,\text{MPa}$ and $S_{l0} = S_{ls}$;

Finally, Table 4.6 shows the list of parameters, and the corresponding units, which are needed in order to use the hysteretic water retention models implemented in Code_Bright.

Table 4.6: Parameters for the hysteretic water retention models implemented in Code_Bright

model	P1	P2	P3	P4	P5	P6	P7	P8	P9	P10
VG (ICL=6, ITYCL=1)	$\bar{P}_{0d}$ [MPa]	$\bar{\sigma}_s$ $\left[\frac{\mathrm{N}}{\mathrm{m}}\right]$	m [-]	S_{lr} [-]	S_{ls} [-]	$\bar{P}_{0w}$ [MPa]	γ_d [-]	$s_0{}^*$ [MPa]	$S_{l0}{}^*$ [-]	γ_w [-]
modVG (ICL=6, ITYCL=17)	$\bar{P}_{0d}$ [MPa]	$\bar{\sigma}_s$ $\left[\frac{\mathrm{N}}{\mathrm{m}}\right]$	m [-]	ξ [-]	S_{ls} [-]	$\bar{P}_{0w}$ [MPa]	γ_d [-]	$s_0{}^*$ [MPa]	$S_{l0}{}^*$ [-]	γ_w [-]

*These parameters are used only to initialize the model at the beginning of the analysis

4.1.7 Other minor changes to Code_Bright

Other minor changes were made to the code in this thesis work and they are briefly listed here.

- The water retention model proposed by Zhang [89] improved at low degree of saturation was initially implemented in Code_Bright. However, it was subsequently not used because the gradient of the SWRC is discontinuous at the transition between funicular state and pendular state. The SWRC modVG model proposed by Fayer and Simmons [88] was used instead.

- The non-hysteretic SWRC modVG model (ICL=6, ITYCL=17) (see Equation 4.25), already present in CB, was slightly modified. In detail, the following condition was added in the model: for $s > s_{dry}$, the degree of saturation is zero, i.e. $S_l = 0$, as well as the different derivatives, i.e. $\partial S_l/\partial p_l = \partial S_l/\partial p_g = \partial S_l/\partial T = 0$.

- Code_Bright gives the user the possibility to choose between different methods of how the relative hydraulic and gas conductivities of an element are calculated (see Section 4.1.4). With one of these methods, the relative conductivity of an element is supposed to be calculated as the minimum of the nodal conductivities, i.e. $k_{rl} = \min\left(k_{rl,n1}, k_{rl,n2}, ...\right)$ and $k_{rg} = \min\left(k_{rg,n1}, k_{rg,n2}, ...\right)$, where $k_{rl,ni}$ and $k_{rg,ni}$ are the relative hydraulic and gas conductivities of the i-th node in a specific element (see IOPTPC=-5 in Section 4.1.4). However, this method worked only for the relative hydraulic conductivity k_{rl} but not for the relative gas conductivity k_{rg}. Some minor changes were subsequently introduced in Code_Bright to calculate also k_{rg} according to this method.

- An error in CB regarding the application of the linear interpolation strategy for the variation of the atmospheric parameters (see Section 4.1.3) was identified. A simple example is used to present the error that was identified in Code_Bright and how it was solved. Let us consider the time history of an atmospheric variable $x(t)$, defined by means of linear interpolation between three points (x_1, t_1), (x_2, t_2) and (x_3, t_3), and two consecutive numerical time steps t_A and t_B, with one of the defined points being intermediate between t_A and t_B, i.e. $t_A < t_2 < t_B$ (see Figure 4.3). The average value of

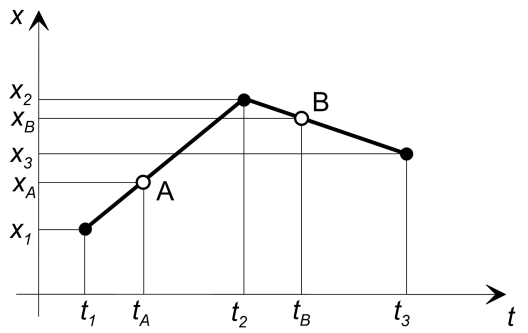

Figure 4.3: Schematic representation of the calculation of an atmospheric variable x between time steps t_A and t_B

the parameter x, i.e. $\bar{x}$, is considered in Code_Bright in the time interval between time t_A and t_B. Given that x_A and x_B are the values of the generic atmospheric parameter at the times t_A and t_B respectively, in the original version of Code_Bright, this average value $\bar{x}$ was calculated as:

$$\bar{x} = \frac{\frac{x_A + x_2}{2}(t_B - t_A) + \frac{x_2 + x_B}{2}(t_B - t_A)}{t_B - t_A} = x_2 + \frac{x_A + x_B}{2} \tag{4.94}$$

Equation 4.94 is clearly wrong because the time interval length $(t_B - t_A)$ is used in both terms of the numerator whereas it should be $(t_2 - t_A)$ for the first term and $(t_B - t_2)$ for the second term. The corrected version of Equation 4.94 is:

$$\bar{x} = \frac{\frac{x_A + x_2}{2}(t_2 - t_A) + \frac{x_2 + x_B}{2}(t_B - t_2)}{t_B - t_A} \tag{4.95}$$

In Code_Bright, a more generalized form of Equation 4.94 was present and, in this work, it was corrected with a more generalized version of Equation 4.95.

4.1.8 Validation of the implemented constitutive models

The validity of the implementation of the new hydraulic constitutive models, i.e. the hydraulic conductivity model (see Section 4.1.5) and the hysteretic water retention models (see Section 4.1.6), was ensured by means of various numerical tests. In this Section, one of these tests is presented.

A one-dimensional hydraulic simulation, with constant temperature $T = 20\,^{\circ}\mathrm{C}$ and constant pore-gas pressure $p_g = 0.1\,\mathrm{MPa}$, was performed considering a 10 cm-thick sample of soil, shown in Figure 4.4. The material hydraulic behaviour of the soil was modelled using the modVG-modM+LF model including water retention hysteresis. The material parameters are shown in Table 4.7. The initial condition for the model was a uniform distribution of pore-liquid pressure with $p_l = 0.08\,\mathrm{MPa}$, which corresponded to a suction value of $s = 0.02\,\mathrm{MPa}$. Given the values of s_0 and S_{l0} shown in Table 4.7, the corresponding initial degree of saturation was equal to $S_l = 0.6565$.

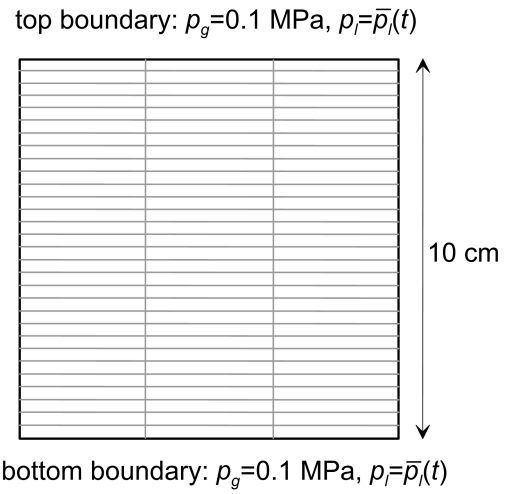

Figure 4.4: Geometry and mesh of the numerical model

Table 4.7: Material parameters for the numerical validation of the models implemented in Code_Bright

Φ [-]	0.45	$s_0{}^*$ [MPa]	0.01
$\bar{P}_{0d}$ [MPa]	0.01962	$S_{l0}{}^*$ [-]	0.685
$\bar{\sigma}_s$ [N/m]	0	γ_w [-]	3
m [-]	0.5	k [m^2]	2.775E-9
ξ [-]	0.0268	$S_{l,BWC/BWD}$ [-]	0.35
S_{ls} [-]	1	C_r^{Film} [MPa$^{-1.5}$]	3.147E-10
$\bar{P}_{0w}$ [MPa]	0.00491	a^{Film} [MPa]	3E-5
γ_d [-]	3	d^{Film} [-]	-1.5

*These parameters are used only to initialize the model at the beginning of the analysis

Several cycles of wetting and drying were simulated applying the same time history of pore-liquid pressure $\overline{p_l}(t)$ at the top and at the bottom boundaries simultaneously. For each cycle, a liquid pressure value was firstly applied at the boundaries. This liquid pressure was maintained until a steady-state condition was reached, which consisted of a uniform distribution of pore-liquid pressure and degree of saturation throughout the soil sample, with the internal liquid pressure in equilibrium with the value applied at the boundaries. At this steady-state condition, the hydraulic gradient was $\nabla h_l = 1$ and, according to Darcy's law (see Equation 2.22), the vertical volumetric liquid flow was $q_l = -k_l$, where k_l is the hydraulic conductivity and the negative sign of q_l means a downward flux. Therefore, at this steady-state condition, the value of the downward liquid flow coincided with the hydraulic conductivity, which was a function of suction s and degree of saturation S_l. After reaching a steady-state condition, a different pore-liquid pressure was applied at the boundaries and a new hydraulic cycle was started. Twelve cycles of wetting and drying were modelled starting from the initial hydraulic state A and ending at the final hydraulic state M (see Figure 4.5).

In order to check the validity of the implementation of the new hydraulic constitutive models implemented in Code_Bright, the hydraulic states at the steady-state conditions obtained with the numerical simulations were compared with the hydraulic paths simulated analytically using the same material parameters. Figures 4.5a and 4.5b show this comparison

in terms of the SWRC and the SHCC respectively. It can be observed that the different cycles involved main drying curve, main wetting curve and scanning curves covering the full range of degree of saturation. The exact coincidence of the analytical predictions and the numerical results confirmed the validity of the implementation in CB of the new models for hydraulic conductivity and water retention hysteresis.

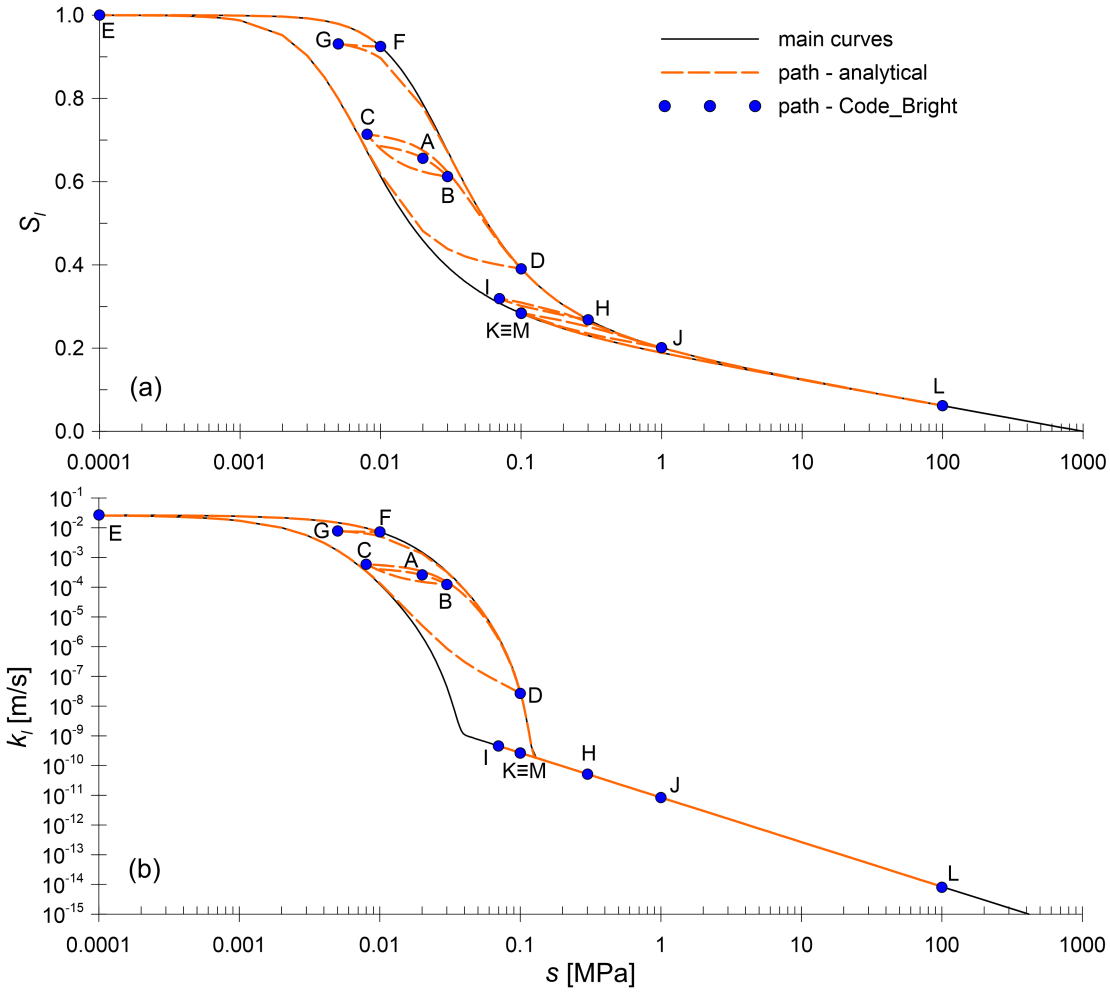

Figure 4.5: Comparison between the hydraulic paths simulated analytically and numerically with Code_Bright, in terms of (a) the SWRC and (b) the SHCC

4.2 LimitState:GEO

4.2.1 Theoretical background

LimitState:GEO (LS) [220] is a commercial software developed at LimitState Ltd in Sheffield, which adopts limit analysis, specifically the upper bound theorem, through a Discontinuity Layout Optimization (DLO) method, to assess failure mechanisms and corresponding factors of safety for a wide variety of geotechnical problems. More precisely, the solution is presented in terms of a failure mechanism and an "adequacy factor". The adequacy factor, which can be applied either to loads or to material strength parameters, is the factor by which loads must be increased or strength parameters must be decreased for the system under consideration to reach

a failure condition. The software is able to assess multiple scenarios and to consider multiple multiplicative partial factors in agreement with modern design codes such as Eurocode 7. In this work, LS was used to model and analyse the stability of unsaturated slopes by means of two-dimensional models. The version LimitState:GEO 3.5 was used in this work.

Limit analysis is rigorously based on the theorems of plasticity. The upper bound theorem of limit analysis [221] is used as the calculation method in LS. Soils are modelled as rigid-perfectly plastic materials. According to the definition given by Chen and Scawthorn [221], the upper bound theorem of limit analysis states: "the soil mass will collapse if there is any compatible pattern of plastic deformation for which the rate of work of the external loads exceeds the part of internal dissipation". Therefore, this method firstly involves the identification of a compatible failure mechanism. Subsequently, for a given compatible failure mechanism, the rate of work done by external loads (including self-weights) is equated to the internal dissipation caused by plastic deformations. As a result, the adequacy factor for loads is identified for given material strength parameters or, alternatively, the adequacy factor for material strength parameters is identified for given loads. The application of the upper bound theorem of limit analysis leads to an upper bound of the exact load adequacy factor, i.e. the predicted load causing failure is higher than the exact one, or to a lower bound of the exact strength adequacy factor, i.e. the predicted strength parameters causing failure are lower than the exact ones. However, the closer the prescribed failure mechanism is to the exact mechanism, the closer the predicted solution is to the exact solution.

LimitState:GEO adopts the Discontinuity Layout Optimization (DLO) numerical procedure, developed by Smith and Gilbert [222], which is an optimization technique used to work out potential failure mechanisms and the corresponding adequacy factors. It firstly involves the definition of a number of potential lines of discontinuity or slip lines, produced by the connection of various nodes, which represent the boundaries between different moving rigid blocks of material. Subsequently, all the compatible potential failure mechanisms are assessed and the critical failure mechanism is identified as the one which minimizes the energy dissipation, as shown in the example of the analysis of the undrained stability of the footing in Figure 4.6. In other words, the DLO method automates the conventional use of upper bound limit analysis by hand calculations. Unlike the traditional hand calculations, a very high number of slipping rigid blocks can be considered with this approach and a more accurate solution is thus generally obtained.

The accuracy of the solution depends on the number and spacing of the nodes defined in the model. The use of a higher number of nodes increases the number of possible potential failure mechanisms, and thus the accuracy of the solution, but increases the computational effort. Simple tests regarding the grid refinement can be done to obtain convergence of the solution.

Compared to the use of "element-based" methods (e.g. finite element method), the DLO method generally provides a strong solution to problems involving failure with much lower computational costs, fewer numerical difficulties and simpler models [222].

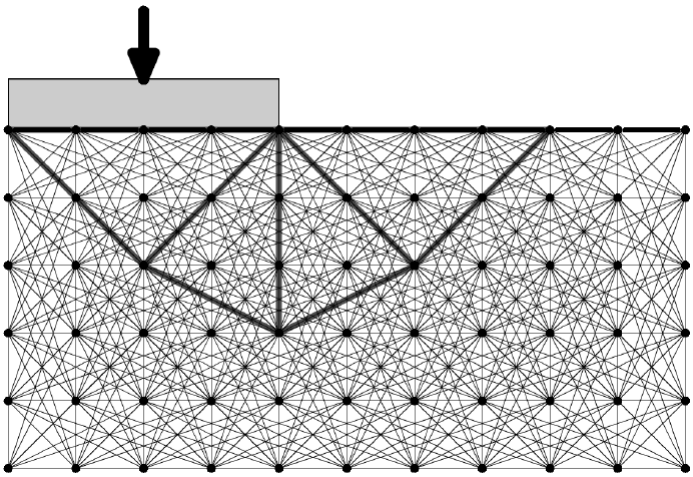

Figure 4.6: Discontinuity Layout Optimization applied to the analysis of the undrained stability of a footing (from LimitState [220])

4.2.2 Description of the model properties

LimitState:GEO offers a large variety of options, material models, element types and conditions. Only the ones used in this thesis work are discussed in this section.

The geometry of the model is firstly created. The geometry is created by defining the boundaries of the solid elements (2D polygons defining a body of soil). From the assigned geometry, a grid is automatically created by the program when the simulation is launched. The user can adjust the density of the grid nodes or the grid node spacing using appropriate parameters.

External boundaries are used to assign conditions on the displacement field whereas internal boundaries are used to divide different solids, e.g. to define the interface between different materials. Two types of external boundaries were assigned in this work: free and fixed. A free boundary is free to displace in any direction whereas, for a fixed boundary, only displacements parallel to the boundary are permitted. If sliding occurs along a fixed boundary, the material properties of the solid will be considered. If sliding occurs along the interface between two materials (i.e. the internal boundary) the properties of the weakest materials will be considered. Alternatively, specific material properties can be defined at the internal boundaries, e.g. representing a geosynthetic present between two materials.

Different materials models can be used in LS (Mohr-Coulomb, tension and/or compression cut off, rigid and engineered elements). In this work, only the Mohr-Coulomb material model was used. According to this model, the material is modelled as rigid-perfectly plastic with Mohr-Coulomb yield criterion and associative plastic flow. This type of material is defined by the following properties: unit weight γ_s, effective cohesion c' and effective friction angle ϕ'.

The Mohr-Coulomb model is defined by the following relationship:

$$\tau_f = c' + \left(\sigma - p_f\right) \tan \phi' \tag{4.96}$$

where τ_f is the shear strength, σ is the total stress normal to the slipping surface and p_f is

the pore fluid pressure. Unsaturated conditions are not directly modelled in LimitState:GEO and the Mohr-Coulomb criterion is not appropriate for unsaturated conditions. However, LimitState:GEO gives the user the possibility to define a spatial distribution of pore fluid pressure p_f in the model and within LS it is implicitly assumed that both total stress σ and pore fluid pressure p_f are expressed relative to the atmospheric pressure (rather than as absolute pressures). Therefore, if, for a situation involving unsaturated conditions, it can be assumed that the pore gas pressure p_g is uniform and equal to atmospheric pressure, then by replacing the distribution of pore-fluid pressure p_f in LS by the distribution of the negative product of suction s and degree of saturation S_l, i.e. $-s \cdot S_l$, Equation 4.96 becomes:

$$\tau_f = c' + (\sigma - p_g + s \cdot S_l) \tan \phi' \tag{4.97}$$

Equation 4.97 coincides with the shear strength criterion for unsaturated soils proposed by Bishop and Blight [67] (see Equation 2.28) where the following assumption is made $\chi = S_l$ [77]. This model was shown to be adequate at describing the shear strength of unsaturated soils [80]. Therefore, in this thesis work, unsaturated conditions were considered in LimitState:GEO by replacing p_f with the negative product $-s \cdot S_l$, under the assumption of uniform pore-gas pressure $p_g = 100\,\text{kPa}$.

In LS, pore fluid pressures can be modelled by defining a water table or by defining a pore fluid pressure regime within a zone of the model. The water table option was not used in this work. The pore fluid regime involves the definition of a distribution of pore-fluid pressure within a certain zone of the model. The following pore fluid pressure regimes are available: constant potential, constant pressure, interpolated grid and aquiclude. Constant potential consists of a linear variation of pore-fluid pressure along the vertical direction by means of two parameters, i.e. slope and intercept of the distribution at a datum level. Constant pressure is self-explanatory and it consists of a uniform pore-fluid pressure over a certain zone of the model. The interpolated grid, which was used extensively in this thesis, involves the definition of the coordinates of grid nodes and the assignment of a fluid pressure value to each grid node. The spatial distribution of pore fluid pressure between grid nodes is then calculated using a bilinear interpolation algorithm. For the final regime, the pore fluid pressure within a zone affected by an aquiclude is zero and this condition is used to prevent the code checking for continuity requirements of pore fluid pressure. LS checks that effective stresses are continuous in the model and, consequently, if total stresses are continuous also pore fluid pressures must be continuous. Discontinuities of pore fluid pressure across an interface are treated by adding artificial internal forces (or total stresses) in order to re-establish the continuity of effective stresses but this in general leads to unexpected results. The aquiclude can be used to prevent LimitState:GEO from generating these artificial internal forces and to admit discontinuities in pore-fluid pressure. This can be applied for instance to the modelling of a retaining wall which separates zones of soils at different pore fluid pressure values.

For the interpolated grid option of defining a regime of pore fluid pressure (as used in this thesis), an interpolated grid is made of a number of grid nodes regularly spaced along the

horizontal and the vertical directions. An interpolated grid is defined in LS by the following quantities: the spatial coordinates of the origin of the grid x_0 and y_0, the spacing of the grid points in the x-direction, dx, and in the y-direction, dy, the number of division of the grid in the x-direction, n_x, and in the y-direction, n_y, and a matrix of pore fluid pressure values associated to each grid node. The interpolated grid can be defined directly in the program or an external file containing the relevant parameters can be imported. A bilinear interpolation is operated in order to calculate the pore fluid pressure at intermediate positions between grid points. Considering four grid points (x_1,y_1), (x_1,y_2), (x_2,y_1) and (x_2,y_2) (see Figure 4.7), the pore fluid pressure in a generic position (x,y) internal to these four grid points, $p_f(x,y)$, is calculated. A linear interpolation is firstly operated in the x-direction:

$$p_f(x,y_1) = \frac{x_2-x}{x_2-x_1}p_f(x_1,y_1) + \frac{x-x_1}{x_2-x_1}p_f(x_2,y_1) \tag{4.98a}$$

$$p_f(x,y_2) = \frac{x_2-x}{x_2-x_1}p_f(x_1,y_2) + \frac{x-x_1}{x_2-x_1}p_f(x_2,y_2) \tag{4.98b}$$

Subsequently an interpolation is applied in the y-direction:

$$p_f(x,y) = \frac{y_2-y}{y_2-y_1}p_f(x,y_1) + \frac{y-y_1}{y_2-y_1}p_f(x,y_2) \tag{4.99}$$

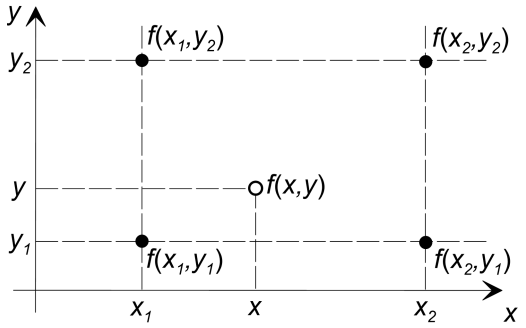

Figure 4.7: Interpolated grid

The interpolated grid was used extensively in this work because it allows the assignment of a generic spatial distribution of pore fluid pressure (or negative product of suction and degree of saturation). However, the application of a pore fluid pressure distribution with values different from zero at the soil surface produces unreliable results. In LS, the soil surface is seen as a boundary where pore-fluid pressure is equal to zero. Therefore, pore fluid pressure values different from zero at the soil surface are treated as discontinuities and external artificial total stresses are generated by the code, thereby leading to incorrect results. In the commercial version of LimitState:GEO, this problem can be avoided with two strategies. The first strategy consists of the application of surface loads equal and opposite to the stresses which the code is expected to generate artificially [223]. For instance if a pore fluid pressure value of -10 kPa is applied at the boundary, a surface load of -10 kPa must be applied at the same boundary, where the negative sign stands for tension and thus a load directed towards the exterior of the model. This strategy can be complicated to apply if pore fluid pressure

varies significantly along a surface boundary. This would imply the discretization of the boundary into a number of different boundaries, with a different load applied to each of them depending on the average value of pore fluid pressure within that section of boundary. A second strategy consists of the creation of a very thin layer of fictitious material on top of the surface boundary and in the application of the aquiclude to this layer. In this way, no artificial forces are generated at the external boundaries and pore fluid pressure distributions varying at the boundaries can be considered. However, the creation of this artificial layer can sometimes lead to numerical difficulties in the solving algorithm. In this thesis work, a non-commercial version of LimitState:GEO was used, developed by the staff at LimitState Ltd. In this non-commercial version, the generation of the artificial external forces at the external boundaries is suppressed, i.e. pore fluid pressure values different from zero at the external boundaries are not treated as discontinuities.

4.3 Link code CB-LS

4.3.1 Motivation

Code_Bright, described in Section 4.1, is a finite element code which was used in this thesis work to perform hydraulic and coupled thermo-hydraulic simulations. In particular, as described in Chapter 8, this code was used to simulate the thermo-hydraulic response of slopes when subjected to realistic atmospheric conditions. The stability of these slopes, highly dependent on the attained values of suction and degree of saturation, could be potentially assessed in Code_Bright performing coupled thermo-hydro-mechanical analyses. However, modelling the failure of slopes using finite element analyses is relatively complex and computationally demanding [222]. On the other hand, limit analysis represents a strong and reliable tool in the assessment of the stability of slopes. Potential failure mechanisms and corresponding factors of safety can be easily identified and the computational effort is often relatively small. However, realistic critical hydraulic conditions (i.e. distributions of suction and degree of saturation) need to be used in limit analysis codes such as LimitState:GEO in order to asses the stability of slopes when subjected to realistic weather conditions. Therefore, in this work, a code called "CB-LS" was written with the purpose of linking finite element thermo-hydraulic analyses including soil-atmosphere interaction performed with Code_Bright and limit analyses for slope stability performed with LimitState:GEO.

The following procedure was adopted in this work. Finite element thermo-hydraulic analyses of slopes, including soil-atmosphere interaction, were firstly performed with Code_Bright. Various critical hydraulic conditions at various specific time steps (e.g. after a heavy rainfall event) were considered. At these time steps, spatial distributions of suction (calculated as $p_g - p_l$) and degree of saturation were exported to external files (extension .txt). These files were then read by the link code CB-LS which generated a corresponding interpolated grid of the quantity $-s \cdot S_l$ and exported the information of this grid to an external file (extension .csv). This file containing the information for the interpolated grid was finally imported to

LimitState:GEO, to be used as the "pore fluid pressure" in that code, in order to perform limit analyses for the assessment of the stability of unsaturated slopes.

The finite element mesh in CB and the interpolated grid in LimitState:GEO cannot be treated in the same way (see Figure 4.8). In CB, values of pore-liquid pressure p_l and pore-gas pressure p_g are nodal quantities and values of degree of saturation S_l are elemental quantities. In LS, the values of $-s \cdot S_l$ are only assigned to the grid nodes. Moreover, the finite element mesh can have irregular shapes, elements aligned along different directions, gradients in the mesh spacing etc. The interpolated grid must be made of regular quadrilaterals, aligned along the x- and y-directions and with regular spacing along x and y. Therefore, an algorithm was implemented in the CB-LS code with the purpose of assigning values of $-s \cdot S_l$ to the LS grid nodes by interpolating or extrapolating the values of suction and degree of saturation in the CB finite element mesh.

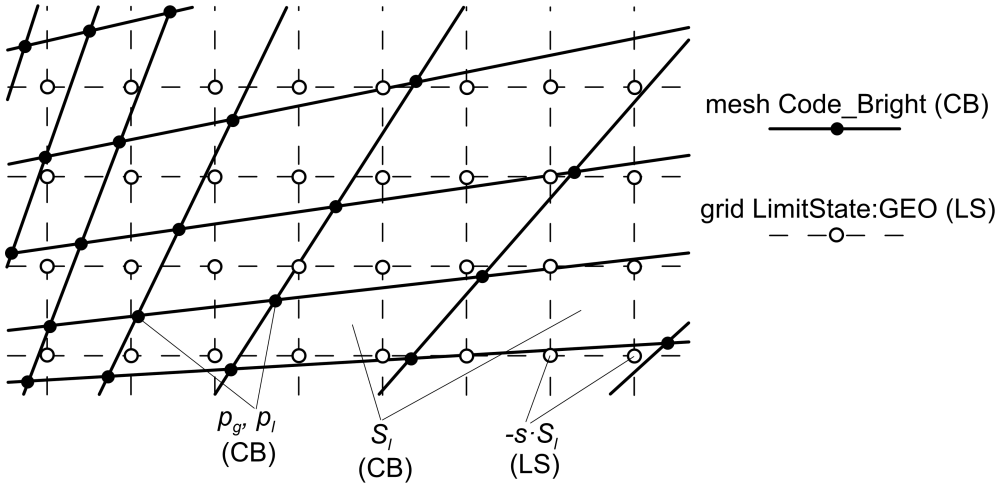

Figure 4.8: Code_Bright finite element mesh and LimitState:GEO interpolated grid

4.3.2 Development of the code

This section describes the structure and the functioning of the CB-LS code and gives instruction on how to use it.

The CB-LS code was written in Matlab. The structure of the code is made of eight different parts which are presented below. For the sake of clarity, the terms nodes and elements will refer to the CB finite element mesh whereas the terms grid and grid points will refer to the LS interpolated grid for pore fluid pressure (or $-s \cdot S_l$).

1) Definition of the input data

Input data for the CB-LS code are initially read. External input data files and the CB-LS code should be all located in the same folder. Input data are: some Code_Bright files with related information, uniform and constant value of the pore-gas pressure p_g adopted in the FE analyses in CB, coordinates of the boundaries of the finite element model, parameters defining the grid in LimitState:GEO and names of input and output files.

Five Code_Bright files are read by the CB-LS code. One is called "root.dat" and contains the name of the Code_Bright model created by the user. Two of them are input files for CB called "root_gen.dat" and "root_gri.dat", where "root" stands for the name of the CB model assigned by the user. These two files are used to read information about the finite element model such as number of nodes, number of elements, nodes belonging to each element and element types (triangular or quadrilateral). The other two files include output information about nodal pore-liquid pressure values (post_file_n) and elemental degree of saturation values (post_file_e) respectively and they need to be generated manually by the user. The following procedure can be used for the generation of post_file_n:

- Open finite element model with GiD > go to the post-process mode > click on "Window" > click on "View results" > select an appropriate time step in the window "Step:" > select "Contour Fill" in the window "View:" > select "Liquid Pressure" > click "Apply" > close the window "View Results & Deformation" > click on the command "List Entities" > choose Nodes > select all the nodes in the mesh > click "Esc" > in the window "List Entities" which has just appeared, click "List" > click "View text" > a window like that shown in Figure 4.9a appears, select all the content of the window (Ctrl+A) > copy the content (Ctrl+C) > open a new text file (e.g. with Notepad) > paste the previous content (Ctrl+V) > save the file.

The following procedure can be used for the generation of post_file_e:

- Open finite element model with GiD > go to the post-process mode > click on "Window" > click on "View results" > select an appropriate time step in the window "Step:" > select "Contour Fill" in the window "View:" > select "Liq Sat Deg" > click "Apply" > close the window "View Results & Deformation" > click on the command "List Entities" > choose Elements > select all the elements in the mesh > click "Esc" > in the window "List Entities" which has just appeared, click "List" > click "View text" > a window like that shown in Figure 4.9b appears, select all the content of the window (Ctrl+A) > copy the content (Ctrl+C) > open a new text file (e.g. with Notepad) > paste the previous content (Ctrl+V) > save the file.

In spite of their description, these two procedures for the generation of the files post_file_n and post_file_e are simple and quick to apply.

The files post_file_n and post_file_e are made of repetitive blocks of data, one for each node or element. In Figure 4.9a, the repetitive block of post_file_n is made of 17 lines whereas, in Figure 4.9b, the repetitive block of post_file_e is made of 22 lines. These two numbers must be specified as input data in the CB-LS code because they are used to read the files post_file_n and post_file_e.

The position of the boundaries of the finite element model are specified by means of the coordinates of the corner points of the geometrical model (see Figure 4.10). In other words, the boundaries are the segments connecting these corner points. These corner points must be defined in a consecutive order, either clockwise or counter clockwise. Figure 4.10 shows an example of the model of a slope where the corner points are ordered consecutively clockwise.

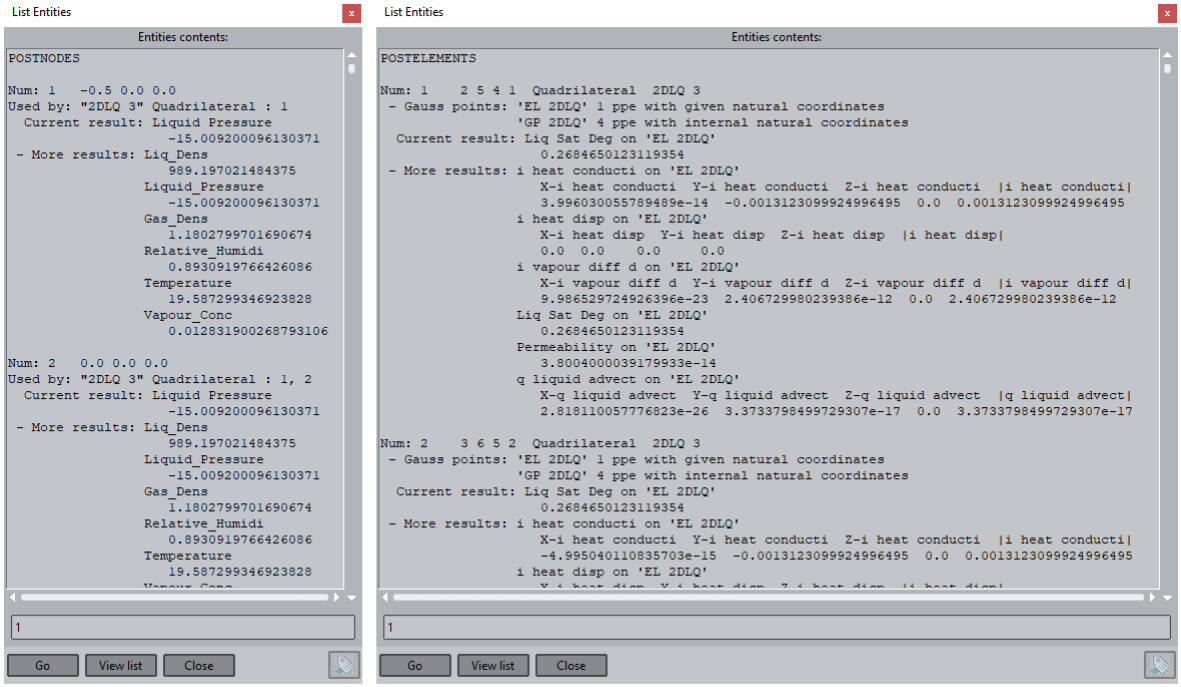

Figure 4.9: Nodal output for post_file_n and elemental output for post_file_e

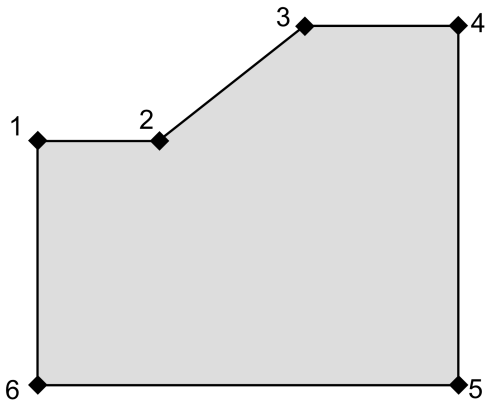

Figure 4.10: Corner points of the FE model of a slope

Parameters for the generation of the LS grid must be defined: the spatial coordinates of the origin of the grid x_0 and y_0, the spacing of the grid points in the x-direction, dx, and in the y-direction, dy, and the number of divisions of the grid in the x-direction, n_x, and in the y-direction, n_y.

Finally, the names of the input files to be read and of the output file to be written are specified.

2) Importation of the finite element mesh data

The link code CB-LS initially reads the file root_gen.dat to identify the number of nodes and elements of the FE mesh. Subsequently, it reads the file post_file_n to obtain the coordinates of each node and the associated pore-liquid pressure values. The file root_gri.dat is then read to identify the type of each element (triangular or quadrilateral) and the mesh nodes

belonging to each element. Finally, the file post_file_e is read to associate the values of degree of saturation to each element.

3) Identification of the boundaries

In this part of the code, the mesh nodes at the boundaries are firstly identified. Subsequently, for each boundary node, the two adjacent boundary nodes are identified (see Figure 4.11). Information about the boundary nodes will be used in the extrapolation of s and S_l for grid points lying outside the finite element mesh.

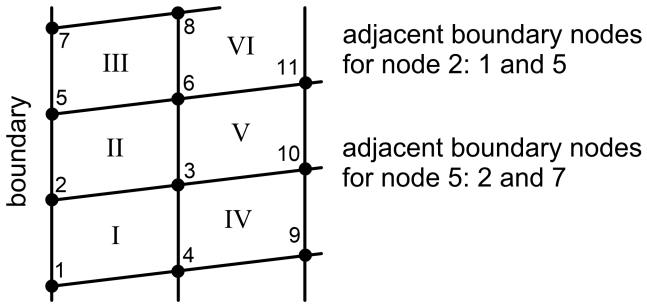

Figure 4.11: Boundary nodes

Given two consecutive boundary corner points A and B, defined as input data, with coordinates (x_A, y_A) and (x_B, y_B) respectively, the boundary line connecting the two points is defined by the following equation:

$$y = y_A + \frac{y_B - y_A}{x_B - x_A}(x - x_A) \tag{4.100}$$

which is valid for $\min(x_A, x_B) < x < \max(x_A, x_B)$. A generic mesh node with coordinates (x, y) belongs to this boundary if it satisfies Equation 4.100 in the range $\min(x_A, x_B) < x < \max(x_A, x_B)$. In the code CB-LS, the boundary nodes of the finite element mesh are identified by comparing the coordinates of every mesh node to each boundary according to the procedure just described.

For each boundary node, the two adjacent boundary nodes are then identified and saved. To do this, each element (e.g. I and II in Figure 4.11) which contains a given boundary node (e.g. 2 in Figure 4.11) is scanned. For each of these elements (e.g. I), the two nodes (e.g. 1 and 3) adjacent to the reference node (e.g. 2) are checked: if one of these nodes is also a boundary node (e.g. 1), this node is associated to the reference boundary node as an adjacent boundary node.

4) Conversion of elemental degrees of saturation into nodal degrees of saturation

Values of degree of saturation are associated to the mesh nodes using the elemental values. The nodal degree of saturation $S_{l,ni}$ of a generic node i is calculated as the average of the

degree of saturation values of the elements including node i:

$$S_{l,ni} = \frac{\sum_{j=1}^{n_{ei}} S_{l,e\,ji}}{n_{ei}} \tag{4.101}$$

where $S_{l,e\,ji}$ is the value of the degree of saturation of the generic element j which includes node i and n_{ei} is the number of elements which include node i. This operation is applied to all the mesh nodes.

5) Creation of the interpolated grid for LimitState:GEO and correlation with the finite element mesh of Code_Bright

The interpolated grid to be used in LimitState:GEO is firstly created: spatial coordinates are assigned to all the grid points according to the parameters defining the grid (i.e. x_0, y_0, dx, dy, n_x and n_y).

Subsequently, each grid point is associated to a FE mesh element. An individual grid point is associated to a specific mesh element if it is included in the same mesh element. The inclusion of a grid node in a given element is verified according to the following procedure (see Figure 4.12). The coordinates of the points at the intersections between the segments connecting the mesh nodes of an element and the horizontal line (i.e. parallel to x-axis) passing through the grid point G are calculated (I_1 and I_2 in Figure 4.12, but also two further points I_3 and I_4 not shown in Figure 4.12). The segments connecting the mesh nodes of an element are represented by an equation of the same form as Equation 4.100. If all the intersection points lie outside the segments (see Figure 4.12a), the grid point G is not associated to the given element because it is located outside the element. If two intersection points I_1 and I_2 lie within the segments but both are on the same side of point G (see Figure 4.12b) (i.e. if $(x_{I_1} - x_G) \cdot (x_{I_2} - x_G) > 0$), the grid point G is not associated to the given element because it is located outside the element. If two intersection points I_1 and I_2 lie within the segments and are on opposite sides of point G (see Figure 4.12c) (i.e. if $(x_{I_1} - x_G) \cdot (x_{I_2} - x_G) \leq 0$), the grid point G is associated to the given element because it is located within the element.

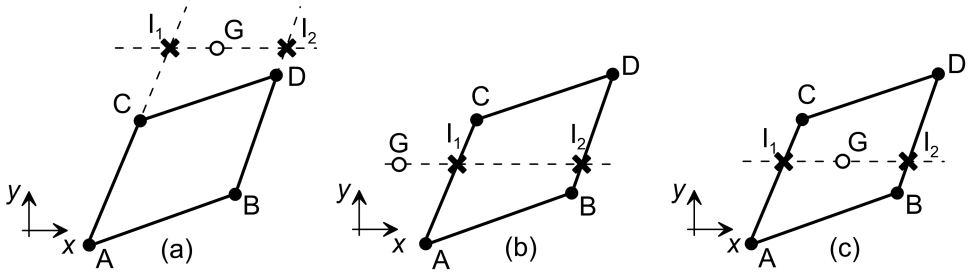

Figure 4.12: Association between grid points and mesh elements

This procedure is applied to all grid points. If a grid point cannot be associated to any mesh element it is treated as a grid point external to the finite element mesh. The distinction between internal grid points and external grid points is important: an interpolation procedure

is applied for the calculation of the values of p_l and S_l for the internal grid points whereas an extrapolation procedure is applied for the external grid points.

6) Interpolation for internal grid points

The values of p_l and S_l for an individual internal grid point are calculated by spatially interpolating the values at the nodes of the associated element. The algorithms of this interpolation are different for a triangular element and a quadrilateral element.

Within a given triangular mesh element, a certain quantity f (which represents either p_l or S_l) is assumed to vary linearly in the space according to the following equation:

$$f(x,y) = a_0 + a_1 x + a_2 y \tag{4.102}$$

where a_0, a_1 and a_2 are three coefficients. Given the coordinates of the three mesh nodes (x_1,y_1), (x_2,y_2) and (x_3,y_3) and the values of the quantity f at these three nodes, f_1, f_2 and f_3 respectively, the coefficients a_0, a_1 and a_2 can be calculated with the following system of equations:

$$\begin{pmatrix} a_0 \\ a_1 \\ a_2 \end{pmatrix} = \begin{bmatrix} 1 & x_1 & y_1 \\ 1 & x_2 & y_2 \\ 1 & x_3 & y_3 \end{bmatrix}^{-1} \cdot \begin{pmatrix} f_1 \\ f_2 \\ f_3 \end{pmatrix} \tag{4.103}$$

Once the coefficients a_0, a_1 and a_2 are calculated for each triangular element and for both p_l and S_l, Equation 4.102 is used to calculate the values of p_l and S_l at the internal grid points associated to the triangular elements.

For quadrilateral elements, a bilinear interpolation algorithm for quadrilateral elements was implemented. In spite of the terminology of bilinear interpolation, this algorithm involves in general non linear relationships. Figure 4.13a shows a generic irregular quadrilateral mesh element made of the mesh nodes P_1, P_2, P_3 and P_4. The position of a grid point G internal to the element is defined by means of the parametric coordinates t and s, which represent the percentage along the different sides to point G (see Figure 4.13a), with $0 \leq t \leq 1$ and $0 \leq s \leq 1$. With reference to Figure 4.13a, point G is identified by the intersection of the segments $\overline{AB}$ and $\overline{CD}$. Points A and B are located respectively on the segments $\overline{P_1P_3}$ and $\overline{P_2P_4}$ at distances from P_1 and P_2 which are given by the lengths of the corresponding segments multiplied by the parameter t. Similarly, points C and D are located respectively on the segments $\overline{P_1P_2}$ and $\overline{P_3P_4}$ at distances from P_1 and P_3 which are given by the lengths of the corresponding segments multiplied by the parameter s.

Given the coordinates of the nodes P_1, P_2, P_3 and P_4, i.e. (x_1,y_1), (x_2,y_2), (x_3,y_3) and (x_4,y_4), the coordinates of the points A, B, C and D, i.e. (x_A,y_A), (x_B,y_B), (x_C,y_C) and (x_D,y_D), can be expressed in a parametric form as follows:

$$x_A = x_1 + (x_3 - x_1) \cdot t \tag{4.104a}$$

$$y_A = y_1 + (y_3 - y_1) \cdot t \tag{4.104b}$$

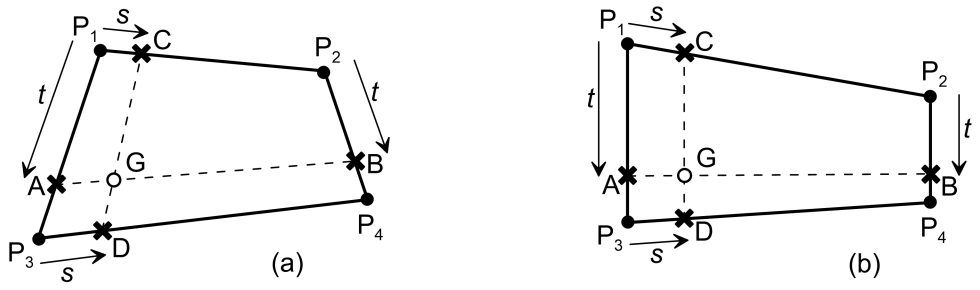

Figure 4.13: Interpolation for irregular quadrilateral elements

$$x_B = x_2 + (x_4 - x_2) \cdot t \tag{4.105a}$$

$$y_B = y_2 + (y_4 - y_2) \cdot t \tag{4.105b}$$

$$x_C = x_1 + (x_2 - x_1) \cdot s \tag{4.106a}$$

$$y_C = y_1 + (y_2 - y_1) \cdot s \tag{4.106b}$$

$$x_D = x_3 + (x_4 - x_3) \cdot s \tag{4.107a}$$

$$y_D = y_3 + (y_4 - y_3) \cdot s \tag{4.107b}$$

The coordinates of the point G, i.e. (x_G, y_G), can be thus obtained in two different ways, either with respect to points A and B and the parameter s:

$$x_G = x_A + (x_B - x_A) \cdot s \tag{4.108a}$$

$$y_G = y_A + (y_B - y_A) \cdot s \tag{4.108b}$$

or with respect to points C and D and the parameter t:

$$x_G = x_C + (x_D - x_C) \cdot t \tag{4.109a}$$

$$y_G = y_C + (y_D - y_C) \cdot t \tag{4.109b}$$

Combining Equations 4.104a,b, 4.105a,b and 4.108a,b, a quadratic equation can be obtained:

$$At^2 + bt + C = 0 \tag{4.110}$$

where the coefficients A, B and C are calculated as follows:

$$A = (x_3 - x_1)(y_4 - y_2) - (y_3 - y_1)(x_4 - x_2) \tag{4.111}$$

$$\begin{aligned} B = y_G(x_4 - x_2 - x_3 + x_1) - x_G(y_4 - y_2 - y_3 + y_1) + (x_3 - x_1)y_2 \\ -(y_3 - y_1)x_2 + x_1(y_4 - y_2) - y_1(x_4 - x_2) \end{aligned} \tag{4.112}$$

$$C = y_G(x_2 - x_1) - x_G(y_2 - y_1) + x_1 y_2 - x_2 y_1 \tag{4.113}$$

In the general case, the two solutions of Equation 4.110 are given by:

$$(t_1, t_2) = \frac{-B \pm \sqrt{B^2 - 4AC}}{2A} \tag{4.114}$$

Among the two solutions of Equation 4.114, only one is of interest for this interpolation algorithm: it must be real and $0 \leq t \leq 1$. If the vertical uprights are parallel (see Figure 4.13b), the coefficient A (see Equation 4.111) is zero, Equation 4.110 is reduced to a linear equation and t is calculated as:

$$t = -\frac{C}{B} \tag{4.115}$$

Once the parameter t is obtained, the parameter s can be calculated by inverting Equation 4.108b and replacing the terms y_A and y_B with Equations 4.104b and 4.105b, thereby obtaining:

$$s = \frac{y_G - y_1 - (y_3 - y_1)t}{y_2 + (y_4 - y_2)t - y_1 - (y_3 - y_1)t} \tag{4.116}$$

Given the values of the quantity f (which represents either p_l or S_l) at the mesh nodes P1, P2, P3 and P4, i.e. respectively f_1, f_2, f_3 and f_4, and once the parameters t and s are known, the value of the quantity f at the grid point G, i.e. f_G, is interpolated as:

$$f_G = f_1 \cdot (1-s) \cdot (1-t) + f_2 \cdot s \cdot (1-t) + f_3 \cdot (1-s) \cdot t + f_4 \cdot s \cdot t \tag{4.117}$$

After the interpolation algorithms for both triangular and quadrilateral elements are applied to calculate p_l and S_l, the quantity $-s \cdot S_l = (p_l - p_g) \cdot S_l$ is calculated at each internal grid point.

7) Extrapolation for external grid points

LimitState:GEO uses also grid points located outside the model to interpolate the pore fluid pressure (or $-s \cdot S_l$) within the model. Therefore, when LS operates a bilinear interpolation between the external grid points and the internal grid points, the values of pore fluid pressure (or $-s \cdot S_l$) assigned to the external grid points must lead to realistic distribution of pore fluid pressure (or $-s \cdot S_l$) in the areas within the model next to the boundaries. The values to be assigned to the external grid points are calculated using an extrapolation algorithm (see Figure 4.14).

Given an external grid point G close to the model boundary (see Figure 4.14) and surrounded by 8 other grid points (from A_1 to A_8), some of the segments connecting G to the surrounding grid points intersect the boundaries (e.g. $\overline{GA_1}$, $\overline{GA_2}$ and $\overline{GA_8}$ in Figure 4.14). Given a point B_i resulting from the intersection between $\overline{GA_i}$ and the boundary, with i between 1 and 8, the value of the quantity f (which represents either p_l or S_l) at the grid point G for the i-th connection, i.e. f_{Gi}, can be calculated. The quantity f_{Gi} can be obtained by extrapolation from the values of f at A_i and B_i, respectively f_{Ai} and f_{Bi}. Considering all the different connections which intersect the boundaries, the values of f at the grid point G, i.e. f_G, can be

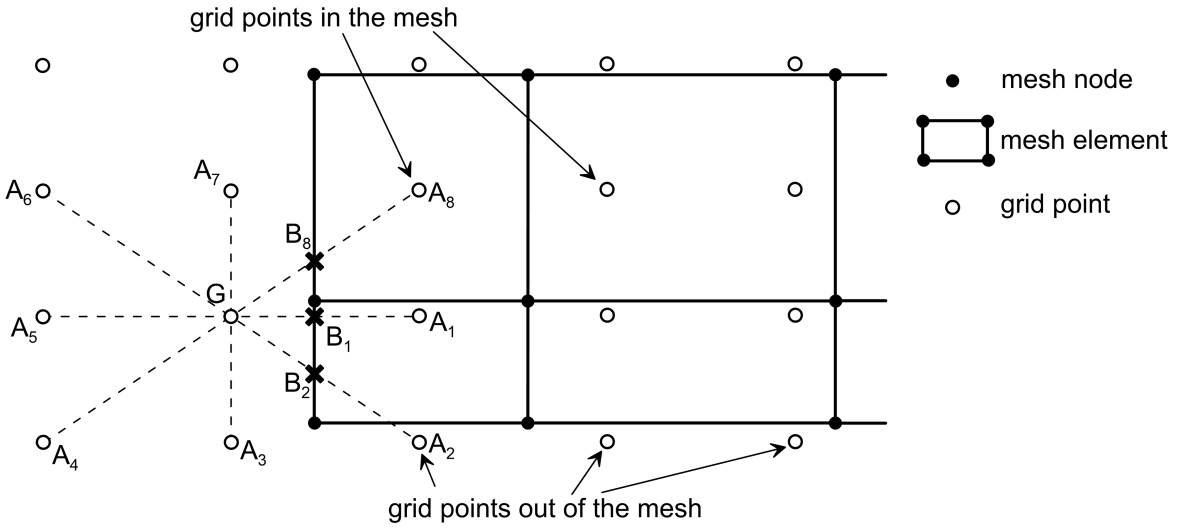

Figure 4.14: External grid points

calculated as the weighted average of the values for the different connections f_{Gi}, as follows:

$$f_G = \frac{\sum_i f_{Gi}/d_{GB_i}}{\sum_i 1/d_{GB_i}} \tag{4.118}$$

where d_{GB_i} is the distance between the grid point G and the point B_i. This weighted average takes into account the distance between G and the intersection points at the boundaries B_i, so that lower distances have higher weights in the average.

Each connection which intersects the boundaries is assessed in the link code CB-LS. Each connection is compared with each boundary segment defined by two adjacent mesh nodes. Given the connection shown in Figure 4.15a, where B_{1a} and B_{1b} are two adjacent boundary mesh nodes, the spatial coordinates of the point B_1 are firstly calculated as:

$$x_{B_1} = \frac{(x_{B_{1a}}y_{B_{1b}} - y_{B_{1a}}x_{B_{1b}})(x_{G_1} - x_{A_1}) - (x_{B_{1a}} - x_{B_{1b}})(x_{G_1}y_{A_1} - y_{G_1}x_{A_1})}{(x_{B_{1a}} - x_{B_{1b}})(y_{G_1} - y_{A_1}) - (y_{B_{1a}} - y_{B_{1b}})(x_{G_1} - x_{A_1})} \tag{4.119a}$$

$$y_{B_1} = \frac{(x_{B_{1a}}y_{B_{1b}} - y_{B_{1a}}x_{B_{1b}})(y_{G_1} - y_{A_1}) - (y_{B_{1a}} - y_{B_{1b}})(x_{G_1}y_{A_1} - y_{G_1}x_{A_1})}{(x_{B_{1a}} - x_{B_{1b}})(y_{G_1} - y_{A_1}) - (y_{B_{1a}} - y_{B_{1b}})(x_{G_1} - x_{A_1})} \tag{4.119b}$$

The quantity f is then calculated at the point B_1, i.e. f_{B_1}, by interpolating the corresponding quantities at the points B_{1a} and B_{1b}, i.e. $f_{B_{1a}}$ and $f_{B_{1b}}$, as follows:

$$f_{B_1} = f_{B_1a} + \frac{\sqrt{(x_{B_1} - x_{B_{1a}})^2 + (y_{B_1} - y_{B_{1a}})^2}}{\sqrt{(x_{B_{1b}} - x_{B_{1a}})^2 + (y_{B_{1b}} - y_{B_{1a}})^2}} \cdot (f_{B_{1b}} - f_{B_{1a}}) \tag{4.120}$$

Finally, the value of f_{G_1} is calculated by extrapolation from the values of f at the points B_1 and A_1, i.e. f_{B_1} and f_{A_1}, as follows:

$$f_{G_1} = f_{A_1} + \frac{\sqrt{(x_{G_1} - x_{A_1})^2 + (y_{G_1} - y_{A_1})^2}}{\sqrt{(x_{B_1} - x_{A_1})^2 + (y_{B_1} - y_{A_1})^2}} \cdot (f_{B_1} - f_{A_1}) \tag{4.121}$$

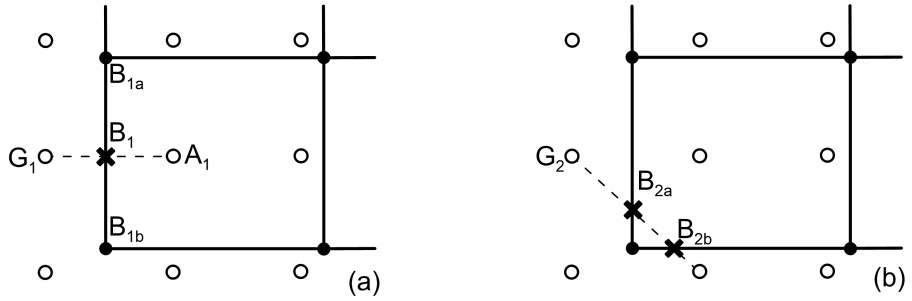

Figure 4.15: Extrapolation for connections intersecting the boundaries (a) in one point or (b) in two points

In case a connection intersects two boundaries (see Figure 4.15b), f_{G_2} is calculated by extrapolation from the values at the two intersection points B_{2a} and B_{2b} on the boundaries, i.e. $f_{B_{2a}}$ and $f_{B_{2b}}$, as follows:

$$f_{G_2} = f_{B_{2b}} + \frac{\sqrt{(x_{G_2} - x_{B_{2b}})^2 + (y_{G_2} - y_{B_{2b}})^2}}{\sqrt{(x_{B_{2a}} - x_{B_{2b}})^2 + (y_{B_{2a}} - y_{B_{2b}})^2}} \cdot (f_{B_{2a}} - f_{B_{2b}}) \tag{4.122}$$

After the extrapolation algorithm is applied to calculate p_l and S_l, the quantity $-s \cdot S_l = (p_l - p_g) \cdot S_l$ is calculated at each external grid point.

8) Creation of the output file to be imported by LimitState:GEO

At the end, the link code CB-LS generates a file (extension .csv) according to the format required by LimitState:GEO for the definition of interpolated grids, including the values of $-s \cdot S_l$ at all grid points. This file can thus be imported into LS for limit analysis of problems involving unsaturated conditions.

4.3.3 Validation

The validity of the implementation of the new CB-LS code was verified with various tests. In this section a simple validation test is described.

A finite element mesh was initially created with Code_Bright (CB). The finite element model, shown in Figure 4.16, consisted of a square with sides of unit length, which was discretized with a mesh of 30x30 elements. Units are not shown because they were not relevant for this test. Uniform distributions of degree of saturation and pore-gas pressure were assigned to the elements, with $S_l = 1$ and $p_g = 0$. Values of p_l were assigned to each mesh node according to the following distribution:

$$p_l(x,y) = \sin(2\pi x + \pi/2) \cdot \sin(2\pi y + \pi/2) \tag{4.123}$$

where x and y are the generic spatial coordinates of the mesh nodes. Equation 4.123 represents the product of two sinusoidal distributions, along x and y respectively. The relevant output files to be read by the link code CB-LS were then generated.

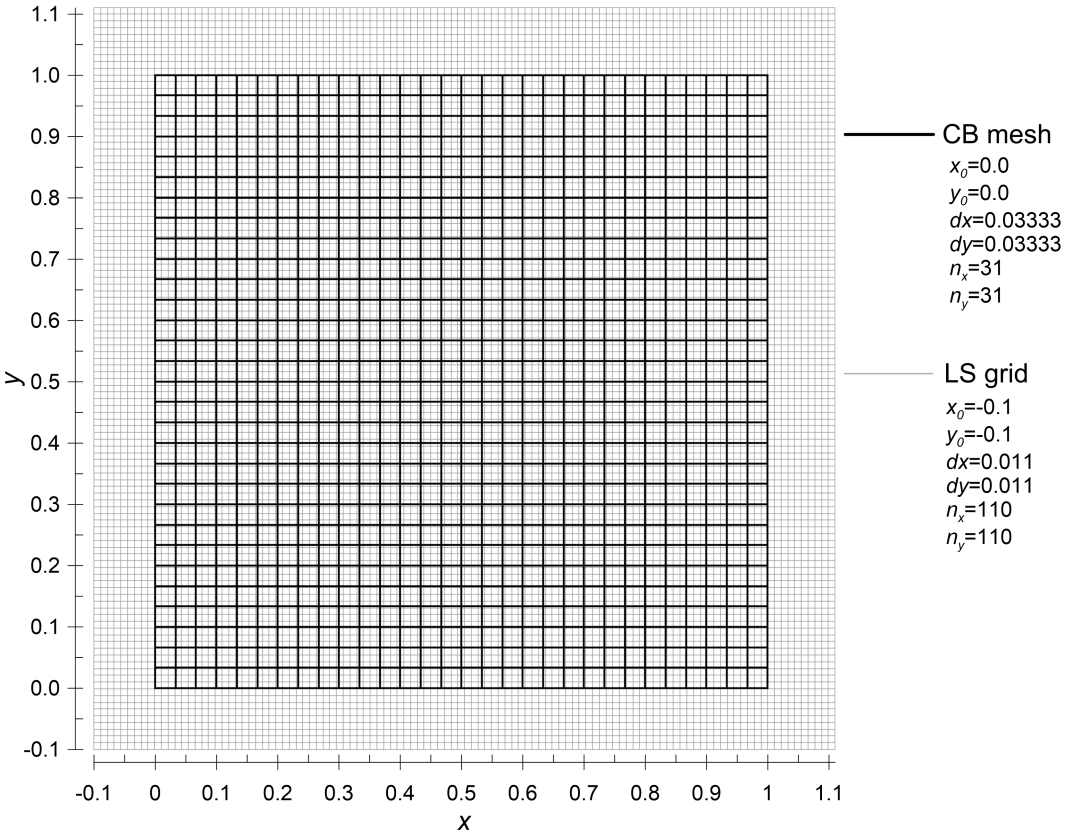

Figure 4.16: Code_Bright (CB) mesh and LimitState:GEO (LS) grid used for the numerical validation test

An interpolated grid to be imported in LimitState:GEO (LS), shown in Figure 4.16, was subsequently created according to the parameters x_0, y_0, dx, dy, n_x and n_y shown in Figure 4.16. It should be noted that the corresponding parameters specified for the CB mesh are only indicative of the position of the mesh nodes since they are not used for the mesh generation. The positions of the points of the LS grid, which was intentionally bigger than the finite element mesh, were not coincident with the position of the finite element nodes so that the values of the quantity $-s \cdot S_l$ were calculated by interpolation and extrapolation.

The code was finally run and the distribution of the quantity $-s \cdot S_l$ obtained for the LS grid by means of interpolation and extrapolation processes was compared with the corresponding distribution assigned to the finite element mesh. The unit of $-s \cdot S_l$ is not shown because it was not relevant in this test.

Figure 4.17 shows the comparison between the distribution of the quantity $-s \cdot S_l$ assigned to the CB finite element mesh (Figure 4.17a) and the distribution of the quantity $-s \cdot S_l$ calculated for the LS grid (Figure 4.17b). In Figure 4.18, these distributions are compared at different sections. These results showed a perfect coincidence between the distribution assigned to the CB mesh and the distribution calculated for the LS grid, both for the internal grid points (e.g. Figures 4.18b and 4.18e) where the interpolation procedure was applied and for the external grid points (e.g. Figures 4.18a, 4.18c, 4.18d and 4.18f) where the extrapolation procedure was applied. The results of this test confirmed the validity of the implementation of the new link code CB-LS.

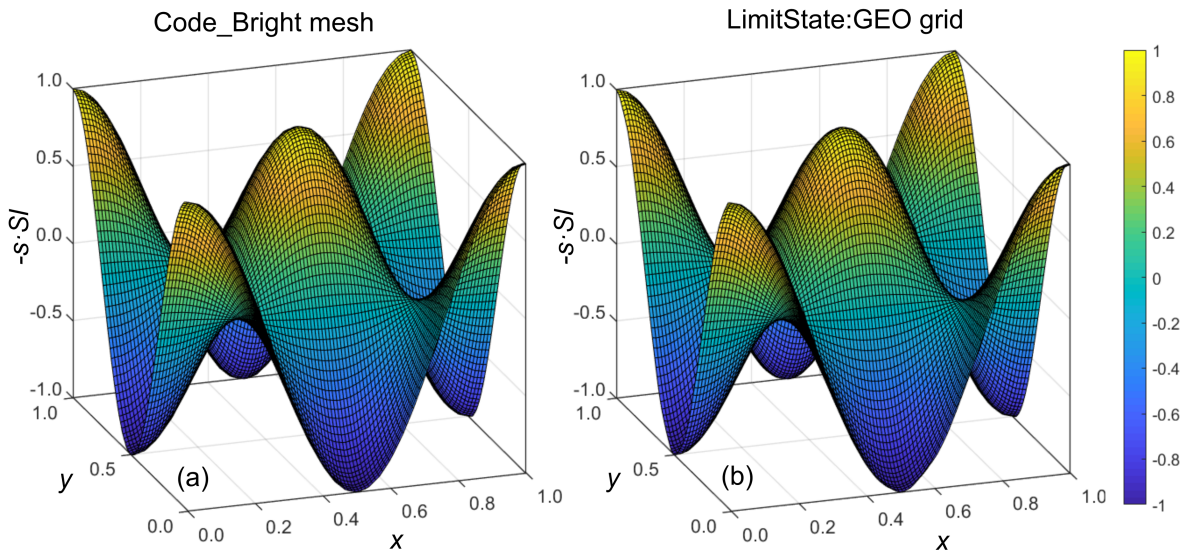

Figure 4.17: Comparison between (a) the distribution of the quantity $-s \cdot S_l$ assigned to the CB finite element mesh and (b) the corresponding distribution obtained for the LS grid

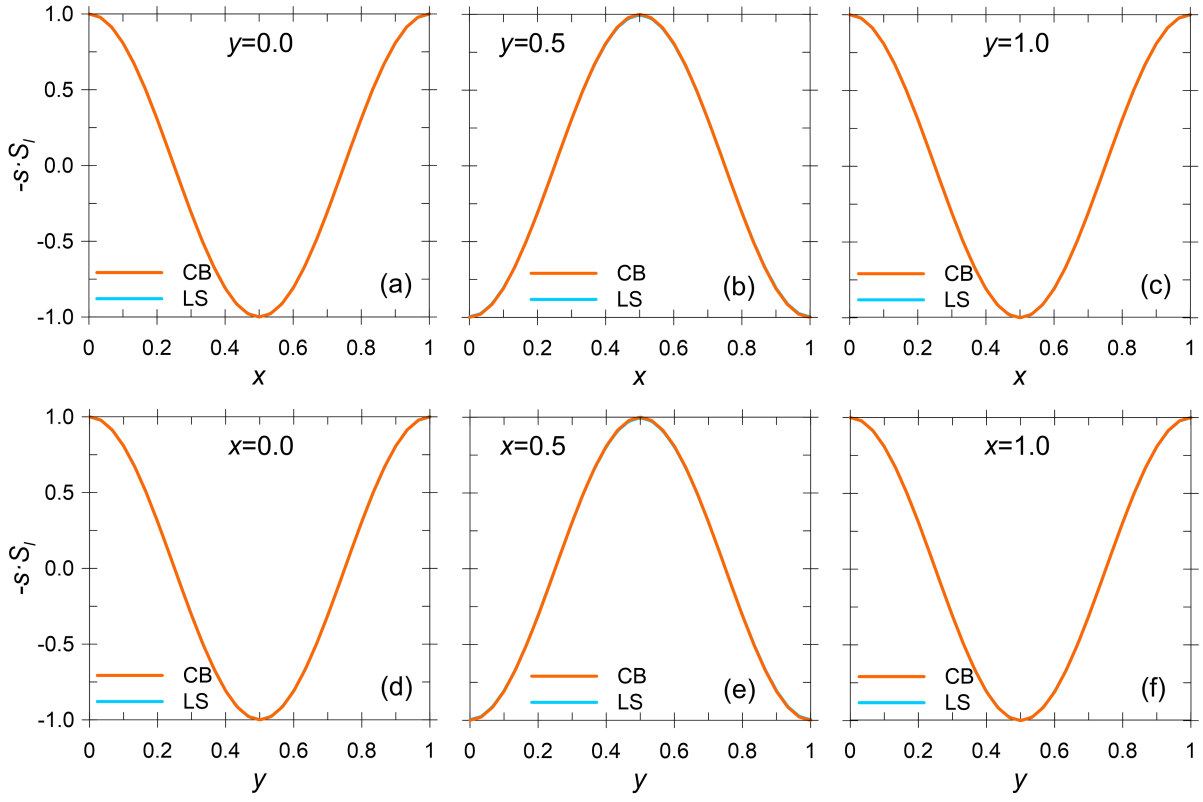

Figure 4.18: Comparison between the distribution of the quantity $-s \cdot S_l$ assigned to the CB finite element mesh and the corresponding distribution obtained for the LS grid at different sections: (a) y=0.0, (b) y=0.5, (c) y=1.0, (d) x=0.0, (e) x=0.5 and (f) x=1.0

Chapter 5

Modelling of air entrapment

Chapter 3 identified key transition points in the soil water retention curve (SWRC) and soil hydraulic conductivity curve (SHCC) and used this as the basis for the subsequent development of a new hydraulic constitutive model. The main areas of focus in developing the new hydraulic constitutive were accurate representation of the SWRC and SHCC at low values of degree of saturation (including the role of film flow in the SHCC), in combination with the influence of hysteresis in the retention behaviour. These aspects of hydraulic behaviour were considered of central importance in accurate numerical modelling of the behaviour of capillary barrier systems, which is the main focus of the second half of this thesis (Chapters 6, 7 and 8). The initial identification of key transition points in the SWRC and SHCC also led, however, to separate considerations of the hydraulic behaviour at the opposite extreme of the full range of degree of saturation, i.e. at very high values of S_l. In particular, it led to some interesting new developments in understanding and modelling of the phenomenon of air-entrapment during wetting to high values of degree of saturation, which are presented in this chapter.

This chapter presents results of analytical and numerical modelling of the phenomenon of air-trapping during wetting, which provide new insights into the differences that will occur between the true SWRC (which represents the fundamental behaviour of the soil) and the apparent SWRC measured in a wetting test performed in the laboratory (which is shown to be affected by various aspects of the test conditions). This has important implications for how to correctly perform numerical modelling of hydraulic behaviour involving wetting at high values of degree of saturation. Although this is not relevant to the numerical modelling of capillary barrier systems, presented in Chapters 6, 7 and 8, it is relevant to numerical modelling of a range of other problems in geotechnical engineering.

5.1 Introduction

Full saturation is often not achieved for an unsaturated soil subjected to wetting, because of the phenomenon of air trapping [56]. As described by Peck [54], Poulovassilis [55] and Stonestrom and Rubin [56], air trapping affects the measured soil water retention curve (SWRC). The occurrence of air trapping means that, during a wetting process, an unsaturated soil may not reach full saturation even though the applied suction becomes zero or negative.

During a wetting process, the liquid phase enters the smaller pores of the soil first and subsequently the larger pores, and the gas phase is consequently expelled. In order for the gas to flow out of the soil during wetting, the gas phase must form continuous gas flow channels. When high values of degree of saturation are attained, larger pores filled with gas may however be entirely surrounded by smaller pores filled with liquid, so that the passageways for gas flow become blocked, as shown in Figure 5.1. At this point, which corresponds to the air-discontinuity point (see Section 3.1), the gas conductivity becomes zero, because the gas phase is discontinuous [224]. From this point, further decreases in the suction applied to the boundary of a soil sample result in an increase in the gas pressure in the trapped bulbs of air. In this situation, the only way for gas to continue to be expelled is through the very slow processes of dissolution of air within the liquid phase and then diffusion of dissolved air within the liquid phase [57]. Diffusion of the dissolved air is driven by a gradient in the dissolved air concentration between the liquid phase around the trapped air bulbs (higher concentration) and the liquid phase adjacent to continuous air voids or adjacent to an external atmospheric boundary (lower concentration).

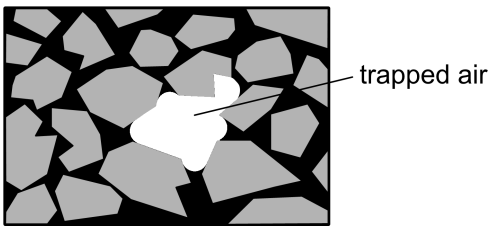

Figure 5.1: Formation of trapped air

Several SWRC models that attempt to include the effects of air trapping have been proposed [121, 133, 134]. All of them involve wetting curves which do not reach full saturation even when suction is reduced to zero. Although this seems a sensible and pragmatic approach, these wetting SWRCs are not a fundamental representation of the soil behaviour, because they are based on use of an apparent suction s_{ext}, which is the suction imposed or monitored at the external boundary of a soil sample. However, once the air becomes trapped, the pore gas pressure p_g in the trapped air bulbs is and remains greater than the gas pressure $p_{g,ext}$ imposed at the boundary of the sample (unless the very slow process of diffusion of dissolved air has finished) and the true suction s internally within the soil is therefore higher than s_{ext}.

The apparent SWRC, of S_l plotted against s_{ext}, is not a property of the material, because it is also affected by various aspects of the wetting test conditions, such as the degree of saturation at the start of wetting [135], the size of the soil sample and the precise time-history of the variation of s_{ext} applied to the sample boundary. In contrast, physical arguments suggest that, for a main wetting curve, the true SWRC, of S_l plotted against the true suction s internally within the soil (based on the gas pressure within the trapped air bulbs), is a fundamental property of the soil (at least for a non-deformable soil). For high values of degree of saturation, above the air-discontinuity point, the apparent SWRC measured in a laboratory test will only coincide with the true SWRC if the test is performed extremely slowly, so that

at each measurement point sufficient time is allowed for the very slow process of diffusion of dissolved air to have finished, so that the value of gas pressure within any trapped air bulbs p_g has equalized with the externally applied gas pressure $p_{g,ext}$.

Physical arguments also suggest that the true SWRC will reach full saturation at a positive value of s. The arguments run as follows. Firstly, if, when the externally applied suction is zero ($s_{ext} = 0$ and hence $p_{g,ext} = p_l$), trapped air temporarily exists within a soil sample, then the curvature of the gas-liquid interfaces (and the constraints imposed by satisfying the contact angle condition if an interface comes into contact with a soil particle) would mean that the gas pressure p_g within trapped air bulbs would be higher than the pore liquid pressure p_l, irrespective of whether a trapped air bulb entirely filled a soil void (so that gas-liquid interfaces come into contact with surrounding soil particles) or was sufficiently small to form an occluded bubble entirely surrounded by water, as also discussed in Section 2.1.1. This means that p_g would be greater than $p_{g,ext}$ and this pressure difference would drive dissolution of air from the trapped air bulb and subsequent diffusion of dissolved air to the external boundary. This diffusion of dissolved air would only cease once the trapped air had completely disappeared. Hence, with an externally applied suction of zero, the only possible final state after diffusion of dissolved air has finished (representing the true SWRC) is a fully saturated condition. In fact, further consideration of this logic suggests that the true SWRC should reach full saturation at a positive value of suction corresponding to the pressure difference across a spherical gas-liquid interface corresponding to the largest sphere that could fit within the largest voids of the soil.

The first aim of the study of air-trapping described in this chapter was to demonstrate the significance of air-trapping through an analytical model representing wetting of an infinitesimally small soil element (with no diffusion of dissolved air) and to show the corresponding differences between the apparent SWRC and the true SWRC for this idealized situation. The second aim was to show, through numerical modelling of realistic wetting tests on soil samples of finite size, that the apparent SWRC, of S_l plotted against s_{ext}, is not a fundamental property of the soil and to demonstrate how various aspects of the wetting test conditions will influence this apparent SWRC. The third and final aim was to show that correct representation of the influence of air trapping during wetting within numerical modelling of boundary value problems can only be achieved by using the true SWRC in combination with an unsaturated gas conductivity expression that goes to zero at the air-discontinuity point.

5.2 Analytical model of wetting of an infinitesimal element

5.2.1 Analytical model

An analytical model for the wetting of an infinitesimally small element of soil (without diffusion of dissolved air) is considered first, to demonstrate the potential impact of air trapping on the apparent SWRC. The approach taken is to assume that the true SWRC, of S_l plotted against the true internal suction s within the soil, is defined and to then calculate

the apparent SWRC, of S_l plotted against s_{ext}, to demonstrate how this differs from the true SWRC. In the interests of simplicity, the soil element is assumed to be incompressible, to avoid any complications caused by changes of element volume induced by changes of suction.

For an infinitesimally small element, liquid flows from the boundary of the element to the interior of the element occur instantaneously, which means that the pore liquid pressure within the interior of the element p_l is always identical to the liquid pressure applied at the boundary. If the degree of saturation S_l of the element is less than the degree of saturation at the air-discontinuity point $S_{l,AD}$, the gas phase is continuous within the element, meaning that gas flows from the interior of the element to the boundary also occur instantaneously, and hence the pore gas pressure within the interior of the element p_g is identical to the gas pressure imposed at the boundary $p_{g,ext}$. However, once the degree of saturation attains or exceeds the air-discontinuity value $S_{l,AD}$, gas flow between the element interior and the boundary is no longer possible, meaning that p_g and $p_{g,ext}$ can take different values (given that diffusion of dissolved air is excluded).

For this situation, the true internal suction s and the externally applied suction s_{ext} are defined as:

$$s = p_g - p_l \tag{5.1}$$

$$s_{ext} = p_{g,ext} - p_l \tag{5.2}$$

For values of S_l below $S_{l,AD}$, p_g and $p_{g,ext}$ are identical, hence s and s_{ext} are identical and the apparent SWRC (S_l plotted against s_{ext}) is the same as the true SWRC (S_l plotted against s). However, for values of S_l above $S_{l,AD}$, p_g and $p_{g,ext}$ differ, hence s and s_{ext} are not the same and the apparent SWRC is different to the true SWRC.

In the example considered here, wetting is assumed to occur with the gas pressure imposed at the element boundary held constant at atmospheric pressure ($p_{g,ext} = p_{atm}$), with p_{atm} taken as 100 kPa, and the pore liquid pressure p_l gradually increased from a negative value relative to p_{atm}. At the air-discontinuity point ($S_l = S_{l,AD}$, $s = s_{AD}$) where air trapping commences, the value of p_g within the trapped air bulbs is equal to p_{atm}. Beyond this point, the value of p_g within the trapped air bulbs increases and it can be related to further increases of S_l by applying the ideal gas law to the fixed mass of gas within the trapped air bulbs (given that diffusion of dissolved air from the trapped air bulbs is excluded):

$$p_g = p_{atm}\frac{1 - S_{l,AD}}{1 - S_l} = p_{atm} + p_{atm}\frac{S_l - S_{l,AD}}{1 - S_l} \tag{5.3}$$

Equation 5.3 assumes no change in the total volume of soil voids within the element (i.e. the soil is assumed to be incompressible) and constant temperature. As a consequence of Equation 5.3, comparing Equations 5.1 and 5.2 gives:

$$s = s_{ext} + p_{atm}\frac{S_l - S_{l,AD}}{1 - S_l} \tag{5.4}$$

or:

$$s_{ext} = s - p_{atm}\frac{S_l - S_{l,AD}}{1 - S_l} \tag{5.5}$$

If the true SWRC is known, the procedure to determine the apparent SWRC, for values of s_{ext} below the air-discontinuity point ($s_{ext} = s = s_{AD}$, $S_l = S_{l,AD}$), where air trapping commences, is as follows:

- Consider a value of true internal suction s slightly lower than the air-discontinuity value s_{AD} and calculate the corresponding value of degree of saturation S_l from the equation of the true SWRC.
- Insert the values of s and S_l in Equation 5.5 to calculate the corresponding value of externally applied suction s_{ext}. The value of S_l and the value of s_{ext} now provide the coordinates of a point on the apparent SWRC.

Repeat the process for gradually decreasing values of s to determine the complete curve of S_l plotted against s_{ext}, defining the apparent SWRC.

5.2.2 Analytical results

Figure 5.2 shows true SWRCs (continuous lines) and apparent SWRCs (dashed lines) calculated using this procedure for two soils; one representative of a sand and one representative of a clay. In each case, the true SWRC was modelled using the van Genuchten [82] model, with the parameter values for the two soils given in Table 5.1. For both soils, the van Genuchten parameter S_{ls}, giving the maximum value of degree of saturation on the true SWRC, was selected as $S_{ls} = 1$. This means that the true SWRCs in Figure 5.2 tend to a fully saturated condition as s tends to zero. As previously noted in Section 5.1, physical arguments suggest that the true SWRC for a main wetting curve should actually reach a fully saturated condition at a positive value of suction, however use of the conventional van Genuchten expression (which mathematically leads to $S_l = 1$ only at $s = 0$ but practically leads to $S_l \approx 1$ for $s \leq s_{AE/AEX}$) is adequate to illustrate the influence of air trapping on the apparent SWRC. For both soils shown in Figure 5.2, the value of the air-discontinuity degree of saturation, where air trapping commences, was taken as $S_{l,AD} = 0.85$, which represents a typical value according to the literature [51, 99]. Hence, in both cases, the apparent SWRC diverges from the true SWRC at $S_l = 0.85$ in Figure 5.2. This occurs at $s_{AD} = 1.90\,\text{kPa}$ for the sand and $s_{AD} = 185\,\text{kPa}$ for the clay.

Table 5.1: Constitutive laws and parameters used for the materials in the analytical model (only SWRC) and in the numerical models (all parameters)

Material	Φ [-]	k [m^2]	$\overline{P_0}$ [MPa]	$\overline{\sigma_s}$ [N/m]	m [-]	S_{lr} [-]	S_{ls} [-]	A_g [-]	λ_g [-]	S_{gs} [-]	S_{gr} [-]
sand	0.40	3E-12	0.003	0	0.6	0.02	1	1	10/3	1	0.15
clay	0.38	1E-16	0.160	0	0.3	0.30	1	1	10/3	1	0.15

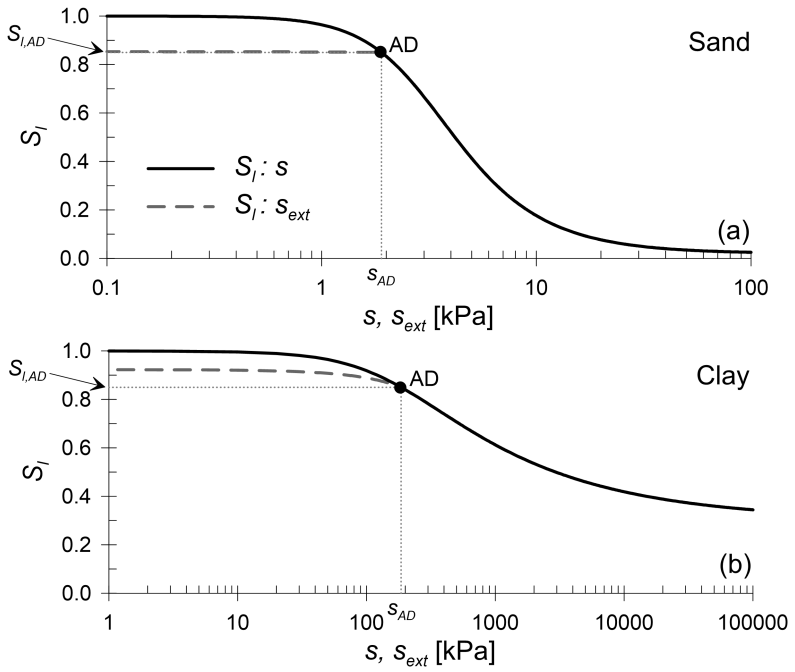

Figure 5.2: Infinitesimal element without diffusion of dissolved air: comparison of true SWRC ($S_l : s$) and apparent SWRC ($S_l : s_{ext}$), for (a) sand and (b) clay

Figure 5.2 shows that, for both soils, the apparent SWRC is significantly different to the true SWRC, with S_l reaching a maximum value significantly less than 1 as s_{ext} is reduced towards zero, demonstrating the influence of air trapping. Inspection of Figure 5.2 also shows that the effect of air trapping is noticeably different for the sand and the clay. The apparent SWRC is almost horizontal for $s_{ext} < s_{AD}$ for the sand, whereas the apparent SWRC shows a noticeable increase of S_l for $s_{ext} < s_{AD}$ for the clay. This is because the compression of the trapped air, as p_g increases above $p_{g,ext} = p_{atm}$, is very small in the case of the sand and more significant in the case of the clay. In the case of the sand, $p_g = p_{atm} = 100\,\text{kPa}$ (as an absolute pressure) at the point where air trapping commences ($s = s_{ext} = s_{AD} = 1.90\,\text{kPa}$) and $p_g = 101.88\,\text{kPa}$ ($s = 1.88\,\text{kPa}$) at the end of wetting when $s_{ext} = 0$. This increase of p_g, from 100 kPa to 101.88 kPa, causes only a very small amount of compression of the trapped air. In contrast, for the clay, p_g increases from $p_g = p_{atm} = 100\,\text{kPa}$ at the onset of air trapping (at $s = s_{ext} = s_{AD} = 185\,\text{kPa}$) to $p_g = 195\,\text{kPa}$ at the end of wetting when $s_{ext} = 0$, and this increase of p_g is sufficient to cause significant compression of the trapped air.

The apparent SWRC curves shown in Figure 5.2 assume no diffusion of dissolved air from the trapped air bulbs, in order to give a first demonstration of the effect of trapped air for an idealised situation. If dissolution of air and diffusion of the dissolved air was included in the analysis of these infinitesimally small soil elements, the apparent SWRC would always be identical to the true SWRC, because diffusion of dissolved gas from the interior of the element to the boundary of the element would occur instantaneously in an infinitesimally small element.

5.3 Numerical modelling of wetting tests on samples of finite size

5.3.1 Numerical model

Numerical modelling of wetting tests on soil samples of finite size was performed, to provide more realistic simulations of the impact of air trapping and to investigate how various aspects of wetting test conditions would influence the apparent SWRC. It must be mentioned that the numerical simulations presented in this section do not represent realistically the common experimental procedures adopted to characterise the SWRC but they may be representative of wetting processes occurring in the field.

Multi-physics numerical modelling was performed with Code_Bright. Advective liquid flow (see Equation 4.26) and gas flow (see Equation 4.27), governed by Darcy's law, were included in all analyses, whereas diffusion of dissolved air within the liquid phase (see Equation 4.34), governed by Fick's law, was included in some analyses but not in others, in order to assess its influence. Diffusion of water vapour within the gas phase was not included, because it would always be insignificant compared to liquid water flow at the high values of S_l occurring in the simulations. The concentration of dissolved air in the liquid phase was governed by Henry's law (see Equation 4.17) and the density of the gas phase was governed by the law of ideal gases. Isothermal conditions were assumed and the soil was assumed to be non-deformable. The default values were used for the phase properties parameters (see Table 4.2) and for the diffusion coefficient D_l^a (see Equation 4.35).

The numerical simulations represented one-dimensional wetting tests performed on soil samples of height 100 mm, with wetting applied from both top and bottom of the samples. The numerical model is shown in Figure 5.3. Taking advantage of symmetry, the finite element model had a height of 50 mm, with wetting applied at the top boundary and an impermeable boundary (to both liquid and gas flows) at the bottom (representing the mid-height of the soil sample). The lateral boundaries were also impermeable to both liquid and gas flows, to give a one-dimensional situation. The FE mesh was characterised by 100 quadrilateral elements in the vertical direction with a refinement mesh gradient of 0/0.05 (finer towards the upper boundary).

Simulations were performed with two different soils; one representative of a sand and the other representative of a clay. The true SWRC for each soil was represented again by the van Genuchten [82] model (see Equation 4.24) and the function for the relative liquid conductivity k_{rl} was given by the Mualem [95] model (see Equation 4.29). The relative gas conductivity k_{rg} was given by Equations 4.30 and 4.31. Constitutive parameter values used for the two soils are given in Table 5.1.

For both soils, the values of A_g in Equation 4.30 and S_{gs} in Equation 4.31 were taken as $A_g = 1$ and $S_{gs} = 1$ and the value of the exponent λ_g was taken as 10/3 [225]. Equation 4.30 used in conjunction with Equation 4.31 predicts that the gas conductivity falls to zero when the degree of gas saturation S_g decreases to a value S_{gr}. The parameter S_{gr} therefore represents

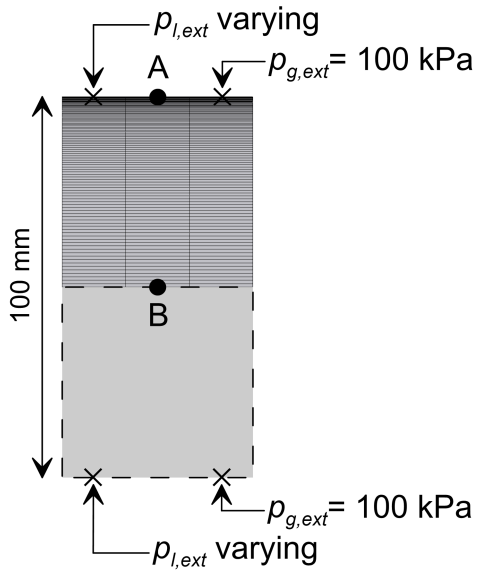

Figure 5.3: Numerical model

the degree of gas saturation at which the gas phase becomes discontinuous, which corresponds to $S_{gr} = 1 - S_{l,AD}$. $S_{gr} = 0.15$ was assumed for both soils, corresponding to $S_{l,AD} = 0.85$. Relative liquid and gas conductivity curves for the sand and the clay are shown in Figure 5.4.

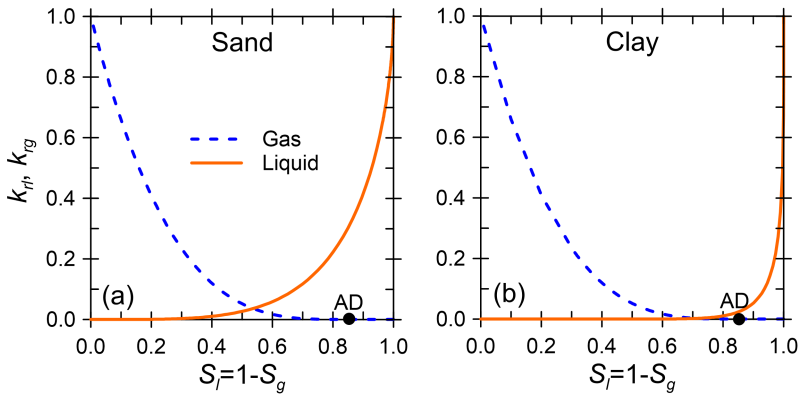

Figure 5.4: Relative liquid conductivity k_{rl} and relative gas conductivity k_{rg} plotted against degree of liquid saturation S_l, for (a) sand and (b) clay

Figure 5.5 shows the variation with time of the suction s_{ext} applied at the top boundary of the numerical model. At this top boundary, the gas pressure $p_{g,ext}$ was held constant at atmospheric pressure p_{atm}, with p_{atm} taken as 100 kPa, and the liquid pressure $p_{l,ext}$ was applied as a negative value relative to p_{atm}, with the value of $p_{l,ext}$ controlled in a stepwise fashion, so that the value of s_{ext} reduced in a series of decrements. Each value of s_{ext} was applied for a fixed interval of time. This fixed time interval for each value of externally applied suction was 6 hours for the sand (see Figure 5.5a) and 600 hours for the clay (see Figure 5.5b). These time intervals were selected as sufficient to allow complete equalization of pore liquid pressure p_l throughout the soil sample (see Section 5.3.3) and were considered representative of what might be used in practice for laboratory determination of SWRCs for samples of sands and clays respectively.

Figure 5.5 shows that, for each of the two soils, the specific values of externally applied

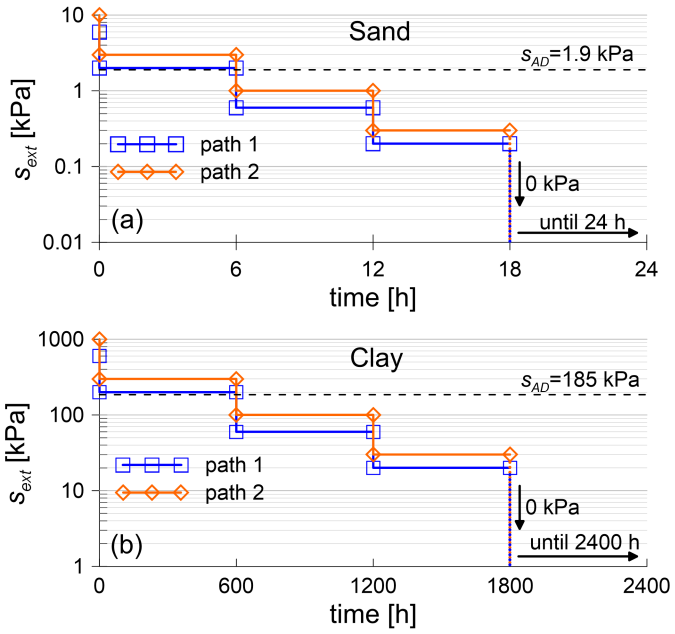

Figure 5.5: Time history of suction applied at the top boundary s_{ext} for (a) sand and (b) clay

suction s_{ext} followed two different sequences, in different simulations. For the sand, for path 1, the initial value of s_{ext} was 6 kPa and the subsequent values of s_{ext} were 2 kPa, 0.6 kPa and 0.2 kPa before a final step to $s_{ext} = 0$, whereas for path 2 the initial value of s_{ext} was 10 kPa and the subsequent values were 3 kPa, 1 kPa and 0.3 kPa, before a final step to $s_{ext} = 0$ (see Figure 5.5a). For both path 1 and path 2, after the first decrement of s_{ext} (to $s_{ext} = 2$ kPa in path 1 or to $s_{ext} = 3$ kPa in path 2) the value of s_{ext} was still above the air-discontinuity value for the sand, $s_{AD} = 1.9$ kPa (see Figure 5.5a), whereas after all subsequent decrements the value of s_{ext} was below s_{AD}. Similarly, for the clay, for path 1 the initial value of s_{ext} was 600 kPa and the subsequent values of s_{ext} were 200 kPa, 60 kPa and 20 kPa before a final step to $s_{ext} = 0$, whereas for path 2 the initial value of s_{ext} was 1000 kPa and the subsequent values were 300 kPa, 100 kPa and 30 kPa, before a final step to $s_{ext} = 0$ (see Figure 5.5b). Again, the values of s_{ext} after the first decrement ($s_{ext} = 200$ kPa in path 1 or 300 kPa in path 2) were above the air-discontinuity value for the clay ($s_{AD} = 185$ kPa), whereas all subsequent values of s_{ext} were below s_{AD}. The intention of using paths 1 and 2 was to investigate the effect of the precise sequence of values of externally applied suction s_{ext} on the apparent SWRC.

The numerical models analysed in this section differ in two respects from common procedures used in laboratory experiments to determine the SWRC: i) the dimensions of the soil sample; ii) the fact that in these numerical models pore liquid pressure and pore gas pressure are both applied at the same boundary of the soil sample (meaning that, during a wetting test, gas has to exit at the same boundary as water is entering), whereas in typical laboratory tests pore liquid pressure and pore gas pressure are applied at opposite boundaries of the soil sample. The differences in sample dimensions would not affect the qualitative nature of the results presented in this section, only the timescales, whereas the application of pore liquid pressure and pore gas pressure at the same boundary or at opposite boundaries is more fundamentally significant, and this is discussed at the end of Section 5.3.5.

5.3.2 Numerical modelling results: apparent SWRC

Figure 5.6 shows the results of the numerical simulations on the sand (Figure 5.6a) and the clay (Figure 5.6b), with the apparent SWRC that would be determined from the wetting test represented as the average degree of liquid saturation of the soil sample $\overline{S_l}$ at the end of each 6 hour (sand) or 600 hour (clay) time interval plotted against the value of externally applied suction s_{ext}. The average degree of liquid saturation of the soil sample $\overline{S_l}$ was calculated as the spatial integral of the degree of saturation over the sample divided by the area of the sample. For each soil, results from 4 different numerical simulations are presented, corresponding to path 1 and path 2, each with diffusion of dissolved air included or excluded. The insets within Figure 5.6a and Figure 5.6b show the results of the final stages of the numerical simulations with s_{ext} plotted on a linear scale, rather than the logarithmic scale of the main figure, allowing the inclusion of results for the final wetting stage to $s_{ext} = 0$. Also shown in Figure 5.6 for each soil is the true SWRC (the smooth continuous curve), which also represents the apparent SWRC for an infinitesimally small element when diffusion of dissolved gas is included (see Section 5.2.2). Finally, the apparent SWRC from the analytical model of the infinitesimally small element when diffusion of dissolved air is excluded is shown by the smooth dashed curve.

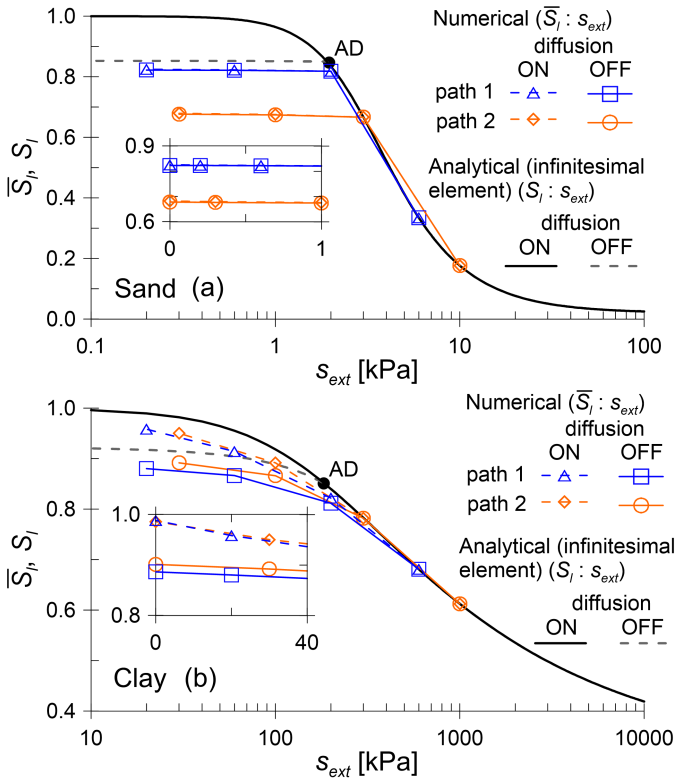

Figure 5.6: Apparent SWRCs, obtained from the numerical analyses for (a) sand and (b) clay, compared against analytical results for an infinitesimal element

Inspection of the numerical modelling results for the sand in Figure 5.6a shows very different results for path 1 and path 2, whereas inclusion or exclusion of diffusion of dissolved air made very little difference. For path 1 and path 2, the apparent SWRC of $\overline{S_l}$ plotted against s_{ext} in Figure 5.6a is almost horizontal from the value of s_{ext} applied immediately before s_{ext}

was first reduced below the air-discontinuity value of suction $s_{AD} = 1.9\,\text{kPa}$. For example, with path 2, the apparent SWRC is almost horizontal from the point $s_{ext} = 3\,\text{kPa}$, because the next decrement of s_{ext} was to $s_{ext} = 1\,\text{kPa}$, which was less than s_{AD}. Air trapping within the soil sample occurred immediately s_{ext} was reduced below s_{AD}, because a thin zone of soil with $s < s_{AD}$, and hence with discontinuous gas phase and gas conductivity of zero, formed immediately at the boundary of the soil sample, preventing any subsequent flow of gas from the remainder of the sample (even though in the majority of the sample s remained greater than s_{AD} and hence S_l remained less than $S_{l,AD}$). Once air trapping commenced in the sand sample, $\overline{S_l}$ showed very little further increase, because subsequent increases of gas pressure p_g in the trapped air were so small that they caused only very small amounts of compression of this trapped air (similar to the infinitesimally small sand sample discussed previously). The behaviour shown in Figure 5.6a means that the final average value of degree of saturation $\overline{S_l}$ in a sand sample of finite size wetted to $s_{ext} = 0$ may be substantially less than the local value of degree of saturation at which air trapping occurs at that location $S_{l,AD}$. Also, the fact that the results of the numerical simulations shown in Figure 5.6a are very different for paths 1 and 2 clearly means that, for sand samples, the apparent SWRC is highly dependent on the precise sequence of values of applied suction s_{ext}.

Figure 5.6b shows that, for the numerical simulations of the clay samples of finite size, the value of $\overline{S_l}$ increased substantially as the wetting test progressed beyond the point where air trapping commenced. In common with the infinitesimally small element of clay discussed previously, the significant increase of $\overline{S_l}$ after air trapping commenced was a consequence of compression of the trapped air, caused by substantial increase of gas pressure within the trapped air. Figure 5.6b also shows relatively similar results for path 1 and path 2 (compared to the sand samples in Figure 5.6a), whereas inclusion or exclusion of diffusion of dissolved air made more difference to the results for the clay samples than it did for the sand samples. Inspection of Figure 5.6b shows that the relatively small difference between the results for path 1 and path 2 for the clay samples is attributable to the significant increase of $\overline{S_l}$ after air trapping commences (so that it matters less where the apparent SWRC diverges from the true SWRC).

5.3.3 Numerical modelling results: gas and liquid pressures

Figure 5.7 shows the variation of pore gas pressure p_g and pore liquid pressure p_l predicted in the numerical simulations of the sand samples (Figures 5.7a and 5.7b) and the clay samples (Figures 5.7c and 5.7d), with the applied time-history of s_{ext} given by path 1 in both cases. Within Figure 5.7, values of p_g and p_l are shown for points A and B (see Figure 5.3), where the former was at the top surface of the numerical model (representing the external boundary of the soil sample, where values of $p_{g,ext}$ and $p_{l,ext}$ were applied) and the latter was at the bottom surface of the model (representing the mid-height of the soil sample). Results for point B are shown for the two different simulations, with diffusion of dissolved air either included or excluded.

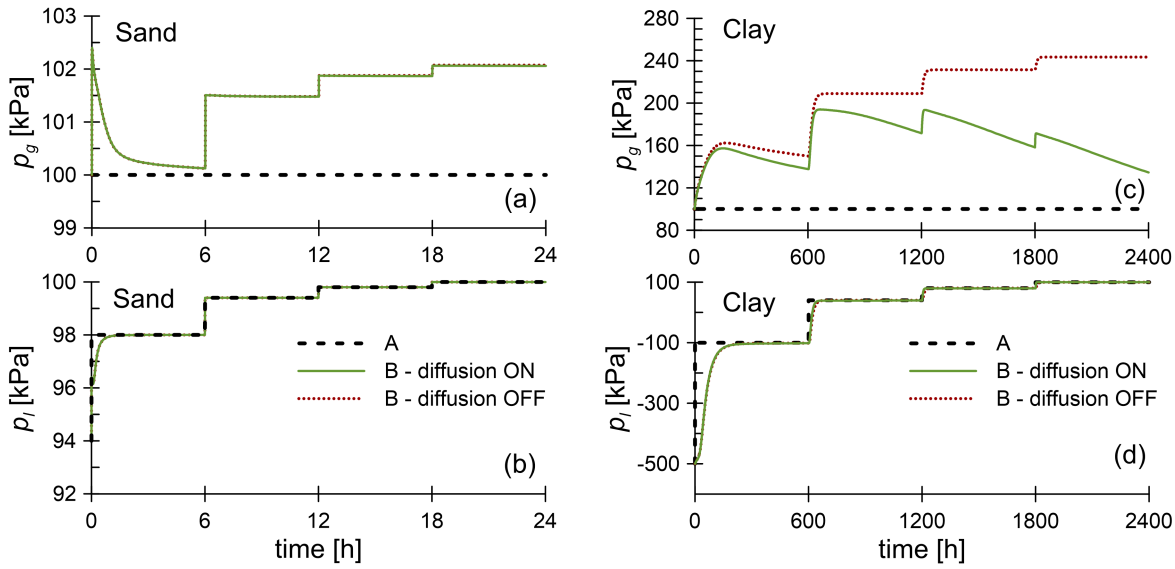

Figure 5.7: Time histories of liquid pressure p_l and gas pressure p_g at positions A and B, for path 1 applied to (a-b) sand and (c-d) clay

Comparison of the values of p_l at points B and A in the sand sample (Figure 5.7b) shows that the time interval of 6 hours used for each wetting stage was more than sufficient to ensure equalisation of pore liquid pressure p_l throughout the sand sample (particularly for the later wetting stages, when S_l was high and the value of liquid conductivity was so high that equalisation of p_l occurred within a few minutes). Similarly, Figure 5.7d shows that the time interval of 600 hours was sufficient to ensure equalisation of p_l throughout the clay sample in each wetting stage.

Inspection of Figure 5.7a shows that, for the first wetting stage, with $s_{ext} = 2\,\text{kPa}$, the time interval of 6 hours was almost sufficient to produce equalisation of pore gas pressure p_g throughout the sand sample, because the value of s_{ext} was slightly above s_{AD} and hence gas flow was possible (even if the value of gas conductivity was much lower than the value at $S_l = 0$, see Figure 5.4). The almost complete equalisation of pore gas pressure throughout the sample explains why the apparent SWRC for path 1 almost coincides with the real SWRC at $s_{ext} = 2\,\text{kPa}$ in Figure 5.6a. However, for all subsequent wetting stages, with $s_{ext} < s_{AD}$, air trapping had occurred and there was no dissipation of p_g at point B within each 6 hour time interval when diffusion of dissolved air was excluded and negligible dissipation of p_g even when diffusion of dissolved air was included (see Figure 5.7a). The excess values of p_g within the soil sample explain why the apparent SWRC diverged from the real SWRC in Figure 5.6a for these lower values of s_{ext}.

Inspection of Figure 5.7c shows that, for the clay samples, even during the first wetting stage, with $s_{ext} = 200\,\text{kPa}$, so that s_{ext} was slightly above s_{AD} and air trapping had not formally commenced, dissipation of the pore gas pressure at point B had only partially occurred within the time interval of 600 hours, because the gas conductivity was so low. Hence, the apparent SWRC does not coincide exactly with the real SWRC at $s_{ext} = 200\,\text{kPa}$ in Figure 5.6b, even though air trapping has not formally commenced. For all subsequent wetting stages, with

$s_{ext} < s_{AD}$, air trapping had occurred and there was no dissipation of p_g at point B within each 600 hour time interval when diffusion of dissolved air was excluded (see Figure 5.7c). For the clay samples, inclusion of diffusion of dissolved air did make a noticeable difference to the dissipation of p_g at point B (see Figure 5.7c), but the diffusion was insufficient to achieve complete equalisation of pore gas pressure within each 600 hour time interval.

5.3.4 Numerical modelling results: factors influencing diffusion and dissolved air

Diffusion of dissolved air had greater influence on the wetting tests on clay shown in Figure 5.6b and Figure 5.7c than on the wetting tests on sand shown in Figure 5.6a and Figure 5.7a. This can be attributed to two different factors. Firstly, in the wetting tests on clay, each value of s_{ext} was maintained for 600 hours, compared to only 6 hours for the wetting tests on sand, meaning that there was simply more time for diffusion of dissolved air in the tests on clay. Secondly, the values of excess gas pressure within the trapped air, which drive the diffusion of dissolved air, were always less than 2 kPa during the tests on sand (compare the values of p_g at points B and A in Figure 5.7a), whereas the values of excess gas pressure within the trapped air were substantially greater during the tests on clay (see Figure 5.7c). This second factor would suggest that, after air trapping commenced, diffusion of dissolved air would dissipate excess pore gas pressure more quickly in tests on clay than in tests on sand. Additional numerical simulations were performed to investigate the relative importance of these two factors.

Figure 5.8 shows the results of numerical simulations of wetting tests on sand for path 1 with each value of s_{ext} maintained for either 6 hours (the original simulations shown in Figure 5.6a) or 600 hours (a new set of simulations). With each wetting stage lasting 600 hours, Figure 5.8 shows that diffusion of dissolved air had a small but noticeable impact on the apparent SWRC, whereas there was negligible impact of diffusion of dissolved air when each wetting stage lasted only 6 hours. However, even with each wetting stage lasting 600 hours, the influence of diffusion of dissolved air during the tests on sand (Figure 5.8) was still much less than in the tests on clay (Figure 5.6b). This means that the higher values of excess gas pressure within the trapped air during tests on clay are of considerable importance, in reducing the time required for dissipation of excess gas pressures in trapped air by diffusion of dissolved air.

The fact that, after air trapping commences, dissipation of excess gas pressures by diffusion of dissolved air occurs more slowly in tests on sands than during tests on clays means that, counter to normal practice, after air trapping commences (at high values of S_l), wetting tests on sand samples should be performed more slowly than wetting tests on clay samples if full equalization of both p_l and p_g throughout the sample is to be achieved. This is, of course, in contrast to the situation at lower values of S_l, when the gas phase is continuous, where it is tests on clay samples that need to be performed slowest, because of the lower values of liquid conductivity for clays.

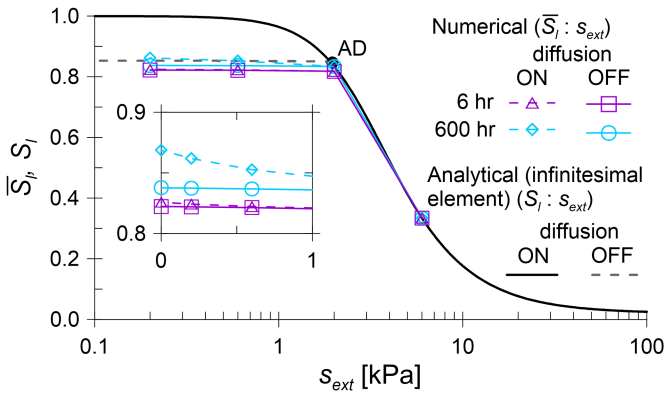

Figure 5.8: Apparent SWRCs: influence of the time duration of each value of applied suction, for path 1 applied to sand

5.3.5 Influence of the method of suction application

The analytical modelling results shown in Figure 5.2 and the numerical modelling results shown in Figures 5.6, 5.7 and 5.8 are all from simulations where wetting was achieved by holding the externally applied gas pressure $p_{g,ext}$ constant at atmospheric pressure and then increasing the externally applied liquid pressure $p_{l,ext}$, with values of $p_{l,ext}$ negative relative to atmospheric pressure. This represents a typical wetting situation in the field and also the type of wetting applied in some laboratory tests. However, other laboratory tests make use of the axis translation technique [226], where elevated values of $p_{g,ext}$ and $p_{l,ext}$ are applied, to ensure that both are above atmospheric pressure. In addition, when the axis translation technique is employed, wetting or drying is often achieved by holding $p_{l,ext}$ constant and varying $p_{g,ext}$. For example in a typical pressure plate test [227] to determine the SWRC, $p_{l,ext}$ is maintained constant at atmospheric pressure p_{atm} and wetting is achieved by progressively reducing the value of $p_{g,ext}$ towards p_{atm}. It is important to investigate whether this different method of applying suction in a laboratory test would affect the apparent SWRC when air trapping occurs.

Figure 5.9 shows the results of analytical calculations (for an infinitesimally small soil element) and numerical simulations (for the sample of finite size shown in Figure 5.3), for wetting tests on the clay, using two different methods of suction application. In one case $p_{g,ext}$ was maintained constant at atmospheric pressure and $p_{l,ext}$ was varied (the simulations shown previously in Figure 5.2b and Figure 5.6b) and in the other case $p_{l,ext}$ was maintained constant at atmospheric pressure and $p_{g,ext}$ was varied (new simulations, representing typical pressure plate tests). All numerical modelling results shown in Figure 5.9 had the same variation of s_{ext} with time, given by path 2 in Figure 5.5b. The smooth continuous curve in Figure 5.9 is the true SWRC, which also represents the apparent SWRC for an infinitesimally small element when diffusion of dissolved gas is included (see earlier). For all other analytical and numerical simulations shown in Figure 5.9, diffusion of dissolved air was not included (to maximise the impact of the change of method of suction application). Note that, for the infinitesimally small element without diffusion of dissolved air, Equations 5.3, 5.4 and 5.5 no longer apply if the externally applied suction is reduced by maintaining $p_{l,ext}$ constant.

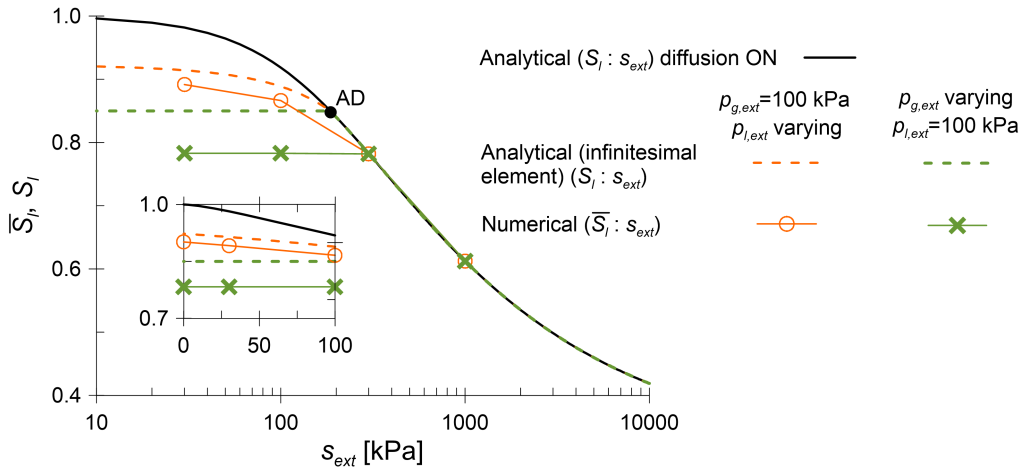

Figure 5.9: Influence of method of suction application ($p_{g,ext}$ = constant or $p_{l,ext}$ = constant) on apparent SWRC, for path 2 applied to clay (diffusion off unless stated otherwise)

Inspection of the results in Figure 5.9 shows that the method of suction application has a major impact on the apparent SWRC. With diffusion of dissolved air not included, when the externally applied suction was reduced by maintaining $p_{l,ext}$ constant, the value of S_l remained constant after air trapping commenced (for both the infinitesimally small element and the sample of finite size), whereas, as shown previously, when the externally applied suction was reduced by maintaining $p_{g,ext}$ constant, the value of S_l increased after air trapping commenced. In the latter case, as discussed previously, after air trapping commences, the increase of p_l produces an increase of gas pressure in the trapped air, leading to compression of this trapped air, whereas this effect does not occur when externally applied suction is reduced by keeping $p_{l,ext}$ constant. Thus, the method of suction application is another aspect of the wetting test conditions that will affect the apparent SWRC once air trapping commences.

As stated in Section 5.3.1, unlike the numerical models analysed in this section where pore liquid pressure and pore gas pressure were applied at the same boundary of the soil sample, in typical laboratory tests pore liquid pressure and pore gas pressure are applied at opposite boundaries. In these numerical analyses, the amount of trapped air is likely to be overestimated compared to typical laboratory tests because all the air present within the sample remains trapped once the suction applied at the boundaries is lower than the air-discontinuity value. Conversely, when pore liquid pressure and pore gas pressure are applied at opposite boundaries, water infiltrates into the sample from the boundary where pore liquid pressure is imposed while a significant amount of air will still flow out at the opposite boundary where pore gas pressure is imposed, even though the applied liquid pressure corresponds to a suction value lower than s_{AD}. Therefore, in absence of diffusion, the SWRC obtained by applying pore liquid pressure and pore gas pressure at opposite boundaries is likely to be more similar to the SWRC estimated for the infinitesimal element of soil (see Section 5.2). Nevertheless, the findings obtained from the numerical analyses may be relevant for different real field conditions, such as an intense water infiltration from the ground surface into a soil layer at low degree of saturation (e.g. sand) underlain by a saturated soil layer (e.g. clay).

5.4 Concluding remarks

At high values of degree of liquid saturation S_l, the apparent SWRC measured in a wetting test in the laboratory ($S_l : s_{ext}$) may differ from the true SWRC ($S_l : s$) within the soil sample due to the occurrence of air trapping. Trapped air is formed when the gas phase becomes discontinuous and the gas pressure within the trapped air will be in general higher than the externally applied gas pressure unless the very slow process of diffusion of dissolved air has finished. Due to the occurrence of air trapping, the apparent SWRC will typically not reach a fully saturated condition as the externally applied suction s_{ext} is reduced to zero whereas physical arguments indicate that the true SWRC will reach full saturation at a positive value of internal suction s.

Analytical and numerical modelling of the phenomenon of air trapping were carried out.

The results of the analytical modelling within an infinitesimally small soil element (without any diffusion of dissolved air) can be summarised as follows.

- If wetting is produced by increasing the externally applied liquid pressure, the gas pressure within the trapped air increases as s_{ext} is reduced towards zero, leading to compression of the trapped air and hence increases of S_l after air trapping commences.

- Increases of S_l due to trapped air compression will be much greater in a test on clay than in a test on sand, because higher values of excess gas pressure within the trapped air are generated in a clay, because the air trapping commences at much higher values of suction in a clay than in a sand.

The results of numerical modelling of wetting tests on soil samples of finite size can be summarised as follows.

- The apparent SWRC is the result of a particular boundary value problem whereas the true SWRC is a fundamental representation of the soil behaviour.

- The apparent SWRC measured in a wetting test will depend upon many aspects of the wetting test conditions, including: the size of the soil sample; the method of suction application (whether the axis translation technique is employed and whether wetting is produced by increasing the externally applied liquid pressure or by decreasing the externally applied gas pressure); the precise sequence of values of externally applied suction; and the time duration used for the application of each value of external suction.

The results lead to the following conclusions.

- The apparent SWRC measured in a wetting test in a laboratory applies only to the specific boundary value problem of this laboratory test and should not be used in numerical modelling of other boundary value problems.

- The only correct way to represent the occurrence of air trapping is to use the true SWRC in combination with a gas conductivity expression that goes to zero at the air-discontinuity point.

- Measurement of the true SWRC in a laboratory test is likely to be problematic for the final part of the main wetting curve, at high values of S_l, when air trapping occurs. The time scales required to achieve this are unlikely to be feasible, in particular for sands because equalization of pore gas pressure within trapped air bulbs by diffusion of dissolved air is much slower in samples of sand than in samples of clay.

Given that laboratory measurement of the final part of the true SWRC for a main wetting curve (at high values of S_l) may not be feasible, it may be best to simply infer a shape for the final part of the curve, based on reliable measurements for the rest of the main wetting SWRC (before air trapping occurs) and information on the shape of the main drying curve at high values of S_l. For example, it might be assumed that the form of the main wetting curve at high values of S_l is simply given by a horizontal translation of the main drying curve in the standard semi-logarithmic plot of S_l against s.

Chapter 6

Numerical study of the fundamental behaviour of capillary barrier systems

The new hydraulic conductivity model and the new hysteretic hydraulic model presented in Chapter 3 and implemented in Code_Bright (see Sections 4.1.5 and 4.1.6), were used to study numerically the fundamental behaviour of capillary barrier systems. In particular, the implications of using these more advanced hydraulic constitutive models were highlighted. This chapter shows the results of numerical simulations performed with Code_Bright, where the roles of improved hydraulic conductivity modelling at low degree of saturation (see Section 6.1) and hydraulic hysteresis (see Section 6.2) on the hydraulic behaviour of capillary barrier systems are highlighted. In addition, numerical simulations performed to identify the minimum water storage capacity of CBSs are shown in Section 6.3. The numerical modelling presented in this chapter is all for one-dimensional problems i.e. use of CBSs on a horizontal ground surface.

6.1 Application of the new hydraulic conductivity model to the study of the fundamental behaviour of capillary barrier systems

Numerical simulations of one-dimensional infiltration tests on a capillary barrier were performed with the new hydraulic constitutive models (modVG-modM+LF) and with the conventional (VG-M) models. Hydraulic hysteresis was not considered in this set of simulations. The aims of these analyses were: i) to show that the new improved hydraulic models are able to describe better the properties of the breakthrough condition from the finer layer to the coarser layer, ii) to assess the role of liquid films in the behaviour of CBSs and iii) to assess the role of vapour diffusion in the phenomenon of water breakthrough from the finer layer to the coarser layer of CBSs. In the analyses, the solid phase was considered as non-deformable and the gas phase as non-mobile. Thus, constant and uniform values of displacements of the solid phase ($\boldsymbol{u} = 0\,\mathrm{m}$) and gas pressure ($p_g = 100\,\mathrm{kPa}$) were imposed. The influence of vapour diffusion within the gas phase was investigated by performing two versions of

each simulation: the first with vapour diffusion not considered and the second with vapour diffusion included. In the analyses in which vapour diffusion was not included, isothermal conditions were imposed with a constant and uniform value of temperature ($T = 20\,^{\circ}\mathrm{C}$) and water transport occurred only through the liquid phase. In the analyses in which vapour diffusion was included, conditions were non-isothermal and water transport occurred through liquid water advection in the liquid phase and through vapour water diffusion in the gas phase.

6.1.1 Description of the numerical models

The numerical model was a vertical column of soil made of two layers: an upper layer, 0.5 m thick, representing the finer layer (F.L.) of a CBS and a lower layer, 0.75 m thick, representing the coarser layer (C.L.) (see Figure 6.1a). The thickness of the coarser layer was unrealistically high in order to have the bottom boundary sufficiently far from the interface so that the phenomenon of breakthrough was not affected by any influence of the bottom boundary.

A structured mesh made of quadrilateral elements was used for the CBS. The mesh of the coarser layer was divided into two parts: from the bottom boundary (0 m) to a height of 0.25 m, 20 uniformly spaced elements were used in the vertical direction; from a height of 0.25 m to the interface with the F.L. (0.75 m), 120 elements were used in the vertical direction with a mesh refinement gradient of 0/0.04 (finer toward the interface). The mesh of the finer layer was characterised by 60 elements in the vertical direction with a mesh refinement gradient of 0.1/0.1 (finer towards the two ends).

The materials forming the two layers were each modelled by defining the hydraulic constitutive models (SWRC and SHCC), porosity and intrinsic permeability. In addition, in the analyses in which vapour diffusion was included, the parameters modelling the thermal conductivity and the vapour diffusivity were also defined. Each of the two layers was considered as a uniform material. The parameters chosen to model the finer layer were representative of a silty sand whereas those of the coarser layer were representative of a pea gravel. The finer layer was modelled using the conventional van Genuchten-Mualem (VG-M) model because, in the analyses, this layer was never at very low degree of saturation. The coarser layer was modelled using the following combinations of models: i) van Genuchten-Mualem (VG-M); ii) modified van Genuchten-modified Mualem (modVG-modM); and iii) modified van Genuchten-modified Mualem + liquid film (modVG-modM+LF). For the modVG-modM+LF modelling, three different values of X_D were used: the default value of $2.35 \times 10^{-9}\,\mathrm{mm.m\,s^{-1}.kPa^{1.5}}$, a value 5 times larger than the default value $1.175 \times 10^{-8}\,\mathrm{mm.m\,s^{-1}.kPa^{1.5}}$ and a value 5 times smaller than the default value $4.7 \times 10^{-10}\,\mathrm{mm.m\,s^{-1}.kPa^{1.5}}$. The default value of X_D was used in the majority of simulations, but some specific simulations were also performed using values for X_D 5 times larger and 5 times smaller than the default value, to explore the impact of uncertainty in the choice of the value for this parameter. The parameter values of the materials are shown in Table 6.1 and the SWRCs and SHCCs are shown in Figures 6.1b and 6.1c respectively. The intrinsic permeability values k shown in Table 6.1 were equivalent

to saturated hydraulic conductivity values of $k_{ls} = 3 \times 10^{-6}\,\mathrm{m\,s^{-1}}$ for the finer layer and $k_{ls} = 1 \times 10^{-2}\,\mathrm{m\,s^{-1}}$ for the coarser layer (see Equation 4.28). The bulk water-continuity value of suction of the coarser layer was $s_{BWC} = 0.7\,\mathrm{kPa}$ and it was identified using the the simplified graphical procedure described in Section 3.3.1. Given s_{BWC}, the corresponding degree of saturation $S_{l,BWC}$ shown in Table 6.1 was obtained from the SWRC expression of the coarser layer. The values of the parameter C_r^{Film} were calculated from knowledge of the parameters X_D, D_{10}, Φ and k_{ls} (see Equations 3.6 and 4.67). The parameter values used for the thermal conductivity and the vapour diffusivity were the default values discussed in Section 4.1.2.

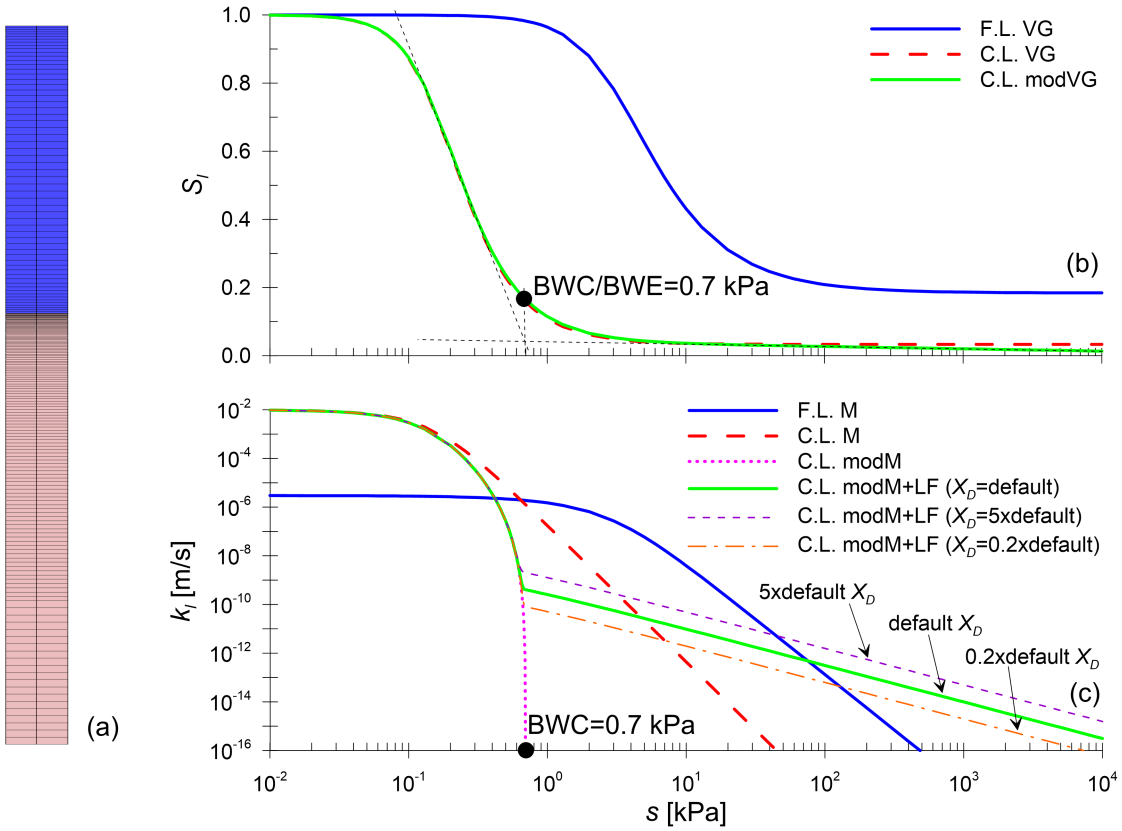

Figure 6.1: Properties of the numerical model: (a) mesh, (b) SWRC models and (c) SHCC models

The initial condition for the numerical analyses was a hydrostatic pore-liquid pressure profile, with $p_l = 100\,\mathrm{kPa}$ ($s = 0\,\mathrm{kPa}$) at the bottom boundary, $p_l = 87.5\,\mathrm{kPa}$ ($s = 12.5\,\mathrm{kPa}$) at the top, and a linear variation between. In this initial condition, the coarser layer was at very low degree of saturation (lower than $S_{l,BWC}$). In the non-isothermal analyses, performed when vapour diffusion was included, an initial uniform temperature profile was applied with $T = 20\,^{\circ}\mathrm{C}$.

For the bottom boundary condition, a constant value of the pore-liquid pressure equal to the initial value was imposed, namely $p_l = 100\,\mathrm{kPa}$ ($s = 0\,\mathrm{kPa}$). For the top boundary condition, a constant value of vertical liquid water flux (the infiltration rate) was imposed. In order to assess the influence of the infiltration rate, two values of water flux were considered: $i_1 = 1 \times 10^{-6}\,\mathrm{m/s}$ and $i_2 = 1 \times 10^{-8}\,\mathrm{m/s}$. The value of i_1 was chosen so that it was comparable with the saturated hydraulic conductivity of the finer layer ($k_{ls} = 3 \times 10^{-6}\,\mathrm{m/s}$) whereas i_2

Table 6.1: Material parameter values for the numerical analyses

Material	Φ [-]	k [m^2]	D_{10} [mm]
	Physical parameters		
F.L.	0.38	3.081E-13	-
C.L.	0.30	1.028E-9	5

	$\overline{P_0}$ [MPa]	$\overline{\sigma_s}$ [N/m]	m [-]	S_{lr} [-]	ξ [-]	S_{ls} [-]
	SWRC parameters					
F.L. VG	3.263E-3	0	0.505	0.1842	-	1
C.L. VG	1.709E-4	0	0.590	0.0313	-	1
C.L. modVG	1.709E-4	0	0.590	-	0.00294	1

	m [-]	S_{lr} [-]	$S_{l,BWC}$ [-]	S_{ls} [-]	C_r^{Film} [MPa$^{-1.5}$]	a^{Film} [MPa]	d^{Film} [-]
	SHCC parameters						
F.L. M	0.505	0.1842	-	1	-	-	-
C.L. M	0.590	0.0313	-	1	-	-	-
C.L. modM	0.590	-	0.165	1	-	-	-
C.L. modM+LF default X_D	0.590	-	0.165	1	9.892E-13	1.454E-4	-1.5
C.L. modM+LF $0.2 \times$ default X_D	0.590	-	0.165	1	1.978E-13	1.454E-4	-1.5
C.L. modM+LF $5 \times$ default X_D	0.590	-	0.165	1	4.946E-12	1.454E-4	-1.5

	λ_{solid} $\left[\frac{\mathrm{W}}{\mathrm{mK}}\right]$	λ_{gas} $\left[\frac{\mathrm{W}}{\mathrm{mK}}\right]$	λ_{liquid} $\left[\frac{\mathrm{W}}{\mathrm{mK}}\right]$	D $\left[\frac{\mathrm{m^2Pa}}{\mathrm{sK^n}}\right]$	n [-]	τ_0 [-]
	Thermal conductivity*			**Vapour diffusivity***		
F.L.	7.7	0.024	0.6	5.9E-6	2.3	1
C.L.	7.7	0.024	0.6	5.9E-6	2.3	1

*Only used in analyses in which vapour diffusion in the gas phase was included

was two orders of magnitude smaller than i_1 and representative of a low rainfall intensity. In the non-isothermal simulations, performed when vapour diffusion was included, a constant temperature equal to $T = 20\,^{\circ}\mathrm{C}$ was applied at the bottom boundary and at the top boundary.

6.1.2 Results and discussion

Three sets of results are presented in this section.

In the first set, the results of numerical analyses obtained with three different hydraulic models describing the coarser layer (i.e. VG-M, modVG-modM and modVG-modM+LF) were compared. In these simulations, vapour diffusion was not included and the default value for X_D (i.e. $2.35 \times 10^{-9}\,\mathrm{mm\,m\,s^{-1}\,kPa^{1.5}}$) was used for the liquid film component of the hydraulic conductivity. The comparison between these results highlights the role of the hydraulic conductivity model used for the coarser layer.

In the second set, the role of the uncertainty on the choice of the value of the parameter X_D is highlighted by means of a sensitivity analysis, where results obtained considering three different values for the parameter X_D are compared. Vapour diffusion was not included in this group of results.

In the third set, the comparison of different results obtained with and without vapour diffusion highlights the role of vapour diffusion in the hydraulic behaviour of capillary barriers during water infiltration. In these analyses, the default value for X_D was used for the liquid film component of the hydraulic conductivity.

Role of the hydraulic conductivity model

The results of the numerical analyses of the infiltration process in a CBS are presented here in order to highlight the influence of the SHCC models used for the coarser layer and the influence of the liquid film conductivity, which is commonly neglected. In these analyses, the default value for X_D was considered for the liquid film component of the hydraulic conductivity.

In this set of analyses, the fitted value of S_{lr} of the coarser layer in the VG model is close to 0 and therefore the VG and modVG models lead to very similar SWRCs (see Figure 6.1b). Hence, the choice between them does not significantly affect the results of the analyses in this case and all the differences which are shown below are attributable to the use of different SHCCs, rather than to the use of different SWRCs. The results shown in Figures 6.2, 6.3 and 6.4 are for the simulations in which vapour diffusion was excluded, but vapour diffusion was found to have negligible effect in most cases, as discussed later.

Figure 6.2 shows the predicted time histories of the effective vertical velocity of the liquid phase (flow rate per unit plan area) predicted at the interface between the finer and coarser layers, obtained using different infiltration rates at the top boundary and different hydraulic constitutive models for the coarser layer. In all the simulations, the effective water velocity at the interface is initially equal to zero. A wetting front then starts moving downwards from the ground surface until it reaches the interface (located at 0.5 m below the top boundary). The suction at the interface then decreases and some time later water starts moving across the interface (breakthrough). The estimated times at breakthrough are indicated by symbols in Figure 6.2. Soon after breakthrough, the water velocity across the interface becomes equal to the infiltration rate applied at the surface (see Figure 6.2).

It can be seen from Figure 6.2 that the predicted breakthrough takes different forms, depending on the infiltration rate and on the model used to describe the hydraulic behaviour of the coarser layer. At the lower infiltration rate i_2, the use of the conventional VG-M model to describe the behaviour of the coarser layer results in prediction that breakthrough would be a relatively gradual phenomenon. In contrast, when the new modVG-modM or modVG-modM+LF models are used for the coarser layer, the numerical simulations show breakthrough as a relatively sudden phenomenon at both infiltration rates. These predictions with the new models are a better qualitative match to experimental observations [23], which show that breakthrough is always a very sudden phenomenon, irrespective of the infiltration

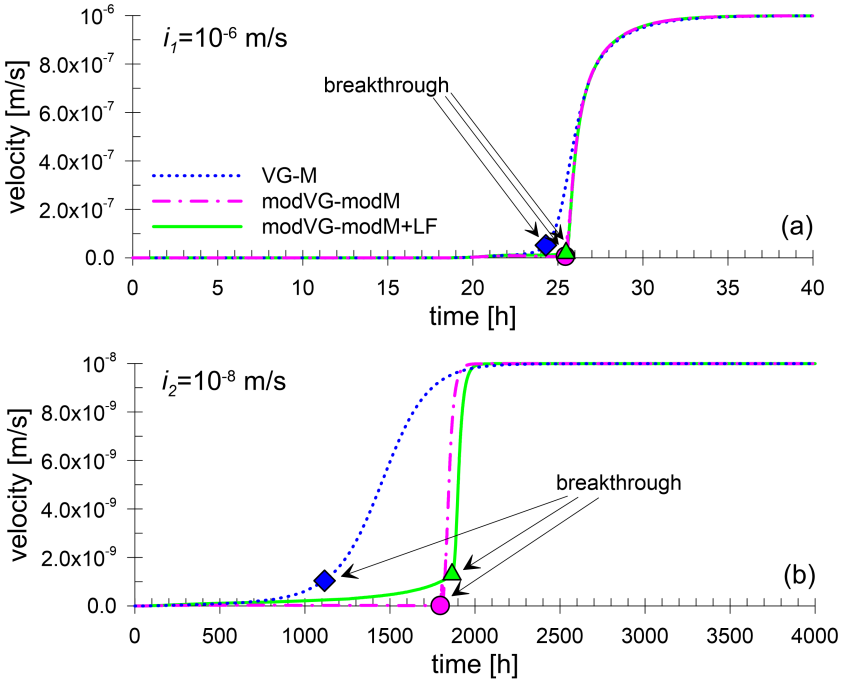

Figure 6.2: Time histories of water velocity across the interface predicted with different hydraulic models, for infiltration rates (a) i_1 and (b) i_2

rate. Inspection of Figure 6.2 also shows that, particularly at the lower infiltration rate i_2, use of the conventional VG-M model results in prediction of an earlier time to breakthrough than is predicted by the new modVG-modM or modVG-modM+LF models. This means that the conventional VG-M model predicts a lower water storage capacity of the finer layer prior to breakthrough than the new models.

The analysis of the suction profile at breakthrough is very important in the study of a CBS because it allows the water content profile at breakthrough to be obtained by means of the SWRC, and this allows the water storage capacity of the barrier to be calculated, where the water storage capacity is defined as the maximum amount of water that can be stored in the barrier before breakthrough occurs [141] (see Section 2.3.3). According to experimental observations, starting from initial conditions when the barrier is generally at low water contents (relatively high suction values), the rainwater infiltrating from the surface causes changes in the suction profile in the finer layer. The infiltrating rainwater is initially stored entirely within the finer layer, which causes the water content to increase and the suction to decrease. When the suction at the interface approaches the BWC value of the coarser layer, this becomes hydraulically conductive and water breaks through from the finer layer to the coarser layer (see Section 2.3.3).

Figures 6.3a and 6.3b show the suction profiles at the time of breakthrough predicted by the numerical analyses for infiltration rates i_1 and i_2 respectively. Also shown, for comparison, are the initial suction profile and a simple empirical suction profile in the finer layer at the time of breakthrough. The latter was obtained by imposing the BWC value of the coarser layer (0.7 kPa) at the interface and above this a hydrostatic profile up to a limiting suction value corresponding to the suction at which the hydraulic conductivity of the finer layer is equal to the applied infiltration rate (this limiting suction is reached only in the case of the higher

infiltration rate i_1) (see Figure 2.22). Various authors [e.g. 141] observed experimentally that the suction profile in the finer layer at the time of breakthrough was always very close to this empirical approximation. From Figures 6.3a and 6.3b, it can be seen that the use of the conventional VG-M model leads to results that are different to the experimental observations from the literature and, again, these differences are more significant for low infiltration rates. In particular, with the VG-M model, breakthrough is predicted when the suction value at the interface is higher than the BWC suction value of the coarser layer and, furthermore, this predicted suction value at the interface varies with the infiltration rate (whereas experimental observations indicate that the suction value at the interface at the time of breakthrough is independent of infiltration rate). By contrast, these inconsistencies with experimental observations are not seen if the new modVG-modM or modVG-modM+LF models are used for the coarser layer. The numerical results for the suction profile in the finer layer at the time of breakthrough (see Figures 6.3a and 6.3b) are then almost identical to the simple empirical suction profile at breakthrough, which was reported to be a good approximation of experimental observations. Using the modVG-modM model, breakthrough is predicted to occur when the suction at the interface exactly reaches the BWC value of the coarser layer, when bulk water starts forming continuous liquid networks across the interface. In addition, the liquid film flow, included in the modVG-modM+LF model, does not affect the suction profiles in the finer layer at the time of breakthrough (see Figures 6.3a and 6.3b).

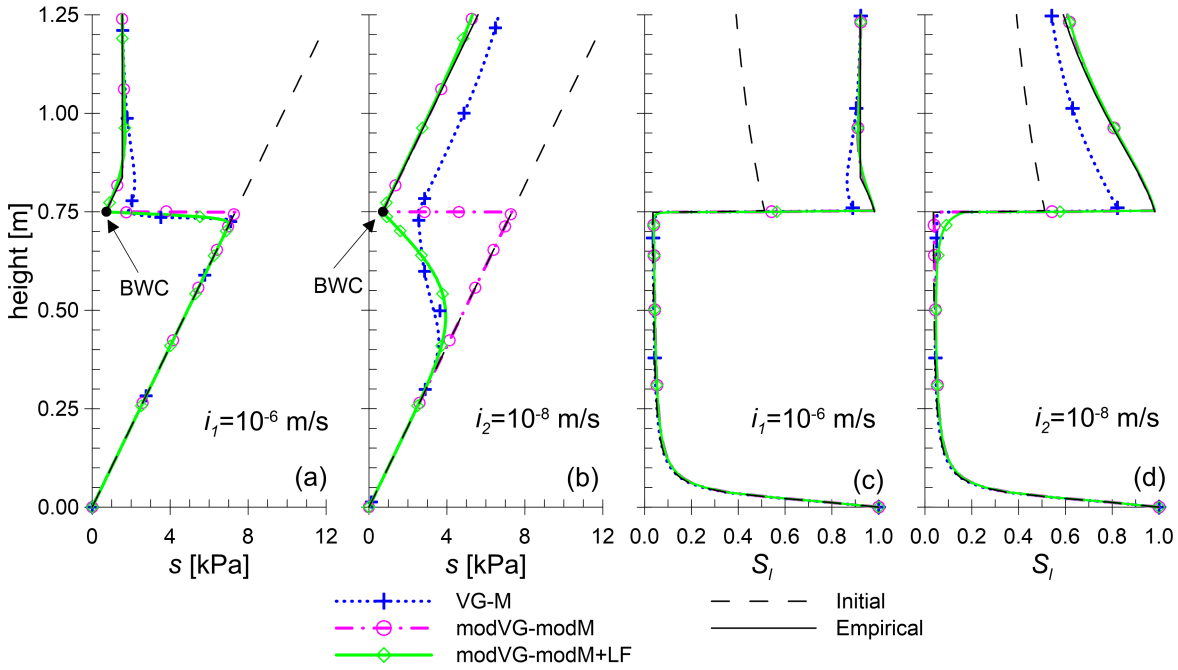

Figure 6.3: Suction (a, b) and degree of saturation (c, d) profiles at breakthrough predicted with different hydraulic models, for infiltration rates i_1 and i_2

The liquid film component of the SHCC may, however, affect significantly the suction profile in the coarser layer at the time of breakthrough. Using the modVG-modM model, the predicted suction profile in the coarser layer at the time of breakthrough is identical to the initial suction profile (see Figures 6.3a and 6.3b), because only bulk water flow is included

in the model and this does not start across the interface until the time of breakthrough. By contrast, when the modVG-modM+LF model, which includes the liquid film flow, is used, the predicted suction profile in the coarser layer at the time of breakthrough is substantially different to the initial suction profile, particularly at the lower infiltration rate (see Figure 6.3b), because even before breakthrough of bulk water occurs, a small amount of water flows across the interface through the continuous liquid film networks. This causes a very small increase in the degree of saturation in the coarser layer immediately below the interface (almost insignificant, as shown in the degree of saturation profiles in Figures 6.3c and 6.3d) but a large decrease in suction (Figures 6.3a and 6.3b). This is explained by the shape of the SWRC at low degree of saturation (below $S_{l,BWE}$), where a small increase of S_l corresponds to a large decrease in suction. The predicted changes in the suction profile in the coarser layer prior to breakthrough may have important consequences when CBSs are used for suction control purposes [e.g. 170].

The values of S_l predicted in the finer layer with the VG-M model are smaller than those predicted by the new models (see Figures 6.3c and 6.3d). This can be explained by the fact that, with the VG-M model, breakthrough occurred earlier and at higher suction values. Therefore, the water storage capacity of the CBS predicted with the VG-M model is lower than that predicted with the new models.

Figure 6.4 shows suction and degree of saturation profiles at different times during infiltration, before and after breakthrough, obtained with the different hydraulic models for the coarser layer and for the infiltration rates i_1 and i_2. In general, as time goes on, water is initially stored in the finer layer with the degree of saturation increasing and suction decreasing. After breakthrough occurs, the wetting front starts moving downwards in the coarser layer. Before breakthrough (t=20 h and 23 h for i_1, and t=445 h and 1000 h for i_2), the different models lead to almost coincident profiles in the finer layer of the CBS for both infiltration rates. By contrast, after breakthrough, the VG-M model results in higher suction values, and hence in lower degree of saturation values, in the finer layer. For the high infiltration rate i_1 (see Figures 6.4a and 6.4b), the degree of saturation profiles in the coarser layer predicted before breakthrough coincide with the initial profiles according to all the hydraulic models. After breakthrough, the VG-M model predicts a faster propagation of the wetting front in the coarser layer and in a lower increase in the degree of saturation. The modVG-modM model and the modVG-modM+LF model lead to almost identical results. Similar concepts apply to the case of the low infiltration rate i_2 (see Figures 6.4c and 6.4d) but, in this case, the effect of liquid film conductivity is not negligible because the modVG-modM model and the modVG-modM+LF model lead to different results in terms of suction profiles in the coarser layer, but the differences are negligible in the degree of saturation profiles. In this case, as observed above, suction profiles in the coarser layer are affected by the liquid film flow before breakthrough occurs. After breakthrough, the bulk water flows in a similar way between the modVG-modM and the modVG-modM+LF models, as suggested by the same degree of saturation profiles, whereas the presence of the liquid films affect the suction profile at depths within the coarser layer greater than the position of the wetting front. Thus, modelling

correctly the hydraulic behaviour of unsaturated soils may have significant implications also in the study of the liquid flow in soils initially at low degree of saturation.

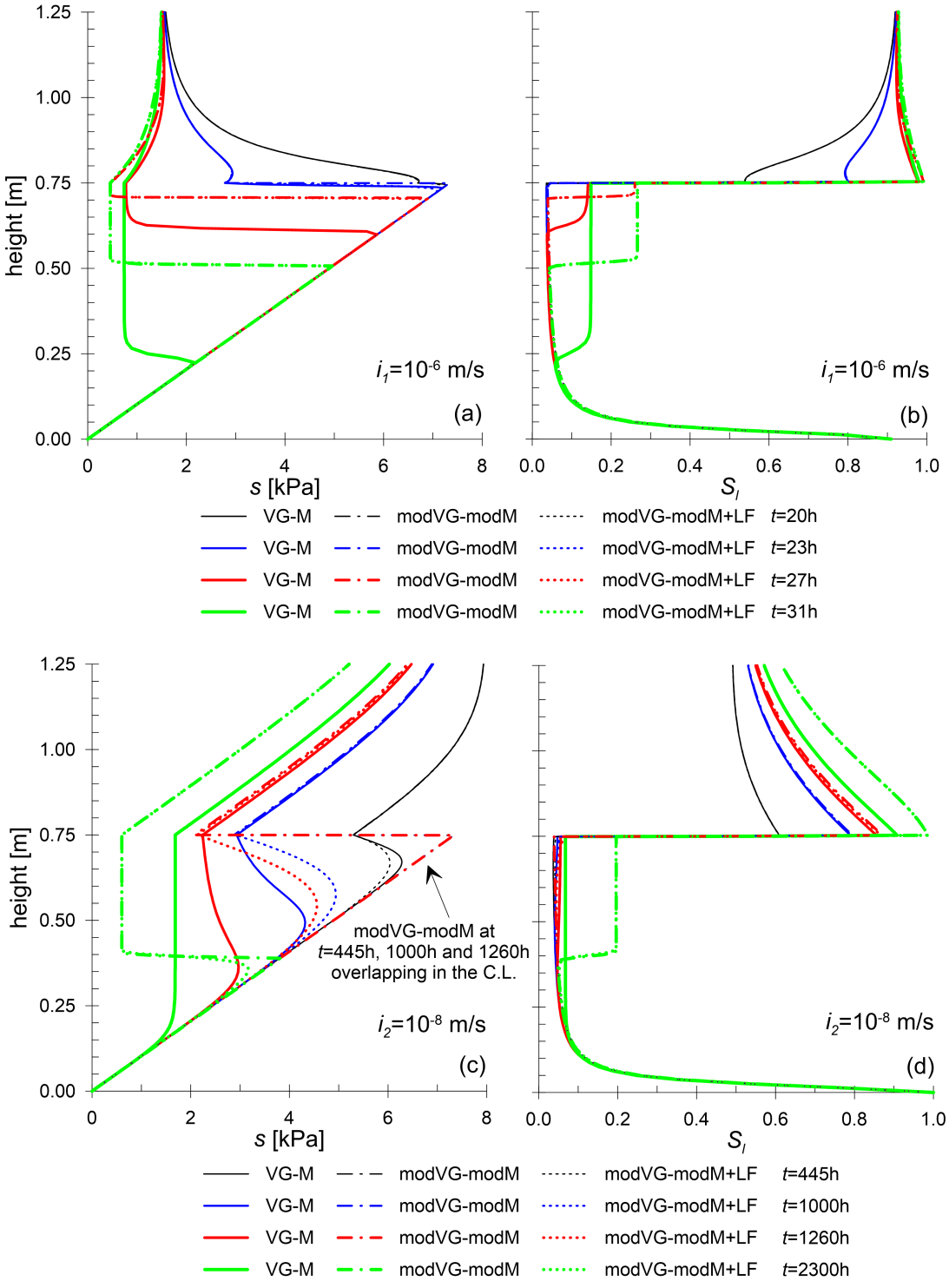

Figure 6.4: Suction (a, c) and degree of saturation (b, d) profiles at different times for infiltration rates i_1 and i_2

Role of the parameter X_D

In order to highlight the role of the parameter X_D, used for the liquid film conductivity of the coarser layer, in the modelling of water infiltration in a CBS, the results of the numerical

analyses obtained considering three different values of the parameter X_D are here compared. This sensitivity analysis shows the role of the statistical uncertainty in the choice of value for the empirical parameter X_D (see Section 3.3.2). The three values used for X_D were: the default value of 2.35×10^{-9} mm.m s^{-1}.kPa$^{1.5}$, 1.175×10^{-8} mm.m s^{-1}.kPa$^{1.5}$ (i.e. 5 times larger than the default value) and 4.7×10^{-10} mm.m s^{-1}.kPa$^{1.5}$ (i.e. 5 times smaller than the default value). The values of X_D 5 times larger than the default value and 5 times smaller than the default value are respectively the expected maximum and minimum value of X_D with a statistical confidence of approximately 95%. The results shown in Figures 6.5 and 6.6 are for the simulations in which vapour diffusion was excluded.

Figure 6.5 shows the predicted time histories of the effective vertical velocity of the liquid phase predicted at the interface between the finer and the coarser layers, obtained using the infiltration rates i_1 and i_2 and different values of X_D for the liquid film conductivity of the coarser layer. At high infiltration rates (see Figure 6.5a), the results obtained with the three different values of X_D are almost indistinguishable. At low infiltration rates (see Figure 6.5b), using the higher value of X_D (i.e. $X_D = 5 \times$ default), the predicted breakthrough is slightly less sudden, as there is a small but detectable gradual increase in the predicted velocity (due to liquid film flow) before the sharp increase in the predicted velocity as breakthrough occurs (when flow of bulk water commences in the coarser layer). The difference due to this uncertainty in the value of X_D in the new modVG-modM+LF model is however much smaller than could be attributed to use of the conventional VG-M model (see Figure 6.2b).

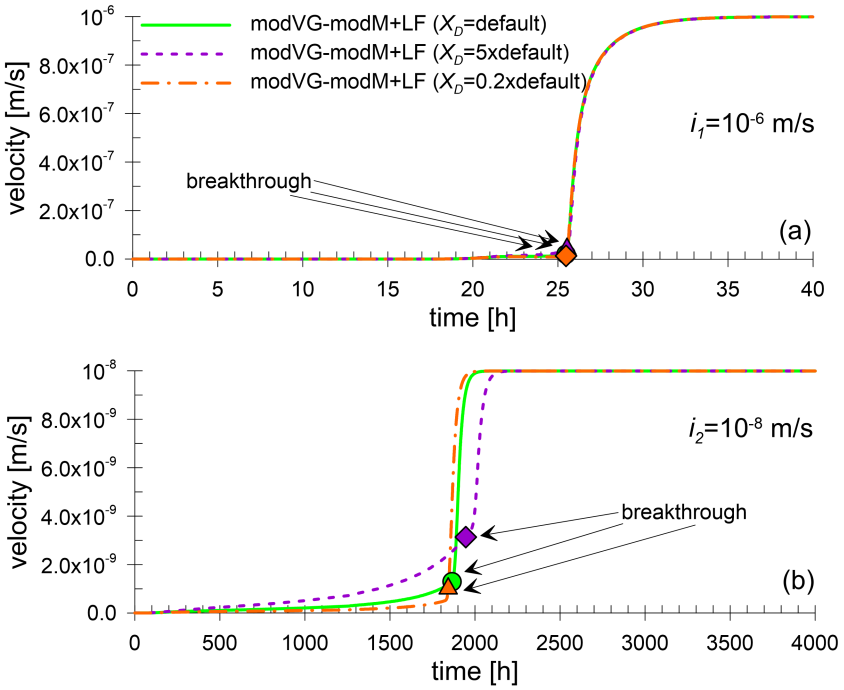

Figure 6.5: Time histories of water velocity across the interface predicted using different values of X_D, for infiltration rates (a) i_1 and (b) i_2

Figure 6.6 shows the suction and degree of saturation profiles at breakthrough predicted using the infiltration rates i_1 and i_2 and different values of X_D for the liquid film conductivity of the coarser layer. At high infiltration rates (see Figures 6.6a and 6.6c), the predicted suction

and degree of saturation profiles are very similar for all three values of X_D. For the lower infiltration rate i_2 (see Figures 6.6b and 6.6d), differences between the suction and degree of saturation profiles predicted with different values of X_D are more significant. In particular, suction and degree of saturation profiles in the finer layer are unaffected by the value of X_D whereas differences can be seen in the coarser layer, in particular with reference to the suction profile. This was expected, because of the previous conclusion that, at the lower infiltration rate, film flow significantly affects the predicted suction profile in the coarser layer at the time of breakthrough (compare the modVG-modM and modVG-modM+LF curves in Figure 6.3b). The influence on the degree of saturation profile is however relatively small (see Figure 6.6d).

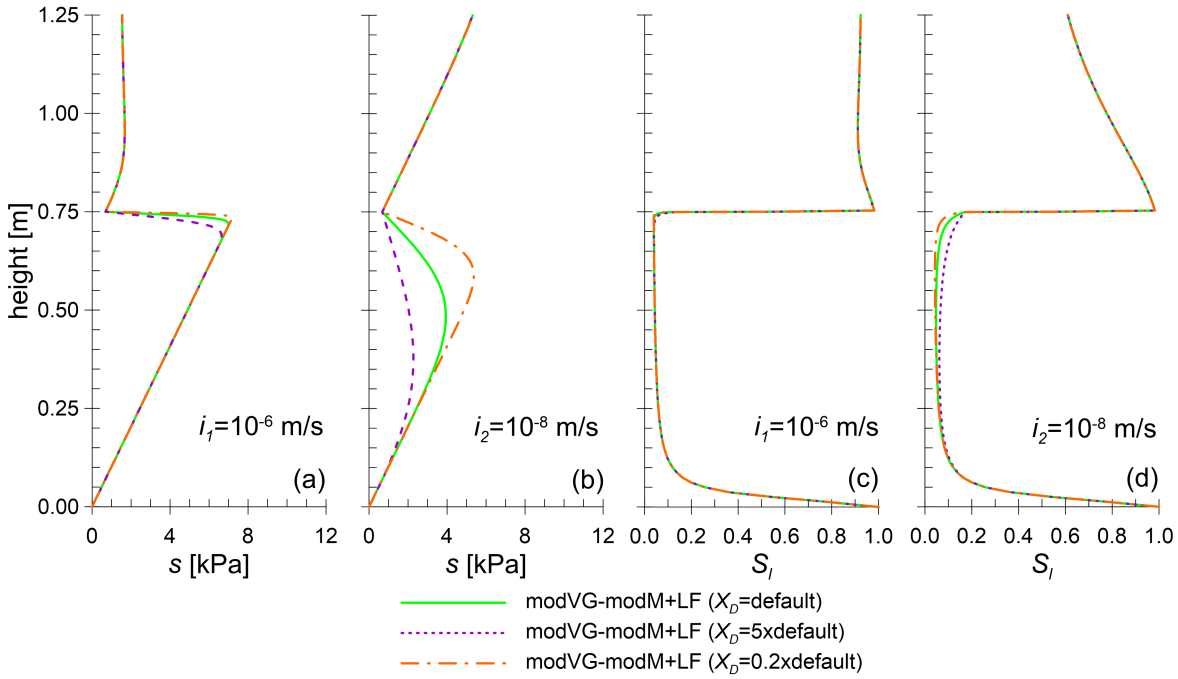

Figure 6.6: Suction (a, b) and degree of saturation (c, d) profiles at breakthrough predicted using different values of X_D, for infiltration rates i_1 and i_2

Role of vapour diffusion

The results previously shown were obtained without modelling water vapour diffusion in the gas phase. As mentioned before, the role of vapour diffusion in the hydraulic behaviour of CBSs during infiltration was investigated by performing two versions of each numerical simulation, with vapour diffusion either included or excluded, as shown in Figures 6.7 and 6.8.

Figure 6.7 shows the time histories of the water velocity across the interface obtained with and without vapour diffusion, for the different hydraulic models and the infiltration rates i_1 and i_2. For the cases in which vapour diffusion was activated, the volumetric water flow across the interface was the sum of the advective liquid water flow and the diffusive water vapour flow. It can be seen that water vapour flow has no noticeable effects on these results.

Figure 6.8 shows suction and degree of saturation profiles at breakthrough obtained with and without vapour diffusion, for the different hydraulic models and the infiltration rates i_1

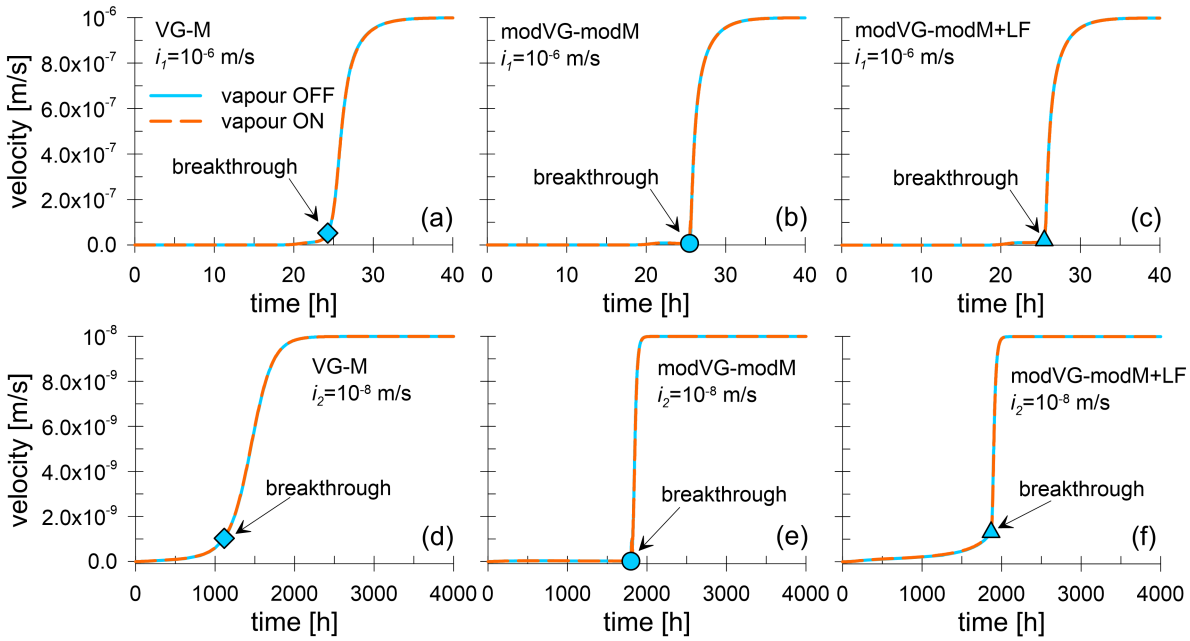

Figure 6.7: Comparison between time histories of water velocity across the interface predicted with and without vapour diffusion, for different models and different infiltration rates

and i_2. As observed for the time histories of the water velocity across the interface, vapour diffusion has negligible effects also on most suction and degree of saturation profiles at breakthrough. Vapour diffusion has no noticeable effects in the simulations where the coarser layer was represented by either the conventional VG-M model or the new modVG-modM+LF model. In both these cases, although only small amounts of liquid water flow into the coarser layer occurs prior to breakthrough, even these small liquid water flows are much greater than the water flows due to vapour diffusion [91]. The effect of vapour diffusion has a small but noticeable effect on the suction profiles employing the modVG-modM model particularly for the low infiltration rate (see Figure 6.8e). With this modVG-modM model, the value of k_l^{Bulk} reduces to zero at the BWC point and there is no liquid film flow. This means that, with this model, vapour diffusion is the only possible mechanism for water flow into the coarser layer prior to breakthrough.

Although the simulations demonstrated that, with the coarser layer represented by either the conventional VG-M model or the new modVG-modM+LF model, vapour diffusion has no noticeable effect on the behaviour of a CBS subjected to a constant rate of infiltration, this does not mean that vapour diffusion will be unimportant in all problems involving unsaturated soils. In particular, water vapour diffusion is likely to be of crucial importance in highly non-isothermal problems, such as nuclear waste disposal [185] and also evaporation from soils [188].

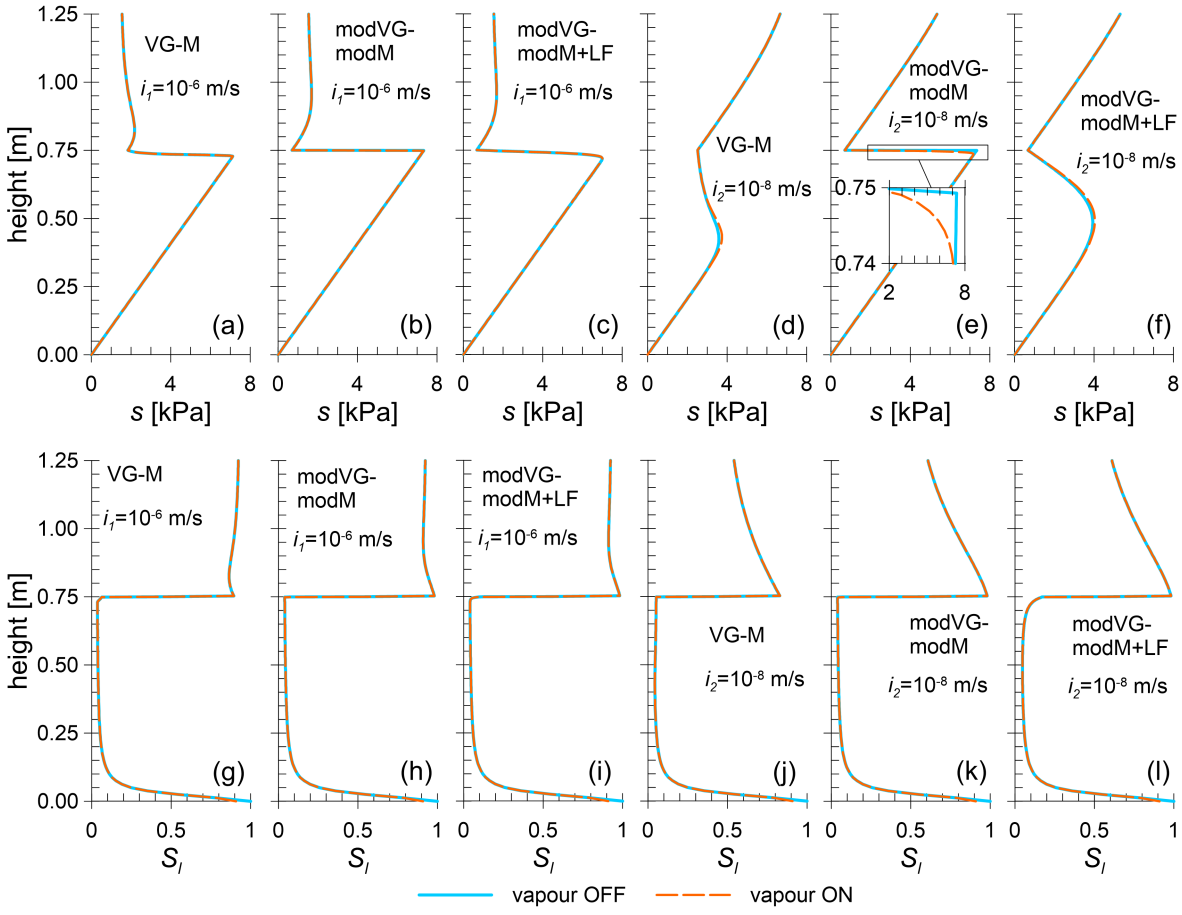

Figure 6.8: Comparison between suction (a, b) and degree of saturation (c, d) profiles at breakthrough predicted with and without vapour diffusion, for different models and the infiltration rates i_1 and i_2

6.2 Application of the new hysteretic hydraulic model to the study of the fundamental behaviour of capillary barrier systems

Numerical one-dimensional simulations of infiltration and evaporation processes in a capillary barrier were performed with the purpose of assessing the role of hydraulic hysteresis in the fundamental hydraulic behaviour of CBSs. Surprisingly, water retention hysteresis is often neglected in the numerical modelling of the hydraulic behaviour of CBSs but, as will be shown in this section, it may have a significant role. In detail, the effects of water retention hysteresis on i) water redistribution within the finer layer, ii) breakthrough and post-breakthrough conditions and iii) evaporation from the ground surface, were studied. This was achieved by comparing results obtained by modelling the hydraulic behaviour of both finer layer and coarser layer using only the main wetting curve, only the main drying curve and the full hysteretic model (i.e. main wetting, main drying and scanning curves).

In these analyses, the solid phase was considered as non-deformable and the gas phase as non-mobile. Thus, constant and uniform values of displacements of the solid phase ($\boldsymbol{u} = 0\,\mathrm{m}$)

and gas pressure ($p_g = 100\,\text{kPa}$) were imposed. The simulations involving the study of the effects of water retention hysteresis on i) water redistribution within the finer layer and ii) breakthrough and post-breakthrough conditions were isothermal and a constant and uniform distribution of temperature was imposed, with $T = 20\,°\text{C}$. The simulations involving the study of the effects of water retention hysteresis on iii) evaporation from the ground surface were non-isothermal and vapour diffusion in the gas phase was also considered in this case.

6.2.1 Description of the numerical models

The model analysed was a vertical column of soil made of two layers: an upper layer, 0.5 m thick, representing the finer layer (F.L.) of a CBS and a lower layer, 0.75 m thick, representing the coarser layer (C.L.) (see Figure 6.9a). The thickness of the coarser layer was unrealistically high in order to have the bottom boundary sufficiently far from the interface so that the phenomenon of breakthrough was not affected by any influence of the bottom boundary.

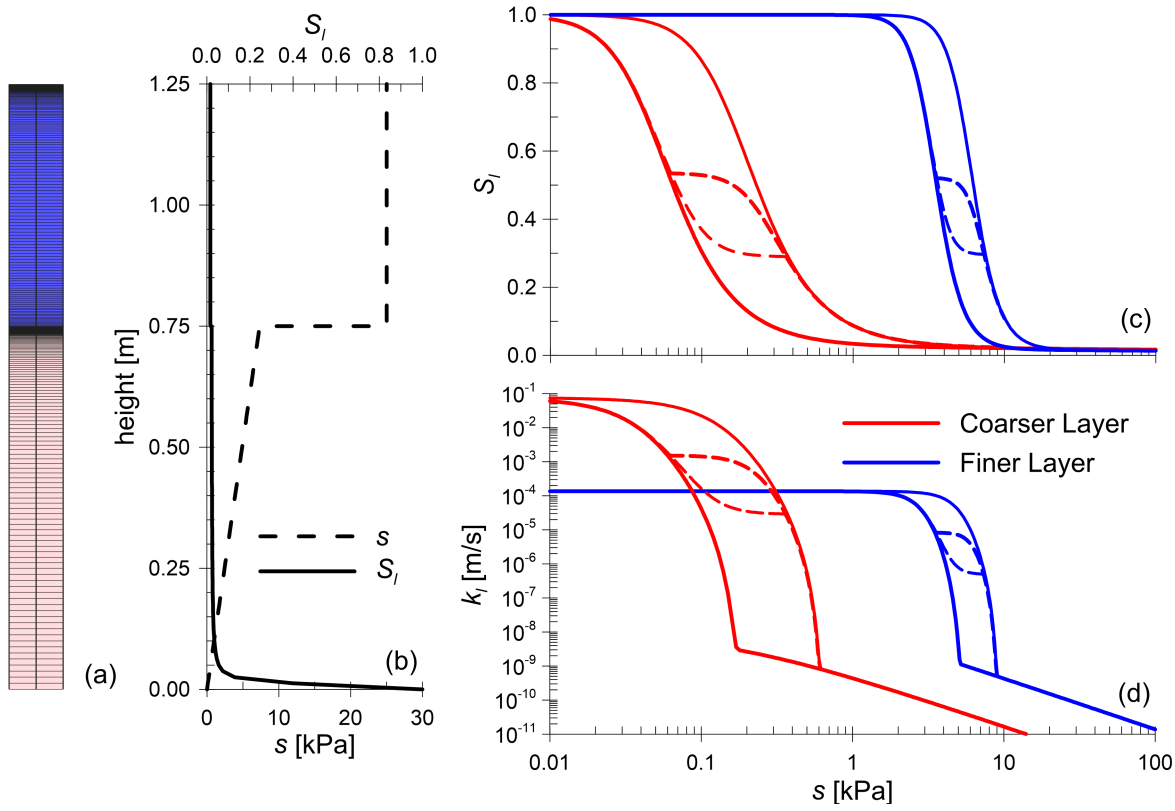

Figure 6.9: Properties of the numerical model: (a) mesh, (b) initial conditions (c) SWRC models and (d) SHCC models

A structured mesh made of quadrilateral elements was used for the CBS. The mesh of the coarser layer was divided into two parts: from the bottom boundary (0 m) to a height of 0.25 m, 20 uniformly spaced elements were used in the vertical direction; from a height of 0.25 m to the interface with the F.L. (0.75 m), 120 elements were used in the vertical direction with a mesh refinement gradient of 0/0.1 (finer toward the interface). The mesh of the finer

layer was characterised by 150 elements in the vertical direction with a mesh refinement gradient of 0.05/0.1 (finer towards the two ends).

The materials forming the two layers were each modelled by defining the hydraulic constitutive models (SWRC and SHCC), the intrinsic permeability and the porosity. In addition, in the thermo-hydraulic simulations, the parameters modelling the thermal conductivity and the vapour diffusivity were also defined. Each of the two layers was considered as a uniform material. The parameters chosen to model the finer layer were representative of a fine sand (see experimental data in Section 7.4) whereas those of the coarser layer were representative of a gravelly sand [197]. The hydraulic behaviour of the materials was modelled using the modVG-modM+LF model, with the liquid film conductivity parameter C_r^{Film} obtained using the default value of parameter X_D. In the simulations, the hydraulic behaviour of both the finer layer and the coarser layer was modelled using three different SWRC models: only the main wetting curve (W), only the main drying curve (D) and the full hysteretic model (i.e. including the main wetting curve, the main drying curve and the scanning curves) (H). The comparison of the results obtained using these three models highlights the role of water retention hysteresis in the modelling of the fundamental behaviour of CBSs.

The parameter values of the materials are shown in Table 6.2 and the SWRCs and SHCCs are shown in Figures 6.9c and 6.9d respectively. The intrinsic permeability values shown in Table 6.2 are equivalent to saturated hydraulic conductivity values of $k_{ls} = 1.36 \times 10^{-4}\,\mathrm{m/s}$ for the finer layer and $k_{ls} = 7.6 \times 10^{-2}\,\mathrm{m/s}$ for the coarser layer (see Equation 4.28). The values for the parameter C_r^{Film} were calculated from knowledge of parameters X_D, D_{10}, Φ and k_{ls} (see Equations 3.6 and 4.67). The parameter values used for the thermal conductivity and the vapour diffusivity are the default values discussed in Section 4.1.2.

The numerical simulations performed can be divided into three different stages. In stage 1, the effect of hydraulic hysteresis on the water redistribution occurring in the finer layer after a period of intense rainfall was analysed. In stage 2, the effect of hydraulic hysteresis on the behaviour of a CBS at breakthrough and post-breakthrough was analysed. In stage 3, the effect of hydraulic hysteresis on evaporation from a CBS to the atmosphere was studied.

In stage 1, isothermal simulations ($T = 20\,^{\circ}\mathrm{C}$) with vapour diffusion excluded were performed. Initial hydraulic conditions imposed for stage 1 are shown in Figure 6.9b. They consisted in a hydrostatic pore-liquid pressure profile in the coarser layer, with a linear variation between $p_l = 100\,\mathrm{kPa}$ ($s = 0\,\mathrm{kPa}$) at the bottom and $p_l = 92.5\,\mathrm{kPa}$ ($s = 7.5\,\mathrm{kPa}$) at the interface, and a uniform pore-liquid pressure profile in the finer layer, with $p_l = 75\,\mathrm{kPa}$ ($s = 25\,\mathrm{kPa}$). The corresponding initial degree of saturation profile (see Figure 6.9b) was automatically fixed when only the main wetting curve (W) or only the main drying curve (D) was used because, in these cases, the relationship between s and S_l was unique. By contrast, when the full hysteretic (H) model was used, the initial degree of saturation profile was obtained by imposing the history parameter values as $s_0 = 1000\,\mathrm{MPa}$ and $S_{l0} = 0$ for both the coarser and the finer layer, which corresponded to initial hydraulic states on the main drying curves. In theory, these initial degree of saturation profiles were different when the models W, D and H were used but, since relatively initial high suction values were imposed (for these

Table 6.2: Material parameter values for the numerical analyses

Material	Φ [-]	k [m^2]	D_{10} [mm]
Physical parameters			
F.L.	0.410	1.398E-11	0.1
C.L.	0.382	7.812E-9	2.7

	$\overline{P_{0d}}$ [MPa]	$\overline{P_{0w}}$ [MPa]	$\overline{\sigma_s}$ [N/m]	m [-]	ξ [-]	S_{ls} [-]	γ_d [-]	γ_w [-]
SWRC parameters								
F.L. W	-	3.34E-3	0	0.812	1.47E-3	1	-	-
F.L. D	5.85E-3	-	0	0.812	1.47E-3	1	-	-
F.L. H	5.85E-3	3.34E-3	0	0.812	1.47E-3	1	9	9
C.L. W	-	4.60E-5	0	0.604	1.82E-3	1	-	-
C.L. D	1.65E-4	-	0	0.604	1.82E-3	1	-	-
C.L. H	1.65E-4	4.60E-5	0	0.604	1.82E-3	1	4	4

	m [-]	$S_{l,BWC/BWD}$ [-]	S_{ls} [-]	C_r^{Film} [MPa$^{-1.5}$]	a^{Film} [MPa]	d^{Film} [-]
SHCC parameters						
F.L.	0.812	0.15	1	3.22E-9	1.454E-4	-1.5
C.L.	0.604	0.15	1	2.24E-13	1.454E-4	-1.5

	Thermal conductivity*			**Vapour diffusivity***		
	λ_{solid} $\left[\frac{\mathrm{W}}{\mathrm{mK}}\right]$	λ_{gas} $\left[\frac{\mathrm{W}}{\mathrm{mK}}\right]$	λ_{liquid} $\left[\frac{\mathrm{W}}{\mathrm{mK}}\right]$	D $\left[\frac{\mathrm{m^2Pa}}{\mathrm{sK^n}}\right]$	n [-]	τ_0 [-]
F.L.	7.7	0.024	0.6	5.9E-6	2.3	1
C.L.	7.7	0.024	0.6	5.9E-6	2.3	1

*Only used in numerical analyses of stage 3

soils), the CBS was initially almost dry with all the models, and all the hydraulic states were in the pendular state, where hydraulic hysteresis is negligible. In this way, the initial degree of saturation profiles were in essence coincident for all 3 cases. The only exception was at the bottom of the coarser layer where, in a layer a few centimetres thick, the initial degree of saturation values were in general high and the corresponding profiles of initial degree of saturation were different for the W, D and H models. However, this difference in the degree of saturation profiles at the bottom of the C.L. did not affect the results of the simulations, because the bottom boundary was placed sufficiently far below the interface between the two layers that initial conditions close to this bottom boundary had no effect on the results in the finer layer or the upper part of the coarser layer. A discontinuity in suction was initially present at the interface between finer and coarser layer in order to have a hydrostatic profile with $s = 0\,\mathrm{kPa}$ at the bottom in the coarser layer and very low degree of saturation in the finer layer. However, this discontinuity had little effect on the simulations of water transport, because both layers were initially almost dry.

In stage 1, a liquid water flow varying with time was imposed at the top boundary (soil

surface). As shown in Figure 6.10a, a high infiltration rate (a mass flow rate per unit plan area of $2 \times 10^{-1}\,\mathrm{kgs^{-1}m^{-2}}$ corresponding to a volumetric infiltration rate per unit plan area i of approximately $2 \times 10^{-4}\,\mathrm{m/s}$) was imposed at the top boundary for 5 minutes. The infiltration was then stopped ($0\,\mathrm{kgs^{-1}m^{-2}}$) allowing the water to redistribute in the finer layer until almost no further redistribution was predicted. During this period of redistribution, a standard boundary condition of zero liquid flux was applied, rather than an atmospheric boundary condition (see Section 4.1.3). As a consequence, there was no evaporation from the ground surface, which simply acted as an impermeable boundary. After 10 days, this cycle was applied again, i.e. 5 minutes of intense infiltration rate ($2 \times 10^{-1}\,\mathrm{kgs^{-1}m^{-2}}$) and then no infiltration until 20 days. In this stage, the amount of water entering at the top boundary was not enough to cause water breakthrough across the interface. A fixed pore-liquid pressure $p_l = 100\,\mathrm{kPa}$ ($s = 0\,\mathrm{kPa}$) was imposed at the bottom boundary. In this stage, the effect of water retention hysteresis on the redistribution of water occurring in the finer layer after a period of intense rainfall was analysed.

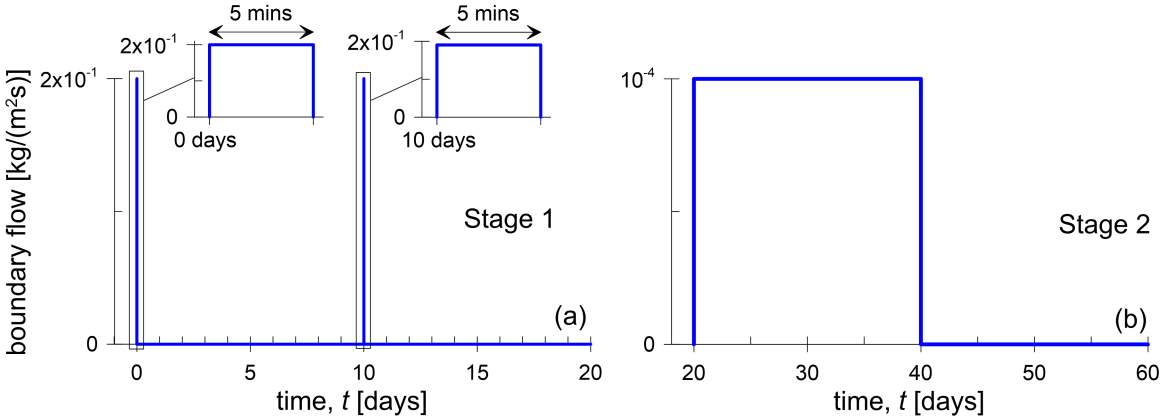

Figure 6.10: Time history of the liquid water flow applied at the top boundary during (a) stage 1 and (b) stage 2

In stage 2, the simulations continued from the end of stage 1 (t=20 days). Therefore, also for stage 2 the analyses were isothermal ($T = 20\,^{\circ}\mathrm{C}$) and water vapour diffusion was excluded. Given that the initial conditions for stage 2 consisted of the final conditions of stage 1, they differed between the analyses in which the models W, D and H were used. The bottom boundary condition in stage 2 still consisted of a fixed pore-liquid pressure $p_l = 100\,\mathrm{kPa}$ ($s = 0\,\mathrm{kPa}$). At the top boundary (see Figure 6.10b), a relatively slow infiltration rate was applied ($1 \times 10^{-4}\,\mathrm{kgs^{-1}m^{-2}}$, corresponding approximately to $i = 1 \times 10^{-7}\,\mathrm{m/s}$) for 20 days (from t=20 days to t=40 days). During this time period, breakthrough occurred with all the models (i.e. W, D and H). At t=40 days, the infiltration was stopped and the simulation was run for other 20 days (from t=40 days to t=60 days) in which post-breakthrough conditions and restoration of the CBS (see Section 2.3.3) were analysed.

In stage 3, non-isothermal simulations were performed in which water vapour diffusion was included. Initial hydraulic conditions were the same as imposed in stage 1 (see Figure 6.9b). In addition, an initial uniform temperature profile, with $T = 25\,^{\circ}\mathrm{C}$ was prescribed. A fixed pore-liquid pressure $p_l = 100\,\mathrm{kPa}$ ($s = 0\,\mathrm{kPa}$) was again imposed at the bottom boundary.

An atmospheric boundary condition was imposed at the soil surface (top boundary), consisting of multiple cycles of rain and evaporation, as shown in Figure 6.11. Each cycle, lasting 12 hours, was composed of 30 minutes of intense rainfall ($P = 1 \times 10^{-2}\,\mathrm{kgs^{-1}m^{-2}}$, corresponding approximately to $i = 1 \times 10^{-5}\,\mathrm{m/s}$) and 11 hours and 30 minutes of evaporation. The evaporation and the different boundary heat fluxes were the result of the assigned atmospheric parameters shown in Table 6.3, where z_0 is the roughness length, z_a is the screen height, ψ is the stability factor, ρ_{ga} is the atmospheric gas density, T_a is the atmospheric temperature, p_{ga} is the atmospheric gas pressure, RH_a is the atmospheric relative humidity, R_n in the radiation and v_a is the wind speed. These atmospheric parameter values are representative of summer weather conditions in Cagliari (Italy) and the choice of these parameter values will be discussed in more detail in Chapter 8. 20 cycles of rain and evaporation were simulated, for a total duration of 240 hours, by means of which the effect of water retention hysteresis on the evaporation from the CBS to the atmosphere was analysed.

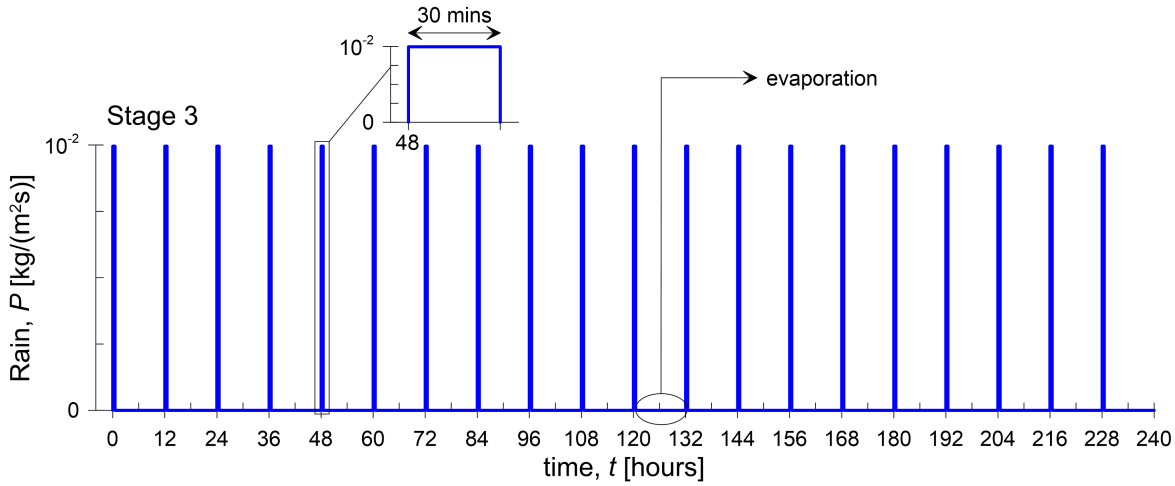

Figure 6.11: Time history of the rain applied at the top boundary during stage 3

Table 6.3: Atmospheric parameters used for numerical analyses during stage 3

z_0 [m]	z_a [m]	ψ [-]	ρ_{ga} [kg/m^3]	T_a [°C]	p_{ga} [MPa]	RH_a [-]	R_n [J m^{-2}s^{-1}]	v_a [m/s]
0.001	2	1	1.1883	25.5	0.1	0.65	325	3.14

6.2.2 Results and discussion

In this Section the results of the numerical simulations of stage 1, stage 2 and stage 3 are presented.

Stage 1: water redistribution

Numerical simulations of stage 1 were performed to analyse the role of water retention hysteresis during water redistribution occurring within the finer layer after intense rainfall

events. With this purpose, short but very intense rainfall events were followed by long periods where no rain was applied (see Figure 6.10a).

Figure 6.12 shows suction and degree of saturation profiles obtained at different times in stage 1, using the main wetting curve model (W), the main drying curve model (D) and the full hysteretic model (H). The results at 4 key times are shown in Figure 6.12: t=5 minutes which is at the end of the first intense rainfall event (Figures 6.12a and 6.12b), t=10 days which is at the end of the water redistribution period following the first intense rainfall event (Figures 6.12c and 6.12d), t=10 days and 5 minutes which is at the end of the second intense rainfall event (Figures 6.12e and 6.12f) and t=20 days which is at the end of the water redistribution period following the second intense rainfall event (Figures 6.12g and 6.12h).

At the end of the first intense rainfall event (t=5 minutes) (see Figures 6.12a and 6.12b), a sharp wetting front is located at a height of approximately 1.10 m. Above this wetting front, the soil is almost saturated whereas, below the wetting front, the CBS is approximately in the initial conditions. This type of infiltration pattern is typical of high ratios of infiltration rate compared to unsaturated hydraulic conductivity [137, 198], i.e. high values of i/k_l where i is the infiltration rate and k_l is the unsaturated hydraulic conductivity. At this time (t=5 minutes), the results obtained with the H model coincide with the results obtained with the W model because only wetting occurred. Slightly higher suction values are predicted with the D model close to the soil surface.

After the first intense infiltration event, water redistribution occurs within the finer layer. After 10 days, further water movements are negligible. At this time, different suction profiles (Figure 6.12c) and degree of saturation profiles (Figure 6.12d) are predicted with the different models. The suction profile in the finer layer obtained with the hysteretic model (H) is intermediate between the profiles obtained with the main wetting model (W) and the main drying model (D). However, a different pattern is found in the degree of saturation profiles in the finer layer. In contrast with the profiles obtained with the W model and the D model, which show S_l monotonically decreasing from the interface to the surface, the degree of saturation profile obtained with the H model is decreasing from point A (the interface) to point B, increasing from point B to point D and again decreasing from point D to point E (the surface). These profiles obtained in the finer layer with the H model can be interpreted more clearly if plotted in the $s : S_l$ plane and compared with the adopted SWRCs of the finer layer, as shown in Figure 6.13a. From the observation of this graph, it can be seen that the hydraulic states of the soil at the heights between point A and point B lie almost on the main wetting curve, between point D and point E they lie almost on the main drying curve and between point B and D they lie on different scanning curves. The following interpretation can be given. During the initial intense rainfall event, the soil in the upper part of the finer layer (from point D to point E) initially reaches high values of degree of saturation and low values of suction. When infiltration is stopped, the water in this zone starts flowing downwards and the soil in the upper part of the finer layer significantly dries out and suction significantly increases, and hence the soil included between points D and E moves along scanning drying curves and onto the main drying curve (see the scanning drying curve followed by the soil at

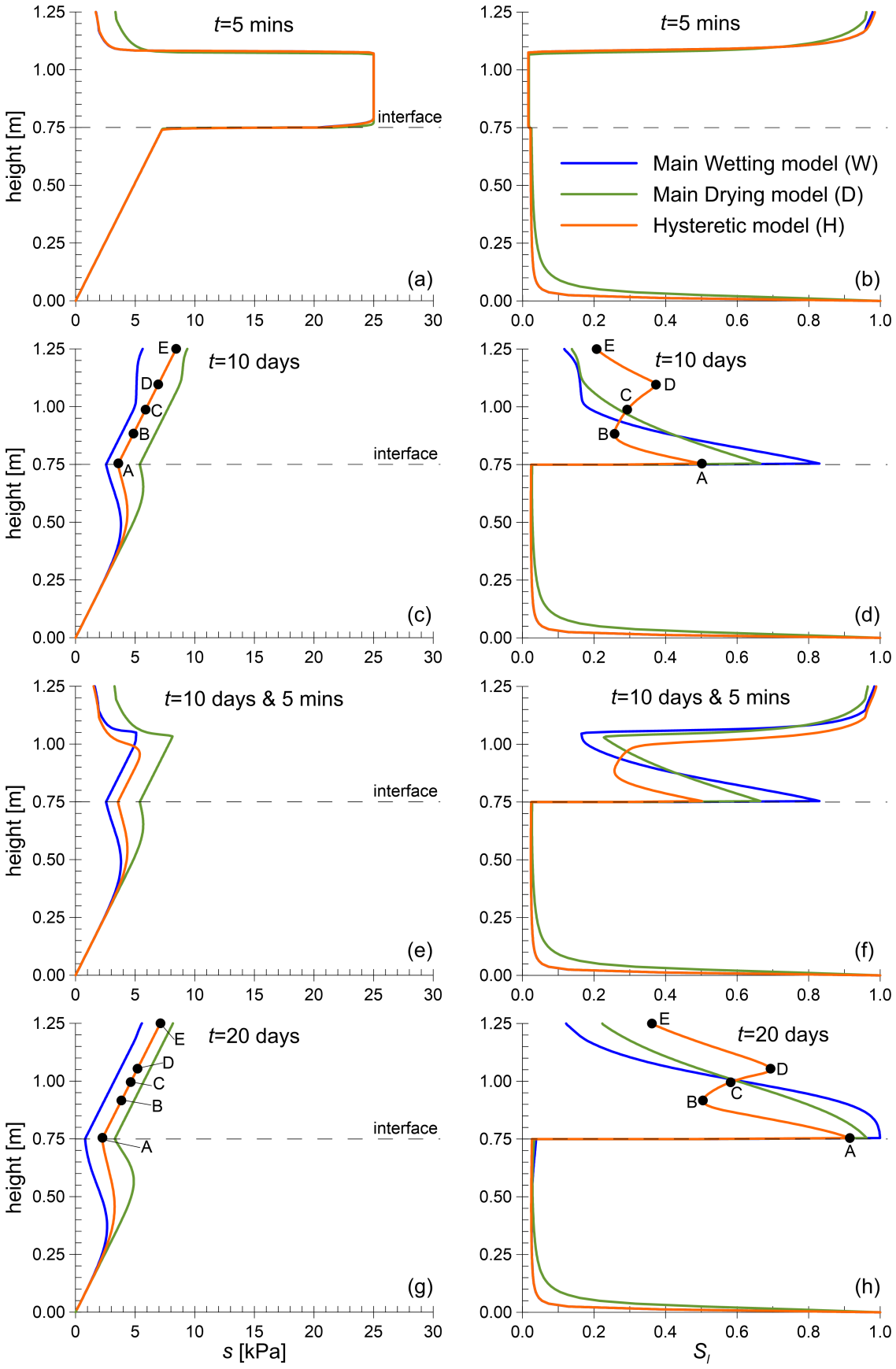

Figure 6.12: Suction (a, c, e, g) and degree of saturation (b, d, f, h) profiles at different times during stage 1

point D, indicated by a dashed line in Figure 6.13a). A similar process occurs in the soil at heights between points B and D but, in this case, the first wetting does not cause high values of degree of saturation and the subsequent increase of suction due to drying is not sufficiently high for the hydraulic states to reach the main drying curve (see the scanning drying curve followed by the soil at point C, indicated by a second dashed line in Figure 6.13a). Therefore, the hydraulic states of the soil at heights between point B and point D are located on different scanning curves. Finally, the soil at heights between point A and point B experience only main wetting paths because these points have experienced only monotonic wetting.

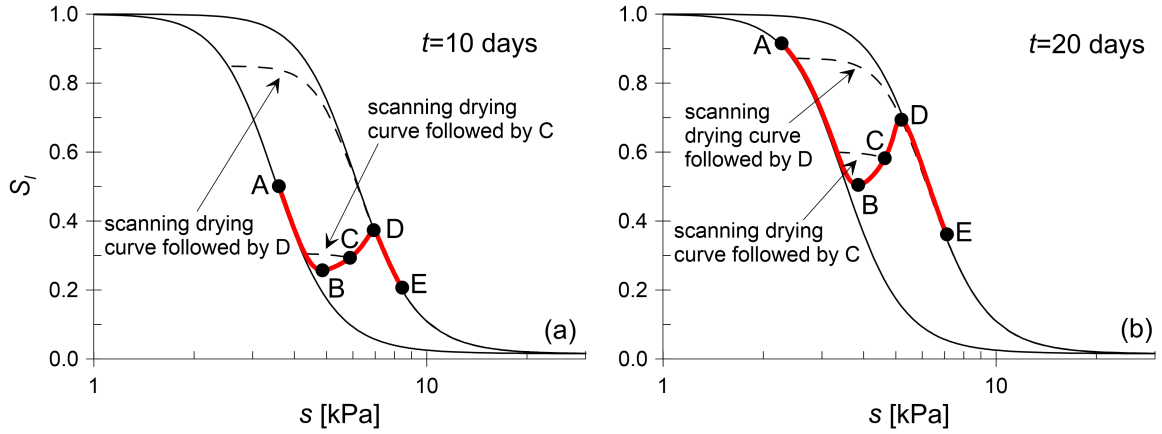

Figure 6.13: Interpretation of the $s : S_l$ profiles in the finer layer at times (a) t=10 days and (b) t=20 days during stage 1

At the end of the second rainfall event (t=10 days and 5 minutes) (see Figures 6.12e and 6.12f), the soil in the upper part of the finer layer is almost saturated and, below a sharp wetting front, the suction and degree of saturation profiles are approximately coincident with those obtained before the beginning of the rainfall event. As a consequence, the finer layer shows a complex variation of degree of saturation (see Figure 6.12f) with very high values of S_l at the top (above the wetting front), moderately high values of S_l at the bottom (caused by the redistribution of water during the previous dry period) and lowest values of S_l within an intermediate zone.

At the end of the second water redistribution period (t=20 days) (see Figures 6.12g and 6.12h), the patterns obtained in the suction and degree of saturation profiles are similar to those obtained at t=10 days. The graphical interpretation in the $s : S_l$ plot of the hydraulic states of the soil in the finer layer is shown in Figure 6.13b. In this case, the higher amount of water stored in the finer layer leads to higher values of degree of saturation and lower values of suction, but the phenomenon of water redistribution within the finer layer of the CBS can be interpreted in the same way as at t=10 days.

Generally speaking, the modelling of water retention hysteresis leads to significantly different predictions of the redistribution of water in the finer layer of a CBS after intense rainfall events than is predicted by using a unique SWRC (irrespective of whether this unique SWRC is a main wetting curve or a main drying curve). Given that rainfall events produce mainly wetting in the soil, it might be expected that the main wetting curve alone would be adequate to model the situation of stage 1. However, the redistribution of water generates

wetting in certain portions of the finer layer and drying in other parts of the finer layer. This explains why the use of the hysteretic model leads to different results compared to the use of only the main wetting curve. Moreover, in contrast with what might be expected, the degree of saturation profiles obtained with the H model are not intermediate between the profiles obtained with the W model and the D model. Finally, the use of the H model leads to the prediction of a more uniform water distribution in the finer layer compared to the W and D models (see, in particular, Figures 6.12d and 6.12h).

Stage 2: breakthrough and post-breakthrough

Numerical simulations of stage 2 were performed to analyse the role of water retention hysteresis on the prediction of water breakthrough from the finer layer to the coarser layer of a CBS and the subsequent restoration of the barrier occurring after breakthrough. Starting from the final conditions of stage 1, rainfall was applied for 20 days during which breakthrough occurred (see Figure 6.10b). After the rain was stopped, further 20 days were simulated to analyse the post-breakthrough and restoration phase.

Figure 6.14 shows the time histories of the downward liquid flows occurring across the interface between finer layer and coarser layer, predicted with the W model, the D model and the H model. The times at breakthrough and at restoration are marked by the symbols in Figure 6.14. The times at breakthrough were identified as the the times at which the water velocity across the interface first dramatically increases whereas the times at restoration were identified as the times at which water infiltration across the interface almost stops. It should be noted that significantly different times at breakthrough are predicted with the different models: the earliest is obtained with the W model, the second with the H model and the latest with the D model. Accordingly, the highest water storage capacity is predicted with the D model and the lowest with the W model.

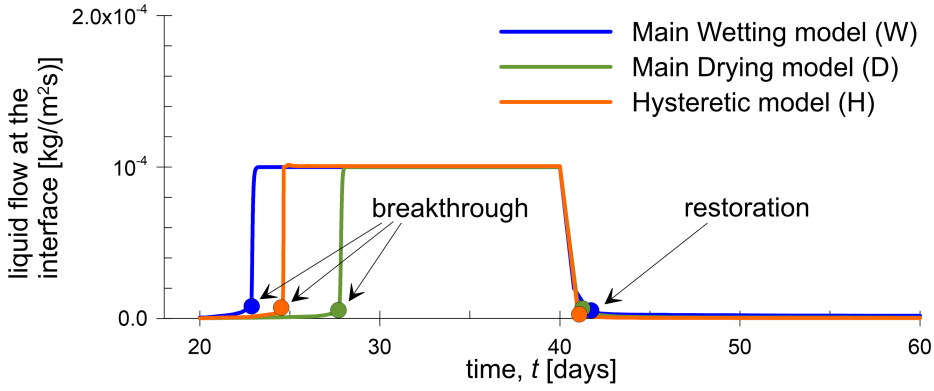

Figure 6.14: Time history of liquid water flow rate across the interface during stage 2

Figure 6.15 shows the suction and degree of saturation profiles at breakthrough (solid lines) and at restoration (dashes lines) obtained with the different models. Figure 6.16 shows the positions of the hydraulic states $s : S_l$ of the soil in the coarser layer at the interface, at breakthrough and at restoration, in comparison with the main drying curve and the main wetting curve of the coarser layer. As expected, when the W model and the H model are

used, the suction at the interface at breakthrough is equal to the BWC value of the coarser layer (see Figures 6.15a and 6.16). However, using the D model, the suction at the interface at breakthrough is equal to the BWD point of the coarser layer (see Figures 6.15a and 6.16) because, in this case, only the main drying curve is used and the BWD point represents the point at which the bulk water component of the main drying SHCC increases from zero. From these suction values at the interface, the suction profiles are approximately hydrostatic in the finer layer, with the exception of the upper part of the profile predicted with the W model which deviates from the linear trend (see Figure 6.15a). Although the suction profiles in the F.L. at breakthrough obtained with the W model and the H model are almost coincident, the corresponding degree of saturation profiles are different because the water redistribution followed different patterns during stage 1. Consequently, the water storage capacity predicted with the H model is slightly higher than that predicted with the W model.

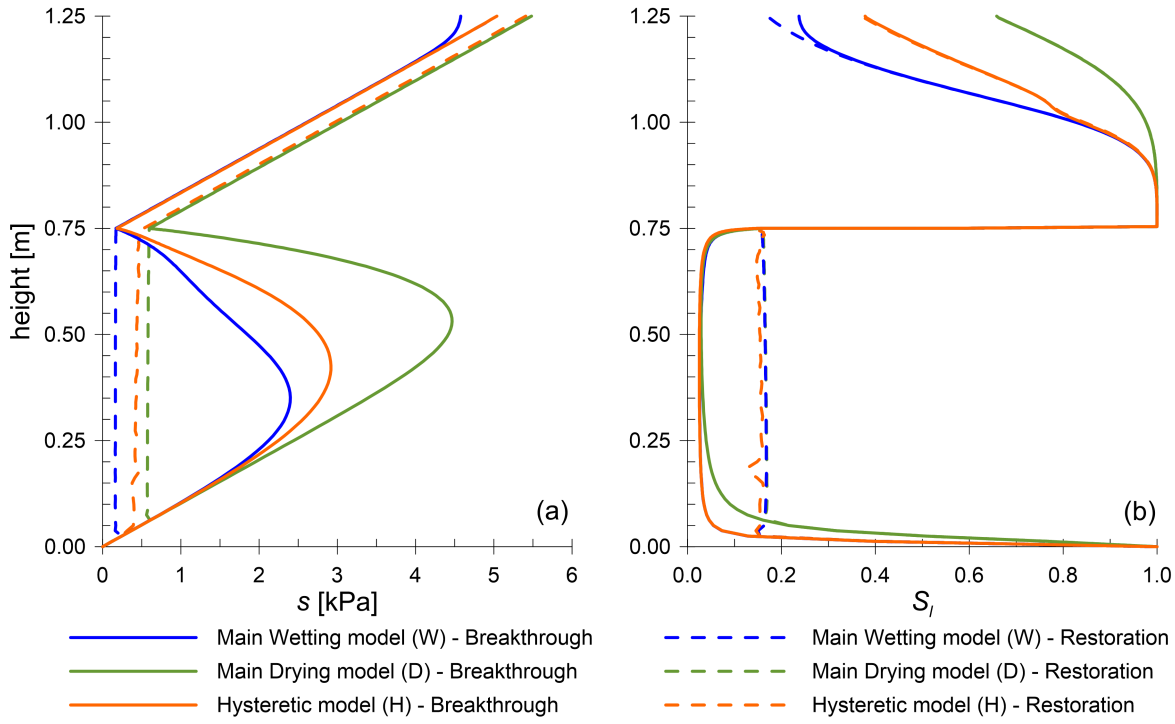

Figure 6.15: Suction (a) and degree of saturation (b) profiles at breakthrough and restoration during stage 2

After infiltration was stopped and the water flow across the interface ceased, at restoration, the suction at the interface and the suction profiles in the F.L. predicted with the W model and the D model remain approximately the same as they are at breakthrough (see Figures 6.15a and 6.16). By contrast, the suction at the interface predicted with the hysteretic model (H) moves from the BWC value of the coarser layer at breakthrough approximately to the BWD value of the coarser layer at post-breakthrough (see Figures 6.15a and 6.16). Consequently, the suction profile predicted with the H model is almost coincident with the profile predicted with the W model at breakthrough whereas it is almost coincident with the profile predicted with the D model at restoration (see Figure 6.15a). This increase of suction at the interface occurring after water breakthrough ceases was observed experimentally by Stormont and Anderson

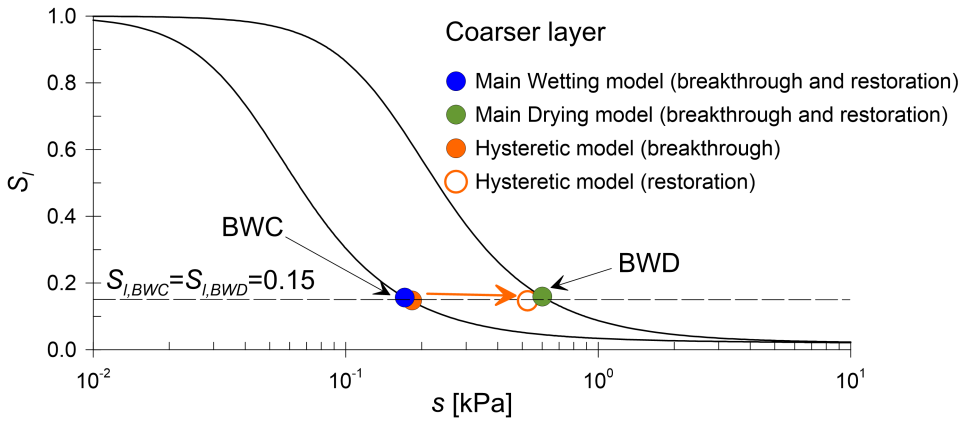

Figure 6.16: Interpretation of the $s : S_l$ points in the coarser layer at the interface at breakthrough and restoration during stage 2

[23] and it was identified with the restoration of the capillary barrier (see Section 2.3.3 and Figure 2.23).

Therefore, whereas the W model may be adequate to represent the hydraulic behaviour of the CBS up to breakthrough it is not able to represent correctly the post-breakthrough and restoration conditions. On the other hand, the D model is able to capture the restoration conditions but it is unable to correctly represent the hydraulic behaviour of the CBS at breakthrough. Only the hysteretic model is able to represent adequately both the breakthrough conditions and the restoration of the CBS after infiltration at the ground surface ceases.

Stage 3: effect of evaporation

Stage 3 was simulated numerically to study the effect of hydraulic hysteresis on the prediction of evaporation to the atmosphere from a CBS. The CBS, which was initially almost dry, was subjected to 20 cycles of 30 minutes of rain and 11 hours and 30 minutes of evaporation (see Figure 6.11) simulating relatively hot and dry weather conditions (representative of summer conditions in Cagliari, Italy).

As results of the simulations, Figure 6.17 shows the time histories of (a) evaporation, (b) cumulative evaporation, (c) water breakthrough across the interface, (d) mean degree of saturation S_l of the finer layer and (e) cumulative inflows and outflows in the finer layer. The cumulative evaporation was obtained by integrating the evaporation over time. The mean degree of saturation of the finer layer was obtained by integrating spatially the degree of saturation over the depth of the finer layer and subsequently dividing it by the thickness of the finer layer. The cumulative flows in Figure 6.17e were obtained by integrating over time the inflow from the top surface (i.e. rain minus evaporation), and the outflow from the finer layer across the interface with the coarser layer (i.e. breakthrough), and the difference between cumulative inflow and cumulative outflow was finally calculated.

In the first 7 cycles (0 h<t<84 h), the evaporation fluxes predicted with the W and D models almost coincide whereas the evaporation predicted with the H model is, in cumulative terms, significantly higher (see Figures 6.17a and 6.17b). In each cycle, the evaporation predicted with the W and D models is indeed initially high but it rapidly decreases whereas

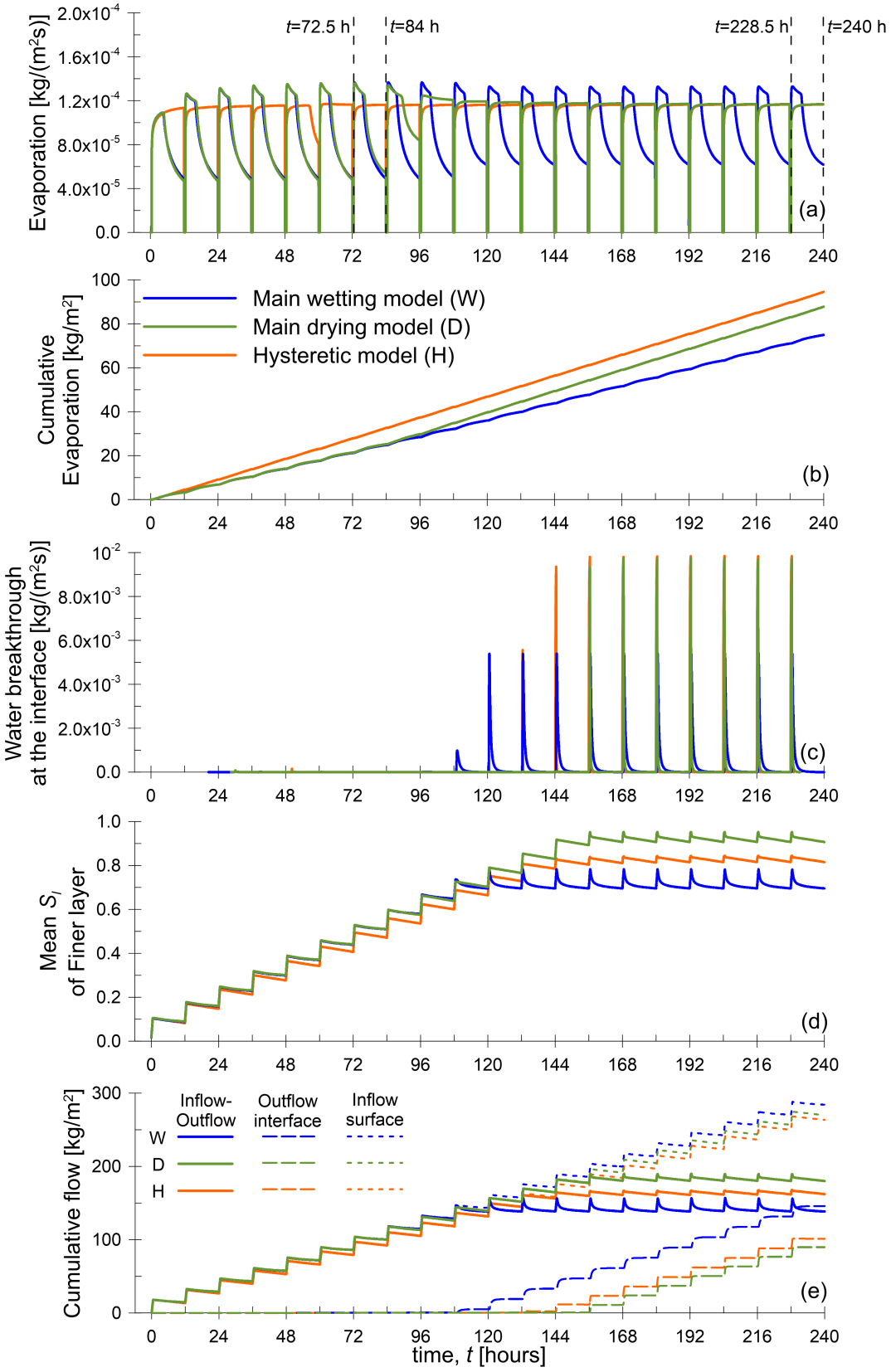

Figure 6.17: Time histories of (a) evaporation, (b) cumulative evaporation, (c) water breakthrough across the interface, (d) mean degree of saturation S_l of the finer layer and (e) cumulative inflow and outflows to/from the finer layer during stage 3

the evaporation predicted with the H model remains relatively high during almost all the evaporation periods (see Figure 6.17a). These different evaporation patterns can be better understood by an inspection of the corresponding degree of saturation profiles at the beginning of a cycle (e.g. t=72.5 h) and at the end of the same cycle (e.g. t=84 h), as shown in Figures 6.18a and 6.18b. At the beginning of a cycle, when the evaporation rate predicted by all the models is relatively high (see Figure 6.17a), the degree of saturation values at the soil surface predicted with all the models are relatively high (see Figure 6.18a). By contrast, at the end of a cycle, when the evaporation rate predicted with the H model is relatively high but that predicted with the W and D models is extremely low (see Figure 6.17a), the degree of saturation at the surface predicted with the H model is moderately high whereas that predicted with the W and D models is very low, approaching zero (see Figure 6.18b). This agrees with the interpretation of the evaporation from soils given in Section 2.4.2, according to which the evaporation rate is higher from wetter soil surfaces (see Figure 2.28) [178]. In other words, with the H model the water distribution is predicted to be more uniform in the finer layer compared to the W and D models, according to which most of the water is stored close to the interface (see Figure 6.18b). With the H model, the higher availability of water close to the surface causes higher evaporation rates being sustained for longer times.

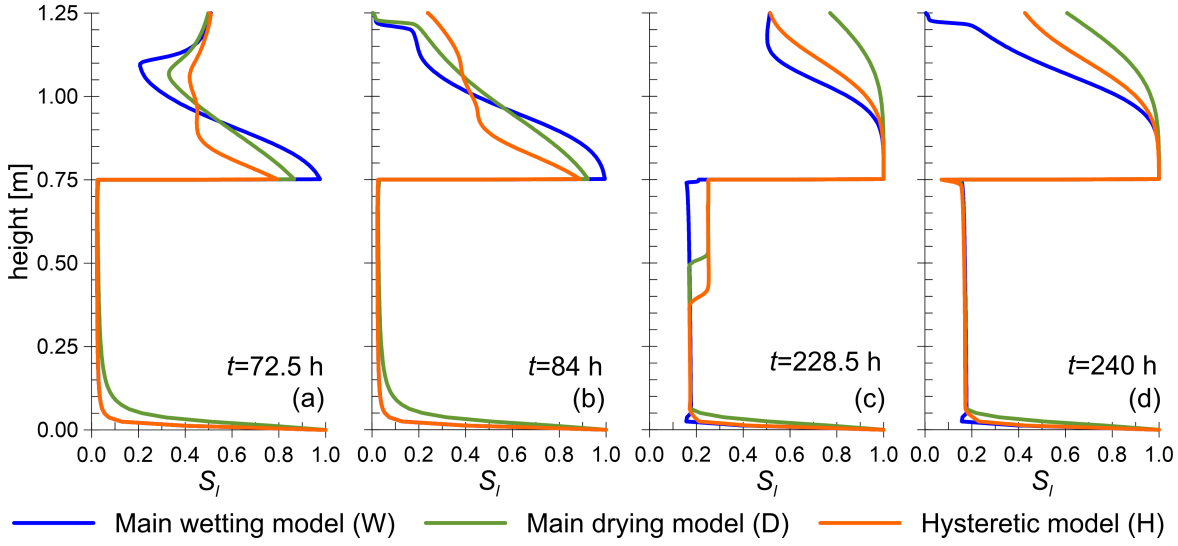

Figure 6.18: Degree of saturation profiles at different times during stage 3: (a) t=72.5 h, (b) t=84 h, (c) t=228.5 h and (d) t=240 h

For subsequent cycles (in particular for t>120 h), the evaporation rate predicted with the W model follows the same patterns as before whereas the evaporation rate predicted with the D model coincides with that predicted with the H model (see Figures 6.17a and 6.17b). This can again be better understood by observing the degree of saturation profiles at the beginning of a cycle (e.g. t=228.5 h) (see Figure 6.18c) and at the end of the same cycle (e.g. t=240 h) (see Figure 6.18d). At the beginning of the cycle, relatively high values of degree of saturation at the surface were predicted with all the models (see Figure 6.18c) as well as relatively high evaporation rates (see Figure 6.17a). In this situation, a higher amount of water is in general stored in the F.L. with respect to the initial cycles (compare Figures 6.18a and 6.18c) and the

water stored close to the surface predicted with the D model is now much higher, even higher than that predicted with the H model. Consequently, at the end of the cycle (see Figure 6.18d), the degree of saturation values predicted with the D and H models at the surface both remain relatively high whereas the degree of saturation value predicted with the W model at the surface is very low, approaching zero.

The time histories of the cumulative inflow at the soil surface (see dotted lines in Figure 6.17e) reflect the evaporation patterns described above because these time histories represent the difference between the cumulative rain and the cumulative evaporation. Therefore, in the first cycles, the cumulative inflows predicted with the D model and with the W model are coincident and they are higher than that predicted with the H model. For subsequent cycles, when a higher amount of water is stored in the finer layer, the cumulative inflows predicted by the D and W models gradually diverge, whereas the cumulative inflows predicted by the D and H models differ by a fixed amount.

The outflow from the finer layer through the interface (i.e. water breakthrough from the finer layer to the coarser layer) (see Figure 6.17c and the dashed lines in Figure 6.17e) is a result of the effects of the evaporation and of the water storage capacity of the CBS. Breakthrough is predicted to start after a lower number of cycles with the W model and, in each cycle, a higher total volume of water flows from the finer layer to the coarser layer. This is due to the low cumulative evaporation and low water storage capacity of the CBS when the W model is used. Comparing the predictions of the H model and of the D model, water breakthrough predicted with the H model starts one cycle earlier than water breakthrough predicted with the D model because a higher water storage capacity of the CBS is predicted with the D model. After breakthrough started with both the H model and the D model, in each cycle a similar amount of cumulative water outflow is predicted because the cumulative evaporations are similar with both models.

The mean degree of saturation of the finer layer (see Figure 6.17d) is a reflection of the difference between the inflow and the outflow in the finer layer (see the solid lines in Figure 6.17e). In the initial cycles, as predicted by all the models, the mean degree of saturation of the finer layer starts increasing because the cumulative rain is higher than the cumulative evaporation and water breakthrough does not occur. In the initial cycles, the mean degree of saturation of the finer layer is predicted to increase more rapidly with the D and W models than with the H model, as a result of the different patterns of evaporation described above. When the water storage capacities of the CBS are attained (higher with the D model, intermediate with the H model, lower with the W model), the variations of the mean degree of saturation of the finer layer predicted with the different models become stable with an overall constant trend where, in each cycle, an initial increase due to the applied rain is followed by a subsequent decrease due to evaporation and water breakthrough.

In general, compared to the use of the main wetting curve alone or the main drying curve alone, the use of the full hysteretic model leads to significantly different predictions of the thermo-hydraulic response of the CBS when subjected to cycles of rain and evaporation. Therefore, the lack of consideration of hydraulic hysteresis in the simulation of the cyclic

behaviour of CBSs may lead to unreliable results. Higher evaporation rates are in general predicted using the H model, as also confirmed by the results of Zhang et al. [166]. Moreover, the water storage capacity and the percolation into the coarser layer predicted with the H model are intermediate between those predicted with the W model and those predicted with the D model.

6.3 Minimum water storage capacity of capillary barrier systems

The water storage capacity (WSC) of a capillary barrier system, namely the maximum amount of water that can be stored in the finer layer before water breakthrough occurs through the interface between finer and coarser layer, is strongly affected by the infiltration rate, as discussed in Section 2.3.3. In general, the water storage capacity of CBSs increases with increasing infiltration rate if this infiltration rate is applied continuously until breakthrough. In this section, it is shown that the water storage capacity associated to a high infiltration rate cannot be relied upon, because an amount of water less than this may produce a delayed breakthrough (some time after infiltration at the ground surface has stopped). The only amount of water that can be stored in the finer layer in the long-term is the minimum water storage capacity. This minimum water storage capacity is that corresponding to the application of a very low constant infiltration rate.

6.3.1 Numerical model

One-dimensional numerical simulations of infiltration processes in a capillary barrier were performed with different infiltration rates applied for different periods of time. In these analyses, a uniform and constant distribution of temperature was considered, the solid phase was considered as non-deformable and the gas phase as non-mobile. Thus, constant and uniform values of displacements of the solid phase ($\boldsymbol{u} = 0\,\text{m}$), gas pressure ($p_g = 100\,\text{kPa}$) and temperature ($T = 20\,^{\circ}\text{C}$) were imposed.

The model analysed was a vertical column of soil made of two layers: an upper layer, 0.8 m thick, representing the finer layer (F.L.) of a CBS and a lower layer, 0.75 m thick, representing the coarser layer (C.L.). The thickness of the coarser layer was unrealistically high in order to have the bottom boundary sufficiently far from the interface so that the phenomenon of breakthrough was not affected by any influence of the bottom boundary.

A structured mesh made of quadrilateral elements was used for the CBS. The mesh of the coarser layer was divided into two parts: from the bottom boundary (0 m) to a height of 0.25 m, 20 uniformly spaced elements were used in the vertical direction; from a height of 0.25 m to the interface with the F.L. (0.75 m), 120 elements were used in the vertical direction with a mesh refinement gradient of 0/0.1 (finer toward the interface). The mesh of the finer layer was characterised by 120 elements uniformly spaced in the vertical direction.

The materials forming the two layers were each modelled by defining the hydraulic constitutive models (SWRC and SHCC), the intrinsic permeability and the porosity. Each of the two layers was considered as a uniform material. The same material properties used in the simulations presented in Section 6.2 were used for these analyses. The parameters chosen to model the finer layer were representative of a fine sand whereas those of the coarser layer were representative of a gravelly sand (see Table 6.2). The hydraulic behaviour of the materials (see Figures 6.9c and 6.9d) were modelled using the full hysteretic modVG-modM+LF model, with the liquid film conductivity parameter C_r^{Film} obtained using the default value of the parameter X_D.

In all the simulations, initial conditions consisted of a hydrostatic linear distribution of pore-water pressure in the coarser layer, with $p_l = 100\,\text{kPa}$ ($s = 0\,\text{kPa}$) at the bottom of the model and $p_l = 92.5\,\text{kPa}$ ($s = 7.5\,\text{kPa}$) at the interface, and a constant value of pore-water pressure in the finer layer, with $p_l = 75\,\text{kPa}$ ($s = 25\,\text{kPa}$). The value of $p_l = 100\,\text{kPa}$ ($s = 0\text{kPa}$) was set as a bottom bottom boundary condition. The initial suction and degree of saturation profiles were similar to those shown in Figure 6.9b but, in the analyses presented in this sub-section, the finer layer is thicker.

Four different simulations were performed and different top boundary conditions were applied for each of them. In the first and second simulations, a constant low infiltration rate $i = 1 \times 10^{-7}\,\text{m/s}$ and a constant high infiltration rate $i = 5 \times 10^{-5}\,\text{m/s}$ were respectively applied at the top boundary for a duration sufficiently long to cause water breakthrough at the interface between finer and coarser layer. With these two simulations, the water storage capacity of the CBS associated to the two corresponding constant infiltration rates was determined.

Subsequently, two further simulations were performed to assess the role of water redistribution on the water storage capacity of the CBS. In the first of these two analyses (path 1), the high infiltration rate $i = 5 \times 10^{-5}\,\text{m/s}$ was applied for a duration of 0.8 hours, such that the total volume of infiltrated water was lower than the water storage capacity obtained from the simulation where a continuous low infiltration rate $i = 1 \times 10^{-7}\,\text{m/s}$ was applied. After 0.8 hours the infiltration at the top boundary was stopped and the hydraulic behaviour of the CBS was monitored during redistribution of water, with an impermeable boundary condition at the ground surface.

In the fourth and last simulation (path 2), the high infiltration rate $i = 5 \times 10^{-5}\,\text{m/s}$ was applied over four time intervals, each with a duration of 0.333 hours (i.e. 0-0.333 hours, 5-5.333 hours, 10-10.333 hours and 15-15.333 hours). These periods of infiltration were alternated with four time intervals in which no infiltration rate was applied (i.e. 0.333-5 hours, 5.333-10 hours, 10.333-15 hours and 15.333-30 hours) i.e. an impermeable boundary condition at the ground surface. In the intervals in which no infiltration rate was applied, the hydraulic behaviour of the CBS was monitored during redistribution of water within the CBS.

6.3.2 Numerical results

Figure 6.19 shows the results of the two simulations in which two different constant infiltration rates were applied at the surface, a low infiltration rate $i = 1 \times 10^{-7}\,\mathrm{m/s}$ (Figures 6.19a and 6.19b) and a high infiltration rate $i = 5 \times 10^{-5}\,\mathrm{m/s}$ (Figures 6.19c and 6.19d). In particular, Figures 6.19a and 6.19c show the time histories of the water velocity applied at the surface (orange lines) and recorded at the interface between finer and coarser layer (blue lines) whereas Figures 6.19b and 6.19d show the corresponding cumulative liquid flows, calculated by integrating the time histories of liquid velocity over time. In addition, Figures 6.19b and 6.19d also show the difference between the cumulative flows applied at the surface and the cumulative flows recorded at the interface (black dashed lines). The water breakthrough at the interface starts after approximately 472 hours for $i = 1 \times 10^{-7}\,\mathrm{m/s}$ and 1.523 hours for $i = 5 \times 10^{-5}\,\mathrm{m/s}$.

In both Figures 6.19b and 6.19d, the difference between the cumulative flow at the surface and at the interface initially increases like the cumulative flow at the surface, because a negligible amount of water initially flows across the interface. When breakthrough occurs, the percolation rate across the interface rapidly increases up to the applied infiltration rate ($i = 1 \times 10^{-7}\,\mathrm{m/s}$ in Figure 6.19a and $i = 5 \times 10^{-5}\,\mathrm{m/s}$ in Figure 6.19c). After breakthrough, the difference between the cumulative flows at the surface and at the interface becomes approximately constant because the percolation rate at the interface approximately equals the infiltration rate at the surface. Therefore, the approximately constant values attained by the differences between the cumulative flows at the surface and at the interface can be seen as the water storage capacities of the CBS respectively for the applied infiltration rate $i = 1 \times 10^{-7}\,\mathrm{m/s}$ (black line in Figure 6.19b) and $i = 5 \times 10^{-5}\,\mathrm{m/s}$ (black line in Figure 6.19d). It can be seen that, as expected, the water storage capacity of the CBS obtained with the higher infiltration rate $i = 5 \times 10^{-5}\,\mathrm{m/s}$, which is 0.288 m, is higher than that obtained with the lower infiltration rate $i = 1 \times 10^{-7}\,\mathrm{m/s}$, which is 0.170 m.

Note that the spikes present in the time histories of liquid velocity at the interface in Figures 6.19a and 6.19c are the results of solving challenging numerical problems but they do not have a real physical relevance. In particular, in the numerical simulations, when the wetting front propagating within the F.L. reaches the interface with the C.L., the suction significantly drops at that location compared to the initial value and a very sharp hydraulic gradient across the interface is attained. This causes a sudden increase of liquid velocity across the interface although the hydraulic conductivity of the C.L. is still very small (i.e. breakthrough has not occurred yet). After this sudden increase of liquid velocity, the hydraulic gradient across the interface becomes rapidly smoother and the liquid velocity suddenly drops and it remains very small until breakthrough. This numerical effect has a negligible impact on the cumulative flows (see Figures 6.19b and 6.19d).

The higher water storage capacity obtained with the application of the higher infiltration rate $i = 5 \times 10^{-5}\,\mathrm{m/s}$ is clarified by inspection of Figure 6.20, which shows the profiles of suction (Figure 6.20a) and degree of saturation (Figure 6.20b) obtained in the finer layer at breakthrough. As already discussed in Section 2.3.3, higher values of suction are attained

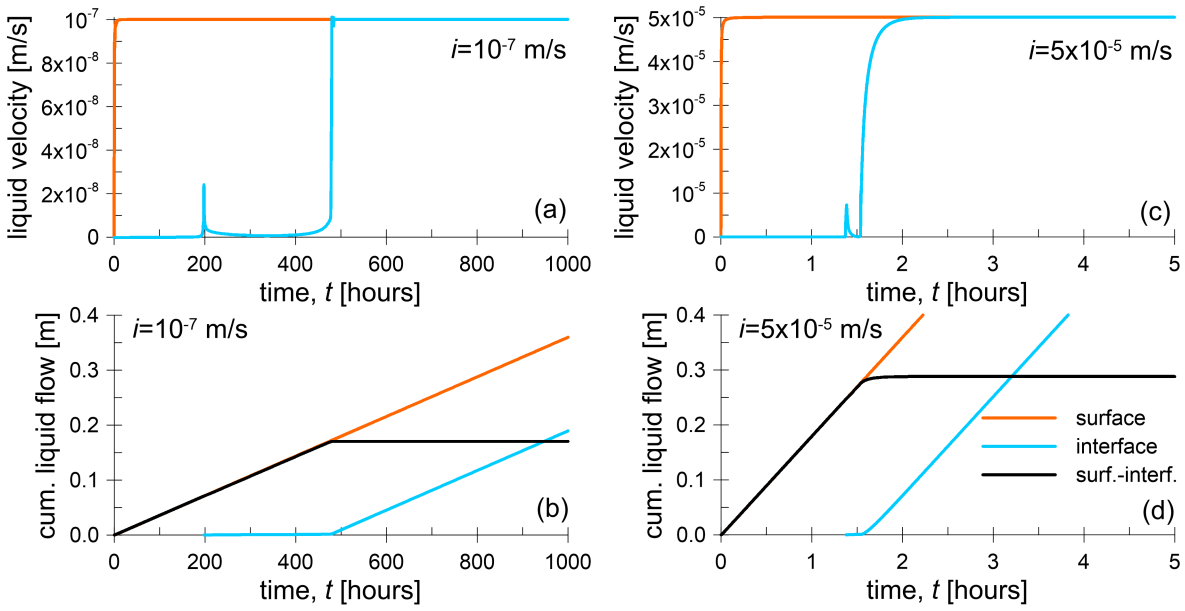

Figure 6.19: Time history of liquid velocity (a-c) and cumulative liquid flow (b-d) at the surface and at the interface for the applied continuous infiltration rates $i = 1 \times 10^{-7}\,\mathrm{m/s}$ and $i = 5 \times 10^{-5}\,\mathrm{m/s}$

in the upper part of the finer layer when the lower infiltration rate is applied. Consequently, lower values of degree of saturation are attained in the upper part of the finer layer, and hence a lower water storage capacity, when the lower infiltration rate is applied.

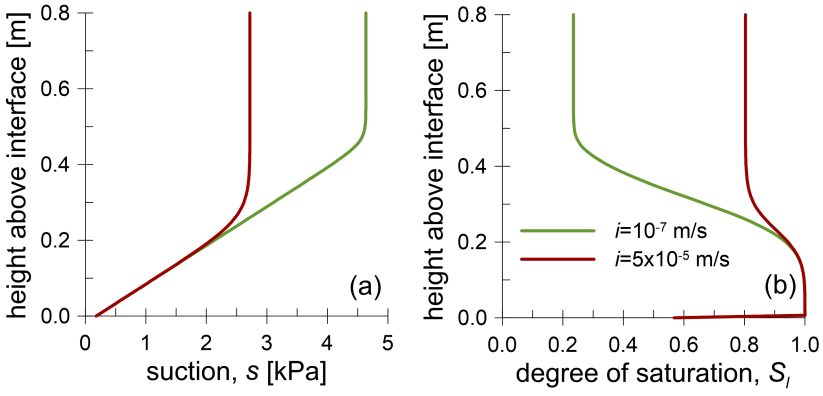

Figure 6.20: Profiles of suction (a) and degree of saturation (b) at breakthrough obtained for the applied continuous infiltration rates $i = 1 \times 10^{-7}\,\mathrm{m/s}$ and $i = 5 \times 10^{-5}\,\mathrm{m/s}$

The higher water storage capacity obtained with a higher constant infiltration rate may not be a reliable quantity for design purposes, due to the effect of water redistribution occurring within the finer layer after the water infiltration at the surface is stopped. In order to analyse this effect, two additional simulations were performed, considering infiltration path 1 and infiltration path 2 described earlier.

Figures 6.21a and 6.21b show the results of the application of infiltration path 1, in terms of the time histories of the water velocity applied at the top surface and predicted at the interface (Figure 6.21a) and the corresponding cumulative flows (Figure 6.21b). In this simulation, the higher infiltration rate $i = 5 \times 10^{-5}\,\mathrm{m/s}$ was applied for a duration of

0.8 hours and subsequently stopped (see orange lines in Figures 6.21a and 6.21b). The total amount of infiltrated water was slightly lower than the water storage capacity (WSC) obtained with the application of the constant lower infiltration rate $i = 1 \times 10^{-7}\,\mathrm{m/s}$, i.e. $WSC\left(i = 1 \times 10^{-7}\,\mathrm{m/s}\right) = 0.170\,\mathrm{m}$. It can be seen that, in this situation, no noticeable water breakthrough is recorded even after redistribution of water in the finer layer occurs.

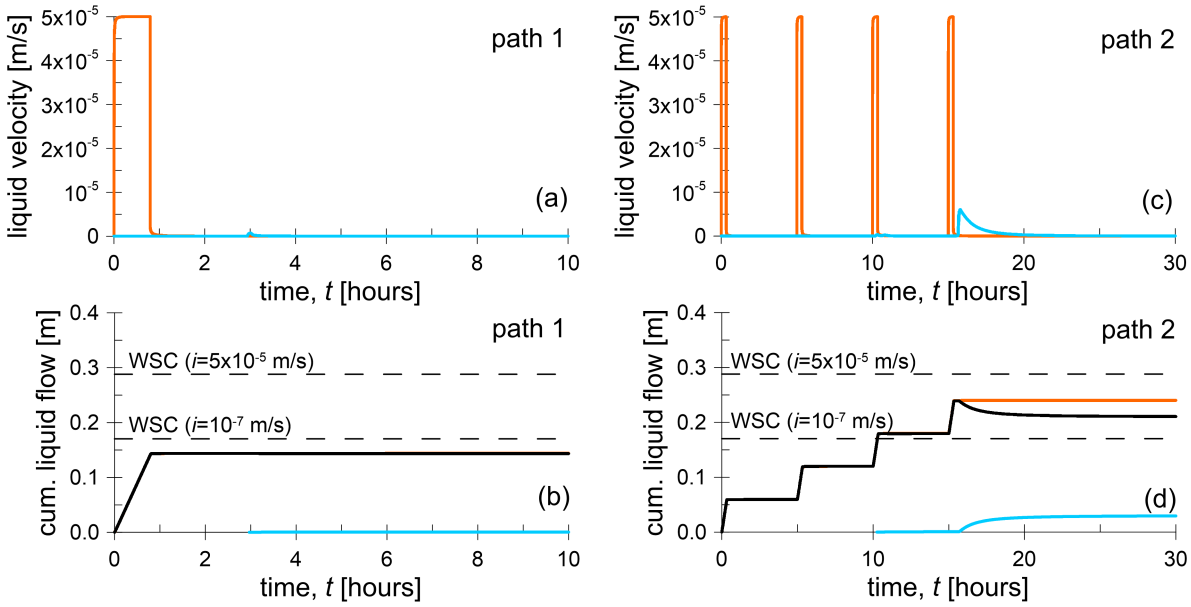

Figure 6.21: Time history of liquid velocity (a-c) and cumulative liquid flow (b-d) at the surface and at the interface for infiltration path 1 (a-b) and infiltration path 2 (c-d)

Figures 6.21c and 6.21d show the results of the application of infiltration path 2, in terms of the time histories of the water velocity applied at the top surface and recorded at the interface (Figure 6.21c) and the corresponding cumulative flows (Figure 6.21d). In this simulation, four time intervals in which the high infiltration rate $i = 5 \times 10^{-5}\,\mathrm{m/s}$ was applied for a duration of 0.333 hours were alternated with four time intervals in which no infiltration rate was applied (see orange lines in Figures 6.21c and 6.21d). In this case, the total amount of infiltrated water was lower than the water storage capacity obtained with the application of the constant higher infiltration rate $i = 5 \times 10^{-5}\,\mathrm{m/s}$, i.e. $WSC\left(i = 5 \times 10^{-5}\,\mathrm{m/s}\right) = 0.288\,\mathrm{m}$, but higher than $WSC\left(i = 1 \times 10^{-7}\,\mathrm{m/s}\right) = 0.170\,\mathrm{m}$. It can be seen that, in this situation, significant water breakthrough occurs at the interface between the finer layer and the coarser layer, during the period of water redistribution after the end of the final period of rainfall.

From these results, it is evident that if the total amount of water infiltrated in the finer layer is lower than the water storage capacity obtained with a very low constant infiltration rate, no significant water breakthrough occurs across the interface between finer layer and coarser layer, regardless of the water infiltration time sequence and the redistribution of water taking place in the finer layer. An amount of water higher than the water storage capacity obtained with a low constant infiltration rate can be injected into the finer layer by means of a relatively high infiltration rate, and this amount of water may be temporarily maintained in the finer layer. However, subsequent redistribution of water within the finer layer may result

in a delayed breakthrough at the interface between the finer layer and the coarser layer.

6.4 Concluding remarks

Subsequent to the successful implementation in Code_Bright (see Chapter 4) of the new hydraulic constitutive models for unsaturated soils (see Chapter 3), these models were applied to the numerical study of the fundamental behaviour of CBS.

The results obtained from simulations of one-dimensional water infiltration tests in which only main wetting curves were considered (i.e. no hysteresis) can be summarised as follows.

- The new hydraulic conductivity model is able to predict the phenomenon of water breakthrough from the F.L. to the C.L. of a CBS much better than the conventional van Genuchten-Mualem model.
- The new hydraulic conductivity model is able to capture the role of liquid film flow, which is often neglected. This can have a significant influence on the variation of suction in the C.L., even prior to breakthrough, particularly for a low infiltration rate. Moreover, it can affect the velocity of water propagation in the C.L. after breakthrough.
- The variability of the parameter X_D within a realistic range of values (i.e. within a 95% confidence interval) has a negligible effect on suction and degree of saturation profiles at breakthrough in the finer layer. In the coarser layer, this variability of X_D affects the suction and degree of saturation profiles only at low infiltration rates.
- Water vapour diffusion has negligible impact in these water infiltration tests.

The impact of hydraulic hysteresis on the behaviour of CBSs was assessed by means of specific one-dimensional simulations in which rainfall, redistribution after rain ceases and evaporation were simulated. The key results can be summarised as follows.

- The inclusion of water retention hysteresis leads to significantly different predictions of the redistribution of water in the finer layer of a CBS after intense rainfall events, compared to predictions employing a unique SWRC, resulting in a more uniform distribution of water in the finer layer.
- Only the full hysteretic constitutive model is able to represent successfully both the condition at breakthrough and the condition at restoration of the CBS.
- Hydraulic hysteresis has a major impact on the prediction of evaporation from a CBS into the atmosphere, because the hysteresis leads to higher water availability in the soil close to the ground surface and hence to the prediction of higher cumulative evaporation.

Simulations of one-dimensional water infiltration tests considering different applied infiltration paths show that, for design purposes, the only reliable water storage capacity of the CBS, which does not result in delayed breakthrough in the long-term, is that obtained with a low constant infiltration rate. This water storage capacity can be approximated by the water storage capacity obtained with a hydrostatic suction profile in the finer layer at breakthrough.

Chapter 7

Multi-layered capillary barrier systems: analytical, numerical and experimental study

Under certain conditions, conventional capillary barrier systems may be highly inefficient in storing water and this strongly depends on the materials used and on the thickness of the layers. In this chapter, the use of multi-layered capillary barrier systems as a means to improve the water storage capacity is analysed. The interpretation of the hydraulic behaviour of multi-layered CBSs is initially given. A simplified analytical model for estimating the water storage capacity of multi-layered CBSs was developed and it is subsequently presented. The simplified model was then validated with the results of rigorous numerical FE analyses and these two approaches, simplified model and numerical FE analyses, were used to perform a parametric analysis of the water storage capacity of multi-layered CBSs. Finally, laboratory column infiltration tests on multi-layered CBSs were carried out in order to validate the use of the simplified analytical model and to show experimentally the improved water storage capacity of multi-layered CBSs.

7.1 Working principle of multi-layered capillary barrier systems

As already mentioned, the water storage capacity (WSC) of a capillary barrier system is defined as the maximum amount of water which can be stored in the barrier before breakthrough occurs. The study of the suction profile $s(z)$ at breakthrough in a CBS is very important because, from this, the corresponding degree of saturation profile and eventually the water storage capacity can be obtained, as was shown in Section 2.3.3 (see Equation 2.61). The suction profile (and hence the degree of saturation profile) in the finer layer at breakthrough depends on the properties of both the finer layer and the coarser layer and on the infiltration rate applied at the surface, as was discussed in Section 2.3.3 (see Figure 2.22).

For relatively low infiltration rates, the suction profile in the finer layer at breakthrough

is approximately hydrostatic. As the infiltration rate i increases, the suction profile tends to deviate from the hydrostatic profile, reaching a maximum suction value equal to s_f^* at the top of the finer layer, such that $k_{l,f}\left(s_f^*\right) = i$, where $k_{l,f}$ is the hydraulic conductivity function of the finer layer [23, 141]. Since the hydraulic conductivity decreases with increasing suction, as the infiltration rate increases, the maximum suction value reached in the finer layer s_f^* decreases. Consequently, the degree of saturation at the top of the finer layer at the time of breakthrough increases as the infiltration rate increases and the water storage capacity therefore increases with increasing infiltration rate. However, as shown in Section 6.3, the design of a CBS cannot rely on the water storage capacity obtained considering high infiltration rates. Only an amount of water lower than the WSC corresponding to very low infiltration rates can be sustained by the barrier in the long term. If an amount of water higher than this value is applied by means of a high infiltration rate, and the infiltration is then stopped, breakthrough will eventually occur, some time after the infiltration at the ground surface has ceased in absence of evapotranspiration (see Section 6.3). Thus, the only reliable value for the WSC is that calculated for a low infiltration rate, i.e. assuming a hydrostatic profile in the finer layer at breakthrough. The influence of the infiltration rate is assessed in the numerical analyses presented in Section 7.3.2.

The term multi-layered capillary barriers refers to CBSs made of the alternation of a given number of finer and coarser layers. If only one finer layer and one coarser layer are considered, a conventional single capillary barrier is obtained. The use of multi-layered CBSs may lead to a significant increase of the water storage capacity, in particular for low infiltration rates. In order to explain this effect, a qualitative comparison of suction and degree of saturation profiles at breakthrough between a conventional single capillary barrier (SCB) and a multi-layered capillary barrier (MCB) is shown in Figure 7.1, for a low infiltration rate. In this example, the MCB is made of two coarser layers (C.L.) and two finer layers (F.L.).

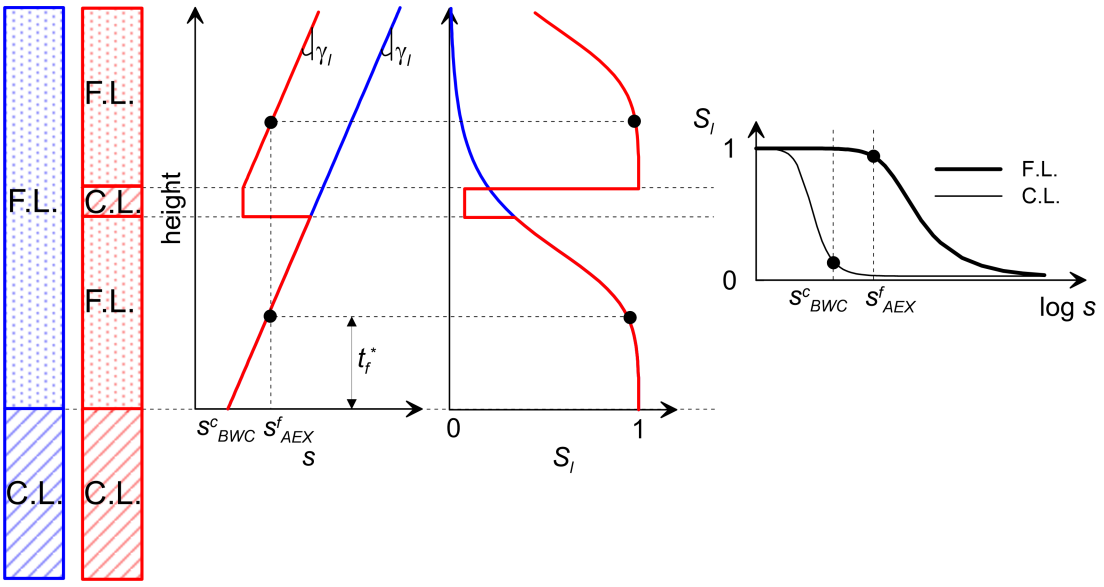

Figure 7.1: Qualitative comparison of suction and degree of saturation profiles at breakthrough for a single CBS (blue) and a multi-layered CBS (red), at a relatively low infiltration rate

For the SCB in Figure 7.1, it can be seen that at breakthrough a large quantity of water is stored in the lower part of the finer layer, immediately above the interface between the finer layer and the coarser layer, where the degree of saturation is generally equal to 1. This applies to a thickness t_f^* where suction is lower than the air-exclusion value of the finer layer s_{AEX}^f. The thickness t_f^* is thus calculated as:

$$t_f^* = \frac{s_{AEX}^f - s_{BWC}^c}{\gamma_l} \tag{7.1}$$

where s_{BWC}^c is the bulk water-continuity value of the coarser layer and γ_l is the unit weight of liquid water. It is worth noting from Equation 7.1 that t_f^* is solely a property of the materials of the coarser and finer layers. Above this thickness t_f^*, the degree of saturation of the finer layer starts decreasing and hence less water is stored far from the interface. In general, increasing the thickness of the finer layer of a capillary barrier leads to an increase of the WSC, but the gain in the WSC becomes lower and lower as the thickness of the finer layer is increased beyond t_f^*. Eventually, no significant gain in WSC is obtained by increasing this thickness of the finer layer beyond the height where suction attains the bulk water-entry value of the finer layer.

For a MCB, breakthrough is the time at which bulk water starts entering the lowest coarser layer of the barrier. The suction profile at breakthrough of a MCB is different from that of a SCB. Although in the lowest finer layer the suction profile is the same as in the corresponding part of the finer layer of a SCB, in an intermediate coarser layer suction typically drops and it is approximately uniform within the coarser layer (see Figure 7.1). In a finer layer above this intermediate coarser layer, the suction profile is continuous at the interface and again hydrostatic within at least the lower part of this upper finer layer [27]. Comparing the degree of saturation profiles of the SCB and the MCB in Figure 7.1, since the intermediate coarser layer in the MCB is typically at low degree of saturation, part of the water storage capacity of a MCB is lost, because of the replacement of some finer material with the intermediate coarser layer. However, this may be more than compensated by the increased storage capacity of the upper finer layer, which is now at much lower suction (and hence much higher degree of saturation) than the corresponding part of the finer layer of a SCB, as a consequence of the presence of the intermediate coarser layer. Thus, the study of a layered capillary barrier is based on weighing these two factors: i) reduction of WSC due to the low degree of saturation in the intermediate coarser layers; ii) increase of WSC due to the potential increase in the degree of saturation in the finer layers overlying intermediate coarser layers.

If relatively high infiltration rates are applied, the situation may be significantly different, as shown in the qualitative comparison between a SCB and a MCB in Figure 7.2. In this case, the suction profile of the SCB is initially hydrostatic up to the value s_f^*, beyond which it is constant. The corresponding degree of saturation remains high over the entire thickness of the single finer layer of the SCB and the WSC is higher than that obtained with lower infiltration rates. In this case, if a coarser layer is introduced in the barrier, part of the WSC is lost within the intermediate coarser layer but no significant gains are obtained in the upper finer layer,

where the degree of saturation was already high. Although the WSC calculated with reference to high infiltration rates is not reliable in the long term and should not be considered for design purposes (as stated earlier), the effect of the infiltration rate in MCBs is analyzed in Section 7.3.2.

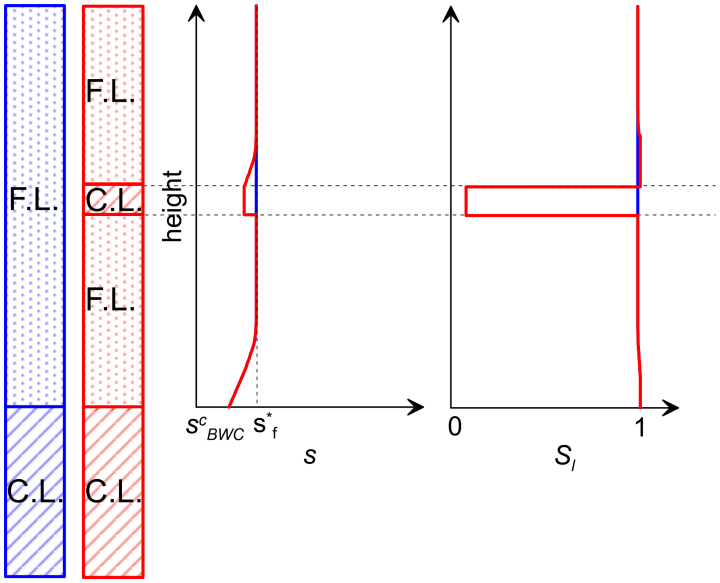

Figure 7.2: Qualitative comparison of suction and degree of saturation profiles at breakthrough for a single CBS (blue) and a multi-layered CBS (red), at a relatively high infiltration rate

7.2 Development of a simplified method for the analysis of multi-layered capillary barrier systems

In this section, a simplified calculation method for multi-layered capillary barriers is proposed. This simplified calculation method involves three steps:

1. determine whether the basic condition for possible use of multi-layered capillary barriers is satisfied;
2. simplified method for a preliminary optimum layout;
3. final verification considering the influence of the infiltration rate.

Step 1: Basic condition for possible use of multi-layered capillary barriers

In Section 7.1, it was shown that, for a conventional SCB, if the thickness of the finer layer $t_{f,SCB}$ is less than the critical thickness t_f^*, given by Equation 7.1, the entire finer layer will be in a fully saturated condition at breakthrough and there is no possibility of increasing the WSC by additional layering. Consequently, if the thickness of the finer layer of a SCB ($t_{f,SCB}$) is such that:

$$t_{f,SCB} \leq t_f^* = \frac{s^f_{AEX} - s^c_{BWC}}{\gamma_l} \tag{7.2}$$

the barrier should not be layered. In this case, the degree of saturation is equal to 1 over the entire thickness of the finer layer of the SCB and the insertion of a new coarser layer leads to a decrease of the WSC. However, $t_{f,SCB} > t_f^*$ does not necessarily mean that the barrier should be layered. The higher the ratio $t_{f,SCB}/t_f^*$ is, the more likely it is that a MCB will have higher WSC than a SCB.

Step 2: Simplified method for a preliminary optimum layout

If the thickness of a SCB is such that $t_{f,SCB} > t_f^*$, the use of a MCB can be considered. In order to find the optimum solution in terms of number and thickness of layers, an iterative procedure for the calculation of the WSC must be used. In particular, the ratio between the water storage capacity of a general multi-layered capillary barrier WSC and the water storage capacity of the corresponding single capillary barrier WSC_{SCB} must be assessed by varying the number of layers in the MCB. This iterative procedure can be executed using numerical methods (e.g. FE), but these can be highly time-demanding and expensive. To avoid this issue, a simplified method is proposed. A simplified suction profile at breakthrough $s(z)$ under constant infiltration rate i is assumed to be valid for MCBs, as shown in Figure 7.3.

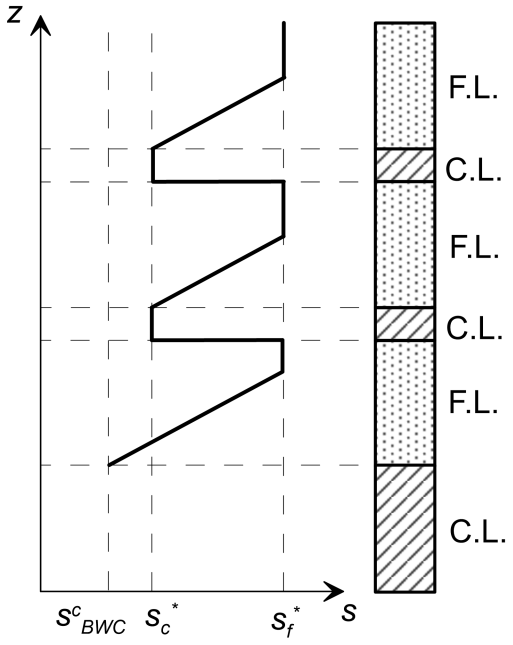

Figure 7.3: Simplified suction profile at breakthrough for multi-layered CBSs

In the finer layers, the suction profile is assumed hydrostatic up to the value s_f^*, beyond which it is constant. This bilinear suction profile within each F.L. agrees with the physical description of the suction profile at breakthrough for single CBSs given in Section 2.3.3. The suction value at the bottom of the lowest finer layer is the bulk-water continuity value of the coarser layer s^c_{BWC}. At the bottom of all the other finer layers, suction is equal to the constant suction value in the intermediate coarser layers, namely s_c^*. The constant suction value in the coarser layers s_c^* is such that $k_{l,c}(s_c^*) = i$, where i is the applied infiltration rate. The reason why a constant suction profile with $s = s_c^*$ is expected within the intermediate coarser layers at breakthrough is similar to the reason why the suction profile in the finer layer

of a SCB at breakthrough tends to become constant in the upper part (see Section 2.3.3). At breakthrough, the water velocity at all depths within a MCB (except the lowest coarser layer) is equal to the infiltration rate i and the suction within the intermediate coarser layers must be a constant value (corresponding to a hydraulic gradient of 1) and this constant value of suction s_c^* must be such that $k_{l,c}(s_c^*) = i$. Given this suction profile at breakthrough $s(z)$ and the main wetting soil water retention curves of the materials $S_l(s)$, the degree of saturation profile at breakthrough $S_l(z)$ can be obtained. Finally, given also the porosities of the materials ϕ, the water storage capacity is calculated as:

$$WSC = \int_{t_{tot}} \phi(z) \cdot S_l(z) \, \mathrm{d}z \tag{7.3}$$

where t_{tot} is the total thickness of the barrier, excluding the lowest coarser layer. The method can be used in hand calculations or can be implemented easily in simple commercial software (e.g. Matlab or Excel) and it allows the storage capacities of MCBs with different numbers of layers to be calculated simply and quickly. It can also take into account the effect of the infiltration rate i. At this step, however, suction profiles at breakthrough should be calculated considering a low infiltration rate. The validity of the method is shown in Section 7.3, by means of a comparison with results obtained using numerical FE analyses, and in Section 7.4, by means of a comparison with experimental results obtained from laboratory column infiltration tests on multi-layered CBSs.

Step 3: Final verification considering the influence of the infiltration rate

After the optimum layout of the barrier is chosen according to Step 2, the influence of the infiltration rate i must be assessed. Although the WSC calculated in correspondence of high infiltration rates is not reliable (see Section 6.3), it is suggested that the behaviour of a MCB under different infiltration rates is assessed because there may be situations in which a temporary water storage greater than the water storage capacity does not necessarily lead to water breakthrough. For instance, when evaporation from the ground surface occurs after a period of high intensity rainfall has ceased this may take water out of the barrier sufficiently quickly to prevent subsequent breakthrough even if the amount of water briefly stored in the barrier exceeds the WSC determined for a low infiltration rate. Hence, in this case, it can be beneficial to have a CBS with a high storage capacity under high infiltration rate, even if this storage capacity cannot be relied upon long-term.

The behaviour of MCBs under high infiltration rates can be assessed again using the simplified approach, but with a different suction profile for each value of i (see previous step). The simplified approach performs very well at low infiltration rates but it may be slightly conservative at relatively high infiltration rates (see Section 7.3.2).

7.3 Numerical and simplified analysis of multi-layered CBSs

In this section, the behaviour of multi-layered capillary barriers is studied numerically using the simplified approach and the rigorous finite element (FE) approach. In particular, several analyses were performed to assess the influence of number of layers, material properties, thickness of the barrier and infiltration rate on the water storage capacity of multi-layered capillary barriers. Moreover, a comparison between the results obtained using the simplified approach and those obtained using numerical FE analyses is shown in order to validate the use of the simplified approach.

7.3.1 Description of the models

Multi-layered capillary barriers were analysed using two approaches: the simplified approach and the numerical FE approach. The simplified approach is described in Section 7.2. Numerical simulations of one-dimensional infiltration tests on MCBs were carried out by means of Code_Bright. Only isothermal liquid water transport was considered in the analyses, with the solid phase considered as non-deformable and the gas phase as nonmobile. Thus, constant and uniform values of temperature ($T = 20\,^{\circ}\mathrm{C}$), displacements of the solid phase ($\boldsymbol{u} = 0\,\mathrm{m}$) and gas pressure ($p_g = 100\,\mathrm{kPa}$) were imposed.

Different geometrical layouts were analysed. All the models were vertical columns of soil made of equal numbers of finer and coarser layers. In all models, the bottom coarser layer was 30 cm thick and all intermediate coarser layers were 5 cm thick. Five values were assigned to t_{tot}, the total thickness of the barrier excluding the bottom coarser layer: 35 cm, 70 cm, 125 cm, 160 cm and 250 cm. The layering factor (κ) is defined as the number of coarser layers or finer layers (the same number) present in the barrier (e.g. the layering factor of a SCB is equal to 1). The layering factor was varied from 1 to 14. The thickness of each individual finer layer t_f for each layout of the barrier is:

$$t_f = \frac{t_{tot} - (\kappa - 1) \cdot t_c}{\kappa} \tag{7.4}$$

where t_c is the thickness of the intermediate coarser layers.

Since only liquid water transport was considered in the analysis, the materials forming the two layers were modelled by defining the hydraulic constitutive models (SWRCs and SHCCs) and the porosities Φ, each of which was considered to be constant and uniform within a layer. Table 7.1 shows the parameters of the materials and Figure 7.4 shows the SWRCs and the SHCCs.

The finer layers were modelled by the conventional VG-M model whereas the coarser layers were modelled by the modVG-modM+LF model (using the default value $X_D = 2.35 \times 10^{-9}\,\mathrm{mm\,m\,s^{-1}\,kPa^{1.5}}$, see Section 3.3.2). Water retention hysteresis was not included in these models because only infiltration tests characterised by a constant infiltration rate were simulated. For this type of simulations, only the definition of the main wetting curve is required.

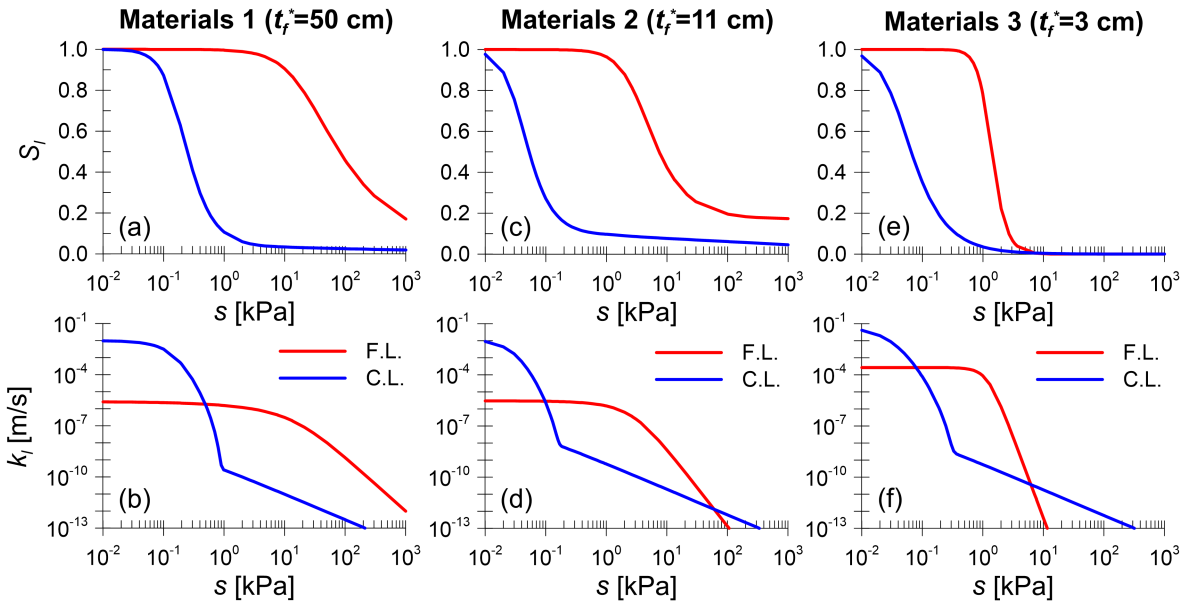

Figure 7.4: SWRCs and SHCCs of the materials used in the analyses

Three pairs of materials for the finer and coarser layers were considered for this study: "Materials 1 (M1)", "Materials 2 (M2)" and "Materials 3 (M3)". For Materials 1, the material properties were taken from Khire et al. [144], with the finer layer a silty sand and the coarser layer a pea gravel. For Materials 2, the material properties were taken from Stormont and Anderson [23], with the finer layer a silty sand and the coarser layer a pea gravel. For Materials 3, the finer layer was a fine sand [143] and the coarser layer was a gravelly sand [197]. The corresponding values for the parameter t_f^* (see Section 7.1) were: 50 cm for Materials 1, 11 cm for Materials 2 and 3 cm for Materials 3.

In the numerical models, initial conditions and boundary conditions were applied. The initial condition was a hydrostatic pore-water pressure profile, with $p_l = 0$ kPa ($s = 100$ kPa) at the bottom boundary. In this initial condition, the coarser layers were at very low degree of saturation, less than $S_{l,BWC}$. Two types of boundary conditions were imposed in the model: the value of pore-water pressure was imposed at the bottom boundary whereas a constant vertical water flux (the infiltration rate i) was imposed at the top boundary. The pore-water pressure imposed at the bottom boundary was equal to the initial value, namely $p_l = 0$ kPa ($s = 100$ kPa). In order to assess the influence of the infiltration rate on the problem, several values of the infiltration rate i imposed at the top boundary were considered.

7.3.2 Results and discussion

Results obtained from numerical FE analyses and simplified analyses are presented in terms of variation of the water storage capacity WSC with the layering factor κ, considering the influence of the total thickness of the barrier above the bottom coarser layer t_{tot}, material properties and infiltration rate i. Moreover, comparisons between the numerical approach and the simplified approach in terms of water storage capacities and suction profiles at breakthrough are shown.

Table 7.1: Properties of the materials

Material	**Physical parameters**		
	Φ [-]	k [m^2]	D_{10} [mm]
M1 F.L.	0.45	2.78E-13	-
M1 C.L.	0.32	1.03E-9	5.0
M2 F.L.	0.41	3.08E-13	-
M2 C.L.	0.33	1.34E-9	2.5
M3 F.L.	0.41	2.78E-11	-
M3 C.L.	0.38	7.81E-9	2.5

	SWRC parameters					
	$\overline{P_0}$ [MPa]	$\overline{\sigma_s}$ [N/m]	m [-]	S_{lr} [-]	ξ [-]	S_{ls} [-]
M1 F.L. VG	1.962E-2	0	0.324	0.022	-	1
M1 C.L. modVG	1.709E-4	0	0.590	-	2.75E-3	1
M2 F.L. VG	3.270E-3	0	0.505	0.171	-	1
M2 C.L. modVG	3.504E-5	0	0.600	-	6.66E-3	1
M3 F.L. VG	1.258E-3	0	0.750	0.000	-	1
M3 C.L. modVG	3.856E-5	0	0.507	-	6.10E-5	1

	SHCC parameters						
	m [-]	S_{lr} [-]	$S_{l,BWC}$ [-]	S_{ls} [-]	C_r^{Film} [MPa$^{-1.5}$]	a^{Film} [MPa]	d^{Film} [-]
M1 F.L. M	0.324	0.022	-	1	-	-	-
M1 C.L. modM+LF	0.590	-	0.107	1	9.89E-13	1.45E-4	-1.5
M2 F.L. M	0.505	0.171	-	1	-	-	-
M2 C.L. modM+LF	0.600	-	0.150	1	1.50E-12	3.00E-5	-1.5
M3 F.L. M	0.750	0.000	-	1	-	-	-
M3 C.L. modM+LF	0.507	-	0.091	1	2.37E-13	3.00E-5	-1.5

Figure 7.5 shows how the water storage capacity varies with the layering factor, considering different materials and different values of the total thickness of the barrier without the bottom coarser layer t_{tot}. In the graphs on the right (Figures 7.5b,d,f), the absolute values of the WSC are plotted against the layering factor whereas the ratios between the water storage capacity WSC and the water storage capacity of the corresponding single capillary barrier WSC_{SCB} are plotted against the layering factor in the graphs on the left (Figures 7.5a,c,e). In Figure 7.5, the infiltration rate applied in all the analyses is $i = 1 \times 10^{-7}\,\mathrm{m/s}$. The (piecewise linear) continuous lines refer to results obtained using the simplified approach whereas the symbols refer to results obtained using the numerical approach.

Values of WSC/WSC_{SCB} higher than 1 in Figure 7.5 mean that the multi-layered barrier has a higher water storage capacity than the conventional single capillary barrier. The higher the ratio WSC/WSC_{SCB}, the more benefit is gained by layering a barrier. It can be seen that, in certain cases, the use of multi-layered barriers leads to a decrease of the WSC (e.g. Materials 1, $t_{tot} = 35\,\mathrm{cm}$) whereas, in other cases, the WSC may be increased substantially by the layering effect (e.g. Materials 3, $t_{tot} = 250\,\mathrm{cm}$). When WSC/WSC_{SCB} is lower than 1, the

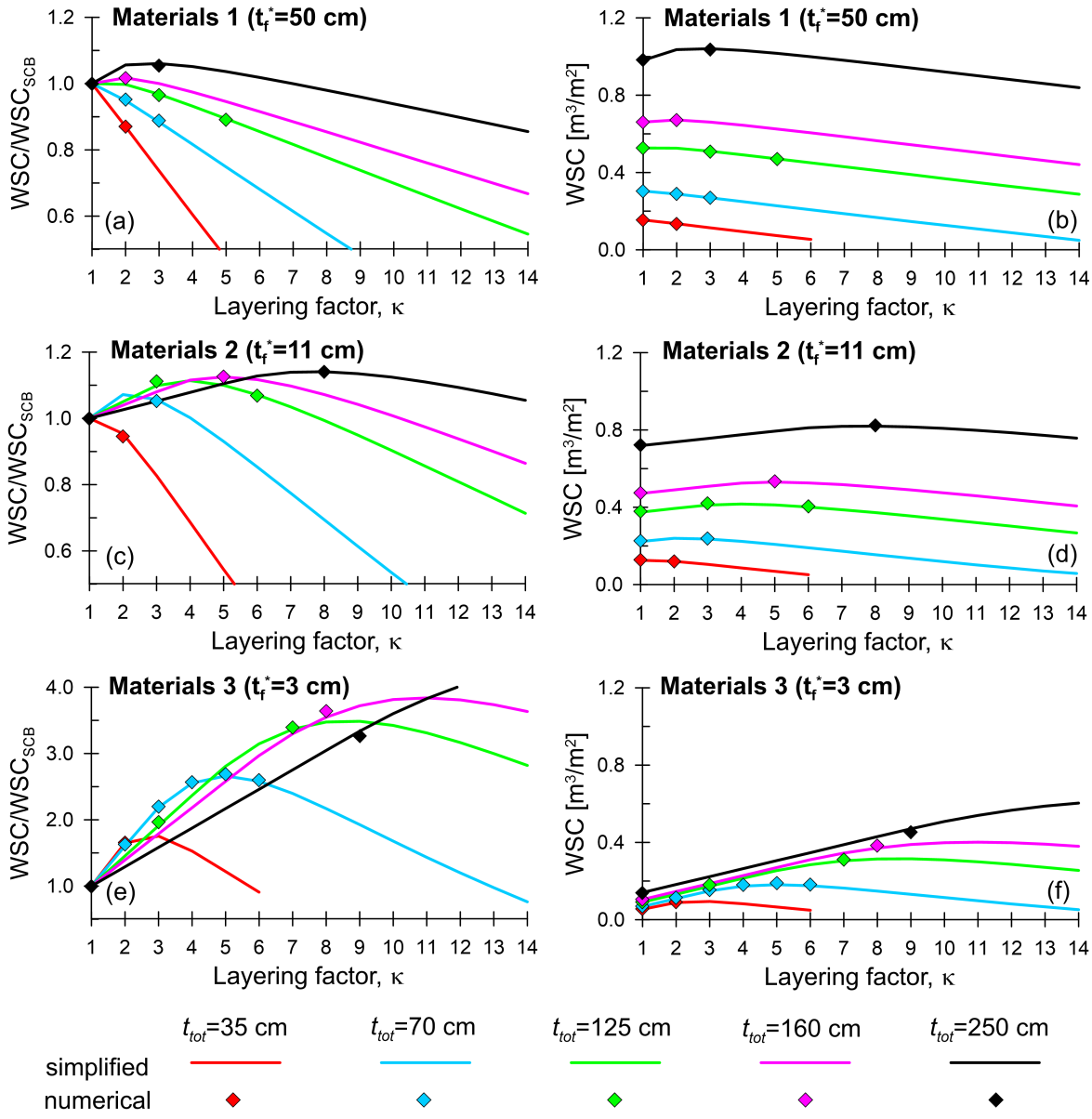

Figure 7.5: Water storage capacities (b,d,f) and ratios between water storage capacity and water storage capacity of a corresponding single capillary barrier (a,c,e) plotted against the layering factor, for a fixed infiltration rate $i = 1 \times 10^{-7}\,\mathrm{m/s}$, varying thickness t_{tot} and materials, obtained from simplified and numerical analyses

reduction in the WSC due to the low degree of saturation in the coarser layers is greater than the increase in WSC due to the reduction of suction in the upper finer layers caused by the introduction of intermediate coarser layers (see Section 7.1).

All the WSC/WSC_{SCB} curves going higher than 1 in Figure 7.5 reach a peak corresponding to the "optimum layering factor" κ_{opt}. For a layering factor higher than the optimum, the curves start decreasing because the reduction of the WSC due to the low degree of saturation in the coarser layers starts outweighing the increase of the WSC due to the reduction of suction in the finer layers. For given materials, the maximum achievable value of WSC/WSC_{SCB} increases with increasing total thickness of the barrier, in agreement with the discussion in Section 7.1, because in thick SCBs the upper part of the finer layer is in general at low degree of saturation and its contribution to the WSC is small. With the introduction of additional coarser layers, suction in the upper part of the barrier may be reduced so that its contribution to the WSC is recovered.

The variation of water storage capacity with the layering factor strongly depends on the materials that the capillary barrier is made of. A coarser layer with high bulk water-continuity value of suction and, in particular, a finer layer with low air-exclusion value of suction (i.e. low value of t_f^*) and low bulk water-entry value (e.g. Materials 3) produces the possibility of a large increase of WSC of a multi-layered capillary barrier compared to a single capillary barrier. On the other hand, for a coarser layer with low bulk water-continuity value and, in particular, for a finer layer with high air-exclusion value (high value of t_f^*) and high bulk water-entry value (e.g. Materials 1) it is unlikely to be worth using a multi-layered barrier unless the barrier is very thick. However, this does not mean that Materials 1 would be a less desirable combination than Materials 3. Observing the absolute values of WSC in the graphs on the right in Figure 7.5, it can be seen that, for a given thickness t_{tot}, the maximum WSC achieved by layering with Materials 3 is lower than the WSC of a SCB made of Materials 1. This means that for finer layers in horizontal capillary barriers, although finer-grained materials like silty sands (e.g. represented by Materials 1) are preferred in terms of WSC, if the availability of materials is limited to coarser-grained materials like fine sands (e.g. represented by Materials 3) the WSC may be increased substantially by means of layering the capillary barrier, in particular if the thickness is high. In this way, recycled or low-cost coarse grained materials (e.g. recycled pavements or construction materials) can be exploited for potential use in CBSs.

The influence of the infiltration rate on the water storage capacity of multi-layered capillary barriers is shown in Figure 7.6. This figure shows different curves representing WSC and WSC/WSC_{SCB} against the layering factor κ, for a fixed value of $t_{tot} = 125\,\text{cm}$ but considering different materials and infiltration rates. In all the right hand graphs (Figures 7.6b,d,f), it can be seen that the WSC increases as the infiltration rate increases, although the higher WSC related to high infiltration rate is not reliable as discussed in Section 6.3. On the other hand, the possible benefit achieved by additional layering, as indicated by the ratio WSC/WSC_{SCB} in the left hand graphs, is always greatest for the low infiltration rates. For instance, the WSC of a layered capillary barrier made of Materials 3 at its optimum layering

factor $\kappa_{opt} = 9$ is approximately 4.4 times higher than the WSC_{SCB} under a low infiltration rate ($i = 1 \times 10^{-8}\,\mathrm{m/s}$), whereas WSC is 20% lower than WSC_{SCB} under an extremely high infiltration rate ($i = 1 \times 10^{-4}\,\mathrm{m/s}$). Considering that the gain obtained for low infiltration rates by layering is much greater than the loss obtained at high infiltration rate and remembering that the WSC obtained at high infiltration rates is not a reliable value since it does not represent the realistic water storage capacity of a CBS, this would suggest that there would be considerable benefit to using a multi-layered capillary barrier if using Materials 3 with $t_{tot} = 125\,\mathrm{cm}$.

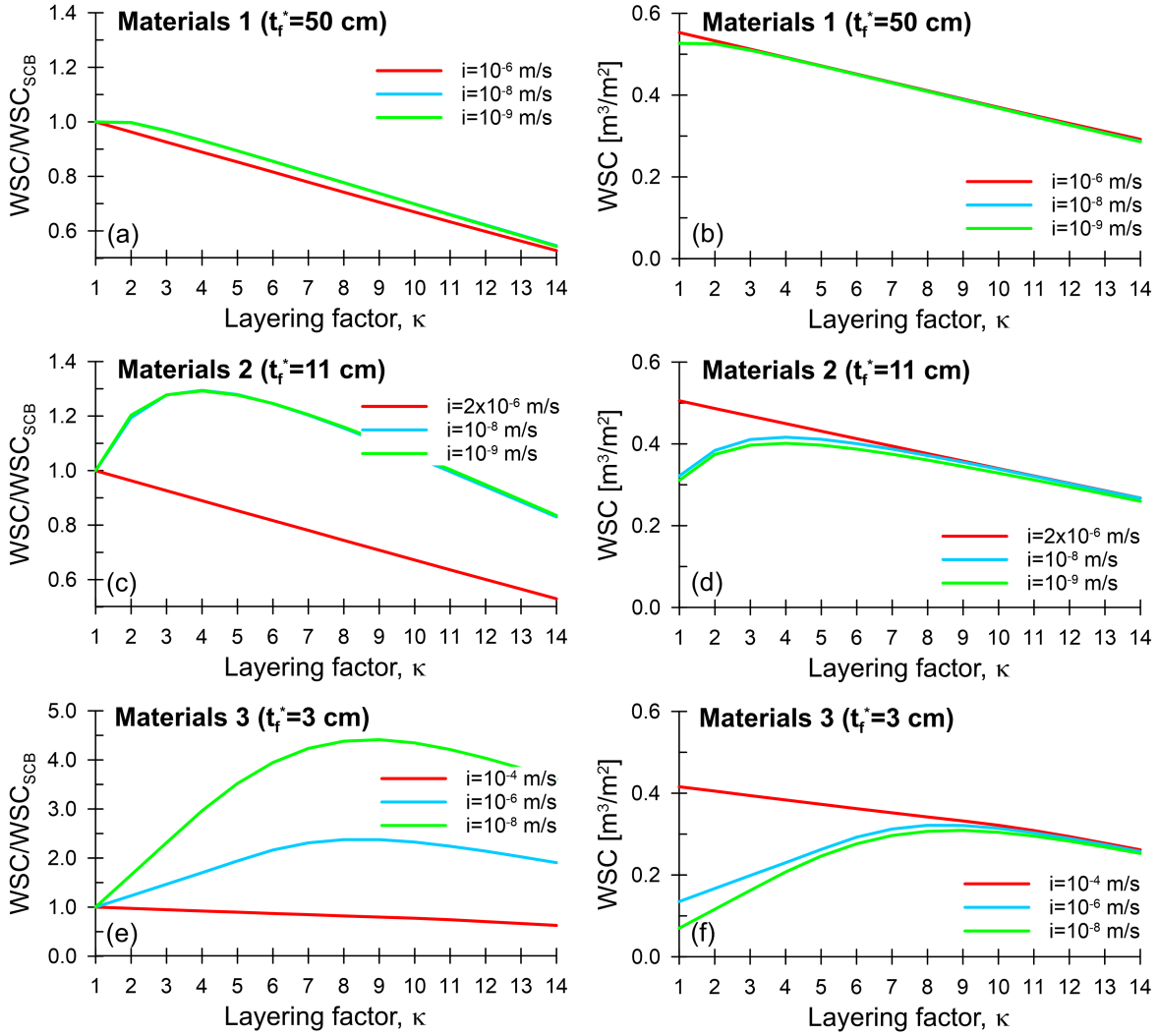

Figure 7.6: Water storage capacities (b,d,f) and ratios between water storage capacity and water storage capacity of a corresponding single capillary barrier (a,c,e) plotted against the layering factor, for a fixed thickness $t_{tot} = 125\,\mathrm{cm}$ and varying infiltration rate i and materials, obtained from simplified analyses

From the comparison between the results shown in Figure 7.5 obtained using the numerical and the simplified approaches, it can be seen that the simplified analyses lead to WSC values approximately equal to those obtained from numerical analyses, where different values of layering factor, thickness t_{tot} and materials are considered. Moreover, a comparison between these two approaches was also done varying the infiltration rate i, as shown in Figure 7.7 and in Figure 7.8.

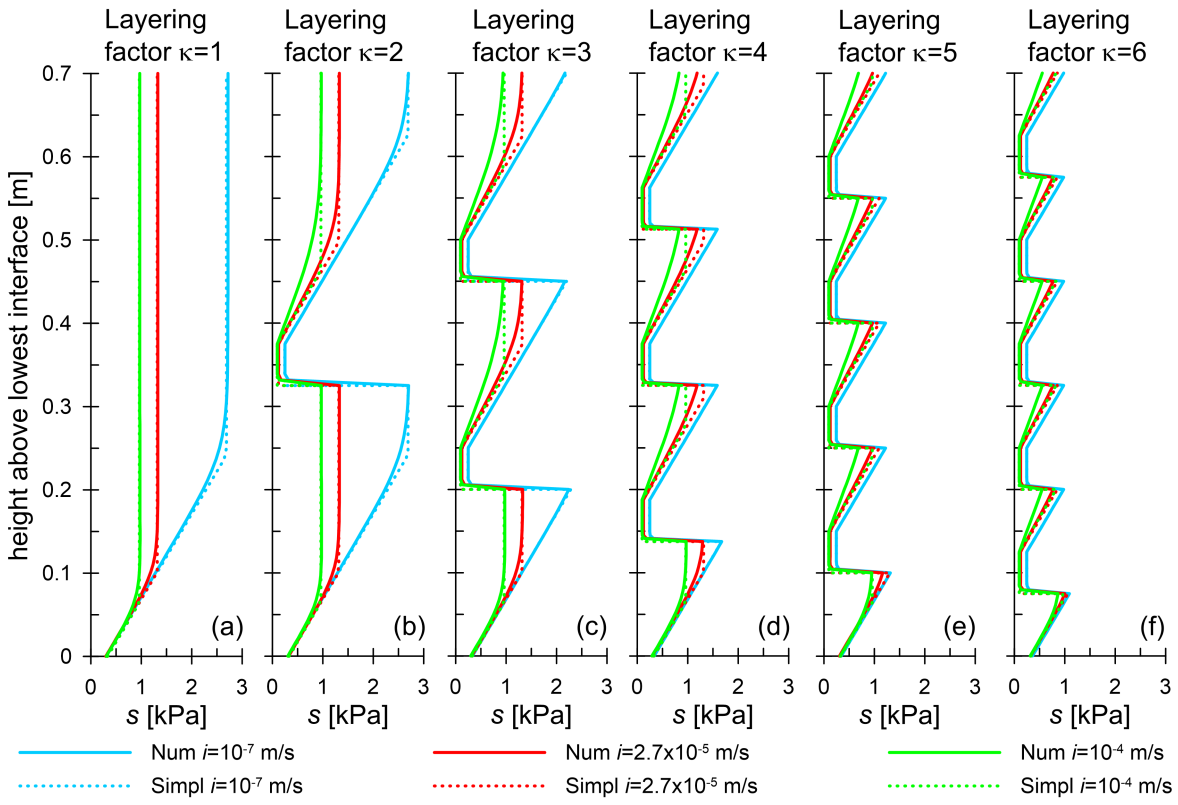

Figure 7.7: Comparison between suction profiles at breakthrough obtained from numerical analyses and simplified analyses, for a fixed thickness $t_{tot} = 70\,\text{cm}$, varying the layering factor and the infiltration rate

In this case, the capillary barrier was modelled with Materials 3, the total thickness was fixed as $t_{tot} = 70\,\text{cm}$, the layering factor κ was varied between 1 and 6 and three values of the infiltration rate i were considered: $i = 1 \times 10^{-7}\,\text{m/s}$, $i = 2.7 \times 10^{-5}\,\text{m/s}$ and $i = 1 \times 10^{-4}\,\text{m/s}$. Figure 7.7 shows the suction profiles obtained above the lowest interface between finer layer and coarser layer at the time of breakthrough. At low infiltration rates, the simplified method predicts very well the suction profiles at breakthrough for the different layering factors. As the infiltration rate increases, the profiles obtained using the simplified method match less accurately those obtained from numerical analyses, although still reasonably well. The simplified method becomes slightly conservative at high infiltration rates, as the suction values obtained using the simplified approach are slightly higher than those obtained from the numerical analyses, leading to lower values of degree of saturation. Figure 7.8 shows the corresponding curves of WSC and WSC/WSC_{SCB} against the layering factor. The curves obtained with the simplified method match very well the curves obtained from FE numerical analyses. This suggests that the simplified method is effective at predicting the water storage capacity of layered capillary barriers, under a wide range of infiltration rates.

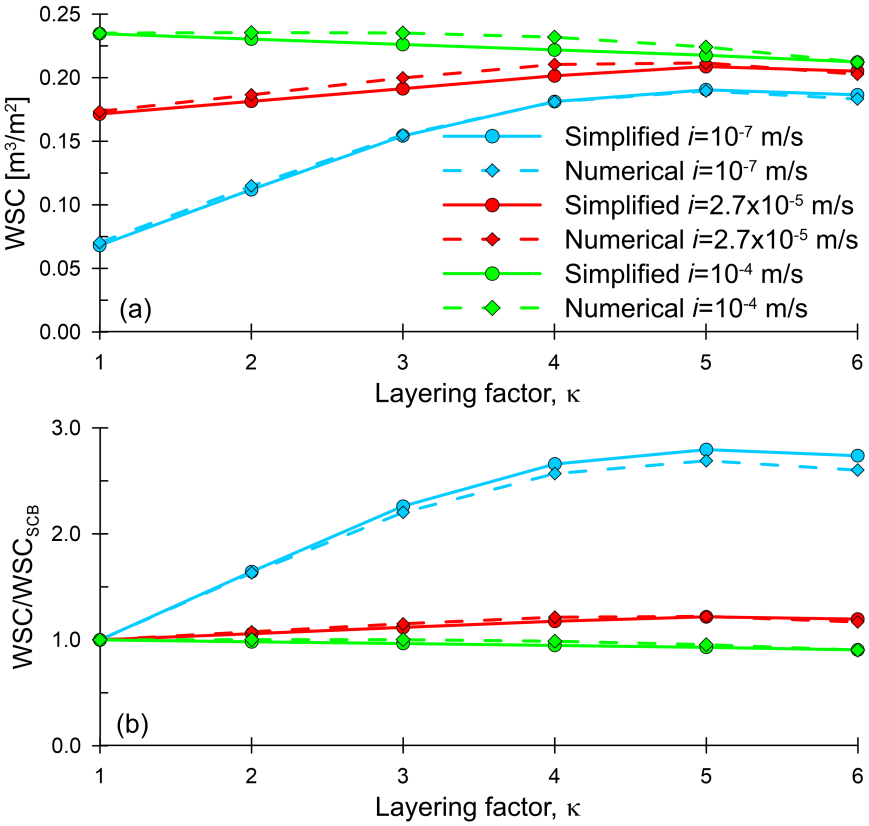

Figure 7.8: Comparison between water storage capacity curves plotted against the layering factor, obtained from numerical analyses and simplified analyses, for a fixed thickness $t_{tot} = 70\,\text{cm}$ and for different infiltration rates

7.4 Laboratory experimental study of multi-layered capillary barrier systems

In the previous sections of this chapter, it was shown that the use of multi-layered capillary barrier systems may lead to a significant increase of the water storage capacity, the parameters affecting the problem were analysed and a simplified analytical method for the prediction of the water storage capacity of MCBs and for their design was proposed. This was done by comparing the results obtained using rigorous FE simulations and the simplified analyses. In this thesis work, these results were also validated experimentally. Water infiltration tests on different instrumented MCBs were performed with two aims: i) to show the water storage capacity of multi-layered CBSs, ii) to validate the use of the simplified calculation method described in Section 7.2.

7.4.1 Description of the experimental programme

The experimental programme involved two main stages:

1. characterization of the materials;

2. column infiltration tests on one conventional single CBS and three multi-layered CBSs.

In the first stage, the properties of two materials used for this experimental work, a fine sand as a finer layer material and a sandy gravel as a coarser layer material, were characterized by specific tests. In particular, the properties analysed were:

- grain-size distribution;
- compaction and relative density;
- solid specific gravity;
- porosity;
- saturated hydraulic conductivity;
- soil water retention curve.

The characterization of the soil water retention curve required the design, manufacturing and installation of a hanging column apparatus. The characterisation of the material properties was done in order to use the simplified calculation method to predict the results of the column infiltration tests on the multi-layered CBSs.

In the second stage, column infiltration tests were performed on a conventional single CBS and on three multi-layered CBSs. This second stage involved different work steps:

- design, manufacturing and installation of the column and its components, including new manufactured low-cost tensiometers for measurements of suction;
- design, manufacturing and installation of an electronic data acquisition system;
- calibration of the instruments;
- set-up of the column infiltration tests on the conventional single CBS and three multi-layered CBSs;
- running the column infiltration tests on the various CBSs.

Four different column infiltration tests were performed. The same materials and the same total height of the CBS were considered in the different tests, but different layering factors (i.e. the number of pairs of layers in a CBS) were adopted: 1 (single CBS), 2, 3 and 5. In each test, the water storage capacity of the CBS, the suction profile and the water content profile at breakthrough were measured and compared with the predictions of the simplified method.

7.4.2 Basic properties of the soils

Two materials were used in this experimental study: a fine sand as a finer layer material and a sandy gravel as coarser layer material. The fine sand was ordered from "Derbyshire Aggregates Ltd" [228] (Product name: 110 Sand Dried 0.1-0.3mm) whereas the sandy gravel was ordered from "A-Grip Systems Ltd" [229] (Product name: Brittany Bronze 1-3mm).

The grain-size distributions of both materials were obtained by sieve tests [230] and they are shown in Figure 7.9. Both materials are relatively uniform with the majority of grains between 0.1 mm and 0.3 mm for the fine sand and between 1 mm and 3 mm for the sandy gravel (as quoted by the suppliers). The grain-size distributions of the two materials were chosen in order to guarantee that no transport of the finer material should have occurred across the coarser material due to liquid flow. For this purpose, the rules for filters suggested by Sherman [231] were adopted. When the infiltration tests were performed on the different multi-layered CBSs, the water which flowed out from the column after breakthrough was always clean, and this confirmed that no finer material was transported through the coarser layer by the liquid flows.

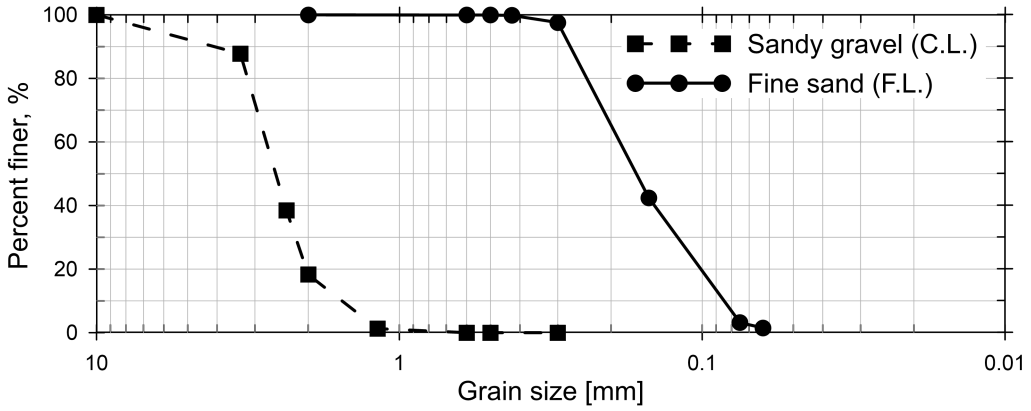

Figure 7.9: Grain-size distributions

The soils were prepared to values of dry density ρ_d which were consistent across the different tests (i.e. constant head permeability tests, water retention tests and main column infiltration tests). The possible range of dry density values were therefore preliminary assessed for both materials: the maximum achievable dry density $\rho_{d,max}$ was determined according to the specifications of ASTM International [232] (D4253) whereas the minimum achievable dry density $\rho_{d,min}$ was determined according to the specifications of ASTM International [233] (D4254) and the results are shown in Table 7.2. In the permeability, retention and column infiltration tests, only a low energy of compaction could be applied for the preparation of the soils to avoid damage to various mechanical components and to the soil containers. The compaction consisted of hand-tamping the surface of the soil, which was always dry during compaction, by means of a flat disk with a handle. Therefore this compaction method was reproduced before performing all the other tests in order to identify a value of the dry density which could be achieved with this compaction method and which was then adopted in all the other tests. As a result, it was decided to use the following values as target dry densities consistently for all the following tests: $\rho_d = 1570\,\mathrm{kg/m^3}$ for the fine sand and $\rho_d = 1600\,\mathrm{kg/m^3}$ for the sandy gravel. The corresponding relative density values D_r were then calculated from:

$$D_r = \frac{\dfrac{1}{\rho_{d,min}} - \dfrac{1}{\rho_d}}{\dfrac{1}{\rho_{d,min}} - \dfrac{1}{\rho_{d,max}}} \tag{7.5}$$

The results are shown in Table 7.2. For the aims of this experimental study, the relative density of the materials was not important in terms of absolute values but it was necessary that the compaction, and hence the dry density, was consistent in all tests.

Table 7.2: Dry densities of the materials: maximum $\rho_{d,max}$, minimum $\rho_{d,min}$, target ρ_d and relative density D_r

	$\rho_{d,max}$ [kg/m^3]	$\rho_{d,min}$ [kg/m^3]	ρ_d [kg/m^3]	D_r [%]
Fine sand (F.L.)	1695	1500	1570	39
Sandy gravel (C.L.)	1653	1553	1600	48

The specific gravity of the soil solids G_s was measured using a water pycnometer, according to the specifications of ASTM International [234] (D854-14). Each test was repeated three times to ensure consistency between the different results. From these tests, the values $G_s = 2.65$ for the fine sand and $G_s = 2.60$ for the sandy gravel were obtained. The porosity values Φ corresponding to the initial dry densities used in the different tests were calculated according to the following equation:

$$\Phi = 1 - \frac{\rho_d}{G_s \rho_l} \tag{7.6}$$

where the value of the liquid density was $\rho_l = 998\,\mathrm{kg/m^3}$. The resulting porosity values were $\Phi = 0.41$ for the fine sand and $\Phi = 0.38$ for the sandy gravel.

The saturated hydraulic conductivities of the two materials were measured by means of constant head permeability tests for granular material, following the specifications given by ASTM International [235] (D2434-68). Figure 7.10 shows the apparatus used for the tests. The bottom part and the top part of the permeameter were filled with cobbles and metallic woven mesh disks were placed between the cobble fillings and the tested material. The soil was poured into the permeameter and compacted in layers of 2.5 cm by hand-tamping to the target dry density (i.e. $\rho_d = 1570\,\mathrm{kg/m^3}$ for the fine sand and $\rho_d = 1600\,\mathrm{kg/m^3}$ for the sandy gravel). The soil sample was then saturated according to the specification given by ASTM International [235]. Subsequently, water tanks with constant water levels were connected to the lower valve and to the upper valve. The water level in the water tank connected to the lower valve was always higher than the water level in the tank connected to the upper valve. Therefore, water flowed into the sample from the lower valve and out of the sample from the upper valve. When a steady-state condition was reached, indicated by stable readings of the water level in the manometers, the saturated hydraulic conductivity was calculated from measurements of water flow and hydraulic gradient, according to ASTM International [235]. For each test, four different values of hydraulic gradient were applied and, for each value of hydraulic gradient, the test was performed two times. Thus, a total of eight measurements of saturated hydraulic conductivity k_{ls} were made for each soil. The results of the different tests were highly consistent and the following average values of saturated hydraulic conductivity were obtained: $k_{ls} = 1.36 \times 10^{-4}\,\mathrm{m/s}$ for the fine sand and $k_{ls} = 2.04 \times 10^{-2}\,\mathrm{m/s}$ for the

sandy gravel.

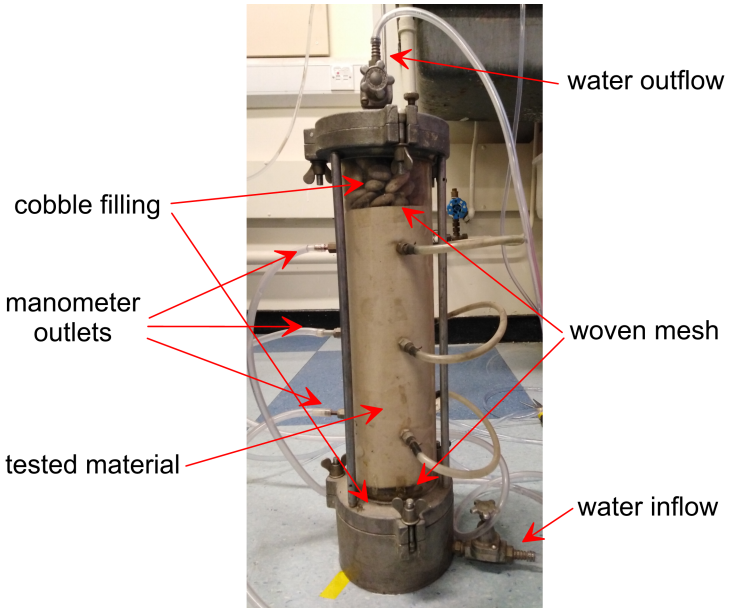

Figure 7.10: Constant head saturated hydraulic conductivity test

The properties of the two materials discussed in this section are summarized in Table 7.3.

Table 7.3: Physical properties of the materials

	D_{10} [mm]	ρ_d [kg/m^3]	G_s [-]	Φ [-]	k_{ls} [m/s]
Fine sand (F.L.)	0.085	1570	2.65	0.41	1.36E-4
Sandy gravel (C.L.)	1.56	1600	2.60	0.38	2.04E-2

7.4.3 Soil water retention curves

Equipment and procedure

The main wetting and main drying SWRCs of the fine sand and the sandy gravel were measured by performing hanging-water column tests [236]. Before the hanging-water column tests were performed, the hanging-water column apparatus was designed, manufactured and set up. Figure 7.11 shows schematically this apparatus. The soil sample was placed and compacted within a plastic chamber (see details of the chamber later) which was located at a height of 3 m from the floor. The soil sample chamber was connected to a burette filled with water by means of a flexible nylon hose. The burette was linked to a vertical metallic rod by means of a clamp so that the vertical position of the burette might be easily varied. A graduated scale was attached to the vertical rod in order to obtain readings of the difference in the vertical height ΔH_w between the water level in the burette and the mid-height of the soil sample. When the burette, the hose and the bottom of the chamber were filled with water and the valve at the bottom of the burette was open, the water pressure was continuous in all the

apparatus. Hence, at equilibrium, the suction s at the mid-height of the soil sample was:

$$s = \Delta H_w \cdot \gamma_l \tag{7.7}$$

where γ_l is the unit weight of liquid. The suction in the soil sample was thus controlled by moving vertically the burette. Changes in the volume of water in the soil sample were monitored over time by recording the water volume changes in the burette. Changes in the average volumetric water content were calculated by dividing the measured changes in the volume of water by the volume of the soil specimen. During the tests, cling films were applied on the top parts of the soil sample chamber and the burette in order to limit evaporation.

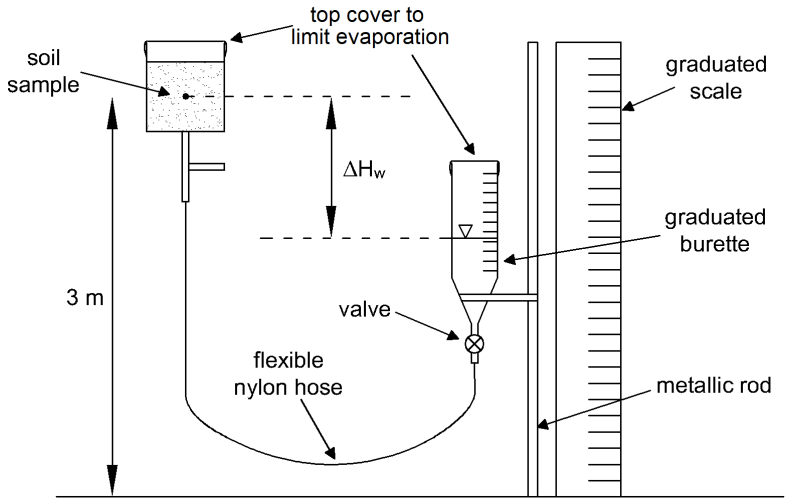

Figure 7.11: Hanging water column test apparatus

Figure 7.12 shows the soil sample chamber used for the SWRC tests. The chamber, made of transparent acrylic, was manufactured by the technical staff at the University of Glasgow by drilling and gluing together different acrylic parts. The chamber was divided into two parts by an intermediate acrylic perforated disk. The lower part was filled with water during the test and it was connected to the burette by means of a flexible nylon hose fitted to the bottom end of the chamber. The lateral neck in the lower part of the chamber was designed to be linked to a pressure sensor in order to carry out simultaneous calibrations of pressure sensors during the SWRC tests. However, the lateral end was closed during the tests and the calibration of the pressure sensors was carried out in a different way (see Section 7.4.4). The upper part of the chamber contained the soil sample. The intermediate perforated acrylic disk supported the soil in the upper part of the chamber and, due to the presence of holes of approximately 1 mm diameter drilled through the thickness of the disk, the liquid phase was continuous across the disk, between the upper part and the lower part of the chamber.

A circular filter paper, a silt filter and the soil sample were sequentially placed above the perforated disk. The filter paper was placed directly on the disk with the aim of preventing transport of solid material from the upper part to the lower part of the chamber. The silt filter, introduced by Stanier and Tarantino [237], acts as a simple high air entry filter. This filter, when fully saturated, allows the flow of water but not the flow of air, thereby maintaining

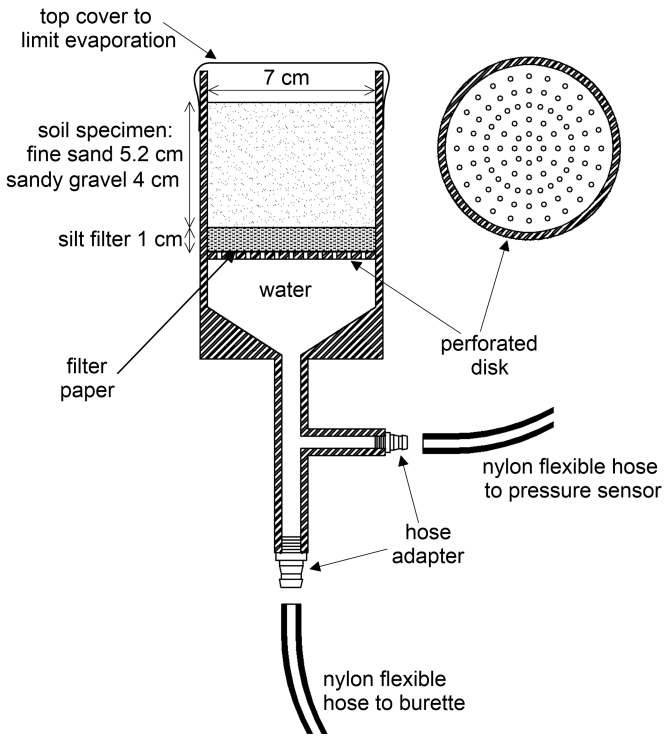

Figure 7.12: Soil sample chamber used for the SWRC tests

suction at the bottom of the soil sample that is placed on the filter. The silt filter remains saturated as long as the suction remains lower than the air-entry value of the filter. Preliminary tests were carried out on the silt filter and showed that the air-entry value was greater than 20 kPa, which is greater than the range of suctions applied in the SWRC tests performed in this work. The silt filter has three advantages over commercial high air entry porous ceramics: i) it is inexpensive (only the cost of a small amount of silt); ii) the hydraulic conductivity is greater than conventional porous ceramics, and hence lower equalisation times are required [237]; iii) given that the surface of the silt filter is rougher than the surface of a porous ceramic, the filter ensures a better contact with the grains of the soil specimen and limits possible wall effects, i.e. it reduces the risk of large pores developing at the interface between filter and soil specimen that would prevent suction being transmitted to the sample [237]. To make the silt filter, the following steps were performed:

1. the chamber was connected to the burette by means of a flexible nylon hose;
2. all the system (i.e. burette, hose and soil sample chamber) was saturated, by raising the burette, with the level of water just above the intermediate acrylic perforated disk;
3. the valve at the bottom of the burette was closed;
4. the filter paper was placed over the intermediate disk;
5. a prescribed quantity of liquefied silt slurry was poured into the chamber;
6. the silt was allowed to settle on the filter paper, producing a 1 cm-thick filter (Figure 7.13a);

7. the valve at the bottom of the burette was reopened allowing the water left in the chamber to drain and flow into the burette (Figure 7.13b).

The initially dry soil sample of mass $M_{0,dry}$ was finally poured directly onto the silt filter and compacted by hand-tamping to the target dry density (i.e. $\rho_d = 1570\,\mathrm{kg/m^3}$ for the fine sand and $\rho_d = 1600\,\mathrm{kg/m^3}$ for the sandy gravel) (Figure 7.13c). In the test on fine sand, the soil sample was 5.2 cm thick whereas in the test on the sandy gravel, the soil sample was 4 cm thick.

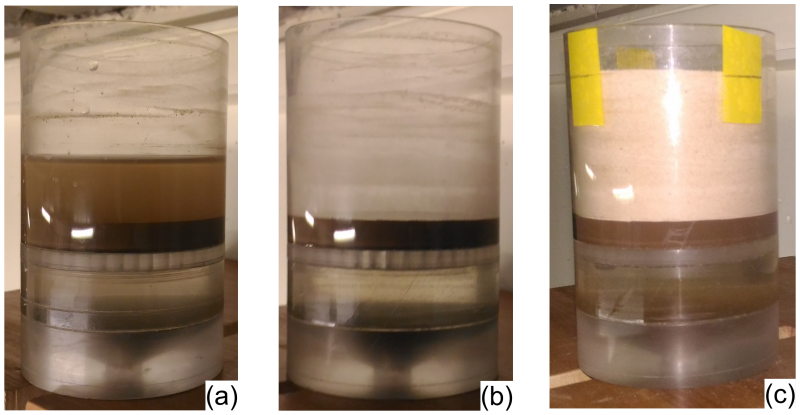

Figure 7.13: Steps for the preparation of the soil specimen in the chamber: (a) preparation of the silt filter during deposition, (b) finished silt filter and (c) preparation of the soil sample through pouring and compaction

Once the SWRC apparatus was set up and the soil specimen was prepared, the SWRC test was started. For each material, the main wetting SWRC was obtained first, starting from oven-dry conditions and finishing at an applied suction value of $s = 0\,\mathrm{kPa}$. The process was then reversed to obtain the main drying SWRC. Although both the main wetting and the main drying SWRCs were obtained, the main wetting SWRC was of major interest in this case because the column infiltration tests, discussed in Sections 7.4.4 and 7.4.5, involved monotonic wetting. The SWRC tests were performed by the following procedure:

1. The hanging column apparatus was set up and the soil specimen was prepared.

2. The difference in water level ΔH_w (see Figure 7.11) was initially high, i.e. an initially high value of suction was applied to the specimen, given by Equation 7.7.

3. Enough time for equalisation of pore-water pressures within the sample was allowed, namely until changes of water volume in the burette were negligible. During this process, the elevation of the burette was continuously adjusted to keep the horizontal elevation of the water surface in the burette at the original position because water flow into the soil (for main wetting) or from the soil (main drying) caused slight variations of the water level in the burette.

4. After equalisation, the change of volumetric water content $\Delta\theta_l$ in the soil specimen (>0 during wetting, <0 during drying) was calculated as the change in the water volume in the burette divided by the total volume of the soil specimen V_0. The change of

volumetric water content $\Delta\theta_l$ was then added to the previous volumetric water content (which was 0 at the beginning of the test) to obtain the current volumetric water content θ_l. The current imposed suction s and the current measured volumetric water content θ_l represent one point on the SWRC.

5. The burette was then moved to a new position, i.e. ΔH_w was reduced during main wetting or increased during main drying, in order to impose a new value of suction s in the soil specimen. Steps 3 and 4 were then repeated. During main wetting this procedure was repeated until reaching $\Delta H_w = 0$ (i.e. $s = 0$).

6. At the end of the main wetting process, the water level was brought above the surface of the soil sample ($\Delta H_w < 0$ and thus $s < 0$) in order to expel as much trapped air as possible and time for equalisation was allowed.

7. The main drying process was then started. Steps 3, 4 and 5 were repeated but, in this case, the initial volumetric water content was high, at each new step ΔH_w was increased (s was increased) and $\Delta\theta_l < 0$.

8. The main drying process and the test finished at an appropriately high value of suction.

9. At the end of the test, the moist soil specimen, or a sub-sample of it, was weighed to obtain the mass $M_{1,wet}$, then oven-dried and weighed again to obtain the dry mass $M_{1,dry}$. Given that the initial mass of the entire dry soil specimen in the test chamber was $M_{0,dry}$, the volumetric water content of the soil specimen at the end of the test $\theta_{l,fin,c}$ was calculated as:

$$\theta_{l,fin,c} = \frac{\left(M_{1,wet} - M_{1,dry}\right) \cdot \left(\dfrac{M_{0,dry}}{M_{1,dry}}\right)}{\rho_l \cdot V_0} \tag{7.8}$$

The value of $\theta_{l,fin,c}$ calculated with this equation should be theoretically equal to the final value of the volumetric water content determined in the test $\theta_{l,fin,0}$.

Results

As discussed above, for each material, the main wetting curve was characterised first and the main drying curve was then characterised by reversing the application of suction at $s = 0\,\text{kPa}$. Therefore, the main drying SWRC test must be interpreted as a continuation of the main wetting SWRC test.

The results of the SWRC tests are here presented in terms of the SWRC data, obtained as the volumetric water content at the end of each equalisation time period plotted against the corresponding applied suction.

Figure 7.14 shows the experimental main wetting curve (MW) and main drying curve (MD) obtained from the test on the fine sand (Figure 7.14a) and on the sandy gravel (Figure 7.14b), with suction s plotted on a linear scale. In addition, Figure 7.14 also shows another pair of

curves for each material: the corrected main wetting curve (MW corrected) and the corrected main drying curve (MD corrected), which take into account the evaporation that occurred during the tests.

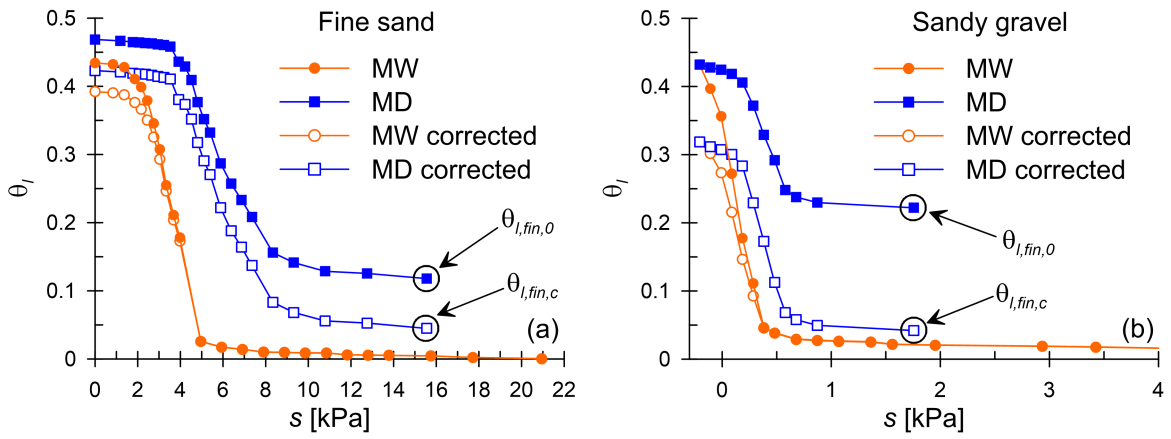

Figure 7.14: Results of the SWRC tests on (a) the fine sand and (b) the sandy gravel: original main wetting (MW) and main drying (MD) points and corrected main wetting (MW corrected) and main drying (MD corrected) after adjusting for the effect of evaporation

Although both the burette and the soil specimen chamber were covered by cling films in order to limit evaporation, the evaporation still had an important role because the duration of the test was relatively high: 44 days for the fine sand and 50 days for the sandy gravel. At the end of the main drying SWRC test, the volumetric water content $\theta_{l,fin,0}$ in the soil specimen obtained from tracking the changes in the volume of water in the burette was compared with the volumetric water content $\theta_{l,fin,c}$ obtained from oven-drying the soil sample and working out the final volumetric water content with Equation 7.8. For both soils, the value of $\theta_{l,fin,0}$ was significantly greater than $\theta_{l,fin,c}$. The latter can be considered the real volumetric water content at the end of the test whereas the former wrongly includes in the soil specimen all the water evaporated during the test. In order to take into account this effect, a correction was applied to the MW and MD curves.

The correction procedure applied to the MW and MD curves can be described as follows. The total volume of water evaporated during the test $V_{w,evap,fin}$ was calculated as:

$$V_{w,evap,fin} = \left(\theta_{fin,0} - \theta_{fin,c}\right) \cdot V_0 \tag{7.9}$$

where V_0 is the volume of the soil specimen. The evaporation was assumed to occur from both the burette and from the soil specimen surface. The evaporation from the burette was assumed to occur at a constant rate of $i_{evap} \cdot A_{burette}$, where i_{evap} is the constant rate of evaporation per unit area of evaporating surface and $A_{burette}$ is the internal area of the burette (i.e. the area of the free water surface). A similar concept can be applied to the soil specimen surface, but only when the volumetric water content is relatively high, or the suction relatively low. Indeed, as discussed in Section 2.4.2, the evaporation from a soil surface is similar to that from a free water surface only when the soil surface is at low values of suction, or at high values of degree of saturation. For simplicity, it was assumed that the evaporation rate from

the soil specimen surface was zero when the suction was greater than the BWC point during wetting and greater than the BWD point during drying, whereas it was assumed to be equal to $i_{evap} \cdot A_0$ when the suction was lower than the BWC point during wetting and lower than the BWD point during drying, where A_0 is the surface area of the soil specimen. Given $t = 0$ the time at the beginning of the test, t_{BWC} the time when the bulk water-continuity point is attained in the soil specimen during the wetting part of the test, t_{BWD} the time when the bulk water-discontinuity point is attained in the soil specimen during the drying part of the test and t_{test} the time when the test ends, then $t_{BWC} < t_{BWD} < t_{test}$ since the main wetting SWRC was characterised before the main drying SWRC. The following equation can be thus written:

$$V_{w,evap,fin} = i_{evap} \cdot A_{burette} \cdot t_{test} + i_{evap} \cdot A_0 \cdot (t_{BWD} - t_{BWC}) \tag{7.10}$$

In Equation 7.10 the total volume of evaporated water $V_{w,evap,fin}$ is split into two components: the water evaporated from the burette throughout the duration of the test t_{test} and the water evaporated from the soil specimen, assumed to occur for a duration $t_{BWD} - t_{BWC}$, namely when the suction was lower than the BWC point during wetting and lower than the BWD point during drying. Equation 7.10 can be inverted to work out the rate of evaporation i_{evap}, as follows:

$$i_{evap} = \frac{V_{w,evap,fin}}{A_{burette} \cdot t_{test} + A_0 \cdot (t_{BWD} - t_{BWC})} \tag{7.11}$$

The volume of water evaporated at any point during the test $V_{w,evap}$ can be finally written as a function of time t as follows:

$$V_{w,evap}(t) = \begin{cases} i_{evap} \cdot A_{burette} \cdot t & \text{if } t < t_{BWC} \\ i_{evap} \cdot A_{burette} \cdot t + i_{evap} \cdot A_0 \cdot (t - t_{BWC}) & \text{if } t_{BWC} < t < t_{BWD} \\ i_{evap} \cdot A_{burette} \cdot t + i_{evap} \cdot A_0 \cdot (t_{BWD} - t_{BWC}) & \text{if } t > t_{BWD} \end{cases} \tag{7.12}$$

The readings of the volume of water in the soil specimen obtained during the test were corrected by subtracting the estimated volume of water evaporated at each value of time.

Figure 7.15 shows, for (a) the fine sand and (b) the sandy gravel, the time histories of the volume of water in the soil specimen obtained at the end of each equalisation stage, corrected and non-corrected, and the time history of the evaporated water predicted using Equation 7.12. The time histories of the applied suction are also shown for information. For both materials, a main wetting path was applied first, and hence the volume of water in the soil specimen initially increased while decreasing values of suction were applied. A main drying path was then applied, and hence the volume of water in the soil specimen decreased while increasing values of suction were applied. The predicted volume of evaporated water increased monotonically during the test although the increase was much more evident at intermediate times, i.e. for $t_{BWC} < t < t_{BWD}$ than at the beginning of the test, i.e. $t < t_{BWC}$, or at the end of the test, i.e. $t > t_{BWD}$. In the first case, the evaporation was assumed to occur from both the burette surface and the soil specimen surface whereas, in the second and in the third case, the evaporation was assumed to occur only from the burette. Given that the internal

area of the burette (1.539 cm^2) was much smaller than the area of the soil specimen (43 cm^2), the calculated evaporation rate from the soil specimen surface, expressed as a volume of evaporated water per unit of time, was much greater than that from the burette. The corrected values of the volume of water in the soil specimen are thus lower than the non-corrected values and this difference increases with the amount of evaporation and thus with time. A similar pattern about the difference between the corrected and non-corrected versions of the SWRCs can be observed in the results shown in Figure 7.14.

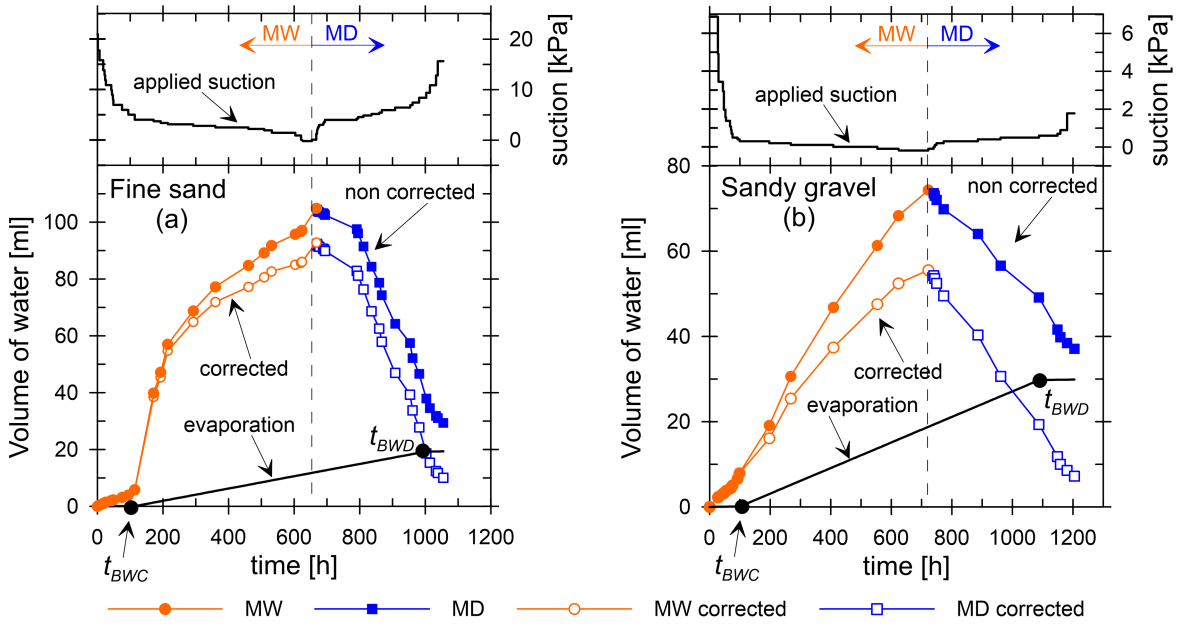

Figure 7.15: Time histories of the volume of water in the soil specimen (non corrected and corrected), evaporated water and applied suction, for (a) the fine sand and (b) the sandy gravel

The use of this correction method produced values of evaporation rate i_{evap} that were of the same order of magnitude for the test on the fine sand and the test on the sandy gravel: $i_{evap} = 1.14 \times 10^{-9}$ m/s in the test on the fine sand and $i_{evap} = 1.94 \times 10^{-9}$ m/s in the test on the sandy gravel. To asses the reliability of the estimation method, the calculated values of i_{evap} were compared to the value obtained from a simple test. A flask with an inner area of 5.72 cm^2 was filled with water and the top was covered with a cling film, as was done for the burette and the soil specimen chamber. The flask was placed for 347 days in the same laboratory environment where the SWRC tests were performed. During this time the volume of water in the flask was regularly monitored in order to calculate the evaporation rate. The average evaporation rate was $i_{evap} = 1.16 \times 10^{-9}$ m/s, which is extremely close to the value estimated in the test on the fine sand and of the same order of magnitude as the value estimated in the test on the sandy gravel.

The corrected values of volumetric water content were used for the SWRCs. For the fine sand, the corrected experimental data were used to directly calibrate the parameters of the modVG SWRC model, which was used to represent the SWRCs of the material. The comparison between the corrected experimental SWRC data and the modVG SWRC model for the fine sand is shown in Figure 7.16a and the resulting model parameters for the fine sand

are shown in Table 7.4. The value of θ_{ls} obtained during the main wetting (MW) test for the fine sand, i.e. $\theta_{ls} = 0.392$, was slightly lower than the value of porosity $\Phi = 0.41$ obtained from a previous test (see Table 7.3), suggesting the occurrence of air trapping. The use of a value of θ_{ls} lower than the value of porosity, i.e. a maximum degree of saturation lower than 1, is relevant to the use of an apparent SWRC (see Chapter 5). At the beginning of the main drying (MD) test, the volumetric water content was similar to the value of porosity obtained in a previous test (in particular slightly higher), i.e. $\theta_{ls} = 0.423$, suggesting the achievement of fully saturated conditions.

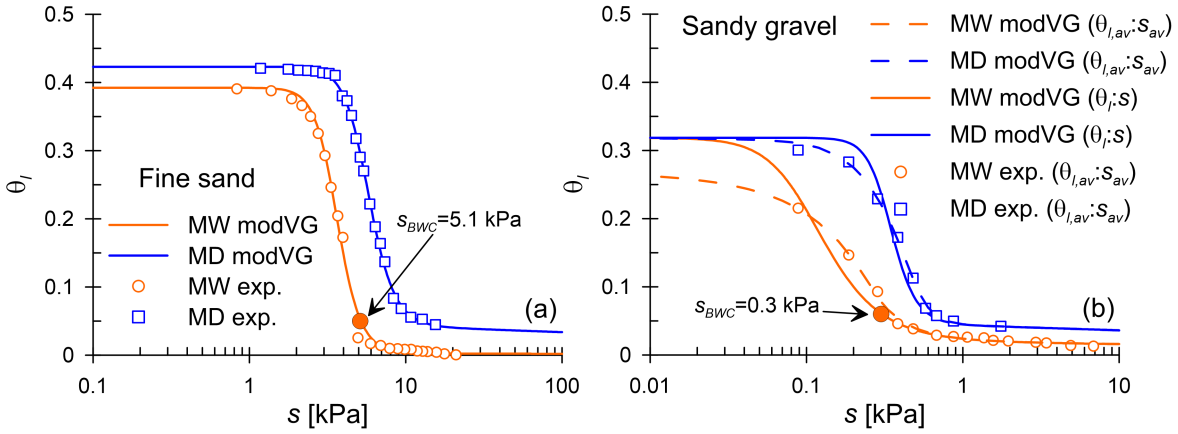

Figure 7.16: SWRCs of (a) the fine sand and (b) the sandy gravel: corrected experimental data and modVG model

Table 7.4: Parameters of the modVG SWRC models

	θ_{ls} [-]	ξ [-]	P_0 [MPa]	m [-]	s_{BWC} [kPa]	s_{BWD} [kPa]
Fine sand MW	0.392	5.319E-4	3.508E-3	0.840	5.1	-
Fine sand MD	0.423	8.940-3	5.532E-3	0.826	-	8.9
Sandy gravel MW	0.319	3.361E-3	1.000E-4	0.642	0.3	-
Sandy gravel MD	0.319	7.675-3	3.331E-4	0.828	-	0.5

For the sandy gravel it was necessary to use an indirect procedure to determine appropriate values for the modVG model parameters, because the values of suction were so low that the variation of suction and hence degree of saturation over the height of the soil specimen was significant. This meant that a plot of the average volumetric water content in the specimen against the suction imposed at the mid-height of the soil specimen (as represented by the experimental data in Figure 7.16) was not the same as the true SWRC, which is the relationship between θ_l (or S_l) and s at a material point. In most cases, specimens as small as those used in these SWRC tests can be considered as material points, rather than having a finite height, committing negligible errors. However, for very coarse materials, this approximation may lead to noticeable errors. In the case of the fine sand (see Figure 7.16a), the soil specimen was considered as a material point and the modVG SWRC model was simply best-fitted to the experimental SWRC data points.

In the case of a soil as coarse as the sandy gravel (see Figure 7.16b), the soil specimen could not be considered as a material point and a different procedure for the calibration of the modVG SWRC model was used. At the end of each equalisation stage, the liquid phase was assumed to be in equilibrium and hence a hydrostatic suction profile was assumed within the soil specimen. This suction profile consisted of the value $\gamma_l \cdot (\Delta H_w - t_0/2)$ at the bottom of the soil specimen, the value $\gamma_l \cdot (\Delta H_w + t_0/2)$ at the top of the soil specimen and a linear variation in between, where t_0 is the height of the soil specimen and ΔH_w is the vertical distance between the water level in the burette and the mid-height of the soil specimen. Using this suction profile and assuming that the SWRC is known, the volumetric water content profile in the soil specimen was obtained. The average volumetric water content in the soil specimen was then calculated by integrating the volumetric water content profile over the height of the specimen and dividing by the total height of the specimen t_0. This calculated average volumetric water content was compared with the measured average volumetric water content. The parameters of the modVG SWRC model for the sandy gravel were calibrated iteratively by best-fitting simultaneously the calculated values of the average volumetric water content to the measured values of the average volumetric water content, for all suction steps. This best-fitting operation was performed independently for the main wetting SWRC and for the main drying SWRC. In Figure 7.16b, the dashed lines represent the modVG model predictions of average volumetric water content $\theta_{l,av}$ plotted against suction at the mid-height s_{av}, which are directly equivalent to the experimental results, whereas the solid lines represent the corresponding true SWRCs at a material point. Values of the modVG model parameters for the sandy gravel are given in Table 7.4. The value of θ_{ls} obtained during the main wetting (MW) test for the sandy gravel, i.e. $\theta_{ls} = 0.319$, was lower than the value of porosity $\Phi = 0.38$ obtained from a previous test (see Table 7.3), suggesting the occurrence of air trapping. The same value of θ_{ls} was recorded at the beginning of the main drying (MD) test.

It should be noticed that, for both materials, the main wetting and the main drying SWRCs (see Figure 7.16) do not coincide at low degree of saturation thereby exhibiting hysteresis. This is in contrast with the analysis of the hydraulic behaviour of unsaturated soils presented in Section 3.1, where it was discussed that water retention hysteresis is typically negligible in the pendular state. The difference between the MW SWRC and the MD SWRC was probably due to the fact that, during the tests, the soil specimens did not reach full hydraulic equilibrium conditions at low values of degree of saturation. Since the hydraulic conductivity at low degree of saturation is extremely low, reaching full hydraulic equilibrium conditions would have probably required extremely long times, much longer times than those actually waited. In the pendular state, the water content at equilibrium should probably have been greater than measured during MW and lower than measured during MD. This error is expected to have little consequence for the application of the hydraulic properties of the materials to the prediction of the results of the column infiltration tests, because, at the time of breakthrough, the suction values at all levels in the column were expected to be less than or equal to the bulk water continuity point for the relevant material.

Once the SWRC properties and the saturated hydraulic conductivities (see Table 7.3) of

the materials were characterised, the SHCCs were predicted using the modM+LF model (see Section 3.3) coupled with the modVG SWRC model. The parameters of the modM model, i.e. m, θ_{ls}, ξ, s_{BWC} and s_{BWD}, are shown in Table 7.4. For the estimation of the parameter C^{Film} of the LF model, the values of the parameters D_{10} and Φ shown in Table 7.3 and the default value of the parameter $X_D = 2.35 \times 10^{-9}\,\mathrm{mm\,ms^{-1}\,kPa^{1.5}}$ were used. The resulting SHCCs are shown in Figure 7.17.

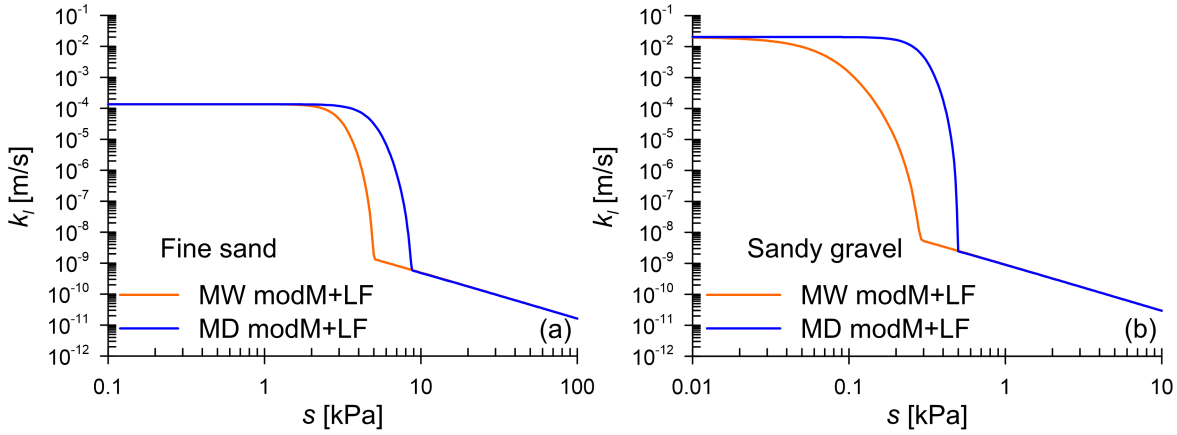

Figure 7.17: Predicted SHCCs of (a) the fine sand and (b) the sandy gravel

7.4.4 Column infiltration tests: equipment and procedure

Test procedure

After the material properties were characterised, one-dimensional column infiltration tests were performed on a conventional single capillary barrier and three different multi-layered CBSs, characterised by different layouts. In particular, with the total height of the CBS fixed at 1 m, excluding the 10 cm thick bottom coarser layer, four different CBSs were tested, with layering factors $\kappa = 1$, $\kappa = 2$, $\kappa = 3$ and $\kappa = 5$, as shown in Figure 7.18. In all the tests, the coarser layers were 10 cm thick whereas the thickness of the finer layer depended upon the layering factor κ according to Equation 7.4.

Figure 7.19 shows a schematic diagram of the column set up. The dry soil was placed in a cylindrical transparent acrylic tube and compacted in 2.5 cm-thick sub-layers by hand-tamping the soil to the target dry density values (i.e. $\rho_d = 1570\,\mathrm{kg/m^3}$ for the fine sand and $\rho_d = 1600\,\mathrm{kg/m^3}$ for the sandy gravel), which were consistent with the saturated hydraulic conductivity tests and the SWRC tests. After compacting each 2.5 cm-thick sub-layer, an initial controlled amount of water was sprayed over the soil surface of each sub-layer with the purpose of preparing the CBS at an initial controlled water content profile. In particular, each column was prepared with an initial water storage which was approximately 80% of the predicted water storage capacity at breakthrough. It was necessary to start the tests with a substantial quantity of water already within the barrier, because a low infiltration rate was subsequently applied (high infiltration rates may lead to unreliable estimations of the water storage capacity, as shown in Section 6.3) and excessively long test durations had to be

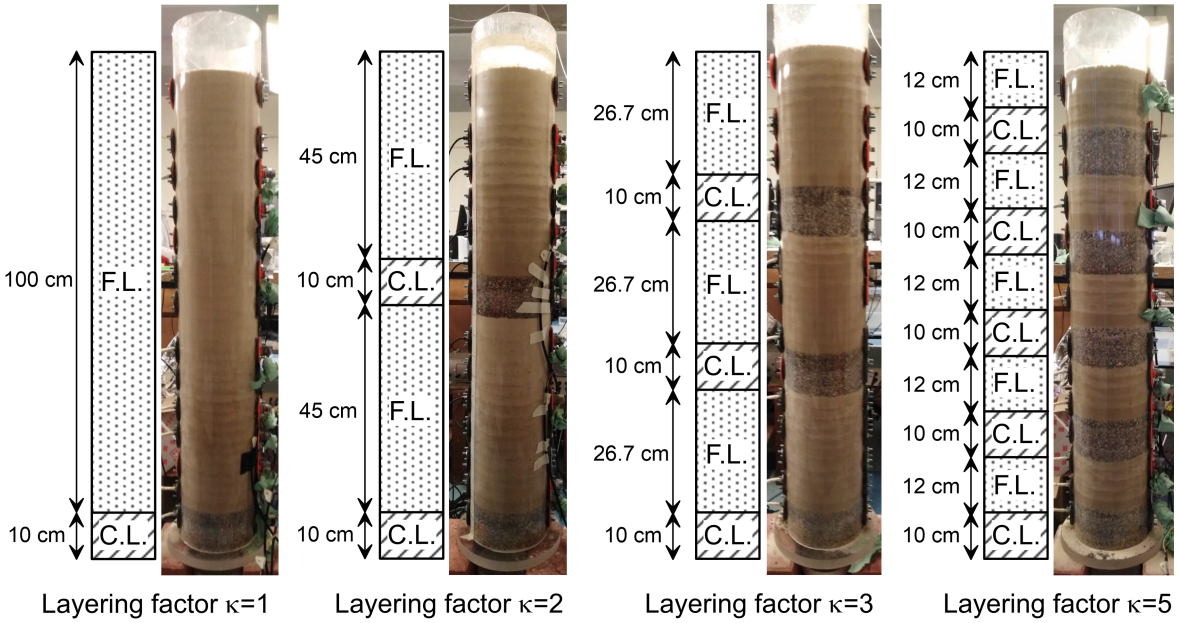

Figure 7.18: Layouts of the multi-layered capillary barrier systems prepared for the infiltration tests

avoided (if starting from dry conditions with a low infiltration rate, the duration of the test would have been very long). This initial amount of water was distributed non-uniformly over the height. In particular, knowing the SWRC properties of the materials, the water was distributed over the height with the aim of achieving a hydrostatic suction profile in each finer layer, with the volume of water within each finer layer corresponding to 80% of the value expected in that layer at breakthrough. The coarser layers were initially dry. Numerical simulations demonstrated that suction and volumetric water content profiles at breakthrough obtained with these initial conditions coincide with suction and volumetric water content profiles at breakthrough obtained starting from fully dry conditions. The initial volumetric water content profiles are shown in Figure 7.20. The initial water storages of the different CBSs were: 4224 ml for $\kappa = 1$; 6319 ml for $\kappa = 2$; 7658 ml for $\kappa = 3$; and 5525 ml for $\kappa = 5$.

A slow and constant flow (corresponding to an infiltration rate between 1.22×10^{-7} m/s and 1.38×10^{-7} m/s) was applied at the top of the column by means of a peristaltic pump (see Figure 7.19). More specifically, a liquid flow was driven to a small reservoir on top of the column. From this reservoir, five tubular wicks made of filter paper transferred the water to a filter paper disk, placed over the column surface in order to guarantee a uniform water infiltration from the top of the column. A similar water supply system (peristaltic pump, reservoir, tubular wicks and filter paper disk) was used by Stormont and Anderson [23] for laboratory infiltration tests on CBSs. A reservoir was connected to the bottom of the column to collect any water outflow occurring after breakthrough. Each test was run until water started being collected at the bottom of the column, indicating that water breakthrough across the lowest finer layer-coarser layer interface had occurred. The bottom reservoir was regularly weighed.

The column was instrumented with a maximum of 8 tensiometers (designed and manufac-

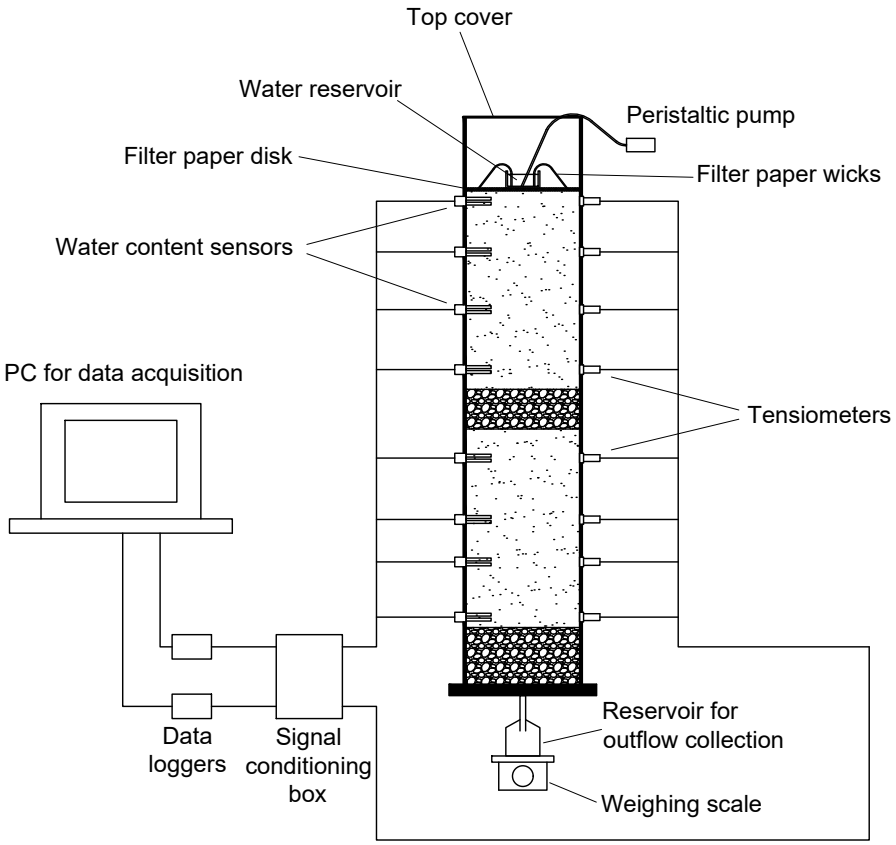

Figure 7.19: Schematic diagram of the column infiltration set up

tured in this thesis work) and a maximum of 8 water content sensors, all placed at different heights in the column, by means of which suction and volumetric water content were respectively recorded over time. In order to acquire automatically readings of suction and volumetric water content, the instruments were connected to a PC by means of a signal conditioning box, working as a power supply and output signal amplifier, and two data loggers. Thus, time histories and profiles at breakthrough of suction and volumetric water content were obtained. Also the water storage capacity of each CBS was obtained by monitoring the amount of water that had flowed into the column until breakthrough. The top of the column was covered with a cling film to limit evaporation.

At the end of each test, before disassembling the set up, samples of soil were taken from the column at different heights. This was done by accessing the lateral ports present in the vertical sides of the column for installation of the instruments. At the end of the test, while water kept being injected from the top of the column at the same constant rate as that used during the test, different lateral ports at different heights were opened and soil samples were extracted by scraping the lateral soil surface with a knife. The samples were subsequently oven-dried in order to work out the final volumetric water contents.

Sensors and electronic system

The volumetric water content in the soil was monitored using ECH_2O EC-5 water content sensors [238]. The EC-5 sensor has two 5 cm-long probes which form a large capacitor. One

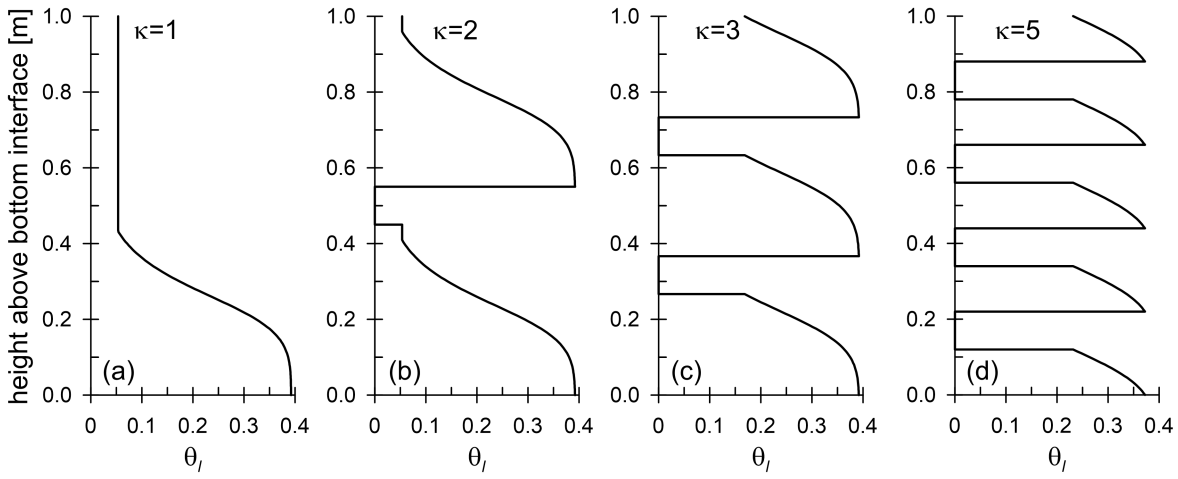

Figure 7.20: Initial volumetric water content profiles: layering factors (a) $\kappa = 1$, (b) $\kappa = 2$, (c) $\kappa = 3$ and (d) $\kappa = 5$

probe acts as a positive plate and the other probe acts as a negative plate, thereby creating an electro-magnetic field in the space between the probes [239]. The space between the probes is filled with soil which acts as a dielectric material with a certain dielectric conductivity. The capacitor charge, which is converted to an output voltage by the sensor circuitry, is directly related to the dielectric conductivity of the soil. The dielectric conductivity of the soil, in turn, is directly related to the volumetric water content [240]. Therefore, the output voltage reading of the EC-5 sensor is related to the volumetric water content in the soil.

The pore-water pressure in the soil was measured using PX26-005DV differential pressure sensors made by Omega Engineering Inc. [241]. These pressure sensors have two ports and a hose filled with a liquid or a gas can be connected to each port. A piezoelectric diaphragm placed inside the sensor is used to measure the difference in pressure between the liquids or gases present in the two ports. In particular, the piezoelectric diaphragm deforms and the direction and magnitude of the deformation depends on the difference in pressure between the two ports. If excited with a certain input voltage, the diaphragm will produce an output voltage. The sign and the absolute value of the output voltage will depend on the direction of the deformation (i.e. in which port the pressure is greater) and on the magnitude of the deformation (i.e. the absolute value of the difference in pressure). In this thesis work, since the aim was to measure the soil suction, one port was connected to a tensiometer filled with water in hydraulic equilibrium with the soil water at a given location, hence subjected to the soil pore-water pressure, whereas the other port was left open to atmosphere, hence subjected to atmospheric pressure. The difference of the two was the corresponding soil suction.

To acquire the readings from the pressure sensors and from the volumetric water content sensors, an electronic system was designed and set up in collaboration with the Electronic Services team of the School of Engineering of the University of Glasgow. Figure 7.21 shows a schematic diagram of the electronic system. The electronic system was set up for a maximum number of 8 pressure sensors and 8 water content sensors. A single power supply provided an input voltage of 12 Vdc. The pressure sensors required an input voltage of 10 Vdc whereas

the water content sensors required an input voltage of 3 Vdc. Therefore, two attenuators were used to decrease the supplied power to these target values of input voltage. For the range of pressures applied, the output voltage of the pressure sensors was in the range of -30 mV to 30 mV whereas the output voltage of the water content sensors was in the range of 300 mV to 1200 mV. These ranges of output voltage were too low compared to the resolution of the data loggers used in this system. Therefore, amplifiers were used to amplify the output signals of the sensors to a maximum of 10 V and a minimum of -10 V, which are the maximum and minimum values of voltage that can be read by the data loggers. Two data loggers were used, one for the pressure sensors and one for the moisture content sensors. The data loggers, which worked as analogue-to-digital converters, were NI USB-6001 DAQ devices purchased from National Instruments [242]. The two data loggers were connected to a personal computer and they were controlled by the PC based software LabVIEW.

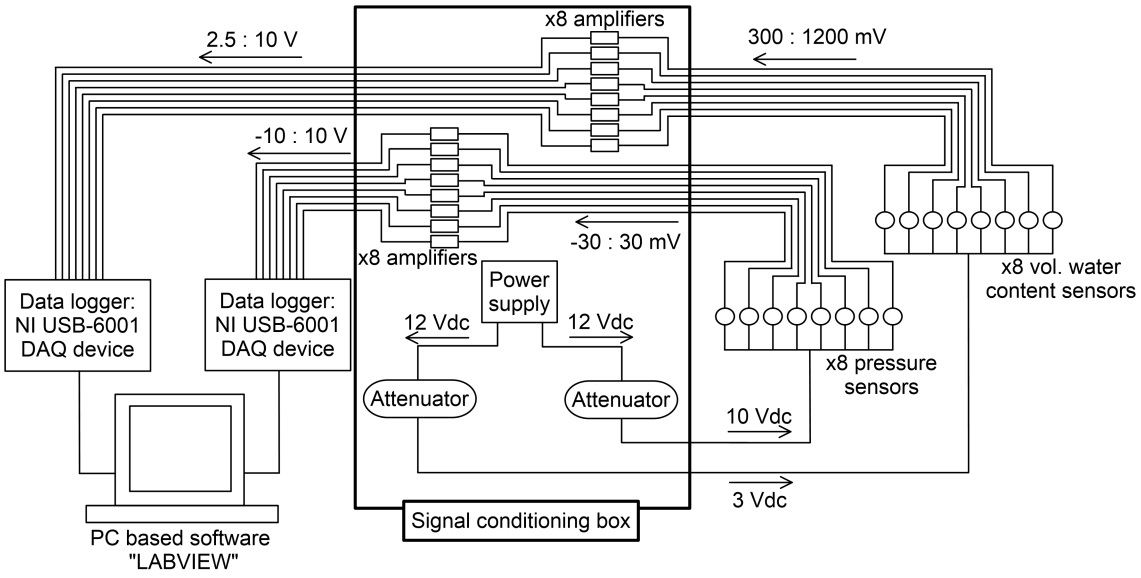

Figure 7.21: Schematic diagram of the electronic system

LabVIEW [243] is a software for the development and use of applications that require test, measurement and control and it uses a graphical programming language named G. A graphical program was developed in LabVIEW for the acquisition and processing of data from the sensors. According to this program, the output signals from the sensors were initially read with a specified frequency, between 3 and 60 readings per minute. Each instrument output signal (a voltage) was processed and converted to the corresponding physical quantity (i.e. pressure or volumetric water content) by using calibration relationships obtained previously. These data were plotted in real-time on the monitor of the PC for monitoring purposes and saved on data files in order to be re-used and analysed.

Calibration tests on the pressure sensors were firstly performed by applying a set of water pressure values to one port, P2, while leaving the other port, P1, open to the atmosphere. Subsequently, the same set of water pressure values were applied to port P1 while leaving port P2 open to the atmosphere. The water pressure was applied to a port of the sensors by connecting a burette filled with water to the port by means of a flexible nylon hose. The entire system of burette, hose and sensor port was filled with water. The water pressure applied to

the port of the sensor was varied by adjusting the difference in height between the pressure sensor and the water level in the burette. Figure 7.22 shows the results of the calibration tests on 8 different pressure sensors. As a reference, the difference between the pressure applied to the port P2 and the pressure applied to the port P1 was considered as positive. It can be seen that all the measurements taken with the different sensors can be very well interpolated by a linear relationship. A linear law was therefore used as calibration relationship between the output voltage and the pressure, in which the parameters of the linear relationship were calibrated by best-fitting the calibration test data, as shown in Figure 7.22. The data shown in Figure 7.22 refer only to the first 8 sensors used. During the whole experimental work, some pressure sensors were damaged and replaced, and thus new calibration tests were performed for the new sensors. Moreover, between each column infiltration test and the following one, the calibration tests were performed again to check that no variation in the behaviour of the sensors occurred during the tests, e.g. due to a plastic deformation of the internal diaphragm. When working correctly, the behaviour of the pressure sensors was always well represented by a linear calibration relationship, similar to those shown in Figure 7.22, and it was very clear when a sensor had been damaged and required replacement.

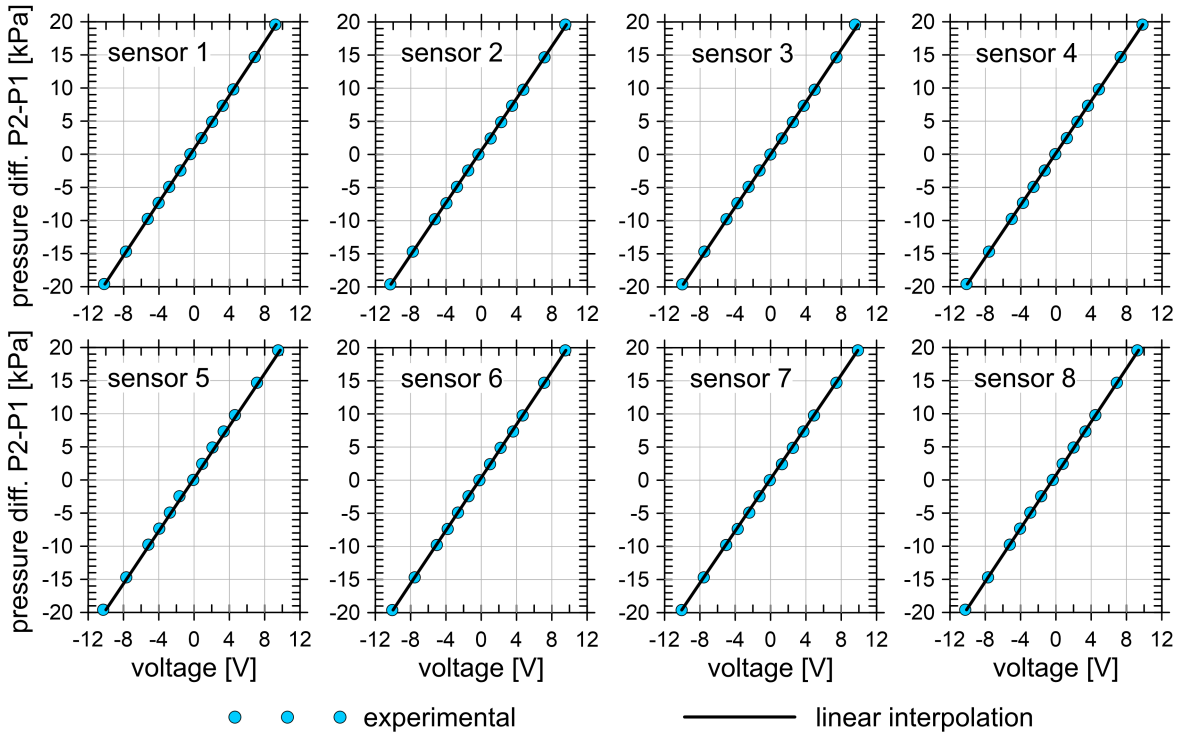

Figure 7.22: Calibration of the pressure sensors

Calibration tests on the volumetric water content sensors were performed by measuring the output voltage values of each sensor when inserted in soil specimens at different controlled volumetric water contents. Specifically, different containers were filled with fine sand prepared at different volumetric water contents. Each water content sensor was inserted into each soil specimen and the output voltage values of the sensors were acquired. The volume and wet mass of each soil specimen were measured. By oven-drying samples of the soils, it was

possible to work out the mass of water, the volume of water and finally the volumetric water content of the soils in each container. Therefore, for each water content sensor, a value of output voltage was related to the corresponding value of volumetric water content. The same operation was also done for the dry soil (i.e. θ_l=0). The results of the calibration tests on 8 water content sensors are shown in Figure 7.23. In agreement with the technical specifications provided by the producer, the response of the sensors can be represented well by a linear relationship in the range of values of volumetric water content in the soil, i.e. from θ_l=0 to θ_l=0.4. Therefore, a linear calibration relationship was used with the parameters obtained by best-fitting the calibration test data, as shown in Figure 7.23.

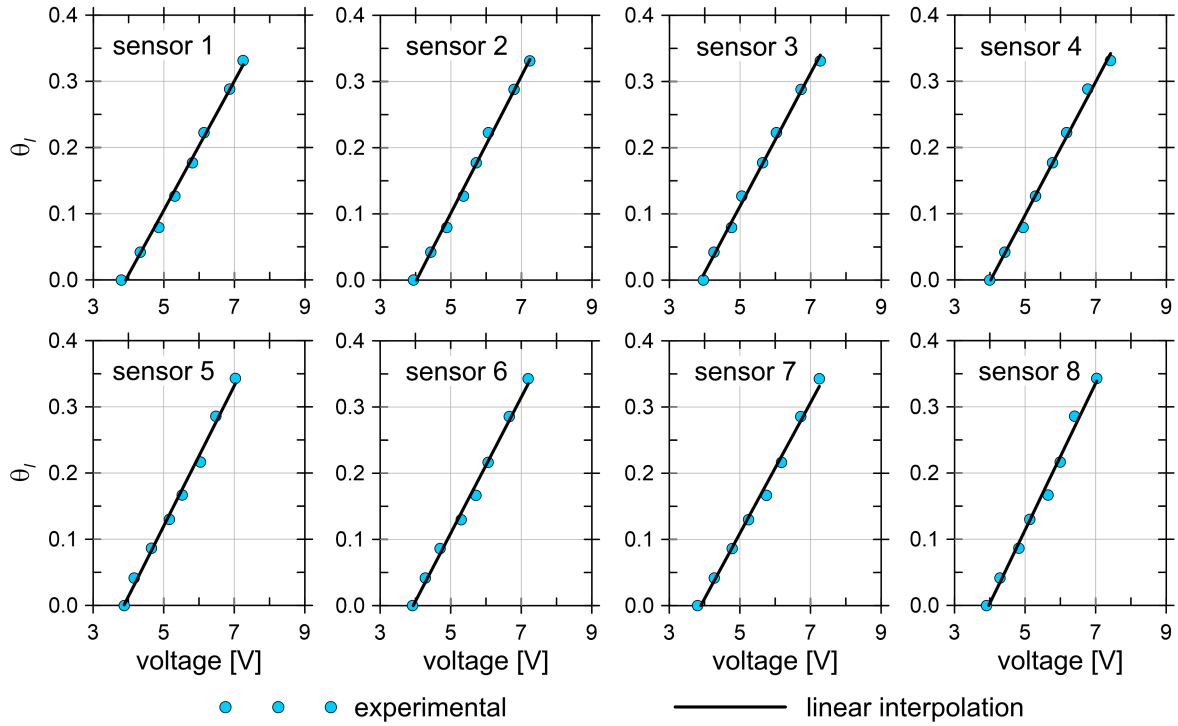

Figure 7.23: Calibration of the volumetric water content sensors

Assembly of the column and the external components

For the column infiltration tests, the column and associated external mechanical components were designed and assembled in collaboration with the Mechanical Services team of the School of Engineering of the University of Glasgow. The function of the column was to sustain the column of soil and to allow the instrumentation of the column of soil.

The soil was prepared inside a transparent acrylic cylindrical tube (see Figure 7.24), 1.2 m high, with an outer diameter of 200 mm and a wall thickness of 3 mm and consequently an inner diameter of 194 mm. The base of the column, glued to the bottom of the acrylic tube, was a 2 cm-thick acrylic plate with a hole drilled in the middle in order to drain any water that percolated to the bottom of the column.

In order to instrument the column of soils with tensiometers and volumetric water content sensors, 28 lateral ports were made symmetrically along two opposite vertical sides of the

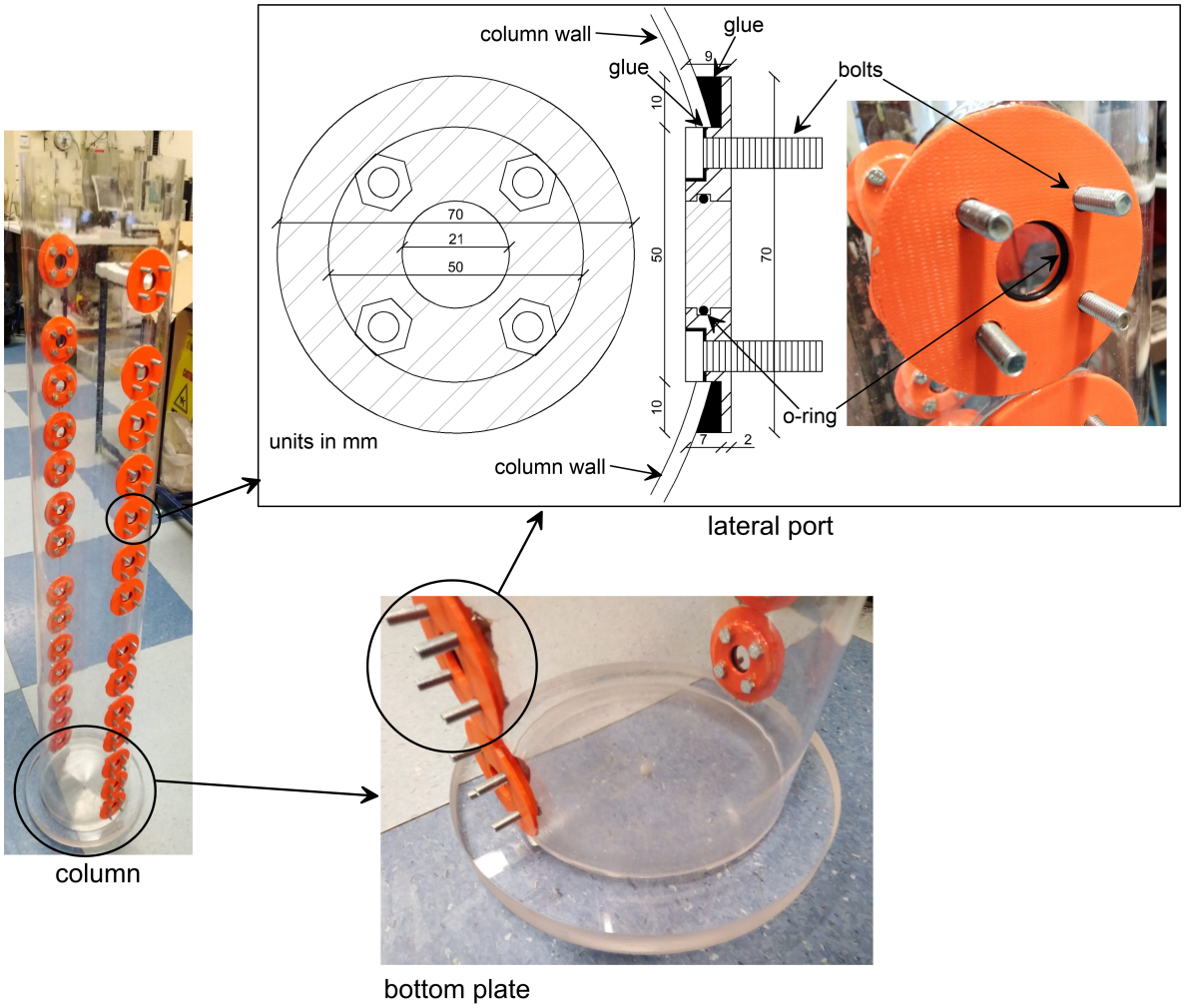

Figure 7.24: Details of the column

tube, 14 on each side, as shown in Figure 7.24. Holes of 52 mm diameter were first drilled in the acrylic tube. Some components made of acrylonitrile butadiene styrene (ABS) (i.e. a thermoplastic polymer) were then designed and 3D-printed and glued in the drilled holes. In particular, each of these 3D-printed components had a thicker central boss (diameter of 50 mm) and a thinner external flange (diameter of 70 mm), with a central circular hole of 21 mm diameter. Four bolts were glued in fours smaller holes spaced around the central hole (see Figure 7.24). The thicker central boss was inserted in the hole drilled in the acrylic column and glued in the space between the external flange and the column wall. The heads of the bolts were on the internal side of the column whereas the threaded shanks were on the external side of the column. Within the central hole of the 3D-printed component, an O-ring was installed.

The central hole of this port served as an access to other fitting components, which could be inserted in this hole. Three types of fitting components were made: a closing plug, the fitting component for the volumetric water content and the fitting component for the tensiometer.

In any given column tests, some of the 28 lateral ports were not used for tensiometers or volumetric water content sensors. These un-used lateral ports were closed during the

column infiltration test with blank plugs, shown in Figure 7.25. This plug, a 3D-printed ABS component, involved a thicker central boss (diameter of 21 mm) and a thinner external flange. The central boss was fitted inside the central hole of the lateral port of the column in order to close it during the column test. Fours holes in the plug matched the locations of the four bolts of the lateral port of the column. When the plug was inserted into the lateral port, the holes of the plugs matched the bolts, and nuts were screwed from the exterior to fix the plug in the lateral port. The O-ring in the lateral port formed a hydraulic seal at the contact between the lateral port and the plug. However, problems of water leakage would not have been expected even if the O-ring had not been installed, because negative values of pore water pressure were always maintained in the soil during the infiltration tests.

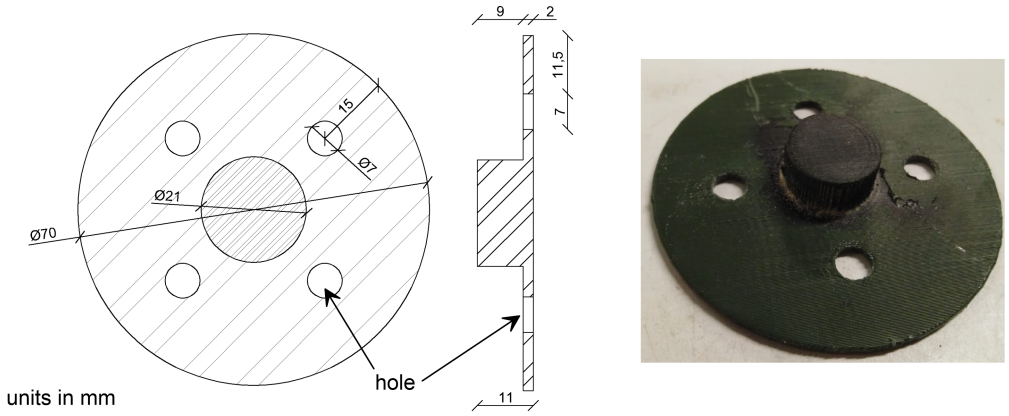

Figure 7.25: Details of the plug

Installation of the water content sensors in the soil column required the design and manufacture of specific components, shown in Figure 7.26. This fitting component was again a 3D-printed ABS object. This fitting component had a similar shape to the closing plug but it was made with a rectangular hole in the middle. The water content sensor was inserted in this central hole and glued in the hole. The water content sensor and its fitting component were then inserted in the lateral port of the column. Similar to the plug, the mechanical stability of the water content sensor was guaranteed by tightening the nuts on the bolts whereas a hydraulic seal was formed by the O-ring in the gap between the fitting component and the hole of the lateral port of the column. When inserted in the column, the 5 cm long sensor probes were located within the soil for their whole length.

For the measurement of suction in the soil, a tensiometer was designed and manufactured in this thesis work. The tensiometer was then glued to a fitting component for insertion in one of the lateral ports of the column. Details of the tensiometer and of the corresponding fitting component are shown in Figure 7.27. The tensiometer body was manufactured from a transparent acrylic cylinder, 20 mm in diameter and 40 mm in length. Two cylindrical holes were drilled in the cylinder, one in the longitudinal direction and one in the transverse direction, and they were connected to each other to form an internal chamber. On one end of the cylinder, connected to the internal chamber, a disk-shaped socket was formed, 17.5 mm in diameter and 7.14 mm deep. A porous ceramic plate was glued in this socket. The porous ceramic plate, purchased from Soilmoisture [244], was 7.14 mm-thick, had a

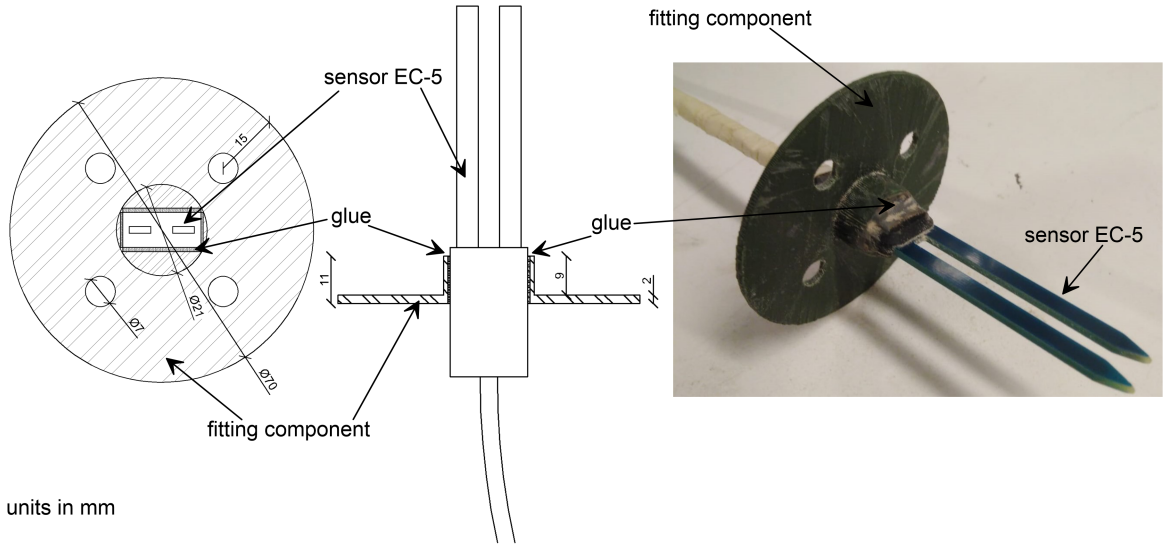

Figure 7.26: Details of the fitting component for the water content sensor

diameter of 15.88 mm, a nominal air-entry value of 50 kPa and it was classified as high flow (high hydraulic conductivity). The porous ceramic was glued to the tensiometer around its perimeter using a rigid epoxy resin from Araldite according to the procedure suggested by Vanapalli et al. [245]. The internal surface of the porous ceramic was in contact with the internal chamber of the tensiometer. The openings in the tensiometer obtained from drilling the internal chamber in the transverse direction were threaded. A hose adapter with an O-ring was screwed in the lower opening whereas a plug with an O-ring was used in the upper opening.

To use the tensiometer, it was initially put in de-aired water for sufficient time (at least 24 hours) to saturate the porous ceramic. Still keeping the tensiometer under water, a pressure sensor was connected to the lower end by means of a short hose connected to the hose adapter (see Figure 7.27). The upper end of the tensiometer was then closed by screwing in a male plug. Finally, the tensiometer was removed from the water and it was ready to be used. In this condition, the internal chamber was completely filled with de-aired water and the porous ceramic was saturated. When placing the ceramic in contact with moist soil, the water in the soil, in the ceramic and in the internal chamber of the tensiometer creates a continuous liquid path. Therefore, at equilibrium, the water pressure in the internal chamber equals the water pressure in the soil. Suction can be maintained in the tensiometer as long as no air flows into the internal chamber (the phenomenon of cavitation is not considered because it occurs at a value of suction much higher than the range of values attained in this work). During operation, the upper male plug and the hose adapter were covered by vacuum grease in order to prevent any possible entrance of air into the tensiometer.

Before being applied to the column infiltration tests, each tensiometer was tested. A thin layer of silt slurry was applied on the porous ceramic and it was progressively dried by tapping the surface with a dry tissue which progressively adsorbed the water from the silt layer. During this process, the pressure in the water chamber was continuously monitored with a pressure sensor. Each test was stopped and considered successful when values of

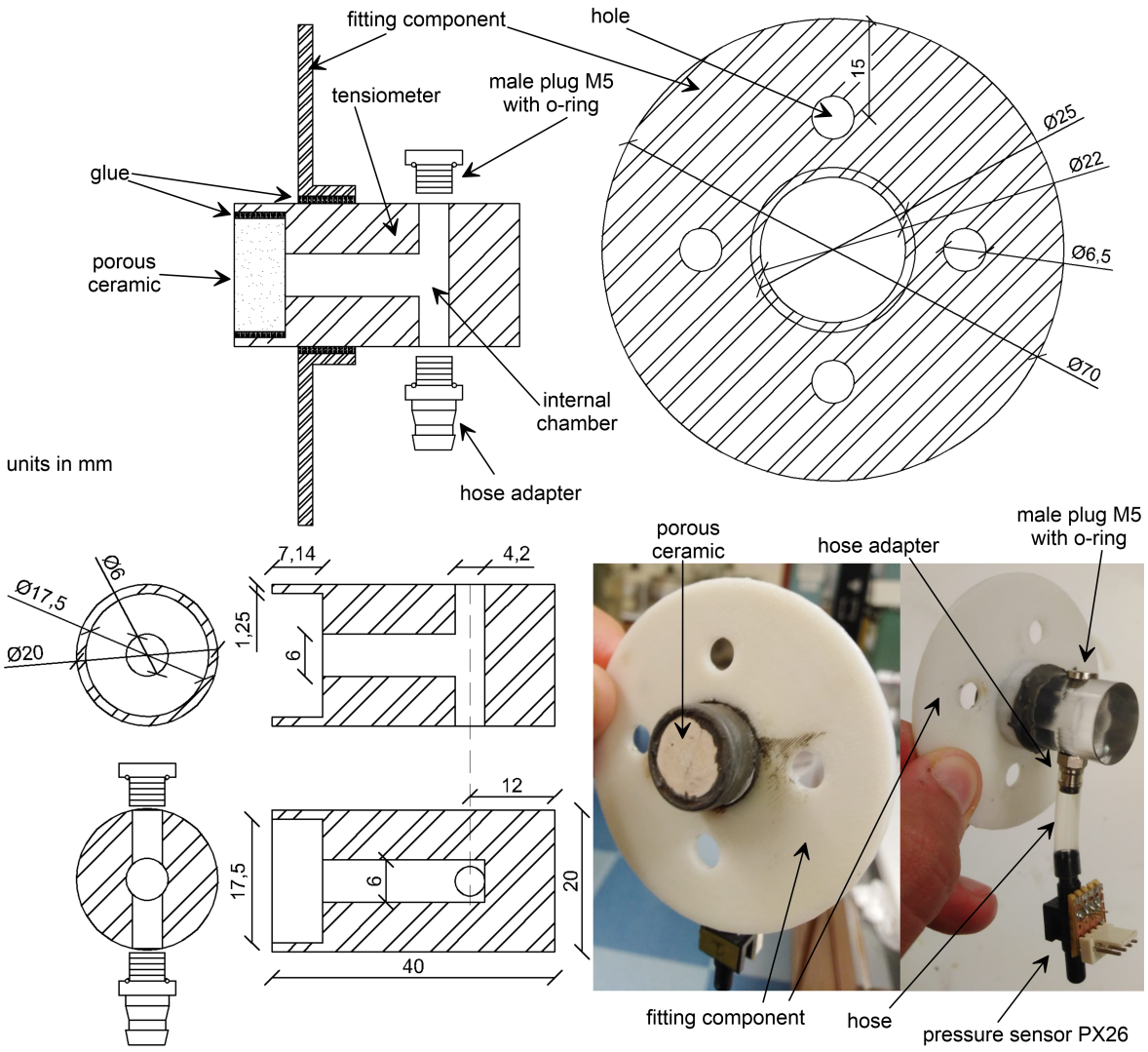

Figure 7.27: Details of the tensiometer and of the corresponding fitting component

suction greater than 20 kPa were reached, which is much greater than the values of suction expected during the infiltration tests. This tensiometer design was cheap and it proved to be reliable at relatively low values of suction. However, it was the result of long iterative work, with several earlier designs of tensiometer not functioning as expected.

In order to install the tensiometers in the column, ABS fitting components were 3D-printed (see Figure 7.27). These fitting components had a shape similar to the fitting components for the water content sensors. In the case of the fitting components for the tensiometers, the central hole was circular. The tensiometer was placed in the central hole and glued to the fitting component. The tensiometer could then be installed in the column, with the end where the porous ceramic was attached going into the lateral port of the column. As before, mechanical stability was guaranteed by screwing the nuts on the bolts passing through the holes of the fitting component whereas a hydraulic seal was formed by the O-ring in the lateral port of the column. Once the tensiometer was inserted, the surface of the porous ceramic was flush with the interior of the column wall and in direct contact with the soil. Before being installed in the column a thin layer of silt slurry was placed on the surface of the porous

ceramic in order to ensure a better contact with the soil and the pore water to limit possible wall effects [237].

7.4.5 Column infiltration tests: results and discussion

The results of column infiltration tests on one conventional SCB ($\kappa = 1$) and three different multi-layered CBSs ($\kappa = 2$, $\kappa = 3$ and $\kappa = 5$) are presented in this section.

Time histories of water inflows and outflows

Figure 7.28 shows the time histories of the cumulative water inflow and water outflow (expressed as volumes of water) for the four column infiltration tests. The water inflow into the column was monitored by regularly weighing the water reservoir from where the water was pumped to the top of the column by the peristaltic pump (see Figure 7.19). The water outflow from the column was monitored by regularly weighing the water reservoir placed at the bottom of the column for outflow collection. In all tests, the water inflow was approximately constant over time and the average values of the infiltration rates, expressed as a volume per unit time and as a volume per unit area per unit time, are shown in Table 7.5. Water outflow from the bottom of the column only started after breakthrough across the lowest interface between finer and coarser layers occurred. After breakthrough occurred, the outflow rate quickly tended to equalise with the inflow rate. The times at breakthrough t_{break} were obtained by inspection of a variety of results, as discussed later.

Table 7.5: Average infiltration rates during the experimental tests

	$\kappa = 1$	$\kappa = 2$	$\kappa = 3$	$\kappa = 5$
Q [ml/h]	14.7	13.0	13.9	14.7
i [m/s]	1.38E-07	1.22E-07	1.31E-07	1.38E-07

Time histories of suction

Figure 7.29 shows the time histories of suction recorded by the tensiometers placed at different locations in the different multi-layered CBSs (the locations of the tensiometers are indicated in the diagram of the column inserted in each sub-plot). The heights z are expressed directed upwards with the origin at the lowest interface between finer layer and coarser layer. Seven tensiometers were used in the tests on the CBSs with $\kappa = 2$ and $\kappa = 5$ whereas eight tensiometers were used in the tests on the CBSs with $\kappa = 1$ and $\kappa = 3$. Only the suction in the finer layers was monitored. The suction in the coarser layer was not monitored because it was difficult to guarantee the continuity of the liquid water between the porous ceramic and the sandy gravel. For the application of the simplified calculation method (see Section 7.2) and for the assessment of the water storage capacity, it is of more interest to assess the suction profiles at breakthrough in the finer layers because most of the water storage capacity is related to the water stored in these layers.

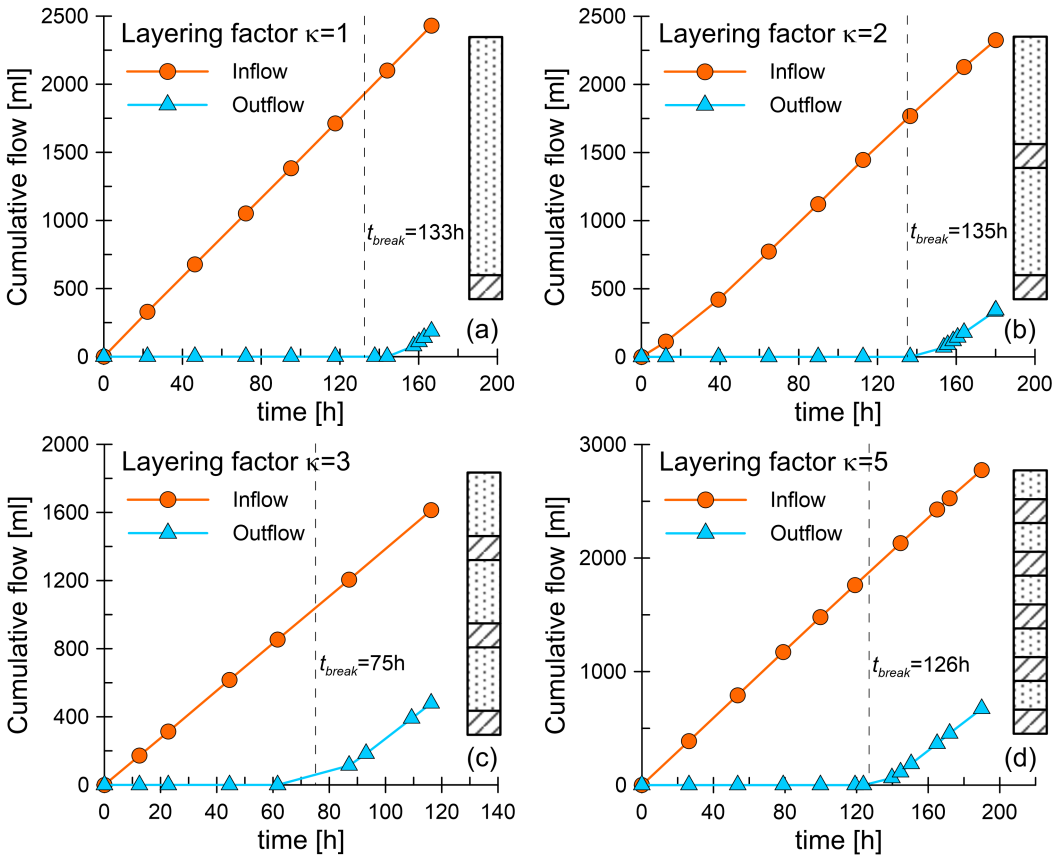

Figure 7.28: Time histories of the cumulative water inflow and outflow during the infiltration tests: (a) $\kappa = 1$, (b) $\kappa = 2$, (c) $\kappa = 3$ and (d) $\kappa = 5$

For the single CBS ($\kappa = 1$) (see Figure 7.29a), the suction values at $z = 80\,\text{cm}$, $z = 72\,\text{cm}$ and $z = 57\,\text{cm}$ were initially equal, suggesting a constant initial suction profile in the upper part of the finer layer. Subsequently, they started decreasing consecutively and at distinct times, at $z = 80\,\text{cm}$ first, at $z = 72\,\text{cm}$ second and at $z = 57\,\text{cm}$ third. The times at which suction starts decreasing at these locations can be seen as the times at which the propagating wetting front hits the corresponding tensiometers. Distinct times can be observed because in the upper part of the finer layer the water content was initially very low (see Figure 7.20a), the unsaturated hydraulic conductivity was very low and the propagating wetting front was thus sharp. After decreasing, these suction values became approximately constant and very similar at the different levels, suggesting that a constant suction profile was attained again in the upper part of the finer layer. By contrast, the suction values at $z = 38\,\text{cm}$, $z = 23\,\text{cm}$, $z = 16\,\text{cm}$, $z = 8\,\text{cm}$ and $z = 1\,\text{cm}$ started decreasing later and approximately at the same time. Moreover, the difference between these suction values remained approximately constant over time and proportional to the difference between the heights. Therefore, rather than the propagation of a sharp wetting front, this indicates that a steady state gradient of suction was maintained in the lower part of the column, with the suction values at different levels in this lower part all decreasing together. In particular, the difference in suction was the consequence of a quasi-hydrostatic profile, i.e. the proportionality between the difference in suction Δs and the difference in heights Δz was given by $\Delta s = \gamma_l \cdot \Delta z$. Therefore, a quasi-hydrostatic profile was always maintained in the lower part of the finer layer and this profile simply translated

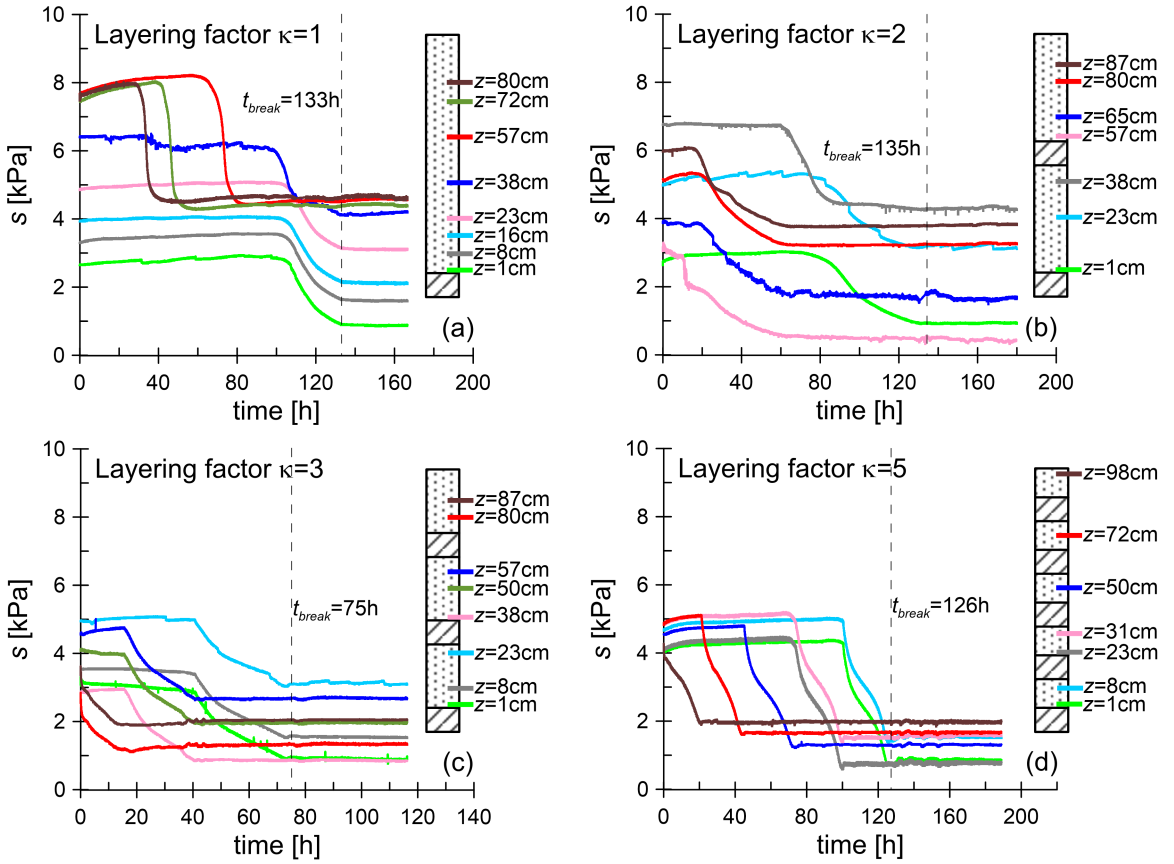

Figure 7.29: Time histories of the measurements of suction during the infiltration tests: (a) $\kappa = 1$, (b) $\kappa = 2$, (c) $\kappa = 3$ and (d) $\kappa = 5$

towards lower values of suction over time. The time at breakthrough can be identified as the time at which the suction values at lower heights stopped decreasing and attained a constant trend ($t_{break} = 133\,\text{h}$).

For the CBS with $\kappa = 2$ (see Figure 7.29b), the suction values recorded in the upper finer layer ($z = 87\,\text{cm}$, $z = 80\,\text{cm}$, $z = 65\,\text{cm}$ and $z = 57\,\text{cm}$) initially decreased approximately contemporaneously since the water contents at these heights were initially relatively high (see Figure 7.20b) as well as the initial hydraulic conductivities. Therefore, there was not the propagation of a sharp wetting front but almost a contemporaneous decrease of suction at the different locations. The suction values in the lower finer layer remained initially constant while water was initially propagating in the upper finer layer, and they started decreasing later than those in the upper finer layer. This indicates that the presence of the intermediate coarser layer acted as a capillary break before breakthrough occurred across the intermediate coarser layer. Breakthrough occurred when the suction values in the upper finer layer stopped decreasing and attained approximately constant values. After water breakthrough across the intermediate coarser layer occurred (approximately at $t = 60\,\text{h}$), the suction values in the lower finer layer ($z = 38\,\text{cm}$, $z = 23\,\text{cm}$ and $z = 1\,\text{cm}$) started decreasing almost immediately. With similarity to the intermediate coarser layer, the time at breakthrough in the lowest coarser layer can be identified as the time at which the suction values in the lower finer layer stopped decreasing and attained a constant trend ($t_{break} = 135\,\text{h}$). Also in this case, the suction profiles in the finer layers were approximately hydrostatic.

The interpretation of these results can be extended to the time histories of suction obtained in the tests on the CBSs with $\kappa = 3$ (see Figure 7.29c) and $\kappa = 5$ (see Figure 7.29d).

Time histories of volumetric water content

Figure 7.30 shows the time histories of the volumetric water content at different locations of the different multi-layered CBSs. For each test, the different coloured curves represent the measurements of different water content sensors located at different heights in the CBS. The locations of the water content sensors are shown in the diagram of the column inserted in each sub-plot. In addition, the corresponding initial volumetric water contents (see symbols at $t = 0$ h) and the corresponding final volumetric water contents (see symbols at the end of the tests) are shown for comparison. The initial volumetric water contents correspond to the values of the volumetric water content used during the initial preparation of the column (see Figure 7.20). To obtain the final volumetric water content, soil samples were extracted from the lateral ports at the end of the tests, before disassembling the columns. These soil samples were then weighed, oven-dried and weighed again to work out the corresponding mass of water and mass of solids, and hence the volumetric water content in the column (knowing the porosity of the soil in the column).

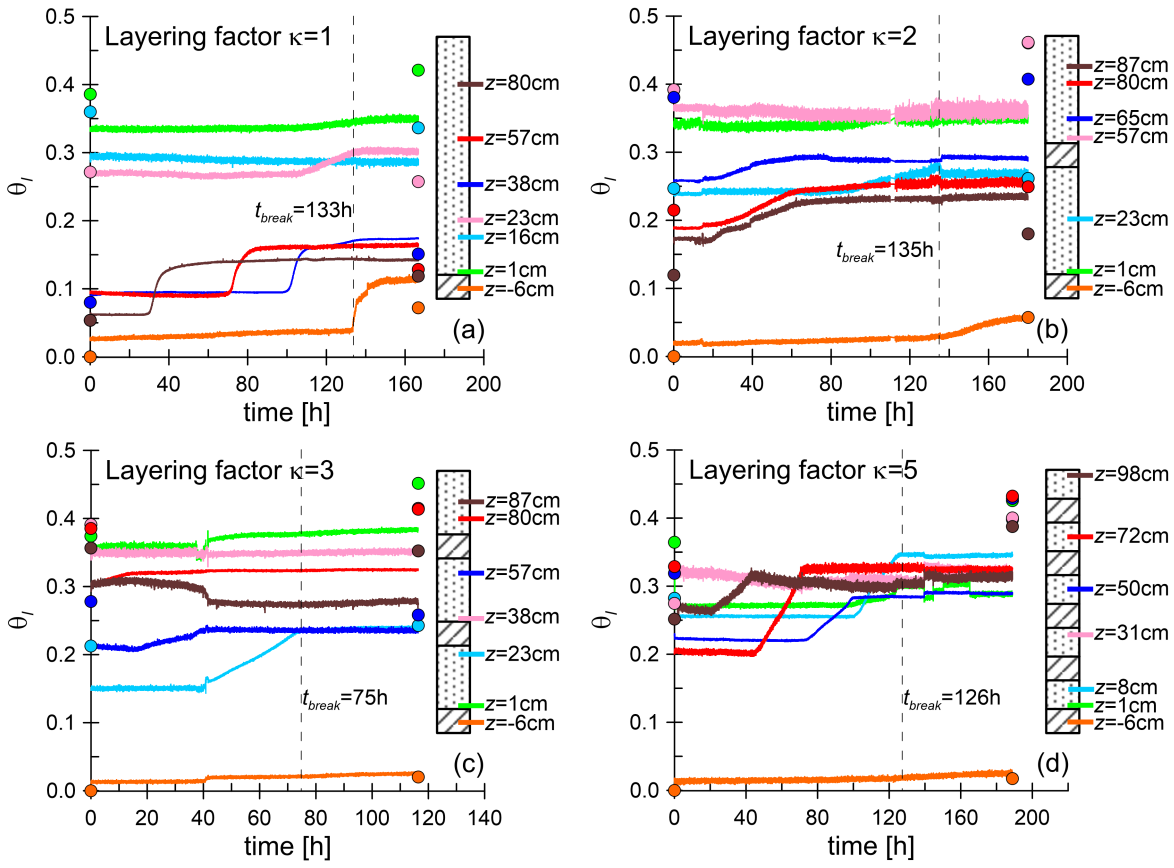

Figure 7.30: Time histories of the volumetric water content measured by the water content sensors (solid lines), initial water contents (symbols at $t = 0$ h) and final water contents (symbols at the final times of the tests) for the different infiltration tests: (a) $\kappa = 1$, (b) $\kappa = 2$, (c) $\kappa = 3$ and (d) $\kappa = 5$

Theoretically speaking, the volumetric water contents recorded by the sensors at the beginning of the test (solid lines at $t = 0\,\text{h}$) should match the initial volumetric water content values (symbols at $t = 0\,\text{h}$) and the volumetric water contents recorded by the sensors at the end of the test (solid lines at the final times) should match the final volumetric water content values (symbols at the final times). In many cases, the initial and final volumetric water contents recorded by the sensors did not match the independently determined initial and final volumetric water contents. There may be a degree of uncertainty in the initial water contents, due to possible water redistributions occurring within the columns between the set-up time and the beginning of a test when monitoring commenced. It is expected, however, that the measurements of final water contents, obtained from the soil samples taken from the column at the end of the test, were accurate and reliable. Hence, the measurements of the water content from the water content sensors were considered unreliable, at least in terms of the absolute values. Nevertheless, they still provided sensible results even if only in terms of the variation of volumetric water content with time. Possible causes of the unreliable response of the volumetric water content sensors were:

- instability of the connection between the water content sensors and the signal conditioning box, i.e. a stereo 3.5 mm Jack connector;
- poor homogeneity of the water content distribution in the volume of soil affecting the sensor measurement, e.g. a discontinuity of water content at the interface between finer layer and coarser layer and, within the same layer, high variation of water content in a little volume of soil;
- poor contact between the sensor probes and the soil, e.g. formation of air gaps between the probes or unrepresentative soil conditions in the soil immediately adjacent to the sensor probes (disturbance caused by the presence of the sensor probes);
- influence of the boundary effects at the outer edge of the soil column;
- for sensors located in the coarser layer, fingering [192] (i.e. unstable non-homogeneous wetting front propagation during infiltration into layered soils) may occur and cause local inhomogeneities in the water content.

Although the electronic system was designed to connect a maximum of 8 water content sensors, one was damaged during the calibration operations. Thus, seven water content sensors were used in each test. Although it is advised [238] not to use these water content sensors in very coarse soils such as a sandy gravel because it may lead to unreliable measurements, one sensor was always placed in the bottom coarser layer at $z = -6\,\text{cm}$ (see Figure 7.30). The purpose of this sensor was only to relate the time at breakthrough across the lowest interface to the measurement of an increase of the water content in the bottom coarser layer. In the tests on the CBSs with layering factors $\kappa = 1$ (see Figure 7.30a) and $\kappa = 2$ (see Figure 7.30b), it was possible to record an increase of the water content whereas no significant increases in water content in the bottom coarser layer were recorded by the sensors in the tests on the CBSs with layering factors $\kappa = 3$ (see Figure 7.30c) and $\kappa = 5$ (see Figure 7.30d).

From the observation of the results for the single CBS ($\kappa = 1$) (see Figure 7.30a), a similar pattern described for the time history of suction can be identified. Consecutive and distinct increases of the water content at the higher locations ($z = 80$ cm first, $z = 57$ cm second and $z = 38$ cm third) can be observed. This suggests the downwards propagation of a sharp wetting front. By contrast, at a lower location in the finer layer $z = 23$ cm, which was initially at a greater value of water content and hydraulic conductivity, the water content increased almost at the same time as at $z = 38$ cm. At $z = 16$ cm and $z = 1$ cm the water contents remained always approximately constant because the initial degrees of saturation were close to the maximum saturation S_{ls}.

For the CBS with $\kappa = 2$ (see Figure 7.30b), the water contents at the heights $z = 87$ cm, $z = 80$ cm and $z = 65$ cm started increasing almost at the same time since the water contents at these heights were initially relatively high (see Figure 7.20b) as well as the initial hydraulic conductivities. Therefore, there was not the propagation of a sharp wetting front but almost a contemporaneous increase of the water content at the different locations. The water content at $z = 23$ cm started increasing later than at $z = 87$ cm, $z = 80$ cm and $z = 65$ cm indicating, as discussed earlier, that the intermediate coarser layer acted as a capillary break until water broke through the intermediate coarser layer. At $z = 57$ cm and $z = 1$ cm, the water contents remained approximately constant because, also in this case, the initial degrees of saturation next to the interfaces with the underlying coarser layers were close to the maximum degree of saturation S_{ls}.

A similar interpretation can be given also to the results of the other two tests $\kappa = 3$ (see Figure 7.30c) and $\kappa = 5$ (see Figure 7.30d). However, for the test with $\kappa = 5$, also the water contents at locations next to the interfaces with the coarser layers (e.g. $z = 1$ cm) increased because the initial water content values were all relatively low (see Figure 7.20d).

These results of volumetric water content measured by the water content sensors must be treated with caution because the quality of the measurements was significantly affected by the weaknesses mentioned earlier. These measurements can only provide sensible information about the time variation patterns but the absolute values are unreliable. On the other hand, the suction measurements through tensiometers were reliable and convincing and they were hence treated with confidence.

Suction and volumetric water content profiles at breakthrough

For each test, the time at breakthrough was identified by comparing the different results shown in Figures 7.28, 7.29 and 7.30. Given that the water breakthrough into the lowest coarser layer is a relatively sudden phenomenon (see Section 6.1), when the outflow from the CBS starts, the outflow rate quickly attains the applied infiltration rate. From the time histories of the outflow shown in Figure 7.28, the times at breakthrough t_{break} can therefore be estimated as the intersection between the horizontal axis and the extrapolation of the linear trend of the cumulative outflow established after breakthrough. From the time histories of suction shown in Figure 7.29, the time at breakthrough t_{break} can be identified as the time at which the suction recorded close to the lowest interface between the finer layer and the

coarser layer stops decreasing and starts following approximately a constant trend. From the time histories of the volumetric water content shown in Figure 7.30, the time at breakthrough t_{break} can be estimated as the time at which the volumetric water content in the lowest coarser layer starts increasing (only detectable for $\kappa = 1$ and $\kappa = 2$). These three interpretations of the phenomenon of breakthrough led to consistent values of the times at breakthrough: $t_{break} = 133\,\text{h}$ for $\kappa = 1$, $t_{break} = 135\,\text{h}$ for $\kappa = 2$, $t_{break} = 75\,\text{h}$ for $\kappa = 3$ and $t_{break} = 126\,\text{h}$ for $\kappa = 5$.

Figure 7.31 shows the suction and volumetric water content profiles at the time of breakthrough for the four infiltration tests. In particular, the symbols represent the experimental data points obtained from the column infiltration tests. The suction data points were obtained from the readings of the tensiometers at the time of breakthrough t_{break}. The volumetric water content data points were obtained from tests on soil specimens extracted from the lateral ports of the column at the end of the test and then oven-dried to work out the volumetric water content, as discussed earlier in this section. The blue dashed lines represent the profiles obtained using the simplified calculation model presented in Section 7.2. The bulk water-continuity value of the coarser layer was $s^c_{BWC} = 0.3\,\text{kPa}$; the constant suction values in the intermediate coarser layers, which depend on the applied infiltration rate, were $s^*_c = 0.259\,\text{kPa}$ for the test with $\kappa = 2$, $s^*_c = 0.258\,\text{kPa}$ for the test with $\kappa = 3$ and $s^*_c = 0.258\,\text{kPa}$ for the test with $\kappa = 5$; the maximum values of suction in the finer layers at breakthrough, which depend on the applied infiltration rate, were $s^*_f = 4.55\,\text{kPa}$ for the test with $\kappa = 1$, $s^*_f = 4.57\,\text{kPa}$ for the test with $\kappa = 2$, $s^*_f = 4.56\,\text{kPa}$ for the test with $\kappa = 3$ and $s^*_f = 4.55\,\text{kPa}$ for the test with $\kappa = 5$. The volumetric water content profiles were obtained from the suction profiles using the main wetting (MW) SWRC modVG models presented in Section 7.4.3.

Comparing the experimental results at breakthrough (symbols) and the results of the simplified model (blue dashed line), it can be seen that, in general, the simplified model is able to capture the general trend of the suction profiles and the water content profiles. At breakthrough, the experimental suction data points tend to be aligned on hydrostatic profiles for suction lower than s^*_f and to be approximately constant in the upper part of a finer layer where suction attains the value of s^*_f (see Figure 7.31a). However, the model always slightly underestimates the suction values at locations where the suction profiles are hydrostatic, due to a difference between the suction values predicted at the interfaces between the finer layers and the underlying coarser layers. This difference between the suction values obtained from the model and those obtained from the experiments is always approximately the same among all the different tests, that is approximately 0.4 kPa. As a consequence of the fact that the suction profiles at breakthrough were slightly underestimated by the simplified model, the volumetric water content profiles at breakthrough were slightly overestimated by the simplified model with comparison to the experimental data (see Figure 7.31). It should be also remembered that the experimental values of θ_l are less reliable than the experimental values of s (see earlier).

The difference between the suction value at the interface between finer layer and coarser layer predicted with the model and that obtained from the experiments, approximately 0.4 kPa, can be explained by referring to Figure 7.32. Figure 7.32a shows a photograph of an interface

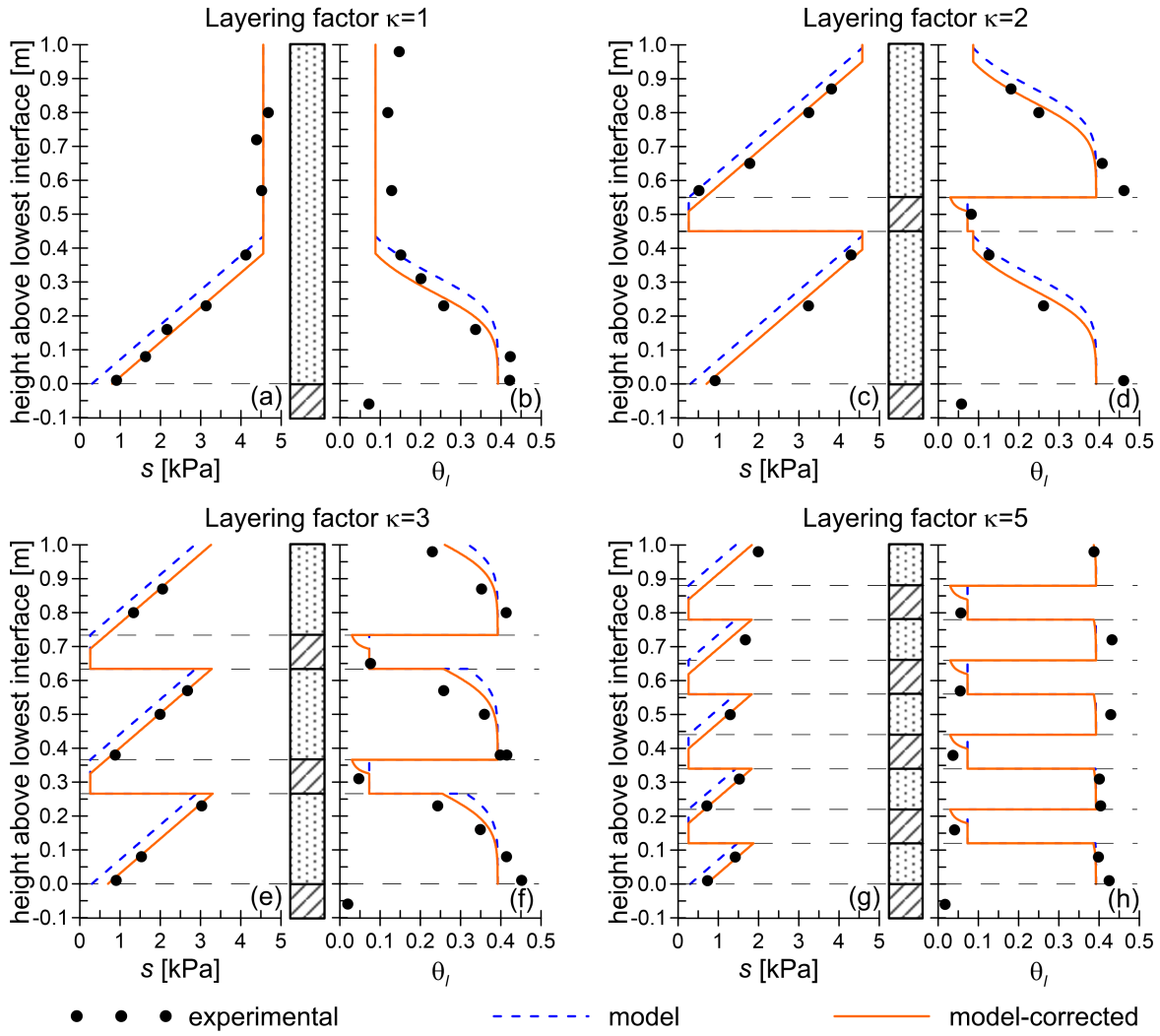

Figure 7.31: Suction and volumetric water content profiles at breakthrough for the different infiltration tests: (a,b) $\kappa = 1$, (c,d) $\kappa = 2$, (e,f) $\kappa = 3$ and (g,h) $\kappa = 5$

between a finer layer and a coarser layer at an early stage of an infiltration test, namely at a much earlier time than the time at breakthrough. After the CBS was set up with an initial amount of stored water that was lower than the water storage capacity of the CBS, the upper few centimetres of each coarser layer, immediately below the interface with a finer layer, quickly became damp. This occurred in all four tests and at all the different interfaces between a finer layer above and a coarser layer underneath. This damp zone was always approximately 4 cm thick (see Figure 7.32a). After being formed, this damp zone did not extend further until water breakthrough across the interface occurred. The formation of this damp zone can be interpreted by the schematic diagram shown in Figure 7.32b. Given that the materials for the finer layer and for the coarser layer have significantly different grain sizes, the coarser layer may be contaminated to some extent by soil grains from the finer layer when the latter is spread and compacted on the coarser layer. When this happens, the finer material occupying the large pores of the coarser material will be at a high value of degree of saturation, similar to that in the finer material above the theoretical interface. The theoretical interface can be considered the design interface or the potential interface if no contamination of material

occurred. When the finer material contaminates the coarser layer, the phenomenon of water breakthrough from the finer layer to the coarser layer will start at a greater depth than the theoretical interface because the water will create continuous liquid paths in the finer material occupying the larger pores of the coarser material. The depth of an effective interface can be defined as the maximum depth reached by the finer material in which the water can create continuous liquid paths within the finer material above the theoretical interface. In this case, water breakthrough will start when suction attains the bulk water continuity value of the coarser layer s^c_{BWC} at the effective interface instead of the theoretical interface. Therefore, the effective suction profile at breakthrough in the finer layer will have a similar form to the theoretical suction profile but its origin will be at the effective interface. As a result, the difference in suction between the theoretical profile and the effective profile at a given height is $\gamma_l \cdot \Delta z$ where Δz is the vertical distance between the theoretical interface and the effective interface. In these tests, identifying the thickness of the damp zone in the coarser layer as the depth of contamination Δz, the difference in suction between the theoretical profile and the effective profile is approximately 0.4 kPa. This value is exactly the difference in suction between the profiles obtained with the simplified model and the experimental profiles in Figure 7.31, thereby confirming the interpretation of the phenomenon just described.

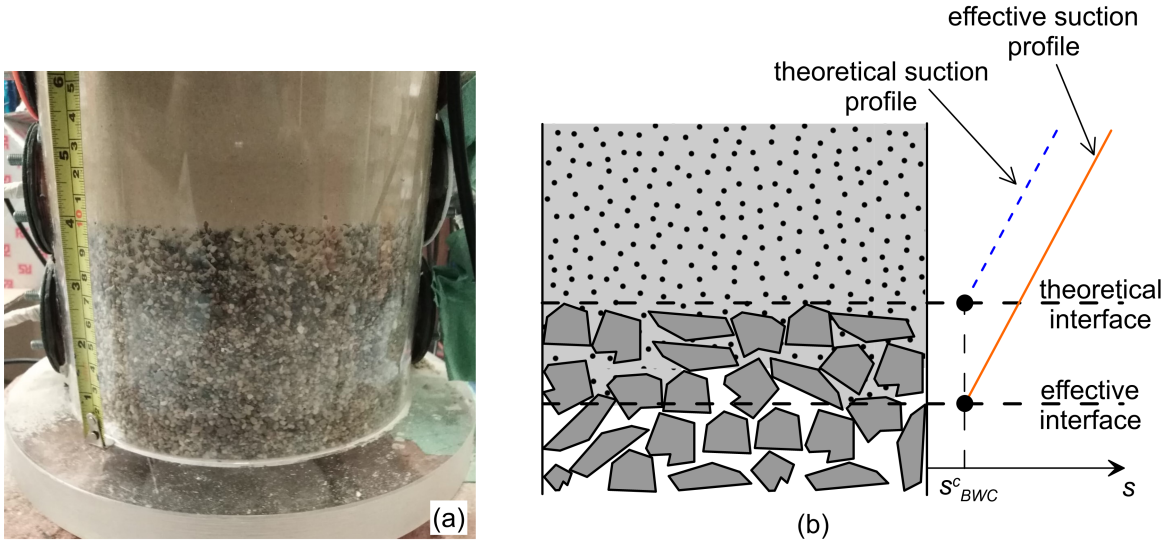

Figure 7.32: Contamination of coarser layer at the interface: (a) photograph during experiment and (b) schematic representation

In order to take into account the difference between the theoretical interface and the effective interface, a correction was introduced in the simplified model. With the corrected model (see orange solid lines in Figure 7.31), the origins of the suction profiles in the finer layers were simply moved lower into the coarser layer by 4 cm. As a result, at a given height where the suction profile is hydrostatic, the suction obtained with the corrected model was approximately 0.4 kPa greater than the suction obtained with the non-corrected model. It can be seen that the suction profiles obtained with the corrected model were all in very good agreement with the experimental data, thereby confirming the validity of the simplified model and the correction introduced to take into account the contamination of material at the

interface.

The volumetric water content values at breakthrough obtained with the corrected model were in general lower than those obtained with the non-corrected model and matched well the experimental data points. However, both the models underestimated the constant value of the volumetric water in the upper part of the single capillary barrier (see Figure 7.31b), which led to an underestimation of the water storage capacity. This difference between the simplified models and the experimental data must be probably attributed to a poor characterization of the SWRC and/or the SHCC of the fine sand around the bulk water-continuity value. Moreover, the maximum volumetric water content in the finer layers obtained close to the interfaces with the underlying coarser layers was slightly underestimated by both models in all the tests (see Figure 7.31b,d,f,h). This was probably due to the presence of a lower amount of trapped air in the column infiltration tests than in the SWRC tests and/or to differences in the porosity of the soil prepared for the infiltration tests with respect to the value obtained during the preliminary tests.

Water storage capacities

Figure 7.33 shows the water storage capacities of the different multi-layered CBSs obtained from the column infiltration tests (black symbols), plotted against the layering factor κ. In particular, Figure 7.33a shows the absolute values of the water storage capacities WSC whereas Figure 7.33b shows the ratio between the water storage capacity of the generic multi-layered CBS, WSC, and the water storage capacity of the corresponding single CBS, WSC_{SCB}. The WSC values of the four different CBSs tested in this work were obtained by summing the initial water storages used during the preparation of the soil columns and the volumes of water infiltrated in the soil columns until the times at breakthrough t_{break}. For comparison, also the water storage capacity curves obtained by applying the simplified model (blue dashed line) and the corrected version of the simplified model taking into account the contamination of the coarser material with the finer material (orange solid line) are plotted in Figure 7.33. In general, the experimental results confirm the interpretation of the hydraulic behaviour of multi-layered CBSs. Indeed, as already described in Sections 7.1 and 7.3, the experimental results show that a significant gain in the WSC was obtained by layering the CBS. The experimental results show that the WSC of the single CBS ($\kappa = 1$) was increased by approximately 30% by using a layering factor of $\kappa = 2$ and by approximately 40% by using a layering factor of $\kappa = 3$. Moreover, experimental results also show that the gain in the WSC does not increase indefinitely with increasing κ, because the effect of the potential increase in the degree of saturation in the finer layers overlying intermediate coarser layers becomes outweighed by the reduction of WSC due to the low degree of saturation in the intermediate coarser layers. This is clearly shown by the fact that the WSC decreases from $\kappa = 3$ to $\kappa = 5$.

Figure 7.33a also shows that both the models are able to capture relatively well the WSC of multi-layered CBSs. Differences between the experimental results and the results obtained with the models are mainly related to a non-perfect characterization of the SWRCs and the SHCCs. This was particularly evident in the calculation of the WSC of the single CBS, which

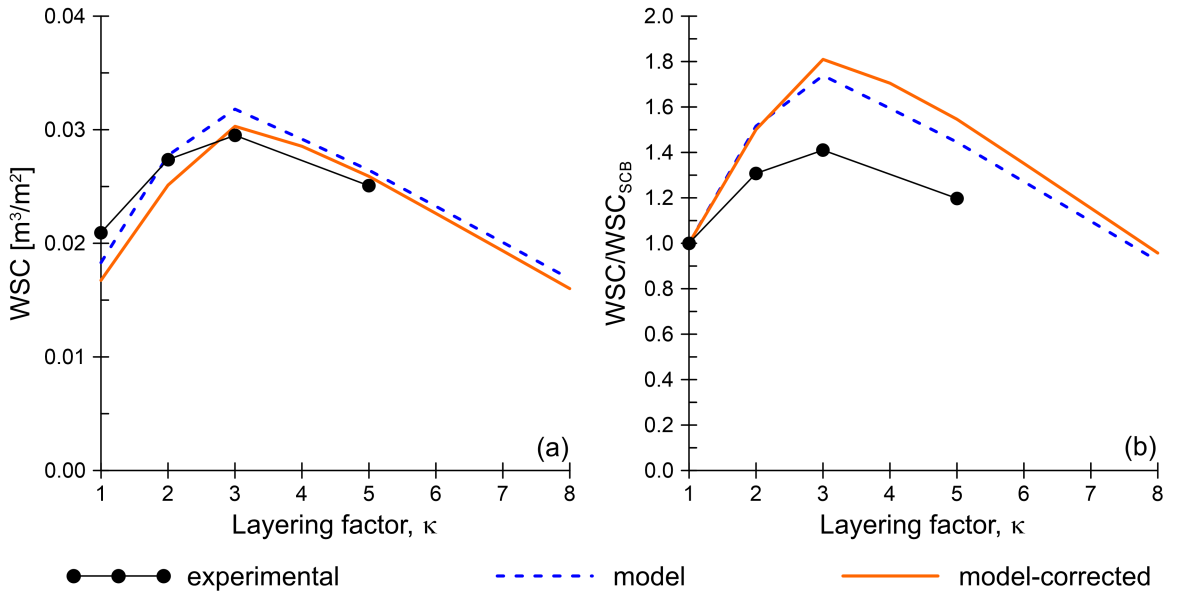

Figure 7.33: Water storage capacities (a) and ratios between the water storage capacity and water storage capacity of the corresponding single capillary barrier (b) plotted against the layering factor for the different infiltration tests

was underestimated by both models. The underestimation of the water storage capacity of the single CBS was the major cause of differences between the experimental curves and the curves from the models, when plotted in terms of the ratio WSC/WSC_{SCB} in Figure 7.33b.

7.5 Concluding remarks

In certain conditions, horizontal conventional CBSs may be highly inefficient at storing water because most of the water is stored in the lower part of the finer layer, close to the interface with the underlying coarser layer, whereas the remaining soil in the F.L. is at low degree of saturation. In such conditions, the use of multiple layers may lead to an increase of water storage capacity.

A simplified approach for the analysis of multi-layered CBSs was proposed. It consists of the definition of a schematic suction profile at breakthrough, depending on infiltration rate and hydraulic properties of the materials, from which the corresponding profile of degree of saturation at breakthrough, and hence the water storage capacity, can be obtained by knowing the SWRCs of the materials. The accuracy of this simplified approach was validated against numerical results of FE analyses and experimental results of laboratory physical tests.

Parametric analyses performed with numerical FE simulations and the simplified method showed the following:

- the gain in WSC obtained by layering may be significant in certain conditions;
- the existence of an optimum layering factor which maximises the gain in water storage capacity;
- the gain obtained by layering increases as the thickness of the CBS increases and if

coarser-grained materials are used, in particular for the finer layer;

- although a high infiltration rate may limit the benefit of using multi-layered CBSs, the WSC obtained using a high infiltration rate is unreliable and should not be adopted.

The behaviour of multi-layered CBSs was finally investigated by means of physical laboratory tests involving column infiltration tests on different CBSs with different layering factors. All the equipment used was designed and manufactured in this work, including tensiometers. These laboratory tests showed that:

- each intermediate coarser layer acts as a "hydraulic break" between different finer layers until breakthrough occurs into that individual coarser layer;
- the suction profile at breakthrough is affected by contamination of the coarser layers from particles of the finer layers;
- suction and water content profiles at final breakthrough into the lowest coarser layer, and hence water storage capacities, obtained from the experimental tests on the CBSs matched well those predicted using the simplified method, after introducing a correction for the contamination of the coarser layers;
- the gain in WSC obtained by layering was significant;
- there is an optimum layering factor which maximises the gain in water storage capacity.

Chapter 8

Numerical study of the long-term application of capillary barrier systems for suction-control purposes

8.1 Introduction

In the previous chapters, the fundamental behaviour of capillary barrier systems was analysed considering relatively simple numerical models (i.e. only one-dimensional analyses) and conditions (e.g. constant liquid flow or constant atmospheric conditions applied at the soil surface). These analyses were performed to study the impact of the new hydraulic constitutive models for unsaturated soils presented in Chapter 3 on the fundamental behaviour of capillary barrier systems (Chapter 6) and to analyse the behaviour of non-conventional multi-layered capillary barrier systems (Chapter 7). The aim of this chapter is to study numerically the long-term application of capillary barrier systems for suction-control and slope stability purposes. Given that the use of CBSs may potentially prevent or limit the percolation of rain water into the underlying soil, relatively high values of suction may potentially be maintained in the underlying soil in the long-term. This can have implications on different geotechnical problems such as slope stability [170], which will be analysed in this chapter.

The analyses presented in this chapter are characterised by a greater level of complexity than those presented in previous chapters. The systems modelled in these analyses included not only the coarser layers (C.L.) and finer layers (F.L.) of the CBSs but also the underlying soil (U.S.). The impact of the use of CBSs for suction-control was analysed in the long term, by modelling several years of realistic weather conditions. These weather conditions were modelled considering the soil-atmosphere interaction and using atmospheric parameters calibrated against real atmospheric data. These atmospheric conditions were representative of a relatively dry and warm European climatic area (Cagliari, Italy) and a relatively wet and cool European climatic area (London, United Kingdom).

Two types of models were analysed: one-dimensional and two-dimensional. The one-dimensional models were used to study the behaviour of horizontal (i.e. unsloping) CBSs whereas the two-dimensional models were used to study the application of CBSs for slope

protection. For both types of models, advanced FE thermo-hydraulic multi-physics simulations were performed in order to analyse the long-term thermo-hydraulic behaviour of CBSs when subjected to realistic weather conditions. In addition, for the two-dimensional models, limit analyses were performed to assess the impact of the use of CBSs on slope stability.

Several simulations were carried out with the aim of highlighting the role of different parameters. The roles of atmospheric conditions, materials of the CBS, thickness of the CBS and height of the slope were studied. In addition, alternative solutions to improve the efficiency of CBSs, such as the use of multi-layered CBSs and multiple drains in sloping CBSs, will be explored in this chapter.

Section 8.2 provides a description of the numerical models employed. Section 8.3 presents the results of the one-dimensional analyses, in which the application of horizontal CBSs is studied, and Section 8.4 shows the results of the two-dimensional analyses, representing the behaviour of sloping CBSs when applied to slope stability. Finally, some concluding remarks for this chapter are presented in Section 8.5.

8.2 Numerical models

One-dimensional analyses were performed to study the long-term performance of horizontal capillary barrier systems when used for suction control purposes. Two-dimensional analyses were performed to study the long-term performance of sloping capillary barrier systems used for slope stability purposes.

For both one-dimensional and two-dimensional models, thermo-hydraulic FE simulations were performed with Code_Bright, in which also the diffusion of water vapour within the gas phase was considered and the atmospheric conditions were modelled using the atmospheric boundary conditions described in Section 4.1.3.

For the two-dimensional models, output hydraulic data, i.e. suction s and degree of saturation S_l, at some specific times critical for the stability of the slope were exported to LimitState:GEO to perform limit analyses. The data transfer between finite element analyses with Code_Bright and limit analyses with LimitState:GEO was done according to the procedure described in Section 4.3. By means of the limit analyses, it was possible to determine the stability of the slope in critical weather conditions, in terms of failure mechanisms and associated factors of safety.

8.2.1 Geometry

In this section, the geometry of the different models is described.

In terms of the geometry, three different one-dimensional models, or soil columns, were considered, as shown in Figure 8.1. The first model consisted of a vertical column representing solely the underlying soil (see Figure 8.1a, "No CBS"). The height of the column, 20 m, was chosen to minimize the impact of the position of the bottom boundary on the soil response close to the surface. This choice was done as a result of preliminary tests in which different

columns characterised by different heights were analysed. It was shown that using a column with a height equal or greater than 20 m has a negligible impact on the soil response close to the surface, which is the location of interest for this study. In the second model, the underlying soil, which is still modelled as in Figure 8.1a, is overlain by a CBS, as shown in Figure 8.1b which is a zoomed view of the top part of the model. The total thickness of this CBS is $t_{CBS} = 60$ cm, the thickness of the coarser layer (C.L.) is 20 cm and the thickness of the finer layer (F.L.) is 40 cm. The third model (see Figure 8.1c) is similar to the second model (Figure 8.1b) but the finer layer is 80 cm thick and, given that the thickness of the coarser layer is fixed to 20 cm, the total thickness of this CBS is $t_{CBS} = 100$ cm. The comparison between the results obtained with these three different geometries was used to assess the role of the CBS and the impact of the thickness of the finer layer on the results.

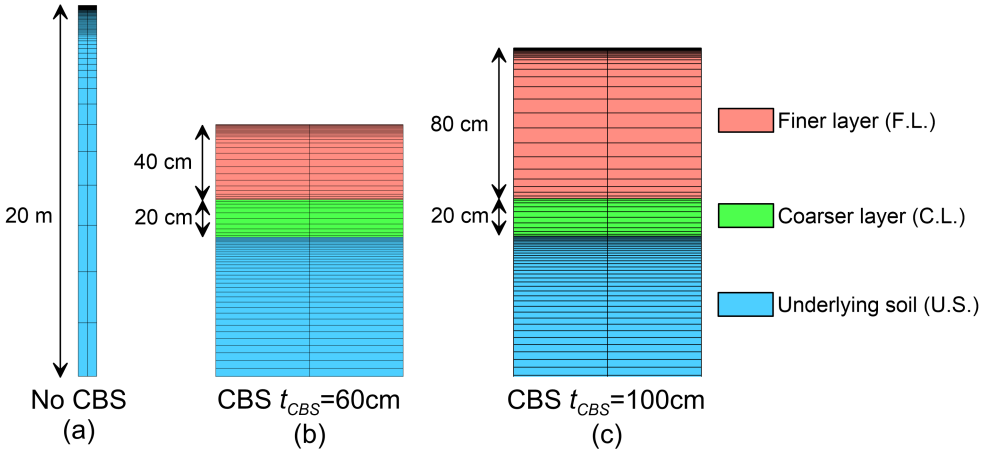

Figure 8.1: Geometry and mesh of the 1D models: (a) model with no CBS, (b) model with CBS of a thickness of $t_{CBS} = 60$ cm (zoomed view) and (c) model with CBS of a thickness of $t_{CBS} = 100$ cm (zoomed view)

The FE mesh was made of quadrilateral elements. In the vertical direction, in all three one-dimensional models, the underlying soil was made of 70 elements: 10 elements from $z = 0$ m (the bottom boundary) to $z = 16.5$ m with a mesh gradient of 0/0.5 (finer upwards), 10 elements from $z = 16.5$ m to $z = 18.5$ m with a mesh gradient of 0/0.4 (finer upwards) and 50 elements from $z = 18.5$ m to $z = 20$ m with a mesh gradient of 0/0.1 (finer upwards). The coarser layer was made of 10 elements with a mesh gradient of 0.7/0.7 (finer towards the boundaries). In the model shown in Figure 8.1b, the finer layer has 26 elements in the vertical direction: 16 elements from $z = 20.2$ m (interface with the coarser layer) to $z = 20.55$ m with a mesh gradient of 0.6/0.6 and 10 elements from $z = 20.55$ m to $z = 20.6$ m (surface) with a mesh gradient of 0/0.2. In the model shown in Figure 8.1c, the finer layer has 26 elements in the vertical direction: 16 elements from $z = 20.2$ m (interface with the coarser layer) to $z = 20.95$ m with a mesh gradient of 0.6/0.6 and 10 elements from $z = 20.95$ m to 21 m (surface) with a mesh gradient of 0/0.2. The mesh close to the top boundaries was very fine because the atmospheric boundary conditions caused high gradients in the state variables (i.e. p_l and T) close to the surface. For all the one-dimensional models only two elements were modelled in the horizontal direction (which is the minimum required by Code_Bright). The general validity of this mesh was assessed by a number of preliminary tests. In particular,

different mesh refinements were considered and it was verified that the results obtained with the mesh described above showed negligible differences when compared with those obtained with finer meshes.

Different geometries were considered for the two-dimensional models, as shown in Figure 8.2. In two models, only the underlying soil was considered (see Figures 8.2a and 8.2b). The geometry of the underlying soil is a slope characterised by an angle of 35°. For the purpose of this thesis, this slope angle could not be too low otherwise the original slope would not be affected by rainfall induced instability problems. On the other hand, the slope angle could not be too high otherwise also the CBS would not be stable. As a rule of thumb, CBSs can be applied for slope stability purposes for slope angles intermediate between the friction angle of the underlying soil (i.e. 20° in these analyses) and the friction angle of the materials of the CBS (40° in these analyses). This rule must be seen just as an indicative guidance. Two slope heights were considered: $H_s = 6\,\text{m}$ (see Figure 8.2a) and $H_s = 10\,\text{m}$ (see Figure 8.2b). The lateral boundaries are located 10.5 m from the top of the slope and 10.5 m from the toe of the slope (see Figures 8.2a and 8.2b). For both of these models, the bottom boundary was located at 20 m below the ground surface, taken from the bottom of the slope. This height is the same used for the one-dimensional models (see Figure 8.1a). The choice of the location of the bottom boundary followed the same logic adopted for the one-dimensional models. The location of the lateral boundaries was chosen by means of preliminary tests in which it was verified that, next to the lateral boundaries, the response of the soil was approximately the same as obtained with corresponding one-dimensional models, meaning that far field conditions were recovered at the lateral boundaries.

Different models in which a capillary barrier system is used to cover the slope surface were created (see Figures 8.2c, 8.2d, 8.2e and 8.2f). In all these models, the underlying slope is identical either to the model shown in Figure 8.2a or to that shown in Figure 8.2b. Figures 8.2c, 8.2d, 8.2e and 8.2f only show a zoomed view of the central part of the model, where the slope is covered by a CBS. In the model shown in Figure 8.2c, the 6 m-high slope presented in Figure 8.2a is covered by a sloping CBS of a total thickness of $t_{CBS} = 60\,\text{cm}$, like that shown in Figure 8.1b for one-dimensional analyses. The slope is totally covered by the CBS whereas at the top and at the toe the CBS covers the horizontal underlying soil surface only for a short length, approximately of 1.3 m. At these locations, the CBS terminates with sloping surfaces, with an angle of 35°. The model shown in Figure 8.2d is similar to that shown in Figure 8.2c but the CBS, which is still 60 cm thick, is applied to the slope of height $H_s = 10\,\text{m}$. In the two-dimensional model shown in Figure 8.2e, a 100 cm-thick CBS equal to that of the one-dimensional model shown in Figure 8.1c is used to cover the slope of a height of $H_s = 10\,\text{m}$. Finally, in the two-dimensional model shown in Figure 8.2f, the 10 m-high slope was covered by a multi-layered CBS (MCB) with a layering factor of 2 and a total thickness of $t_{CBS} = 60\,\text{cm}$. In this MCB, the thickness of the finer layers is 27.5 cm, the thickness of the bottom coarser layer is 20 cm whereas the thickness of the intermediate coarser layer is 5 cm. All quoted layer thicknesses for MCBs on slopes refer to vertical dimensions (e.g. see inset of Figure 8.2f), rather than thicknesses measured perpendicular to

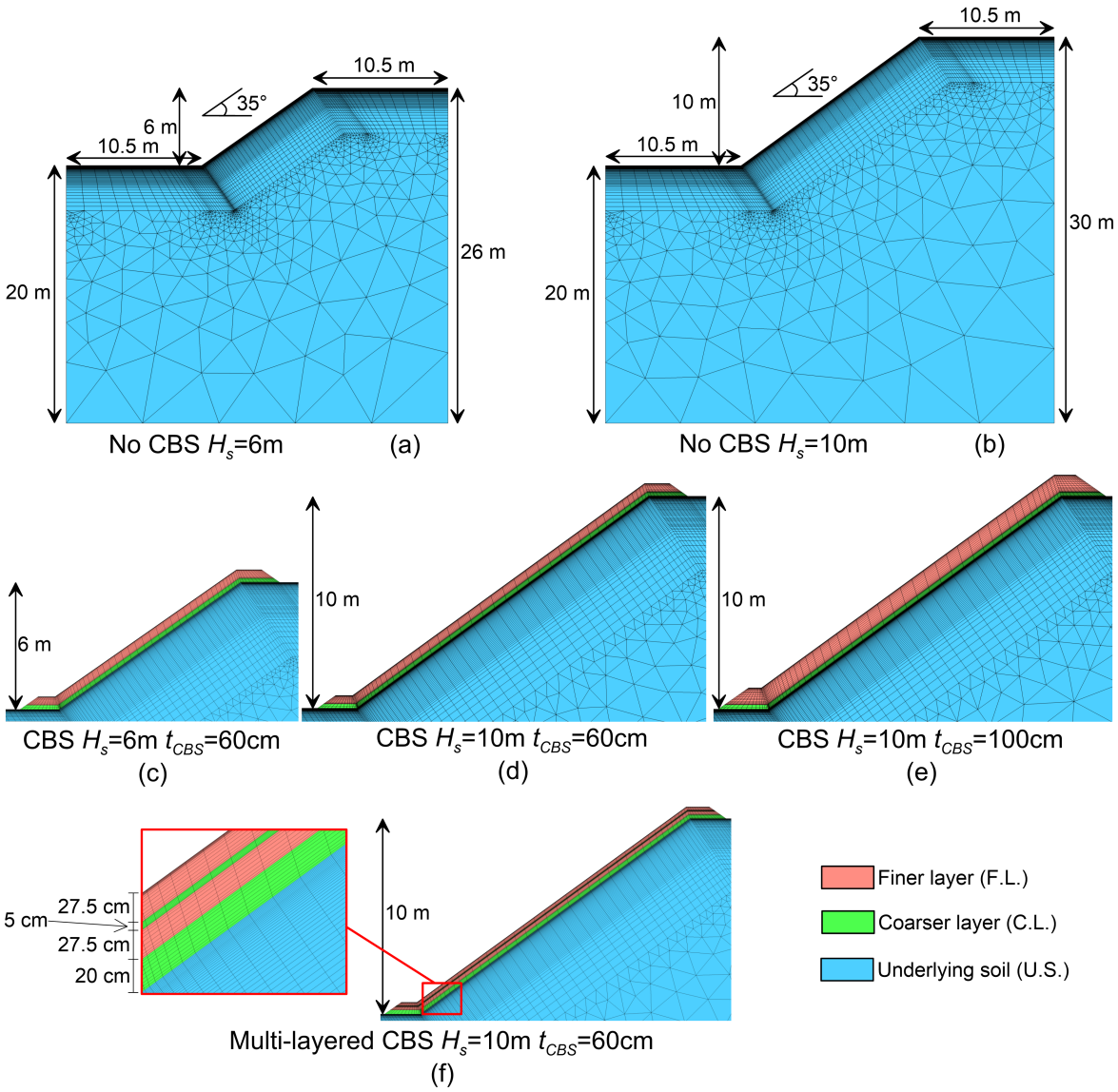

Figure 8.2: Geometry and FE mesh of the 2D models: (a) model with slope height $H_s = 6\,\text{m}$ with no CBS, (b) model with slope height $H_s = 10\,\text{m}$ with no CBS, (c) model with slope height $H_s = 6\,\text{m}$ with CBS of thickness $t_{CBS} = 60\,\text{cm}$, (d) model with slope height $H_s = 10\,\text{m}$ with CBS of thickness $t_{CBS} = 60\,\text{cm}$, (e) model with slope height $H_s = 10\,\text{m}$ with CBS of thickness $t_{CBS} = 100\,\text{cm}$ and (f) model with slope height $H_s = 10\,\text{m}$ with multi-layered CBS of thickness $t_{CBS} = 60\,\text{cm}$

the slope.

As discussed in Section 2.3.4, sloping CBSs may potentially transport water down the slope due to the effect of gravity. For this reason, a drain should be placed at the toe of the slope with the purpose of collecting any water transported by the sloping CBS. Figure 8.3 shows a schematic representation of these drains, as expected in reality (insets on the left) and as modelled in Code_Bright. This figure shows the presence of two drains: a bottom drain and an intermediate drain. The bottom drain was present in all the models whereas the intermediate drain was considered only in one model in order to assess the influence of the presence of an intermediate drain in a sloping CBS. In reality, these drains are tubes which collect water transported from the finer layer and divert it away. The lateral sides and the bottom side of the tube in contact with the coarser layer are closed and impermeable whereas the upper part in contact with the finer layer is perforated. In this way, the water can percolate from the finer layer into the drain where it is diverted away. Around the drain, geotextiles can be placed at the interface between the finer layer and the coarser layer in order to convey the water directly into the drain and avoid water breakthrough into the coarser layer around the drain. In the numerical FE models, the drains were modelled by applying particular surface boundary conditions to some specific mesh elements in the coarser layer, whose location is highlighted by the dashed red line in Figure 8.3. These drainage surface boundary conditions can be seen as a surface liquid water outflow occurring orthogonal to the 2D plane. This out-of-plane outflow q_l was modelled by the following expression:

$$q_l = \begin{cases} 0 & \text{if } s > s^c_{BWC} \\ \gamma_w \cdot \left(s - s^c_{BWC}\right) & \text{if } s \leq s^c_{BWC} \end{cases} \tag{8.1}$$

where s is the suction in the drain element, s^c_{BWC} is the bulk-water continuity value of suction of the coarser layer and γ_w is a leakage coefficient. Equation 8.1 suggests that when the suction in the drain element s is greater than s^c_{BWC}, the drain is inactive and no out-of-plane water flow occurs. When s attains the value of s^c_{BWC}, the drain starts working and the water is removed from the drain element as long as $s \leq s^c_{BWC}$. By imposing a high value to the leakage coefficient γ_w, the suction in the drain element remains approximately constant $s \approx s^c_{BWC}$ as long as water enters the drain. Practically speaking, as long as the suction at the interface between F.L. and C.L. is greater than the BWC value of the coarser layer, the water is stored in the finer layer and the drain is inactive, whereas, when the suction at the interface attains the BWC value of the coarser layer, water breakthrough from the finer layer into the coarser layer occurs but this water is removed out of the model by the drain elements.

The finite element meshes adopted for the two-dimensional models are shown in Figures 8.2 and 8.3. The capillary barrier systems and the upper part of the underlying soil, from the surface to a depth of 3.5 m, were modelled with quadrilateral elements whereas the lower part of the underlying soil was modelled with triangular elements in order to avoid the use of highly distorted mesh elements. Two principal orientations of the quadrilateral elements can be identified: perpendicular to the soil surface and parallel to the soil surface. In the

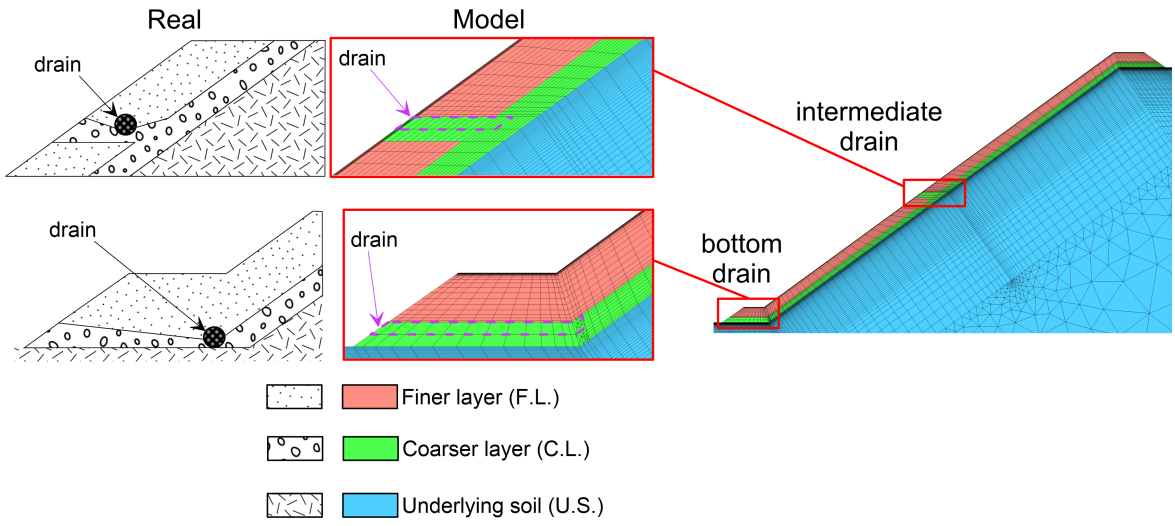

Figure 8.3: Modelling of the drains

underlying soil, the mesh was finer moving vertically from the bottom boundary to the top boundary. The mesh spacing of the quadrilateral elements in the orientation perpendicular to the soil surface was the same as used in the one-dimensional models, for both the underlying soil and the single CBSs. For the multi-layered CBS (see Figure 8.2f), the mesh spacing for the lower coarser layer was the same as used for the other models. The lower finer layer was modelled with 9 elements in the perpendicular orientation with a mesh gradient of 0.6/0.6 (finer towards the edges). The intermediate coarser layer was modelled with 6 elements and a mesh gradient of 0.6/0.6. The upper 5 cm-thick sub-layer of the upper finer layer was modelled with 10 elements with a mesh gradient of 0/0.2 (finer towards the soil surface) whereas the remaining thickness of the upper finer layer was modelled with 9 elements with a mesh gradient of 0.6/0.6. In the orientation parallel to the soil surface, the mesh becomes finer moving from the lateral boundaries towards the slope and, in the centre of the model, it becomes finer moving from the middle towards the toe and the top of the slope. In the underlying soil, along the lateral horizontal edges not covered by the CBSs, the mesh is made of 14 elements along the parallel orientation with mesh gradients of 0/0.4 down the slope and 0.4/0 up the slope. In the locations where the underlying soil is covered by a CBS, the same mesh spacing in the parallel orientation was used for both the CBS and the underlying soil. At the top and at the toe of the slope, in the parts where the CBS is horizontal, the mesh was made of 14 elements with mesh gradients of 0.2/0.35 at the top and 0.4/0.5 at the toe. The mesh of the slope was made of 48 elements in the parallel direction with a mesh gradient of 0.25/0.18. In the model with the multiple drains, the mesh of the slope was slightly different: both above and below the intermediate drain the CBS was made of 30 elements in the parallel orientation, with mesh gradients of 0.25/0.18 and 0.32/0.18 respectively.

The geometries of the two-dimensional models created with LimitState:GEO for limit analyses were the same as those created for the FE analyses in Code_Bright. Figure 8.4 shows an example of the geometry of a LimitState:GEO model (i.e. CBS with $H_s = 10\,\text{m}$ and $t_{CBS} = 60\,\text{cm}$) and the corresponding grid used for limit analyses. In the underlying

soil, the grid spacing along both the x-direction and y-direction was 0.4453 m, except for a sub-layer of 50 cm under the surface. In this sub-layer the grid spacing was much smaller, i.e. 0.089 06 m along both the x-direction and y-direction. The grid spacing in the coarser layer is 0.044 53 m along both the x-direction and y-direction. The grid spacing in the finer layer is 0.089 06 m along both x-direction and y-direction. Note that in thin or irregular shapes, such as the the 50 cm thick sub-layer in the underlying soil, the coarser layer and the finer layer, the LS grid will not be spaced regularly because the code will automatically adapt it to the irregular elements, while maintaining a regular spacing of the grid nodes lying on the boundaries. A fine grid in the coarser layer and in the finer layer was necessary to capture failure mechanisms involving the CBS. A fine grid in the upper part of the underlying soil close to the surface was necessary to capture shallow failure mechanisms. Deep failure mechanisms could be modelled with a coarser grid.

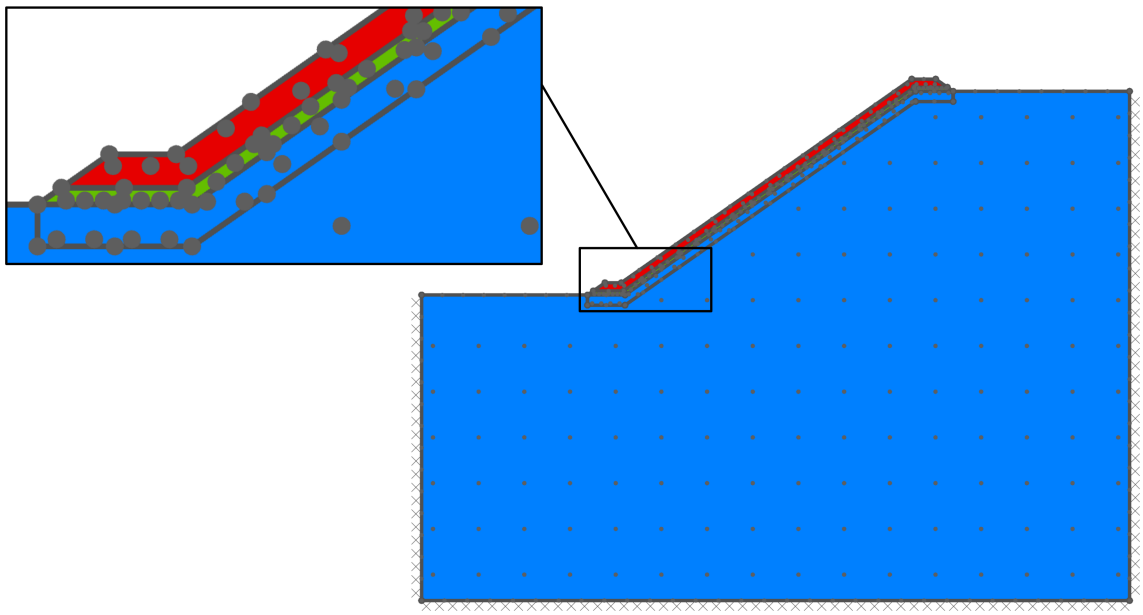

Figure 8.4: LimitState:GEO grid

The general validity of the FE mesh for the two-dimensional models was assessed by some preliminary tests. In particular, different mesh refinements were considered and it was verified that the results obtained with the mesh described above showed negligible differences when compared with those obtained with finer meshes. In a similar manner, the validity of the limit analysis grids was verified by ensuring that finer grids led to negligible differences in the results.

8.2.2 Materials

Four different materials were considered in this numerical study. The material properties used for the underlying soil were representative of a silt. The material properties used for the coarser layer were representative of a gravelly sand. Two materials were considered for the finer layer, with properties representative of either a fine sand or a silty sand. From the comparison of the results obtained considering these two materials, it was possible to assess

the role of the material properties of the F.L. on the response of the system.

The material parameters used for the FE models are shown in Table 8.1 and the SWRCs and SHCCs are shown in Figure 8.5. The hydraulic behaviour of the fine sand, silty sand and gravelly sand was modelled using the modVG-modM+LF model. The hydraulic behaviour of the silt was modelled using the modVG-modM model, i.e. without the liquid film conductivity component, because in such a fine material the liquid film conductivity is negligible or becomes significant only at very high values of suction, beyond the range of interest for this study. In this particular case, since the parameter ξ of the modVG model is $\xi = 0$ for the silt, the modVG model coincided with the VG model. Hydraulic hysteresis was modelled in all the materials using the bounding surface approach presented in Section 3.4.

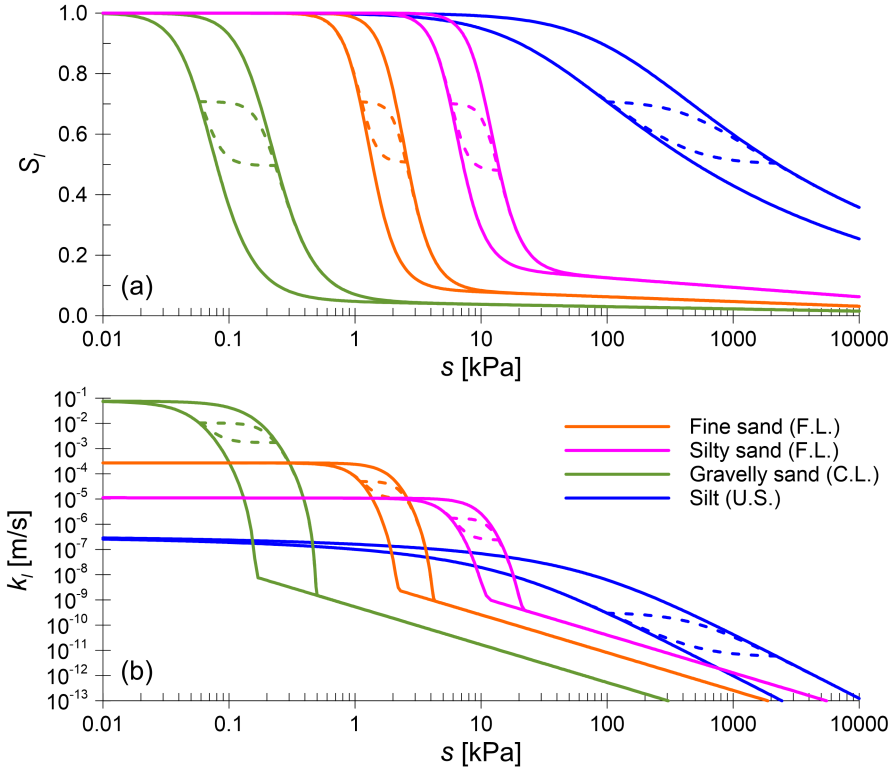

Figure 8.5: Hydraulic properties of the materials: (a) SWRCs and (b) SHCCs

The thermal conductivity and the vapour diffusivity were modelled respectively by Fourier's law and Fick's law (see Section 4.1.2).

The material parameters for the limit analyses in LimitState:GEO were the unit weight γ, the friction angle ϕ' and the effective cohesion c'. The parameter values adopted in these analyses are shown in Table 8.2. The values adopted for the unit weight reflect the porosity, the specific gravity and the range of degree of saturation expected during intense rainfall events. The friction angle values used for the materials of the CBSs, i.e. fine sand, silty sand and gravelly sand, are close to the upper bounds of the range of possible values for these materials [246], corresponding to a high relative density state. This is however a reasonable assumption because the materials of the CBS are designed to be compacted on site, and hence the degree of compaction is controlled by the designer. A relatively low value of friction angle was used to represent the silt [246], which represents a natural material already present on site.

Table 8.1: Material parameter values for the FE numerical analyses

Material	**Model**	**Physical parameters** Φ [-]	k [m^2]	D_{10} [mm]
Fine sand	modVG-modM+LF	0.411	2.77E-11	0.17
Silty sand	modVG-modM+LF	0.411	1.11E-12	0.034
Gravelly sand	modVG-modM+LF	0.382	7.81E-9	2.73
Silt	modVG-modM	0.480	3.80E-14	-

	SWRC parameters $\overline{P_{0d}}$ [MPa]	$\overline{P_{0w}}$ [MPa]	$\overline{\sigma_s}$ [N/m]	m [-]	ξ [-]	S_{ls} [-]	γ_d [-]	γ_w [-]
Fine sand	2.31E-3	1.21E-3	0.072	0.779	6.79E-3	1	8	8
Silty sand	1.16E-2	6.05E-3	0.072	0.779	1.36E-2	1	8	8
Gravelly sand	1.93E-4	6.45E-5	0.072	0.688	3.27E-3	1	6	6
Silt	1.124E-1	2.52E-2	0.072	0.186	0.00E-3	1	2	2

	SHCC parameters m [-]	$S_{l,BWC/BWD}$ [-]	S_{ls} [-]	C_r^{Film} [MPa$^{-1.5}$]	a^{Film} [MPa]	d^{Film} [-]
Fine sand	0.779	0.18	1	9.54E-10	4.0E-5	-1.5
Silty sand	0.779	0.22	1	1.19E-7	2.0E-4	-1.5
Gravelly sand	0.688	0.16	1	2.21E-13	1.5E-7	-1.5
Silt	0.186	0.00	1	-	-	-

	Thermal conductivity λ_{solid} $\left[\frac{\mathrm{W}}{\mathrm{m\,K}}\right]$	λ_{gas} $\left[\frac{\mathrm{W}}{\mathrm{m\,K}}\right]$	λ_{liquid} $\left[\frac{\mathrm{W}}{\mathrm{m\,K}}\right]$	**Vapour diffusivity** D $\left[\frac{\mathrm{m^2 Pa}}{\mathrm{s K^n}}\right]$	n [-]	τ_0 [-]
Fine sand	7.7	0.024	0.6	5.9E-6	2.3	1
Silty sand	7.7	0.024	0.6	5.9E-6	2.3	1
Gravelly sand	7.7	0.024	0.6	5.9E-6	2.3	1
Silt	7.7	0.024	0.6	5.9E-6	2.3	1

Finally, a small value of effective cohesion (i.e. $c' = 0.1\,\mathrm{kPa}$) was assigned to all materials in order to avoid numerical instabilities in the analyses.

8.2.3 Initial conditions, boundary conditions and modelling of the atmosphere

The response of the models presented in Sections 8.2.1 and 8.2.2 was analysed when subjected to realistic atmospheric boundary conditions. In particular, two different climatic conditions were considered in this study: Cagliari (Italy) and London (United Kingdom). The former was chosen because it is representative of a European dry and warm climate whereas the latter was chosen because it is representative of a European wet and cool climate. Historical data for the weather in Cagliari were obtained from the meteorological office of the Italian air force

Table 8.2: Material parameter values for the limit analyses

Material	γ [kN/m^3]	ϕ' [°]	c' [kPa]
Fine sand	17	40	0.1
Silty sand	19	35	0.1
Gravelly sand	16	40	0.1
Silt	19	20	0.1

(Servizio metereologico Aeronautica Militare [247]) whereas data for the weather in London were obtained from the meteorological office of the UK Government (Met Office [248]).

The atmospheric data processed for the modelling of the atmospheric boundary conditions were air temperature T_a, wind speed v_a, atmospheric relative humidity RH_a, cloud index I_n, radiation R_n and precipitation P. The average monthly values of these parameters were calculated for years 1981-2010 and they are represented by the histograms in Figures 8.6a-l. In order to be modelled in Code_Bright, these data, with exception of the net radiation, were fitted by yearly sinusoidal distributions, represented by the solid lines in Figures 8.6a-h and 8.6k-l. The parameter values for the yearly sinusoidal distributions, shown in Table 8.3a, were obtained by fitting this distribution (see Equation 4.45 with $x_d = 0$) to the atmospheric data. The net radiation was modelled using the model implemented in Code_Bright and discussed in Section 4.1.3 (see Equations 2.74 and 4.46-4.54).

Figures 8.6m,n show daily rainfall data for particularly wet 10-year periods for each location, i.e. 1984-1993 for Cagliari and 1993-2002 for London.

Table 8.3b shows the general parameters used for the modelling of the atmospheric conditions. See Section 4.1.3 and Table 4.4 for further information about the atmospheric boundary conditions and the description of the different parameters. The parameter values shown in Table 8.3b are representative of: sites at the latitudes of Cagliari and London respectively, starting times for the analyses at midnight of the 1st of January, neutrally stable atmosphere, soil surface roughness and surface albedos representative of a surface covered by short grass.

Three different analysis stages were considered for the modelling of the atmospheric boundary conditions. In all these three stages, the quantities related to the energy transfer and evaporation (i.e. air temperature T_a, wind speed v_a, atmospheric relative humidity RH_a, cloud index I_n and net radiation R_n) were modelled by sinusoidal yearly time variations (see black lines in Figures 8.6a-j). The three analysis stages differed for the modelling of rainfall, as explained below.

1. For the first 20 years of analysis (stage 1), only the presence of the underlying soil is considered, representing the stage before the construction of the CBS; rain P is applied according to the sinusoidal yearly distributions shown in Figures 8.6k and 8.6l.

2. For the subsequent 10 years of analysis (stage 2), the CBS is included in the models (only those which consider the presence of a CBS), representing the stage after the

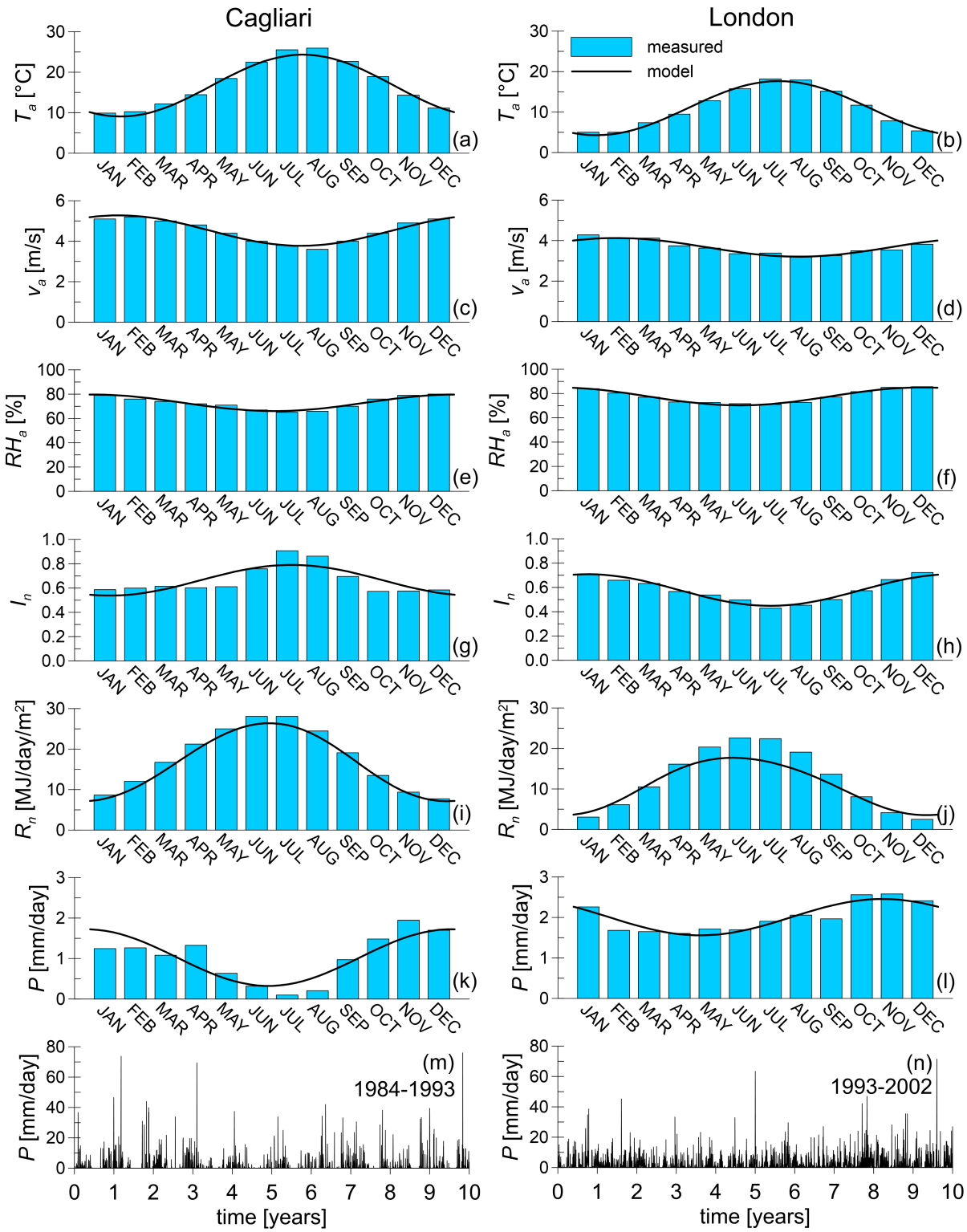

Figure 8.6: Measured data and modelling of atmospheric conditions for (a,c,e,g,i,k,m) Cagliari (Italy) and (b,d,f,h,j,l,n) London (UK)

Table 8.3: Parameters for the atmospheric boundary conditions

(a) Atmospheric parameters

	Cagliari			London		
	x_m	x_a	t_a [s]	x_m	x_a	t_a [s]
T_a [°C]	16.70	7.64	1.058E+7	10.98	6.69	9.935E+6
v_a [m/s]	3.593	0.598	2.618E+7	2.911	0.366	2.741E+7
RH_a [%]	0.729	0.068	2.386E+7	0.777	0.074	2.227E+7
I_n [-]	0.664	0.126	9.556E+6	0.579	0.130	2.490E+7
P^* [$\mathrm{kg\,m^{-2}\,s^{-1}}$]	1.180E-5	8.062E-6	2.004E+7	2.318E-5	5.178E-6	1.884E+7

(b) General parameters

		Cagliari	London
φ_l	[rad]	0.6845	0.8990
t_s	[s]	2.28096E+7	2.28096E+7
t_m	[s]	4.32E+4	4.32E+4
z_0	[m]	0.001	0.001
z_a	[m]	1.5	1.5
ψ	[-]	1	1
ρ_{ga}	[$\mathrm{kg\,m^{-3}}$]	1.2	1.2
A_{ld}	[-]	0.2	0.2
A_{lw}	[-]	0.2	0.2
γ_g	[$\mathrm{kg\,m^{-2}\,s^{-1}\,MPa^{-1}}$]	1E+6	1E+6
γ_l	[$\mathrm{kg\,m^{-2}\,s^{-1}\,MPa^{-1}}$]	-1E+6	-1E+6

construction of the CBS; rain P is applied according to the sinusoidal yearly distributions shown in Figures 8.6k and 8.6l. In the models in which only the underlying soil is considered (e.g. Figures 8.1a, 8.2a and 8.2b), this stage represents a repetition of stage 1 for a further 10 years.

3. For the final 10 years of analysis (stage 3), rain is applied to the soil surface (either underlying soil or CBS) using the daily rainfall data shown in Figures 8.6m and 8.6n.

The first two stages were preliminary stages needed to set up realistic conditions in the underlying soils and in the CBS, whereas only stage 3 was of interest for this study. In particular, stage 1 was used to set up realistic initial thermo-hydraulic conditions in the underlying soil in relatively short computational times. Similarly, stage 2 was used to set up realistic initial thermo-hydraulic conditions in the CBS after construction (in the models in which a CBS was present) in relatively short computational times. Finally, stage 3 was used to analyse the response of the models to more accurate time histories of rainfall, characterised by a particularly wet 10-year sequence of recorded daily data.

Initial conditions and bottom boundary conditions used for the analyses in which the weather of Cagliari was simulated were different from those in which the weather of London was simulated.

For the weather of Cagliari, it was shown that the application of the weather conditions described in stage 1 for a sufficiently high number of years (i.e. cycles) will ultimately lead to

a situation in which the soil state quantities and the surface mass and energy fluxes follow the same cyclic behaviour every year. This is obtained because, after a certain number of simulated years, the yearly cumulative evaporation equals the yearly cumulative rain. The bottom boundary was modelled as impermeable to liquid water and energy flux, in both the one-dimensional and two-dimensional models. In the long term, this bottom boundary condition was consistent with the fact that, after a certain number of years, major cyclic variation were predicted close to the soil surface whereas negligible variations were predicted at greater depths. The impact of the location of the bottom boundary was analysed by means of preliminary tests in which it was verified that variations of the state quantities in the very long term (i.e. >10000 years) were negligible close to the bottom of the model. The lateral boundary conditions, only relevant to the two-dimensional models, were also modelled as impermeable to liquid flow and heat flow because they were located sufficiently far from the slope to achieve one-dimensional conditions, as also verified by means of some preliminary numerical tests. For both the one-dimensional models and the two-dimensional models, the initial conditions for the underlying soil were chosen in order to minimise the number of years required to attain a cyclic annual response of the underlying soil, i.e. to minimise the time required to achieve conditions in which the yearly cumulative evaporation equals the yearly cumulative rain. These initial conditions consisted of i) a hydrostatic pore-liquid pressure profile with $p_l = -15\,\text{MPa}$ ($s = 15.1\,\text{MPa}$) at the bottom of the model and ii) a homogeneous temperature profile with $T = 19.65\,^{\circ}\text{C}$. The initial reversal point for the underlying soil, needed to identify the degree of saturation from suction if the hysteretic model is used (see Section 4.1.6), was given by $s_0 = 16.5\,\text{MPa}$ and $S_{l0} = 0.2671$. The initial conditions of the materials of the CBS, when this was introduced in stage 2 of the analysis, were representative of a relatively dry state. In particular, a homogeneous initial distribution of pore-liquid pressure, i.e. $p_l = 90\,\text{kPa}$ ($s = 10\,\text{kPa}$) for the gravelly sand and for the fine sand and $p_l = 80\,\text{kPa}$ ($s = 20\,\text{kPa}$) for the silty sand, and a homogeneous temperature profile with $T = 19.65\,^{\circ}\text{C}$ were adopted.

For the weather of London, the approach used for the weather of Cagliari would lead to results of little significance for this study. Over a year, the cumulative amount of rain would always be greater than the cumulative amount of evaporation. Therefore, the application of an impermeable bottom boundary condition, regardless how deep it is, provokes an overall increase of the water stored in the model until reaching a situation in which every winter the underlying soil becomes fully saturated and suction at the surface becomes equal to zero. This situation will not make sense in the logic of this study, because the aim of the CBS is maintaining relatively high values of suction during extreme rainfall events. If the beneficial effect of suction is lost for each ordinary rainfall event, the use of a CBS will not make sense because a slope will not be stable even before the application of a CBS.

For the weather of London, the bottom boundary condition was modelled as impermeable to heat flow, but a constant pore-liquid pressure of $p_l = 0.247\,\text{MPa}$ ($s = -0.147\,\text{MPa}$) was applied. In hydrostatic conditions, the latter corresponds to a position of the water table of approximately 15 m above the bottom boundary, i.e. 5 m below the surface of the underlying

soil for the one-dimensional models and 5 m below the lower part of the slope for the two-dimensional models. In other words, the idea of the model was to fix approximately the location of the water table at a certain depth, although this might vary depending on the atmospheric conditions, i.e. during winter the overall water flux is directed downwards and the level of the water table is higher whereas during summer the overall water flux is directed upwards and the level of the water table is lower. This represents a situation where the mean level of the water level is set by conditions in a deep aquifer, within which lateral drainage can occur. By preliminary specific tests, it was verified that the location of the bottom boundary was deep enough to have a negligible effect on the response of the system close to the surface. The lateral boundaries were modelled as impermeable to liquid and heat flows. Also for the weather of London, the initial conditions for the underlying soil were chosen in order to minimise the number of years required to attain an annual cyclic response of the underlying soil. These initial conditions consisted of i) a hydrostatic pore-liquid pressure profile with $p_l = 0.247\,\text{MPa}$ ($s = -0.147\,\text{MPa}$) at the bottom of the model, consistent with the bottom boundary condition, and ii) a homogeneous temperature profile with $T = 6.32\,^{\circ}\text{C}$. The initial reversal point for the underlying soil was given by $s_0 = 1000\,\text{MPa}$ and $S_{l0} = 0.0$ (i.e. initial states were on the main wetting curve). The initial conditions of the materials of the CBS, when this was introduced in stage 2 of the analysis, were representative of a relatively dry state. In particular, a homogeneous initial distribution of pore-liquid pressure, i.e. $p_l = 90\,\text{kPa}$ ($s = 10\,\text{kPa}$) for the gravelly sand and for the fine sand and $p_l = 80\,\text{kPa}$ ($s = 20\,\text{kPa}$) for the silty sand, and a homogeneous temperature profile with $T = 6.32\,^{\circ}\text{C}$ were adopted.

The time period of interest in these simulations was that represented by stage 3 of the analyses, i.e. the particularly wet 10-year period in which rainfall was applied according to daily recorded data. Therefore, the results shown in Sections 8.3 and 8.4 will refer only to this stage and the initial time $t = 0$ will refer to the beginning of stage 3. It is worth stressing the fact that, for both sets of simulations (with the weather of Cagliari and London), the initial conditions used for the models (at the start of stage 1) are not of primary importance for stage 3 of the analyses because more realistic initial conditions in the underlying soil and in the CBS at the start of stage 3 were initialised by means of stages 1 and 2 of the analyses.

Finally, an apparent form of inconsistency in the choice of the time variation of the weather conditions in stage 3 must be discussed. In this stage, the rain was modelled using a daily "resolution", i.e. daily values of rainfall height were transformed into daily values of constant water fluxes, whereas all the atmospheric parameters regarding evaporation and heat flux at the surface were modelled using a yearly sinusoidal variation, which is less accurate. This can be potentially far from the reality, e.g. temperature excursion from day to night is typically significant. This choice was done as a result of some preliminary numerical tests. In particular, different simulations were performed in which the weather conditions were modelled using the following time resolutions: i) daily resolution of rain and daily resolution of evaporation and heat flux, ii) daily resolution of rain and yearly sinusoidal variation of atmospheric parameters related to evaporation and heat flux and iii) yearly sinusoidal variation of rain and yearly sinusoidal variation of atmospheric parameters related to evaporation and

heat flux. From the comparison of the results obtained with these three approaches, it was observed that:

- modelling rain using a daily resolution had a major impact on the predicted response of the system;
- modelling evaporation and heat flux using a daily resolution had a minor impact on the predicted response of the system;
- modelling rain using a daily resolution slightly increased the computational time;
- modelling evaporation and heat flux using a daily resolution enormously increased the computational time.

As a consequence of these results, it was decided to adopt a daily resolution for rain, because it leads to more accurate results with a minor impact on the computational times, and a yearly sinusoidal variation for the atmospheric parameters related to evaporation and heat flux, because the error of neglecting the daily resolution is small but the impact on the computational times is enormous.

The lateral and bottom boundaries of the LS:GEO models for limit analysis were modelled as fixed, that is only displacements parallel to the boundary were permitted. The top boundaries were modelled as free, meaning that movements both parallel and perpendicular to the boundaries were permitted.

8.3 Application of horizontal capillary barrier systems: 1D models

In this section the results of the one-dimensional FE thermo-hydraulic analyses are presented. These models are representative of CBSs on horizontal ground. Ten different simulations were performed combining the different weather conditions, materials and thicknesses of the finer layer of the CBS presented in Section 8.2. The list of the one-dimensional analyses performed is shown in Table 8.4. All the results shown in this section refer to stage 3 of the analyses (see Section 8.2.3) and the initial time $t = 0$ corresponds to the beginning of stage 3. In particular, the initial time $t = 0$ corresponds to midnight of the 1st of January (1984 for Cagliari or 1993 for London).

Figure 8.7 shows the time histories of rain, evaporation into the atmosphere, surface runoff, net infiltration at the surface and water breakthrough into the coarser layer obtained for the different models, as a consequence of the application of the weather conditions of Cagliari (Figures 8.7 a-e) and London (Figures 8.7 f-j). Net infiltration was obtained as the sum of rain, evaporation and runoff, where the positive sign means a water flow entering the soil surface (e.g. rain) whereas the negative sign means a water flow leaving the soil surface (e.g. runoff). Evaporation typically assumes negative values (i.e. water leaving the soil surface) but, occasionally, it may assume positive values (i.e. water entering the surface)

Table 8.4: Summary of the 1D analyses

Analysis ID	Weather	CBS	
		material F.L.	t_{CBS} [cm]
Cag_NOCBS	Cagliari	No CBS	
Cag_FS_60	Cagliari	Fine sand	60
Cag_FS_100	Cagliari	Fine sand	100
Cag_SS_60	Cagliari	Silty sand	60
Cag_SS_100	Cagliari	Silty sand	100
Lon_NOCBS	London	No CBS	
Lon_FS_60	London	Fine sand	60
Lon_FS_100	London	Fine sand	100
Lon_SS_60	London	Silty sand	60
Lon_SS_100	London	Silty sand	100

when the absolute humidity of the atmosphere is greater than that at the soil surface. Water breakthrough into the coarser layer was obtained as the sum of liquid water flow and vapour water flow occurring across the interface between the finer layer and the coarser layer of the CBS, where the positive sign means an upward flow whereas the negative sign means a downward flow. Figure 8.8 shows the water flows of Figure 8.7 expressed in cumulative terms, obtained by integrating over time the water flows shown in Figure 8.7.

In the 10-year period analysed, the total amount of rainfall in London was almost twice the amount in Cagliari (see Figures 8.8a and 8.8f), i.e. approximately 7575 mm in London and 4297 mm in Cagliari. Although the amount of rainfall in the long term is significantly different between Cagliari and London, extreme rainfall events are comparable at these locations. In particular, the daily rainfall was above 60 mm (a mean intensity of 6.94×10^{-4} kg/s/m^2 in Figure 8.7a or 8.7f) on three different days in Cagliari over the 10 year period and on two different days in London. The most critical rainfall event in Cagliari consisted of a daily rainfall of 73.8 mm on 7th of March 1985, corresponding to the time $t = 1.182\,74$ years in the analyses, whereas the most critical rainfall event in London consisted of a daily rainfall of 63.4 mm on 1st of January 1998, corresponding to the time $t = 5.002\,14$ years in the analyses, after a particularly wet period. Further results will be shown at these particular critical rainfall events.

The maximum peaks of evaporation rate attained with the weather of Cagliari are higher than those attained with the weather of London (see Figures 8.7b and 8.7g), as a consequence of drier and warmer summers. However, the cumulative evaporation obtained from the different models with the weather of London is in general slightly greater than that obtained with the weather of Cagliari (see Figures 8.8b and 8.8g). This might seem counter-intuitive but it can be explained as follows. Although the potential for evaporation is greater in Cagliari, due to a warmer and drier weather, the amount of rainfall is greater in London. Hence, in London, a higher amount of water is in general available for evaporation whereas, in Cagliari, the evaporation rate is high after rainfall but it rapidly drops after the soil surface dries out.

Common points can be observed in the time histories of cumulative evaporation obtained

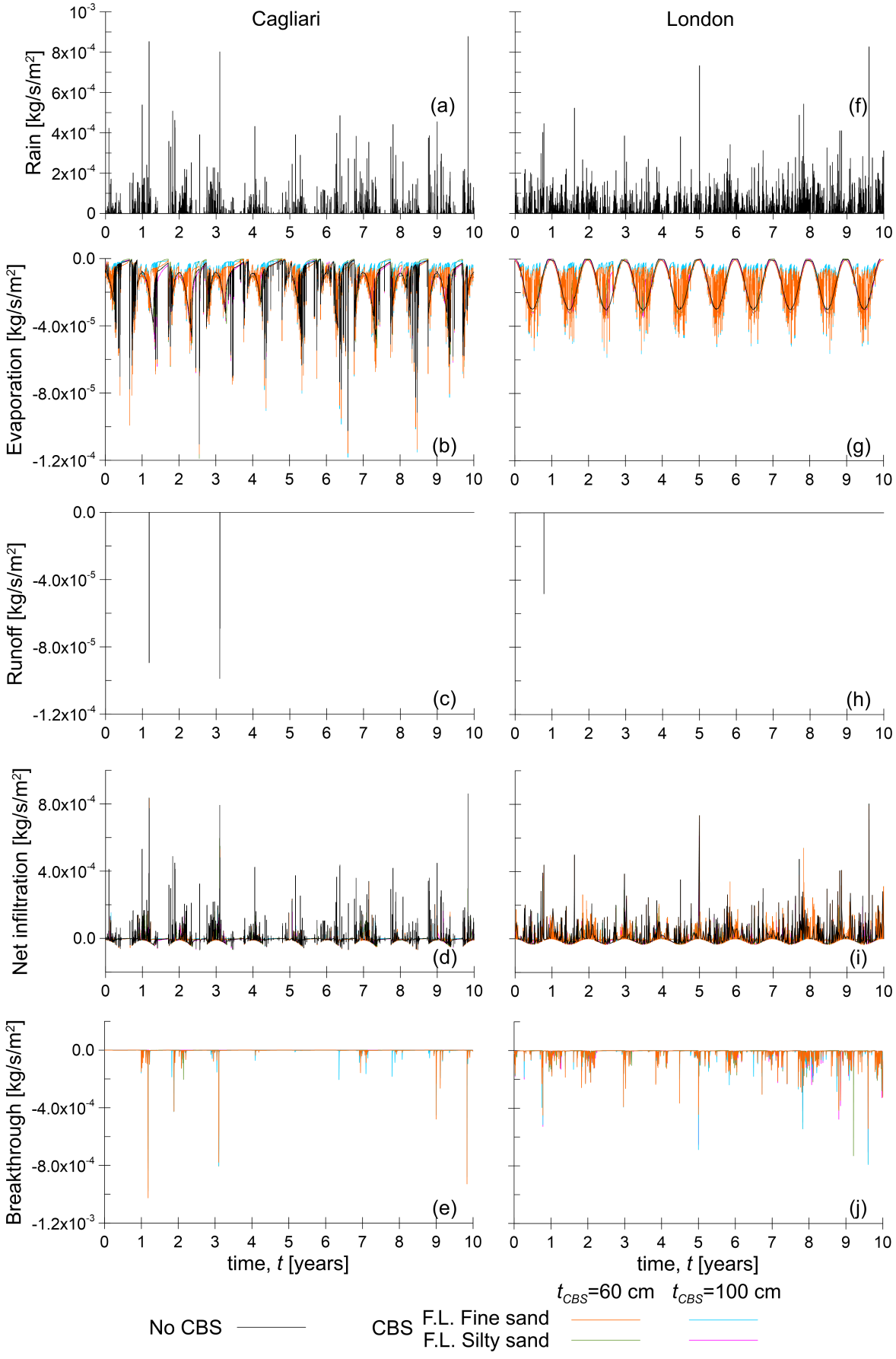

Figure 8.7: Time histories of (a,f) rain, (b,g) evaporation, (c,h) runoff, (d,i) net infiltration into the soil surface and (e,f) water breakthrough into the coarser layer obtained from one-dimensional simulations for the weather conditions of (a-e) Cagliari and (f-j) London

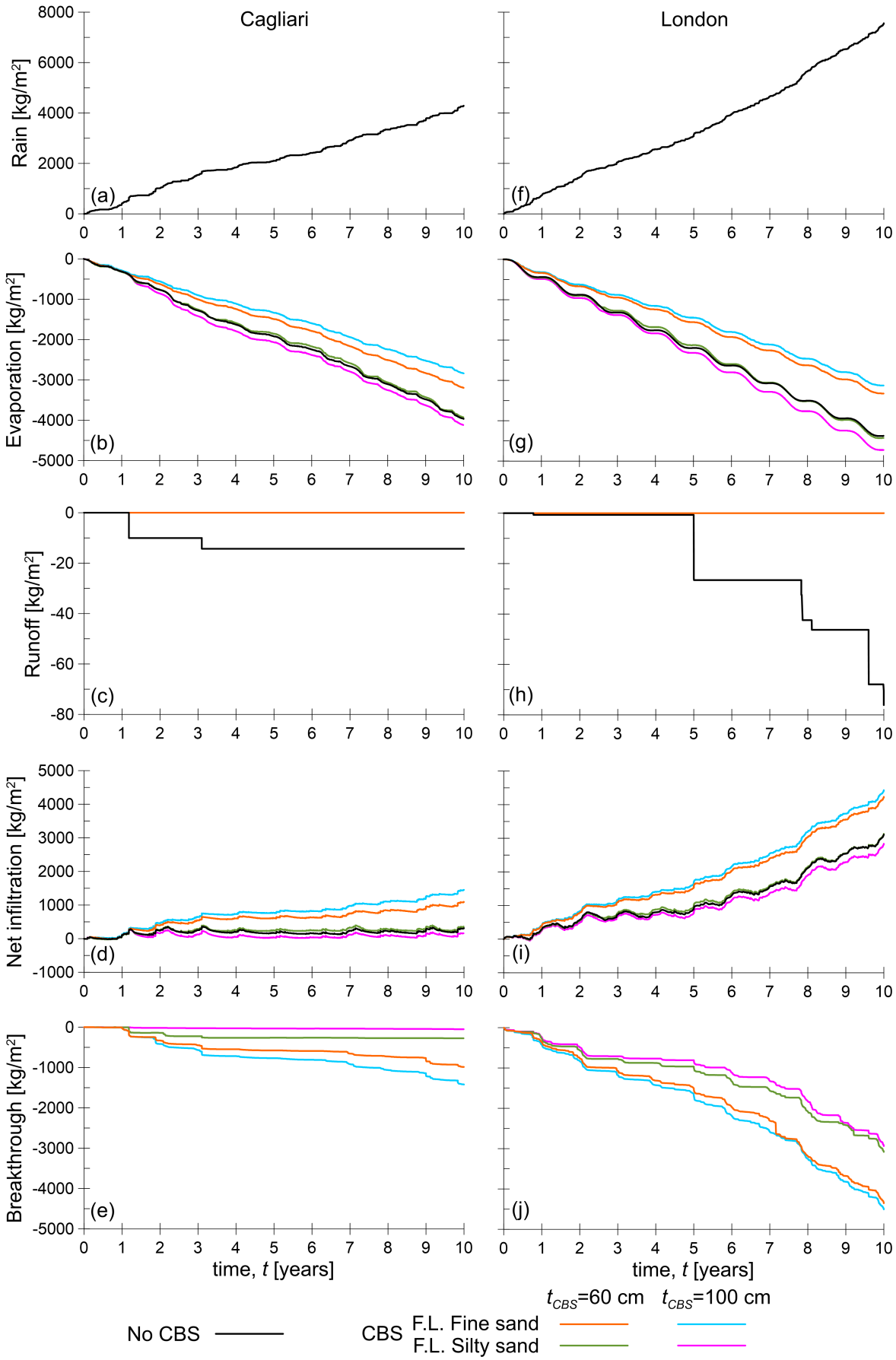

Figure 8.8: Time histories of cumulative flows of (a,f) rain, (b,g) evaporation, (c,h) runoff, (d,i) net infiltration into the soil surface and (e,f) water breakthrough into the coarser layer obtained from one-dimensional simulations for the weather conditions of (a-e) Cagliari and (f-j) London

with the weather of Cagliari and London (see Figures 8.8b and 8.8g). The cumulative evaporation obtained from the CBSs with the F.L. made of fine sand is lower than the cumulative evaporation predicted from both the underlying soil (in the model without CBS) and from the CBSs with the F.L. made of silty sand. This can be explained by the fact that, after rain ceases, in a relatively coarse material such as fine sand, the rainwater flows rapidly downwards due to the effect of gravity and the soil surface tends to dry relatively quickly after rainfall ceases. Consequently, the evaporation rate from a dry soil surface is generally low (see Section 2.4.2). Conversely, higher values of degree of saturation are generally maintained at the soil surface when the silty sand is used as a material for the F.L. The cumulative evaporation is consequently higher than that obtained with the fine sand and comparable with that obtained with the underlying soil, which is made of silt.

Increasing the thickness of the finer layer has opposite effects on the cumulative evaporation for the cases where fine sand or silty sand are used for the F.L. of the CBSs. For the fine sand, a higher thickness of the F.L. results in a lower cumulative evaporation because most of the water, which is stored close to the interface with the C.L., is located further from the soil surface, which results in drier conditions and higher values of suction at the ground surface. Conversely, for the silty sand, a higher thickness of the F.L. results in a higher cumulative evaporation because, in this case, the water storage capacity strongly increases with increasing thickness of the F.L. and, hence, the water available for evaporation increases.

For both weather conditions, surface runoff never occurs when a CBS is modelled on top of the U.S., regardless of the material used for the F.L, because the saturated hydraulic conductivity of the materials used for the F.L. is much greater than the maximum infiltration rate (see Figures 8.7c, 8.7h, 8.8c and 8.8h). Without a CBS, a very small amount of runoff is predicted with both weathers of Cagliari and London, as a consequence of particularly intense rainfall events. It must be acknowledged that the amount of runoff, which is related to the ratio between the rainfall intensity and the saturated hydraulic conductivity of the soil at the surface, might be higher if a more accurate resolution (e.g. hourly) for the rainfall was used because it would capture the possibility of shorter but more intense rainfall events.

Given that the amount of rainfall is fixed for a given location (Cagliari or London) and that runoff can be considered as negligible for the different models, the net infiltration is a direct reflection of the effect of evaporation (see Figures 8.7d, 8.7i, 8.8d and 8.8i). In the simulations in which the cumulative evaporation is higher, the cumulative net infiltration is lower. It must be noted that for the weather of Cagliari (see Figure 8.8d), the cumulative net infiltration has a general increasing trend for the simulations in which the F.L. is made of fine sand whereas it has a general constant trend for the simulations in which the F.L. is made of silty sand or in which no CBS is present. This suggests that, for the models with no CBS or with a CBS having the F.L. made of silty sand, the amount of evaporation and rain are approximately balanced in the long term whereas, for the models with a CBS having the F.L. made of fine sand, the amount of evaporation is always lower than the amount of rainfall over the long term. Conversely, for the weather of London (see Figure 8.8i), the amount of evaporation is lower than the amount of rainfall over the long term for all the models.

In all the models with a CBS and with the weather of London (see Figures 8.7j and 8.8j), water breakthrough into the coarser layer and subsequently into the underlying soil occurs at several times. In particular, a higher cumulative breakthrough occurs when the F.L. is modelled with the fine sand compared to silty sand. As discussed before, a higher thickness of the F.L. leads to a lower cumulative breakthrough when silty sand is adopted for the F.L. whereas it leads to a higher cumulative breakthrough when fine sand is adopted for the F.L. Similar aspects can be observed with the weather of Cagliari (see Figures 8.7e and 8.8e) although the cumulative amounts of breakthrough are in general lower than those predicted with the weather of London. Moreover, it can be seen that the only CBS able to prevent water breakthrough for all the duration of the analysis is that with the F.L. made of silty sand and with a thickness of $t_{CBS} = 100\,\text{cm}$, but only when adopted with the weather of Cagliari.

To evaluate the impact of the presence of the CBS on the hydraulic response of the underlying soil, Figures 8.9 and 8.10 show the time histories of suction and degree of saturation respectively predicted at the surface of the underlying soil (i.e. interface between C.L. and U.S. in the presence of a CBS) for all the different models. It must be noted that, in Figure 8.9, suction is plotted on a logarithmic scale. In the models without a CBS (Figures 8.9a, 8.9f, 8.10a, and 8.10f), strong seasonal fluctuations of suction and degree of saturation occur at the soil surface. In summer, relatively high values of suction and low values of degree of saturation are predicted although these peaks are more extreme for Cagliari, where summers are drier and warmer. Conversely, in winter, relatively low values of suction and high values of degree of saturation are in general predicted as a consequence of wetter and cooler weather conditions. Both in Cagliari and London, suction is often above 10 kPa also during winter although some critical rainfall events cause the suction to drop down to very low values, approaching 0 kPa. For the weather conditions of Cagliari, this occurs twice (i.e. $t = 1.182\,\text{years}$ and $t = 3.102\,\text{years}$) whereas, for those of London, this occurs five times (i.e. $t = 0.783\,\text{years}$, $t = 5.001\,\text{years}$, $t = 8.808\,\text{years}$, and $t = 9.601\,\text{years}$). At these times, the surface of the soil attains fully saturated conditions $S_l = 1$ (see Figures 8.10a and 8.10f).

By introducing a CBS (see Figures 8.9b-e, 8.9g-j, 8.10b-e and 8.10g-j), suction and degree of saturation in the underlying soil exhibit a more stable trend, with fewer and less extreme peaks and troughs. Hence, when the underlying soil is covered by a CBS, seasonal fluctuations of suction and degree of saturation in the underlying soil are reduced. Also the temperature variation (not shown) is more stable. The CBS indeed limits both the percolation of water into the underlying soil and the evaporation from the underlying soil. The more stable trend of s and S_l is more evident in Cagliari, where water breakthrough into the underlying soil occurs fewer times than in London. Moreover, in London, values of degree of saturation at the top of the underlying soil are generally greater than in Cagliari, and hence values of suction generally lower. This is related not only to the fact that London is characterised by a wetter and cooler climate but also to the fact that in London the imposed bottom boundary condition results in a water table relatively close to the soil surface.

In Cagliari, it can be seen that the CBSs having fine sand as a material for the F.L. (see Figures 8.9b,c and 8.10b,c), regardless of the thickness t_{CBS}, are not able to prevent water

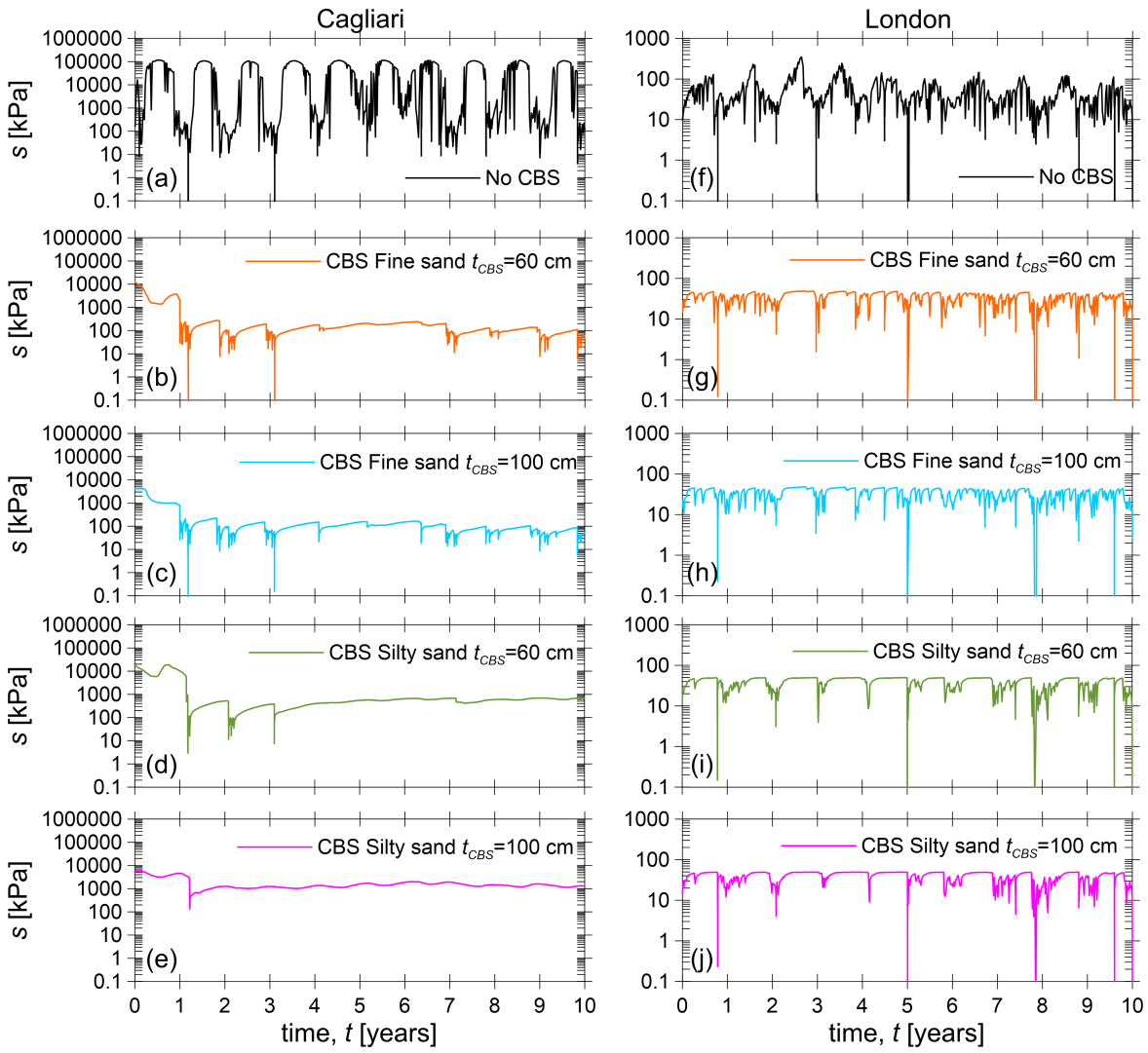

Figure 8.9: Time histories of suction at the surface of the underlying soil obtained from one-dimensional simulations for the weather conditions in (a-e) Cagliari and (f-j) London

breakthrough at the most extreme rainfall events (i.e. $t = 1.182$ years and $t = 3.102$ years). At these times, suction vanishes, i.e. $s \leq 0$ kPa, and full saturation is achieved, i.e. $S_l = 1$ at the top of the underlying soil. Conversely, a CBS with silty sand as the F.L. (see Figures 8.9d,e and 8.10d,e), is more effective at maintaining suction in the underlying soil. For the CBS with silty sand and a thickness of $t_{CBS} = 60$ cm, breakthrough occurs and low values of suction are attained, i.e. between 3 kPa and 10 kPa at the top of the underlying soil, although suction does not fully vanish. The CBS with a thickness of $t_{CBS} = 100$ cm is highly effective at preventing breakthrough, and maintains relatively high values of suction and low values of degree of saturation at the top of the underlying soil at all times.

In London, all the CBSs considered in these simulations are unable to maintain relatively high values of suction and low values of degree of saturation at the top of the underlying soil (see Figures 8.9g-j and 8.10g-j). In all these models, full saturation is attained and suction vanishes at different times.

Figure 8.11 shows suction (a,c) and degree of saturation (b,d) vertical profiles at the end of

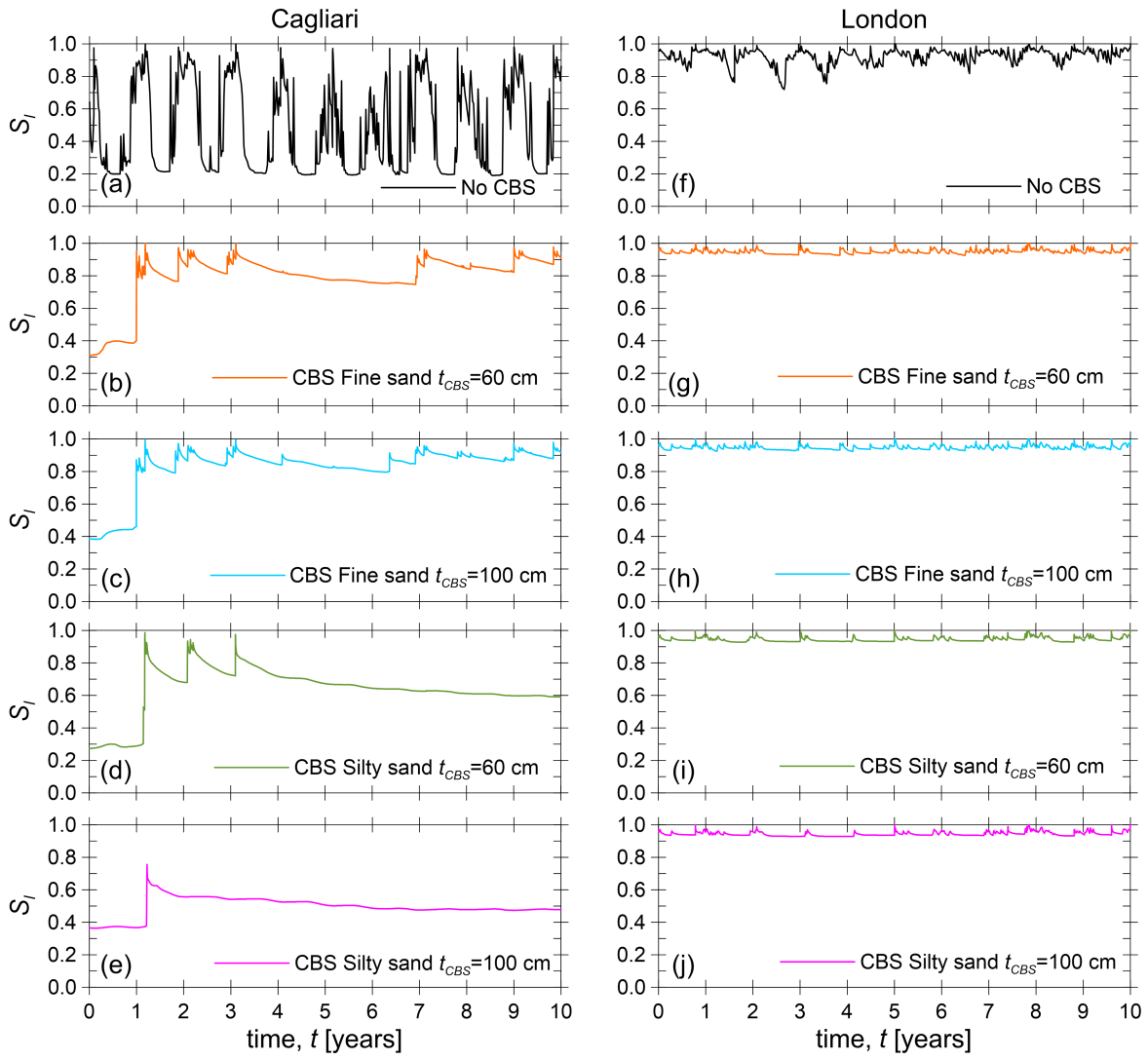

Figure 8.10: Time histories of degree of saturation at the surface of the underlying soil obtained from one-dimensional simulations for the weather conditions in (a-e) Cagliari and (f-j) London

the most critical rainfall events in Cagliari (a,b) and London (c,e), for all the one-dimensional models analysed. The most critical time for Cagliari is at $t = 1.182\,74$ years, at the end of the most intense rainfall event corresponding to the 7th of March 1985, whereas the most critical time for London is at $t = 5.002\,14$ years, at the end of the most intense rainfall event corresponding to the 1st January 1998. In this figure, the reference height at 0 m corresponds to the location of the surface of the underlying soil and, hence, the underlying soil is located at negative values of height whereas the CBSs are located at positive values of height. The insets in the different sub-plots are zoomed views of the profiles in the CBS and at the surface of the underlying soil.

For the simulations with the weather of Cagliari (see Figures 8.11a,b), the different suction and degree of saturation profiles are approximately similar in the underlying soil at heights between -4 m and -20 m approximately. These correspond to high values of suction and low values of degree of saturation. The situation is significantly different close to the underlying soil surface. Without a CBS, the underlying soil reaches almost fully saturated conditions

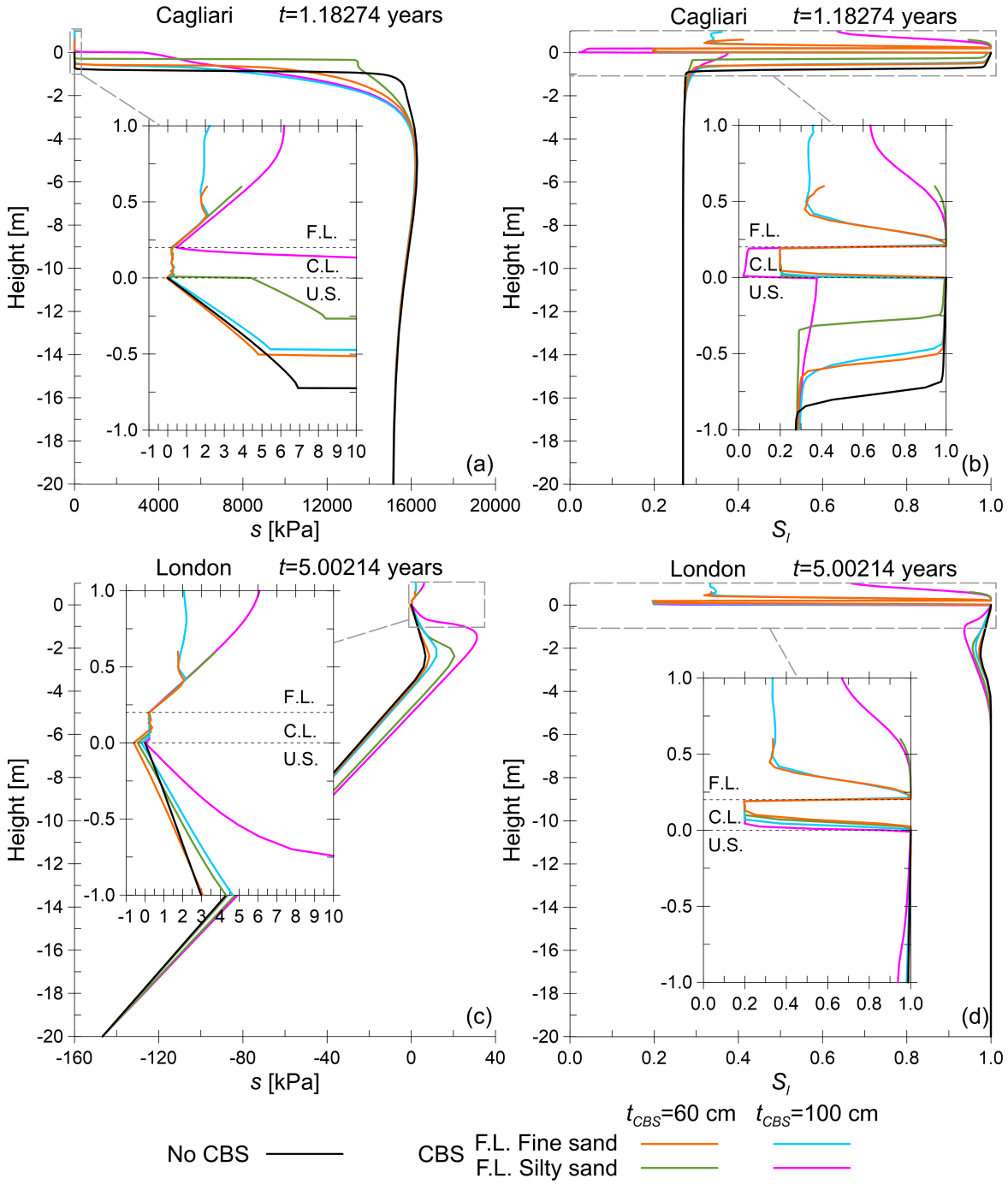

Figure 8.11: (a,c) Suction and (b,d) degree of saturation profiles obtained at the end of the most critical rainfall event from one-dimensional simulations for the weather conditions in (a,b) Cagliari and (c,d) London

at locations between 0 m and −0.75 m, with values of suction between 0 kPa and 7 kPa, as a consequence of the massive infiltration of rainwater. A sharp wetting front divides this almost saturated area from the remaining underlying soil at low values of degree of saturation. This sharp wetting front is identified by a sharp decrease of degree of saturation and a sharp increase of suction. As discussed above, both the CBSs having fine sand as a material for the F.L. are not effective at maintaining high values of suction in the underlying soil. Suction and degree of saturation profiles obtained with these CBSs at heights between 0 m and −0.5 m are approximately similar to those obtained without CBS. The only difference is represented by the location of the wetting front which, for these CBSs, is higher (i.e. −0.5 m) than that without CBS (i.e. −0.75 m). Conversely, the CBSs having silty sand as a material for the F.L. are more effective at maintaining higher values of suction in the underlying soil. In the model with a thickness of $t_{CBS} = 60$ cm, the underlying soil is almost saturated at heights between 0 m and −0.25 m but higher values of suction are maintained compared to the models without a CBS or with the CBSs made of fine sand. In the model with $t_{CBS} = 100$ cm, water breakthrough in the underlying soil never occurs and, even during the most critical rainfall event, the underlying soil is at low values of degree of saturation and high values of suction. The better performance of the CBSs made of silty sand at maintaining higher values of suction in the underlying soil is a consequence of the higher water storage capacity, as can be seen from the degree of saturation profiles in the F.L. in Figure 8.11b. When silty sand is used, higher values of degree of saturation, and thus higher water storage capacities, are predicted in the F.L. compared to the use of fine sand. Moreover, comparing the upper part of the F.L. of the two CBSs with $t_{CBS} = 100$ cm, it can be seen that the F.L. made of silty sand is able to store a higher amount of water than the F.L. made of fine sand. Therefore, a higher thickness of the F.L. is beneficial for the CBS made of silty sand whereas it is detrimental for the CBS made of fine sand because, in the latter case, an increase of the thickness of the F.L. does not add significant extra water storage capacity but leads to a reduction of the evaporation from the F.L. into the atmosphere.

For the simulations with the weather of London (see Figures 8.11c,d), the suction profiles at heights between approximately −3 m and −20 m are linear and the degree of saturation close to $S_l = 1$ at the most critical time. The profiles are approximately hydrostatic for the models with CBSs with a F.L. consisting of silty sand, corresponding to a location of the water table (i.e. $s = 0$ kPa) at approximately −5 m. Without a CBS or with a CBS with the F.L. consisting of fine sand, the location of the water table is higher, approximately at −4 m, as a consequence of the higher amount of downward water filtration. Close to the surface, suction values in the soil predicted without the CBS are very small, between $s = 0$ kPa at 0 m and $s = 3$ kPa at −1 m. The CBSs made of fine sand, with both thicknesses $t_{CBS} = 60$ cm and $t_{CBS} = 100$ cm, and the CBS made of silty sand with a thickness of $t_{CBS} = 60$ cm are not able to limit the decrease of suction in the top metre of the underlying soil, which attains even small negative values at the interface between coarser layer and underlying soil. The use of the CBS having the F.L. made of silty sand with a thickness of $t_{CBS} = 100$ cm leads to the prediction of slightly higher values of suction in the underlying soil at locations between 0 m

and -2 m although suction still attains the value of $s = 0$ kPa at the top of the underlying soil.

8.4 Application of capillary barrier systems to slopes: 2D models

This section presents the results of the two-dimensional FE thermo-hydraulic analyses of slopes and limit analyses for slope stability. Fourteen different simulations were performed combining different weather conditions, materials and thicknesses of the finer layer and slope heights. In addition, the effects of the use of multiple drains along the height of the slope and the use of multi-layered CBSs were investigated. The modelling of all these different aspects is described in Section 8.2. The list of these fourteen two-dimensional analyses is shown in Table 8.5. The comparison of the results obtained from the different simulations highlights the general role of the CBS applied for slope protection and the roles of the different key parameters and conditions.

Table 8.5: Summary of the 2D analyses of slopes

Analysis ID	Weather	H_s [m]	CBS			Drain
			type	material F.L.	t_{CBS} [cm]	
Cag_10_NOCBS	Cagliari	10	No CBS	-	-	-
Cag_10_SCB_FS_60_SD	Cagliari	10	Single	Fine sand	60	Single
Cag_10_SCB_FS_100_SD	Cagliari	10	Single	Fine sand	100	Single
Cag_10_SCB_SS_60_SD	Cagliari	10	Single	Silty sand	60	Single
Cag_10_SCB_SS_100_SD	Cagliari	10	Single	Silty sand	100	Single
Lon_10_NOCBS	London	10	No CBS	-	-	-
Lon_10_SCB_FS_60_SD	London	10	Single	Fine sand	60	Single
Lon_10_SCB_FS_100_SD	London	10	Single	Fine sand	100	Single
Lon_10_SCB_SS_60_SD	London	10	Single	Silty sand	60	Single
Lon_10_SCB_SS_100_SD	London	10	Single	Silty sand	100	Single
Cag_6_NOCBS	Cagliari	6	No CBS	-	-	-
Cag_6_SCB_FS_60_SD	Cagliari	6	Single	Fine sand	60	Single
Cag_10_SCB_FS_60_MD	Cagliari	10	Single	Fine sand	60	Multiple
Cag_10_MCB_FS_60_SD	Cagliari	10	Layered	Fine sand	60	Single

8.4.1 Effect of thickness and materials of the CBS in Cagliari

This section shows the results of five two-dimensional simulations. In all these simulations, the weather conditions of Cagliari were considered and the slope height was $H_s = 10$ m. One of the five models was the bare slope, i.e. no CBS. The other four models included single capillary barrier systems with a single drain at the bottom of the slope and with the following materials for the finer layer and thickness of the CBS t_{CBS}: fine sand with $t_{CBS} = 60$ cm, fine sand with $t_{CBS} = 100$ cm, silty sand with $t_{CBS} = 60$ cm and silty sand with $t_{CBS} = 100$ cm. These five models correspond to the following analyses

shown in Table 8.5: Cag_10_NOCBS, Cag_10_SCB_FS_60_SD, Cag_10_SCB_FS_100_SD, Cag_10_SCB_SS_60_SD and Cag_10_SCB_SS_100_SD.

Figure 8.12 and Figure 8.13 show contours of degree of saturation and suction respectively at the end of the most critical rainfall event, i.e. $t = 1.182\,74$ years, for the different models. It must be noted that these are views only of the central upper part of the models, where the slope is located. The insets in Figures 8.12 and 8.13 are zoomed views of the toe of the slope for the models with CBSs. In the absence of the CBS (see Figures 8.12a and 8.13a), the soil surface is fully saturated down to a depth of approximately 80 cm, where a sharp wetting front separates the overlying saturated zone at very low values of suction from the underlying zone at lower degree of saturation ($S_l \approx 0.27$) and high values of suction. In the presence of the different CBSs (see Figures 8.12b-e and 8.13b-e), the soil under the footprint of the CBSs is in general maintained at lower degree of saturation even during the most critical rainfall event, unlike the lateral areas not covered by the CBS. However, close to the toe of the slope, breakthrough has occurred into the C.L. and into the underlying soil in the models shown in Figures 8.12b-d and 8.13b-d, causing an increase of the degree of saturation and decrease of suction in very small areas of the underlying soil under the footprint of the CBSs. The only exception is represented by the model with the CBS having the F.L. made of silty sand and a thickness of $t_{CBS} = 100$ cm (see Figures 8.12e and 8.13e) in which no water breakthrough occurs throughout the simulation, even at the toe of the slope.

In the two CBSs having the F.L. made of fine sand (Figures 8.12b,c), the lower part of the F.L. close to the interface with the C.L. attains high values of degree of saturation ($S_l > 0.99$) whereas the upper part attains low values of degree of saturation. In the CBS having the F.L. made of silty sand and the thickness of $t_{CBS} = 60$ cm (Figure 8.12d), the F.L. is almost all fully saturated whereas the degree of saturation attains lower values in the F.L. of the CBS having the F.L. made of silty sand and a thickness of $t_{CBS} = 100$ cm (Figure 8.12e).

Figure 8.14 shows the suction and degree of saturation profiles at the end of the most critical rainfall event. Three different sections along the slope height were considered: toe (section A-A), middle (section B-B) and top (section C-C). The location of these sections are shown in Figures 8.12 and 8.13. In these profiles and in all the profiles shown in the remainder of this section, the reference height of 0 m is located at the surface of the underlying soil, i.e. at the interface with the C.L. in the models in which a CBS covers the slope surface. Without the CBS, as identified in Figures 8.12a and 8.13a, the upper part of the underlying soil, approximately 80 cm thick, is fully saturated and suction approaches very low values, between 0 kPa and 6 kPa, at all sections (see Figure 8.14). When a CBS is used, high values of suction and low values of degree of saturation are maintained in the middle and top sections. In the models with the CBSs having the F.L. made of fine sand, with both $t_{CBS} = 60$ cm and $t_{CBS} = 100$ cm, and in the model with the CBS having the F.L. made of silty sand and a thickness of 60 cm, low values of suction and almost full saturation are attained at the toe section in a very small depth of the underlying soil close to the surface. By contrast, high values of suction and low values of degree of saturation are maintained at the toe section in the model having the CBS made of silty sand and a thickness of $t_{CBS} = 100$ cm. Based on

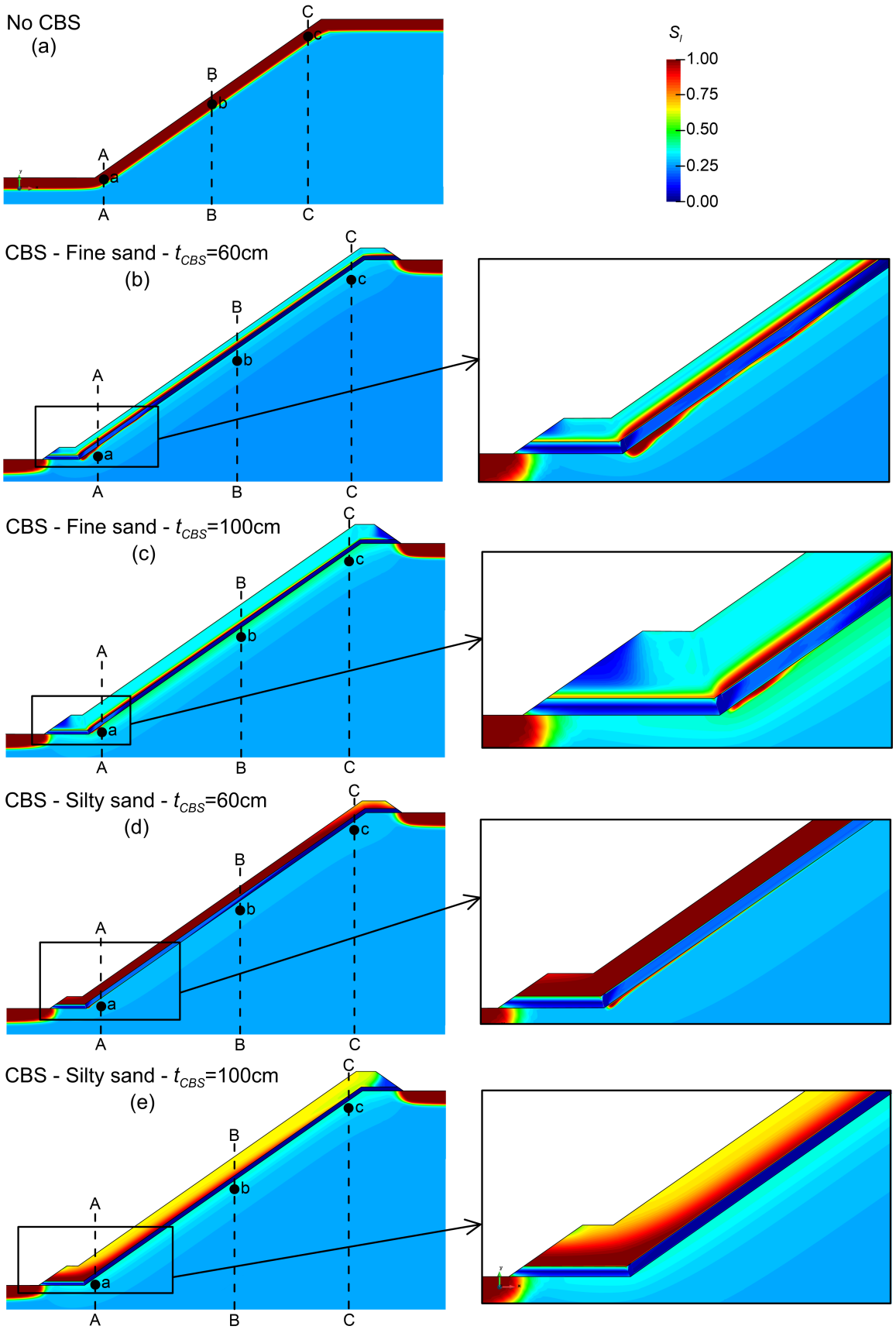

Figure 8.12: Degree of saturation contours at the most critical rainfall event, i.e. $t = 1.182\,74$ years, for the different models

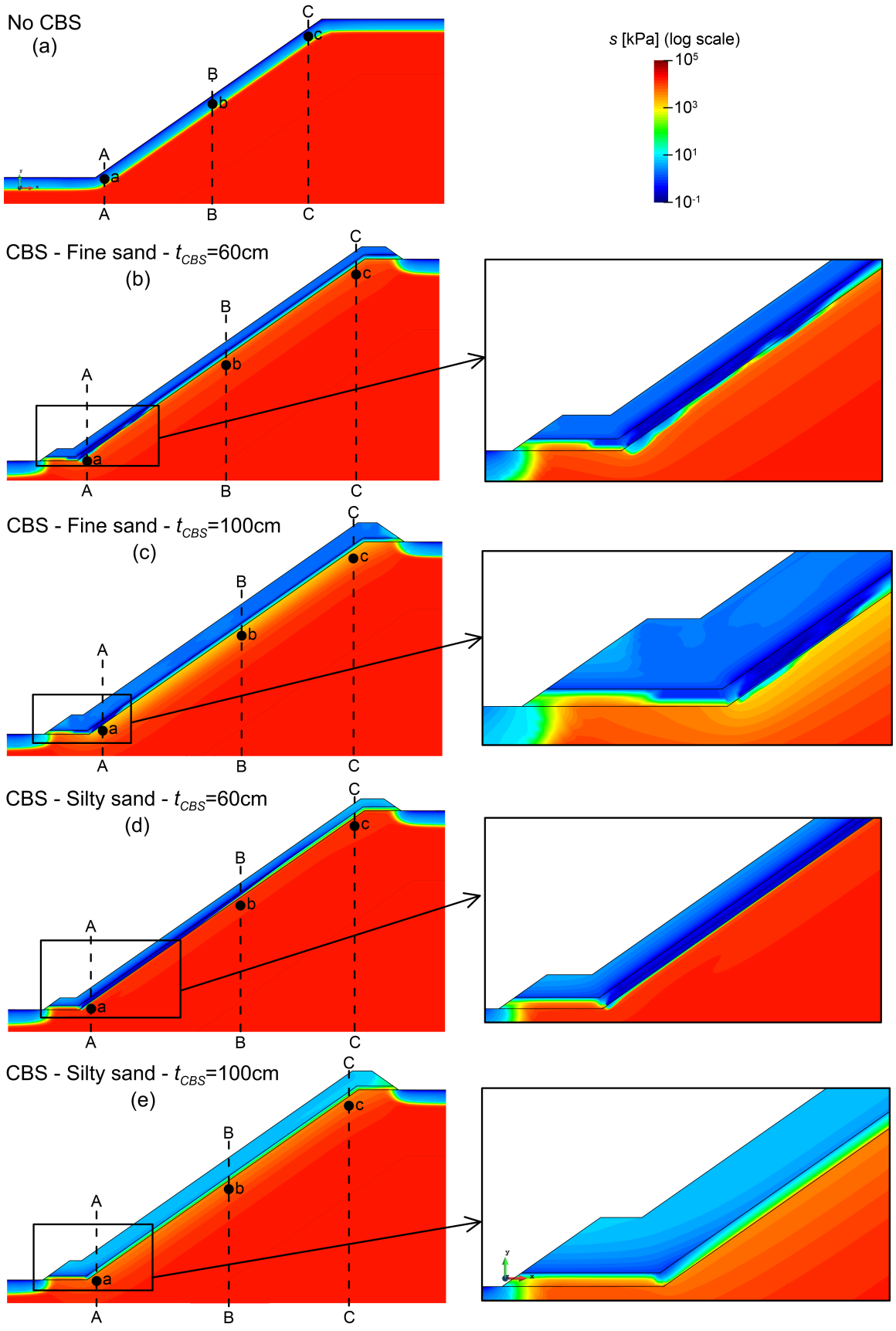

Figure 8.13: Suction contours at the most critical rainfall event, i.e. $t = 1.182\,74$ years, for the different models

the minimum values of suction attained and on the extension of the areas of underlying soil affected by the reduction in suction and increase in degree of saturation, the silty sand is more effective than the fine sand as a material of the F.L. in these analyses. Moreover, for both materials, the use of a thicker F.L. improves the effectiveness of the CBS.

The impact of the CBSs on the hydraulic response of the underlying soil over time can be better understood by observing Figure 8.15, which shows the time histories of suction and degree of saturation obtained at the points a (toe), b (middle) and c (top). These points are located 5 cm under the surface of the underlying soil when measured perpendicularly to the ground surface. The locations of these points are shown in Figure 8.12 and 8.13. It can be seen that, when a CBS is used, the fluctuations of s and S_l due to rain and evaporation have a lower amplitude than in the absence of a CBS. At points b and c, all the CBSs maintain high values of suction and low values of degree of saturation even during rainfall, i.e. when the model without CBS attains very low values of suction. At the toe of the slope (point a), the two CBSs having the F.L. made of fine sand are unable to prevent a significant decrease in suction in two intense rainfall events whereas the CBS having the F.L. made of silty sand and a thickness of 60 cm is ineffective on one occasion, i.e. the most critical rainfall event. As discussed before, only the CBS having the F.L. made of silty sand and a thickness of $t_{CBS} = 100$ cm is able to maintain high values of suction and low values of degree of saturation in the underlying soil at all sections and for all the time analysed.

In general, the CBSs are able to limit significantly or prevent totally the percolation of water into the underlying soil during a particular rainy period for the location of Cagliari. In order to understand the working principle of these sloping CBSs, Figure 8.16 shows the absolute liquid velocity and degree of saturation profiles within the CBSs at the toe, middle and top sections, at the end of the most critical rainfall event. The insets in Figures 8.16a-c are zoomed views of the absolute liquid velocity profiles in the finer layer. The direction of the liquid velocity is mainly orientated in a direction parallel to the interface between the F.L. and the C.L. Hence, the lateral water diversion of the CBS (see Section 2.3.4), which is given by the integral of the downslope component of water velocity profile over the perpendicular cross-section of the F.L. can be approximated by the area under under the liquid velocity profiles in the F.L. in Figures 8.16a-c multiplied by a constant (the cosine of the slope angle). From the comparison between the liquid velocity and the degree of saturation profiles obtained in the F.L. for the CBSs made of fine sand and those made of silty sand, two different working mechanisms can be identified. The finer layers made of fine sand are characterised by relatively low values of degree of saturation over most of their depth (the degree of saturation is high only in a thin region close to the interface with the C.L.) and relatively high downslope liquid velocity values in the thin layer at high degree of saturation, i.e. high lateral water diversion. By contrast, the finer layers made of silty sand are characterised by relatively high values of degree of saturation over their entire depth and low downslope liquid velocity values over their entire depth, i.e. low lateral water diversion. This means that the key response of the CBSs having the F.L. made of fine sand is to divert rainwater laterally down to the drain located at the toe. On the other hand, the key response of the CBSs having the F.L. made of

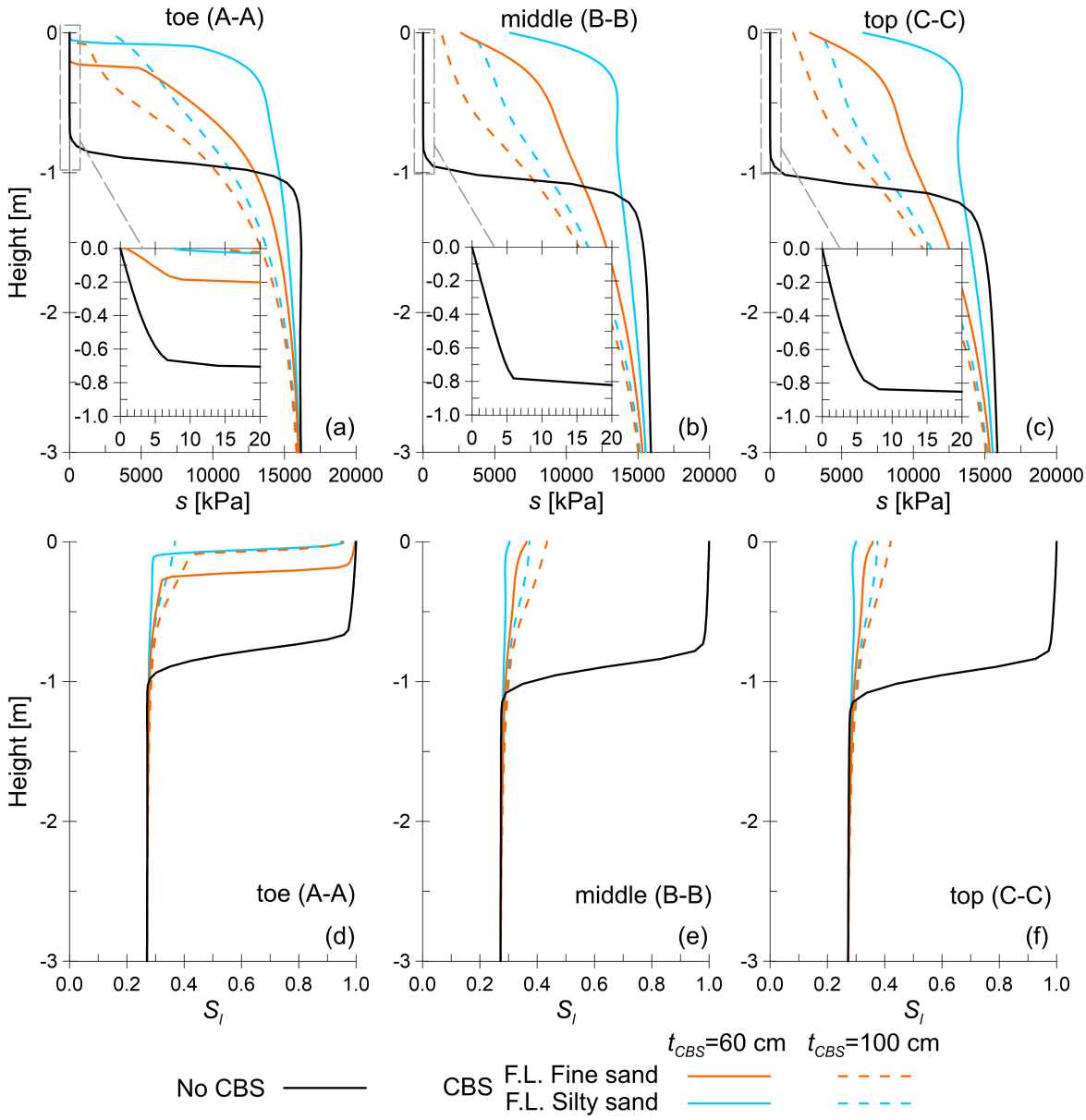

Figure 8.14: Suction (a-c) and degree of saturation (d-f) profiles at different sections in the underlying soil at the end of the most critical rainfall event, i.e. $t = 1.18274$ years, for different models

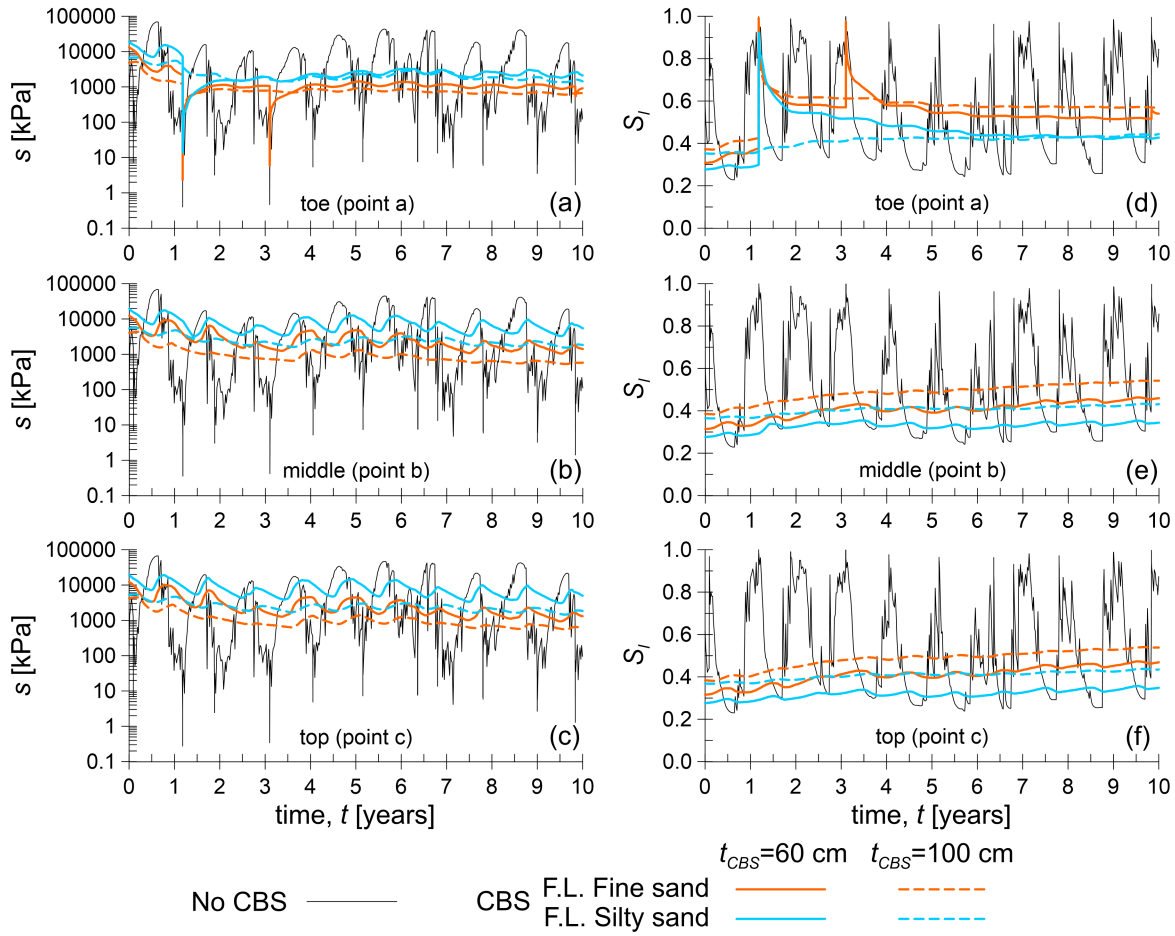

Figure 8.15: Time histories of suction (a-c) and degree of saturation (d-f) at the points a (toe), b (middle) and c (top) for different models

silty sand is to store water in the F.L. and subsequently remove it by evaporation, as occurs for the horizontal CBSs. For the finer layers made of fine sand, most of the water is diverted in a thin zone close to the interface with the C.L. where the degree of saturation is high, as shown by the liquid velocity profiles. For these CBSs, the values of degree of saturation and liquid velocity significantly increase moving down the slope (i.e. from section C-C to section A-A), as a result of the increase of the amount of diverted water. By contrast, the increase in degree of saturation and liquid velocity from the top to the toe is less significant for the finer layers made of silty sand because the lateral water diversion plays a minor role. For the finer layer made of fine sand, using a higher thickness does not lead to a significantly improved performance of the CBS because the upper part of the F.L. remains at low values of degree of saturation and contributes little to the lateral water diversion capacity of the CBS, as shown by the comparison between the profiles obtained for $t_{CBS} = 60\,\text{cm}$ and $t_{CBS} = 100\,\text{cm}$. By contrast, increasing the thickness of the F.L. when this is made of silty sand leads to a significant improvement of the performance of the CBS because the upper part of the F.L. significantly contributes to the water storage capacity, as shown by the comparison between the degree of saturation profiles obtained for $t_{CBS} = 60\,\text{cm}$ and $t_{CBS} = 100\,\text{cm}$.

Given that the behaviour of a sloping CBS having the F.L. made of silty sand is similar to that of a corresponding horizontal CBS due to its limited lateral diversion capacity, the results

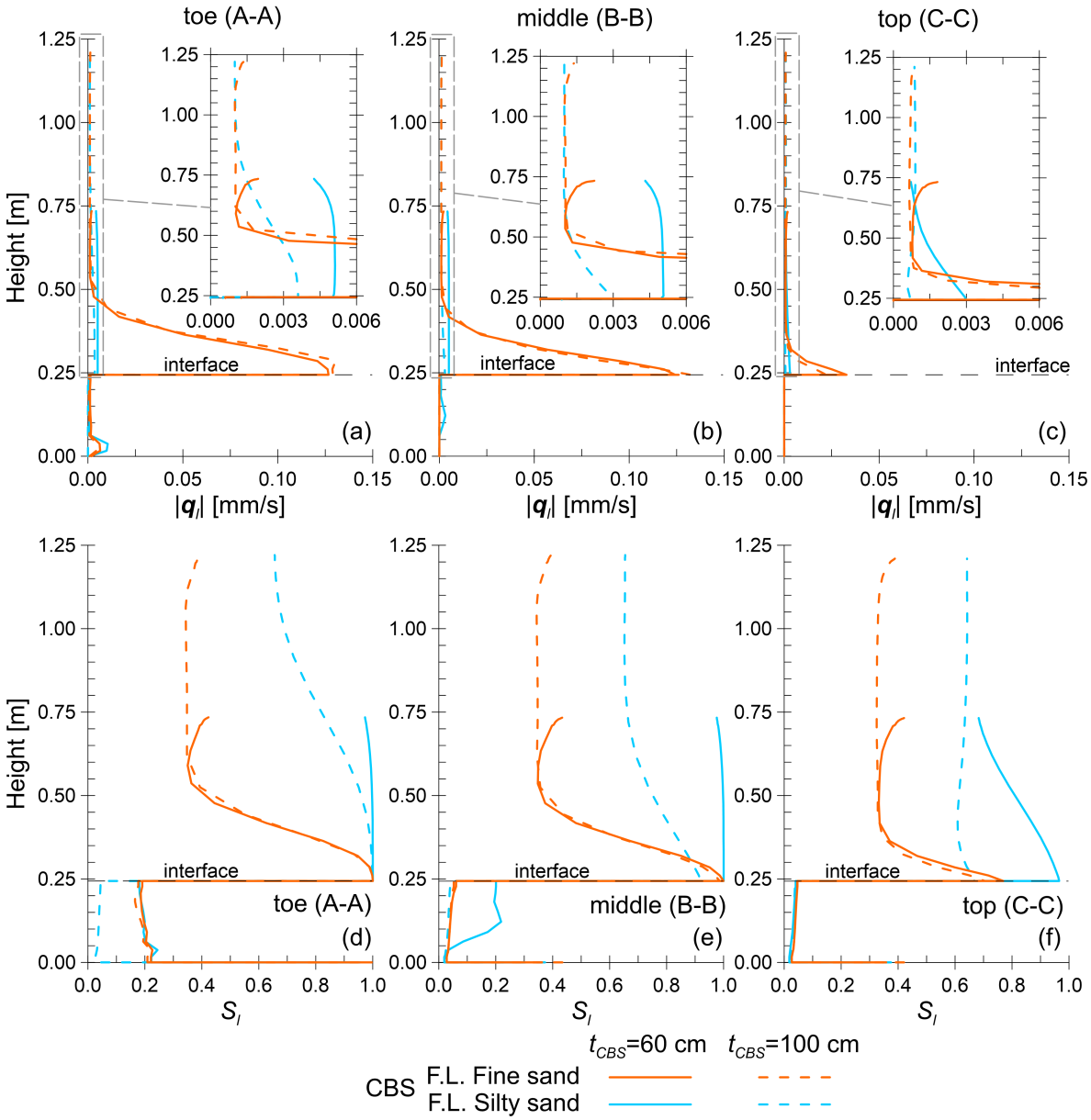

Figure 8.16: Absolute liquid velocity (a-c) and degree of saturation (d-f) profiles at different sections in the CBS at the most critical rainfall event, i.e. $t = 1.182\,74$ years, for different models

observed from the two-dimensional models of sloping CBSs qualitatively confirm the results obtained from one-dimensional models of horizontal CBSs (see Section 8.3). As observed for the one-dimensional models, the 100 cm-thick sloping CBS having the F.L. made of silty sand never leads to water breakthrough into the underlying soil at any sections whereas the corresponding 60 cm-thick sloping CBS leads to water breakthrough at the toe at the most critical rainfall event.

The impact of the four CBSs considered in this section on the stability of the slope was assessed by performing limit analyses with LimitState:GEO. Different models were considered for the limit analyses. The first model was represented by the bare slope (BS), i.e. with no CBS. This model was used to assess the stability of the original slope when a CBS is not constructed. For each FE model with a CBS, two different LS:GEO models were considered:

- one model represents the whole system which is the slope covered by a CBS (CS), hence made of the CBS plus the underlying soil (CS-CBS+U.S.), in which the overall stability is assessed;
- the other model consists of the slope covered by a CBS, in which only the stability of the underlying soil is assessed (CS-U.S.).

In other words, the same distribution of the product $-s \cdot S_l$ (from Code_Bright) was used in these two models but the difference is that in the latter model the CBS is not modelled in LS:GEO and only the stability of the underlying soil is assessed. The reason for this distinction is related to the fact that LS:GEO only shows the failure mechanism with the minimum corresponding factor of safety. As will be shown, many failure mechanisms are restricted to the CBS and, in these cases, the stability of the original slope would be hidden by failure mechanisms involving the CBS. Therefore, the latter model was considered to investigate the effect of the CBS on the stability of the original slope.

Most results of the limit analyses in this and in the following sections are presented in terms of the factor of safety (FoS). Considering that the shear strength was modelled by the relationship proposed by Bishop and Blight [67] (see Equation 4.97), the factor of safety is here defined as:

$$FoS = \frac{\tan \phi'}{\tan \phi_{lim}} = \frac{c'}{c_{lim}} \tag{8.2}$$

where ϕ_{lim} and c_{lim} are respectively the limit friction angle and the limit effective cohesion which together would cause collapse (i.e. for FoS=1). Note that FoS is therefore a scaling factor which acts simultaneously on ϕ' and c'.

Figure 8.17 shows the failure mechanisms and the corresponding FoSs at the end of the most critical rainfall event for three models analysed. The model in Figure 8.17a refers to the model with no CBS using degree of saturation and suction contours shown in Figures 8.12a and 8.13a whereas the models shown in Figures 8.17b and 8.17c refer to the model with the CBS having the F.L. made of fine sand and a thickness of $t_{CBS} = 60$ cm. The degree of saturation and suction contours shown in Figures 8.12b and 8.13b are used for the models

shown in Figures 8.17b and 8.17c. The BS model has a shallow failure line passing though the fully saturated area (see Figure 8.12a). The corresponding FoS is lower than 1, i.e. FoS=0.82, suggesting that, without a CBS, the slope is unstable at the end of the most critical rainfall event. The use of a CBS significantly improves the stability of the original soil, as shown by the CS–U.S. model (see Figure 8.17c), thanks to the higher suction values maintained in the underlying soil. The failure line is much deeper and the corresponding FoS was enormously higher than 1 (FoS=52). For the CS-CBS+U.S. model, the stability of the CBS becomes more critical than that of the U.S. The failure mechanism of the model CS–CBS+U.S. involves only the C.L. and the F.L. of the CBS but the corresponding FoS is higher than 1 (FoS=1.29) which corresponds to a stable condition.

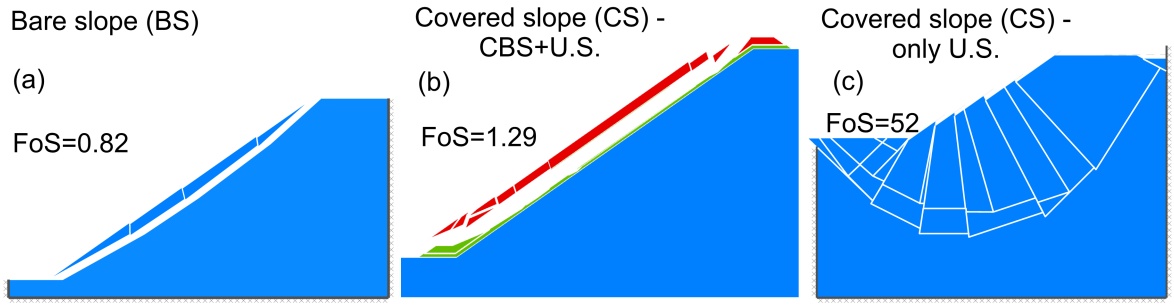

Figure 8.17: Collapse mechanisms at the most critical time, i.e. $t = 1.18274$ years, for the models: (a) bare slope, (b) slope covered by the CBS (fine sand $t_{CBS} = 60$ cm) and (c) underlying soil with hydraulic conditions of the slope covered by the CBS

Figure 8.18 shows the FoSs of the three models analysed above in 9 different critical rainfall events. It can be seen that in two events (i.e. 1.18274 years and 3.10203 years) the FoS of the BS is lower than 1. Introducing the CBS, the underlying soil is now permanently stable with corresponding FoSs always very high, above 40. The stability of the CBS is almost unaffected by the weather conditions, indicated by an approximately constant trend of the FoS, always higher than 1. This stable trend is related to the fact that the suction values attained in the materials used for a CBS, which are generally coarse-grained soils, are typically relatively low. The stability of the CBS is thus hardly affected by variations in suction and hence weather conditions. For these materials, the stability is mainly related to the shear strength parameters, i.e. ϕ' and c', and the value of ϕ' is often high for this type of materials. These shear strength parameters of the CBS materials are affected by fewer uncertainties and by a minor variability compared to the impact of suction on the shear strength of the underlying soil. The prediction of the minimum values of suction attained in the underlying soil is often the result of predictive methods characterised by a higher number of uncertainties compared to laboratory and field tests used to characterise the shear strength parameters of the CBS materials.

The histogram in Figure 8.19 shows the minimum factors of safety obtained for all the different models analysed in this section. The collapse mechanisms obtained for the different models including CBSs (not shown) are all similar to those shown in Figures 8.17b and 8.17c, which were obtained for the model with CBS having the F.L. made of fine sand

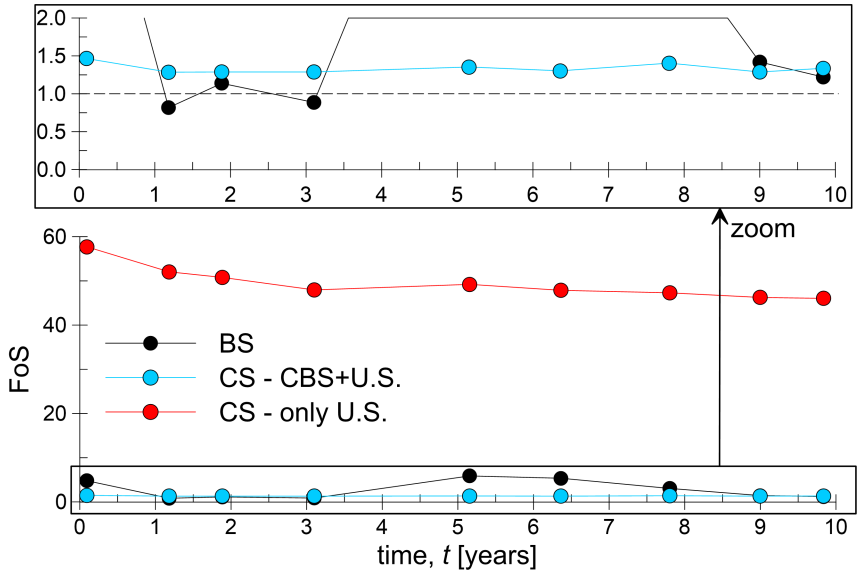

Figure 8.18: Time histories of the factor of safety for the models for 9 critical rainfall events: bare slope (BS), slope covered by the CBS (fine sand $t_{CBS} = 60\,\text{cm}$) (CS-CBS+U.S.) and underlying soil with hydraulic conditions of the slope covered by the CBS (CS-U.S.)

and a thickness of $t_{CBS} = 60\,\text{cm}$. From the comparison of the FoSs obtained for the BS model and CS-CBS+U.S. models, it can be seen that all the CBSs are effective at maintaining the stability of the slope, which, without the use of any of these CBSs, would be unstable during intense rainfall events. The factors of safety of the underlying soil when covered by a CBS (CS-U.S.) obtained for the different models are very high and similar to each other. Therefore, although water breakthrough into the underlying soil occurs in three of these models (see Figures 8.12b-d and 8.13b-d), only a very small area of the U.S. is affected by significant decreases in suction and the stability of the slope is thus unaffected by these events of breakthrough. All the CBSs are stable at the most critical rainfall events, with similar factors of safety included between 1.16 for the model with silty sand and $t_{CBS} = 60\,\text{cm}$ and 1.32 for the model with silty sand $t_{CBS} = 100\,\text{cm}$. The minimum factor of safety for the CBSs with fine sand is less affected by the thickness of the CBS, i.e. FoS=1.29 for $t_{CBS} = 60\,\text{cm}$ and FoS=1.31 for $t_{CBS} = 100\,\text{cm}$. The higher sensitivity of the minimum factor of safety to t_{CBS} observed for the CBS having the F.L. made of silty sand is due to the higher range of suction values attained by a material such as silty sand. At the end of the most critical rainfall event, the CBS with silty sand and $t_{CBS} = 60\,\text{cm}$ experiences lower values of suction than the CBS with silty sand and $t_{CBS} = 100\,\text{cm}$ (see Figures 8.13d and 8.13e). For the CBSs with $t_{CBS} = 60\,\text{cm}$, the factor of safety is lower when silty sand is used for the F.L. than when fine sand is used, because the friction angle of the silty sand ($\phi' = 35°$) is less than the friction angle of the fine sand ($\phi' = 40°$), see Table 8.2.

8.4.2 Effect of thickness and materials of the CBS in London

Similar to the results shown in Section 8.4.1, this section shows the results of five two-dimensional simulations, in which the slope height was $H_s = 10\,\text{m}$ but the weather con-

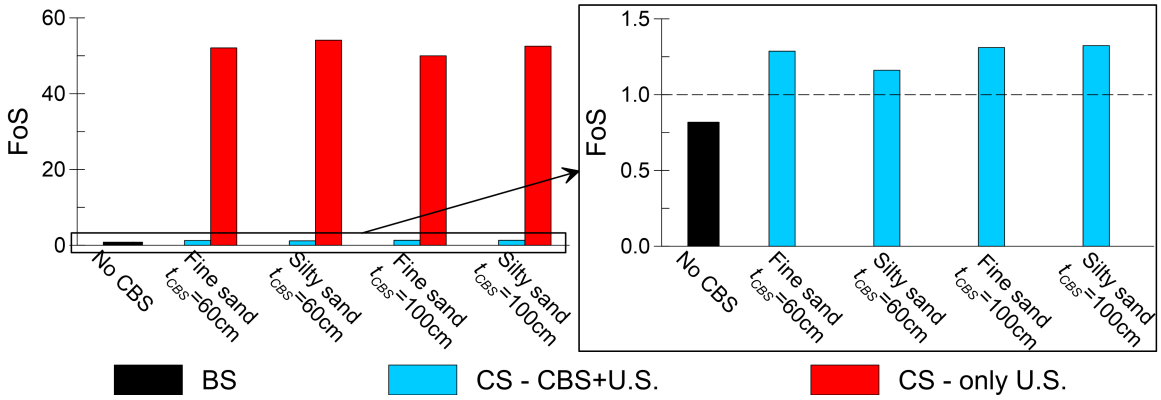

Figure 8.19: Minimum factors of safety obtained for the different models

ditions were representative of London. One of the five models was the bare slope, i.e. no CBS. The other four models included single capillary barrier systems with a single drain at the bottom of the slope and with the following materials and thickness: fine sand with $t_{CBS} = 60\,\text{cm}$, fine sand with $t_{CBS} = 100\,\text{cm}$, silty sand with $t_{CBS} = 60\,\text{cm}$ and silty sand with $t_{CBS} = 100\,\text{cm}$. These five models correspond to the following analyses shown in Table 8.5: Lon_10_NOCBS, Lon_10_SCB_FS_60_SD, Lon_10_SCB_FS_100_SD, Lon_10_SCB_SS_60_SD and Cag_10_SCB_SS_100_SD. From the analysis of these results, and comparing with what was observed in Section 8.4.1, in which the same models were analysed with the weather of Cagliari, it is possible to understand the effect of different climatic conditions on the application of CBSs for slope protection.

Figure 8.20 and Figure 8.21 respectively show the degree of saturation and suction contours at the end of the most critical rainfall event, i.e. $t = 5.002\,14\,\text{years}$, for the different models. It must be noted again that these are views only of the central upper part of the models, where the slope is located. Compared to the results obtained for Cagliari, the degree of saturation values in the underlying soil are in general always relatively high even in the areas little affected by intense rainfall events. This is due to the different initial and boundary conditions adopted for the models considering the weather of London. The initial and boundary conditions were representative of a situation in which the location of the water table was relatively high, i.e. 5 m below the ground level from the lower part of the slope in hydrostatic conditions, and oscillating around this equilibrium position in different seasons. Although the values of degree of saturation are in general relatively high in the underlying soil, suction may still attain significant values which may assume a crucial role in the slope stability.

In the absence of a CBS (see Figures 8.20a and 8.21a), very low values of suction are attained close to the soil surface down to a depth of approximately 1.7 m, where an almost fully saturated area is underlain by soil at lower degree of saturation and higher values of suction. In the presence of the different CBSs (see Figures 8.20b-e and 8.21b-e), higher values of suction are maintained in the soil underlying the CBSs even at the end of the most critical rainfall event, unlike the lateral zones not covered by the CBS. However, close to the toe of the slope, breakthrough has occurred into the C.L. and into the underlying soil in the models

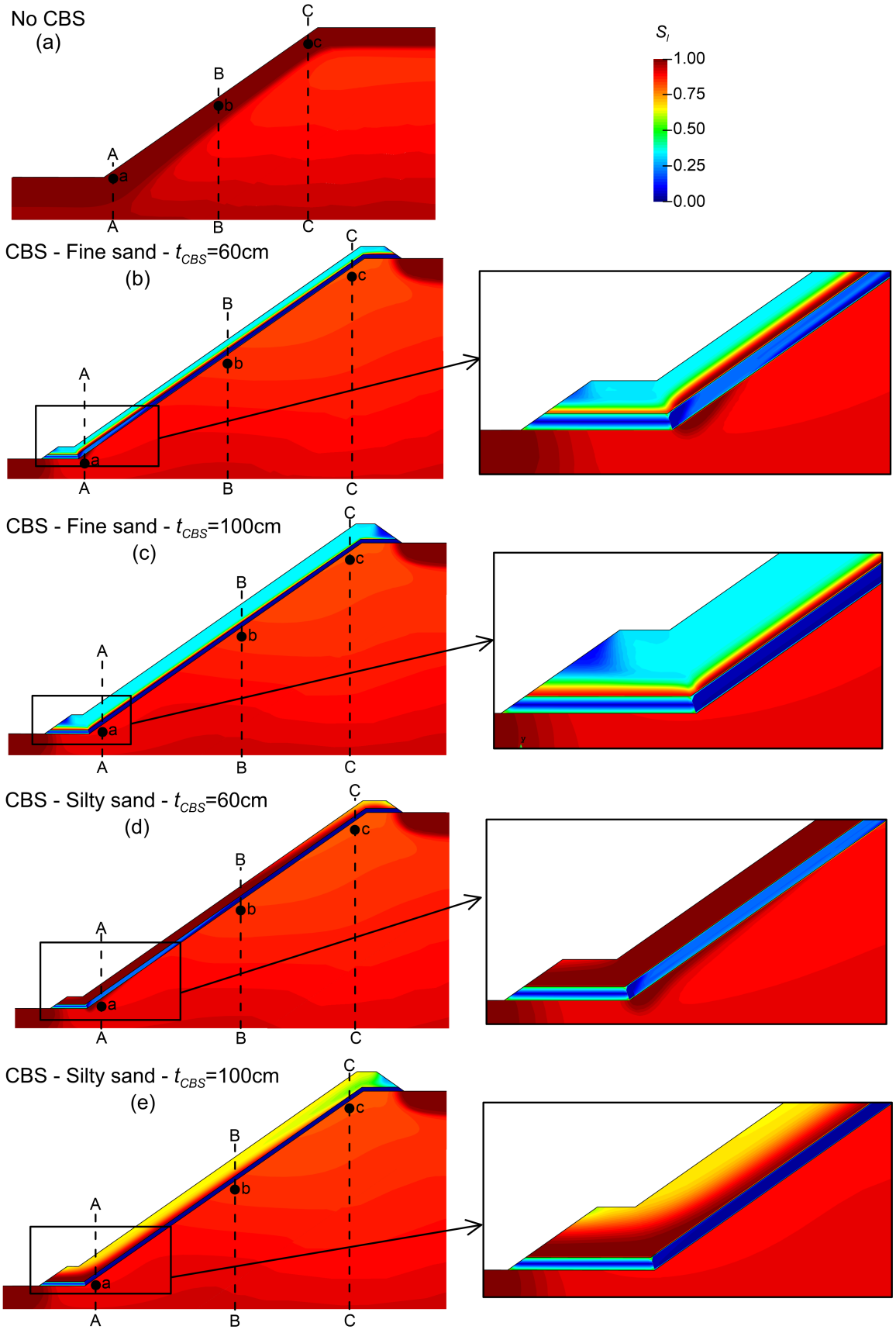

Figure 8.20: Degree of saturation contours at the most critical rainfall event, i.e. $t = 5.002\,14$ years, for the different models

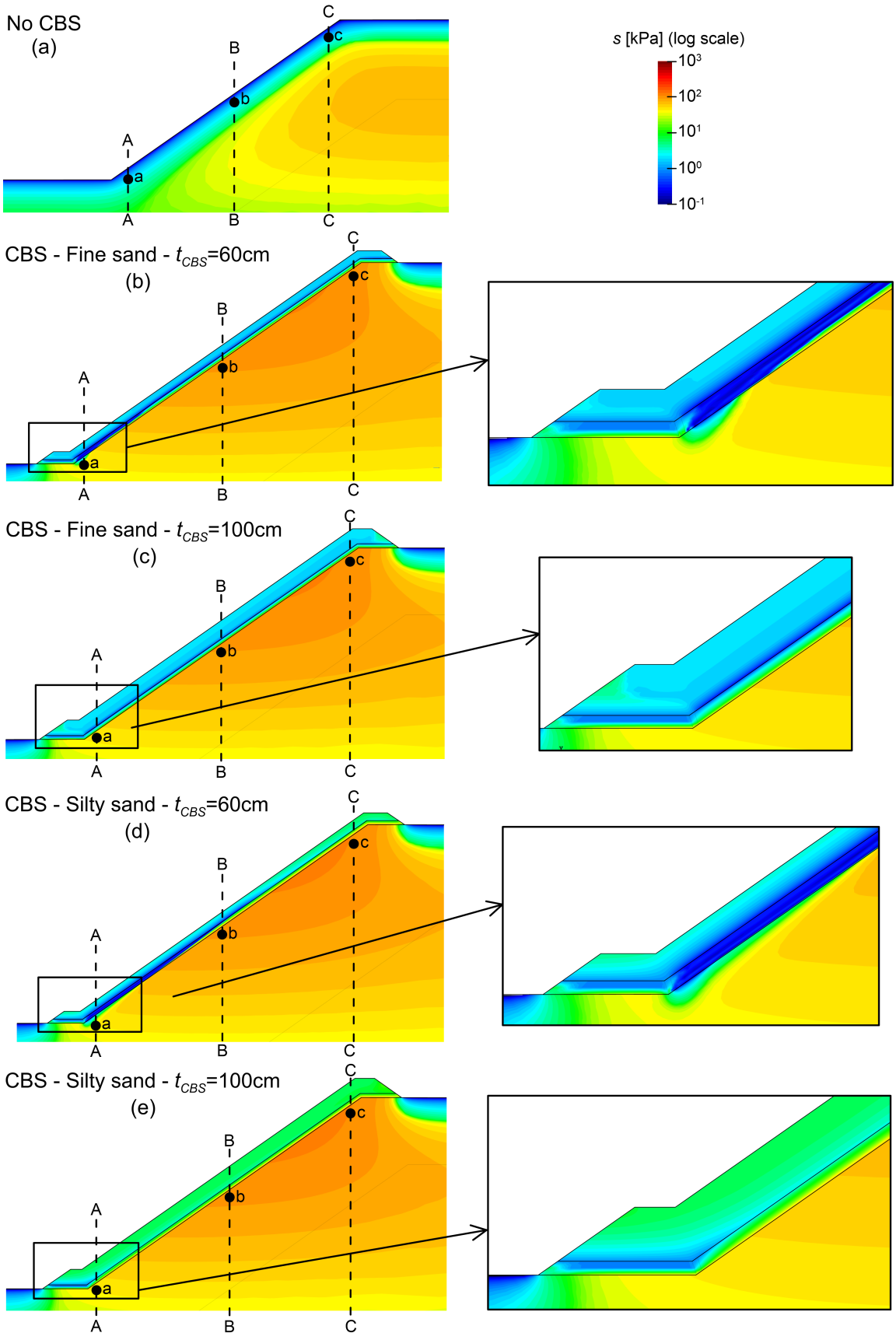

Figure 8.21: Suction contours at the most critical rainfall event, i.e. $t = 5.002\,14$ years, for the different models

with thinner CBSs ($t_{CBS} = 60\,\text{cm}$) shown in Figures 8.20b,d and 8.21b,d. This causes a slight increase of degree of saturation and in particular a decrease of suction in very small areas of the underlying soil under the CBS. By contrast, no water breakthrough has occurred in the models with the thicker CBSs ($t_{CBS} = 100\,\text{cm}$) (see Figures 8.20c,e and 8.21c,e).

Suction and degree of saturation contours obtained within the CBSs at the end of the most critical rainfall event (see Figures 8.20b-e and 8.21b-e) are similar to those obtained at the most critical rainfall event in Cagliari (see Figures 8.12b-e and 8.13b-e) and hence similar considerations made in that case apply to these results.

Figure 8.22 shows the suction and degree of saturation profiles in the underlying soil at the end of the most critical rainfall event in the three reference sections: toe (section A-A), middle (section B-B) and top (section C-C). Without the CBS, as also identified in Figures 8.20a and 8.21a, the upper part of the underlying soil, approximately 1.7 m thick, is fully saturated and suction approaches very low values, between 0 kPa and 6 kPa, at the middle and top section. At the toe section, this zone of full saturation and very low values of suction extends beyond a depth of 3 m. When a CBS is used, high values of suction and low values of degree of saturation are maintained in the middle and top sections at the end of most critical rainfall event. At the toe section, in the models with the thinner CBSs ($t_{CBS} = 60\,\text{cm}$), low values of suction and almost full saturation are attained in a very small area of the underlying soil close to the surface, regardless of the material used for the F.L. By contrast, high values of suction and low values of degree of saturation are maintained at the toe section with the two CBSs with a thickness of $t_{CBS} = 100\,\text{cm}$.

A higher thickness of the CBS improves the effectiveness of the CBS for both materials considered. Considering the two CBSs of a thickness of $t_{CBS} = 60\,\text{cm}$ and based on the observation of the extension of the area of underlying soil affected by significant decreases in suction and increases in degree of saturation, the fine sand is more effective than the silty sand as a material for the F.L. This is in contrast with what is observed from the simulations with the weather of Cagliari (see Figure 8.14), according to which the silty sand was shown to be more effective as a material for the F.L. The reason for this difference between the results observed for the weathers of Cagliari and London is related to the two different working mechanisms of the CBSs made of fine sand and silty sand and how they interact with weather conditions. As described in Section 8.4.1, the CBS having the F.L. made of silty sand works in a manner more similar to horizontal CBSs, in which the water storage capacity plays an important role because rainwater is stored in the finer layer and removed by evaporation in the periods between rainfall events. The CBS having the F.L. made of fine sand has a low water storage capacity but it is more effective in diverting water laterally down the slope. The usefulness of a high water storage capacity (relevant to the CBS with silty sand) is strongly related to the general amounts of rain and evaporation (because these influence how much water is already likely to be stored in the CBS before an extreme rainfall event occurs) whereas the usefulness of a high lateral water diversion capacity (relevant to the CBS with fine sand) is strongly related to the maximum rainfall intensity [148], and hence to extreme rainfall events. In Cagliari, which is characterised by a relatively dry and warm weather, a CBS made of

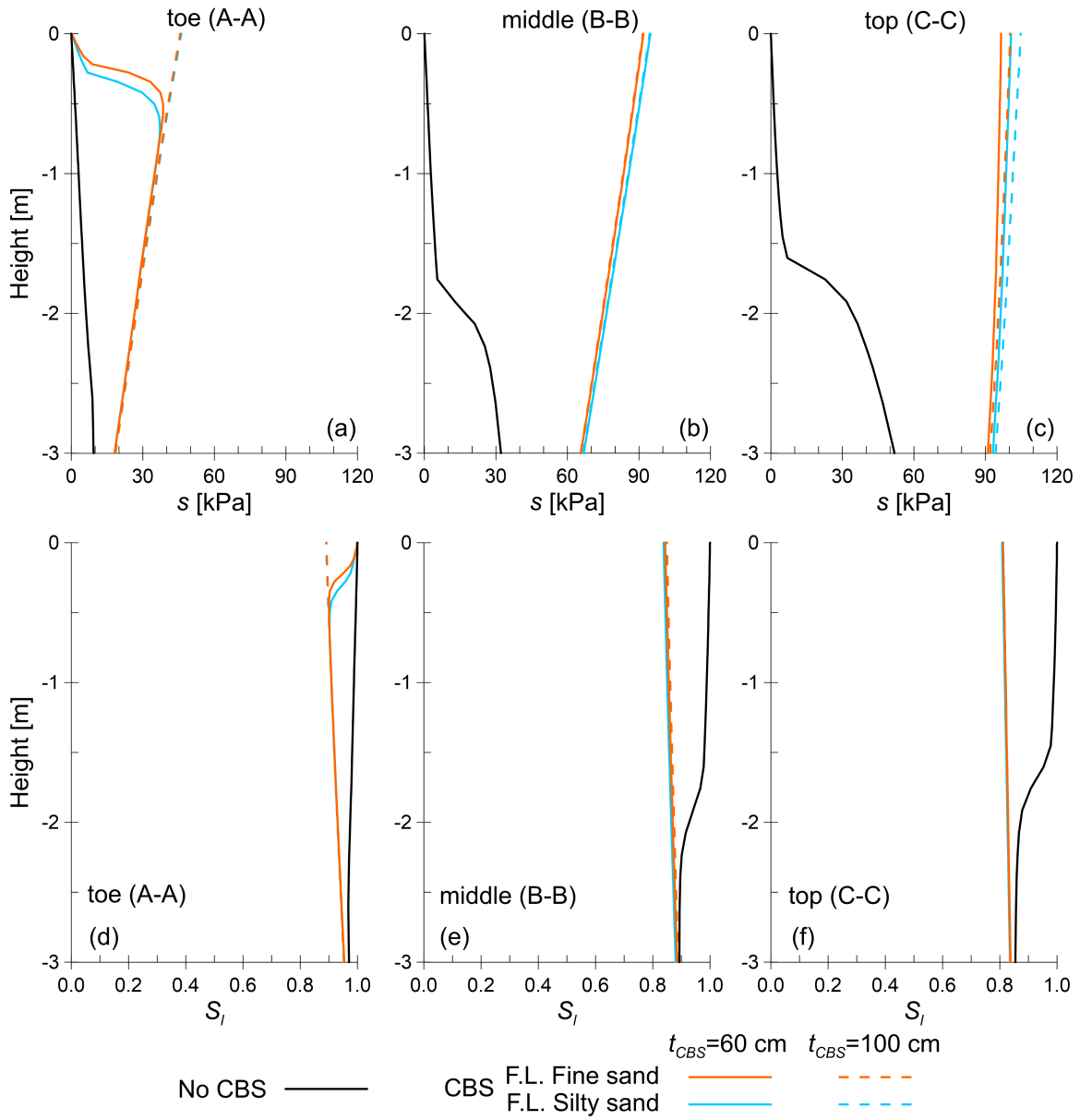

Figure 8.22: Suction (a-c) and degree of saturation (d-f) profiles in different sections in the underlying soil at the most critical rainfall event, i.e. $t = 5.002\,14$ years, for different models

silty sand works better because a high amount of evaporation and a relatively low amount of rainfall means that a large proportion of its high water storage capacity is typically available when an extreme rainfall event occurs. In London, which is characterised by a relatively wet and cool weather, a CBS made of silty sand is not effective because the amount of evaporation is always much lower than the amount of rainfall, so much of the high water storage capacity is already filled even before an extreme rainfall event occurs. These observations also agree with the results obtained for the horizontal CBSs (see Section 8.3). In London, where the extreme individual rainfall events are comparable or less extreme than the extreme rainfall events recorded in Cagliari (i.e. maximum daily rainfall values of 63.4 mm for London and 73.8 mm for Cagliari), a CBS made of fine sand works better on a slope because it uses the high lateral water diversion capacity.

Figure 8.23 shows the time histories of suction and degree of saturation obtained at the points a (toe), b (middle) and c (top). These points are located 5 cm under the surface of

the underlying soil when measured perpendicularly to the ground surface. The locations of these points can be seen in Figure 8.20 and 8.21. As already observed in Section 8.4.1 for the weather of Cagliari, when a CBS is used the fluctuations of s and S_l due to rain and evaporation have lower amplitudes than those obtained in the absence of a CBS. They indeed exhibit almost a constant trend. At points b and c, all the CBSs maintain relatively high values of suction and full saturation is not reached even during rainfall. At the toe of the slope (point a), the CBSs of a thickness of $t_{CBS} = 60\,\text{cm}$ are unable to prevent a significant decrease in suction in all the duration of the analyses whereas the CBSs of a thickness of $t_{CBS} = 100\,\text{cm}$ are able to maintain high values of suction and to avoid full saturation in all the underlying soil for all the time analysed.

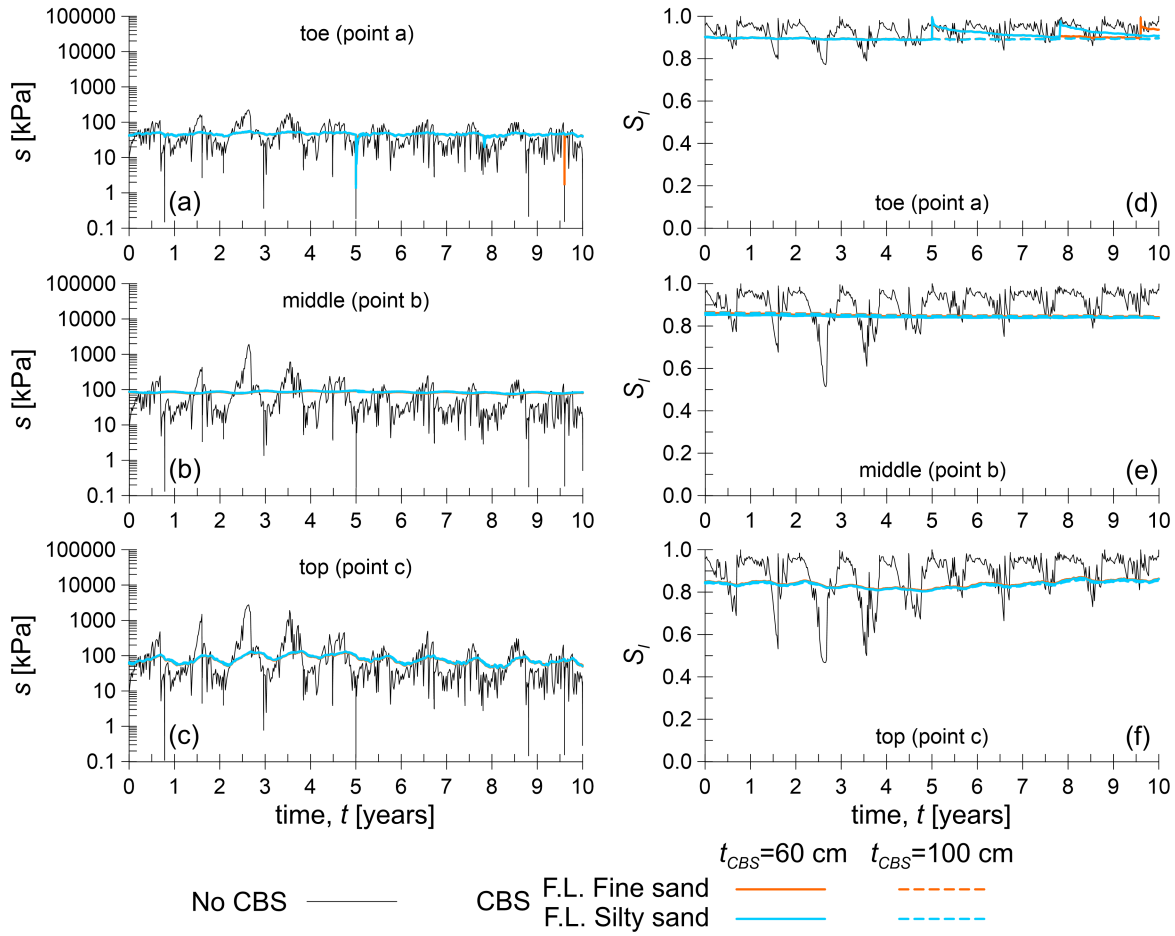

Figure 8.23: Time histories of suction (a-c) and degree of saturation (d-f) at the points a (toe), b (middle) and c (top) for different models

The slope stability of the models discussed in this section was assessed using LS:GEO. As was done in Section 8.4.1, LS:GEO was used to assess the stability of the bare slope (BS) and, for each model with a CBS, the stability of the whole model (CS-CBS+U.S.) and only the underlying soil (CS-U.S.).

Figure 8.24 shows the time history of the factors of safety obtained at the end of thirteen intense rainfall events. The LS:GEO model bare slope (BS) uses the results obtained from the FE model Lon_10_NOCBS whereas the two LS:GEO models CS-CBS+U.S. and CS-U.S. use the results obtained from the FE model Lon_10_SCB_FS_60_SD (i.e. the model

with the CBS having the F.L. made of fine sand and a thickness of $t_{CBS} = 60\,\text{cm}$). From inspection of Figure 8.24 it can be seen that the bare slope is predicted to be unstable (FoS<1) in many rainfall events in the 10-year period analysed. The failure mechanisms of the bare slope always involve the instability of a shallow portion of soil, which is directly affected by significant decreases in suction, similar to the mechanism shown in Figure 8.17a. The application of the CBS plays an important role for the slope stability. It can be seen that, as a result of the application of the CBS, the original slope is always stable (FoS>1.26), as shown by the CS-U.S. model. The collapse mechanisms related to the CS-U.S. model are similar to that shown in Figure 8.17c, involving deep areas of underlying soil. As observed for Cagliari (see Figure 8.18), the stability of the CBS becomes more critical than that of the U.S. Indeed, the failure mechanism of the model CS–CBS+U.S. involves both the F.L. and the C.L. of the CBS, with a collapse mechanism similar to that shown in Figure 8.17b, and the corresponding FoS is always higher than 1 (FoS>1.26) which suggests a stable condition. Moreover, this factor of safety exhibits a constant trend over time suggesting that the weather conditions have little influence on the stability of the CBS.

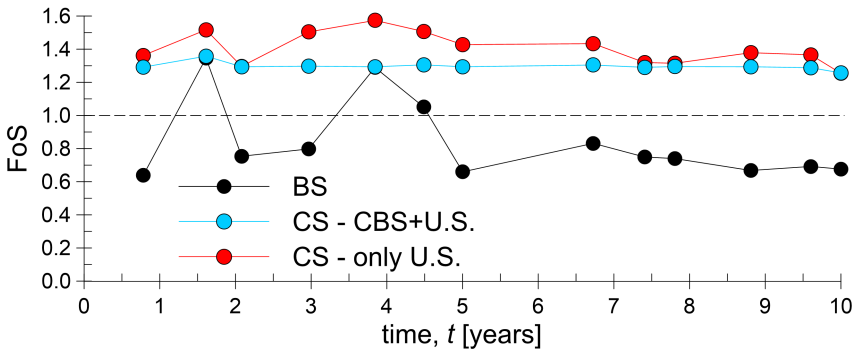

Figure 8.24: Time history of the factors of safety for the models for 13 intense rainfall events: bare slope (BS), slope covered by the CBS (fine sand and $t_{CBS} = 60\,\text{cm}$) (CS-CBS+U.S.) and underlying soil with hydraulic conditions of slope covered by CBS (CS-U.S.)

Figure 8.25 shows a comparison of the minimum factors of safety obtained for all the models analysed in this section. It can be seen that all the CBSs represent an effective method of slope stabilization, as a result of corresponding factors of safety always greater than 1. On the other hand, the minimum factor of safety of the bare slope is 0.66. The different CBSs lead to similar minimum factors of safety of the underlying soil (model CS-U.S.). The minimum factor of safety of the CBS having the F.L. made of silty sand and a thickness of $t_{CBS} = 60\,\text{cm}$ is slightly lower compared to the values obtained for the other CBSs because the silty sand is modelled with a lower value of friction angle than that used for the fine sand (see Table 8.2) and the minimum values of suction attained in the F.L. (see Figure 8.21d) are lower than those obtained with the corresponding CBS with $t_{CBS} = 100\,\text{cm}$ (see Figure 8.21e).

It must be noted that the small amount of water breakthrough into the underlying soil that occurred in some models does not significantly affect the stability of the slope.

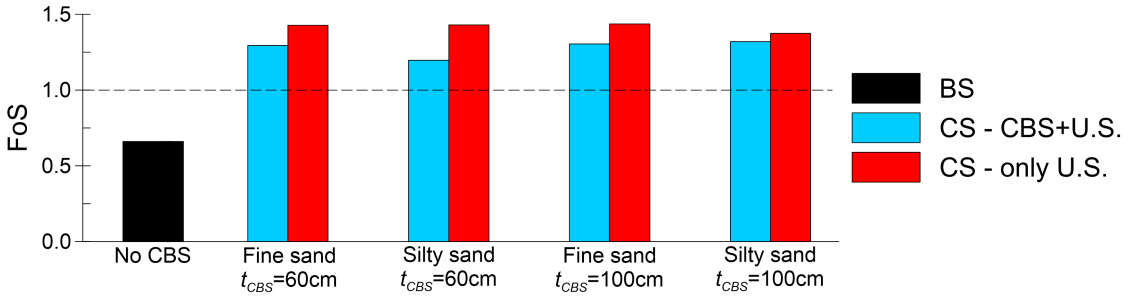

Figure 8.25: Minimum factors of safety obtained for the different models

8.4.3 Effect of the slope height

The aim of this section is to show the effect of the slope height on the application of capillary barrier systems for slope stability. The results of two two-dimensional simulations are shown in this section: a bare slope and a slope covered with a single CBS having the F.L. made of fine sand and a thickness of $t_{CBS} = 60\,\text{cm}$, with a single drain at the toe of the slope. Weather conditions of Cagliari were considered. For both models, the slope height was $H_s = 6\,\text{m}$, which is different from that considered in the models presented in Sections 8.4.1 and 8.4.2, i.e. $H_s = 10\,\text{m}$. The two models correspond to the following analyses shown in Table 8.5: Cag_6_NOCBS and Cag_6_SCB_FS_60_SD. The results shown for these models will be systematically compared with the results obtained from the corresponding models characterised by a slope height of $H_s = 10\,\text{m}$, i.e. Cag_10_NOCBS and Cag_10_SCB_FS_60_SD, already presented in Section 8.4.1.

Figure 8.26 shows the suction and degree of saturation contours at the end of the most critical rainfall event, i.e. $t = 1.18274\,\text{years}$, for the models with and without a CBS. The contours predicted in the model without a CBS are very similar to those obtained for the corresponding model with a slope height of $H_s = 10\,\text{m}$ (see Figures 8.12a and 8.13a). This consisted of a sharp wetting front located at a depth of approximately 80 cm separating the upper soil, fully saturated and at very low values of suction, and the lower soil, which is at low values of degree of saturation and high values of suction. In the model with the CBS (see Figures 8.12c,d), low values of degree of saturation and high values of suction are maintained under the CBS along the whole length. By contrast, water breakthrough into the underlying soil is predicted at the toe of the corresponding model with a slope height of $H_s = 10\,\text{m}$ (see Figures 8.12b and 8.13b).

Similar comments can be made by observing Figures 8.27 and 8.28. In particular, Figure 8.27 shows the suction and degree of saturation profiles at the end of the most critical rainfall event, i.e. $t = 1.18274\,\text{years}$, at the three reference sections A-A (toe), B-B (middle) and C-C (top). From this figure it can be seen that, in contrast with the bare slope where very low values of suction and high values of degree of saturation are attained in the top metre of soil at all sections, the CBS is effective at preventing water breakthrough and hence at maintaining high values of suction and low values of degree of saturation in the underlying soil at all sections. Figure 8.28 shows the time histories of suction and degree of saturation at the points a, b and c, located at the toe, middle and top sections respectively at a depth of 5 cm

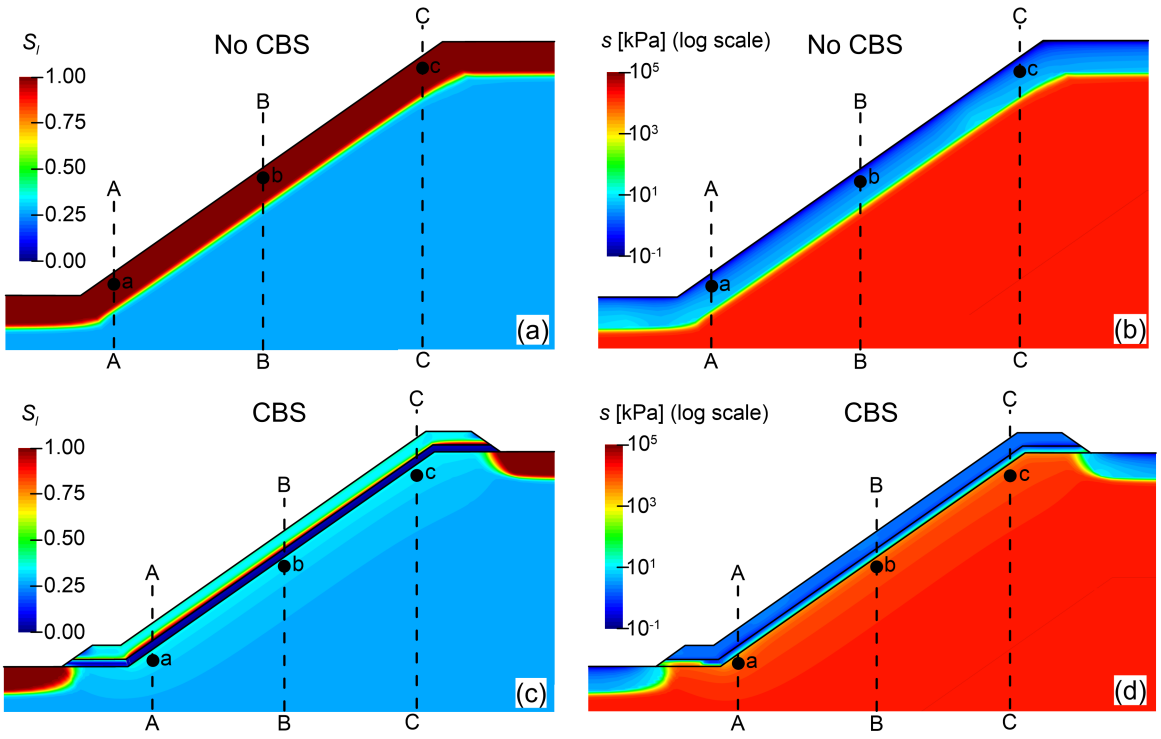

Figure 8.26: Slope height $H_S = 6\,\text{m}$; (a,c) degree of saturation and (b,d) suction contours at the end of the most critical rainfall event, i.e. $t = 1.182\,74\,\text{years}$, for the models (a,b) with no CBS and (c,d) with CBS

below the surface of the underlying soil, measured perpendicular to the ground surface. The comparison between the bare slope (BS) and the covered slope (CS) confirms the effectiveness of the CBS at maintaining high values of suction and low values of degree of saturation during all the 10-year period analysed.

Figure 8.29 shows the absolute liquid velocity and degree of saturation profiles obtained within the CBS at sections A-A (toe), B-B (middle) and C-C (top). From the observation of these profiles it is evident that the effectiveness of the CBS at preventing breakthrough relies on the lateral water diversion capacity of the CBS. This is clearly represented by an increase of the water diverted laterally from the top to the toe of the slope, shown in the form of an increase of the degree of saturation and absolute liquid velocity. At all these sections, the coarser layer remains at very low values of degree of saturation and no significant amount of water enters it.

As described in Section 2.3.4, the diversion length of a CBS, i.e. the length in the down-dip direction to a point where breakthrough commences and the barrier does not divert any additional water, is related to the slope angle, weather conditions, materials of the CBS and thickness of the F.L. As already stated above, the same CBS (fine sand for the F.L. and thickness of $t_{CBS} = 60\,\text{cm}$) under the same weather conditions (Cagliari) led to water breakthrough into the underlying soil at the toe when applied to a slope with a height of $H_s = 10\,\text{m}$ whereas it does not cause any water breakthrough when applied to a slope with a height of $H_s = 6\,\text{m}$. In the two cases the diversion length was the same. However, in the higher slope ($H_s = 10\,\text{m}$) the distance between the top of the slope and the bottom drain is greater than the diversion length of the CBS whereas in the smaller slope ($H_s = 6\,\text{m}$) the

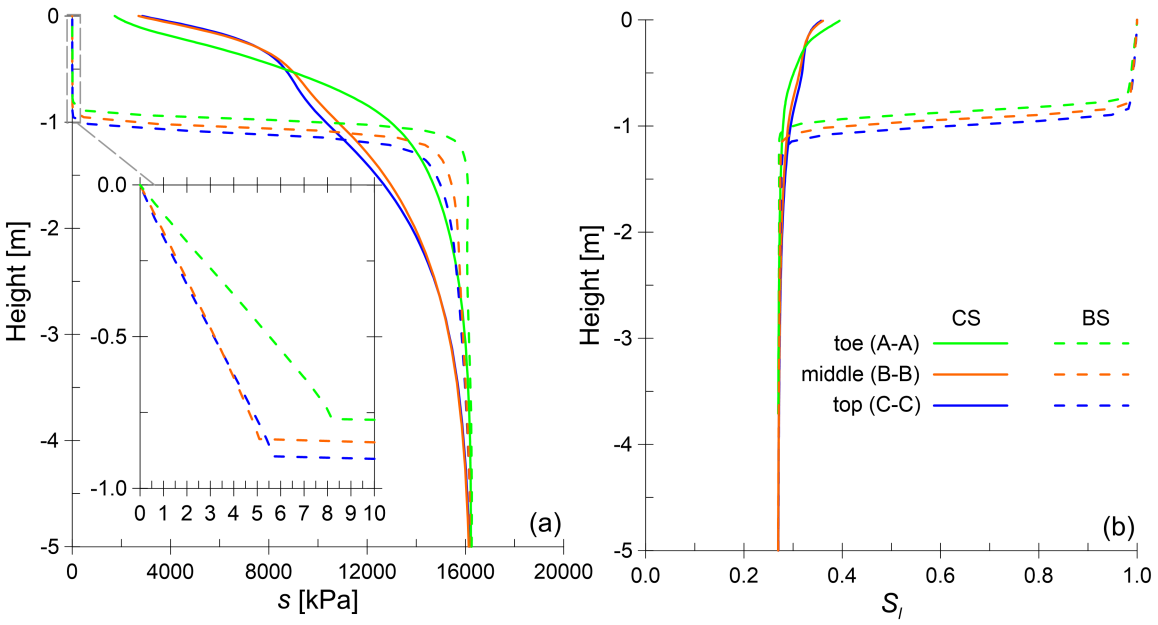

Figure 8.27: (a) Suction and (b) degree of saturation profiles at the end of the most critical rainfall event, i.e. $t = 1.18274$ years, at the sections A-A (toe), B-B (middle) and C-C (top)

distance between the top of the slope and the bottom drain is lower than the diversion length of the CBS. Therefore, according to the results shown so far, the application of CBSs whose main working mechanism is lateral water diversion are proved to be effective for relatively small slopes but they may be potentially non suitable to protect tall slopes. Solutions for extending the applicability of such CBSs to taller slopes and the corresponding results are presented and discussed in Sections 8.4.4 and 8.4.5. In contrast, it seems likely that a CBS whose main working mechanism is based on water storage (e.g. a CBS with silty sand as the F.L. operating under the weather conditions of Cagliari, as discussed earlier) may work almost as well for taller slopes as it does for lower slopes.

Limit analyses were performed considering the two models discussed in this section, both with a slope height of $H_s = 6$ m. For the model with the CBS (CS), two limit analysis models were analysed: the whole model (CS-CBS+U.S.) and only the underlying soil (CS-U.S.). The minimum factors of safety obtained from these models were compared with those obtained from the corresponding models with a slope height of $H_s = 10$ m. The results of this comparison are shown in Figure 8.30. The main points identified in Section 8.4.1 regarding the stability of the slopes in the models with $H_s = 10$ m apply also to those with $H_s = 6$ m. The minimum factors of safety obtained for the models BS and CS-CBS+U.S. are hardly affected by the slope height. The failure mechanisms of both these models are almost planar (see Figures 8.17a and 8.17b) and affected very little by the slope height. Conversely, the stability of the underlying soil in the models CS-U.S., which are characterised by deep failure mechanisms (see Figure 8.17c), is significantly affected by the slope height. In particular, the factor of safety decreases with increasing slope height. Nevertheless, the factors of safety are very high in both cases.

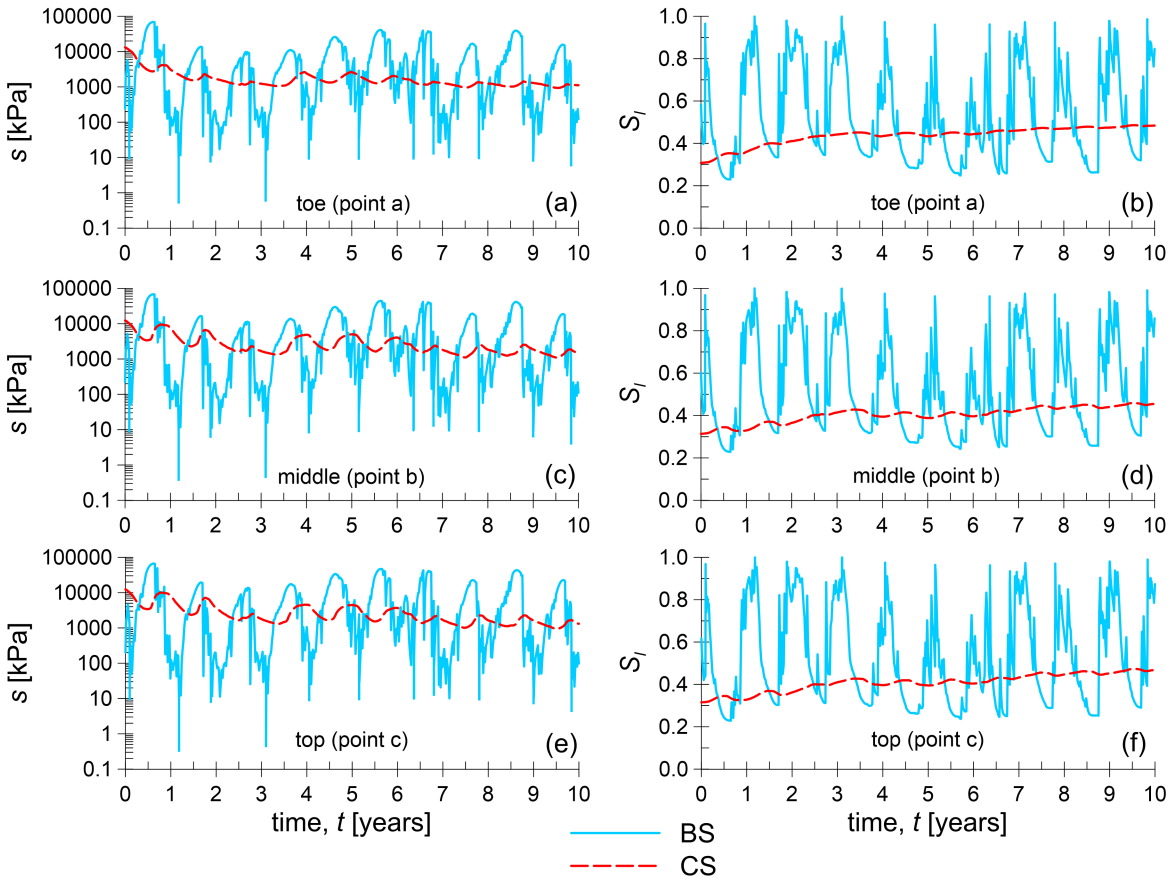

Figure 8.28: Time histories of (a,c,e) suction and (b,d,f) degree of saturation at the points a (toe), b (middle) and c (top)

8.4.4 Effect of the use of multiple drains

In Section 8.4.2 it was shown that, particularly in a wet and cool climatic area such as London, CBSs which work mainly by diverting water laterally (e.g. CBSs with fine sand) should be preferred to CBSs which work mainly by storing rain water in the F.L., which is then removed by evaporation (e.g. CBSs with silty sand). However, in Section 8.4.3 it was discussed that CBSs working mainly by diverting water laterally may not be effective at preventing water breakthrough into the underlying soil when applied to tall slopes, due to limits in the water diversion length. A possible solution to this limitation is to use multiple drains placed in the CBS at intermediate heights. The idea behind this solution is to reduce the distance between the top of the slope, where the lateral water diversion starts, and the drain, where the water is collected, to make it lower than the maximum diversion length of the CBS. In other words, the intention is that in the CBS below an intermediate drain the ability of diverting water should be fully restored, because all the water transported from the section of slope above is collected by this intermediate drain.

This section shows the results obtained from three simulations. In all these simulations, weather conditions of Cagliari were considered and the slope height was $H_s = 10\,\text{m}$. One of the three models was the bare slope, i.e. no CBS. The other two models included single capillary barrier systems, both having the F.L. made of fine sand and a thickness of $t_{CBS} = 60\,\text{cm}$. In

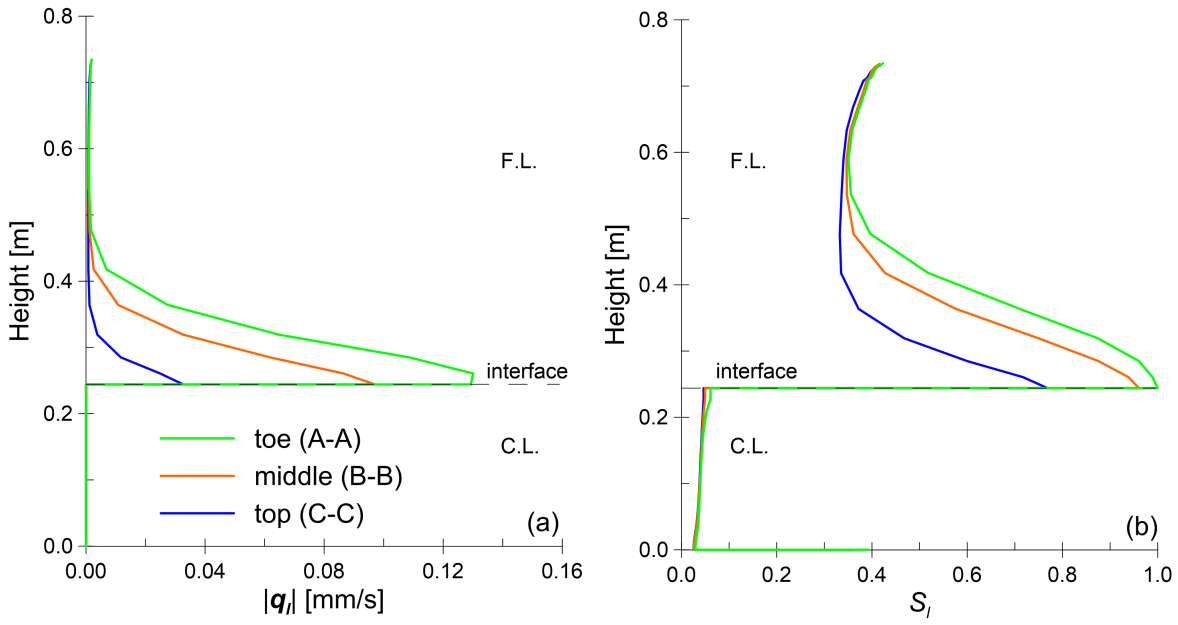

Figure 8.29: (a) Absolute liquid velocity and (b) degree of saturation profiles at the end of the most critical rainfall event, $t = 1.182\,74$ years, at the sections A-A (toe), B-B (middle) and C-C (top)

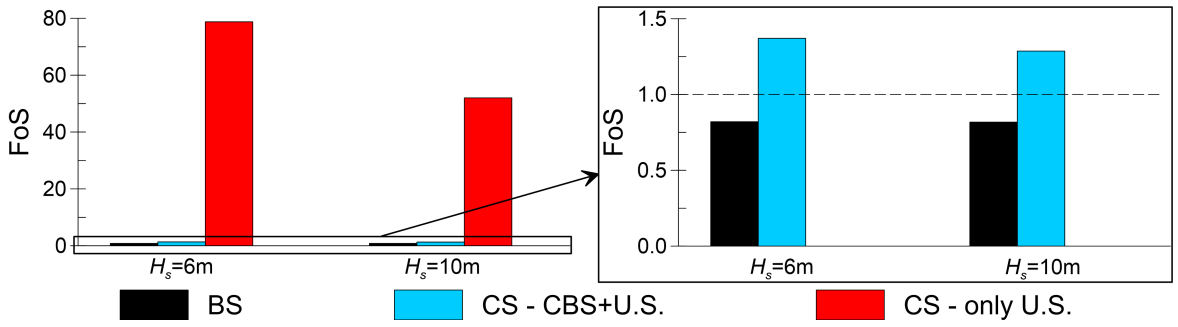

Figure 8.30: Comparison between the minimum factors of safety obtained with slope heights of $H_s = 6\,\text{m}$ and $H_s = 10\,\text{m}$ for different models

one model, only a single drain was modelled at the toe of the slope whereas in the other model two drains were modelled, one at the toe of the slope and one at an intermediate location (see Figure 8.3). These three models correspond to the following analyses shown in Table 8.5: Cag_10_NOCBS, Cag_10_SCB_FS_60_SD and Cag_10_SCB_FS_60_MD. In this section, for simplicity, these three models will be referred to as no CBS, single drain and multi-drain respectively. The results from the first two of these three models were already presented and discussed in Section 8.4.1. Therefore, this section will focus only on the comparison with the results obtained from the multi-drain model Cag_10_SCB_FS_60_MD.

Figure 8.31 shows the degree of saturation contours at the end of the most critical rainfall event for the models with CBSs with a single drain and multiple drains. Compared to the CBS with a single drain, which leads to water breakthrough into the underlying soil at the toe of the slope, in the model with multiple drains low values of degree of saturation are maintained in the underlying soil at the end of the most critical rainfall event. This can be explained by

observing the degree of saturation contour in the CBS at the location of the intermediate drain. At this location, all the water diverted by the CBS in the upper part of the slope is collected by this intermediate drain. Below this, the F.L. of the CBS is again at low degree of saturation suggesting that the lateral water diversion capacity is fully restored below the intermediate drain.

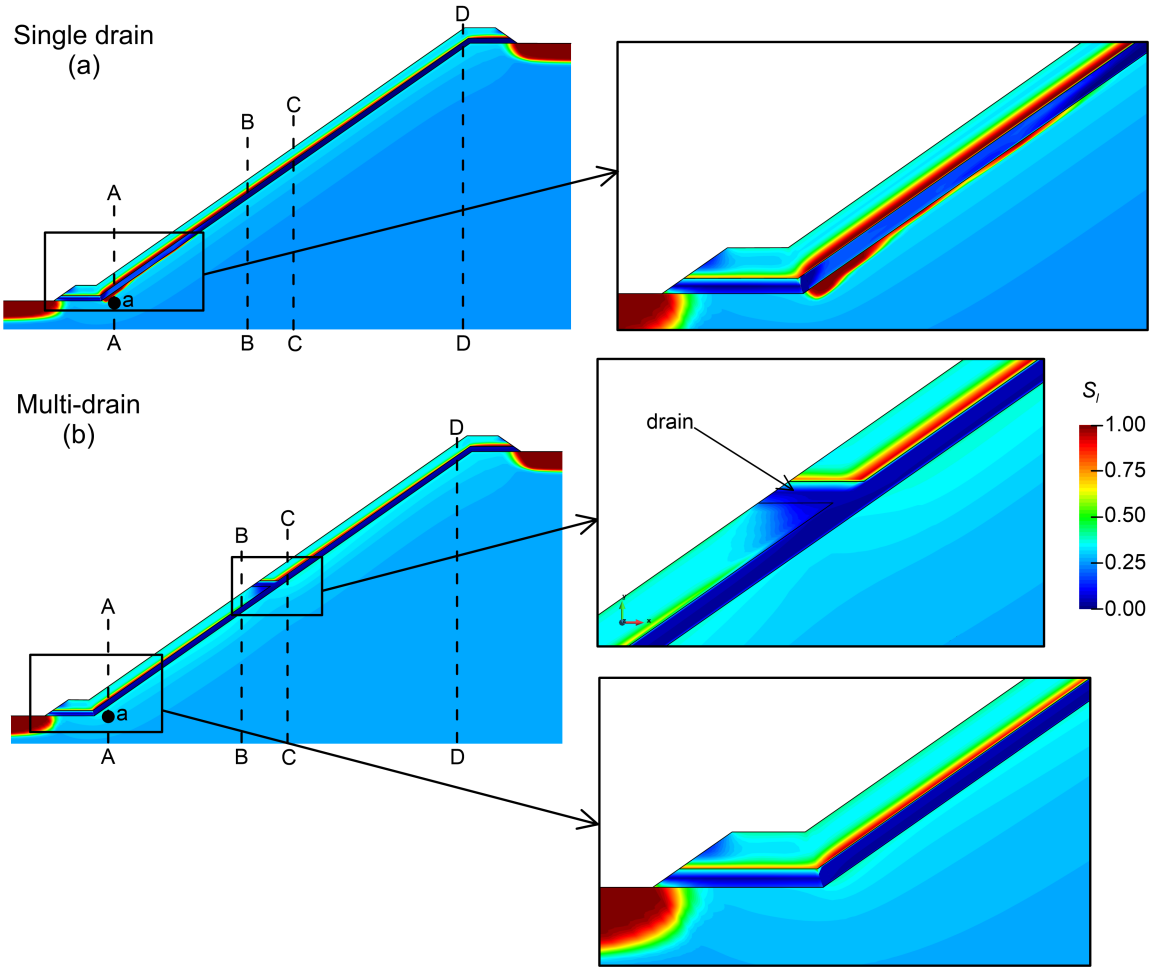

Figure 8.31: Degree of saturation contours at the end of the most critical rainfall event, i.e. $t = 1.182\,74$ years, for the models with CBSs with (a) a single drain and (b) multiple drains

Figure 8.32 shows the time histories of suction and degree of saturation obtained in the underlying soil at point a, which is located in the underlying soil at the toe of the slope, at a depth of 5 cm measured perpendicular to the underlying soil surface. The location of this point is shown in Figure 8.31. It can be seen that, using the CBS with a single drain, water breakthrough into the underlying soil occurs in two intense rainfall events, as suggested by the low peaks of suction and high peaks of degree of saturation. By contrast, no water breakthrough into the underlying soil occurs in the model with multiple drains, as suggested by the stable trend of suction, at high values, and degree of saturation, at low values.

Figure 8.33 shows the absolute liquid velocity and degree of saturation profiles in the CBSs at four different sections. The location of these fours sections are shown in Figure 8.31. These sections are located progressively from section A-A at the toe of the slope, section B-B beneath the intermediate drain, section C-C above the intermediate drain and section D-D at

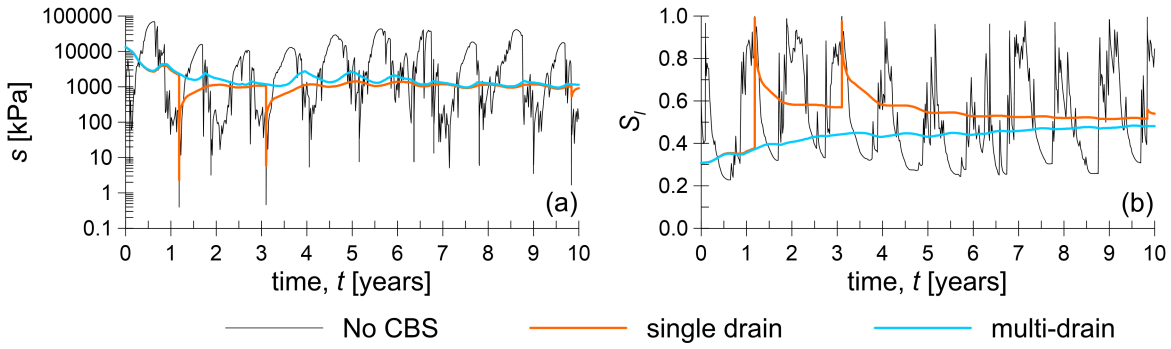

Figure 8.32: Time histories of (a) suction and (b) degree of saturation obtained in the underlying soil at the toe of the slope (point a)

the top of the slope. Comparing the results obtained for the single drain model and the multi-drain model, it can be seen that the profiles above the intermediate drain (Figures 8.33c,d,g,h) are approximately coincident, meaning that the water is diverted laterally in the same way at these locations. Beneath the intermediate drain (Figures 8.33a,b,e,f), the models with a single drain and with multiple drains lead to significantly different results. The degree of saturation and the absolute liquid velocity profiles obtained with a single drain attain much greater values than those attained with multiple drains. Indeed, unlike the model with a single drain, in the model with multiple drains all the lateral water diversion capacity is restored beneath the intermediate drain because the water transported from upwards is collected into the intermediate drain. Therefore, the CBS can be seen as divided into two parts which work separately, one above and one below the intermediate drain.

Defining L_{CBS} the length of the CBS, measured from the top to the toe of the slope and defining L_D the diversion length of the CBS, a CBS with a single drain is efficient at preventing water breakthrough into the underlying soil if the following condition is verified:

$$L_{CBS} \leq L_D \tag{8.3}$$

In the numerical model with a single drain, water breakthrough occurs into the coarser layer and hence into the underlying soil because the condition expressed by Equation 8.3 is not verified. For a CBS in which a number of n_{drains} drains are present in the CBS, all spaced uniformly, the condition for the prevention of breakthrough becomes:

$$\frac{L_{CBS}}{n_{drains}} \leq L_D \tag{8.4}$$

which means that the total length of the CBS can be divided in different parts introducing different drains. For this reason, in the numerical model with multiple drains analysed in this section ($n_{drains} = 2$), no water breakthrough occurs into the coarser layer and hence into the underlying soil. Theoretically, this concept can be extended to any number of drains and, thus, to slopes of any height.

Figure 8.34 finally shows the minimum factors of safety obtained for the different models

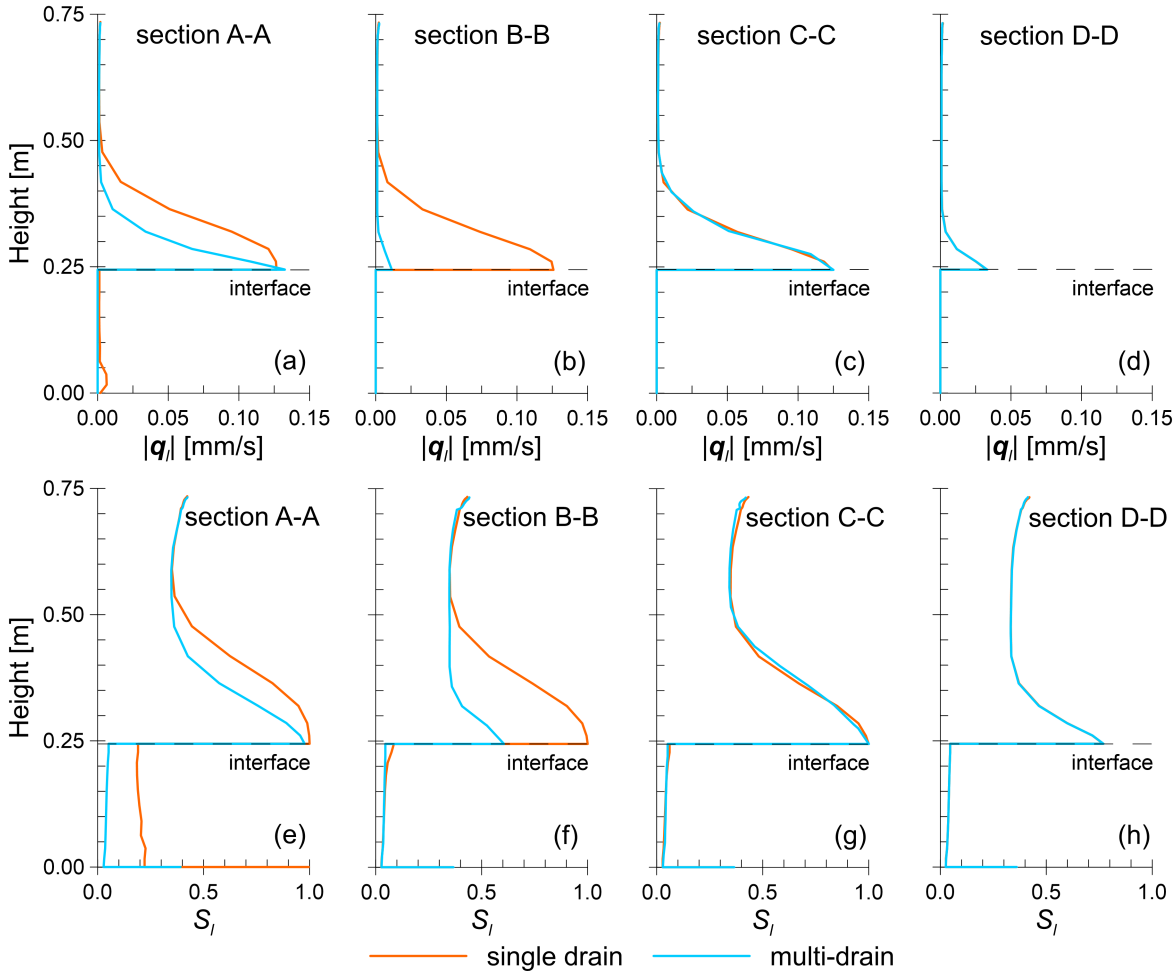

Figure 8.33: (a-d) Absolute liquid velocity and (e-h) degree of saturation profiles at the end of the most critical rainfall event, i.e. $t = 1.182\,74$ years, at four different sections

analysed in this section. It can be seen that the results obtained from the single drain model and those obtained from the multi-drain model are approximately identical. The small amount of water breakthrough that occurred at the toe of the slope in the single drain model does not affect the failure mechanism and the corresponding factor of safety. However, for taller slopes with a single drain, water breakthrough may affect larger areas of underlying soil and, hence, also the failure mechanism and the corresponding factor of safety. On the other hand, the use of multiple drains along the height of the slope should guarantee the stability of slopes of any height.

8.4.5 Effect of the use of multi-layered CBSs

A method to extend the applicability of sloping CBSs to higher slopes by means of the use of multiple drains was discussed in Section 8.4.4. An alternative method consisting of the use of multi-layered sloping CBSs is discussed in this section. The idea of using multi-layered CBSs was already analysed and discussed in Chapter 7 with reference to the water storage capacity of horizontal CBSs. In this section, the application of multi-layered CBSs for slope protection purposes is analysed.

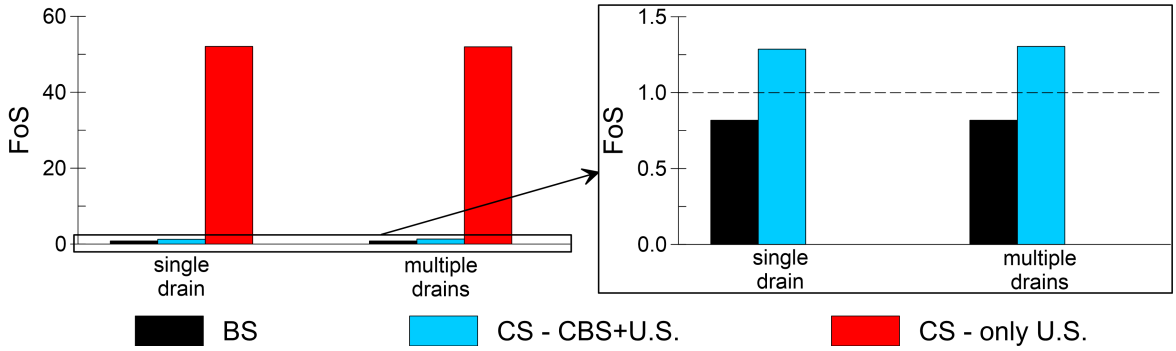

Figure 8.34: Minimum factors of safety obtained for the different models

This section shows the results obtained from three simulations. In all these simulations, weather conditions of Cagliari were considered and the slope height was $H_s = 10\,\text{m}$. One of the three models was the bare slope, i.e. no CBS. The other two models included a single capillary barrier system and a multi-layered CBS. The geometry of the multi-layered CBS is shown in Figure 8.2. The material used for the finer layers of both CBSs was the fine sand and the total thickness was equal to $t_{CBS} = 60\,\text{cm}$. A single drain was located at the toe of both the CBSs. These three models correspond to the following analyses shown in Table 8.5: Cag_10_NOCBS, Cag_10_SCB_FS_60_SD and Cag_10_MCB_FS_60_SD. In this section, for simplicity, these three models will be referred to as no CBS, single CBS and multi-layered CBS (or MCB) respectively. The results from the first two of these three models were already presented and discussed in Section 8.4.1. Therefore, this section will focus on the comparison with the results obtained from the multi-layered CBS model Cag_10_MCB_FS_60_SD.

Figure 8.35 shows the degree of saturation contours at the end of the most critical rainfall event for the single CBS model and for the multi-layered CBS model. Compared to the single CBS, which leads to water breakthrough into the underlying soil at the toe of the slope, in the MCB model low values of degree of saturation are maintained in the underlying soil at the end of the most critical rainfall event at all points under the footprint of the CBS. Two insets are present in Figure 8.35b, showing zoomed views of the contours at the toe of the slope (inset I) and at an upper location between the top and the middle of the slope (inset II). In inset II, it can be seen that the upper finer layer of the MCB attains high values of degree of saturation whereas the other three layers, i.e. intermediate and lower coarser layers and lower finer layer, attain very low values of degree of saturation. This suggests that, at this location, all the rainwater is transported only by the upper finer layer. From the observation of inset I, water breakthrough from the upper finer layer into the intermediate coarser layer, and then into the lower finer layer, occurs in the bottom few metres of the slope. The rainwater which enters the lower finer layer in this lower part of the slope is then diverted laterally by the lower finer layer. In proximity of the toe, where the CBS is horizontal, all the rainwater still transported by the upper finer layer breaks through the underlying layers of the CBS and finally enters the drain. Similarly, the small amount of water diverted by the lower finer layer is directly collected by the drain located at the toe.

The effectiveness of the multi-layered CBS is confirmed also by the observation of

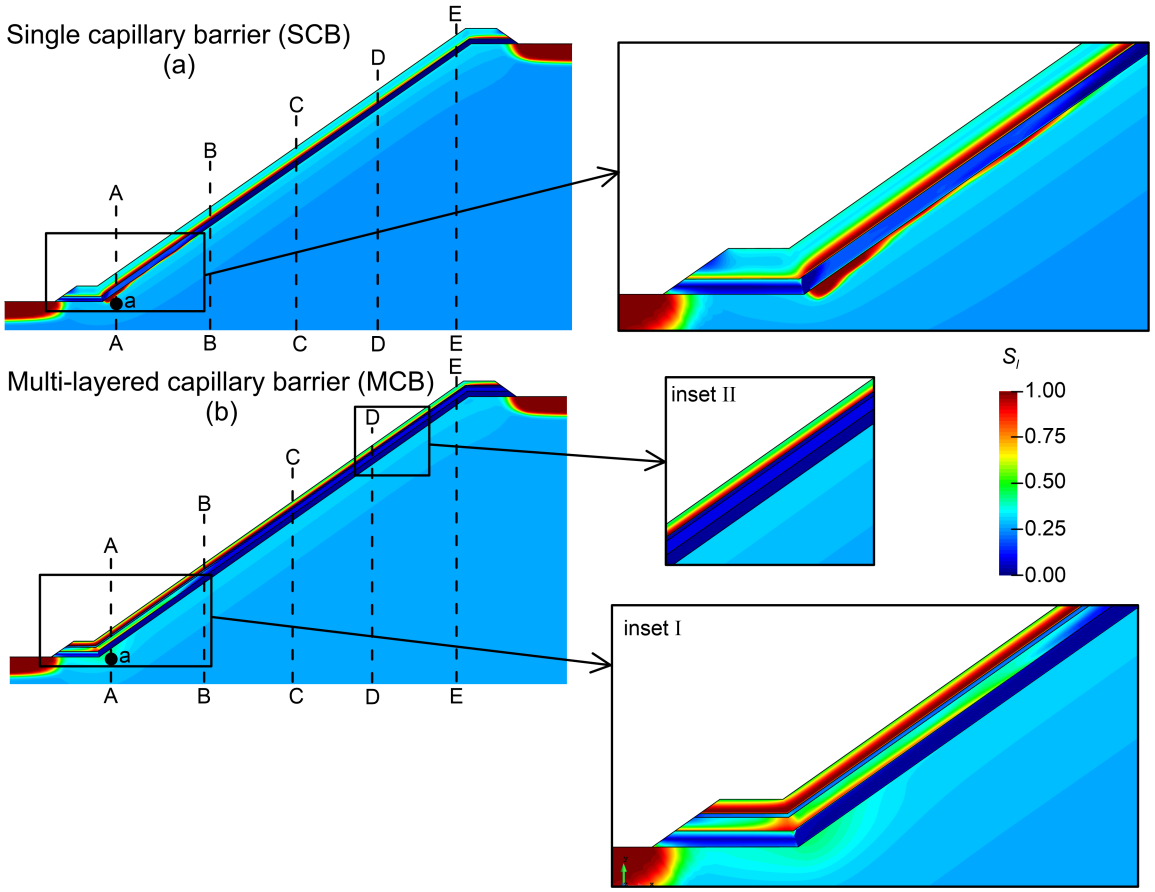

Figure 8.35: Degree of saturation contours at the end of the most critical rainfall event, i.e. $t = 1.182\,74$ years, for the models with (a) a single CBS and (b) a multi-layered CBS

Figure 8.36, which shows the time histories of suction and degree of saturation at point a, which is located in the underlying soil at the toe of the slope. The location of point a, shown in Figure 8.35, is at a depth of 5 cm measured perpendicular to the underlying soil surface. It can be seen that water breakthrough into the underlying soil occurs in two intense rainfall events in the single CBS model. By contrast, no water breakthrough into the underlying soil occurs in the model with the multi-layered CBS, as suggested by the stable trend of suction, maintaining high values, and degree of saturation, maintaining low values.

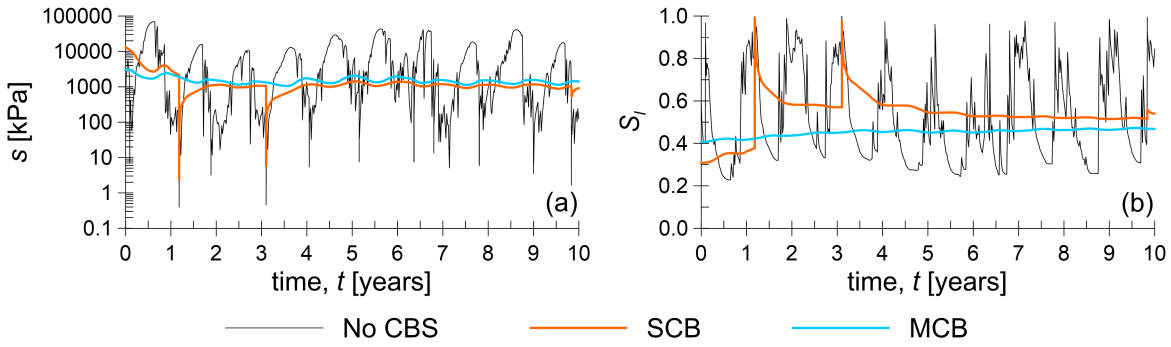

Figure 8.36: Time histories of (a) suction and (b) degree of saturation obtained in the underlying soil at the toe of the slope (point a)

In order to understand how the sloping multi-layered CBS is more effective than the

sloping single CBS at preventing water breakthrough into the underlying soil, the absolute liquid velocity profiles and the degree of saturation profiles at the end of the most critical rainfall event in the two CBSs are compared in Figure 8.37. Five different sections are considered in this figure, progressively from section A-A at the toe to section E-E at the top. The locations of these sections are shown in Figure 8.35. In the single CBS, values of absolute liquid velocity (Figure 8.37a) and degree of saturation (Figure 8.37b) increase from the top of the slope (section E-E) in the down-dip direction until section B-B. Beyond B-B, the absolute liquid velocity and degree of saturation profiles in section A-A (toe) are approximately coincident with those obtained in section B-B, hence suggesting that at section B-B the water diversion capacity of the single CBS is reached and no further water can be diverted laterally. Hence, additional rainwater at that location results in water breakthrough, as can be observed in higher values of degree of saturation in the C.L. obtained at sections B-B and A-A compared to the other sections. A different pattern can be observed for the profiles of absolute liquid velocity (Figure 8.37c) and degree of saturation (Figure 8.37d) obtained in the multi-layered CBS. Moving from section E-E (top of the slope) down to section C-C, the degree of saturation and absolute liquid velocity in the upper finer layer increase whereas no water is transported in the other layers, which remain at relatively low values of degree of saturation. All the rainwater is thus diverted by the upper finer layer between sections E-E and C-C. At sections B-B and A-A, the absolute liquid velocity and degree of saturation profiles in the upper finer layer remain similar to those obtained in section C-C suggesting that at section B-B the upper finer layer reaches the diversion capacity and does not divert any extra water. Therefore, from section B-B downwards, all extra rainwater breaks through into the intermediate coarser layer and then into the lower finer layer. Indeed, at section B-B the degree of saturation in the lower finer layer starts increasing although the liquid water velocity is still negligible. From section B-B to section A-A, the degree of saturation in the lower finer layer increases as well as the absolute liquid velocity. Therefore, between section B-B and section A-A also the lower finer layer starts diverting rainwater laterally, in addition to the water diverted by the upper finer layer. Therefore, the functioning of this sloping multi-layered CBS can be seen schematically as follows:

- at the top of the slope rainwater is diverted laterally by the upper finer layer;
- when the diversion capacity of the upper F.L. is attained, breakthrough into the underlying coarser layer and then into the lower finer layer occurs;
- from this point, in addition to the upper finer layer which keeps diverting an amount of water equal to the diversion capacity, the lower finer layer starts diverting water;
- this mechanism is expected to be replicable for multiple layers, i.e. for a layering factor greater than 2.

According to this mechanism, the diversion capacity of the multi-layered CBS analysed in this section is expected to be approximately twice that of the single CBS, considering that the

contribution of the upper part of the F.L. of the single CBS to the lateral water diversion is negligible.

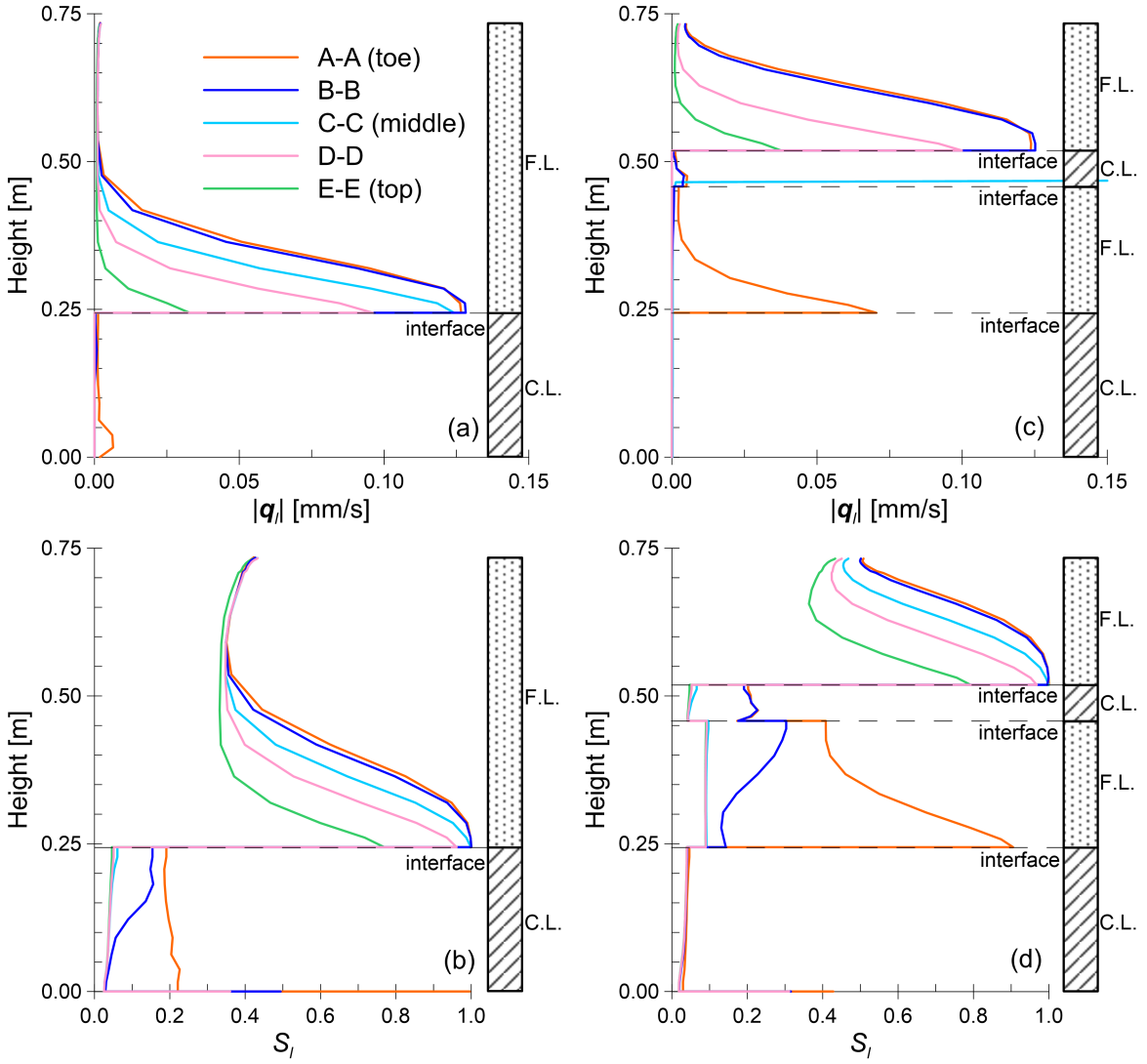

Figure 8.37: (a,c) Absolute liquid velocity and (b,d) degree of saturation profiles at the end of the most critical rainfall event, i.e. $t = 1.182\,74$ years, at five different sections, (a,b) for the single CBS and (c,d) for the multi-layered CBS

Figure 8.38 shows the minimum factors of safety obtained from limit analyses of the different models considered in this section. It can be seen that changing from a single CBS to a multi-layered CBS does not affect the stability of the underlying soil (CS-U.S.) since the collapse mechanism with the simple CBS is not influenced by the little amount of water percolation that occurred into the underlying soil. However, for taller slopes covered by a single CBS, water breakthrough may affect larger areas of underlying soil, and hence the failure mechanism and the corresponding factor of safety. On the other hand, the use of multi-layered CBSs may guarantee the stability of taller slopes compared to the single CBS by preventing water breakthrough into the underlying soil. In the models CS-CBS+U.S., the failure mechanism involves only the CBS, for both the models with a single CBS and a multi-layered CBS. The corresponding factors of safety for the two CBSs are very similar and both greater than 1.

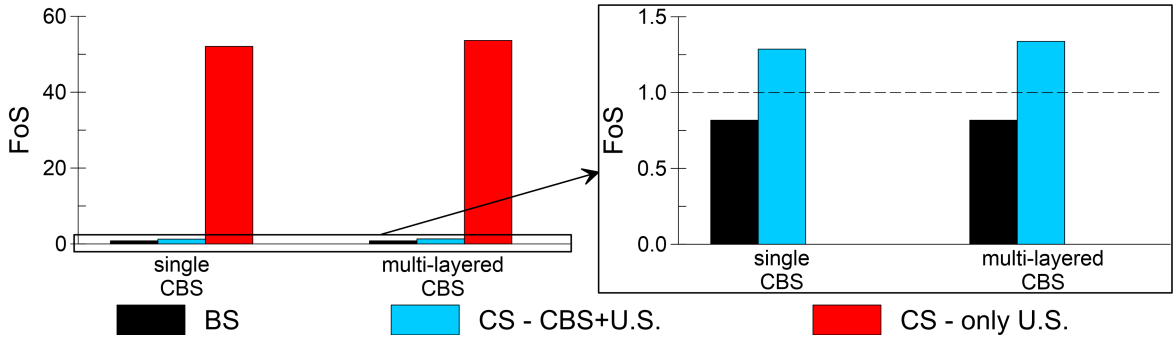

Figure 8.38: Minimum factors of safety obtained for the different models

8.5 Concluding remarks

In this section, the long-term behaviour of CBSs and application to slope stability were studied numerically using thermo-hydraulic FE analyses coupled with limit analyses. Realistic weather conditions of two representative European climatic zones were considered: Cagliari (Italy), having a dry and warm climate, and London (UK), having a wet and cool climate. For both these cities, records of a particularly wet 10-year period were used to model the rainfall whereas average annual cycles of other atmospheric conditions controlling evaporation and radiation were used. The hydraulic behaviour of the materials was modelled using the new hydraulic constitutive models for the hydraulic conductivity and hydraulic hysteresis presented in Chapter 3. Two different sets of analyses were performed: one-dimensional analyses, representative of horizontal CBSs, and two-dimensional analyses, representative of sloping CBSs applied for suction control and slope stability purposes. For each of these sets of analyses, different parameters and conditions were considered and the corresponding results were compared to assess the role of the materials of the CBS, thickness of the CBS and weather conditions. In addition, for the two-dimensional analyses, the role of slope height, use of multiple drains and use of multi-layered CBSs were also considered.

The key results obtained from the one-dimensional analyses, which are representative of horizontal CBSs, can be summarised as follows:

- without the use of a CBS, the original underlying soil close to the ground surface often attains fully saturated conditions during intense rainfall events, resulting in frequent and extended losses of suction;
- the evaporation into the atmosphere from the finer layer of a CBS made of silty sand is typically greater than that from a finer layer made of fine sand;
- percolation into the underlying soil is greater when fine sand is used for the F.L. instead of silty sand, because of the lower amount of evaporation and the lower water storage capacity;
- under the weather conditions of London, breakthrough into the underlying soil regularly occurs with all the CBSs analysed, as a consequence of the higher overall amount of

rainfall compared to the overall amount of evaporation, and suction in the underlying soil often decreases to zero;

- under the weather conditions of Cagliari, the amount of evaporation is comparable to the amount of rainfall; however, breakthrough occasionally occurs with certain CBSs during particularly intense rainfall events;
- silty sand is better than fine sand as a material for the F.L. of a horizontal CBS, due to the higher amount of evaporation and the higher water storage capacity;
- a greater thickness of the F.L. of a horizontal CBS is beneficial if the F.L. is made of silty sand because it leads to a higher water storage capacity;
- a greater thickness of the F.L. of a horizontal CBS is detrimental if the F.L. is made of fine sand because it leads to a reduction of the amount of evaporation and the increase of water storage capacity is negligible ;
- under the weather conditions of Cagliari, all the CBSs analysed help to limit the loss of suction and the depth of soil affected by loss of suction; however, only one CBS was effective at preventing breakthrough and at maintaining high values of suction and low values of degree of saturation at all times, i.e. the CBS with the F.L. made of silty sand and with a thickness of $t_{CBS} = 100\,\text{cm}$.

The results of the two-dimensional analyses of slopes can be summarised as follows:

- without the use of a CBS, suction vanishes during several rainfall events in an area of soil close to the ground surface, causing the bare slope to be unstable, under the weather conditions of both Cagliari and London;
- generally speaking, unlike the horizontal CBSs (one-dimensional models), all the different sloping CBSs were proven to be an effective way to prevent or limit the percolation of water into the underlying soil, to maintain high values of suction in the underlying soil and to maintain the stability of the slope even during intense rainfall events;
- the main working principle of CBSs having the F.L. made of fine sand is to divert water laterally down to a drain, where the rainwater is collected; the effectiveness of these CBSs is mainly related to the occurrence of extreme rainfall events; in an European context, they can be effective both in dry and warm climates (e.g. Cagliari) and in wet and cool climates (e.g. London);
- the main working principle of CBSs having the F.L. made of silty sand is to store rainwater in the F.L. and release it to the atmosphere by evaporation, similar to the working principle of horizontal CBSs; the effectiveness of these CBSs is mainly related to the overall amount of rainfall (not simply the severity of extreme rainfall events) and evaporation; in an European context, they can be efficient in dry and warm climates

(e.g. Cagliari) but not in wet and cool climates (e.g. London) where the overall amount of rainfall is greater than the overall amount of evaporation;

- the thickness of the F.L. has a major impact when silty sand is used for the F.L. because, as this thickness increases, the water storage capacity increases accordingly; the thickness of the F.L. has a minor impact when fine sand is used for the F.L. because the upper part of the F.L. does not contribute to the lateral water diversion;

- CBSs are more efficient at preventing water breakthrough into the underlying soil when applied to smaller slopes (i.e. $H_s = 6\,\text{m}$ in these analyses) than taller slopes (i.e. $H_s = 10\,\text{m}$ in these analyses);

- the application of CBSs can be extended to slopes of any height by placing multiple drains along the height of the slope; in this way, the CBS can be divided into different parts, each of which must divert water for a shorter distance compared to a corresponding CBS with one drain at the bottom;

- multi-layered CBSs are more efficient at diverting water laterally and, hence, at limiting and preventing water breakthrough into the underlying soil; each finer layer starts diverting water when water breakthrough from the overlying finer layer occurs, while the latter keeps diverting the maximum amount of water corresponding to the water diversion capacity;

- all the CBSs analysed in this thesis are effective at preventing rainfall induced instability of the slope in the long-term;

- once a CBS is used to cover the slope, the stability problem becomes controlled by the stability of the CBS; however this is less sensitive to weather conditions and it is mainly influenced by the shear strength properties of the materials (i.e. friction angle), which are typically good for the materials used for the CBS and can be controlled and established during the construction of the CBS (i.e. by means of compaction).

Chapter 9

Conclusions and recommendations

9.1 Conclusions

The reduction of carbon emissions due to anthropogenic activities is one of the most important research challenges of our time because of the impact of the concentration of CO_2 in the atmosphere on climate change. Since a significant component of carbon emissions is due to the production of cement, which is widely used in many applications within geotechnical engineering, the development and application of low-carbon solutions in geotechnical engineering practice is essential for the mitigation of the effects of climate change. The conclusions of this PhD project, funded by the EU H2020 programme via the Marie Skłodowska-Curie Innovative Training Networks (ITN-ETN) project TERRE, should therefore be viewed in this context.

Under unsaturated condition, soil suction may impart significant strength gains to soil but this effect is generally neglected in geotechnical design because of its unreliability. Suction may easily vanish (or be reduced) after a heavy rainfall event. This is the cause, for example, of rainfall-induced slope instabilities. Geotechnical engineers can take advantage of the effect of suction as a natural and green soil reinforcement if a system able to limit or prevent rainwater infiltration into the soil is applied. For this purpose, the application of capillary barrier systems (CBSs) was analysed in this thesis. A CBS is a soil cover made of a finer layer overlying a coarser layer. The coarser layer of a CBS is typically at very low degree of saturation and hence the corresponding unsaturated hydraulic conductivity is also very low. Thus, the coarser layer acts as an almost impermeable barrier and the rainwater is stored in the upper finer layer. The rainwater stored in the finer layer is then removed by evapotranspiration or lateral drainage. The coarser layer will continue to behave as an impermeable layer unless it reaches a critical condition (breakthrough), which typically corresponds to high degree of saturation of the finer layer. Advantages of capillary barrier systems are low cost, high durability, simplicity of installation and possibility to use low-quality or recycled materials.

The working principle of capillary barrier systems is fundamentally related to the hydraulic behaviour of unsaturated soils. A correct knowledge and modelling of the hydraulic behaviour of relatively coarse-grained materials (i.e. gravel, sand and silt), in particular at low degree of saturation, is crucial for accurate interpretation and prediction of the behaviour of capillary

barrier systems.

The research work carried out can be divided in three general parts. In the first part, new constitutive models describing the hydraulic behaviour of unsaturated soils were developed, validated against experimental data, implemented in a numerical FE code and applied to the study of the fundamental behaviour of CBSs. In the second part of the work, non-conventional horizontal multi-layered capillary barrier systems were analysed from a theoretical point of view, with a new simplified analytical method, with subsequent validation by numerical FE analyses and laboratory physical tests. In the third part of the work, the long-term application of horizontal and sloping CBSs for suction control and slope stability purposes was studied numerically using FE analyses and limit analyses.

9.1.1 Modelling of the hydraulic behaviour of unsaturated soils

Inaccuracies in the interpretation and modelling of the hydraulic behaviour of unsaturated soils were identified by a critical literature review. These inaccuracies particularly regarded the hydraulic behaviour at very high degree of saturation, with the formation of trapped air during wetting, and at very low degree of saturation. A more accurate and physically-based interpretation of the hydraulic behaviour of unsaturated soils was consequently given. Key transition points in the SWRC and in the SHCC were identified and defined: air-entry (AE) point, air-exclusion (AEX) point, air-continuity (AC) point, air-discontinuity (AD) point, bulk water-discontinuity (BWD) point, bulk water-continuity (BWC) point, bulk water-exclusion (BWEX) point and bulk water-entry (BWE) point. This served as the physical basis for a rigorous interpretation and modelling of the phenomenon of air entrapment and the development of a new predictive hydraulic conductivity model, intended for use over the full range of degree of liquid saturation S_l, particularly for coarse-grained soils.

Air entrapment

At high values of degree of liquid saturation S_l, the apparent soil water retention curve (SWRC) measured in a wetting test in the laboratory (S_l plotted against the externally applied suction s_{ext}) may differ from the true SWRC (S_l plotted against the internal suction s within the soil sample). This is because of the occurrence of air trapping within the soil, when the gas phase becomes discontinuous, and the fact that the gas pressure within the trapped air will then be higher than the externally applied gas pressure unless the very slow process of diffusion of dissolved air has finished. Due to the occurrence of air trapping, the apparent SWRC will typically not reach a fully saturated condition as the externally applied suction s_{ext} is reduced to zero. In contrast, physical arguments indicate that the true SWRC will reach full saturation at a positive value of internal suction s.

Analytical modelling of air trapping within an infinitesimally small soil element (without any diffusion of dissolved air) demonstrated how the apparent SWRC can differ from the true SWRC. If wetting is produced by increasing the externally applied liquid pressure (rather than by decreasing the externally applied gas pressure), this results in increases in the gas

pressure within the trapped air as s_{ext} is reduced towards zero, leading to compression of the trapped air and hence increases of S_l after air trapping commences (even when diffusion of dissolved air is excluded). The analytical modelling demonstrated that these increases of S_l after air trapping commences will be much greater in a test on clay than in a test on sand, because higher values of excess gas pressure within the trapped air are generated in a clay, because the air trapping commences at much higher values of suction in a clay than in a sand.

Numerical modelling of wetting tests on soil samples of finite size (involving simulations where diffusion of dissolved air was included and simulations where this diffusion was excluded) showed that, once air trapping commences, the apparent SWRC measured in a wetting test will depend upon many aspects of the wetting test conditions. These include: the size of the soil sample; the method of suction application (whether the axis translation technique is employed and whether wetting is produced by increasing the externally applied liquid pressure or by decreasing the externally applied gas pressure); the precise sequence of values of externally applied suction; and the time duration used for the application of each value of external suction. Hence, the apparent SWRC is the result of a particular boundary value problem (the wetting test on the soil sample), rather than a fundamental representation of the soil behaviour. In contrast, the true SWRC is a fundamental representation of the soil behaviour.

Given that the apparent SWRC measured in a wetting test in a laboratory applies only to the specific boundary value problem of this laboratory test, this apparent SWRC is not applicable to any other boundary value problem. Hence, the apparent SWRC from the laboratory test should not be used in numerical modelling of other boundary value problems. The only correct way to represent the occurrence and influence of air trapping during wetting in numerical modelling of boundary value problems is to use the true SWRC in combination with a gas conductivity expression that goes to zero at the air-discontinuity point.

Measurement of the true SWRC in a laboratory test is likely to be problematic for the final part of the main wetting curve, at high values of S_l, when air trapping occurs, because this can only be done by performing the test extremely slowly, such that diffusion of dissolved air has finished for each value of externally applied suction. The time scales required to achieve this are unlikely to be feasible. This is particularly true for sands, because the numerical simulations presented here indicate that equalization of pore gas pressure within trapped air by diffusion of dissolved air is much slower in samples of sand than in samples of clay (because it is the excess gas pressures in the trapped air that drive the diffusion of dissolved air and these excess gas pressures are much lower in sand samples than in clay samples). Given that laboratory measurement of the final part of the true SWRC for a main wetting curve (at high values of S_l) may not be feasible, because of the excessive time scales required once air trapping occurs, it may be best to simply infer a shape for the final part of the curve, based on reliable measurements for the rest of the main wetting SWRC (before air trapping occurs). Information on the shape of the main drying curve at high values of S_l may also be useful. For example, it might be assumed that the form of the main wetting curve at high values of S_l is simply given by a horizontal translation of the main drying curve in the standard

semi-logarithmic plot of S_l against s.

Hydraulic constitutive models for unsaturated soils and application to capillary barrier systems

Conventional hydraulic constitutive models for unsaturated soils (e.g. Brooks and Corey [81], van Genuchten [82] and Kosugi [83]) are not adequate to represent the hydraulic behaviour of unsaturated soils at low degree of saturation. More recent models for the SWRC and for the soil hydraulic conductivity curve (SHCC) have been proposed, some of which are intended to improve the performance at low degree of saturation. However, among these models, those for the SHCC are mathematically complex [96], not predictive [91, 97] or involve parameter values that must be determined from experimental data that are difficult to obtain with sufficient accuracy [49]. Moreover, hydraulic hysteresis has not previously been satisfactorily included in hydraulic constitutive models improved at low degree of saturation.

A new hydraulic conductivity model which is reliable, predictive, easy to apply and avoids some inconsistencies of conventional hydraulic conductivity models (e.g. the van Genuchten-Mualem model) which are apparent at low values of S_l was proposed in this thesis. In the new model, the hydraulic conductivity is split into two components: the bulk water component and the liquid film component. The bulk water component is represented by a new modified version of the Mualem [95] model, i.e. modM model, able to capture the fact that bulk water flow ceases when the bulk water network becomes discontinuous. As in the conventional Mualem model, the bulk water component of hydraulic conductivity in the new model can be predicted simply from knowledge of the saturated hydraulic conductivity k_{ls} and information about the SWRC. The liquid film component of hydraulic conductivity is represented by a semi-empirical relationship (LF model). This relationship involves a soil constant that can either be evaluated by fitting experimental values of hydraulic conductivity in the low degree of saturation range (where water flow is only in the liquid films) or it can be estimated from the effective particle size D_{10} and the porosity Φ. This means that, in the absence of experimental measurements of hydraulic conductivity under unsaturated conditions, the new model can be used to predict the SHCC over the full range of S_l based solely on knowledge of the SWRC and the values of k_{ls}, D_{10} and Φ. This new SHCC model was coupled with improved versions at low degree of saturation of the SWRC models of Brooks and Corey (i.e. modBC), van Genuchten (i.e. modVG) and Kosugi (i.e. modK). The modVG-modM+LF model was used as the reference model for the remainder of the thesis. The new model was validated against experimental data.

Hydraulic hysteresis was subsequently introduced using an original bounding surface approach coupled with the SWRC and SHCC models improved at low degree of saturation. In the new hysteretic hydraulic constitutive model, main wetting and main drying SWRCs can be modelled using any of the models modVG, modBC or modK. Scanning curves were modelled using a bounding surface approach, which leads to simple closed-form expressions for the scanning curves. Introducing certain parameter constraints in the hysteretic SWRC model means that the bulk water component of hydraulic conductivity k_l^{Bulk} is assumed non-

hysteretic when plotted against degree of saturation S_l, whereas the liquid film component k_l^{Film} is non-hysteretic when plotted against suction s.

The new hysteretic hydraulic constitutive model was validated against experimental SWRC and SHCC data from different soils. The model was able to represent well the hysteretic hydraulic behaviour of relatively coarse-grained unsaturated soils (gravels, sands and silts) over the full range of degree of saturation. Moreover, the model is easy to apply (it involves simple closed-form expressions), it is flexible (the same approach can be applied with different expressions for the main drying and main wetting SWRCs) and it requires a relatively low number of parameters (once the main SWRCs and SHCCs are defined, only a single pair of additional parameters, γ_d and γ_w, are required for the definition of the scanning SWRC and SHCC curves). In addition, the simplicity of the model makes it suitable for implementation in numerical codes.

The new hysteretic hydraulic constitutive models for SWRC and SHCC (hysteretic modVG-modM+LF) were successfully implemented in the numerical finite element software Code_Bright. After implementation, the new hydraulic constitutive models were employed to assess the impact that their use has on predictions of the fundamental behaviour of CBSs.

From simulations of one-dimensional water infiltration tests in which only main wetting curves were considered (i.e. no hysteresis), it was shown that the new hydraulic conductivity model is able to predict the phenomenon of water breakthrough from the finer layer to the coarser layer of a CBS much better than the conventional van Genuchten-Mualem model. Moreover, the new model is able to capture the role of the liquid film flow, which is often neglected in numerical modelling. The simulations presented in the thesis show that the liquid film flow can have a significant influence on the variation of suction in the coarser layer of a capillary barrier system, even prior to breakthrough, particularly at low infiltration rates. The new hydraulic constitutive model is expected to find many other applications in situations where liquid flow occurs in coarse-grained soils at very low degree of saturation, such as during evaporation from a ground surface consisting of a coarse-grained soil.

The impact of hydraulic hysteresis on the behaviour of CBSs was assessed by means of specific one-dimensional simulations in which rainfall, redistribution of water after rain ceases and evaporation were simulated. It was shown that inclusion of water retention hysteresis leads to significantly different predictions of the redistribution of water in the finer layer of a CBS after intense rainfall events, compared to predictions employing a unique SWRC. The full hysteretic constitutive model leads to a more uniform distribution of water in the finer layer after redistribution than a non-hysteretic model. The reason why use of a unique SWRC based on the main wetting curve is not adequate, even when there is no evaporation or other removal of water from a CBS, is that redistribution of water within the finer layer after rainfall ceases means that the upper part of the finer layer experiences drying during this redistribution.

The numerical study of CBSs also demonstrated that only the full hysteretic constitutive model is able to represent successfully both the condition at breakthrough (with suction at the interface attaining the BWC point of the coarser layer) and the condition at restoration of the

CBS (with suction at the interface attaining the BWD point of the coarser layer). Finally, it was shown that hydraulic hysteresis has a major impact on the prediction of evaporation from a CBS into the atmosphere, because the hysteresis leads to higher water availability in the soil close to the ground surface and hence to the prediction of higher cumulative evaporation.

9.1.2 Multi-layered capillary barrier systems

In certain conditions, horizontal conventional capillary barrier systems may be highly inefficient at storing water, depending on the material and the thickness of the finer layer. In particular, prior to breakthrough, the degree of saturation may attain high values only in a small part of the finer layer immediately above the interface with the coarser layer whereas the remaining portion of the finer layer remains at low degree of saturation. The contribution of the upper part of the finer layer to the water storage capacity is thus small. In these conditions, increasing the thickness of the finer layer leads to negligible improvements in the water storage capacity.

The use of multi-layered CBSs, made of the alternation of multiple finer layers and coarser layers, may lead to a substantial increase in the water storage capacity. Compared to the use of a single CBS, the insertion of an intermediate coarser layer induces a reduction in the suction profile at breakthrough above this intermediate coarser layer and, hence, a corresponding increase of the degree of saturation in an overlying finer layer. The insertion of an intermediate coarser layer may therefore lead to an increase of the water storage capacity of the CBS. The intermediate coarser layer itself is, however, typically at very low degree of saturation, and part of the water storage capacity of a multi-layered CBS is therefore lost, because of the replacement of some finer material with the intermediate coarser layer. The design of the layout of a multi-layered CBS must always weigh these two counter-acting factors.

A simplified approach for the analysis of multi-layered CBSs was proposed in this thesis. This simplified approach first consists of the definition of a schematic suction profile at breakthrough, depending on the infiltration rate and the hydraulic properties of the materials of the CBS. Subsequently, from the schematic suction profile, the degree of saturation profile at breakthrough is obtained using the SWRCs of the materials. The water storage capacity of the CBS is then obtained by integrating the degree of saturation profile over the thickness of the CBS. This simplified approach can be easily used for hand-calculations or automatized in a simple commercial software (e.g. Excel or Matlab). Moreover, with this simplified approach, expensive and time-consuming FE analyses can be avoided. The accuracy of this simplified approach was first validated against the results of numerical FE analyses and then against experimental results of laboratory physical tests on different multi-layered CBSs.

Parametric analyses were performed to assess the performance of multi-layered CBSs and the impact of different parameters (i.e. number of layers, thickness of the CBS, materials and infiltration rate) on the water storage capacity. These parametric analyses were performed using both the simplified method and rigorous FE simulations, with the two methods leading to similar results. Generally speaking, it was shown that the use of multi-layered CBSs may

lead to a significant increase of the water storage capacity under certain conditions. The maximum gain in water storage capacity which can be achieved by layering increases with increasing thickness of the CBS and with the use of coarser materials, in particular for the finer layer. For each multi-layered CBS, there is an optimum number of layers which maximises the gain in water storage capacity. Adopting a number of layers greater than the optimum will reduce the water storage capacity because the beneficial effect of the additional water stored in the finer layers is outweighed by the detrimental effect of the replacement of some material of the finer layer with material of the coarser layer at lower degree of saturation. The application of a high infiltration rate may limit the benefit of using multi-layered CBSs but it was shown that the prediction of water storage capacity of a CBS subjected to a high infiltration rate is unreliable and should not be adopted (breakthrough may occur some time after the high infiltration rate is stopped due to water redistribution).

The behaviour of multi-layered CBSs was finally analysed by means of physical laboratory tests. The basic properties of the materials used (i.e. grain size distribution, relative density, solid specific gravity, porosity, saturated hydraulic conductivity and soil water retention curve) were firstly determined by means of appropriate tests. A hanging column apparatus was designed, manufactured and set up for the determination of the SWRCs. The main physical model tests consisted of one-dimensional column infiltration tests on four different capillary barrier systems characterised by different layering factors, i.e. 1 (single CBS), 2, 3 and 5, where the layering factor is the number of coarser layers or finer layers (same number) in the CBS. The columns were instrumented with tensiometers and water content sensors for recording suction and volumetric water content respectively. All the equipment, including column, external components for instrument installation, tensiometers and data acquisition system, was designed, manufactured and set up in-house specifically for this project. The infiltration tests were conducted by applying a constant infiltration rate at the top of the column until breakthrough occurred at the bottom of the column. Records of suction over time along the height of the CBSs showed that intermediate coarser layers act as "hydraulic breaks", meaning that the suction profile beneath an intermediate coarser layer is unaffected by the infiltration process until breakthrough across this coarser layer occurs. Suction and volumetric water content profiles recorded at breakthrough for the different multi-layered CBSs matched well those predicted using the simplified method, after introducing a correction to take into account the small amount of contamination of material of the finer layer into the coarser layer. Similarly, the water storage capacities of the different multi-layered CBSs were in good agreement with those predicted with the simplified method, thereby confirming the validity of the method. As suggested by the numerical and simplified analyses, the experimental tests confirmed that using multi-layered CBSs may lead to a significant increase of the water storage capacity. The water storage capacity initially increases with increasing layering factor until reaching a maximum, corresponding to the optimum layering factor. Beyond the optimum layering factor, the water storage capacity decreases with increasing layering factor.

9.1.3 Long term application of capillary barrier systems for suction control and slope stability

The application of capillary barrier systems for suction control and slope stability was finally studied numerically. The aim was to analyse the performance of CBSs and the response of the underlying soil in the long term (i.e. decades) when subjected to realistic weather conditions. In particular, the aims of the analyses were: to understand if the use of CBSs may represent an effective solution for maintaining suction in the ground and preventing rainfall-induced instability; to assess the role of the different parameters involved in the problem; and to explore alternative design solutions for improving the performance of CBSs. The application of CBSs was studied in this context with reference to European climates. To capture the variability of the climate within Europe, two different climatic areas were considered: Cagliari (Italy), which is representative of a relatively dry and warm European climate, and London (UK), which is representative of wet and cool European weather. A wide range of European climatic areas have conditions intermediate between these two cases.

Several numerical models were analysed. These models included both the bare underlying soil and the underlying soil covered by different types of CBS. One-dimensional models and two-dimensional models were analysed. The former were representative of a horizontal (non-sloping) ground whereas the latter were used to model slopes. Different thicknesses of the CBS (60 cm and 100 cm) and materials of the finer layer (fine sand and silty sand) were considered. The atmospheric conditions were modelled using measured historical data of the weather conditions of Cagliari (Italy) and London (UK). In particular, after setting up realistic initial conditions in the underlying soil and the CBS through preliminary simulations of simplified atmospheric conditions for 30 years, the subsequent response of the different models to particularly rainy 10-year periods was analysed.

The thermo-hydraulic response of the soil was analysed using advanced thermo-hydraulic finite element simulations with Code_Bright (CB) whereas the stability of the slope was assessed using the limit analysis software LimitState:GEO (LS:GEO). Limit analyses in LS:GEO were performed using hydraulic conditions (i.e. contours of suction and degree of saturation) from CB. A Matlab code was written *ad hoc* to link CB and LS:GEO. This code imports the suction and degree of saturation contours obtained from CB and creates a new interpolated grid of the product $-s \cdot S_l$, which is finally exported to LS:GEO. This product is used to model the effect of unsaturated conditions on shear strength with the strength relationship of Bishop and Blight [67] (assuming $\chi = S_l$ in the effective stress expression of Bishop [64]).

From one-dimensional analyses it was possible to understand the behaviour of horizontal CBSs applied for suction control purposes. Generally speaking, horizontal CBSs were shown to be a relatively ineffective solution in a European context. They do limit the amount of water infiltrating into the underlying soil, thereby reducing the depth of soil affected by significant reductions of suction and reducing the frequency of occurrence of suction losses. Nevertheless, water breakthrough occurred with most CBSs, leading to significant reductions or loss of

suction in a shallow zone of the underlying soil, in particular for the climatic conditions of London. The only CBS that was effective in completely preventing breakthrough and maintaining suction throughout the analysis was the CBS having the F.L. made of silty sand and a thickness of the CBS of 100 cm, when applied in the climatic conditions of Cagliari. Compared to fine sand, silty sand was shown to be more effective as a material for the finer layer of horizontal CBSs, for two reasons: it leads to a higher water storage capacity; and it leads to higher amount of evaporation because the soil surface is typically at higher degree of saturation than that of the F.L. made of fine sand. Increasing the thickness of the CBS is beneficial when silty sand is used as a material for the F.L. because it leads to a higher water storage capacity. By contrast, increasing the thickness of a F.L. made of fine sand beyond a certain limit is detrimental because it has a negligible effect on the water storage capacity but it leads to a reduction of evaporation.

On the basis of these results, horizontal CBSs are unlikely to find wide application for suction control purposes in a European context. Their application should probably be limited to arid and semi-arid climatic areas.

Sloping CBSs may find application for slopes made of relatively weak materials being at risk of rainfall-induced slope instability. The slope angle of these slopes should not be too low, otherwise the slope would be stable without the CBS, and should not be too high, otherwise the CBS itself would be unstable. As a rule of thumb, the slope angle should be between the friction angle of the material of the underlying soil, i.e. the lower bound, and the friction angle of the materials of the CBS, i.e. the upper bound. It follows that use of materials with higher friction angle for the CBSs will extend their range of application.

From two-dimensional analyses it was possible to assess the applicability of sloping CBSs for suction control and slope stability. Generally speaking, unlike the horizontal CBSs, all the different sloping CBSs were proven to be effective at preventing or limiting the percolation of water into the underlying soil, to maintain high values of suction in the underlying soil and to maintain the stability of the slope even during intense rainfall events, for the different weather conditions analysed. In some models, a small amount of water breakthrough into the underlying soil was predicted at the toe of the slope but this did not affect the stability of the slope. If CBSs are used for suction control and slope stability purposes, a small amount of water breakthrough into the underlying soil can be thus tolerated without affecting the slope stability, as long as this breakthrough affects only a small area of underlying soil and the potential failure mechanisms do not involve this area.

Depending upon the material used for the finer layer, two key working principles of sloping CBSs were identified. Using a finer material for the finer layer, such as a silty sand, the lateral water diversion ability of the CBS is limited and the behaviour is hence similar to that of a horizontal CBS, i.e. rainwater is stored in the finer layer and released into the atmosphere by evaporation. Using a coarser material for the finer layer, such as a fine sand, rainwater entering the finer layer is diverted laterally in the down-dip direction due to the effect of gravity. A drain is placed at the toe of the slope with the purpose of collecting this diverted water. If the CBS is perfectly effective, all rainwater is diverted to the bottom drain

and water breakthrough never occurs. Given that the amount of water diverted increases in the down-dip direction, if the lateral diversion capacity is attained at a location higher than that of the drain, the CBS cannot divert any additional amount of water and, beyond that point, any further rainwater becomes percolation into the coarser layer (i.e. breakthrough occurs). The effectiveness of the former type of CBS, with the finer layer made of finer materials, strongly depends on the overall climatic conditions and on the balance between long-term rain and evaporation. This type of CBS is more effective if applied in regions with a warm and dry climate where the amounts of evaporation and rain are comparable. For this type of CBS, using a thick finer layer is typically beneficial because they are characterised by a higher water storage capacity. The effectiveness of the other type of CBS, with the finer layer made of slightly coarser materials, is little affected by the overall climatic conditions but it strongly depends on extreme rainfall events. It can be applied in regions with both a warm and dry climate and a cool and wet climate, as long as rainfall events are not too extreme. For this type of CBS, using a thick finer layer, such as 100 cm, does not improve significantly the water diversion capacity because most of the water is diverted within a thin sub-layer of the finer layer, next to the interface with the coarser layer.

All the sloping CBSs were shown to be effective for suction control and slope stability for slopes of height up to 10 m. However, it was shown that the effectiveness of CBSs at preventing water breakthrough decreases with the increasing slope height, in particular for CBSs whose main working principle is lateral water diversion. For higher slopes, water breakthrough might involve large volumes of underlying soil and hence affect the stability of slopes covered by CBSs. For this reason, two solutions aimed to widen the range of applicability of CBSs to higher slopes were analysed and discussed: the use of multi-layered CBSs and the use of multiple drains.

It is possible to increase the diversion length of a CBS by introducing multiple finer and coarser layers, as was done for horizontal CBSs. When the finer layer is made of a relatively coarse material, such as fine sand, high flow rates may be attained but the part of soil actively diverting water is limited to a thin sub-layer next to the interface with the coarser layer. Beyond a certain thickness, the upper part of the finer layer gives negligible contribution to the water diversion capacity. By introducing multiple coarser and finer layers, this water diversion mechanism can be replicated within sub-layers at the bottom of each finer layer. At the top of the slope, the upper finer layer firstly diverts water down-dip until a point where the water diversion capacity of the upper finer layer is attained. Beyond this point, the upper finer layer cannot divert any extra amount of water and further rainwater enters the underlying coarser layer and the next finer layer. The underlying finer layer is thus "activated" at this point and starts diverting water laterally until a point where the diversion capacity of this finer layer is attained. This mechanism is then replicated for the different layers. With this solution, the diversion length of a multi-layered CBS with a layering factor of 2 may be up to twice that of a corresponding single CBS, that of a multi-layered CBS with a layering factor of 3 may be up to three times that of a corresponding single CBS.

The previous solution of using multi-layered CBS is effective at widening the range of

application to taller slopes but it requires the use of additional quantities of material for the construction of different layers. In order to apply sloping CBSs to slopes of any height avoiding the construction of very thick CBSs, multiple drains may be placed along the slope height at different locations. In a sloping CBS with a single drain at the toe, water must be diverted from the top of the slope to the bottom drain and this distance can be very long. Using multiple drains, the whole CBS can be seen as divided into multiple CBSs. Each of them must divert water for a shorter distance, that is the distance between two consecutive drains. This is possible because the water diversion capacity of the CBS is fully restored beneath each intermediate drain. Each drain therefore collects only the water diverted by the part of the CBS on the section of slope up to the next drain.

As mentioned above, all the CBSs tested under both Cagliari and London climatic conditions were effective at preventing rainfall-induced slope instability. Without the use of a CBS, the analysed bare slopes were unstable in critical rainfall conditions and they were characterised by shallow failure mechanisms. The application of CBSs made the original slopes stable, with very high factors of safety. All the CBSs were also always stable but characterised by lower factors of safety than those related to the underlying original slopes. After the application of CBSs, the problem of the stability became thus controlled by the stability of the CBS. However, CBSs are typically made of relatively coarse-grained materials, having good mechanical properties and shear strength little affected by variability of suction and thus weather conditions. In other words, unlike the stability of slopes made of weak fine materials which rely on the effect of suction, the stability of the CBSs mainly relies on the value of friction angle, which is characterised by fewer uncertainties compared to those involved in the prediction of suction. In addition, the friction angle of the materials used for the CBS can be controlled during construction because the friction angle of these coarse materials strongly depends on the degree of compaction and void ratio.

9.2 Recommendations for future work

As often happens, while answering the initial research questions other ideas and further research questions turned up. This final section presents ideas, opportunities and suggestions for further research work regarding the topics addressed in this thesis.

9.2.1 Modelling the hydraulic behaviour of unsaturated soils

A conceptual and numerical interpretation of the phenomenon of air entrapment was given in Chapter 5. An experimental validation of these findings would provide a more solid base to this conceptual and numerical interpretation. An experimental campaign might involve tests at the macroscopic scale and at the microscopic scale. Tests at the macroscopic scale could consist of reproducing in the laboratory the SWRC tests which were simulated numerically in Chapter 5. Tests at the microscopic scale would involve measuring the gas pressure in bulbs of trapped air and comparing these measurements with the numerical and analytical

predictions. Measuring directly the gas pressure within trapped air is likely to be complicated. Indirect measurements might however be feasible. Ideas for indirect measurements might involve the use of X-Ray Computed Tomography or microscopic imaging techniques to reconstruct the shape of the interfaces between trapped air bulbs and the surrounding water. From knowledge of the shape of these interfaces and of the pore-water pressure and by using the Young-Laplace equation (Equation 2.2), the gas pressure within the trapped air could be obtained. In addition, a numerical study of suitable boundary value problems could be carried out in order to show the consequences of incorrect constitutive modelling of air trapping (i.e. use of an apparent SWRC), compared to correct constitutive modelling (true SWRC combined with a gas conductivity curve going to zero at AC/AD point).

The liquid film component of the new hydraulic conductivity model presented in Section 3.3 was calibrated using experimental data of hydraulic conductivity plotted against suction at very low degree of saturation. The concept of liquid film flow is still poorly known or understood in the geotechnical engineering community. In addition, measuring the hydraulic conductivity at low values of degree of saturation is in general complex and time-consuming. As a consequence, the availability of experimental hydraulic conductivity data at low degree of saturation is still very poor. It would be very helpful to improve the experimental techniques for characterization of hydraulic conductivity at low degree of saturation, to design apparatuses able to distinguish liquid water flow and water vapour flow at low degree of saturation and to enrich the availability of data of hydraulic conductivity at low degree of saturation.

The hydraulic behaviour and the mechanical behaviour of unsaturated soils are in general coupled. The full hydraulic constitutive model presented in Chapter 3, including improvements of SWRC and SHCC at low degree of saturation and hydraulic hysteresis, is complete from the hydraulic point of view but it was used only considering rigid materials. The new hydraulic constitutive model could be used in conjunction with existing mechanical constitutive models for unsaturated soils, such as the Barcelona Basic Model [69] which is already implemented in Code_Bright. Numerical analyses of suitable boundary value problems could be performed in order to assess the impact of the new full hydraulic constitutive model on the mechanical behaviour of unsaturated soils.

9.2.2 Multi-layered capillary barrier systems

A new concept of multi-layered CBS was analysed in Chapter 7, focusing on the water storage capacity. It would be interesting to study also the recharge ability of these multi-layered CBSs after rainfall ceases. The expectation is that the use of multiple layers can have a beneficial effect also on the recharge ability as a consequence of an increase of the total amount of evaporation. In a multi-layered CBS, the water is initially stored in the upper finer layer and, if breakthrough occurs from this finer layer into the underlying coarser layer and the next finer layer, the water starts being stored in the underlying finer layer and so on. Therefore, compared to a single CBS of the same total thickness, where most of the water is stored next

to the interface with the bottom coarser layer, a higher amount of water is in general stored in the upper part of a multi-layered CBS. This is expected to mean that the soil surface maintains lower values of suction for longer time and, consequently, a higher amount of evaporation will occur. This expected behaviour should be verified with numerical simulations and validated against experimental tests.

Similar to what was done for the water storage capacity of horizontal multi-layered CBSs, it would be interesting to develop a simplified method for the estimation of the lateral water diversion capacity of sloping multi-layered CBSs. An approach similar to that used by Parent and Cabral [150] (see Section 2.3.4) for the estimation of the diversion capacity of single CBSs could be adopted for multi-layered CBSs. The approach of Parent and Cabral [150] consists of the calculation of the lateral water diversion capacity of a single CBS starting from the knowledge of a simplified suction profile at breakthrough. In a similar manner, a schematic suction profile at breakthrough for sloping multi-layered CBSs could be developed (similarly to what was done for the simplified suction profile at breakthrough for horizontal multi-layered CBSs) and used for calculation of their water diversion capacity.

9.2.3 Long term application of capillary barrier systems for suction control and slope stability

The numerical analyses regarding the long-term performance of CBSs showed that they can be potentially used for suction control purposes and slope stability in a European climatic context and the roles of different parameters and conditions were analysed (see Chapter 8). However, some aspects must still be studied prior to extensive application in the construction field.

Durability is typically recognised as an advantage of capillary barrier systems. However, an aspect which should be assessed with more attention is the risk of surface erosion. The main cause of surface erosion is generally the generation of surface water runoff, which may transport soil particles. In the cases analysed, the materials of the finer layer were coarse enough not to generate runoff. However, erosion could be also caused by the impact of raindrops on the soil surface. This risk should be analysed and, if it reveals to be a serious problem for the durability of CBSs, potential solutions should be studied, such as the use of a surface protection layer (e.g. a vegetated layer).

The capillary barrier systems analysed in this thesis were bare. Vegetation can be however present on the soil surface and may have a significant impact on the hydro-mechanical behaviour of soils. The growth of vegetation may change the SWRC and SHCC properties of the soil by modifying the void ratio and changing the soil structure. Shear strength typically increases due to the presence of roots. In addition, vegetation affects water extraction from soil. On one hand, it reduces the amount of evaporation by covering the soil surface exposed to the atmosphere. On the other hand, the vegetation is able to extract water from the soil and release it into the atmosphere by transpiration. The relevance of these aspects to capillary barrier systems should be studied.

From the results of preliminary numerical analyses, it was discussed that modelling rainfall by using a daily resolution was more appropriate than using a yearly resolution. This was valid in particular for the CBSs having the finer layer made of fine sand, whose efficiency is limited by the occurrence of extreme rainfall events. The use of time resolutions smaller than daily for the rainfall application were not investigated because of the lack of rainfall data at small time resolution in the particular time periods analysed and because of the high computing time requirements. The effect of the use of smaller time resolutions, e.g. hourly or sub-hourly, should be studied, perhaps focusing on single extreme rainfall events.

All the long-term applications of CBSs analysed were virtual case studies useful to isolate and assess the role of the different parameters considered. At this point, it would be useful to try to assess the application of CBSs on real case studies. For instance, it could be useful to consider a slope which collapsed in the past due to the effect of rainfall, for which data of materials, geometry and weather conditions are available, and to try to reproduce the effect of the application of CBSs on the stability. Moreover, it is important to perform field tests. Field tests on the application of CBSs have been already performed but they usually involved artificial and/or small-sized slopes [168–170]. Field tests should be expanded to the application of CBSs to big natural slopes.

One of the main future challenges is the development of specific design methods for the application of CBSs for suction control. The numerical analyses carried out in this thesis for the study of the long-term application of CBSs can be considered advanced and hence characterised by a degree of complexity often far from that used in engineering practice. In order to make the application of CBSs for suction control more appealing in the construction industry, simple design methods should be developed. The simplification of the design method should involve three aspects: material behaviour, method of analysis and modelling of the weather conditions.

Finally, the suitability of CBSs for other applications in geotechnical engineering should be addressed, for problems where maintaining suction in the ground and using its beneficial effect on shear strength can have an impact on geotechnical design. For instance, CBSs might be potentially constructed around foundations to maintain suction beneath the foundation footprint. In this way, consideration of the effect of suction on shear strength might lead to the design of smaller foundations. The construction of a CBS on top of the ground behind a retaining wall might prevent rainwater infiltration into the retained soil, thereby leading to a smaller earth pressure on the retaining wall and hence to a reduction of the required size of the wall.

References

[1] Pachauri, R. K., Allen, M. R., Barros, V. R., Broome, J., Cramer, W., Christ, R., Church, J. A., Clarke, L., Dahe, Q., Dasgupta, P., Dubash, N. K., Edenhofer, O., Elgizouli, I., Field, C. B., Forster, P., Friedlingstein, P., Fuglestvedt, J., Gomez-Echeverri, L., Hallegatte, S., Hegerl, G., Howden, M., Jiang, K., Jimenez Cisneroz, B., Kattsov, V., Lee, H., Mach, K. J., Marotzke, J., Mastrandrea, M. D., Meyer, L., Minx, J., Mulugetta, Y., O'Brien, K., Oppenheimer, M., Pereira, J. J., Pichs-Madruga, R., Plattner, G.-K., Pörtner, H.-O., Power, S. B., Preston, B., Ravindranath, N. H., Reisinger, A., Riahi, K., Rusticucci, M., Scholes, R., Seyboth, K., Sokona, Y., Stavins, R., Stocker, T. F., Tschakert, P., van Vuuren, D., and van Ypserle, J.-P. *Climate Change 2014: Synthesis Report. Contribution of Working Groups I, II and III to the Fifth Assessment Report of the Intergovernmental Panel on Climate Change*. IPCC, Geneva, Switzerland, 2014.

[2] van Aalst, M. K. The impacts of climate change on the risk of natural disasters. *Disasters*, 30(1):5–18, 2006.

[3] Trenberth, K. E. Changes in precipitation with climate change. *Climate Research*, 47 (1-2):123–138, 2011.

[4] Rodhe, H. A comparison of the contribution of various gases to the greenhouse effect. *Science*, 248(4960):1217–1219, 1990.

[5] US Department of Commerce, NOAA. ESRL Global Monitoring Division - Global Greenhouse Gas Reference Network. `https://www.esrl.noaa.gov/gmd/ccgg/trends/mlo.html`, Last accessed on 2019-09-16.

[6] Goddard Institute for Space Studies (GISS) at The National Aeronautics and Space Administration (NASA). Global Land-Ocean Temperature Index. `https://climate.nasa.gov/vital-signs/global-temperature`, Last accessed on 2019-09-16.

[7] United States Geological Survey (USGS). Cement Statistics and Information. `https://www.usgs.gov/centers/nmic/cement-statistics-and-information`, Last accessed on 2019-09-16.

[8] Chang, I., Lee, M., and Cho, G.-C. Global CO_2 Emission-Related Geotechnical Engineering Hazards and the Mission for Sustainable Geotechnical Engineering. *Energies*, 12(13), 2019.

[9] Zornberg, J. G., LaFountain, L., and Caldwell, J. A. Analysis and design of evapotranspirative cover for hazardous waste landfill. *Journal of Geotechnical and Geoenvironmental Engineering*, 129(5):427–438, 2003.

[10] Waugh, W. J., Petersen, K. L., Link, S. O., Bjornstad, B. N., and Gee, G. W. Natural analogs of the long-term performance of engineered covers. *In-situ remediation: Scientific basis for current and future technologies. Part 1*, 1994.

[11] Albright, W. H., Benson, C. H., Gee, G. W., Abichou, T., Tyler, S. W., and Rock, S. A. Field performance of three compacted clay landfill covers. *Vadose Zone Journal*, 5(4): 1157–1171, 2006.

[12] Dwyer, S. F. Alternaltive landfill covers pass the test. *Civil engineering*, 68(9):50, 1998.

[13] Benson, C. H., Daniel, D. E., and Boutwell, G. P. Field performance of compacted clay liners. *Journal of Geotechnical and Geoenvironmental Engineering*, 125(5):390–403, 1999.

[14] Suter, G. W., Luxmoore, R. J., and Smith, E. D. Compacted soil barriers at abandoned landfill sites are likely to fail in the long term. *Journal of Environmental Quality*, 22 (2):217–226, 1993.

[15] Kleppe, J. H. and Olson, R. E. Desiccation cracking of soil barriers. In *Hydraulic barriers in soil and rock*. ASTM International, 1985.

[16] Benson, C. H. and Othman, M. A. Hydraulic conductivity of compacted clay frozen and thawed in situ. *Journal of Geotechnical Engineering*, 119(2):276–294, 1993.

[17] Benson, C. H., Chamberlain, E. J., Erickson, A. E., and Wang, X. Assessing frost damage in compacted clay liners. *Geotechnical Testing Journal*, 18(3):324–333, 1995.

[18] Albrecht, B. A. and Benson, C. H. Effect of desiccation on compacted natural clays. *Journal of Geotechnical and Geoenvironmental Engineering*, 127(1):67–75, 2001.

[19] Rowe, R. K. Long-term performance of contaminant barrier systems. *Géotechnique*, 55(9):631–678, 2005.

[20] Bouazza, A. Geosynthetic clay liners. *Geotextiles and Geomembranes*, 20(1):3–17, 2002.

[21] Zornberg, J. G., Bouazza, A., and McCartney, J. S. Geosynthetic capillary barriers: current state of knowledge. *Geosynthetics International*, 17(5):273–300, 2010.

[22] Shackelford, C. D., Chang, C. K., and Chiu, T. F. The capillary barrier effect in unsaturated flow through soil barriers. In *1st ICEG Conference, Edmonton, CA*, pages 789–793, 1994.

[23] Stormont, J. C. and Anderson, C. E. Capillary barrier effect from underlying coarser soil layer. *Journal of Geotechnical and Geoenvironmental Engineering*, 125(8):641–648, 1999.

[24] Müller, W. W. and Saathoff, F. Geosynthetics in geoenvironmental engineering. *Science and technology of advanced materials*, 16(3):034605, 2015.

[25] Haiderand, N. and Karlsson, S. Loss of Chimassorb 944 from LDPE and identification of additive degradation products after exposure to water, air and compost. *Polymer degradation and stability*, 74(1):103–112, 2001.

[26] Beißmann, S., Stiftinger, M., Grabmayer, K., Wallner, G., Nitsche, D., and Buchberger, W. Monitoring the degradation of stabilization systems in polypropylene during accelerated aging tests by liquid chromatography combined with atmospheric pressure chemical ionization mass spectrometry. *Polymer degradation and stability*, 98(9): 1655–1661, 2013.

[27] Harnas, F. R., Rahardjo, H., Leong, E. C., and Wang, J. Y. Experimental study on dual capillary barrier using recycled asphalt pavement materials. *Canadian Geotechnical Journal*, 51(10):1165–1177, 2014.

[28] Henken-Mellies, W. U. and Schweizer, A. Long-term performance of landfill covers-results of lysimeter test fields in Bavaria (Germany). *Waste Management & Research*, 29(1):59–68, 2011.

[29] Morris, C. E. and Stormont, J. C. Evaluation of numerical simulations of capillary barrier field tests. *Geotechnical & Geological Engineering*, 16(3):201–213, 1998.

[30] Zhang, Z. F. Evaluating the long-term hydrology of an evapotranspiration-capillary barrier with a 1000 year design life. *Water Resources Research*, 52(6):4883–4904, 2016.

[31] Fredlund, D. G. and Rahardjo, H. *Soil mechanics for unsaturated soils*. John Wiley & Sons, 1993.

[32] Krahn, J. and Fredlund, D. G. On total, matric and osmotic suction. *Soil Science*, 114 (5):339–348, 1972.

[33] Aitchison, G. D. Engineering concepts of moisture equilibria and moisture changes in soils. In *in Moisture Equilibria and Moisture Changes in Soils Beneath Covered Areas, A Symposium-in-print (Australia), Butterworths*, pages 7–21, 1964.

[34] Siddiqua, S., Blatz, J., and Siemens, G. Evaluation of the impact of pore fluid chemistry on the hydromechanical behaviour of clay-based sealing materials. *Canadian Geotechnical Journal*, 48(2):199–213, 2011.

[35] Young, T. An essay on the cohesion of fluids. *Philosophical transactions of the royal society of London*, (95):65–87, 1805.

[36] Laplace, P. Supplement to the tenth edition. *Méchanique céleste*, 10:1985–1990, 1806.

[37] Kaye, G. W. C. and Laby, T. H. *Tables of physical and chemical constants and some mathematical functions*. Longmans, Green and Company, 1911.

[38] Henry, W. Experiments on the quantity of gases absorbed by water, at different temperatures, and under different pressures. *Philosophical Transactions of the Royal Society of London*, (93):29–274, 1803.

[39] Hillel, D. and Hatfield, J. L. *Encyclopedia of Soils in the Environment*, volume 3. Elsevier Amsterdam, 2005.

[40] Crawford, C. B. and Quinn, B. The interactions of microplastics and chemical pollutants. In *Microplastic Pollutants*, pages 131–157. Elsevier Science, 2017.

[41] Haines, W. B. Studies in the physical properties of soils: II. A note on the cohesion developed by capillary forces in an ideal soil. *The Journal of Agricultural Science*, 15 (4):529–535, 1925.

[42] Fisher, R. A. On the capillary forces in an ideal soil; correction of formulae given by WB Haines. *The Journal of Agricultural Science*, 16(3):492–505, 1926.

[43] Brunauer, S., Emmett, P. H., and Teller, E. Adsorption of gases in multimolecular layers. *Journal of the American chemical society*, 60(2):309–319, 1938.

[44] Derjaguin, B. V., Churaev, N. V., Muller, V. M., and Kisin, V. I. *Surface forces*. Springer, 1987.

[45] Derjaguin, B. V. and Churaev, N. V. Structural component of disjoining pressure. *Journal of Colloid and Interface Science*, 49(2):249–255, 1974.

[46] Langmuir, I. Repulsive forces between charged surfaces in water, and the cause of the Jones-Ray effect. *Science*, 88(2288):430–432, 1938.

[47] Israelachvili, J. N. *Intermolecular and surface forces*. Academic press, 2015.

[48] Tuller, M. and Or, D. Water films and scaling of soil characteristic curves at low water contents. *Water Resources Research*, 41(9), 2005.

[49] Lebeau, M. and Konrad, J.-M. A new capillary and thin film flow model for predicting the hydraulic conductivity of unsaturated porous media. *Water Resources Research*, 46 (12), 2010.

[50] Haines, W. B. Studies in the physical properties of soil. V. The hysteresis effect in capillary properties, and the modes of moisture distribution associated therewith. *The Journal of Agricultural Science*, 20(1):97–116, 1930.

[51] Likos, W. J., Lu, N., and Godt, J. W. Hysteresis and uncertainty in soil water-retention curve parameters. *Journal of Geotechnical and Geoenvironmental Engineering*, 140 (4):04013050, 2013.

[52] Klausner, Y. *Fundamentals of continuum mechanics of soils*. Springer Science & Business Media, 2012.

[53] Lourenco, S., Gallipoli, D., Augarde, C. E., Toll, D. G., Fisher, P. C., and Congreve, A. Formation and evolution of water menisci in unsaturated granular media. *Géotechnique*, 62(3):193–199, 2012.

[54] Peck, A. J. Change of moisture tension with temperature and air pressure: Theoretical. *Soil Science*, 89(6):303–310, 1960.

[55] Poulovassilis, A. The effect of the entrapped air on the hysteresis curves of a porous body and on its hydraulic conductivity. *Soil Science*, 109(3):154–162, 1970.

[56] Stonestrom, D. A. and Rubin, J. Water content dependence of trapped air in two soils. *Water Resources Research*, 25(9):1947–1958, 1989.

[57] Williams, P. J. Movement of air through water in partly saturated soils. *Nature*, 212 (5069):1463, 1966.

[58] Gallipoli, D., Wheeler, S., and Karstunen, M. Modelling the variation of degree of saturation in a deformable unsaturated soil. *Géotechnique*, 53(1):105–112, 2003.

[59] Chapuis, R. P. and Aubertin, M. On the use of the Kozeny Carman equation to predict the hydraulic conductivity of soils. *Canadian Geotechnical Journal*, 40(3):616–628, 2003.

[60] Richards, L. A. Capillary conduction of liquids through porous mediums. *Physics*, 1 (5):318–333, 1931.

[61] Lu, N. and Likos, W. J. Suction stress characteristic curve for unsaturated soil. *Journal of Geotechnical and Geoenvironmental Engineering*, 132(2):131–142, 2006.

[62] Wheeler, S. J., Sharma, R. S., and Buisson, M. S. R. Coupling of hydraulic hysteresis and stress–strain behaviour in unsaturated soils. *Géotechnique*, 53(1):41–54, 2003.

[63] Gallipoli, D., Gens, A., Sharma, R., and Vaunat, J. An elasto-plastic model for unsaturated soil incorporating the effects of suction and degree of saturation on mechanical behaviour. *Géotechnique*, 53(1):123–136, 2003.

[64] Bishop, A. W. The principle of effective stress. *Teknisk ukeblad*, 39:859–863, 1959.

[65] Jennings, J. E. B. and Burland, J. B. Limitations to the use of effective stresses in partly saturated soils. *Géotechnique*, 12(2):125–144, 1962.

[66] Wheeler, S. J. and Sivakumar, V. An elasto-plastic critical state framework for unsaturated soil. *Géotechnique*, 45(1):35–53, 1995.

[67] Bishop, A. W. and Blight, G. E. Some aspects of effective stress in saturated and partly saturated soils. *Géotechnique*, 13(3):177–197, 1963.

[68] Gens, A., Sánchez, M., and Sheng, D. On constitutive modelling of unsaturated soils. *Acta Geotechnica*, 1(3):137, 2006.

[69] Alonso, E. E., Gens, A., and Josa, A. A constitutive model for partially saturated soils. *Géotechnique*, 40(3):405–430, 1990.

[70] Chiu, C. F. and Ng, C. W. W. A state-dependent elasto-plastic model for saturated and unsaturated soils. *Géotechnique*, 53(9):809–829, 2003.

[71] Sheng, D., Fredlund, D. G., and Gens, A. A new modelling approach for unsaturated soils using independent stress variables. *Canadian Geotechnical Journal*, 45(4):511–534, 2008.

[72] Khalili, N., Geiser, F., and Blight, G. E. Effective stress in unsaturated soils: Review with new evidence. *International journal of Geomechanics*, 4(2):115–126, 2004.

[73] Nuth, M. and Laloui, L. Effective stress concept in unsaturated soils: Clarification and validation of a unified framework. *International journal for numerical and analytical methods in Geomechanics*, 32(7):771–801, 2008.

[74] Fredlund, D. G., Morgenstern, N. R., and Widger, R. A. The shear strength of unsaturated soils. *Canadian Geotechnical Journal*, 15(3):313–321, 1978.

[75] Escario, V. and Saez, J. The shear strength of partly saturated soils. *Géotechnique*, 36 (3):453–456, 1986.

[76] Gan, J. K. M., Fredlund, D. G., and Rahardjo, H. Determination of the shear strength parameters of an unsaturated soil using the direct shear test. *Canadian Geotechnical Journal*, 25(3):500–510, 1988.

[77] Öberg, A. L. and Sällfors, G. Determination of shear strength parameters of unsaturated silts and sands based on the water retention curve. *Geotechnical Testing Journal*, 20 (1):40–48, 1997.

[78] Khalili, N. and Khabbaz, M. H. A unique relationship of chi for the determination of the shear strength of unsaturated soils. *Géotechnique*, 48(5), 1998.

[79] Tarantino, A. and Tombolato, S. Coupling of hydraulic and mechanical behaviour in unsaturated compacted clay. *Géotechnique*, 55(4):307–317, 2005.

[80] Gallipoli, D., Gens, A., Chen, G., and D'Onza, F. Modelling unsaturated soil behaviour during normal consolidation and at critical state. *Computers and Geotechnics*, 35(6): 825–834, 2008.

[81] Brooks, R. H. and Corey, A. T. Hydraulic properties of porous media. *Hydrology Papers, Colorado State University*, 24:37, 1964.

[82] van Genuchten, M. T. A closed-form equation for predicting the hydraulic conductivity of unsaturated soils 1. *Soil science society of America journal*, 44(5):892–898, 1980.

[83] Kosugi, K. Lognormal distribution model for unsaturated soil hydraulic properties. *Water Resources Research*, 32(9):2697–2703, 1996.

[84] Campbell, G. S. and Shiozawa, S. Prediction of hydraulic properties of soils using particle-size distribution and bulk density data. *Indirect methods for estimating the hydraulic properties of unsaturated soils*, pages 317–328, 1992.

[85] Richards, B. G. Measurement of free energy of soil moisture by the psychrometric technique, using thermistors. In *in Moisture Equilibria and Moisture Changes in Soils Beneath Covered Areas, A Symposium-in-print (Australia), Butterworths*, pages 35–46, 1965.

[86] Fredlund, D. G. and Xing, A. Equations for the soil-water characteristic curve. *Canadian Geotechnical Journal*, 31(4):521–532, 1994.

[87] Rossi, C. and Nimmo, J. R. Modeling of soil water retention from saturation to oven dryness. *Water Resources Research*, 30(3):701–708, 1994.

[88] Fayer, M. J. and Simmons, C. S. Modified soil water retention functions for all matric suctions. *Water Resources Research*, 31(5):1233–1238, 1995.

[89] Zhang, Z. F. Soil water retention and relative permeability for conditions from oven-dry to full saturation. *Vadose Zone Journal*, 10(4):1299–1308, 2011.

[90] Khlosi, M., Cornelis, W. M., Gabriels, D., and Sin, G. Simple modification to describe the soil water retention curve between saturation and oven dryness. *Water Resources Research*, 42(11), 2006.

[91] Peters, A. Simple consistent models for water retention and hydraulic conductivity in the complete moisture range. *Water Resources Research*, 49(10):6765–6780, 2013.

[92] Iden, S. C. and Durner, W. Comment on "Simple consistent models for water retention and hydraulic conductivity in the complete moisture range" by A. Peters. *Water Resources Research*, 50(9):7530–7534, 2014.

[93] Peters, A. Reply to comment by S. Iden and W. Durner on "Simple consistent models for water retention and hydraulic conductivity in the complete moisture range". *Water Resources Research*, 50(9):7535–7539, 2014.

[94] Burdine, N. Relative permeability calculations from pore size distribution data. *Journal of Petroleum Technology*, 5(3):71–78, 1953.

[95] Mualem, Y. A new model for predicting the hydraulic conductivity of unsaturated porous media. *Water Resources Research*, 12(3):513–522, 1976.

[96] Tuller, M. and Or, D. Hydraulic conductivity of variably saturated porous media: Film and corner flow in angular pore space. *Water Resources Research*, 37(5):1257–1276, 2001.

[97] Peters, A. and Durner, W. A simple model for describing hydraulic conductivity in unsaturated porous media accounting for film and capillary flow. *Water Resources Research*, 44(11), 2008.

[98] Tokunaga, T. K. Hydraulic properties of adsorbed water films in unsaturated porous media. *Water Resources Research*, 45(6), 2009.

[99] Pham, H. Q., Fredlund, D. G., and Barbour, S. L. A study of hysteresis models for soil-water characteristic curves. *Canadian Geotechnical Journal*, 42(6):1548–1568, 2005.

[100] Néel, L. Théories des lois d'aimantation de Lord Rayleigh, 1. *Cahiers de physique*, 12: 1–20, 1942.

[101] Néel, L. Théorie des lois d'aimantation de Lord Rayleigh, 2. *Cahiers de physique*, 13 (861):18–30, 1943.

[102] Everett, D. H. A general approach to hysteresis. Part 4. An alternative formulation of the domain model. *Transactions of the Faraday Society*, 51:1551–1557, 1955.

[103] Poulovassilis, A. Hysteresis of pore water, an application of the concept of independent domains. *Soil Science*, 93(6):405–412, 1962.

[104] Philip, J. R. Similarity hypothesis for capillary hysteresis in porous materials. *Journal of geophysical research*, 69(8):1553–1562, 1964.

[105] Mualem, Y. Modified approach to capillary hysteresis based on a similarity hypothesis. *Water Resources Research*, 9(5):1324–1331, 1973.

[106] Mualem, Y. A conceptual model of hysteresis. *Water Resources Research*, 10(3): 514–520, 1974.

[107] Mualem, Y. Extension of the similarity hypothesis used for modeling the soil water characteristics. *Water Resources Research*, 13(4):773–780, 1977.

[108] Mualem, Y. Prediction of the soil boundary wetting curve. *Soil Science*, 137(6): 379–390, 1984.

[109] Topp, G. C. Soil-water hysteresis: the domain theory extended to pore interaction conditions 1. *Soil Science Society of America Journal*, 35(2):219–225, 1971.

[110] Poulovassilis, A. and Childs, E. C. The hysteresis of pore water: the non-independence of domains. *Soil Science*, 112(5):301–312, 1971.

[111] Mualem, Y. A modified dependent-domain theory of hysteresis. *Soil Science*, 137(5): 283–291, 1984.

[112] Pham, H. Q. An engineering model of hysteresis for soil-water characteristic curves. Master's thesis, University of Saskatchewan, 2001.

[113] Hanks, R. J., Klute, A., and Bresler, E. A numeric method for estimating infiltration, redistribution, drainage, and evaporation of water from soil. *Water Resources Research*, 5(5):1064–1069, 1969.

[114] Khalili, N., Habte, M. A., and Zargarbashi, S. A fully coupled flow deformation model for cyclic analysis of unsaturated soils including hydraulic and mechanical hystereses. *Computers and Geotechnics*, 35(6):872–889, 2008.

[115] Nuth, M. and Laloui, L. Advances in modelling hysteretic water retention curve in deformable soils. *Computers and Geotechnics*, 35(6):835–844, 2008.

[116] Dane, J. H. and Wierenga, P. J. Effect of hysteresis on the prediction of infiltration, redistribution and drainage of water in a layered soil. *Journal of Hydrology*, 25(3-4): 229–242, 1975.

[117] Jaynes, D. Comparison of soil-water hysteresis models. *Journal of Hydrology*, 75(1-4): 287–299, 1984.

[118] Li, X. Modelling of hysteresis response for arbitrary wetting/drying paths. *Computers and Geotechnics*, 32(2):133–137, 2005.

[119] Zhou, A.-N., Sheng, D., Sloan, S. W., and Gens, A. Interpretation of unsaturated soil behaviour in the stress–saturation space, I: volume change and water retention behaviour. *Computers and Geotechnics*, 43:178–187, 2012.

[120] Gallipoli, D., Bruno, A. W., D'onza, F., and Mancuso, C. A bounding surface hysteretic water retention model for deformable soils. *Géotechnique*, 65(10):793–804, 2015.

[121] Kool, J. B. and Parker, J. C. Development and evaluation of closed-form expressions for hysteretic soil hydraulic properties. *Water Resources Research*, 23(1):105–114, 1987.

[122] Nimmo, J. R. Semiempirical model of soil water hysteresis. *Soil Science Society of America Journal*, 56(6):1723–1730, 1992.

[123] Scott, P. S., Farquhar, G. J., and Kouwen, N. Hysteretic effects on net infiltration. In *Advances in infiltration*, pages 163–170. American Society of Agricultural Engineers, St. Joseph, Mich., 1983.

[124] Gardner, W. R. Some steady-state solutions of the unsaturated moisture flow equation with application to evaporation from a water table. *Soil science*, 85(4):228–232, 1958.

[125] Šimůnek, J., van Genuchten, M. T., and Šejna, M. *The HYDRUS-1D software package for simulating the movement of water, heat, and multiple solutes in variably saturated media, Version 4.0, HYDRUS Software Ser. 3*. Department of Environmental Sciences, University of California, Riverside, California, 2008.

[126] Kroes, J. G., van Dam, J., Groenendijk, P., Hendriks, R. F. A., and Jacobs, C. M. J. *SWAP version 3.2. Theory description and user manual*. Alterra, Wageningen, Netherlands, 2009.

[127] Fayer, M. J. *UNSAT-H version 3.0: Unsaturated soil water and heat flow model theory, user manual, and examples*. Pacific Northwest National Lab., Richland, WA (US), 2000.

[128] Klute, A. and Heermann, D. Soil water profile development under a periodic boundary condition. *Soil Science*, 117(5):265–271, 1974.

[129] Parker, J. C. and Lenhard, R. J. A model for hysteretic constitutive relations governing multiphase flow: 1. Saturation-pressure relations. *Water Resources Research*, 23(12): 2187–2196, 1987.

[130] Pedroso, D. M., Sheng, D., and Zhao, J. The concept of reference curves for constitutive modelling in soil mechanics. *Computers and Geotechnics*, 36(1-2):149–165, 2009.

[131] Mualem, Y. Hydraulic conductivity of unsaturated soils: prediction and formulas. *Methods of Soil Analysis: Part 1—Physical and Mineralogical Methods*, pages 799–823, 1986.

[132] Rudiyanto, Sakai, M., van Genuchten, M. T., Alazba, A. A., Setiawan, B. I., and Minasny, B. A complete soil hydraulic model accounting for capillary and adsorptive water retention, capillary and film conductivity, and hysteresis. *Water Resources Research*, 51(11):8757–8772, 2015.

[133] van Geel, P. J. and Sykes, J. F. The importance of fluid entrapment, saturation hysteresis and residual saturations on the distribution of a lighter-than-water non-aqueous phase liquid in a variably saturated sand medium. *Journal of Contaminant Hydrology*, 25 (3-4):249–270, 1997.

[134] Chen, P., Wei, C., and Ma, T. Analytical model of soil-water characteristics considering the effect of air entrapment. *International Journal of Geomechanics*, 15(6):04014102, 2014.

[135] Sharma, R. S. and Mohamed, M. H. A. An experimental investigation of LNAPL migration in an unsaturated/saturated sand. *Engineering Geology*, 70(3-4):305–313, 2003.

[136] Stormont, J. The effectiveness of two capillary barriers on a 10% slope. *Geotechnical & Geological Engineering*, 14(4):243–267, 1996.

[137] Zhang, L. L., Fredlund, D. G., Zhang, L. M., and Tang, W. H. Numerical study of soil conditions under which matric suction can be maintained. *Canadian Geotechnical Journal*, 41(4):569–582, 2004.

[138] Yang, H., Rahardjo, H., and Leong, E.-C. Behavior of unsaturated layered soil columns during infiltration. *Journal of Hydrologic Engineering*, 11(4):329–337, 2006.

[139] Smith, P. G. C., Potts, D. M., and Addenbrooke, T. I. A precipitation boundary condition for finite element analysis. In *Proceedings of the 1st European Conference on Unsaturated Soils*, volume 773, page 778, 2008.

[140] Benson, C., Abichou, T., Albright, W., Gee, G., and Roesler, A. Field evaluation of alternative earthen final covers. *International Journal of Phytoremediation*, 3(1): 105–127, 2001.

[141] Stormont, J. C. and Morris, C. E. Method to estimate water storage capacity of capillary barriers. *Journal of Geotechnical and Geoenvironmental Engineering*, 124(4):297–302, 1998.

[142] Baker, R. S. and Hillel, D. Laboratory tests of a theory of fingering during infiltration into layered soils. *Soil Science Society of America Journal*, 54(1):20–30, 1990.

[143] Yang, H., Rahardjo, H., Leong, E. C., and Fredlund, D. G. A study of infiltration on three sand capillary barriers. *Canadian Geotechnical Journal*, 41(4):629–643, 2004.

[144] Khire, M. V., Benson, C. H., and Bosscher, P. J. Capillary barriers: Design variables and water balance. *Journal of Geotechnical and Geoenvironmental Engineering*, 126 (8):695–708, 2000.

[145] Yang, H., Rahardjo, H., Wibawa, B., and Leong, E.-C. A soil column apparatus for laboratory infiltration study. *Geotechnical Testing Journal*, 27(4):347–355, 2004.

[146] Rahardjo, H., Tami, D., and Leong, E. C. Effectiveness of sloping capillary barriers under high precipitation rates. In *Proc., 2nd Int. Conf. on Problematic Soils*, pages 39–54, 2006.

[147] Barbour, S. L. and Yanful, E. K. A column study of static nonequilibrium fluid pressures in sand during prolonged drainage. *Canadian Geotechnical Journal*, 31(2): 299–303, 1994.

[148] Ross, B. The diversion capacity of capillary barriers. *Water Resources Research*, 26 (10):2625–2629, 1990.

[149] Pease, R. E. and Stormont, J. C. Effectiveness of sloping capillary barriers under high precipitation rates. In *Joint Conference on the Environment*, 1996.

[150] Parent, S.-É. and Cabral, A. Design of inclined covers with capillary barrier effect. *Geotechnical & Geological Engineering*, 24(3):689–710, 2006.

[151] Steenhuis, T. S., Parlange, J.-Y., and Kung, K.-J. S. Comment on "The diversion capacity of capillary barriers" by Benjamin Ross. *Water Resources Research*, 27(8): 2155–2156, 1991.

[152] Stormont, J. C. The effect of constant anisotropy on capillary barrier performance. *Water Resources Research*, 31(3):783–785, 1995.

[153] Oldenburg, C. M. and Pruess, K. On numerical modeling of capillary barriers. *Water Resources Research*, 29(4):1045–1056, 1993.

[154] Webb, S. W. Generalization of ross' tilted capillary barrier diversion formula for different two-phase characteristic curves. *Water Resources Research*, 33(8):1855–1859, 1997.

[155] Abdolahzadeh, A. M., Lacroix Vachon, B., and Cabral, A. R. Evaluation of the effectiveness of a cover with capillary barrier effect to control percolation into a waste disposal facility. *Canadian Geotechnical Journal*, 48(7):996–1009, 2011.

[156] Zhan, T. L. T., Li, H., Jia, G. W., Chen, Y. M., and Fredlund, D. G. Physical and numerical study of lateral diversion by three-layer inclined capillary barrier covers under humid climatic conditions. *Canadian Geotechnical Journal*, 51(12):1438–1448, 2014.

[157] Lacroix Vachon, B., Abdolahzadeh, A. M., and Cabral, A. R. Predicting the diversion length of capillary barriers using steady state and transient state numerical modeling: case study of the Saint-Tite-des-Caps landfill final cover. *Canadian Geotechnical Journal*, 52(12):2141–2148, 2015.

[158] Walter, M. T., Kim, J.-S., Steenhuis, T. S., Parlange, J.-Y., Heilig, A., Braddock, R. D., Selker, J. S., and Boll, J. Funneled flow mechanisms in a sloping layered soil. *Water Resources Research*, 36(4):841–849, 2000.

[159] Kämpf, M. and Montenegro, H. On the performance of capillary barriers as landfill cover. *Hydrology and Earth System Sciences*, 1(4):925–930, 1997.

[160] Morris, C. E. and Stormont, J. C. Parametric study of unsaturated drainage layers in a capillary barrier. *Journal of Geotechnical and Geoenvironmental Engineering*, 125 (12):1057–1065, 1999.

[161] Stormont, J. C. and Morris, C. E. Unsaturated drainage layers for diversion of infiltrating water. *Journal of irrigation and drainage engineering*, 123(5):364–366, 1997.

[162] Ng, C. W. W., Coo, J. L., Chen, Z. K., and Chen, R. Water infiltration into a new three-layer landfill cover system. *Journal of Environmental Engineering*, 142(5):04016007, 2016.

[163] Ng, C. W. W., Liu, J., Chen, R., and Coo, J. L. Numerical parametric study of an alternative three-layer capillary barrier cover system. *Environmental earth sciences*, 74 (5):4419–4429, 2015.

[164] Ng, C. W. W., Liu, J., Chen, R., and Xu, J. Physical and numerical modeling of an inclined three-layer (silt/gravelly sand/clay) capillary barrier cover system under extreme rainfall. *Waste Management*, 38:210–221, 2015.

[165] Harnas, F. R., Rahardjo, H., Leong, E. C., and Wang, J. Y. Physical model for the investigation of capillary-barrier performance made using recycled asphalt. *Geotechnical Testing Journal*, 39(6):977–990, 2016.

[166] Zhang, Q., Werner, A. D., Aviyanto, R. F., and Hutson, J. L. Influence of soil moisture hysteresis on the functioning of capillary barriers. *Hydrological Processes: An International Journal*, 23(9):1369–1375, 2009.

[167] Rahardjo, H., Satyanaga, A., and Leong, E. C. Unsaturated soil mechanics for slope stabilization. In *Proceedings of 5th Asia–Pacific conference on unsaturated soils*, page 103–117, 2011.

[168] Rahardjo, H., Santoso, V. A., Leong, E. C., Ng, Y. S., Tam, C. P. H., and Satyanaga, A. Use of recycled crushed concrete and Secudrain in capillary barriers for slope stabilization. *Canadian Geotechnical Journal*, 50(6):662–673, 2013.

[169] Rahardjo, H., Satyanaga, A., and Leong, E. C. Characteristics of pore-water pressure response in slopes during rainfall. In *Proceedings of 3rd Asian Conference on Unsaturated Soils*, pages 493–498, 2007.

[170] Rahardjo, H., Santoso, V. A., Leong, E. C., Ng, Y. S., and Hua, C. J. Performance of an instrumented slope covered by a capillary barrier system. *Journal of Geotechnical and Geoenvironmental Engineering*, 138(4):481–490, 2011.

[171] Rahardjo, H., Gofar, N., Satyanaga, A., Leong, E. C., Wang, C. L., and Wong, L. H. J. Effect of rainfall infiltration on deformation of geobarrier wall. *Geotechnical and Geological Engineering*, 37(3):1383–1399, 2019.

[172] Matsuoka, H. and Liu, S. *A new earth reinforcement method using soilbags*. CRC Press, 2005.

[173] Rahardjo, H., Satyanaga, A., Harnas, F., and Leong, E. C. Use of dual capillary barrier as cover system for a sanitary landfill in singapore. *Indian Geotechnical Journal*, 46 (3):228–238, 2016.

[174] Zhang, W., Sun, C., and Qiu, Q. Characterizing of a capillary barrier evapotranspirative cover under high precipitation conditions. *Environmental Earth Sciences*, 75(6):513, 2016.

[175] Blight, G. E. Interactions between the atmosphere and the earth. *Géotechnique*, 47(4): 715–767, 1997.

[176] Fredlund, D., Rahardjo, H., and Fredlund, M. *Unsaturated Soil Mechanics in Engineering Practice*. John Wiley & Sons, New York, United States of America, 2012.

[177] Elia, G., Cotecchia, F., Pedone, G., Vaunat, J., Vardon, P. J., Pereira, C., Springman, S. M., Rouainia, M., van Esch, J., Koda, E., et al. Numerical modelling of slope–vegetation–atmosphere interaction: an overview. *Quarterly Journal of Engineering Geology and Hydrogeology*, 50(3):249–270, 2017.

[178] Brutsaert, W. Evaporation into the atmosphere: Theory, history and applications. 1982.

[179] Penman, H. L. Natural evaporation from open water, bare soil and grass. *Proceedings of the Royal Society of London. Series A. Mathematical and Physical Sciences*, 193 (1032):120–145, 1948.

[180] Monteith, J. L. Evaporation and environment. In *Symposia of the society for experimental biology*, volume 19, pages 205–234. Cambridge University Press (CUP) Cambridge, 1965.

[181] Priestley, C. H. B. and Taylor, R. J. On the assessment of surface heat flux and evaporation using large-scale parameters. *Monthly weather review*, 100(2):81–92, 1972.

[182] Thornthwaite, C. W. An approach toward a rational classification of climate. *Geographical review*, 38(1):55–94, 1948.

[183] Brutsaert, W. and Stricker, H. An advection-aridity approach to estimate actual regional evapotranspiration. *Water Resources Research*, 15(2):443–450, 1979.

[184] Allen, R. G., Pereira, L. S., Raes, D., Smith, M., et al. Crop evapotranspiration - Guidelines for computing crop water requirements - FAO Irrigation and drainage paper 56. *Fao, Rome*, 300(9):D05109, 1998.

[185] Gens, A. Soil-environment interactions in geotechnical engineering. *Géotechnique*, 60 (1):3, 2010.

[186] Wilson, G. W., Fredlund, D. G., and Barbour, S. L. Coupled soil-atmosphere modelling for soil evaporation. *Canadian Geotechnical Journal*, 31(2):151–161, 1994.

[187] Schneider-Zapp, K., Ippisch, O., and Roth, K. Numerical study of the evaporation process and parameter estimation analysis of an evaporation experiment. *Hydrology and Earth System Sciences*, 14(5):765–781, 2010.

[188] Gran, M., Carrera, J., Olivella, S., and Saaltink, M. W. Modeling evaporation processes in a saline soil from saturation to oven dry conditions. *Hydrology and Earth System Sciences*, 15(7):2077–2089, 2011.

[189] Han, J. and Zhou, Z. Dynamics of soil water evaporation during soil drying: laboratory experiment and numerical analysis. *The Scientific World Journal*, 2013, 2013.

[190] Vanapalli, S. K., Sillers, W. S., and Fredlund, M. D. The meaning and relevance of residual state to unsaturated soils. In *51st Canadian Geotechnical Conference*, pages 4–7, 1998.

[191] Luckner, L., van Genuchten, M. T., and Nielsen, D. R. A consistent set of parametric models for the two-phase flow of immiscible fluids in the subsurface. *Water Resources Research*, 25(10):2187–2193, 1989.

[192] Hillel, D. and Baker, R. S. A descriptive theory of fingering during infiltration into layered soils. *Soil Science*, 146(1):51–56, 1988.

[193] Bouwer, H. Rapid field measurement of air entry value and hydraulic conductivity of soil as significant parameters in flow system analysis. *Water Resources Research*, 2(4): 729–738, 1966.

[194] Schubert, H., Herrmann, W., and Rumpf, H. Deformation behaviour of agglomerates under tensile stress. *Powder technology*, 11(2):121–131, 1975.

[195] Lu, N. and Khorshidi, M. Mechanisms for soil-water retention and hysteresis at high suction range. *Journal of Geotechnical and Geoenvironmental Engineering*, 141(8): 04015032, 2015.

[196] Schelle, H., Heise, L., Jänicke, K., and Durner, W. Water retention characteristics of soils over the whole moisture range: a comparison of laboratory methods. *European journal of soil science*, 64(6):814–821, 2013.

[197] Tami, D., Rahardjo, H., Leong, E.-C., and Fredlund, D. G. Design and laboratory verification of a physical model of sloping capillary barrier. *Canadian Geotechnical Journal*, 41(5):814–830, 2004.

[198] Zhan, T. L. T. and Ng, C. W. W. Analytical analysis of rainfall infiltration mechanism in unsaturated soils. *International Journal of Geomechanics*, 4(4):273–284, 2004.

[199] Kemper, W. D. Movement of water as effected by free energy and pressure gradients: I. Application of classic equations for viscous and diffusive movements to the liquid phase in finely porous media 1. *Soil Science Society of America Journal*, 25(4):255–260, 1961.

[200] Vachaud, G. and Thony, J.-L. Hysteresis during infiltration and redistribution in a soil column at different initial water contents. *Water Resources Research*, 7(1):111–127, 1971.

[201] Mehta, B. K., Shiozawa, S. H. O., and Nakano, M. Hydraulic properties of a sandy soil at low water contents. *Soil science*, 157(4):208–214, 1994.

[202] Akin, I. D. and Likos, W. J. Implications of surface hydration and capillary condensation for strength and stiffness of compacted clay. *Journal of Engineering Mechanics*, 143(8):04017054, 2017.

[203] Vanapalli, S. K., Fredlund, D. G., and Pufahl, D. E. The influence of soil structure and stress history on the soil–water characteristics of a compacted till. *Géotechnique*, 49 (2):143–159, 1999.

[204] Reinson, J. R., Fredlund, D. G., and Wilson, G. W. Unsaturated flow in coarse porous media. *Canadian Geotechnical Journal*, 42(1):252–262, 2005.

[205] Olivella, S., Gens, A., Carrera, J., and Alonso, E. E. Numerical formulation for a simulator (CODE_BRIGHT) for the coupled analysis of saline media. *Engineering computations*, 13(7):87–112, 1996.

[206] Nemes, A. d., Schaap, M. G., Leij, F. J., and Wösten, J. H. M. Description of the unsaturated soil hydraulic database UNSODA version 2.0. *Journal of Hydrology*, 251 (3-4):151–162, 2001.

[207] Mualem, Y. A catalogue of the hydraulic properties of unsaturated soils. 100 pp. *Technion-Israel Inst. of Technol., Haifa, Israel*, 1976.

[208] Sakai, M. and Toride, N. Soil water hydraulic functions for a sandy soil and an aggregated soil. *Journal of the Japanese Society of Soil Physics (Japan)*, 2007.

[209] Gillham, R. W., Klute, A., and Heermann, D. F. Hydraulic properties of a porous medium: Measurement and empirical representation 1. *Soil Science Society of America Journal*, 40(2):203–207, 1976.

[210] Londra, P. A. Simultaneous determination of water retention curve and unsaturated hydraulic conductivity of substrates using a steady-state laboratory method. *HortScience*, 45(7):1106–1112, 2010.

[211] Gallage, C., Kodikara, J., and Uchimura, T. Laboratory measurement of hydraulic conductivity functions of two unsaturated sandy soils during drying and wetting processes. *Soils and Foundations*, 53(3):417–430, 2013.

[212] Topp, G. C. and Miller, E. E. Hysteretic moisture characteristics and hydraulic conductivities for glass-bead media 1. *Soil Science Society of America Journal*, 30(2): 156–162, 1966.

[213] Olivella, S., Carrera, J., Gens, A., and Alonso, E. E. Nonisothermal multiphase flow of brine and gas through saline media. *Transport in porous media*, 15(3):271–293, 1994.

[214] Ribó, R., Pasenau, M., Escolano, E., Ronda, J., Gonzalez, L., and Rosa, E. Gid user manual. *CIMNE, Barcelona*, 1999.

[215] Bear, J. *Dynamics of fluids in porous media*. American Elsevier, New York, 1972.

[216] Olivella, S., Carrera, J., Gens, A., and Alonso, E. E. Porosity variations in saline media caused by temperature gradients coupled to multiphase flow and dissolution/precipitation. *Transport in Porous Media*, 25(1):1–25, 1996.

[217] Laloui, L. and Loria, A. F. R. *Analysis and Design of Energy Geostructures: Theoretical Essentials and Practical Application*. Academic Press, 2019.

[218] Orlander, T., Adamopoulou, E., Asmussen, J. J., Marczyński, A. A., Milsch, H., Pasquinelli, L., and Fabricius, I. L. Thermal conductivity of sandstones from Biot's coefficient. *Geophysics*, 83(5):D173–D185, 2018.

[219] Carrera, J., Alfageme, M., Galarza, G., Medina, A., and De Andres, M. Estudio de la infiltración a través de la cobertera de la FUA. Publicación Técnica núm. 02/92, ENRESA, 1992.

[220] LimitState. *LimitState:GEO Manual VERSION 3.5.d, March 2019 edn*. LimitState Ltd, 2019.

[221] Chen, W.-F. and Scawthorn, C. R. Limit analysis and limit equilibrium solutions in soil mechanics. *Soils and Foundations*, 10(3):13–49, 1970.

[222] Smith, C. C. and Gilbert, M. Application of discontinuity layout optimization to plane plasticity problems. *Proceedings of the Royal Society A: Mathematical, Physical and Engineering Sciences*, 463(2086):2461–2484, 2007.

[223] Smith, C. C. and Gilbert, M. New upper bound solutions for layered soil bearing capacity problems using discontinuity layout optimization. In *10th Australia New Zealand Conference on Geomechanics, Brisbane*, pages 250–255, 2007.

[224] Fischer, U., Dury, O., Flühler, H., and van Genuchten, M. T. Modeling nonwetting-phase relative permeability accounting for a discontinuous nonwetting phase. *Soil Science Society of America Journal*, 61(5):1348–1354, 1997.

[225] Millington, R. J. and Quirk, J. P. Permeability of porous solids. *Transactions of the Faraday Society*, 57:1200–1207, 1961.

[226] Hilf, J. W. *An investigation of pore water pressure in compacted cohesive soils*. PhD thesis, Design and Construction Division, Bureau of Reclamation, United States Department of the Interior, Denver, 1956. Technical Memorandum No. 654.

[227] Richards, L. A. and Fireman, M. Pressure-plate apparatus for measuring moisture sorption and transmission by soils. *Soil Science*, 56(6):395–404, 1943.

[228] Derbyshire Aggregates Ltd. `http://derbyshireaggregates.com/resin-bonded/110-sand-dried-0-1-0-3mm/`, Last accessed on 2020-01-13.

[229] A-Grip Systems Ltd. `https://a-grip.co.uk/product/autumn-gold-1-3mm/`, Last accessed on 2020-01-13.

[230] ASTM International. Standard test methods for particle-size distribution (gradation) of soils using sieve analysis. In *ASTM D6913*. West Conshohocken, PA: American Society for Testing and Materials, 2017.

[231] Sherman, W. C. Filter experiments and design criteria. Technical report, ARMY ENGINEER WATERWAYS EXPERIMENT STATION VICKSBURG MISS, 1953.

[232] ASTM International. Standard test methods for maximum index density and unit weight of soils using a vibratory table. In *ASTM D4253*. West Conshohocken, PA: American Society for Testing and Materials, 2006.

[233] ASTM International. Standard test methods for minimum index density and unit weight of soils and calculation of relative density. In *ASTM D4254*. West Conshohocken, PA: American Society for Testing and Materials, 2006.

[234] ASTM International. Standard test methods for specific gravity of soil solids by water pycnometer. In *ASTM D854-14*. West Conshohocken, PA: American Society for Testing and Materials, 2010.

[235] ASTM International. Standard test method for permeability of granular soils (constant head). In *ASTM D2434-68*. West Conshohocken, PA: American Society for Testing and Materials, 2006.

[236] Dane, J. H., Hopmans, J. W., and Topp, G. C. Hanging water column. In *Methods of soil analysis. Part 4*, pages 680–683. 2002.

[237] Stanier, S. A. and Tarantino, A. An approach for predicting the stability of vertical cuts in cohesionless soils above the water table. *Engineering geology*, 158:98–108, 2013.

[238] METER Group Inc. `https://www.metergroup.com/environment/products/ec-5-soil-moisture-sensor/`, Last accessed on 2020-01-20.

[239] Bogena, H. R., Huisman, J. A., Oberdörster, C., and Vereecken, H. Evaluation of a low-cost soil water content sensor for wireless network applications. *Journal of Hydrology*, 344(1-2):32–42, 2007.

[240] Topp, G. C., Davis, J. L., and Annan, A. P. Electromagnetic determination of soil water content: Measurements in coaxial transmission lines. *Water Resources Research*, 16 (3):574–582, 1980.

[241] Omega Engineering Inc. https://www.omega.co.uk/pptst/PX26.html, Last accessed on 2020-01-20.

[242] National Instruments. https://www.ni.com/en-gb/support/model.usb-6001.html, Last accessed on 2020-01-21.

[243] Johnson, G. W. *LabVIEW graphical programming*. Tata McGraw-Hill Education, 1997.

[244] Soilmoisture Equipment Corp. https://www.soilmoisture.com/POROUS-CERAMIC-PLATE-0.5-DIAM.-1/2-BAR/, Last accessed on 2020-01-22.

[245] Vanapalli, S. K., Nicotera, M. V., and Sharma, R. S. Axis translation and negative water column techniques for suction control. In *Laboratory and field testing of unsaturated soils*, pages 33–48. Springer, 2008.

[246] Swiss Standard SN 670 010b. Characteristic coefficients of soils, association of swiss road and traffic engineers. 1999.

[247] Servizio metereologico Aeronautica Militare. http://www.meteoam.it/, Last accessed on 2018-09-28.

[248] Met Office. https://www.metoffice.gov.uk/, Last accessed on 2018-09-28.